Transactions of the ASME®

Technical Editor,
H. L. JULIEN (1998)
Associate Technical Editors
Advanced Energy Systems
M. J. MORAN (1996)
Fuels and Combustion Technologies
D. W. PACER (1994)
Gas Turbine
E. M. GREITZER (1994)
Internal Combustion Engine
J. A. CATON (1994)
Nuclear Engineering
H. H. CHUNG (1996)
Power
P. H. GILSON (1996)

BOARD ON COMMUNICATIONS
Chairman and Vice-President
R. D. ROCKE

Members-at-Large
T. BARLOW, T. DEAR, L. KEER,
J. KITTO, W. MORGAN, E. M. PATTON,
S. PATULSKI, R. E. REDER,
R. SHAH, A. VAN DER SLUYS,
F. M. WHITE, J. WHITEHEAD

OFFICERS OF THE ASME
President, J. H. FERNANDES
Exec. Director
D. L. BELDEN
Treasurer
R. A. BENNETT

PUBLISHING STAFF
Mng. Dir., Publ.
CHARLES W. BEARDSLEY
Managing Editor,
CORNELIA MONAHAN
Sr. Production Editor,
VALERIE WINTERS
Production Assistant,
MARISOL ANDINO

Transactions of the ASME, Journal of Engineering for Gas Turbines and Power (ISSN 0742-4795) is published quarterly (Jan., Apr., July, Oct.) for $130.00 per year by The American Society of Mechanical Engineers, 345 East 47th Street, New York, NY 10017. Second class postage paid at New York, NY and additional mailing offices. POSTMASTER: Send address changes to Transactions of the ASME, Journal of Engineering for Gas Turbines and Power, c/o THE AMERICAN SOCIETY OF MECHANICAL ENGINEERS, 22 Law Drive, Box 2300, Fairfield, NJ 07007-2300.
CHANGES OF ADDRESS must be received at Society headquarters seven weeks before they are to be effective. Please send old label and new address.
PRICES: To members, $40.00, annually: to nonmembers, $136.00.
Add $24.00 for postage to countries outside the United States and Canada.
STATEMENT from By-Laws. The Society shall not be responsible for statements or opinions advanced in papers or . . . printed in its publications (B 7.1, para. 3).
COPYRIGHT © 1993 by The American Society of Mechanical Engineers. Authorization to photocopy material for internal or personal use under circumstances not falling within the fair use provisions of the Copyright Act is granted by ASME to libraries and other users registered with the Copyright Clearance Center (CCC) Transactional Reporting Service provided that the base fee of $3.00 per article is paid directly to CCC, 27 Congress St., Salem, MA 01970. Request for special permission or bulk copying should be addressed to Reprints/Permission Department.
INDEXED by Applied Mechanics Reviews and Engineering Information, Inc.
Canadian Goods & Services Tax Registration #126148048

Journal of Engineering for Gas Turbines and Power

Published Quarterly by The American Society of Mechanical Engineers
VOLUME 115 • NUMBER 3 • JULY 1993

TECHNICAL PAPERS

433 Influence of Flow Conditions on Deposits From Heated Hydrocarbon Fuels (92-GT-114)
J. S. Chin and A. H. Lefebvre

439 Innovative High-Temperature Aircraft Engine Fuel Nozzle Design (92-GT-132)
R. W. Stickles, W. J. Dodds, T. R. Koblish, J. Sager, and S. Clouser

447 Factors Influencing the Circumferential Liquid Distribution From Pressure-Swirl Atomizers
S. K. Chen, A. H. Lefebvre, and J. Rollbuhler

453 Scaling of the Two-Phase Flow Downstream of a Gas Turbine Combustor Swirl Cup: Part I—Mean Quantities (92-GT-207)
H. Y. Wang, V. G. McDonnell, W. A. Sowa, and G. S. Samuelsen

461 Liquid Sheet Disintegration and Atomization Process on a Simplified Airblast Atomizer (92-GT-107)
G. Lavergne, P. Trichet, P. Hebrard, and Y. Biscos

467 Effects of Variable Liquid Properties on Multicomponent Droplet Vaporization (92-GT-131)
R. Kneer, M. Schneider, B. Noll, and S. Wittig

473 Multijet Annulus/Core-Flow Mixing—Experiments and Calculations (92-GT-111)
S. J. Baker and J. J. McGuirk

480 Studies of Jet Fuel Thermal Stability in a Flowing System (92-GT-106)
S. P. Heneghan, C. R. Martel, T. F. Williams, and D. R. Ballal

486 Effects of Back-Pressure in a Lean Blowout Research Combustor (92-GT-81)
G. J. Sturgess, S. P. Heneghan, M. D. Vangsness, D. R. Ballal, A. L. Lesmerises, and D. Shouse

499 Particle Diagnostics and Turbulence Measurements in a Confined Isothermal Liquid Spray (92-GT-113)
A. Breña de la Rosa, S. V. Sankar, G. Wang, and W. D. Bachalo

507 Direct Measurements of Skin Friction in Supersonic Combustion Flow Fields (92-GT-320)
K. M. Chadwick, D. J. DeTurris, and J. A. Schetz

515 Coherent Anti-Stokes Raman Scattering (CARS) Thermometry in a Model Gas Turbine Can Combustor (92-GT-134)
J. Y. Zhu, T. Tsuruda, W. A. Sowa, and G. S. Samuelsen

522 The Combustion of Droplets Within Gas Turbine Combustors: Some Recent Observations on Combustion Efficiency (92-GT-135)
J. Odgers, D. Kretschmer, and G. F. Pearce

533 Second-Generation Low-Emission Combustors for ABB Gas Turbines: Field Measurements With GT11N-EV (92-GT-322)
M. Aigner and G. Müller

537 Combustion System Performance and Field Test Results of the MS7001F Gas Turbine (92-GT-314)
J. P. Claeys, K. M. Elward, W. J. Mick, and R. A. Symonds

547 Low NO_x Combustor for Automotive Ceramic Gas Turbine—Reliability Assurance (92-GT-109)
H. Kumakura, M. Sasaki, and D. Suzuki

554 Development of a Liquid-Fueled, Lean-Premixed Gas Turbine Combustor (92-GT-112)
L. H. Cowell and K. O. Smith

563 Emissions Reduction by Varying the Swirler Airflow Split in Advanced Gas Turbine Combustors (92-GT-110)
G. J. Micklow, S. Roychoudhury, H. L. Nguyen, and M. C. Cline

570 Modification of Combustor Stoichiometry Distribution for Reduced NO_x Emission From Aircraft Engines (92-GT-108)
G. J. Sturgess, R. G. McKinney, and S. A. Morford

581 Evaluation of Low-NO_x Combustor Concepts for Aeroderivative Gas Turbine Engines (92-GT-133)
J. B. McVey, F. C. Padget, T. J. Rosfjord, A. S. Hu, A. A. Peracchio, B. Schlein, and D. R. Tegel

588 Carbon Monoxide Emissions From Gas Turbines as Influenced by Ambient Temperature and Turbine Load (92-GT-105)
W. S. Y. Hung

594 The Flow Inside a Model Gas Turbine Combustor: Calculations
J. J. McGuirk and J. M. L. M. Palma

603 Three-Dimensional Gas Turbine Combustor Emissions Modeling (92-GT-129)
N. K. Rizk and H. C. Mongia

(Contents continued on page 446)

Downloaded 03 Jun 2010 to 171.66.16.159. Redistribution subject to ASME license or copyright; see http://www.asme.org/terms/Terms_Use.cfm

Contents (continued)

612 **Semianalytical Correlations for NO_x, CO, and UHC Emissions** (92-GT-130)
N. K. Rizk and H. C. Mongia

620 **Comparison of Spectrometric Techniques for the Analysis of Liquid Gas Turbine Fuels** (92-GT-202)
M. Lukas

628 **Coal Gas Cleaning and Purification With Inorganic Membranes** (92-GT-359)
D. E. Fain and G. E. Roettger

634 **Coal Mineral Matter Transformation During Combustion and Its Effects on Gas Turbine Blade Deposition and Erosion**
S. Rajan and J. K. Raghavan

641 **Deposition of Volcanic Materials in the Hot Sections of Two Gas Turbine Engines** (92-GT-219)
J. Kim, M. G. Dunn, A. J. Baran, D. P. Wade, and E. L. Tremba

652 **What Affects the Cost of Hot Gas Filter Stations?** (92-GT-221)
J. F. Zievers, P. Eggerstedt, E. C. Zievers, and D. Nicolai

658 **Development of Hot Gas Cleaning Systems for Advanced, Coal-Based Gas Turbine Cycles** (92-GT-431)
T. E. Lippert, R. A. Newby, M. A. Alvin, D. M. Bachovchin, G. J. Bruck, and E. E. Smeltzer

665 **Ceramic Filters for Hot Gas Cleanup** (92-GT-313)
L. R. White, T. L. Tompkins, K. C. Hsieh, and D. D. Johnson

670 **Utility Perspective of Selecting Air Filter for Simple-Cycle, Heavy-Duty Combustion Turbines** (92-GT-321)
J. W. Lyons and A. Morrison

674 **Performance of Gas Turbine Compressor Cleaners** (92-GT-360)
H. J. Kolkman

ANNOUNCEMENTS

479 **Change of address form for subscribers**

678 **Information for authors**

Downloaded 03 Jun 2010 to 171.66.16.159. Redistribution subject to ASME license or copyright; see http://www.asme.org/terms/Terms_Use.cfm

Influence of Flow Conditions on Deposits From Heated Hydrocarbon Fuels

J. S. Chin
Visiting Professor.

A. H. Lefebvre
Reilly Professor of Combustion Engineering.

Thermal Science and Propulsion Center,
Purdue University,
West Lafayette, IN 47907

The thermal stability characteristics of two liquid hydrocarbon fuels are examined using a single-pass system whereby the fuel under test flows only once through a heated tube which is maintained at constant temperature throughout a test duration of six hours. Deposition rates on the tube walls are measured by weighing the tube before and after each test. The experimental data are used to derive empirical equations for predicting the effects on deposition rates of variation in fuel temperature, wall temperature, and Reynolds number. It is found that deposition rates are enhanced by increases in fuel temperature, wall temperature and flow velocity, and by reductions in tube diameter. Pressure has no effect on deposition rates provided it is high enough to prevent fuel boiling.

Introduction

Right from its inception, the continuing trend in turbojet engine design has been toward higher compression ratios and higher turbine inlet temperatures. These advances have resulted in the fuel becoming subject to a wide range of thermal stresses. Heat must be extracted from lubricating oil, with the fuel providing the heat sink. A further rise in fuel temperature occurs as the fuel flows through the burner feed arm due to the high rate of convective heat transfer from the compressor outlet air. In some fuel nozzle designs, the fuel may experience further additional heating by radiative heat transfer from the combustion gases. The combined effect of these various heat inputs is that by the time the fuel is sprayed into the combustion zone, its temperature is appreciably higher than when it left the fuel tank. Unfortunately, this elevation in fuel temperature stimulates oxidation reactions, which lead to the formation of gums and other insoluble materials (including carbon), which tend to deposit on heat exchanger walls and control surfaces. Deposition within the fuel nozzle is especially harmful because it can distort the fuel spray pattern to such an extent that it causes overheating of liner walls, turbine blades, and nozzle guide vanes.

The deposits formed in fuel nozzles and on other heated surfaces are a manifestation of thermal degradation of the fuel. Fuels that have a high thermal stability also have a low tendency to form deposits. Current aircraft fuels do not present a major problem in this regard, but the situation could worsen appreciably in the future due to anticipated higher fuel temperatures in heat exchangers and fuel nozzles and to the more widespread use of fuels of broader chemical composition. Several different methods have been developed to evaluate fuel thermal stability and the published literature in this field is quite extensive. Useful descriptions of the various experimental techniques employed are contained in the CRC literature survey on the thermal oxidation stability of jet fuel (1979), Taylor (1979), Cohen (1980), Peat (1982), Baker et al. (1983), Roback et al. (1983), TeVelde and Glickstein (1983), TeVelde et al. (1983), Mills and Kendall (1986), Marteney and Spadaccini (1986), and Chin and Lefebvre (1992). None of the experimental methods developed so far is entirely free from defects. Even so, they have provided a considerable body of information on the effects of fuel temperature, wall surface temperature, and fuel composition on deposition rates. In contrast, the fluid dynamic aspects of the thermal stability problem have received comparative neglect. The present work represents an attempt to remedy this deficiency. Evidence is presented to show the important effects of fuel and wall temperatures on deposition rates, but consideration is also given to the effect on deposition rates of variations in flow conditions, notably liquid flow rate, velocity, pressure, and Reynolds number. It is hoped that the results obtained will be of interest and value to the designers of aircraft heat exchangers, fuel control systems, and fuel nozzles.

Apparatus

The apparatus employed in this experimental study on fuel thermal stability is essentially a single-pass system in which the test fuel flows only once through a heated tube, which is maintained at constant temperature throughout the test duration. It is basically the same as the apparatus described in a previous publication by Chin and Lefebvre (1992) except that various minor modifications to the original apparatus have been made as part of a continuing effort to upgrade the facility and thereby improve the accuracy and consistency of the experimental data. The apparatus in its present form is shown schematically in

Contributed by the International Gas Turbine Institute and presented at the 37th International Gas Turbine and Aeroengine Congress and Exposition, Cologne, Germany, June 1–4, 1992. Manuscript received by the International Gas Turbine Institute February 6, 1992. Paper No. 92-GT-114. Associate Technical Editor: L. S. Langston.

Copyright © 1993 by ASME
Downloaded 02 Jun 2010 to 171.66.16.121. Redistribution subject to ASME license or copyright; see http://www.asme.org/terms/Terms_Use.cfm

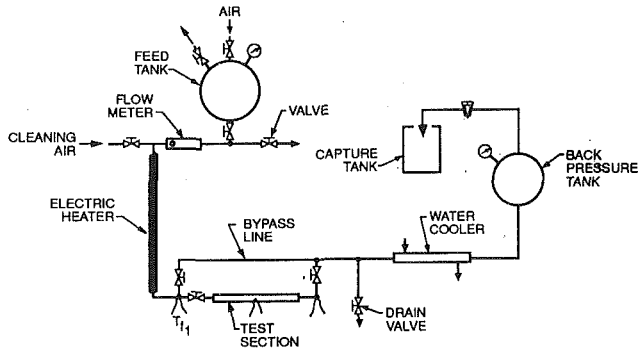

Fig. 1 Schematic diagram of test facility

Fig. 1. The main components are a feed tank that contains the test fuel, a flow meter, a fuel heater, a heated test section, a water cooler, a back-pressure tank, and a drain tank. In operation, the test fuel flow from the storage tank into the electric heater that raises its temperature to the desired value at entry to the test section. The fuel usually experiences a small increase in temperature as it flows through the test section to an extent that depends on the flow rate and the temperature difference between the fuel and the tube wall.

In some experiments the tube wall is maintained at exactly the same temperature as the fuel flowing through it. This is done to eliminate heat transfer between the tube and the fuel so that as the fuel flows through the tube its temperature remains constant. After emerging from the test section, the fuel flows through a water cooler, which reduces its temperature to around 300 K before it flows into the back-pressure tank and out of the system. The fuel pressure within the test section can be varied up to around 4 MPa (580 psia), but most tests are carried out a pressures of 2.5 MPa (363 psia) and below.

The back-pressure tank represents a comparatively recent addition to the test facility. Although its presence does not contribute directly to greater accuracy of the experimental data, it makes a useful indirect contribution in that it improves appreciably the flow stability of the system. Before this addition, the throttle valve that controlled the fuel flow rate was located in a hot fuel section. As the pressure drop across this valve was always extremely high [typically 2.5 MPa (363 psia) at inlet and 0.12 MPa (17 psia) at outlet], this meant that the throttle valve was usually barely "cracked open." As the hot fuel flowed through this very small opening, it tended to form deposits that caused a continuous decline in flow rate that required frequent adjustment of the valve. Fitting the back-pressure tank allowed the throttle valve to be located in a region where fuel temperatures and pressures differentials are both low. The valve now has a much wider opening and deposits no longer form. This improvement in the method of flow control, in conjunction with the large-volume back-pressure tank, has virtually eliminated flow instabilities and flow-rate drift from the system.

The test section, instrumentation, tube preparation, and weighing procedures have been fully described in two previous publications (Chin et al., 1992; Chin and Lefebvre, 1992). The main component of the test section is a thin-walled stainless steel tube of length 152 mm. This tube is clamped between two electrically heated copper segments. Semicircular grooves cut into the two segments provide good thermal contact between the tube and the copper segments when the latter are clamped together. Thermocouples are used to measure tube-wall temperatures at six equispaced intervals along the tube length. Fuel temperatures are measured only at the tube inlet and outlet.

Table 1 Fuel properties

(a) Kinematic viscosity

Fuel Temp., °C	Viscosity, $m^2/s \times 10^{-6}$	
	DF 2	Kerosine
100	1.15	0.79
140	0.78	0.58
170	0.62	0.48
200	0.54	0.41
250	0.40	0.29

(b) Density

Fuel Temp., °C	Density, kg/m^2	
	DF 2	Kerosine
20	840	820
140	740	725
250	630	620

(c) Aromatics content

DF 2	30 - 35 percent
Kerosine	20 - 25 percent

For any given fuel, the fuel pressure and flow rate are set at suitable values and the heaters for the fuel and test section are both switched on. During the fuel heatup period, which is usually less than ten minutes, the flowing fuel bypasses the test section. When the fuel and tube-wall temperature have both attained the desired values, the bypass valves are operated to divert the hot fuel through the test section. At the same time the water supply to the fuel cooler is turned on.

A feedback system between the fuel and tube-wall thermocouples and the fuel and test section heaters, respectively, allows both fuel and tube-wall temperatures to be maintained within 1°C of preset values throughout the test duration. Deposition rates are measured by weighing the tube before and after each test. The deposits usually weigh between 2 and 100 mg depending on the fuel composition and test conditions.

Experience has shown that for good repeatability of results, the fuel preheater should be cleaned after each test run. This is done by supplying electrical power to the preheater so that its inner wall attains a high temperature. At the same time, air is passed through the preheater, where it is heated to a temperature of around 500 K at outlet. This procedure has been found to be very effective in removing all deposits from the preheater wall.

Experimental

The fuels selected for this study are DF 2 and kerosine. The relevant properties of these two fuels are listed in Table 1. The fuels were chosen partly on the basis of low costs, since long test runs call for large amounts of fuel, and also because they encompass the aromatic contents of present and anticipated future aviation fuels.

The flow variables of principal interest for their influence on deposition rates are the pressure, temperature, velocity, and

Nomenclature

d = tube diameter
D.I. = deposit index, $\mu g/cm \cdot kg$
D.R. = deposition rate, $\mu g/cm^2 \cdot h$
$\dot{m}_F$ = mass flow rate of fuel
$\dot{m}_{VF}$ = volumetric flow rate of fuel
Re = Reynolds number = $Ud\rho/\mu$
T_F = fuel temperature, K
T_W = wall temperature, K
U = flow velocity
μ = fuel viscosity
ρ = fuel density

Downloaded 02 Jun 2010 to 171.66.16.121. Redistribution subject to ASME license or copyright; see http://www.asme.org/terms/Terms_Use.cfm

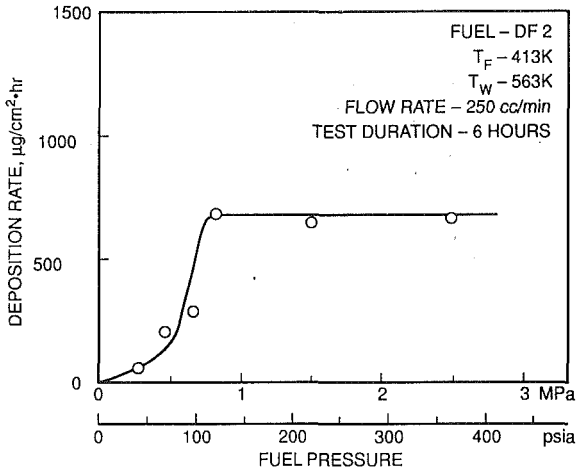

Fig. 2 Influence of pressure on deposition rates

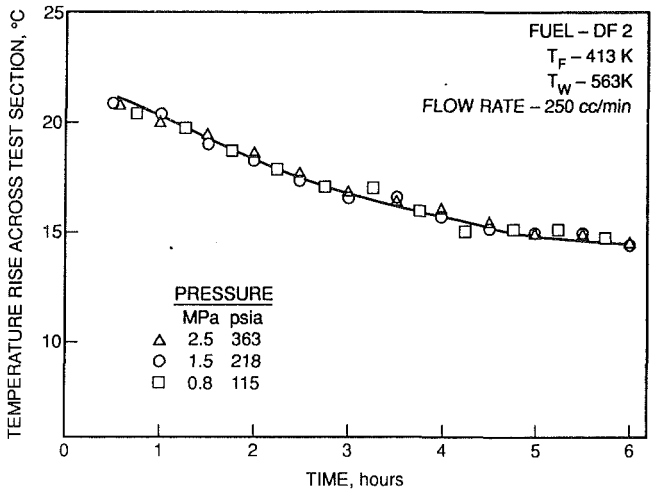

Fig. 3 Influence of deposit thickness on fuel temperature rise

Reynolds number of the flowing fuel. Also of interest is the influence of tubewall temperature, since this affects both the temperature and the velocity profile in the boundary layer adjacent to the tube wall. The separate effects of these various parameters are discussed below in turn.

Pressure. In general, the results contained in the literature show little effect of fuel pressure on deposition rates. Vranos and Marteney (1980) found no effect of pressure on deposition rates for No. 2 home heating oil or for Jet A fuel when the pressure was higher than 1.5 MPa (218 psia). Marteney and Spadaccini (1986) also reported for JP 5 fuel that a wide variation in pressure from 17.2 to 5.5 MPa (250 to 800 psia) had no effect on deposit formation rates. High-pressure deposition tests were also conducted and reported by Roback et al. (1981). The fuel pressures generally exceeded 13.8 MPa (2000 psia). The results showed no significant change in wall temperatures as a consequence of increasing pressure, suggesting that the rate of deposit formation was relatively independent of pressure over the pressure range from 13.8 to 34 MPa (2000 to 4930 psia). However, Watt et al. (1968) reached rather different conclusions. According to these workers, the influence of fuel pressure, while not entirely consistent from fuel to fuel, was to diminish both local and total deposits with increasing pressure.

Some of the results obtained on the effect of pressure using DF 2 as the test fuel are shown in Fig. 2. The data contained in this figure were obtained using a 400 series stainless steel tube of length 152 mm, outer diameter 3.08 mm, and inner diameter 2.59 mm. They show the average rate of deposition in $\mu g/cm^2 \cdot h$ plotted against fuel pressure for a fuel flow rate of 250 cc/min and a test duration of six hours.

It is clear from Fig. 2 that above a certain minimum pressure the deposition rate is independent of fuel pressure. For the DF 2 fuel used in these experiments, this minimum pressure is around 0.8 MPa (115 psia). A limited number of tests carried out on other fuels indicates that the minimum pressure may be higher or lower than 0.8 MPa, depending on the temperature and volatility of the fuel. In general, the minimum pressure above which pressure has no effect on deposition rates decreases with increases in fuel temperature and/or fuel volatility. This suggests that the low deposition rates associated with low fuel pressures may be the results of fuel boiling and the production of fuel vapor. Autoxidation deposit formation rates are lower in the vapor phase than in the liquid phase at the same temperature. Another effect of fuel boiling is to convert the normally smooth flow of fuel through the section into a two-phase, turbulent flow of relatively high velocity. This produces a vigorous scrubbing action at the tube surface, which tends to inhibit deposition and also remove any deposits that might form on the surface despite the adverse conditions. However, it should be noted that measurements of deposition rates for JP 4 and JP 5 fuels made by Szetela (1976) led him to an opposite conclusion. He found deposits to be higher for JP 4, which he attributed to the fact that "boiling increases the deposition tendency." Clearly, the effect of fuel boiling on deposition rates merits further investigation.

Further evidence on the insensitivity of deposition rates to variations in fuel pressure above the critical value is presented in Fig. 3. This figure illustrates the manner in which the temperature rise experienced by the fuel as it flows through the heated tube varies with time. Initially, the tube wall is perfected clean and the fuel temperature rise is relatively high. With the passage of time, the accumulation of deposit on the tube wall creates a thermal barrier between the tube and the flowing fuel, which gradually diminishes the heat flux from the tube to the fuel, thereby causing a continuous decline in the temperature rise of the fuel, as illustrated in Fig. 3. Thus the temperature rise of the fuel provides a useful indication of the amount of deposition on the tube wall. Figure 3 shows that for constant conditions of fuel temperature, wall temperature, and fuel flow rate, pressure has no effect on deposition rates for DF 2 over a pressure range from 0.8 to 2.5 MPa (115 to 363 psia).

Reynolds Number. On aircraft fuel systems, as the fuel flows from the tank and through various engine components into the fuel nozzle, it experiences a variety of flow conditions corresponding to a wide range of Reynolds numbers. It is therefore of some practical interest and importance to examine the impact of variations in this flow parameter on deposition rates. For experimental purposes, Reynolds number can be varied readily by changing one or more of the following:

1 mass flow rate (velocity)
2 tube diameter
3 fuel temperature

Unfortunately, variations in fuel temperature not only serve to change the Reynolds number, they also have a pronounced effect on the auto-oxidation reactions that promote deposition. This leaves mass flow rate and tube diameter as the only two practical options for achieving variations in Reynolds number.

For the results presented in Fig. 4, the variation in Reynolds number was accomplished by varying the fuel flow rate. The four curves shown in this figure correspond to the following conditions:

(*a*) Fuel—DF 2
T_F = 473 K, T_W = 623 K, P = 2.5 MPa
$\dot{m}_{VF}$ = 100–400 cc/min

Downloaded 02 Jun 2010 to 171.66.16.121. Redistribution subject to ASME license or copyright; see http://www.asme.org/terms/Terms_Use.cfm

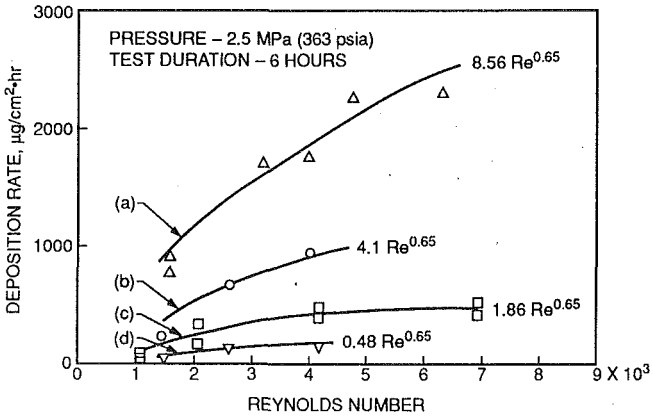

Fig. 4 Influence of Reynolds number on deposition rate

Stainless steel tube, 400 series; i.d. = 2.59 mm, o.d. = 3.08 mm

(*b*) Fuel—DF 2
T_F = 413 K, T_W = 563 K, P = 2.5 MPa
$\dot{m}_{VF}$ = 100–400 cc/min
Stainless steel tube, 400 series; i.d., = 2.59 mm, o.d. = 3.08 mm

(*c*) Fuel—kerosine
T_F = 523 K, T_W = 673 K, P = 2.5 MPa
$\dot{m}_{VF}$ = 50–200 cc/min
Stainless steel tube (316); i.d. = 2.10 mm, o.d. = 3.08 mm

(*d*) Fuel—DF 2
T_F = 413 K, T_W = 413 K, P = 2.5 MPa
$\dot{m}_{VF}$ = 150–400 cc/min
Stainless steel tube, 400 series; i.d. = 2.59 mm, o.d. = 3.08 mm

Inspection of the above table shows that in three cases the wall temperature was 150°C higher than the fuel temperature, while in case (*d*) the fuel and tube wall were both at the same temperature. In all cases, regardless of fuel type, fuel temperature, or wall temperature, it is found that the effect of variation in Reynolds number on deposition rate (D.R.) can be expressed as

$$\text{D.R.} = \text{const} \cdot \text{Re}^{0.65} \tag{1}$$

The effect on deposition rates of a change in Reynolds number caused by a change in tube diameter is illustrated in Fig. 5. This figure contains the same data shown as (*d*) in Fig. 4 plus additional data obtained for the same fuel, at the same conditions of pressure and temperature, but with the tube internal diameter increased from 2.59 to 4.60 mm. Figure 5 shows that both sets of data tend to fall on the same curve, which conforms to the relationship

$$\text{D.R.} = 0.48\ \text{Re}^{0.65} \tag{2}$$

This increase in deposition rate with increase in Reynolds number is attributed to the higher heat transfer between the wall and the fuel and the higher transverse velocity components which are more effective in transporting material from the mainstream fuel flow to the tube walls.

Interest is sometimes expressed in the amount of deposit produced by a given mass of fuel. To examine this situation a "deposit index," D.I., is first defined as

$$\text{D.I.} = \frac{\text{mass of deposit per unit length of tube}}{\text{mass of fuel}} = \frac{\mu\text{g/cm}}{\text{kg}} \tag{3}$$

Also, we have

$$\text{Re} = \frac{\rho U d}{\mu} = \frac{4}{\pi} \cdot \frac{\dot{m}_{VF}}{d\nu} \tag{4}$$

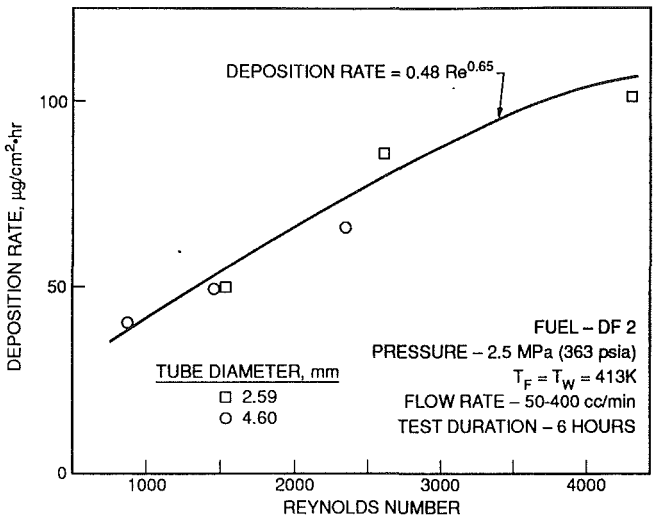

Fig. 5 Influence of tube diameter on deposition rate

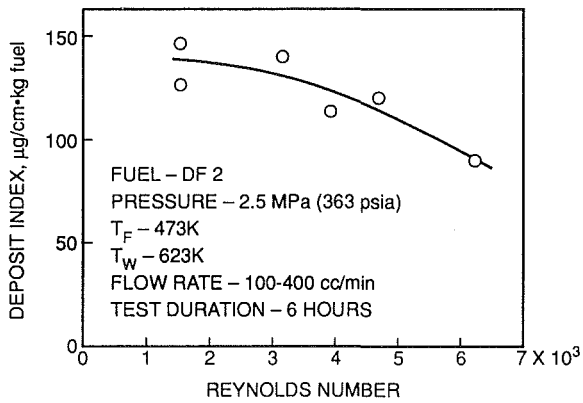

Fig. 6 Influence of Reynolds number on Deposit Index

By appropriate combinations of Eqs. (1), (3), and (4), the following relationships between deposition rate, deposit index, and Reynolds number are derived

$$\text{D.R.} \propto \text{Re}^{0.65} \tag{1}$$

$$\text{D.I.} \propto \text{Re}^{-0.35} \mu^{-1} \tag{5}$$

$$\frac{\text{D.R.}}{\text{D.I.}} \propto \text{Re}\ \mu \tag{6}$$

Figure 6 shows the deposit index plotted against Reynolds number for DF 2 fuel flowing through a 400 series stainless steel tube having an inside diameter of 2.59 mm and an outside diameter of 3.08 mm. One practical implication of the results presented in Figs. 5 and 6 is that for any given fuel flow rate a reduction in tube diameter will cause an increase in deposit thickness. However, it should be noted that in the present experiments on the effect of Reynolds number on deposition rates, the flow velocity is always less than a few meters per second. With continual reduction in tube diameter, the scrubbing action along the tube walls could eventually reach a point at which any further increase in flow velocity would cause deposition rates to decline.

Fuel Temperature. As mentioned earlier, the effect of an increase in temperature on deposition rate is twofold: (1) By reducing the fuel viscosity it raises the Reynolds number and hence also the deposition rate, as shown in Fig. 5; (2) it accelerates the auto-oxidation reactions responsible for deposit formation. The extent to which deposition rates are enhanced by an increase in fuel temperature depends on whether the fuel

Downloaded 02 Jun 2010 to 171.66.16.121. Redistribution subject to ASME license or copyright; see http://www.asme.org/terms/Terms_Use.cfm

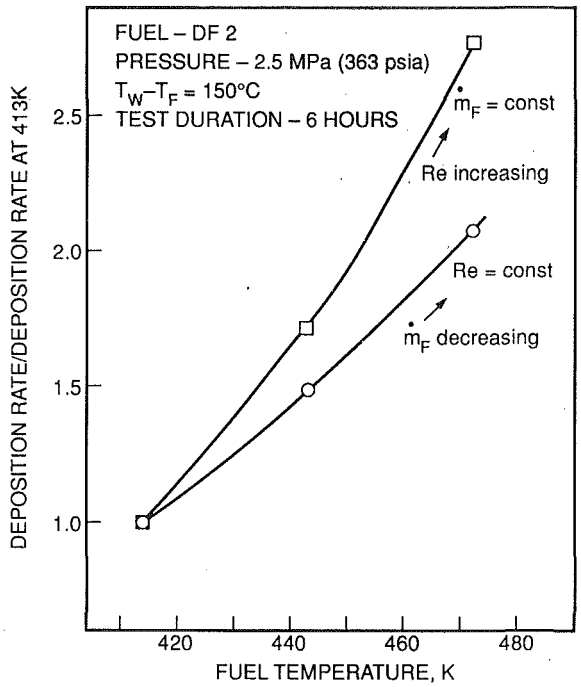

Fig. 7 Influence of fuel temperature on deposition rate

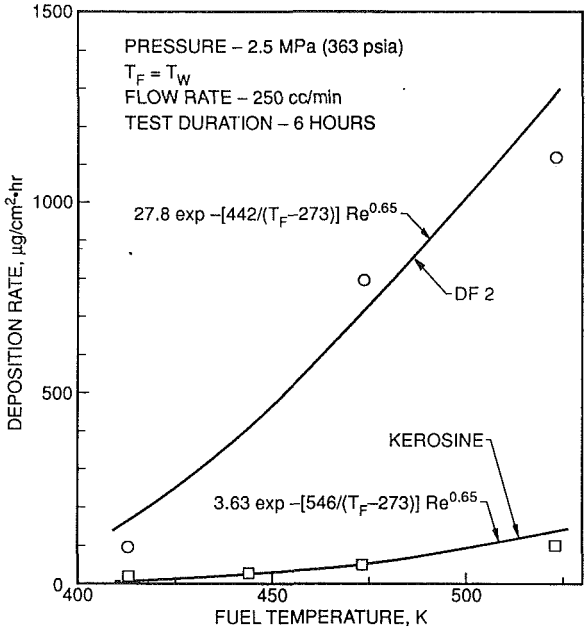

Fig. 8 Correlation of data for various fuel temperatures

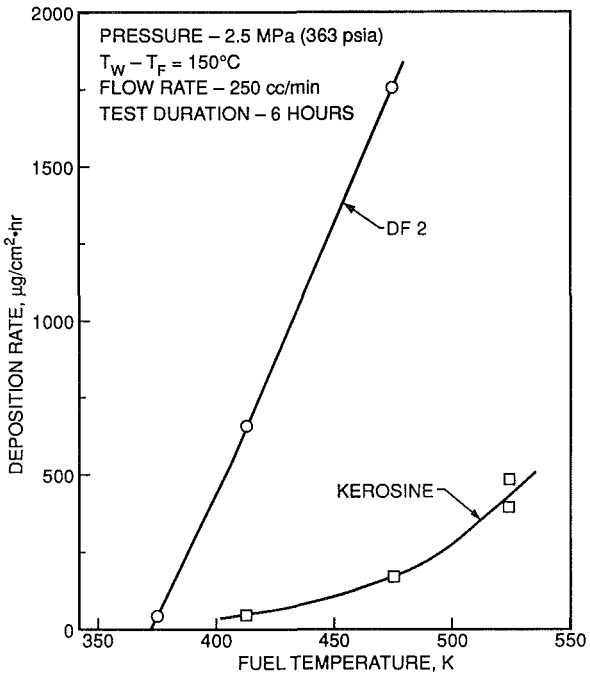

Fig. 9 Influence of fuel temperature on deposition rate

flow rate is held constant and the Reynolds number allowed to increase, or whether the flow rate is allowed to decline in order to maintain a constant Reynolds number. These effects are illustrated in Fig. 7.

In many experiments that are performed to show the influence of fuel temperature on deposition rates, the temperature of the tube wall is often appreciably higher than the temperature of the fuel flowing through it. This is done for many reasons, not the least being to simulate the conditions that exist in aircraft fuel systems and fuel injectors. Unfortunately, it produces a steep temperature gradient in the fuel adjacent to the wall, which prohibits a precise definition of temperature in the region where the deposition process is actually taking place. To avoid this problem, and to obtain experimental data on the influence of fuel temperature on deposition rates of more fundamental significance, the fuel and tube wall should ideally be at the same temperature. By eliminating heat transfer between the fuel and the tube wall, the effect of wall temperature is removed, so that any observed changes in deposition rates are due solely to variations in fuel temperature.

Some results obtained for kerosine and DF 2 under conditions where $T_W = T_F$ are shown in Fig. 8. Over a range of fuel temperatures from 413 to 523 K, it is found that deposition rates are correlated satisfactorily by an expression of the form

$$\text{D.R.} = C_1 \exp -[C_2/(T_F - 273)]\text{Re}^{0.65} \quad (7)$$

where C_1 is a constant whose value depends mainly on fuel composition and the material and condition of the tube wall, and C_2 depends solely on fuel composition (including additives). C_2 represents the activation energy of the auto-oxidation reaction that leads to the formation of deposits.

For kerosine, we have

$$\text{D.R.} = 36.3 \exp -[546/(T_F - 273)]\ \text{Re}^{0.65} \quad (8)$$

while for DF 2

$$\text{D.R.} = 27.8 \exp -[442/(T_F - 273)]\ \text{Re}^{0.65} \quad (9)$$

In these equations, deposition rate is expressed in terms of $\mu g/cm^2 \cdot h$.

Tube-Wall Temperature. If the tube-wall temperature exceeds the fuel temperature, the deposition rate is increased. This is evident from inspection of the data contained in Figs. 8 and 9, which were obtained under identical test condition except that in one case (Fig. 8) the fuel and wall temperatures were the same, whereas in the second case (Fig. 9) the wall temperature was 150°C higher than the fuel temperature. Comparison of these two figures reveals that an increase in wall temperature leads to a higher rate of deposition. For the two fuels employed in this investigation, kerosine and DF 2, the effect of wall temperature on deposition rates can be accounted for by including the term $\exp[(T_W - T_F)/166]$ into Eqs. (8) and (9), which then become, respectively:

For kerosine

$$\text{D.R.} = 3.63 \exp -[546/(T_F - 273)] \times \exp[(T_W - T_F)/166]\text{Re}^{0.65} \quad (10)$$

Downloaded 02 Jun 2010 to 171.66.16.121. Redistribution subject to ASME license or copyright; see http://www.asme.org/terms/Terms_Use.cfm

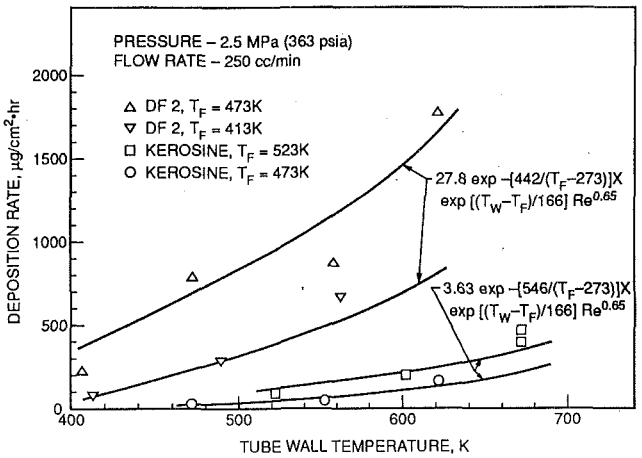

Fig. 10 Influence of tube-wall temperature on deposition rate

For DF 2

$$\text{D.R.} = 27.8 \exp - [422/T_F - 273)] \times \exp\ [(T_W - T_F)/166]\ \text{Re}^{0.65} \quad (11)$$

These equations are shown plotted in Fig. 10 alongside the corresponding experimental data for DF 2 and kerosine.

Discussion

Although Eqs. (10) and (11) have little fundamental significance, they have some practical value because they provide a useful indication of the relative importance of the relevant fuel and flow parameters on deposition rates. For example, they show that the most important factor influencing deposition rates is fuel temperature. Also of importance is the tube-wall temperature, specifically the difference in temperature between the wall surface and the adjacent fuel ($T_W - T_F$). Finally, they show that flow velocity and tube diameter affect deposition rates via their influence on Reynolds number. Over the range of flow velocities covered in these experiments, deposition rates are enhanced by increases in flow velocity and reductions in tube diameter.

Equations (10) and (11) contain no term to account for the influence of fuel pressure on deposition rates. This is because the present study has shown that provided it is high enough to prevent fuel boiling, pressure has no effect on deposition rates.

References

Baker, C. E., Bittker, D. A., Cohen, S. M., and Seng, G. T., 1983, "Research on Aviation Fuel Instability," *Combustion Problems in Turbine Engines*, AGARD Conference Proceedings No. 353, pp. 2/1–2/10.

Chin, J. S., Lefebvre, A. H., and Sun, F. T.-Y, 1992, "Temperature Effects of Fuel Thermal Stability," ASME JOURNAL OF ENGINEERING FOR GAS TURBINES AND POWER, Vol. 114, pp. 353–358.

Chin, J. S., and Lefebvre, A. H., 1992, "Experimental Techniques for the Assessment of Fuel Thermal Stability," AIAA Paper No. 92-0685.

Cohen, S. M., 1980, "Fuels Research—Fuel Thermal Stability Overview," *Aircraft Research and Technology for Future Fuels*, NASA CP-2146, pp. 161–168.

Coordinating Research Council Inc., 1979, "Thermal Oxidation Stability of Jet Fuels—A Literature Survey," CRC Report No. 509.

Marteney, P. J., and Spadaccini, L. J., 1986, "Thermal Decomposition of Aircraft Fuel," ASME JOURNAL OF ENGINEERING FOR GAS TURBINES AND POWER, Vol. 108, pp. 648–653.

Mills, J. S., and Kendall, D. R., 1986, "The Quantification and Improvement of the Thermal Stability of Aviation Turbine Fuel," ASME JOURNAL OF ENGINEERING FOR GAS TURBINES AND POWER, Vol. 108, pp. 381–386.

Peat, A. E., 1982, "Thermal Decomposition of Aviation Fuel," ASME Paper No. 82-GT-27.

Roback, R., Szetela, E. J., and Spadaccini, L. J., 1981, "Deposit Formation in Hydrocarbon Rocket Fuels," NASA CR 179579.

Roback, R., Szetela, E. J., and Spadaccini, L. J., 1983, "Deposit Formation in Hydrocarbon Fuels," ASME JOURNAL OF ENGINEERING FOR GAS TURBINES AND POWER, Vol. 105, pp. 55–65.

Szetela, E. J., 1976, "Deposits From Heated Gas Turbine Fuels," ASME Paper No. 76-GT-9.

Szetela, E. J., Giovanetti, A. J., and Cohen, S., 1985, "Fuel Deposit Characteristics at Low Velocity," ASME Paper No. 85-IGT-130.

Taylor, W. F., 1979, "Jet Fuel Thermal Stability," NASA TM-79231.

TeVelde, J. A., and Glickstein, M. R., 1983, "Heat Transfer and Stability of Alternative Aircraft Fuels," Vol. 1, Report AD A137404.

TeVelde, J. A., Spadaccini, L. J., Szetela, E. J., and Glickstein, M. R., 1983, "Alternative Fuel Deposit Formation," *Combustion Problems in Turbine Engines*, AGARD Conference Proceedings No. 353, pp. 3/1–3/10.

Vranos, A., and Marteney, P. T., 1980, "Experimental Study of the Stability of Aircraft Fuels at Elevated Temperatures," NASA CR 165165.

Watt, J. J., Evans, A., and Hibbard, R. R., 1968, "Fouling Characteristics of ASTM Jet A Fuel When Heated to 700°F in a Simulated Heat Exchanger Tube," NASA TN D-4958.

Downloaded 02 Jun 2010 to 171.66.16.121. Redistribution subject to ASME license or copyright; see http://www.asme.org/terms/Terms_Use.cfm

R. W. Stickles

W. J. Dodds

Advanced Engine Combustor Aero Design,
GE Aircraft Engines,
Cincinnati, OH 45215

T. R. Koblish

J. Sager

New Products Development,
Fuel Systems Textron,
Zeeland, MI 49464

S. Clouser

Naval Air Propulsion Center,
Trenton, NJ 08628

Innovative High-Temperature Aircraft Engine Fuel Nozzle Design

The objective of the Innovative High-Temperature Aircraft Engine Fuel Nozzle Program was to design and evaluate a nozzle capable of operating at a combustor inlet air temperature of 1600°F (1144 K) and a fuel temperature of 350°F (450 K). The nozzle was designed to meet the same performance requirements and fit within the size envelope of a current production F404 dual orifice fuel nozzle. The design approach was to use improved thermal protection and fuel passage geometry in combination with fuel passage surface treatment to minimize coking at these extreme fuel and air temperatures. Heat transfer models of several fuel injector concepts were used to optimize the thermal protection, while a series of sample tube coking tests were run to evaluate the effect of surface finish, coatings, and tube material on the coking rate. Based on heat transfer analysis, additional air gaps, reduced fuel passage flow area, and ceramic tip components reduced local fuel wetted wall temperatures by more than 200°F (110 K) when compared to a current production F404 fuel nozzle. Sample tube coking test results showed the importance of surface finish on the fuel coking rate. Therefore, a 1 μin. (0.025 μm) roughness was specified for all fuel passage surfaces. A novel flow divider valve in the tip was also employed to reduce weight, allow room for additional thermal protection, and provide back pressure to reduce the risk of fuel vaporization. Phase II of this program will evaluate the fuel nozzle with a series of contaminated fuel and coking tests.

Introduction

Advanced military high-performance gas turbines will require both increased pressure ratio for improved cycle efficiency and increased use of fuel as a heat sink for both airframe and engine cooling. These two trends will increase both combustor inlet air and fuel temperatures. Therefore, innovative fuel injector designs will be required to operate successfully in this thermally hostile environment.

The primary concern in the design of high-temperature fuel injectors is the phenomenon of fuel coking. Coking is the formation of insoluble hydrocarbon compounds in the fuel by autoxidation. This results in deposits of gum, tars, varnish, and solid carbon on fuel passage surfaces. The deposits restrict flow, and can in turn lead to a significant reduction in combustor performance and life. Coking rates depend on many factors, such as wetted wall temperatures, fuel residence time at temperature, total volume of fuel passed through the system, and fuel thermal stability (Lyon, 1992). Therefore, a simple bulk fuel or wetted wall temperature design limit does not exist. However, GEAE experience has shown that fuel nozzle coking becomes a significant problem in current production fuel injectors when wetted wall temperatures approach 400°F (477 K). Maintaining the 400°F maximum wetted wall temperature guideline at the design goals of this program (Table 1) is an extreme challenge.

There are four basic approaches used to minimize fuel injector coking: (1) change to a more thermally stable fuel; (2) actively cool the fuel injector with air or fuel in a separate cooling circuit; (3) improve fuel passage geometry and thermal protection to reduce wetted wall temperatures; (4) treat fuel passage surfaces to inhibit coking.

Changing fuels is not an option in this program. In fact, in the future, fuel thermal stability will probably decrease (Lyon, 1992). Actively cooling the injector would reduce coking, but it is in conflict with the continuous effort to reduce weight and simplify the fuel system. Thermal protection alone will not meet the goals of this program. However, fuel passage surface treatment offers the potential to reduce the coking rate to acceptable levels at elevated wetted wall temperatures. Therefore, the GEAE/Fuel Systems Textron approach was a combination of improved thermal protection and surface treatment.

The innovative fuel nozzle designed for this program meets the flow and spray requirements and fits within the size en-

Table 1 Innovative fuel nozzle design goals

Air temperature	1600°F (1144 K)
Fuel temperature	350°F (450 K)
Operability	Full envelope
Smoke	Invisible with JP-5 and 12.5 percent H2 fuel
Life	Full aircraft life
Fuel capability	JP-5, DFM (JFTOT ≥ 477 K)

Contributed by the International Gas Turbine Institute and presented at the 37th International Gas Turbine and Aeroengine Congress and Exposition, Cologne, Germany, June 1-4, 1992. Manuscript received by the International Gas Turbine Institute February 6, 1992. Paper No. 92-GT-132. Associate Technical Editor: L. S. Langston.

Copyright © 1993 by ASME
Downloaded 02 Jun 2010 to 171.66.16.121. Redistribution subject to ASME license or copyright; see http://www.asme.org/terms/Terms_Use.cfm

velope of the Textron F404 dual orifice fuel nozzle shown in Fig. 1. All temperature predictions and design features will be compared to the F404 baseline.

Heat Transfer Analysis

Heat transfer analysis was conducted to develop insulating and hydraulic tip designs that would minimize wetted wall temperatures. Past experience has shown that maximum wetted wall temperatures along with the associated coking problems occur in the nozzle tip. This is due to a lack of adequate space for proper heat shielding, combined with the smaller fuel flow passages that are easily plugged by coke particles. More specifically, because it is the outer fuel annulus, the secondary fuel passage in a dual orifice nozzle is where the most severe wetted wall temperatures occur.

Analytical Model. An axisymmetric heat transfer model of the F404 tip is shown in Fig. 2. The analysis was done with the GEAE three-dimensional transient numerical heat transfer code THTD. Maximum steady-state wetted wall temperatures in the F404 fuel nozzle occur at a cruise condition rather than at maximum combustor inlet air temperature (T_3) condition, such as takeoff or sea level dash. This is due to the cooling effect of the high fuel flow rate at the maximum T_3 condition. At cruise, T_3 is still fairly high but fuel flow is much lower; thus wetted wall temperatures are at a maximum. An F404 cruise condition with T_3 extrapolated from 774°F to 1166°F (669 K to 903 K), to represent the 1600°F (1144 K) maximum T_3 program goal, was used to compare tip designs. The fuel inlet temperature was also increased from 200°F to 350°F (366 K to 450 K), while combustor inlet pressure, air flow, and fuel flow were unchanged. Figure 3 shows baseline Textron F404 fuel nozzle wetted wall temperatures at this extrapolated condition. As expected, wetted wall temperatures are well above 400°F (477 K).

A total of 27 tip designs was evaluated at the extrapolated cruise point. The design features included reduced fuel flow area, additional air gaps, modifications to the tip inlet (elbow), ceramic nozzle body, ceramic inserts, thermal barrier coatings, reduced emissivity coatings, and vacuum sealed insulating gaps. All designs maintained the basic F404 dual orifice fuel passages and fit within the baseline envelope.

Fuel Flow Area. The highest temperature region in the baseline F404 nozzle was the tip entrance or elbow. In this region fuel is dumped from the secondary fuel delivery tube in the support, to a collecting area at the elbow. Low fuel flow velocity leads to very high wetted wall temperatures. Figure 4 shows the dramatic reduction in wetted wall temperatures when the flow area in the elbow region is reduced.

Figure 5 shows the relationship between secondary fuel flow area, heat transfer coefficients, and wetted wall temperatures. This also confirms the need for maintaining high fuel velocity throughout the nozzle. In addition to heat transfer considerations, increased fuel velocity also reduces residence time in the fuel nozzle, which reduces the time available for the coking process.

Air Gaps Versus Solid Ceramics. Current fuel nozzle thermal protection in the tip is generally an insulating air gap that separates the fuel wall from T_3 air. An alternative would be to use insulating materials such as ceramics. However, replacing the baseline secondary stainless steel/air gap construction with a solid piece of partially stabilized zirconia actually increased wetted wall temperatures by nearly 100°F (56 K).

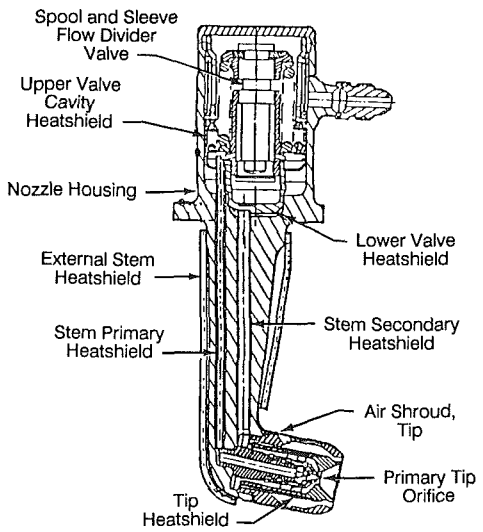

Fig. 1 Production F404 fuel nozzle used as baseline for innovative design

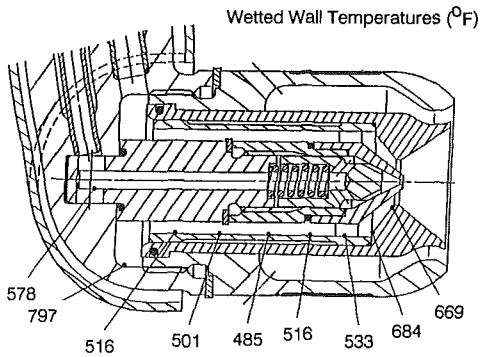

Fig. 3 F404 baseline wetted wall temperatures at extrapolated cruise condition well above acceptable levels

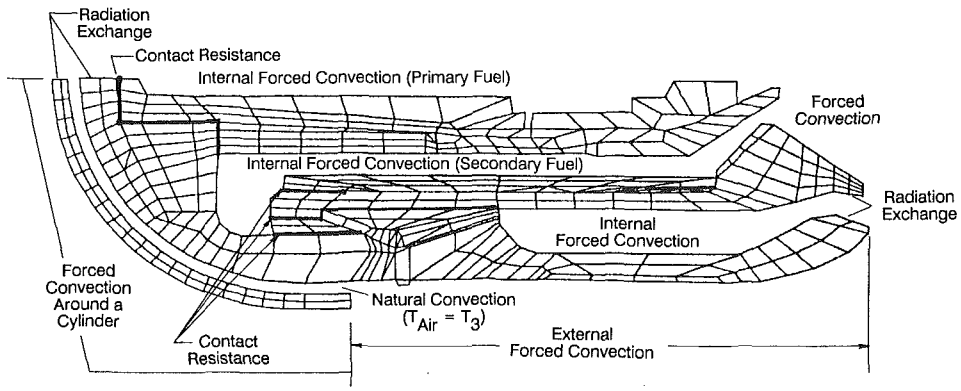

Fig. 2 F404 fuel nozzle tip heat transfer model

Downloaded 02 Jun 2010 to 171.66.16.121. Redistribution subject to ASME license or copyright; see http://www.asme.org/terms/Terms_Use.cfm

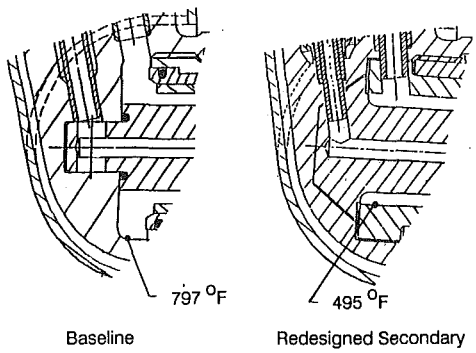

Fig. 4 Redesign of elbow significantly reduces wetted wall temperatures

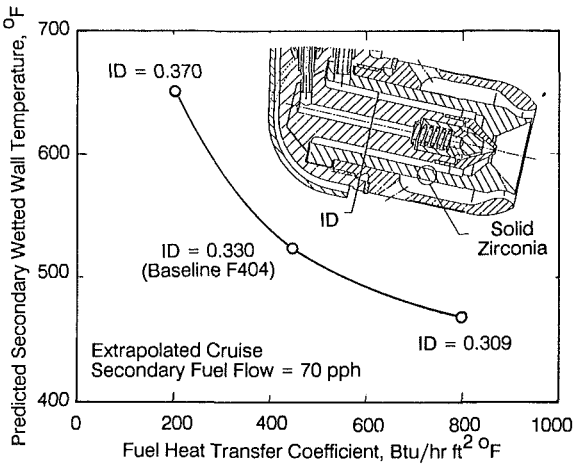

Fig. 5 Reducing fuel flow area lowers wetted wall temperature

The wetted wall temperature was reduced 20°F (11 K) from the baseline when the stainless steel/air gap design was replaced with an identical zirconia/air gap design. However, this is a manufacturing challenge because of the thin ceramic walls.

Super Insulated Fuel Delivery Tube. In addition to heat transfer analysis on the injector tip, a superinsulated delivery tube was designed to minimize fuel temperature rise in the injector support. Under steady-state cruise conditions, fuel flow is high enough to minimize bulk fuel temperature rise, but improved insulation becomes crucial to prevent heat soak-back at the low flow rates associated with idle descent. State-of-the-art tube insulation designs utilize annular air gaps surrounding the fuel delivery tube. This appears to be effective for current engine cycles at high fuel flow rates. In this program the high temperature level will add a substantial radiative heat load along with the existing convective heat flux on the injector support. In order to compensate for the increased radiation load, a double wall fuel transfer delivery tube (as shown in Fig. 6) has been developed. A normal air gap will continue to be utilized between the strut (structure) and the outer shell of the transfer tube. However, the double wall construction of the tube will be filled with Perlite powder and insulative trapped air cells. Perlite is an insulative material used extensively for applications where radiation is a significant heat transfer mode. As shown in Fig. 6, a slip joint was incorporated to compensate for the substantial thermal gradients that will be encountered during full power, cruise and soak-back conditions. As the outer structure grows with the surrounding air temperature, the innermost tube length will be relatively constant at the 350°F (450 K) fuel temperature. The slip seal is designed to retain the Perlite bulk packing density while allowing the outer tube wall to grow with radiation load. Calculated inner wetted

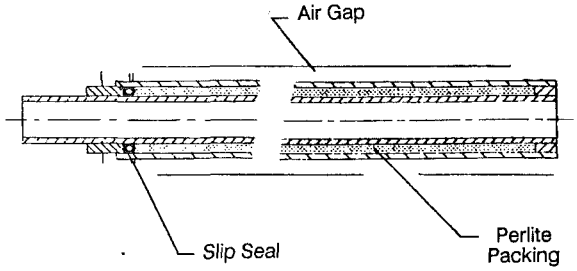

Fig. 6 Slip seal allows for thermal differences

wall temperatures at the conditions investigated for the Perlite tube were:

Compressor discharge temperature (T_3):
1200°F (922 K) 1600°F (1144 K)
Fuel velocity:
20 fps (6 mps) 40 fps (12 mps)
Wetted wall temperature:
365°F (458 K) 360°F (455 K)

At these conditions, bulk fuel temperature rise through the support will be minimal.

Key Thermal Design Features. Heat transfer analysis confirmed that heat shields and insulation alone will not meet the goals of this program. In all tip designs evaluated wetted wall temperatures were well above the 400°F (477 K) limit. However, the analysis did point to important design features for reducing wetted wall temperatures:

- Reduce fuel flow passage area.
  - Increases fuel velocity
  - Increases heat transfer coefficients
  - Reduces wetted wall temperatures
  - Reduces fuel residence time
- Add air gaps.
  - Metal with air gaps more effective than solid ceramics
- Substitute ceramic for metal parts.
  - Ceramics in combination with air gaps
- Avoid bends and steps in the fuel flow path.
  - Causes stagnant fuel regions with low heat transfer coefficients and thus high wetted wall temperatures
  - Provides coking initiation sites
- Add the Perlite filled superinsulated fuel delivery tube in the injector support.
  - Minimizes bulk fuel temperature rise in support.

Reduced emissivity coatings, vacuum gaps, and thermal barrier coatings did not demonstrate a significant reduction in wetted wall temperatures.

Fuel Passage Surface Treatment

Heat transfer analysis has shown that thermal protection alone will not meet the goals of this program. Therefore, an attempt was made to reduce the fuel coking rate with surface treatment, including surface finish and composition. Previous data have clearly shown that certain elements in the fuel system dramatically increase fuel coking. Table 2 from Taylor and

Table 2 Effect of metal surface on carbon deposition (Taylor and Frankenfeld, 1975)

Metal surface	Deposit formation rate at 400°F (mg/sq cm h)
Copper	0.00525
Ti-6Al-4V	0.00375
Ti-8Al-1V-1Mo	0.00240
Pure titanium	0.00093
Stainless steel 304	0.00093
Aluminum	0.00093

Downloaded 02 Jun 2010 to 171.66.16.121. Redistribution subject to ASME license or copyright; see http://www.asme.org/terms/Terms_Use.cfm

Frankenfeld (1975) shows the effect of some metals on the coking rate of JP-5. Thus, various inert surface coatings were evaluated under this program to investigate the potential for coking reduction.

Marteney and Spadaccini (1986) suggested two basic coking processes: (1) a homogeneous oxidation reaction occurring in the fuel free-stream forming coke particles that adhere to the fuel passage surface; (2) a heterogeneous catalytic reaction occurring at the fuel passage surface. If mechanism #2 dominates, an inert surface should reduce the coking rate. If mechanism #1 dominates, a polished surface may prevent carbon from adhering. Figure 7 indicates that both processes occur but the dominant one depends on wetted wall temperature. Below wetted wall temperatures of 530°F (550 K), a line representing an activation energy of 10 kcal/mole fits the data. This is typical of a heterogeneous reaction system like what might occur at the wall. Above 530°F, the 40 kcal/mole activation energy line is typical of a homogeneous oxidation reaction (liquid phase) (Marteney and Spadaccini, 1986). At very high fuel temperatures (> 800°F (700 K)) the coking mechanism is pyrolysis controlled (Chin et al., 1992).

Coking Test Rig. Evaluation of the various approaches to eliminate or reduce fuel coking was conducted in a heat transfer/coking rig described as follows and as shown in Fig. 8. The main consideration in the design of the fuel heat-up circuit was to minimize the potential for thermally prestressing the fuel in local stagnant zones of high heat flux. Therefore, a low heat flux heating unit consistent with aircraft heat exchanger designs (fuel/oil coolers) was selected. Two electric rod heat exchanger units were utilized in the rig to obtain fuel temperatures as high as 400°F (477 K). A constant flow pump provided continued recirculation of the fuel within the two heater units to prevent stagnant thermal stress zones. Wetted wall temperatures inside the heaters did not exceed 430°F (494 K). Subsequent checks of the fuel (JP-5) break point temperatures for both unheated and heated samples showed prestressing in the heater did not affect fuel thermal stability. JFTOT tests of all samples indicated 518°F (543 K) break points. JFTOT tests on fuel samples after 40 μm. filters were installed also indicated the same results. In order to promote fuel thermal decomposition, the supply fuel was bubbled with air to ensure oxygen saturation. An oxygen concentration meter provided constant monitoring of the fuel supplied to the test.

In addition to the fuel heater, the test stand also provided electrically heated air to supply the heat source for conducting either coking or heat transfer tests of the various specimens. Air temperatures of 1600°F (1144 K) to simulate the engine compressor discharge temperature levels and heat transfer coefficients were also obtained.

The test fixture is shown in Figs. 9 and 10. All sample coking specimens tested were 3.35 in. (8.5 cm) long by 0.43 in. (1.1 cm) diameter tubes. As shown, the test fixture was designed to accommodate two specimens in series. All test specimen candidates were evaluated relative to a reference specimen (Stainless 347, standard surface finish) typical of the F404 nozzle passage design. Heated air flowed through the i.d. passage of the specimen tube while heated fuel flowed over the o.d. surface through an annulus that simulated typical nozzle design flow passages (i.e., flow velocities and fluid residence times). During a coking evaluation the outer surface of the specimen tube was set at a specific temperature (wetted wall temperature). A constant surface temperature was maintained by adjusting the heated air temperature and/or mass flow.

A fluoroptic thermometry system was utilized to measure the wetted wall temperature without obstructing the fuel flow or surface geometry. The unit measured the fluorescent decay of a small phosphor patch applied at two stations along the candidate and reference specimen tubes. An emitter/collector probe was mounted in line with each phosphor patch (two on each tube). The probe emits a light beam to the phosphor patch, while the collector picks up the phosphor's fluorescence. The decay time of the fluorescent signal is calibrated as a

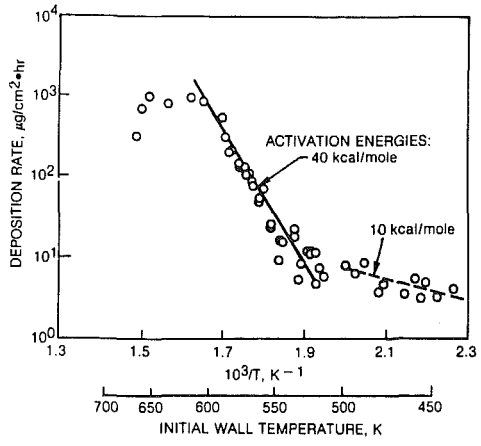

Fig. 7 Coking mechanism changes around 530°F (550 K) (from Marteney and Spadaccini, 1986)

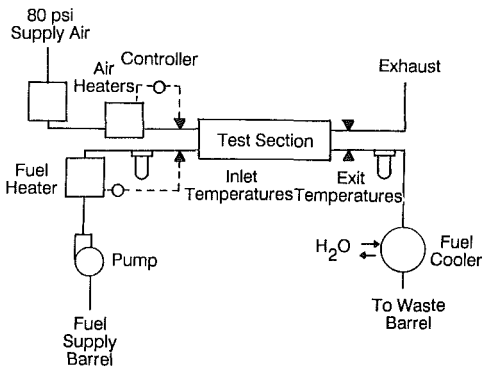

Fig. 8 Heat transfer/coking test rig

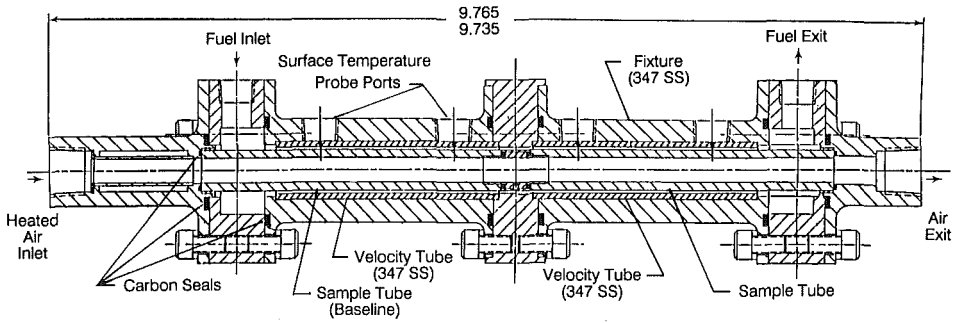

Fig. 9 Tandem tube test fixture

Downloaded 02 Jun 2010 to 171.66.16.121. Redistribution subject to ASME license or copyright; see http://www.asme.org/terms/Terms_Use.cfm

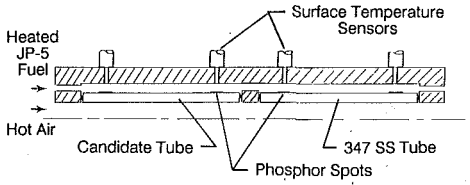

Fig. 10 Wetted wall temperatures monitored optically

Table 3 Coking specimen tubes

Material	Surface finish, μin.	Surface finish, μm
347 stainless steel	125	3.18
347 Stainless steel	65	1.65
347 Stainless steel	10	0.25
Aluminum oxide coated 347	Rough	
Pyrolytic glass coated 347	10	0.25
Chromium carbide coated 347	10	0.25
Titanium nitride coated 347	10	0.25
Catalytic glass coated 347	10	0.25
Zirconia	10	0.25
High-temperature glass coated 347	10	0.25

function of the surface temperature. Testing at Fuel Systems Textron confirmed claims by the manufacturer (Luxtron) that distillate fuels would not affect the transmission of fluorescent signals and that system accuracy is within the quoted ±1°C (Wickesheim and Sun, 1985).

Test Procedure. The test procedure was based on determining test conditions that would produce a measurable deposition within a practical test period. The conditions of 350°F fuel inlet temperature, surface temperature levels of 400 to 600°F, and fuel flow velocities from 5 to 15 fps were considered. The results of baseline testing identified an 8-hour test cycle, which would be utilized in all subsequent screening tests. Evaluation of deposition rate was determined by measurement of weight gained by the candidate specimen in conjunction with the tandem reference baseline specimen. Promising candidates were subjected to 30-hour evaluation tests to confirm their potential effectiveness. In all evaluations and baseline testing of specimens, JP-5 fuel was oxygenated, heated, and passed over the surface on a one pass basis in order to simulate actual operational conditions.

8 Hour Coking Tests. Table 3 shows the specimen tubes that were tested.

Initial tests were run with baseline 347 stainless steel tubes to determine test conditions that gave a measurable carbon buildup in 8 hours. The conditions selected from these tests were as follows:

Inlet fuel temperature = 350°F (450 K)
Inlet wetted wall temperature = 575°F (575 K)
Fuel velocity = 10 fps (3 mps)
Test time = 8 hours

All the specimen tubes were evaluated at these conditions. Visual observation suggested that the zirconia and the chromium carbide coated tubes were more resistant to carbon deposits. Attempts to quantify the deposition were unsuccessful because the phosphor patch on all the sample tubes used for optical surface temperature measurements eroded during the tests. This skewed the before and after the weight difference. A second problem with the tests was that the wetted wall temperature was set high (575°F) to accelerate the coking rate for an 8 hour test. However, as discussed earlier this could have affected the coking mechanism.

30 Hour Coking Tests. A second series of tests was run at the following conditions:

Table 4 Total carbon deposition results—475°F tests

Material	Finish, μin.	Carbon deposition, mg.	Rate, mg/sq cm h
347 SS	10	2.0	0.00228
Zirconia	10	2.2	0.00251
Chromium carbide	10	2.6	0.00297
347 SS	125	2.7	0.00308

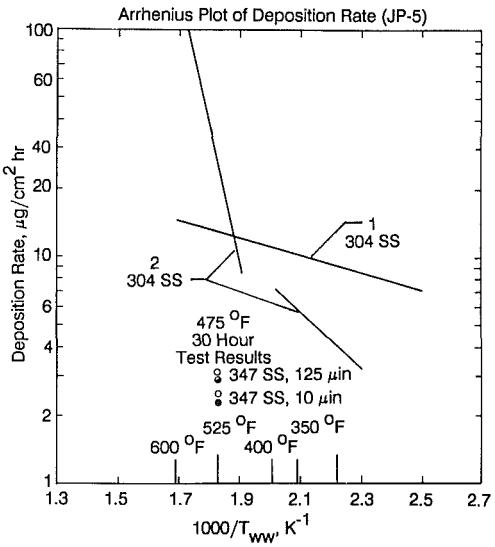

Fig. 11 Coking rate much lower than other reported data: (1) Taylor and Frankenfeld (1975); (2) Marteney and Spadaccini (1986)

Inlet fuel temperature = 350°F (450 K)
Inlet wetted wall temperature = 475°F (519 K)
Fuel velocity = 10 fps (3 mps)
Test time = 30 hours

In these tests both tubes were identical and the phosphor patch was only used on the forward tube to set the conditions. This allowed accurate before and after weights of the aft tube to be obtained. Table 4 summarizes the carbon deposition rates. Wetted wall temperature increased along the length of the tubes. The average wetted wall temperature on the aft tube was 50°F (29 K) above the inlet wetted wall temperature, so the deposition rates quoted are for an average wetted wall temperature of 525°F (547 K).

Deposition rates for all tubes were similar. Polished 347 stainless steel was the most coke-resistant material tested. Both Taylor and Frankenfeld (1975) and Meyers et al. (1992) also found stainless steels superior to other candidate fuel passage materials. However, the difference between the coking rates of the two 347 SS sample tubes does indicate a surface finish effect.

Figure 11 shows the deposition rate as compared to other available JP-5 data. There is a great deal of scatter, but the deposition rates measured in this program are significantly lower. A possible explanation for this is that in both Taylor and Frankenfeld (1975) and Marteney and Spadaccini (1986) fuel was not preheated before introduction to the hot stainless steel surface. In this study the fuel was preheated to a 350°F (450 K) bulk temperature and carbon particles were filtered out before entering the test section. Therefore, it may be possible that the fuel was prestressed to a point where fewer radicals were available to participate in the coking process inside the test section. Marteney et al. (1982) also observed a reduction in diesel fuel coking rate when it was preheated to 300°F (422 K).

Downloaded 02 Jun 2010 to 171.66.16.121. Redistribution subject to ASME license or copyright; see http://www.asme.org/terms/Terms_Use.cfm

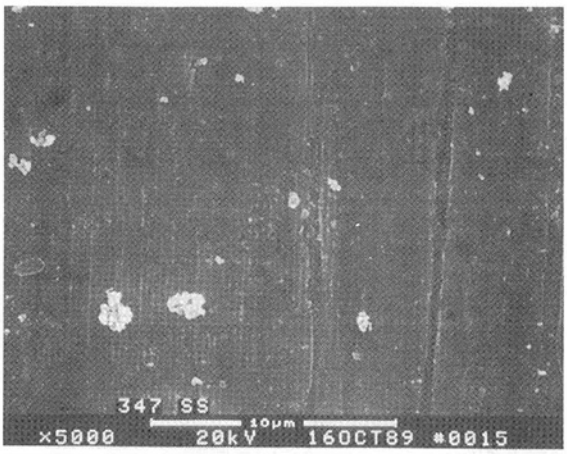

T_{ww} = 475°F

Note: Bright flakes in photo are from gold sputter, not carbon

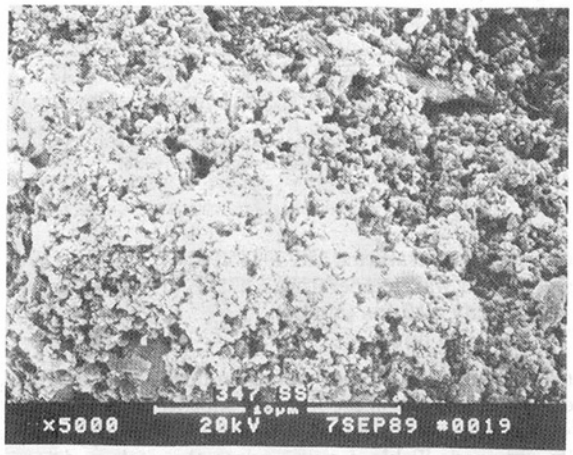

T_{ww} = 575°F

Fig. 12 Varnish forms on 10 μin. 347 SS at T_{ww} = 475° while soft carbon deposited at 575°F

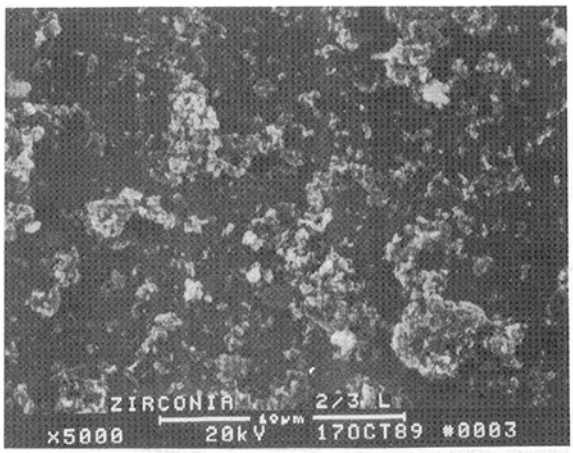

T_{ww} = 475°F

Fig. 13 10 μin. zirconia tube had soft carbon rather than varnish deposits at 475°F (5000 ×)

SEM Analysis of Deposits. Examination of the carbon depositions with a scanning electron microscope (SEM) provided some interesting details. SEM photographs clearly showed two distinct types of depositions: a soft carbon and a hard varnish. All of the 575°F wall temperature test specimen tubes had a soft carbon deposit. On the other hand, most of the same specimen tubes had a varnish deposit when run at the 475°F wall temperature condition. Figure 12 compares the two types of deposition on 347 stainless steel tubes. Possibly, deposition may start out as a varnish on the surface, but the exposure to the higher 575°F wall temperature continues the hydrocarbon breakdown until only soft carbon is left.

With one tube the type of deposition was not a function of temperature. Partially stabilized zirconia tubes had soft carbon as shown in Fig. 13 at both the 475°F and 575°F test conditions. Although the exact cause is not clear, this result does suggest that the fuel tube composition does affect the coking mechanism.

Based on this result, partially stabilized zirconia may be an excellent material for the tip fuel passages since it only forms soft carbon, which could be washed out of the tip at high fuel flow conditions. Varnish, on the other hand, tends to build up and then spall off in larger chucks that could plug the nozzle secondary spin slots. In addition, zirconia has lower thermal conductivity than stainless steel; therefore it acts as an insulator to minimize wetted wall temperatures.

Effect of Surface Finish. In addition to the two types of deposition observed from SEM inspections, the effect of surface finish was also evident. Figure 14 shows SEM back-scatter photographs of 347 stainless steel tubes of 125 and 10 μin. surface roughness after the 575°F coking tests. Machine lines are clearly visible on the 125 μin. surface at 100×. Carbon deposits concentrated on those machine lines (carbon is dark on back scatter). On the 10 μin. finish the machine lines have been polished out, but some other surface defects are visible. Once again carbon deposition is evident on the surface defects.

Quantitative measurements (Table 2) indicated a 26 percent reduction in carbon deposition when the surface roughness was reduced from 125 to 10 μin. To help verify this trend and to take it one step further, 2 stainless steel tubes were polished to a 1 μin. finish with a grit polishing process. One tube was left uncoated and the other was coated with chromium carbide vapor deposition. Both tubes were run at the 475°F, 30 hour test. Although there was some discoloration of the tubes, there was no measurable (<0.1 mg) deposition on either tube. These results strongly suggest that surface finish plays an important role in coke initiation.

The Reed Valve

A design approach to reduce heat transfer surfaces and provide additional room for thermal protection resulted in the incorporation of a simplistic reed valve concept as shown in Fig. 15. The standard sliding spool and sleeve valve configuration of the baseline F404 integral valve body/support design was replaced by a single curvilinear-cantilever leaf spring valve located in the tip of the fuel injector. This concept combines the functions of the sliding spool, which meters and divides fuel flow to both primary and secondary passages of the nozzle tip. In addition, the tip location of the reed valve eliminates one of the two (primary and secondary) fuel delivery tubes down the support structure of the fuel injector. A single fuel feed simplifies construction and affords improved thermal protection along the support path. The reed valve also reduces the risk of fuel vaporization by maintaining back pressure

Downloaded 02 Jun 2010 to 171.66.16.121. Redistribution subject to ASME license or copyright; see http://www.asme.org/terms/Terms_Use.cfm

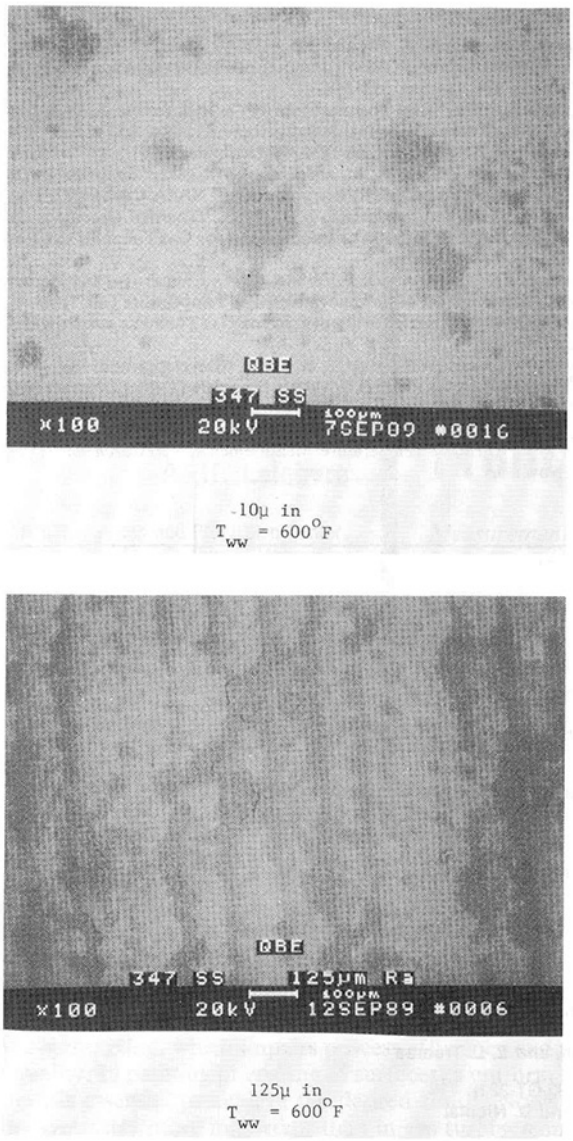

Fig. 14 Dark spots are carbon on 100 × back scatter analysis; machine lines and surface defects are initiation sites

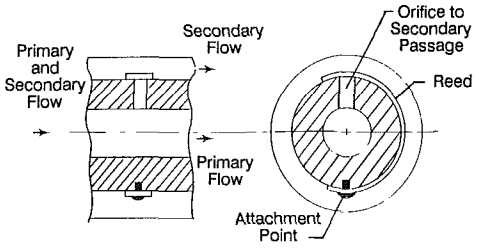

Fig. 15 Reed valve divides primary/secondary flow in tip

during heat soak-back conditions. Reed valve design considerations include geometric relations between leaf movement and the discharge orifice, material selection, cantilever geometry, and flow chamber shape. Development tests of the reed valve included 10^7 on/off cycles, hot and cold fuel flow checks, and limited contamination testing. The baseline F404 flow curve was matched, with the exception of a delayed reed valve closing hysteresis, as shown in Fig. 16. The hysteresis was repeatable so it was considered acceptable for this program. Moving the flow divider valve into the high temperature flowpath does increase the risk of leakage and valve hysteresis

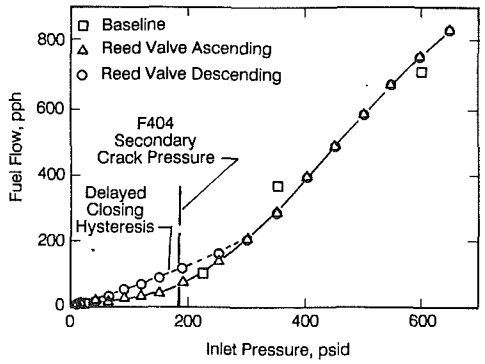

Fig. 16 Delayed closing hysteresis is very repeatable

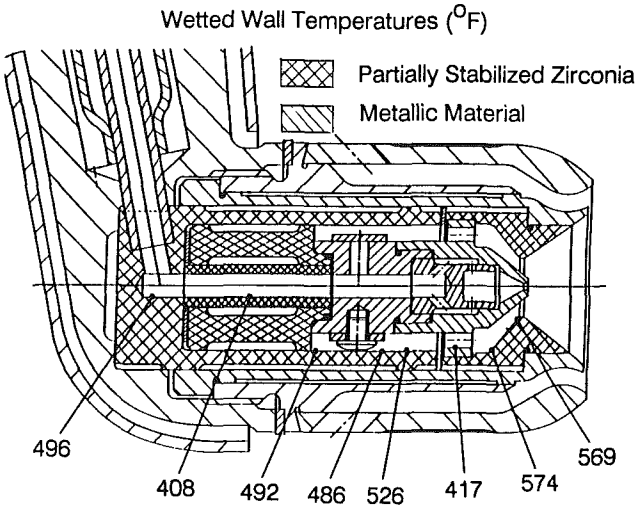

Fig. 17 Wetted wall temperatures are significantly lower than the baseline F404; hot spots are downstream of secondary spin slots

due to coke or varnish formation. However, the simple reed valve design and potential payoffs warrant the risk.

Innovative Fuel Nozzle Design

The innovative nozzle tip design is shown in Fig. 17. The reed valve in the tip provides the primary/secondary fuel flow dividing function. The valve saves weight (over 5 lb on a set of 18 nozzles), allows extra room for insulating air gaps, and back pressures the fuel flow to reduce the risk of vaporization. The partially stabilized zirconia in the tip provides additional insulation and inhibits the formation of hard varnish. Several additional insulative air gaps have been added to the tip. A Perlite-filled superinsulating fuel delivery tube is included in the support. All fuel passages have been polished to a mirrorlike 1 μin. roughness. Figure 17 shows that local wetted wall temperatures have been reduced by more than 200°F when the final nozzle tip design is compared to the baseline F404.

Conclusions

An innovative single inlet dual orifice fuel nozzle was designed to operate at maximum combustor air and fuel temperatures of 1600°F (1144 K) and 350°F (450 K), respectively. The design approach was to minimize fuel passage wetted wall temperatures with improved heat shielding and reduce the fuel coking rate by treating the fuel passage surfaces. A novel flow divider valve in the tip was also included in the design.

Heat transfer analysis showed that reduced fuel passage flow area, additional insulating air gaps, and replacement of metallic tip components with ceramics minimized the wetted wall temperatures. Vacuum gaps, reduced emissivity coatings, and

Downloaded 02 Jun 2010 to 171.66.16.121. Redistribution subject to ASME license or copyright; see http://www.asme.org/terms/Terms_Use.cfm

thermal barrier coatings did not offer significant wetted wall temperature reductions.

Sample tube coking tests showed that polishing the fuel passage surface reduced the coking rate. The coking tests also demonstrated that the type of deposition depended on the wetted wall temperature. Hard varnish formed at wetted wall temperatures of 475°F (519 K) and soft carbon deposits occurred at wetted wall temperatures of 575°F (575 K). However, partially stabilized zirconia formed soft carbon at both 475 and 575°F. Therefore, zirconia may act as a catalyst to form soft carbon at lower wetted wall temperatures.

Phase II of the program will evaluate the fuel nozzle with a series of contaminated fuel and cyclic coking tests.

Acknowledgments

This work was funded by the Naval Air Propulsion Center (NAPC) under contract No. N00140-87-C-6321.

References

Chin, J. S., Lefebvre, A. H., and Sun, F. T.-Y., 1992, "Temperature Effects on Fuel Thermal Stability," ASME JOURNAL OF ENGINEERING FOR GAS TURBINES AND POWER, Vol. 114, pp. 353–358.

Lyon, T. F., 1992, "Fuel Thermal Stability Outlook for GE Aircraft Engines in 1991," Aviation Fuel: Thermal Stability Requirements, ASTM STP 1138, P. W. Kirklin and P. David, eds., ASTM, Philadelphia, PA.

Marteney, P. J., Colket, M. B., and Vranos, A., 1982, "Experimental Study of the Thermal Stability of Hydrocarbon Fuels," NASA CR-168027, Dec.

Marteney, P. J., and Spadaccini, L. J., 1986, "Thermal Decomposition of Aircraft Fuel," ASME JOURNAL OF ENGINEERING FOR GAS TURBINES AND POWER, Vol. 108, pp. 648–653.

Myers, G. D., Armstrong, J. P., White, C. D., Clouser, S., and Harvey, R. J., 1992, "Development of an Innovative High-Temperature Gas Turbine Fuel Nozzle," ASME JOURNAL OF ENGINEERING FOR GAS TURBINES AND POWER, Vol. 114, pp. 401–408.

Taylor, W. F., and Frankenfeld, J. W., 1975, "Development of High Stability Fuel," Final Report for Phase II Naval Air Propulsion Center Contract N00140-74-C-0618, Dec.

Wickesheim, K., and Sun, M., 1985, "Phosphors and Fiber Optics Remove Doubt From Difficult Temperature Measurements," *Research and Development*, Nov.

Downloaded 02 Jun 2010 to 171.66.16.121. Redistribution subject to ASME license or copyright; see http://www.asme.org/terms/Terms_Use.cfm

Factors Influencing the Circumferential Liquid Distribution From Pressure-Swirl Atomizers

S. K. Chen

A. H. Lefebvre

Thermal Sciences and Propulsion Center,
Purdue University,
West Lafayette, IN 47907

J. Rollbuhler

NASA Lewis Research Center,
Cleveland, OH 44135

Measurements of circumferential liquid distribution are carried out over ranges of injection pressure from 0.34 to 1.72 MPa (50 to 250 psi) using five different simplex nozzles to achieve variations in the discharge orifice length/diameter ratio from 0.5 to 4.0. Two additional simplex nozzles of the same flow number are also examined in order to ascertain the effect of variations in the number of swirl chamber feed slots on circumferential liquid distribution. Mixtures of water and glycerine are used to provide a twelve to one variation in liquid viscosity. The results obtained show that spray uniformity improves markedly at higher injection pressures. Increase in liquid viscosity also has a beneficial effect on spray uniformity. The most uniform circumferential liquid distributions are obtained with nozzles having a discharge orifice length/diameter ratio of between 1 1/2 and 2.

Introduction

The symmetry of the spray patterns produced by atomizers is an important variable in most practical applications. In spray drying, for example, an unsymmetric spray may cause poor liquid–gas mixing, which impairs process efficiency and product quality. In painting or coating of surfaces, a uniform spray pattern is essential to achieve the desired finish. Nowhere is spray symmetry more important than in gas turbine combustors, where nonuniformities in circumferential fuel distribution can give rise to local pockets of fuel-lean mixture in which burning rates are low, thereby producing high concentrations of carbon monoxide and unburned hydrocarbons. By the same token, other regions of the spray in which the fuel concentration exceeds the mean value are characterized by high soot formation, leading to excessive flame radiation and exhaust smoke. Irregularities in circumferential fuel distribution can also adversely affect liner wall temperatures and turbine blade life.

The term "patternation" is often used to describe the uniformity of the circumferential distribution of liquid in a conical spray. Despite its importance to spray coating applications and to many key aspects of gas turbine combustion performance, the number of reported studies on spray patternation is surprisingly few. Some 30 years ago, Tate (1960a) observed that patternation criteria are quite arbitrary and empirical; this fairly describes the situation today. Although spray symmetry can be measured and expressed quantitatively, few efforts have been made to relate patternation to liquid properties, nozzle design features, and nozzle operating conditions. A notable exception is the recent study carried out by Cohen and Rosfjord (1992). These workers examined the spray patternation behavior of a dual-orifice pressure atomizer with nozzle shroud airflow of the type used in many in-service engines. This research led to the acquisition of spray patternation data at realistic engine conditions of high pressure and temperature. However, the results of this investigation are clouded to some extent by the dominant effect of the nozzle shroud air, which caused the spray cone to collapse at some operating conditions.

Experience with hollow-cone simplex atomizers has shown that patternation is sensitive to the degree of eccentricity between the swirl chamber and the final discharge orifice. Nozzle quality is also important, and spray patternation may be impaired by poor surface finish, orifice imperfections, plugged or contaminated flow passages, eccentric alignment of key nozzle components, and other conditions. For airblast atomizers, lack of symmetry in the various air passages and swirlers can also have an adverse effect on spray patternation (Lefebvre, 1983).

In this study, emphasis is placed on simplex nozzles of low flow number, of the type that are generally used in small gas turbines and that also serve as "primary" or "pilot" atomizers in the dual-orifice and hybrid airblast injectors fitted to large turbojet engines. Such nozzles are of special interest because relatively small variations in certain critical dimensions can have a disproportionately large impact on spray patternation. The most critical geometric feature is the final discharge orifice, since this is where the liquid attains its maximum velocity before it is ejected from the nozzle in the form of a conical spray. As viscous losses tend to be high in this region of maximum flow velocity, normal design practice is to make the length/diameter ratio of the final discharge orifice (l_o/d_o) as small as possible without creating a sharp edge that would be difficult to manufacture consistently and would also be susceptible to damage during handling.

Contributed by the International Gas Turbine Institute and presented at the ASME COGEN-TURBO IV, New Orleans, Louisiana, August 1990. Manuscript received by the International Gas Turbine Institute February 27, 1992. Associate Technical Editor: L. S. Langston.

Copyright © 1993 by ASME
Downloaded 02 Jun 2010 to 171.66.16.121. Redistribution subject to ASME license or copyright; see http://www.asme.org/terms/Terms_Use.cfm

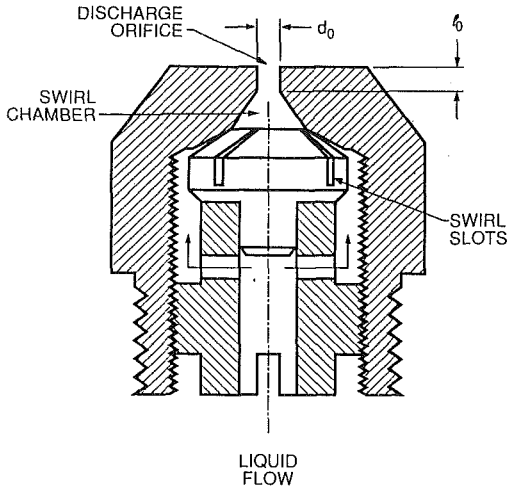

Fig. 1 Simplex pressure-swirl atomizer

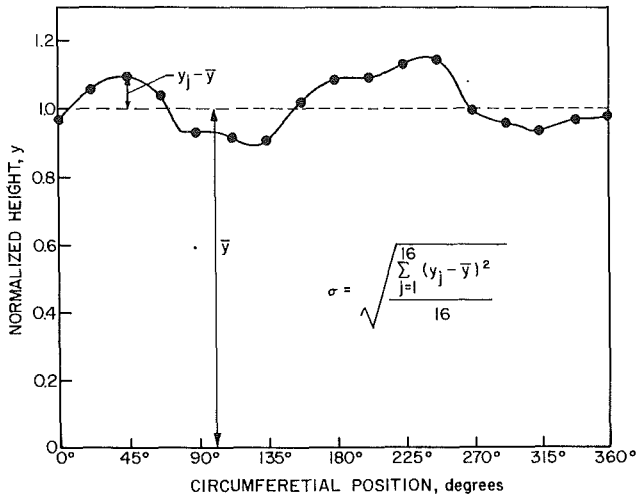

Fig. 3 Calculation procedure for determining standard deviation

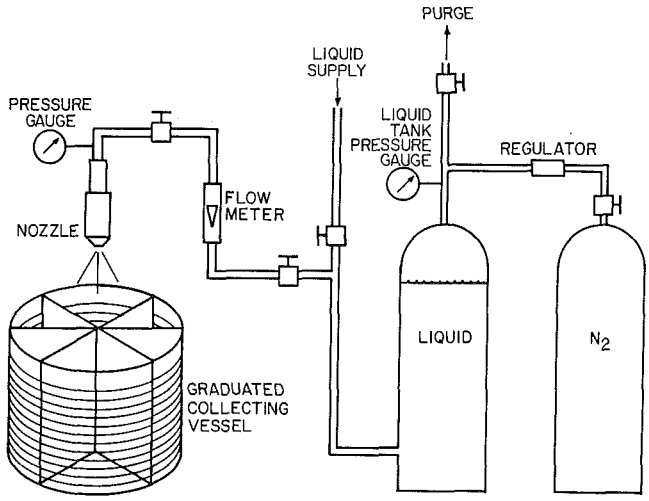

Fig. 2 Schematic diagram of test rig

Experimental

Seven simplex nozzles conforming to the basic design shown in Fig. 1 were specially manufactured for this program by the Delavan Company, all having the same flow number of $8 \times 10^{-8} m^2$ and the same discharge orifice diameter, d_o, of 0.457 mm. The length/diameter ratio of the discharge orifice is different for five of these nozzles, the actual values being 0.5, 1.0, 2.0, 3.0, and 4.0. Two additional nozzles were manufactured with an l_o/d_o of 1.0 to examine the influence of number of feed slots on patternation. One nozzle features two diametrically opposite feed slots, while the other has a single feed slot. Both the single-slot and the double-slot nozzles have the same total inlet port area as the standard three-slot nozzles, so the flow number should be almost identical for all nozzles.

The apparatus employed is essentially the same as that used in previous experimental studies carried out by Chen et al. (1991, 1992) on the factors influencing the atomization performance and cone angles of the sprays produced in pressure-swirl atomization. This apparatus is shown schematically in Fig. 2. Liquid is supplied to the nozzle from a nitrogen-pressurized tank. The amount of liquid ejected from the nozzle is controlled by a hand-operated valve located in the bypass line. A number of valves, pressure gages, and flow meters are located in the nozzle feed line to provide the desired nozzle operating conditions in terms of liquid injection pressure and mass flow rate. The method used to measure the circumferential liquid distribution, or "patternation," is one that originated many years ago in the gas turbine industry, when circular-sectored vessels were developed to measure symmetry about the spray axis of hollow-cone fuel nozzles. In this method the nozzle is centered above the vessel and sprays down into a graduated cylindrical collection tray that is partitioned into a number of pie-shaped sectors, usually 12 or 16. The height of the nozzle above the patternator is determined by the need to ensure that the entire spray is always collected, even for the widest spray cone angle. The duration of each test is governed by the time required for one of the sectors to become nearly full. At this point the liquid supply is turned off and the residual flow is diverted away from the patternator. The height of the liquid in each tube is measured by visually locating the meniscus between lines scribed into the clear plastic of the patternator.

After the level of liquid in each sector is measured and recorded, the values are averaged to get a mean height. The levels of the sectors are normalized against the mean, and the standard deviation of the normalized values is calculated as indicated in Fig. 3, using the following definition for standard deviation:

$$\sigma = \left[\frac{\sum_{j=1}^{n} (y_j - \bar{y})^2}{n} \right]^{0.5} \quad (1)$$

Nomenclature

d_o = discharge orifice diameter, m
FN = flow number of atomizer $= \dot{m}_L/(\Delta P_L \cdot \rho_L)^{0.5}$, m^2
l_o = length of discharge orifice, m
$\dot{m}_L$ = liquid flow rate, kg/s
n = number of sectors in patternator
ΔP_L = injection pressure, P_a
t = liquid film thickness in discharge orifice, m
y_j = normalized height of liquid level in sector j
$\bar{y}$ = average value of y_j
μ_L = absolute liquid viscosity, kg/ms
ρ_L = liquid density, kg/m^3
σ = standard deviation of circumferential liquid distribution

Downloaded 02 Jun 2010 to 171.66.16.121. Redistribution subject to ASME license or copyright; see http://www.asme.org/terms/Terms_Use.cfm

Table 1 Properties of glycerine-water solutions at 20°C

Percentage glycerine by mass	Viscosity, kg / ms	Density, kg / m^3	Surface tension, kg / s^2
0	0.001	1000	0.0734
30	0.006	1110	0.0701
61	0.012	1152	0.0685

where n is the number of sectors, y_j is the normalized height of the liquid level in sector j ($j=1,2, \ldots, n$), and $\bar{y}$ is the average value of y_j, i.e.,

$$\bar{y} = \left(\sum_{j=1}^{n} y_j\right)/n \tag{2}$$

The normalized standard deviation, as calculated from Eq. (1), is indicative of the circumferential irregularity of the spray. However, as pointed out by Tate (1960a), the measured standard deviation varies appreciably with the total number of sectors employed; with fewer sectors the patternation appears better. This variable should therefore, be specified when reporting results. The patternator employed in the present study features 16 sectors.

Although the method described above is basically simple, there is a risk that the sampling technique itself might introduce errors into the measurement. To circumvent this possibility, the collecting vessel should be mounted on a flat, horizontal surface. The nozzle itself should not be skewed relative to the axis of the collecting vessel, which should be accurately centered and located at the appropriate distance from the nozzle.

The relevant properties of the liquids employed in this investigation are listed in Table 1. As indicated in this table, variation of liquid viscosity was accomplished by mixing water with glycerine to achieve viscosities of 0.001, 0.006, and 0.012 kg/ms. The viscosity was measured using a Haake model viscometer and was checked periodically to make sure that no significant change occurred when the mixture was recycled. Although the densities and surface tensions of the three liquids employed were slightly different, the variation of liquid viscosity by a factor of 12 may be considered to be dominant.

Results

In the course of this investigation a large amount of data was collected to demonstrate the effects of nozzle design features, nozzle operating conditions, and liquid viscosity on circumferential patternation (Chen, 1989). The data presented in Figs. 4–12 are typical of the results obtained.

Injection Pressure. Figures 4 and 5 illustrate the influence of injection pressure on circumferential distribution. Figure 4 shows the variation of σ with ΔP_L for l_o/d_o ratios of 0.5, 1.0, and 2.0, while Fig. 5 contains similar data for l_o/d_o ratios of 2, 3, and 4. Both figures show identical trends, namely, that σ declines, i.e., patternation improves with increase in injection pressure. This result is to be expected, because at low injection pressures the spray is not fully developed. Increase in injection pressure improves patternation by promoting more turbulence and better mixing in the swirl chamber. Although the data presented in Figs. 4 and 5 tend to suggest that patternation should continue to improve with further increases of injection pressure, Tate (1960b) noted that when the injection pressure is raised above around 2.4 MPa (350 psi), the patternation deteriorates. He attributes this to the disruptive effect on the spray of the highly turbulent air induced into the spray by the strong ejector action of the high-velocity liquid issuing from the nozzle.

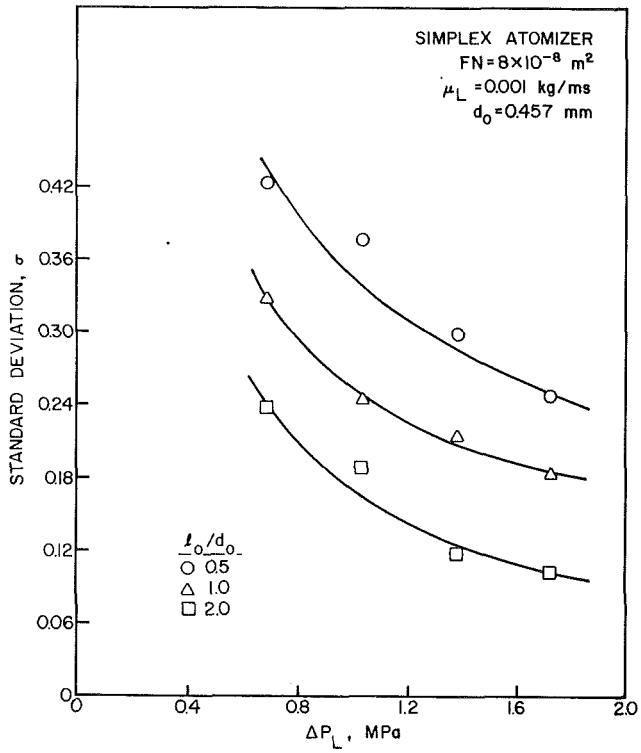

Fig. 4 Influence of injection pressure and l_o/d_o ratio on circumferential patternation

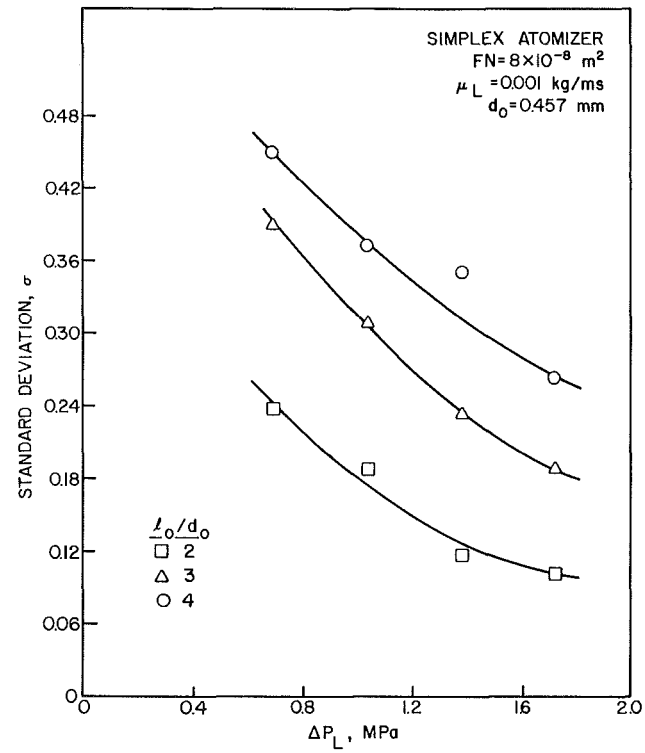

Fig. 5 Influence of injection pressure and l_o/d_o ratio on circumferential patternation

All simplex nozzles, including those employed here, have a limited flow range. To overcome this problem, various so-called "wide-range" atomizers have been proposed, of which the most widely used are the "duplex" and "dual-orifice." The duplex nozzle retains the single swirl chamber of the sim-

Downloaded 02 Jun 2010 to 171.66.16.121. Redistribution subject to ASME license or copyright; see http://www.asme.org/terms/Terms_Use.cfm

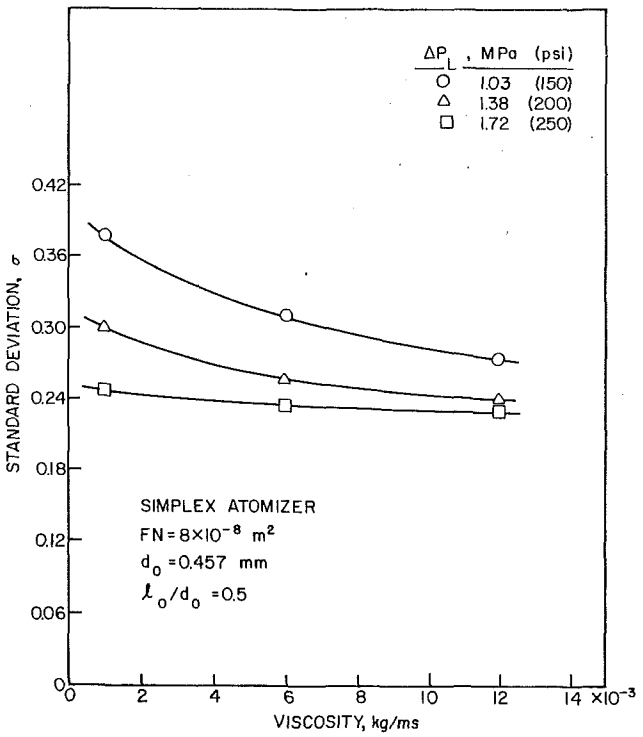

Fig. 6 Influence of liquid viscosity on circumferential patternation for an l_o/d_o ratio of 0.5

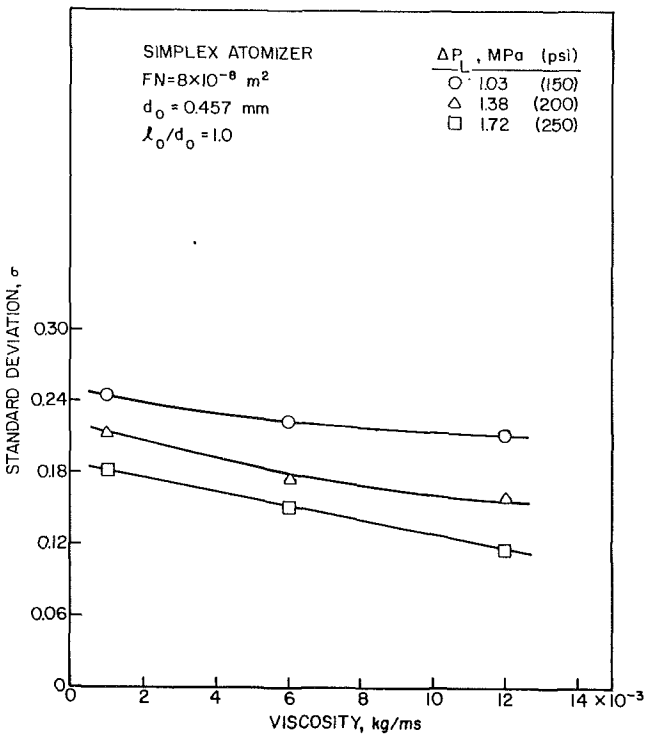

Fig. 7 Influence of liquid viscosity on circumferential patternation for an l_o/d_o ratio of 1.0

plex nozzle, but has two sets of feed slots, each having its own separate liquid supply. One set of slots is much smaller in cross-sectional area than the other. The small slots are termed *primary* and the large slots *secondary*. At low flow rates all the liquid to be atomized flows through the primary slots. At high flow rates liquid continues to be supplied to the primary slots but most of the liquid flows through the secondary slots. The dual-orifice atomizer is similar to the duplex nozzle except that two separate swirl chambers are provided, one for the primary flow and the other for the secondary flow. With both types of atomizer, when the secondary liquid first starts to flow it draws its energy for atomization from the primary spray, thereby reducing the effective injection pressure and hence also the quality of atomization. The results presented in Figs. 4 and 5 show that, at this condition of low effective injection pressure and reduced atomization quality, the circumferential patternation is also at its worst.

Liquid Viscosity. The beneficial effect of higher injection pressure on circumferential patternation, as illustrated in Figs. 4 and 5, is fully confirmed by the data presented in Figs. 6–8. These figures also show that patternation improves with increase in viscosity, but the effect is generally quite small except for the nozzle having an l_o/d_o of 0.5, which exhibits a significant reduction in σ with increase in viscosity at the lowest injection pressure.

The mechanism whereby liquid viscosity affects patternation is not obvious. By reducing the Reynolds number of the nozzle internal flow, and thereby reducing the energy available for mixing, an increase in viscosity might be expected to have an adverse effect on circumferential patternation. However, an increase in viscosity is known to increase the thickness of the annular liquid film formed in the final discharge orifice. According to Rizk and Lefebvre (1985) this thickness is proportional to the liquid viscosity raised to the one fourth power ($t \propto \mu_L^{0.25}$). Clearly a thicker liquid film will make the distributions of velocity and turbulence across the film less sensitive to the geometric imperfections on the wall surface. Moreover,

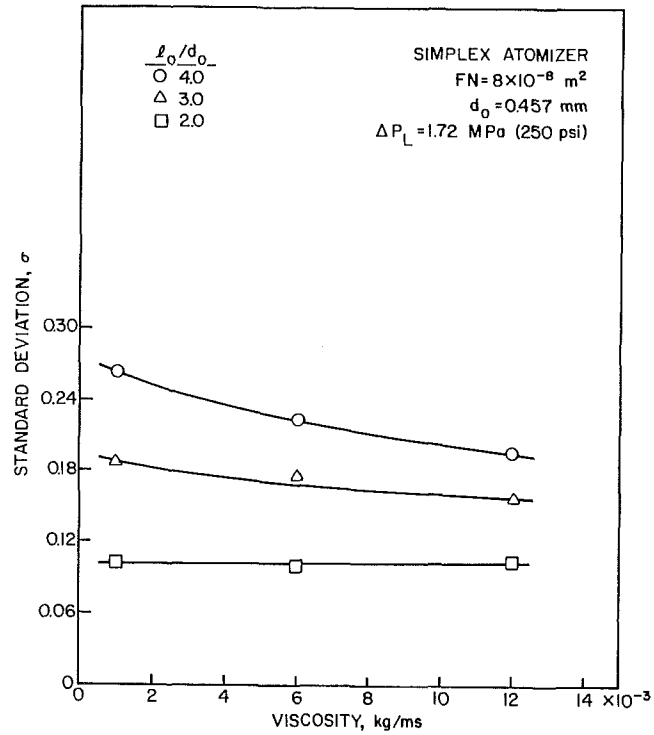

Fig. 8 Influence of liquid viscosity on circumferential patternation for high l_o/d_o ratios

a thicker film is likely to have a more uniform thickness. Which of these two different mechanisms will dominate at any given flow condition will depend on the nozzle geometric design features and the injection pressure. For the range of viscosities encompassed in this investigation, an increase in liquid viscosity tends to improve patternation, but the effect is generally quite small in comparison to the ΔP_L effect.

Downloaded 02 Jun 2010 to 171.66.16.121. Redistribution subject to ASME license or copyright; see http://www.asme.org/terms/Terms_Use.cfm

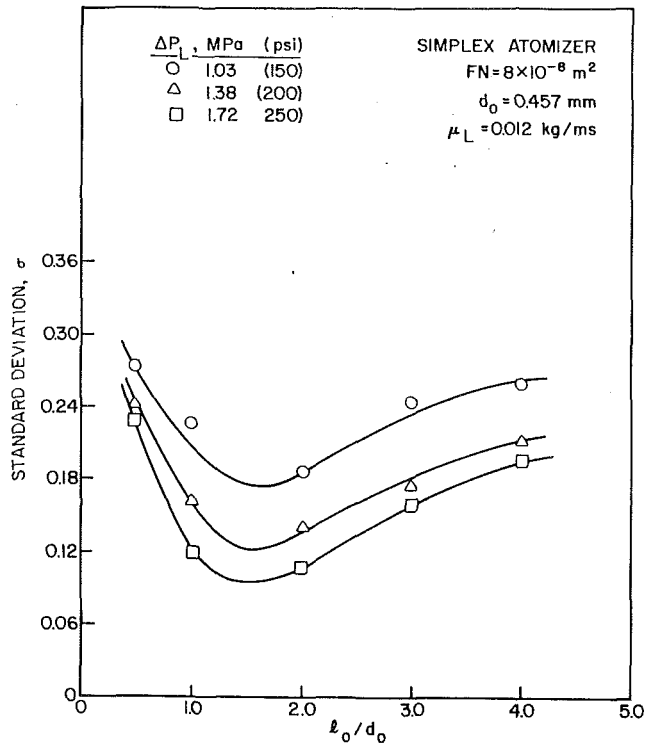

Fig. 9 Influence of l_o/d_o ratio and injection pressure on circumferential patternation

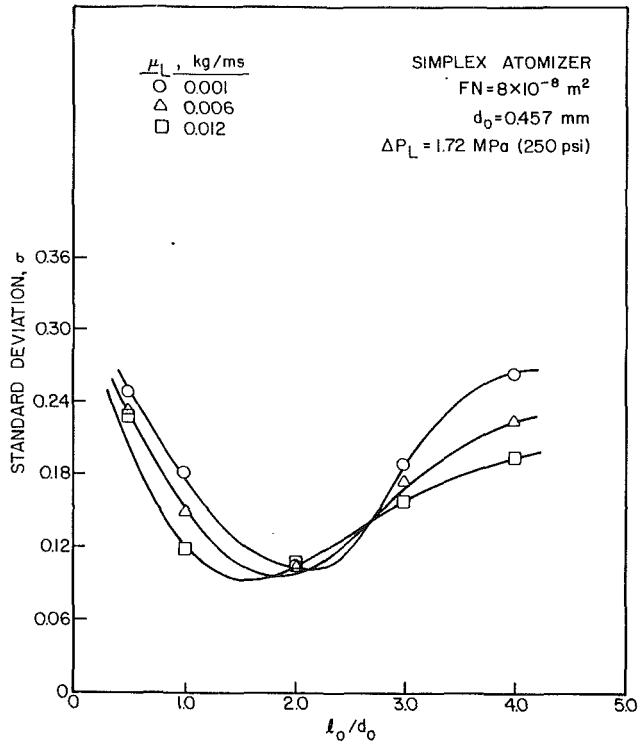

Fig. 11 Influence of l_o/d_o ratio and liquid viscosity on circumferential patternation for $\Delta P_L = 1.72$ MPa

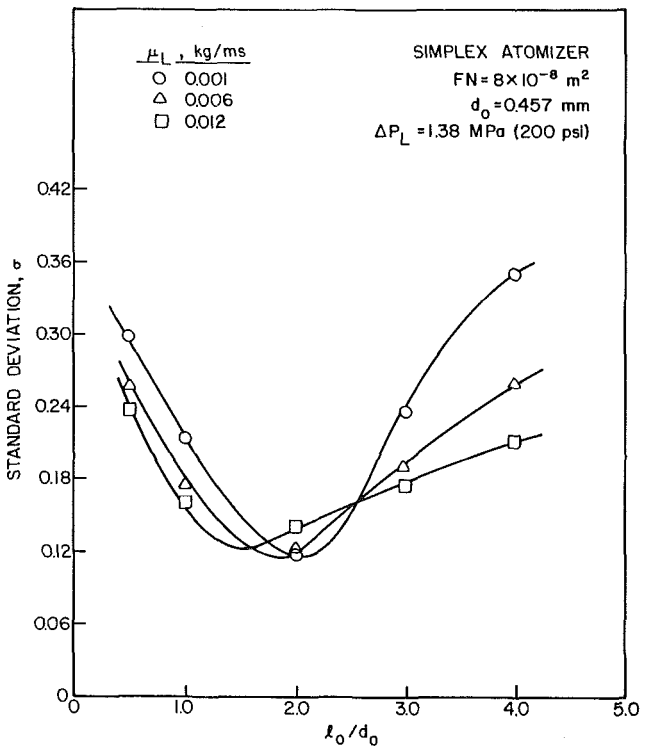

Fig. 10 Influence of l_o/d_o ratio and liquid viscosity on circumferential patternation for $\Delta P_L = 1.38$ MPa

Discharge Orifice Length/Diameter Ratio. The influence of nozzle l_o/d_o ratio on patternation is illustrated in Figs. 9–11. Figure 9 shows, for all values of injection pressure, that an increase in l_o/d_o over the range from 0.5 to approximately 2.0 causes the standard deviation σ to decline, i.e., the circumferential liquid distribution becomes more uniform. However, further increase in l_o/d_o beyond a value of around 2.0 has an adverse effect on spray patternation. It is believed, for the range of l_o/d_o from 0.5 to around 2.0, that continual increase in orifice length tends to produce a thicker and more uniform film at the orifice exit, thereby creating a more uniform circumferential distribution of liquid in the spray. The factors underlying the increase in σ for l_o/d_o ratios higher than around two are unclear. One possibility is that a longer discharge orifice causes the circumferential uniformity of the liquid film to become more dependent on the surface condition of the inside of the final orifice, thus a nonuniform liquid film might reappear if the final orifice is too long. It is interesting to note that one of the authors (AHL) made a similar observation some years ago when attempting to determine the optimum length for the prefilming surface of an airblast atomizer. It was noted that striations in the liquid sheet, caused by the feed jets emerging from a finite number of slots onto the prefilming surface, almost disappeared at a certain distance along the prefilming surface, only to reappear again in the flow region farther downstream. At the time, it was concluded that either too long or too short a prefilming surface would result in nonuniformities in the thickness of the liquid film formed at the prefilming edge. It is possible that a similar flow phenomenon is responsible for the results outlined above on the influence of discharge orifice length/diameter ratio on spray patternation.

Also of interest in Figs. 10 and 11 is that a higher liquid viscosity moves the value of l_o/d_o at which the standard deviation is a minimum toward a lower value.

Number of Distributor Slots. The effect of the number of feed slots on circumferential distribution is shown in Fig. 12. The baseline atomizer has three equispaced slots. For this atomizer, the effect of an increase in injection pressure from 0.69 to 1.72 MPa (100 to 250 psi) is to improve patternation by reducing the value of σ from 0.33 to 0.18. Reducing the number of equispaced slots from three to two has little effect on circumferential patternation. The curve drawn in Fig. 12

Downloaded 02 Jun 2010 to 171.66.16.121. Redistribution subject to ASME license or copyright; see http://www.asme.org/terms/Terms_Use.cfm

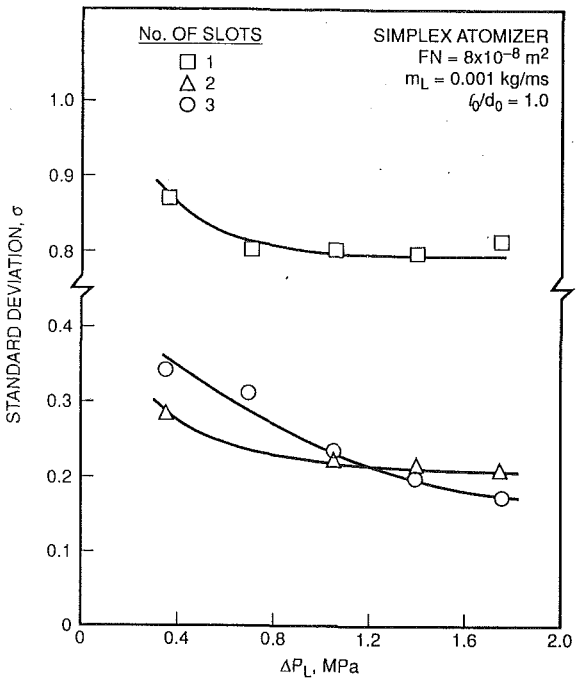

Fig. 12 Effect of number of feed slots on circumferential patternation

through the data points obtained with this nozzle exhibits a lower dependence on injection pressure than the three-slot nozzle, but on the average the values of σ are about the same. If the number of feed slots is further reduced, so that all the liquid is injected into the swirl chamber through a single slot, the resulting circumferential distribution is extremely poor, as shown in Fig. 12.

Summary and Conclusions

The experimental work conducted in this investigation was undertaken to study the effects of several parameters on the circumferential liquid distribution of the sprays produced by simplex atomizers featuring three equispaced distributor slots. The injection pressures employed were in the range from 0.34 to 1.72 MPa (50 to 250 psi). Liquid viscosity was varied from 0.001 to 0.012 kg/ms. Variation in discharge orifice length/diameter ratio was from 0.5 to 4.0. Two additional nozzles, having either one or two feed slots of the same total flow area as the three-slot nozzles, were also tested.

From the results obtained during this investigation, the following conclusions are drawn:

1 Spray patternation improves, i.e., the circumferential liquid distribution becomes more uniform, with increase in injection pressure over the range from 0.34 to 1.72 MPa (50 to 250 psi).
2 Patternation is improved slightly by an increase in liquid viscosity.
3 An increase in l_o/d_o from 0.5 to 2.0 improves the patternation. However, further increase in l_o/d_o, in the range from 2.0 to 4.0, has an adverse effect on patternation. This has important implications for the design of pressure-swirl atomizers.
4 The optimum value of l_o/d_o for the best patternation is reduced by an increase in liquid viscosity.

References

Chen, S. K., 1989, "An Investigation on Performance of Pressure-Swirl Atomizers for Small Gas Turbines," M.S. thesis, School of Mechanical Engineering, Purdue University, West Lafayette, IN.

Chen, S. K., Lefebvre, A. H., and Rollbuhler, J., 1991, "Influence of Liquid Viscosity on Pressure-Swirl Atomizer Performance," *Atomization and Sprays*, Vol. 1, No. 1, pp. 1–22.

Chen, S. K., Lefebvre, A. H., and Rollbuhler, J., 1992, "Factors Influencing the Spray Cone Angle of Pressure-Swirl Atomizers," ASME JOURNAL OF ENGINEERING FOR GAS TURBINES AND POWER, Vol. 114, pp. 97–103.

Cohen, J. M., and Rosfjord, T. J., 1992, "Spray Patternation at High Pressure," *AIAA J. Propul. Power*, Vol. 7, No. 4, pp. 481–487.

Lefebvre, A. H., 1983, *Gas Turbine Combustion*, Hemisphere Publishing Corp., New York.

Rizk, N. K., and Lefebvre, A. H., 1985, "Internal Flow Characteristics of Simplex Swirl Atomizers," *AIAA J. Propul. Power*, Vol. 1, No. 3, pp. 193–199.

Tate, R. W., 1960a, "Spray Patternation," *Ind. Eng. Chem.*, Vol. 52, No. 10, pp. 49–52.

Tate, R. W., 1960b, "Spray Patternation; a Significant Variable in Fuel Combustion and Chemical Processes Using Atomizing Nozzles," *Equipment and Design*, Vol. 50, No. 10, pp. 49A–55A.

Downloaded 02 Jun 2010 to 171.66.16.121. Redistribution subject to ASME license or copyright; see http://www.asme.org/terms/Terms_Use.cfm

Scaling of the Two-Phase Flow Downstream of a Gas Turbine Combustor Swirl Cup: Part I—Mean Quantities

H. Y. Wang

V. G. McDonell

W. A. Sowa

G. S. Samuelsen

UCI Combustion Laboratory,
University of California,
Irvine, CA 92717-3550

A production gas turbine combustor swirl cup and a 3 ×-scale model (both featuring co-axial, counterswirling air streams) are characterized at atmospheric pressure. Such a study provides an opportunity to assess the effect of scale on the behavior of the continuous phase (gas in the presence of spray) and droplets by comparing the continuous phase velocity, droplet size, and droplet velocity at geometrically analogous positions. Spatially resolved velocity measurements of the continuous phase, droplet size, and droplet velocity were acquired downstream of the production and 3 ×-scale swirl cups by using two-component phase-Doppler interferometry in the absence of reaction. While the continuous phase flow fields scale well at the exit of the swirl cup, the similarity deviates at downstream locations due to (1) differences in entrainment, and (2) a flow asymmetry in the case of the production hardware. The droplet velocities scale reasonably well with notable exceptions. More significant differences are noted in droplet size, although the presence of the swirl cup assemblies substantially reduces the differences in size that are otherwise produced by the two atomizers when operated independent of the swirl cup.

Introduction

Co-axial, counterswirling air streams have been studied for a variety of applications in combustion and other systems. Most of the studies have been conducted at nonreacting, single-phase (i.e., gas phase in the absence of spray) conditions. Some of these studies (e.g., Habib and Whitelaw, 1980; Vu and Gouldin, 1982; Gouldin et al., 1983) observe that only counterswirl produces recirculation, while others (e.g., Samimy and Langenfeld, 1988; Mehta et al., 1989) find that both coswirl and counterswirl can generate a recirculation zone.

One of the practical applications featuring two co-axial counterswirling streams is the GE SNECMA CFM56 engine combustor swirl cup (Fig. 1). Fuel is injected by a simplex atomizer mounted in the center of the swirl cup. A portion of the droplets convect directly downstream while the remainder impinge onto the inner surface of a primary venturi (which separates the primary swirling air from the secondary swirling air), form a thin liquid film, and are re-atomized in the shear field produced between the two counterswirling air streams. A goal of this swirl cup assembly is to produce a uniformly distributed field of similarly sized fine droplets.

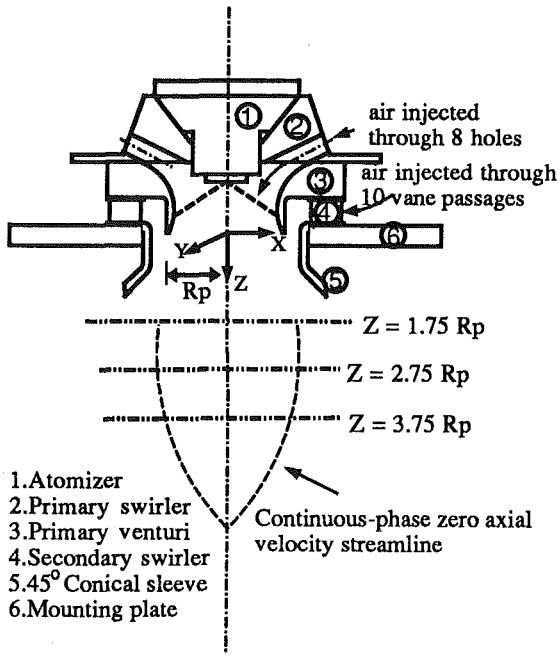

Fig. 1 Swirl cup assembly

Contributed by the International Gas Turbine Institute and presented at the 37th International Gas Turbine and Aeroengine Congress and Exposition, Cologne, Germany, June 1-4, 1992. Manuscript received by the International Gas Turbine Institute February 6, 1992. Paper No. 92-GT-207. Associate Technical Editor: L. S. Langston.

Copyright © 1993 by ASME
Downloaded 02 Jun 2010 to 171.66.16.121. Redistribution subject to ASME license or copyright; see http://www.asme.org/terms/Terms_Use.cfm

Table 1 Characteristics of the PDI

	1×	3×
Transmitter		
0.5145 μm line (U, D)*		
Fringe spacing (μm)	9.03	9.88
Waist (μm)	223.32	187.17
0.4880 μm line (V or W)[2]		
Fringe spacing (μm)	9.31	9.84
Waist (μm)	211.82	177.53
Receiver		
Collection lens (mm)	629 f/5.7	1000 f/9.3
Focusing lens (mm)	238	238
Spatial filter (μm)	100	100
Collection angle	30 deg off-axis forward	

*U, V, W, and D are axial, radial, tangential velocity, and droplet diameter, respectively.

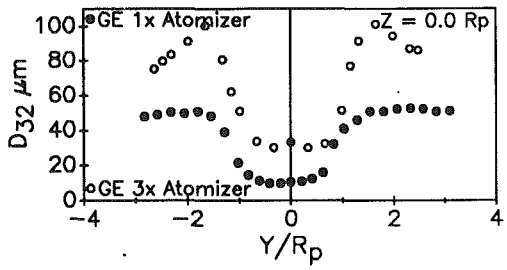

Fig. 2 Comparison of D_{32} between atomizers in the absence of the swirl cup assemblies

Due to the complexity of the co-axial, counterswirling air flows and the lack of adequate advanced diagnostics, few studies have been conducted on the two-phase behavior in the presence of such flows. Only recently have such flows been considered in a series of tests conducted at the UCI Combustion Laboratory (e.g., Wang et al., 1991a, b, c; 1992a).

The studies have been conducted at two scales. First, tests have been completed in a 3×-scale model. Secondly, measurements have been acquired in production hardware (i.e., "1×-scale"). While the purpose of the tests was to provide data in support of spray modeling, the results offer a unique opportunity as well to study (1) the extent to which the results scale on the basis of geometric similarity, and (2) the behavior of droplets at two geometrically similar scales.

In the present study, the time-averaged droplet size and velocity distributions are compared downstream of the production hardware and the 3×-scale model of the swirl cup. The liquid and air mass flow rates in the 1× test are about 1/9 of those in the 3× test, following the ratio of the air inlet area of the practical swirl cup to that of the 3×-scale model swirl cup. The purpose of this choice was to maintain a constant velocity from the swirling air outlet and a constant liquid loading rate (or air-to-liquid ratio) for both the 1×- and 3×-scale tests.

Experiment

Swirl Cup Assembly. Hago simplex atomizers, having flow numbers of 0.65 and 7.30 (based on ratio of flow rate, in lb/hr, to square root of injection pressure differential, in lb/in.[2]), were used in the 1×- and 3×-scale tests, respectively. A 6.35 mm polycarbonate honeycomb (101.6 mm thick) was placed 50 mm above the top of the swirl cup in both cases to provide a uniform velocity profile at the entrance plane to the swirlers.

Characterization Chamber. Two different characterization chambers were utilized. Although not specifically designed for these tests, each chamber was similar in design, and that used for the 3×-scale test was a 2.7-scale version of that used for the 1×-scale tests. In both chambers, the test article was centrally located within a square duct (495 mm × 495 mm for 1×-scale; 1330 mm × 1330 mm for 3×-scale) and oriented downward. The test article was attached to a vertical traverse, which was connected to the chamber. The chamber itself was suspended from an optical table using a two-dimensional traverse, thus giving the test article three degrees of freedom. In each case, the diagnostics were fixed, and the test article was moved. Additional details about each facility are available elsewhere (3×-scale: Wang et al., 1990; 1×-scale: Wang et al., 1991c, and McDonell and Samuelsen, 1991).

Instruments. A two-component phase-Doppler interferometer (PDI) (Aerometrics Model 3100-S) was used to measure the droplet size and velocities. An Ar^+ laser provided the laser beams for the PDI measurements. The PDI setup used for both tests is shown in Table 1.

Test Condition and Sample Points

Test Condition. The inlet area of the swirlers for the production swirl cup is 1/9 of the 3×-scale model. To make the air outlet velocities through the 1× swirlers the same as those of the 3×-scale model, the 1×-scale tests were conducted at an air flow rate of 0.017 kg/s (30.2 scfm), which is 1/9 of the air flow rate used in the 3×-scale test.

Water was used in both tests. To maintain the liquid-to-air ratio the same as a stoichiometric ratio of a kerosene fuel (about 14.78), the liquid flow rate of the production and 3×-scale swirl cups should be 1.1 g/s and 10.0 g/s, respectively. While the 3×-scale tests were conducted at 10.0 g/s (Wang et al., 1991a, b), the 1×-scale hardware was operated at 0.86 g/s due to flow limitations in the test stand. This provided a liquid-to-air loading rate of 5.0 percent rather than 6.5 percent in the 3×-scale model test. However, the swirl cup flow field is dominated by the aerodynamics (Wang et al., 1991a, b), and this difference is considered negligible with respect to affecting both the gas-phase flow and droplet dispersion.

Sample Points. The measurements were conducted at three axial locations: Z = 1.75, 2.75, and 3.75 R_p (where R_p is the radius of the primary venturi exit plane), and along the centerline of the swirl cup. The origin of the coordinates is at the center of the primary venturi exit plane. R_p for the 1×- and 3×-scale fixtures is 9.7 mm and 29.2 mm, respectively.

Results and Discussion

From the myriad of data collected, selected measurements are presented and specific characteristics are identified that are particularly germane to the behavior observed at both scales.

Atomizer Comparison in the Absence of the Swirl Cup. The two atomizers were characterized in the absence of the swirl cup assemblies to provide a baseline against which to compare differences observed in the presence of the swirl cup. An example is shown in Fig. 2. While large differences in D_{32} are observed due to the geometric difference in size and the order of magnitude difference in mass flow, far less difference is observed in the presence of the swirl cup assemblies.

Comparison of 1×- and 3×-Scale Swirl Cup Results. In the following, comparisons are presented for radial profiles at three axial planes (Z = 1.75 R_p, 2.75 R_p, and 3.75 R_p). In addition, for the velocity results, a centerline profile is included and appears in the top portion of the figure. Data are provided for the following representative droplet size groups:

- "Small" 11–20 μm
- "Medium-Sized" 30–40 μm
- "Large" 74–88 μm

Droplet Size and Data Rate. As shown in Fig. 3, the dif-

Downloaded 02 Jun 2010 to 171.66.16.121. Redistribution subject to ASME license or copyright; see http://www.asme.org/terms/Terms_Use.cfm

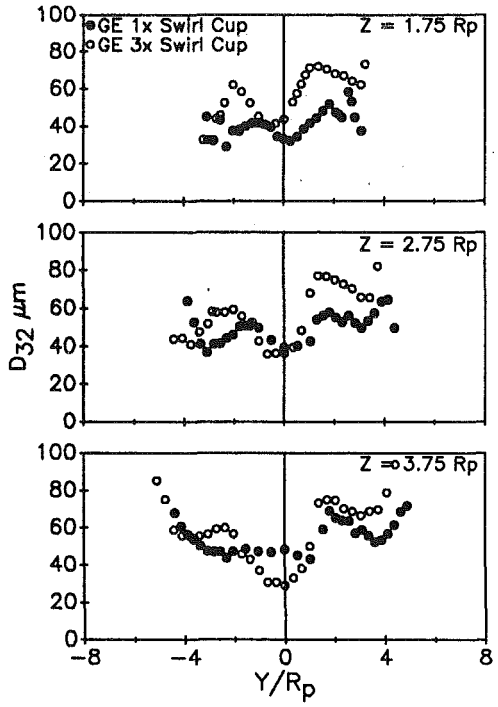

Fig. 3 Comparison of droplet distribution D_{32}

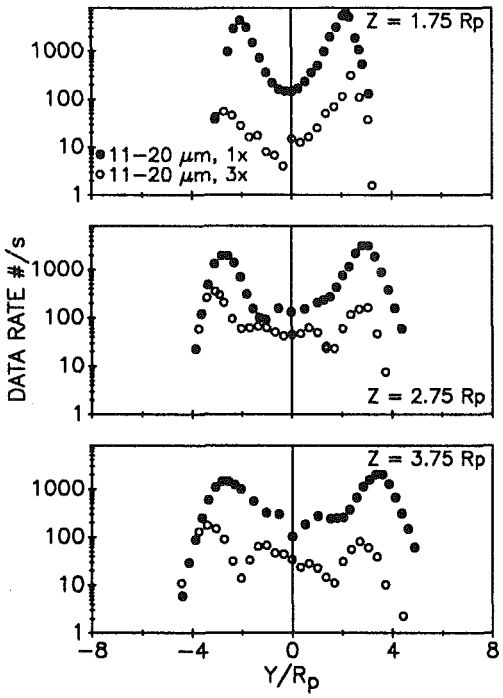

Fig. 4(*a*) Small droplets

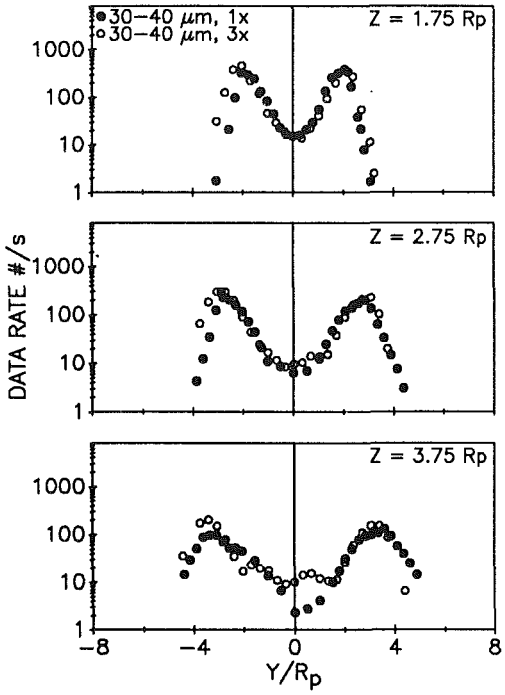

Fig. 4(*b*) Medium-sized droplets

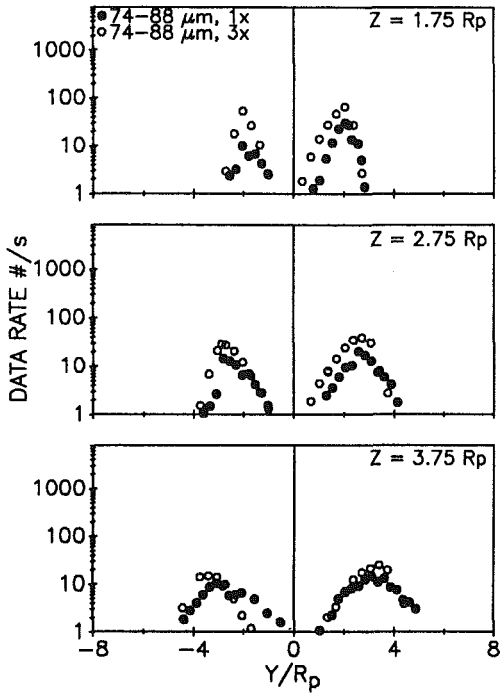

Fig. 4(*c*) Large droplets

Fig. 4 Comparison of droplet data rate

ferences in D_{32} are substantially reduced in the case of the swirl cup. While the D_{32} in the 3×-scale case is systematically greater than in the 1× case, the differences are reduced as the flow evolves downstream. The larger droplet size distribution for the 3×-scale case is attributed to the differences in the initial droplet size distribution.

Additional insight is offered by the data rate results shown in Fig. 4. Compare, for example, the data rate of droplet arrival for the large and small droplets. At the first axial location ($Z = 1.75\ R_p$), the data rate of the small droplets is greater for the 1×-scale (Fig. 4*a*), and the data rate for the larger droplets is greater for the 3×-scale (Fig. 4*c*). Note the remarkable correspondence for the medium-sized droplets (Fig. 4*b*). This is the one large population of droplets that both scales share in common. This data set also reveals the first evidence of the effect of scale on droplet entrainment. At the centerline of the $Z = 3.75\ R_p$ location, the data rate of the 1×-scale falls relative to the 3×-scale. These data, along with the mean axial and radial velocity data, reveal a dispropor-

Downloaded 02 Jun 2010 to 171.66.16.121. Redistribution subject to ASME license or copyright; see http://www.asme.org/terms/Terms_Use.cfm

tionate entrainment of medium-sized droplets in the 3×-scale case. Note also the associated impact on the D_{32} results at $Z = 3.75\ R_p$ (Fig. 3). The twin-peak droplet data rate distributions in both cases suggest that the region downstream of the primary venturi is highly populated with droplets and thus high in liquid volume flux.

Mean Axial Velocities. Figure 5 presents results for the mean axial velocity. At the exit of the swirl cup, the axial velocity profiles of the continuous phase are identical for both cases (Fig. 5*a*). Downstream, modest but significant deviations occur. For example, the centerline profile reveals that a slightly longer recirculation zone exists downstream in the 3×-scale test and the $Z = 3.75\ R_p$ profile shows that the recirculation zone is wider as well. This is attributed to differences in entrainment rates between the two cases.

The 1×-scale data at $Z = 3.75\ R_p$ also reveal an asymmetry in the flow of the practical hardware. The flow field of the 3×-scale model swirl cup is, in contrast, symmetric due to a stronger axial momentum.

The behavior of the droplets is shown in Figs. 5(*b–d*). The small droplets for both the 1×- and 3×-scale tests mirror the continuous phase (Fig. 5*b*) with one notable exception. At $Z = 1.75\ R_p$, the small droplets in the 1×-scale test have not fully relaxed to the continuous phase velocity. This is the first concrete example of the differences in time between the two scales for droplets to acclimate. The medium-sized droplets in the 3×-scale test also reflect this (Fig. 5*c*). In addition, the large droplets in the 3×-scale case are recirculated at $Z = 3.75\ R_p$, whereas those in the 1×-scale case are not (Fig. 5*d*). The differences are attributed to the relatively long distance traveled from the atomizer to the same geometrically analogous points in the 3×-scale test compared to the 1×-scale test. Given that the droplet velocities are similar in each case, the medium-sized droplets have more time to approach the velocity of the continuous phase at the same geometrically analogous point in the 3×-scale test than in the 1×-scale test. Note the relatively analogous mean axial velocities at the first axial location for both cases.

Mean Radial Velocities. Figure 6(*a*) compares the mean radial velocities of the continuous phase. Positive values on the $+Y$ side and negative values on the $-Y$ side indicate velocities away from the centerline.

Near the swirl cup, the velocities scale remarkably well. Note in particular the evolution of the 3×-scale mean radial velocities downstream. At $Z = 3.75\ R_p$, for example, away from the centerline the flow is radially outward, whereas close to the centerline the flow is toward the centerline. Downstream of the $Z = 1.75\ R_p$ location, the asymmetry in the production hardware is clearly evident. Both the centerline and radial profiles reveal a nonzero centerline velocity due to a mismatch of the aerodynamic and geometric centerlines.

As with the mean axial velocity, the radial velocities of the droplets are well scaled at the upstream location $Z = 1.75\ R_p$. Downstream, the mean radial velocities for the small (Fig. 6*b*)

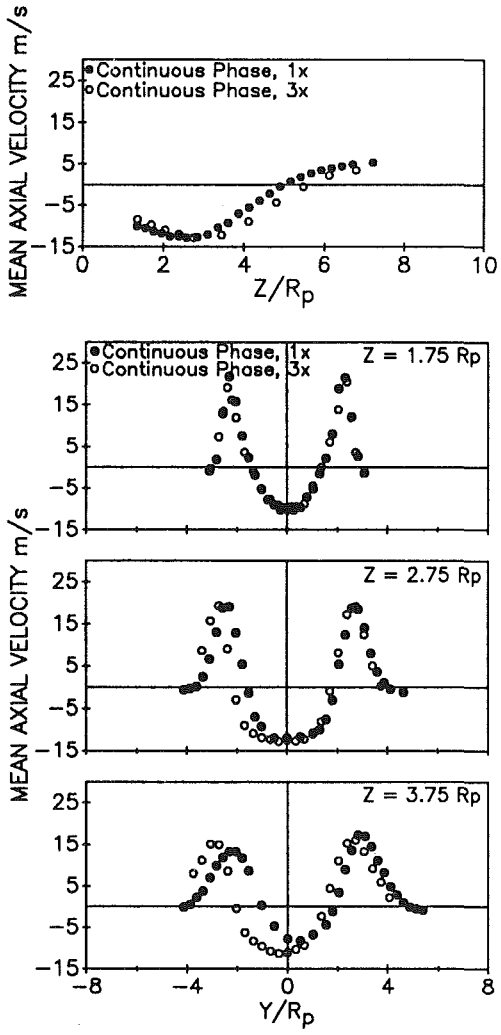

Fig. 5(*a*) Continuous phase

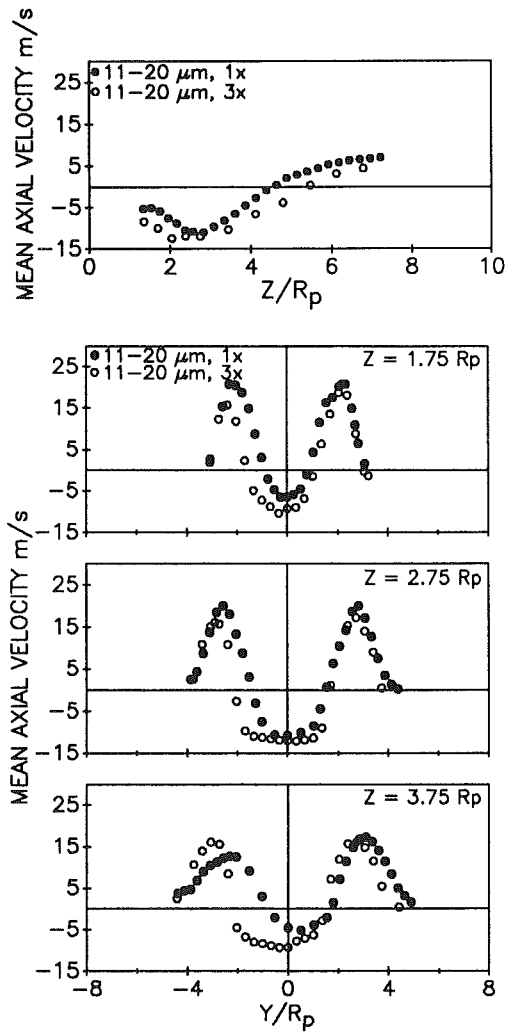

Fig. 5(*b*) Small droplets

Fig. 5 Comparison of mean axial velocity

Downloaded 02 Jun 2010 to 171.66.16.121. Redistribution subject to ASME license or copyright; see http://www.asme.org/terms/Terms_Use.cfm

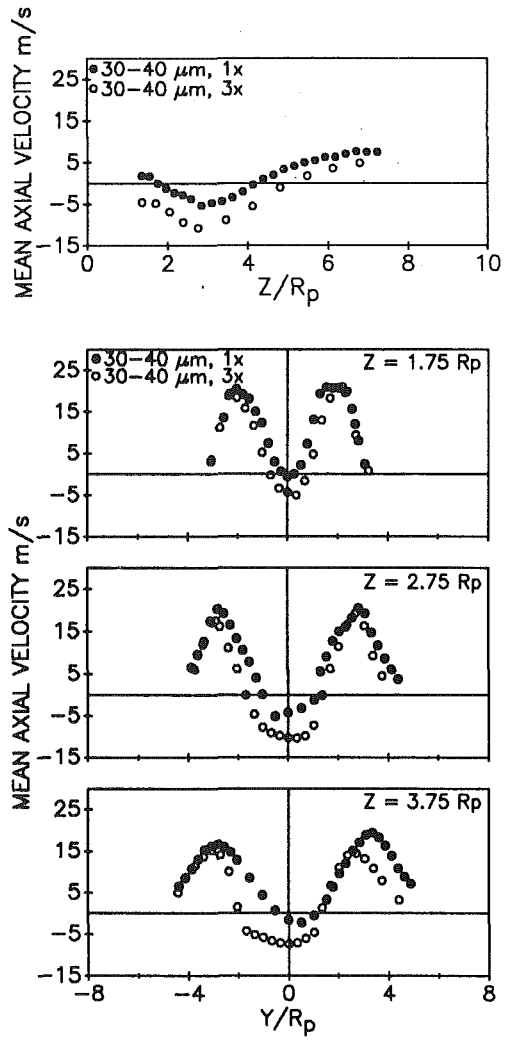

Fig. 5(c) Medium-sized droplets

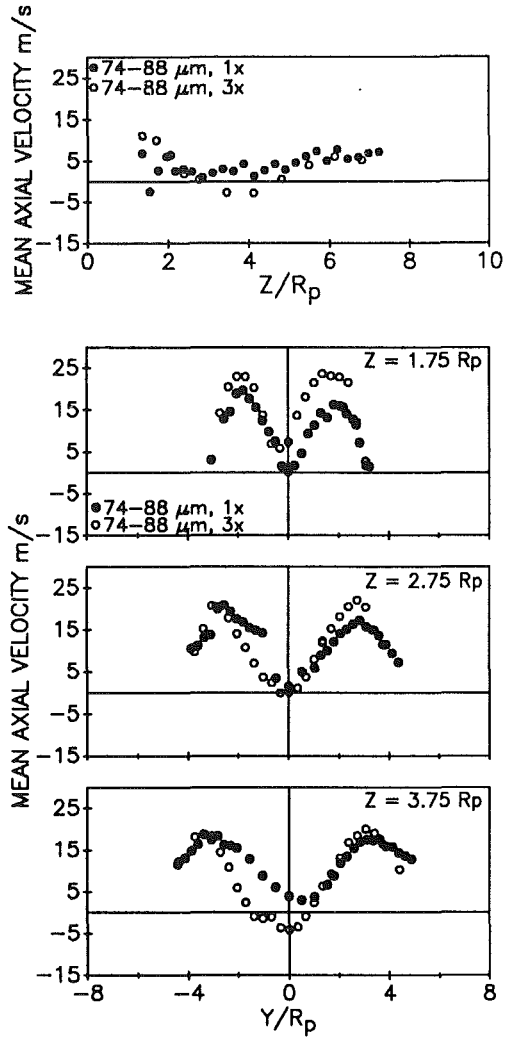

Fig. 5(d) Large droplets

Fig. 5 (continued)

and medium-sized (Fig. 6*c*) droplets reflect an asymmetry in the 1× test observed in the continuous phase. Because of the insensitivity of the large droplets to the influence of the gas-phase flow field, the mean radial velocity of the large droplets is more symmetric, in the 1× test, than that of the small and medium-sized droplets (Fig. 6*d*).

Noteworthy at $Z = 3.75\ R_p$ is the inward flow of small- and medium-sized droplets to the centerline for the 3×-scale case. This again mirrors the continuous phase. The large droplets are unaffected.

Mean Tangential Velocities. The continuous phase mean tangential velocities are presented in Fig. 7(*a*). Looking downstream from the swirl cup, positive values on the $+X$ side and negative values on the $-X$ side reflect counterclockwise rotation. At $Z = 1.75\ R_p$, the results appear "noisy." In fact, the data reflect a subtle behavior and, at $Z = 2.75\ R_p$, the results are similar. Specifically, the radial location where the peak tangential velocities occur is the same and the decay of the profiles is similar. Unlike the mean axial and radial velocities, the tangential velocities of both scales are not precisely matched at $Z = 1.75\ R_p$. The droplet behavior provides the explanation.

The droplet mean tangential velocities, presented in Figs. 7(*b–d*), provide especially interesting insights with respect to the effect of scale. In particular, the droplet mean tangential velocity distributions display differences in magnitude and trend not observed in either the axial or radial velocity.

The mean tangential velocity distribution of the small droplets is presented in Fig. 7(*b*). The data for the small and medium-sized droplets in the 1×-scale test reveal a twin-peak distribution on either side of the centerline, with one inside the recirculation zone and the other outside of it. To understand the peaks, the sources from which droplets emanate to this point must be identified: (1) droplets recirculating while swirling counterclockwise, (2) droplets produced from the edge of the venturi (dominated by the counterclockwise-swirling secondary air), and (3) droplets injected directly from the atomizer, which are dominated by the clockwise rotating primary air. The relative contribution of these three sources results in strong bimodal velocity distributions (Wang et al., 1991b). What is different here is how the scale affects the sign of the peak. The major question is whether droplets directly injected from the atomizer with clockwise rotation can overcome the negative pressure gradient of the recirculation zone and penetrate to this point.

The small droplets (Fig. 7*b*) show two positive peaks at $Z = 1.75\ R_p$. Outside the recirculation zone, the counterclockwise rotating secondary air is dominant, and inside the recirculation zone the counterclockwise rotating circulation overpowers the clockwise rotating droplets emanated from the atomizer directly. Note that the 3×-scale data are significantly

Downloaded 02 Jun 2010 to 171.66.16.121. Redistribution subject to ASME license or copyright; see http://www.asme.org/terms/Terms_Use.cfm

less precise than the mean axial and radial velocities at $Z = 1.75\ R_p$. Clearly, scale and the associated differences in entrainment, and droplet residence time have a major impact.

The behavior of the medium-sized droplets is especially insightful. The 3×-scale data at $Z = 1.75\ R_p$ mirror the small droplet data. The 1×-scale data, however, reveal a strong counterclockwise rotation in the recirculation zone, indicating that insufficient droplet residence time is available for these sized droplets to accelerate to the locally counterclockwise swirling flow.

Large droplets penetrate farther in the axial direction, as shown in Fig. 7(*d*). In this case, only two of the above sources contribute because very few large droplets are recirculated. As a result, the measurements consist of clockwise rotating droplets, which arrive directly from the atomizer and counterclockwise droplets arriving from the venturi. The behavior of the large droplets is similar for both cases because, compared to the small- and medium-sized droplets, their relaxation time is longer whereas their residence time is relatively shorter.

In both cases, with increasing axial distance downstream, the twin-peak distribution transitions into a single-peak distribution because the flow is dominated by the counterclockwise swirling secondary air flow.

Conclusions

The behavior of the continuous phase and droplets in the flow field downstream of a production and a 3×-scale model engine combustor swirl cup has been studied. Conclusions drawn from the study are as follows:

- The continuous phase scales well at the exit of the swirl cup in the present cases because the low liquid loading ratio has little affect on the flow. Farther downstream, scaling is difficult to evaluate because of differences in entrainment and the presence of asymmetries, especially with the production hardware.
- The droplets reflect the continuous-phase flow field to a varying degree depending upon droplet size or droplet relaxation time scale. The different behavior of droplets of different size can be explained successfully in terms of droplet relaxation time scale and the sources of droplets. The different behavior of droplets of same size in both cases can be interpreted by different droplet residence time reaching the same geometrically analogous point and the origins of these droplets.
- In spite of the differences in the atomizer characteristics, the behavior of the droplet size and velocity is similar in both the production (1×-scale) and 3×-scale swirl cups, indicating that, for this particular hardware and operating condition, the continuous phase dominates the flow field and droplet dispersion.
- The droplet D_{32} in the 3×-scale is generally greater than that in the 1×-scale. This is due, in part, to differences in the initial droplet size distribution produced by the two atomizers.

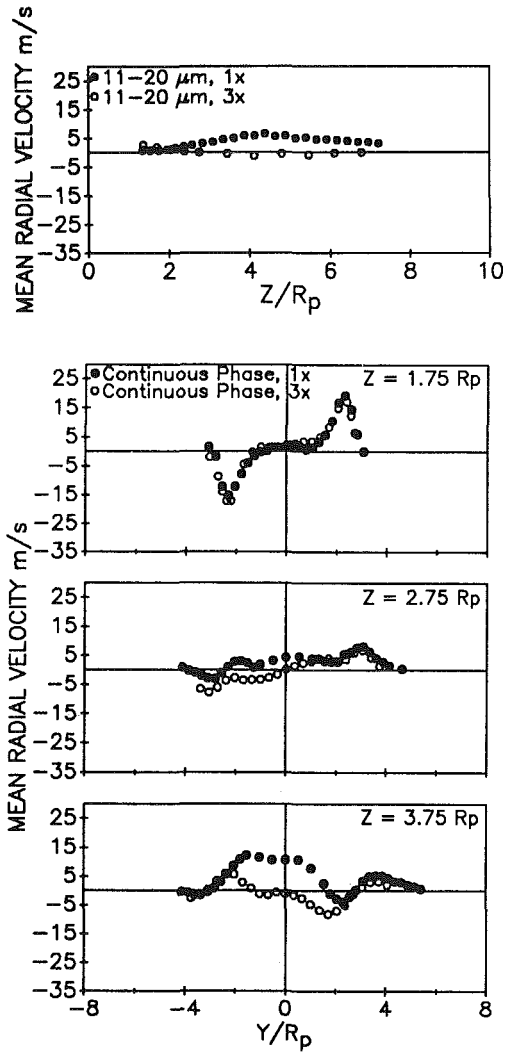

Fig. 6(*a*) Continuous phase

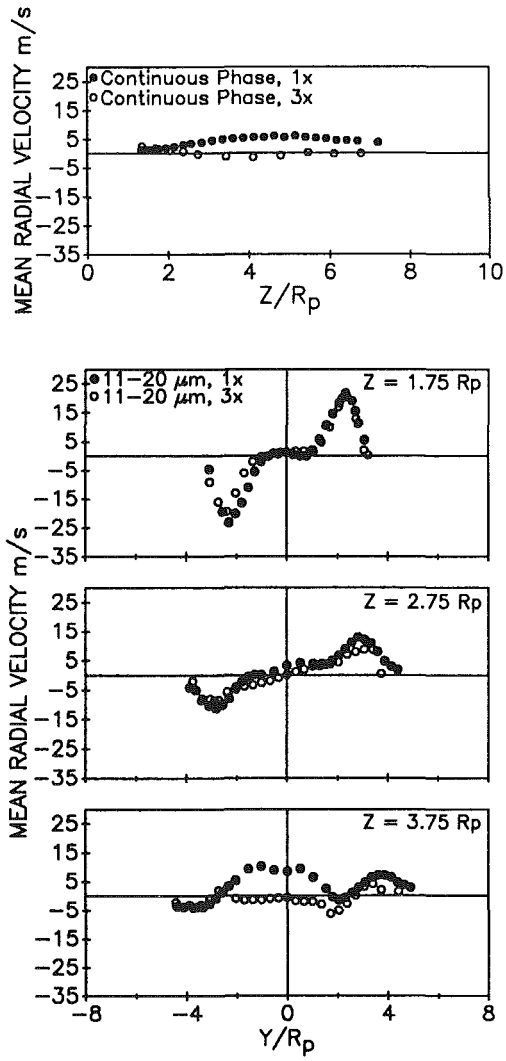

Fig. 6(*b*) Small droplets

Fig. 6 Comparison of mean radial velocity

Downloaded 02 Jun 2010 to 171.66.16.121. Redistribution subject to ASME license or copyright; see http://www.asme.org/terms/Terms_Use.cfm

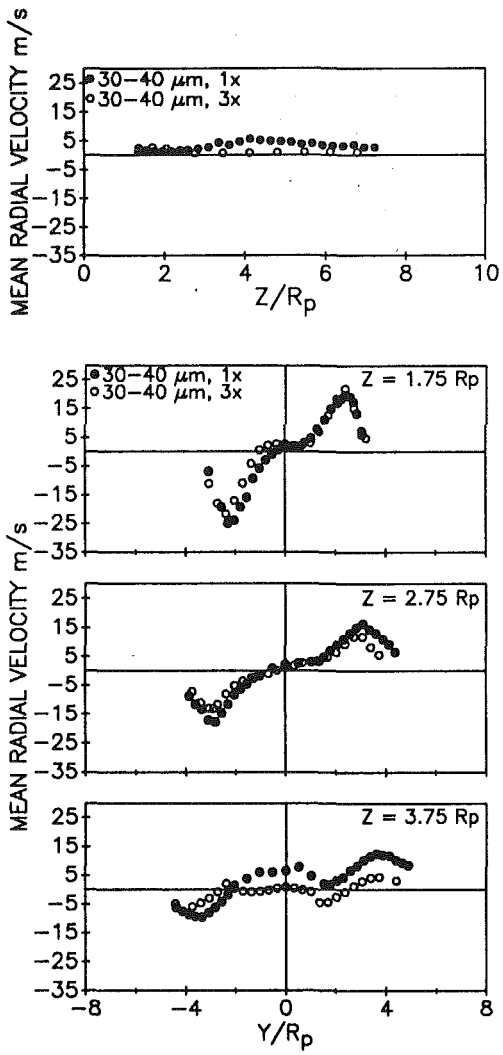

Fig. 6(*c*) Medium-sized droplets

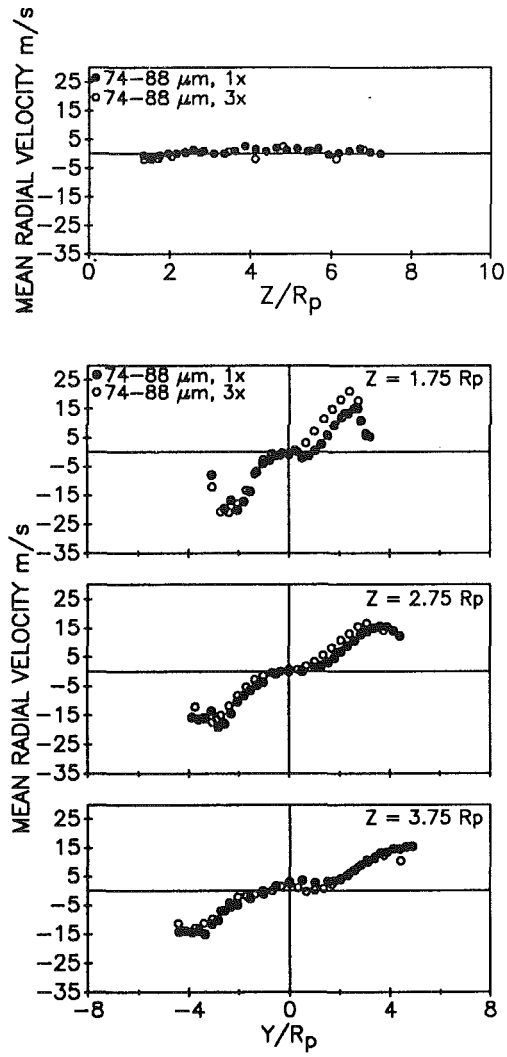

Fig. 6(*d*) Large droplets

Fig. 6 (continued)

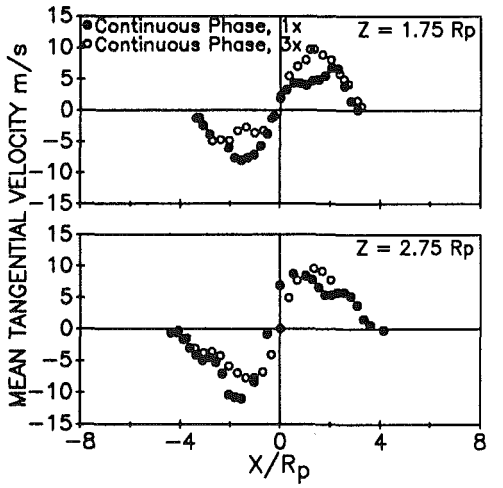

Fig. 7(*a*) Continuous phase

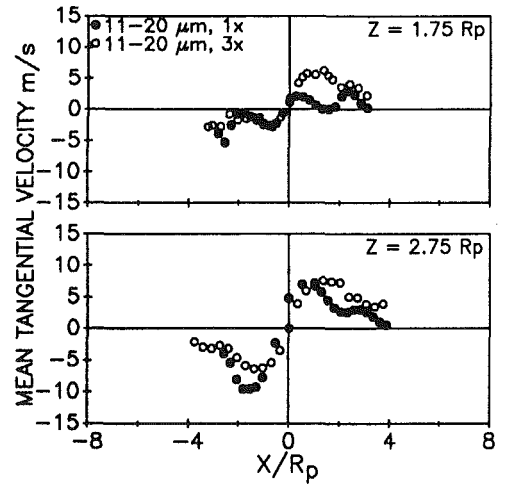

Fig. 7(*b*) Small droplets

Fig. 7 Comparison of mean tangential velocity

Nevertheless, the presence of the swirl cup tends to reduce these differences and provides more uniform and smaller droplet size distribution than using atomizer alone. The extent to which the aerodynamic flow and droplet formation from the primary venturi contribute to differences observed cannot be determined at this point.

- The shear layer has a high droplet population and thus a high liquid volume flux for both 1×- and 3×-scale tests.

Downloaded 02 Jun 2010 to 171.66.16.121. Redistribution subject to ASME license or copyright; see http://www.asme.org/terms/Terms_Use.cfm

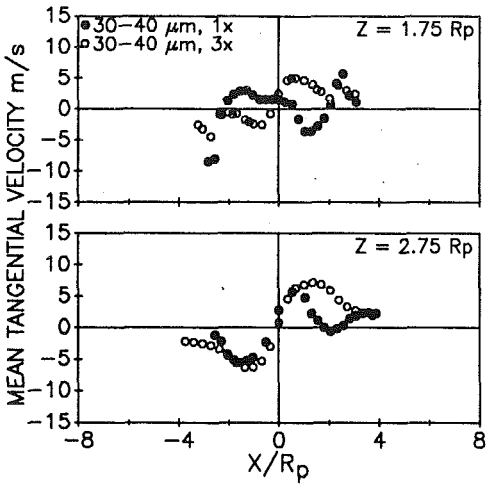

Fig. 7(c) Medium-sized droplets

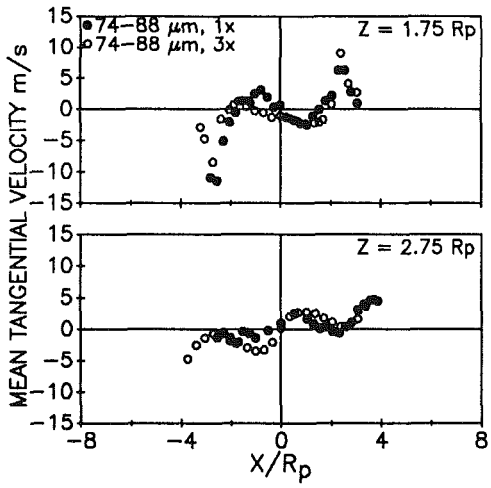

Fig. 7(d) Large droplets

Fig. 7 (continued)

Although the time-averaged information of the continuous phase and the droplets is essential to the understanding of the gas-phase flow field and droplet dispersion, the information on the corresponding velocity rms and pdf is necessary for further insight into the gas-phase/droplet interaction, which will be discussed in the second part of this series study (Wang et al., 1992b).

Acknowledgments

The authors acknowledge financial support from GE Aircraft Engines, and the assistance of S. W. Lee with plotting part of the data and H. D. Crum with assembling the swirl cup hardware.

References

Gouldin, F. C., Depsky, J. S., and Lee, S. L., 1983, "Velocity Field Characteristics of a Swirling Flow Combustor," AIAA Paper No. AIAA-83-0314.

Habib, M. A., and Whitelaw, J. H., 1980, "Velocity Characteristics of Confined Coaxial Jets With and Without Swirl," ASME *Journal of Fluids Engineering*, Vol. 102, pp. 47–53.

McDonell, V. G., and Samuelsen, G. S., 1991, "Gas and Drop Behavior in Reacting and Non-reacting Air-Blast Atomizer Sprays," *AIAA Journal of Propulsion and Power*, Vol. 7, pp. 684–691.

Mehta, J. M., Shin, H. W., and Wisler, D. C., 1989, "Mean Velocity and Turbulent Flow Field Characteristics Inside an Advanced Combustor Swirl Cup," AIAA Paper No. AIAA-89-0215.

Samimy, M., and Langenfeld, C. A., 1988, "Experimental Study of Isothermal Swirling Flow in a Dump Combustor," *AIAA Journal*, Vol. 26, No. 12, pp. 1442–1449.

Vu, B. T., and Gouldin, F. C., 1982, "Flow Measurements in a Model Swirl Flow," *AIAA Journal*, Vol. 20, pp. 652–659.

Wang, H. Y., McDonell, V. G., Sowa, W. A., and Samuelsen, G. S., 1990, "Swirl Cup Continuous and Discrete Phase Measurements in a 3× Scale Module," Final Report, UCI-ARTR-90-11, UCI Combustion Laboratory, University of California, Irvine.

Wang, H. Y., Sowa, W. A., McDonell, V. G., and Samuelsen, G. S., 1991a, "Spray Gas-Phase Interaction Downstream of a Co-axial Counter-swirling Dome Swirl Cup," *Proceedings of the Fifth International Conference on Liquid Atomization and Spray Systems* (*ICLASS*), pp. 687–694.

Wang, H. Y., Sowa, W. A., McDonell, V. G., and Samuelsen, G. S., 1991b, "Dynamics of Discrete Phase in a Gas Turbine Co-axial, Counter-swirling, Combustor Dome Swirl Cup," AIAA Paper No. AIAA-91-2353.

Wang, H. Y., McDonell, V. G., Sowa, W. A., and Samuelsen, G. S., 1991c, "Experimental Study of Single-Phase and Two-Phase Flow Fields Downstream of a Gas Turbine and a 3× Scale Model Combustor Swirl Cup," UCI-ARTR-91-6, UCI Combustion Laboratory, University of California, Irvine, CA.

Wang, H. Y., McDonell, V. G., Sowa, W. A., and Samuelsen, G. S., 1992a, "Characterization of a Two-Phase Flow Field Downstream of a Gas Turbine Co-axial, Counter-swirling, Combustor Swirl Cup," AIAA Paper No. AIAA-92-0229.

Wang, H. Y., McDonell, V. G., Sowa, W. A., and Samuelsen, G. S., 1992b, "Scaling the Two-Phase Flow Downstream of a Gas Turbine Combustor Swirl Cup: Part II—Fluctuating Quantities and Droplet Correlations," to be submitted to ASME JOURNAL OF ENGINEERING FOR GAS TURBINES AND POWER.

Downloaded 02 Jun 2010 to 171.66.16.121. Redistribution subject to ASME license or copyright; see http://www.asme.org/terms/Terms_Use.cfm

Liquid Sheet Disintegration and Atomization Process on a Simplified Airblast Atomizer

G. Lavergne

P. Trichet

P. Hebrard

Y. Biscos

CERT/ONERA/DERMES,
31055 Toulouse Cedex, France

Liquid sheet break-up in coflowing shear flow is the mean by which liquids are atomized in practical injectors for gas turbine combustors. The present study explores experimentally the mechanisms of liquid sheet instabilities and spray formation. Experiments are conducted on four airblast geometries. A high-speed video camera associated with an image processing unit was used to study the liquid sheet instabilities. A microphone and a frequency analyzer were used to track the disintegration frequency. Instability amplitude and disintegration length of the liquid sheet were measured. A two-component Phase Doppler Particle Analyzer was used to characterize the resultant spray. The spatial distribution of the particle size is influenced by the swirling flow field. These experimental results will be used to assess models of fuel sheet instabilities and disintegration.

Introduction

There is an important need for the development of low NO_x combustors for gas turbines to meet stringent NO_x regulations in many countries. To meet the EC (European Community) program goal of reducing current aircraft pollutants emissions, future fuel injectors must produce a fine spray and good droplet air mixing. The specific aims of the program are summarized in Table 1.

The work was subdivided into interlaboratory tasks over the course of one and half years.

Prefilming airblast atomizers are widely employed in modern gas turbines. Inside an atomizer, liquid fuel is forced through an annular orifice and exits under relatively low pressure in the form of an annular sheet. High-velocity air passes along both sides of the liquid sheet. The shear forces at the liquid–air interface promote the generation of instabilities in the sheet, which amplify until the sheet disintegrates (Dombrowski and Johns, 1963; Lefebvre, 1980; Eroglu and Chigier, 1992). Atomization occurs within a short distance from the atomizer edge.

The first objective of this research was to obtain a better understanding of the physical process: liquid sheet behavior at low and moderate velocities to obtain qualitative and quantitative results (Table 1: Disintegration process) for numerical code assessment (Coria, Table 1; Camatte and Ledoux, 1991). These experimental results will help to validate analytical models that can accurately describe these processes.

The second objective was to characterize the spray behavior and to utilize the phase Doppler analyzer to provide both droplet size and velocity information at higher air speed, corresponding to practical values in a combustor and develop a data base as boundary conditions for the liquid phase for droplets transport numerical codes (Table 1, Turbomeca).

Approach

The approach taken was to characterize the two-phase flow produced by a simplified airblast atomizer.

The break-up mechanisms of the annular liquid sheet at the various air and liquid flow conditions was investigated. Next the resulting two-phase flow (droplet size and velocity) was characterized. Finally the single-phase flow (in the absence of the dispersed phase) will be characterized: mean and fluctuating axial, radial, and tangential velocities.

Experimental Arrangement

The spray behavior of an atomizer has a direct effect on combustion performance. As a result, the interest in fuel atomization is renewed. As diagnostics have evolved from photography to video and laser-based instruments (Swithenbank et al., 1977), the details of scrutiny have increased.

Table 1 Matrix of current fundamental program of in-house research activities with universities

	ANALYTICAL MODELS	MODEL VERIFICATION EXPERIMENTS	FUNDAMENTAL EXPERIMENTS
DISINTEGRATION PROCESS	CORIA	ONERA/CERT	
SPRAY			ONERA/CERT
FLOW FIELD	TURBOMECA		IST

Contributed by the International Gas Turbine Institute and presented at the 37th International Gas Turbine and Aeroengine Congress and Exposition, Cologne, Germany, June 1-4, 1992. Manuscript received by the International Gas Turbine Institute February 6, 1992. Paper No. 92-GT-107. Associate Technical Editor: L. S. Langston.

Copyright © 1993 by ASME
Downloaded 02 Jun 2010 to 171.66.16.121. Redistribution subject to ASME license or copyright; see http://www.asme.org/terms/Terms_Use.cfm

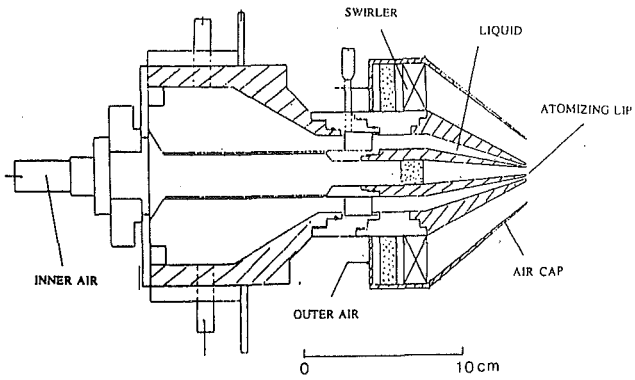

Fig. 1 Schematic of experimental airblast atomizer

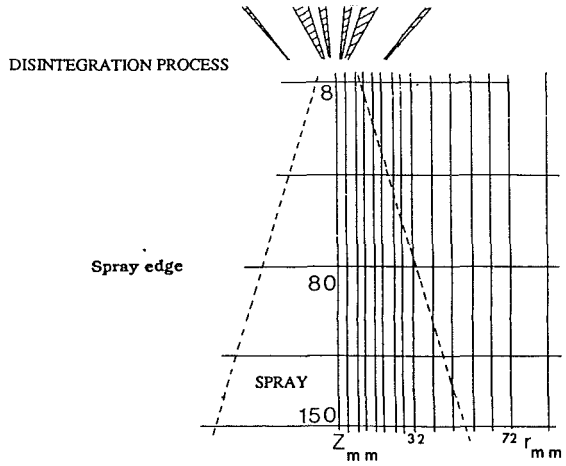

Fig. 2 PDPA measurement coordinate system and measurement mesh

Atomizer. The atomizer used in this study, shown in Fig. 1, was developed specifically as an airblast research atomizer by Coria (Rouen). This atomizer has a high degree of modularity: variable liquid sheet thickness, variable swirl angle, and variable inner and outer air velocities. For this study, we can note that the liquid sheet (400 μm thickness) lies between two coflowing air streams. The primary air is without swirl, the secondary air has a swirl component (swirl vane angle is 30 deg). Four geometries were studied:

1 400 μm liquid sheet + primary air
2 400 μm liquid sheet + primary air + secondary air
3 400 μm liquid sheet + primary air + swirling secondary air
4 Same as (3) but with different liquid sheet thickness (600 μm)

Facility. The facility used was the injector test rig at CERT/DERMES. The atomizer is mounted on an adapter, which provided both liquid flow and atomizing air. Three degrees of translational freedom were provided to the atomizer.

The experimental systems used for the current study encompass three circuits: two air circuits (inner air and outer air), one liquid circuit. All fluids (air and water) were monitored with a rotameter, so velocities for water or air are given as mean values.

Flow Visualization. A relatively new visualization technique, high-speed video, has some advantage over high-speed cinematography: ease of use, and the video recordings are immediately accessible. A Kodak High-Speed Video Camera (Kodak, 1986) has been used to observe the liquid sheet behavior at the outlet of the injector. The high-speed video system provided 1000 fps (full frame) to 6000 fps (1/6 full frame). This high-speed video was associated with an image processing unit (Biscos et al., 1991). For all experiments reported here, the lighting technique was shadowgraphy.

Microphone. During the experiments it was noticed that the disintegration phenomenon was producing a discernible frequency related to the air speed. By positioning a microphone near the disintegration zone, it was possible to compare the characteristic disintegration frequency measured from image analysis to an acoustic frequency measured by the microphone and frequency analyzer; the comparison was successful, so the microphone method was validated and used to monitor the disintegration frequency when image analysis was no longer feasible.

Phase-Doppler Particle Analyzer. The phase-Doppler anemometer used in this study was a two-component, dual beam, Phase-Doppler Particle Analyzer (PDPA) from Aerometrics, Inc. The principles of phase-Doppler anemometry have been reported previously by Bachalo and Houser (1984). An XMT 1200 optical transmitter and an RCV 2200 optical receiver were used to measure, simultaneously, the size and velocity of individual droplets. The receiving and transmitting lenses were 495 mm focal length. A collimating lens (300 mm) and slit width of 100 μm were used in the receiving optics. The PDPA configuration was off axis 30 deg backscatter.

The measurements were made across three axial planes starting at $z = 8$ mm, the two other planes being at $z = 80$ mm and $z = 150$ mm (Fig. 2). At each plane two perpendicular scans were performed. These two sets of measurements give access to the three components of velocity: axial, radial, and tangential. For each diametral scan, data were collected as a function of radius. Throughout the spray 4000 data points were collected for each location.

Results

The overall goal of the visualization studies was qualitatively and quantitatively to determine the physical process of liquid atomization. The first objective was to evaluate the influence of nozzle geometry, AFR, and swirl angle. The second objective was to assess the computer code.

Break-up of an Annular Liquid Sheet. The results reveal three distinct break-up mechanisms. For bubble formation (at low primary airflow), the bubble regime is shown in Fig. 3. From video images analysis, the bubble size was measured and found to be nearly twice the annular sheet diameter, as found by Lee and Chen (1990). As the air flow rate was increased, the spacing between bubbles decreased and the bubble shape flattened. At much higher air velocities, we observe liquid sheet instabilities as shown in Figs. 4 and 5. The third regime, prompt atomization (Lefebvre, 1991) was observed above an air velocity of 60 ms.

Break-up Length. From video recordings like Fig. 6 we could see the liquid sheet behavior and define a break-up length when coherent ligaments or sheet no longer exist. From 100 recordings we have determined a mean value for break-up

Nomenclature

V1 = inner air velocity, m/s
V2 = outer air velocity, m/s
SMD = Sauter mean diameter, μm
AFR = air-fuel ratio

Downloaded 02 Jun 2010 to 171.66.16.121. Redistribution subject to ASME license or copyright; see http://www.asme.org/terms/Terms_Use.cfm

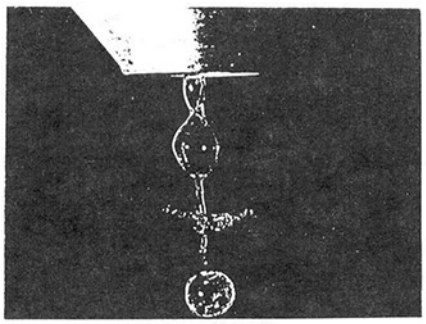

Fig. 3 Bubble formation ($V1 = 10$ m/s)

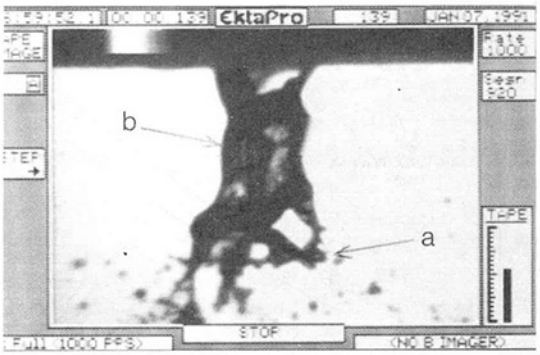

Fig. 6 Liquid sheet disintegration: (*a*) break-up length; (*b*) frequency

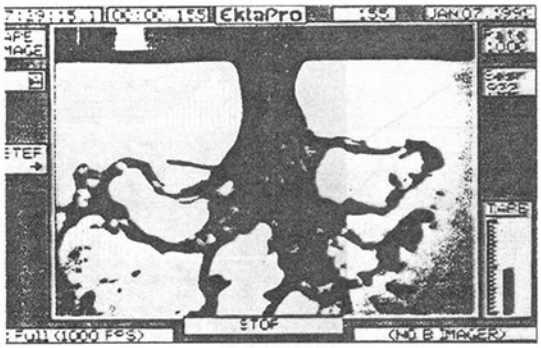

Fig. 4 Stretched streamwise ligament disintegration ($V1 = 10$ m/s, $V2 = 33$ m/s)

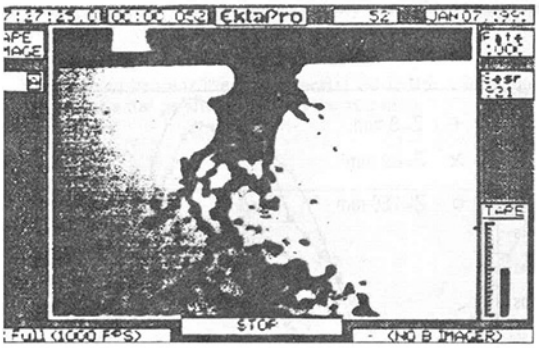

Fig. 5 Cellular break-up ($V1 = 27$ m/s, $V2 = 33$ m/s)

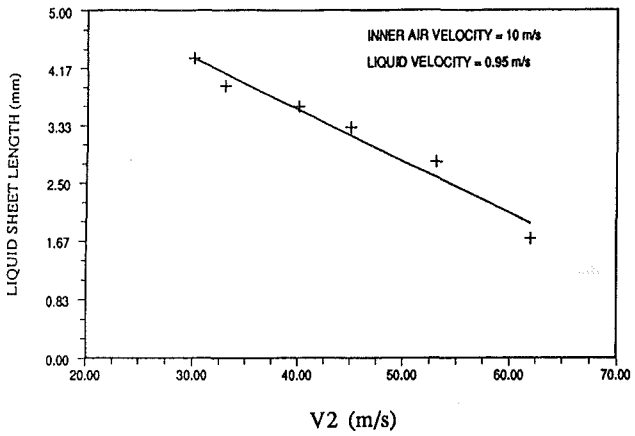

Fig. 7 Break-up length versus air velocity

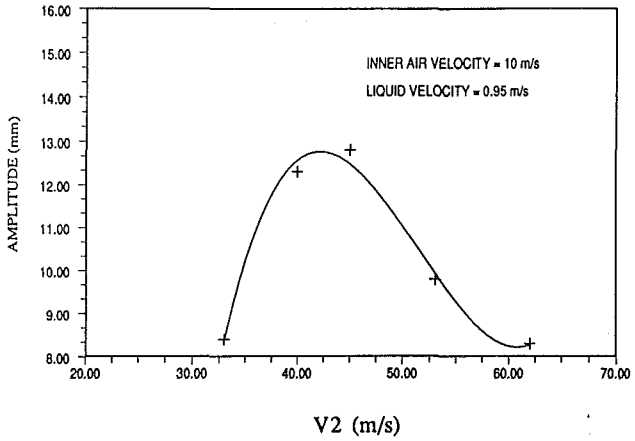

Fig. 8 Liquid sheet instability amplitudes

length for each airflow setting (Fig. 7). As observed by many authors (Rizk and Lefebvre, 1980; Lefebvre, 1989; Stapper and Samuelsen, 1990), for plane or annular sheet, we measured a decreasing break-up length with increasing air velocity. By increasing the air velocity, break-up length recedes to the nozzle exit, leading surely to the prompt atomization process.

Instability Amplitude. From the same high-speed video camera recordings used for the break-up measurements, we determined the instability amplitudes of the liquid sheet (Fig. 8). We can note that the instabilities reach a maximum value near 40–50 m/s and after that they decrease rapidly. At higher velocities (above 60 m/s) we observed a not-too-well-defined instability amplitude again, proof of a new atomization process.

Instability Frequency With/Without Swirl. The liquid sheet instabilities were measured by high-speed video image processing (Fig. 6). As mentioned above we have also used a microphone linked to a B&K analyzer. The results are presented in Fig. 9. The frequency increases with the air velocity. This behavior has been found by many authors (Chigier, 1991; Mansour and Chigier, 1990) and we can note on the same figure that the introduction of swirling airflow increases the frequency slightly. As the image analysis and the microphone gave the same results, we have selected the acoustic measurements, when the high-speed video images could no longer be processed due to high number of droplets, and blurred the disintegration zone. On the microphone spectra, the frequency peaks, characteristic of the atomization phenomenon, disappeared in the environmental noise above 900 Hz.

Spray Characterization. The break-up mechanism affects the spatial distribution of droplets in the resultant spray. Contrary to liquid sheet disintegration studies, which were per-

Downloaded 02 Jun 2010 to 171.66.16.121. Redistribution subject to ASME license or copyright; see http://www.asme.org/terms/Terms_Use.cfm

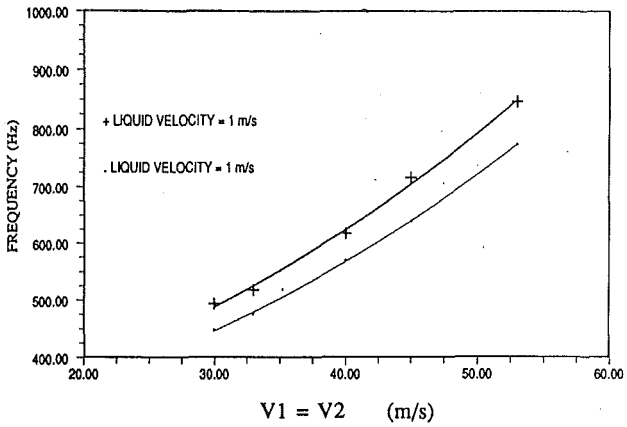

Fig. 9 Liquid sheet instability frequencies, with swirling air (+); without swirling air (·)

Table 2 Experimental conditions

Experiments were conducted at atmospheric pressure and ambient temperature	
Airblast geometry	**3**
Swirl vanes angle	**30 deg**
Liquid	**water**
Liquid flowrate	**50 l/h**
Slot width	**400 μm**
Swirler outlet velocity	**100 m/s**
Inner air velocity	

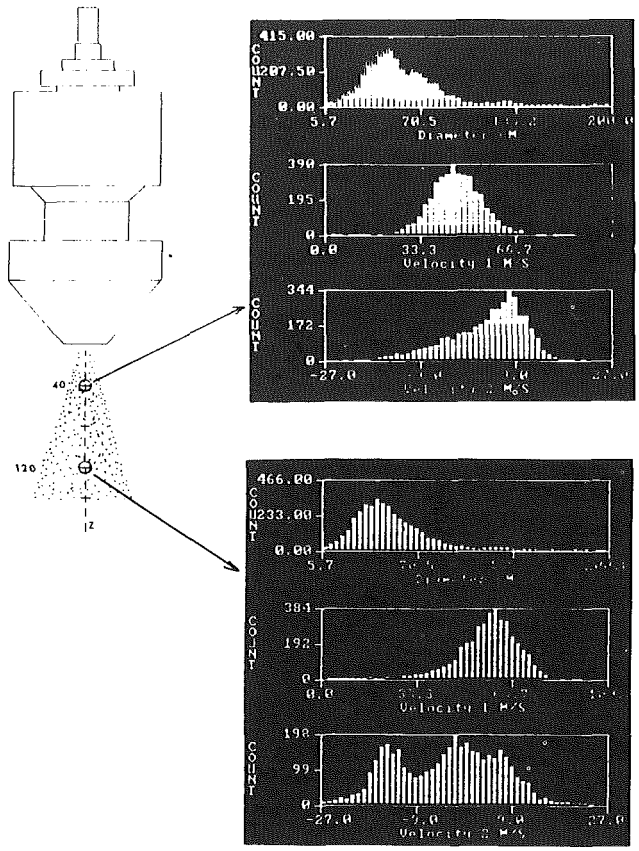

Fig. 10 Representative size and velocities histograms on the spray centerline ($V1 = V2 = 100$ m/s)

formed at low speeds, the spray investigation was conducted at higher velocities, more representative of a practical system in a combustor. The operating conditions for spray analysis are given in Table 2. Although detailed size distributions and droplet velocities data are available for each point surveyed (Fig. 10), the data presented here are the mean size and velocity values. Measurements have been performed at three axial planes, close to the injector ($z = 8$ mm) and downstream ($z = 80$ mm, $z = 150$ mm). At each plane only two orthogonal scans have been done. These two sets of measurements give information on the axial, radial, and tangential velocities.

Mean Axial Velocities. Figure 11 gives a plot of the mean axial velocities in the three measurement planes. Close to the injector ($z = 8$ mm), the droplet velocity presents two peaks, as found on practical airblast injectors (McDonnell and Samuelsen, 1988; Hebrard et al., 1991). Within the injector passages the liquid velocity is slow (mean value: 1 m/s) but high-velocity air passes along both sides of the sheet and the droplets are accelerated ($z = 8$ mm). Between the two measurement planes $z = 8$ mm and $z = 80$ mm the liquid flow gains moment of momentum, but farther downstream ($z = 150$ mm) the axial velocity profile does not change much, indicating a dilute spray behavior. Also noteworthy, downstream, is the plain jet velocity profile. In this simplified airblast atomizer, we have noticed no recirculating flow close to the injector. This experimental airblast atomizer has been designed mainly for annular sheet behavior.

Mean Radial Velocities. Figure 12 gives a plot of the radial velocity evolution. For the two measurement planes ($z = 8$ mm and $z = 80$ mm) the radial velocity depicts an expanding spray: Droplets flow outward from the injector axis. On the last measurement plane ($z = 150$ mm), the near-symmetric behavior of the spray is no longer valid. A large zone of negative

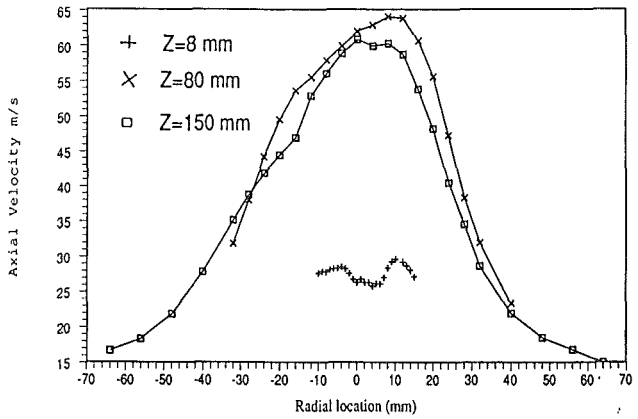

Fig. 11 Variation of droplet mean axial velocities with radial position at different axial positions ($V1 = V2 = 100$ m/s)

radial velocity is found near the injector axis. We are far away from the injector outlet; if we take the liquid sheet diameter as the reference dimension, we are at 30 times this distance.

Mean Tangential Velocities. From the mean tangential profiles in the three axial planes (Fig. 13) we find much less variation than on axial and radial velocity distributions. For the three positions we note a solid body rotation for the central core surrounded by a free vortex flow. All these data indicate a conservation of the swirling flow within the spray from close to the injector ($z = 8$ mm) to far downstream ($z = 150$ mm).

Sauter Mean Diameter. The spatial distribution of SMD is given in Fig. 14. At 8 mm from the injector outlet, the

Downloaded 02 Jun 2010 to 171.66.16.121. Redistribution subject to ASME license or copyright; see http://www.asme.org/terms/Terms_Use.cfm

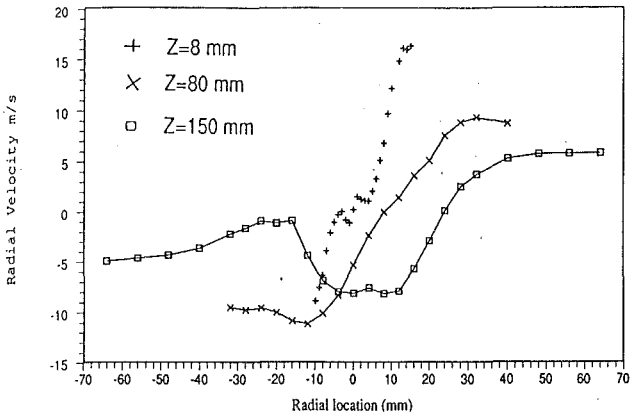

Fig. 12 Variation of droplet mean radial velocities with radial position at different axial positions ($V1 = V2 = 100$ m/s)

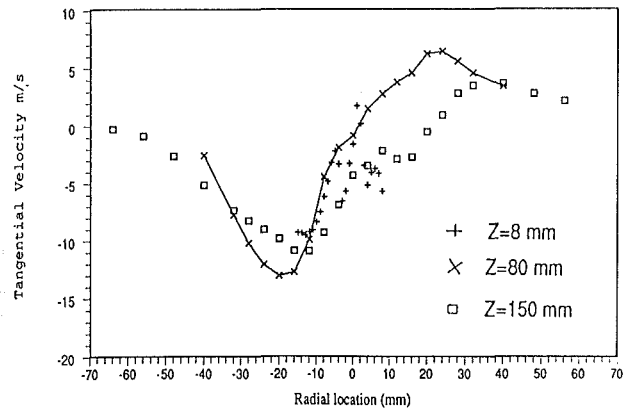

Fig. 13 Variation of droplet mean tangential velocities with radial positions at different axial positions ($V1 = V2 = 100$ m/s)

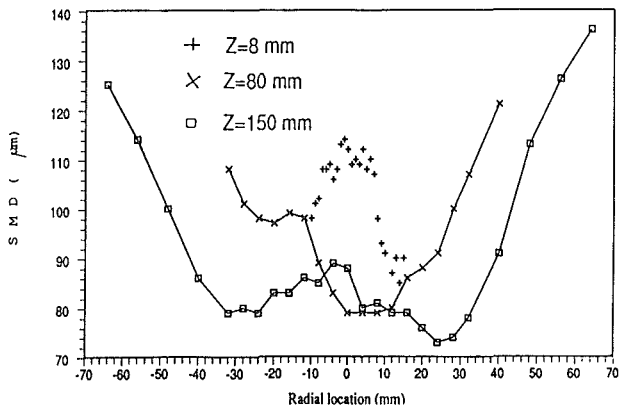

Fig. 14 Variation of droplet SMD with radial position at different axial positions ($V1 = V2 = 100$ m/s)

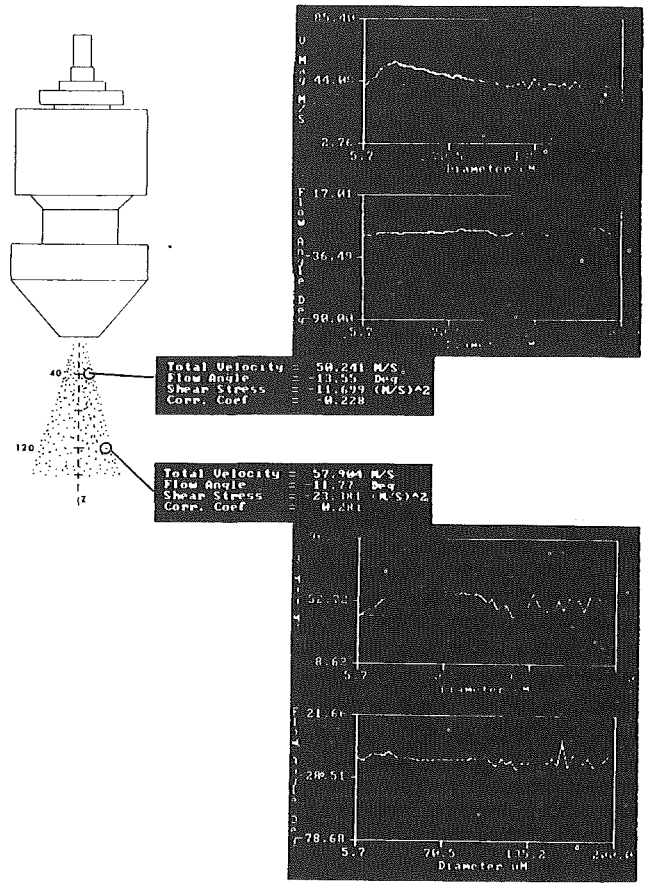

Fig. 15 Mean angle of droplet trajectory ($V1 = V2 = 100$ m/s)

atomization is terminated. In the inner part of the spray we have droplets of nearly equal size (110 μm). This result on atomization corroborates the Stapper and Samuelsen (1990) values for similar liquid sheet thickness. These droplets come from the ligament break-up. Close to this uniform size distribution we have smaller droplets generated by the thin liquid sheet between the ligaments. Farther downstream the swirl effect, noted in Fig. 11, has modified the size distribution, as observed by many authors (Brena de la Rosa, 1990, 1992). Droplet SMD near the spray boundaries is larger than that near the spray centerline. At the lower measurement plane, we note some large droplets near the spray axis, which may be a result of the air entrainment.

Flow Angle. The angle of trajectory of the liquid droplets was measured in the maximum concentration zone (Fig. 15). The droplet angle varies slightly from 18 to 11 deg. Theses small values, if compared to the swirl vane angle (30 deg), come from a very long swirler shroud and also from the absence of swirling water flow.

These experimental results for spray characteristics will be compared to laser diffraction (Malvern) measurements with kerosene as the atomized fluid. This will permit us to investigate the effect of liquid properties (viscosity, surface tension) on the atomization process. These data will be used as boundary conditions for the liquid phase for droplets transport numerical codes, in the interlaboratory work (Table 1, Turbomeca).

Conclusion

In this paper we have taken a brief look at the atomization process for a simplified airblast injector. On the basis of the insights gained in this investigation so far, we offer the following observations and opinions:

The high-speed video camera coupled to an image analysis is a useful tool for liquid sheet behavior study, giving both qualitative and quantitative results.

Different flow structure/atomization processes occur for various airflow conditions: bubble regime; liquid sheet instabilities; prompt atomization.

Depending on the flow regime, instability frequencies, amplitudes, and disintegration length were measured. The results are in accordance with published data.

These measurements are to be compared with the results

Downloaded 02 Jun 2010 to 171.66.16.121. Redistribution subject to ASME license or copyright; see http://www.asme.org/terms/Terms_Use.cfm

measured in a cylindrical liquid sheet instability model (Ledoux, 1991; CORIA, Table 1).

The spray behavior is representative of an airblast injector: These measurements have shown the overall effect of swirling flow on the properties of spatial distribution of droplets, on their velocity field, and on their number density, for example: Droplet SMD near the spray boundaries is larger than that near the spray centerline. However, due to small inner air diameter we have not observed a recirculating two-phase flow.

Future work will include the influence of air temperature on the disintegration process, and the influence swirl has on the velocity and turbulence gas field in the absence of the spray.

Acknowledgments

The work reported in this paper resulted from the efforts of researchers in the Departement de Mécanique et Energetique des Systemes. The authors wish specifically to acknowledge the contribution of F. Bismes for the spray rig installation and data acquisition.

This work is part of a larger effort to investigate "Low Emission Combustors," at the initiative of EC and sponsored by SNECMA and TURBOMECA.

References

Bachalo, W. D., and Houser, M. J., 1984, "Phase Doppler Spray Analyzer for Simultaneous Measurements of Drop Size and Velocity Distribution," *Optical Engineering*, Vol. 23, No. 5, p. 583.

Biscos, Y., Berthoumieu, P., Hebrard, P., Lavergne, G., 1991, "Developpement d'une méthode de trajectographie 2D de gouttes par traitemement d'images obtenues en video rapide," presented at the XIV Colloque National de l'ANRT, Paris, Dec.

Brena de la Rosa, A., Bachalo, W. D., and Rudoff, R. C., 1990, "Spray Characterization and Turbulence Properties in an Isothermal Spray With Swirl," ASME JOURNAL OF ENGINEERING FOR GAS TURBINES AND POWER, Vol. 112, pp. 60–66.

Brena de la Rosa, A., Wang, G., and Bachalo, W. D., 1992, "The Effect of Swirl on the Velocity and Turbulence Fields of a Liquid Spray," ASME JOURNAL OF ENGINEERING FOR GAS TURBINES AND POWER, Vol. 114, pp. 72–81.

Camatte, P., and Ledoux, M., 1991, "Airblast Atomization: Instability of an Annular Liquid Sheet surrounded by Two Airflows of Different Velocities," *Proceedings, 5th International Conference on Liquid Atomization and Spray Systems*, NIST, Gaithersburg, MD, pp. 695–702.

Chigier, N. A., 1991, "The Physics of Atomization," *Proceedings, 5th International Conference on Liquid Atomization and Spray Systems*, NIST, Gaithersburg, MD, pp. 1–15.

Dombrowski, N., and Johns, W. R., 1963, "The Aerodynamic Instability and Disintegration of Viscous Liquid Sheets," *Chemical Engineering Science*, Vol. 18, pp. 203–214.

Eroglu, H., and Chigier, N. A., 1992, "Wave Characteristics of Liquid Sheets in Cocurrent Air Flow," *Atomization and Sprays*, Vol. 2.

Hebrard, P., Trichet, P., and Bardey, X., 1991, "Experimental Investigation of Two-Phase Flow in the Near Field of an Airblast Atomizer," *Proceedings, 5th International Conference on Liquid Atomization and Spray Sytems*, NIST, Gaithersburg, MD, pp. 669–678.

Kodak, 1986, Ektapro 1000 Motion Analyzer.

Lee, J., and Chen, L, 1990, "A Linear Stability Analysis of Gas-Liquid Interface," AIAA Paper No. 90-0446.

Lefebvre, A. H., 1980, "Airblast Atomization," *Prog. Energy Combustion Sci.*, Vol. 6, pp. 233–261.

Lefebvre, A., 1989, *Atomization and Sprays*, Hemisphere Publishing Corporation, New York.

Lefebvre, A. H., 1991, "Twin Fluid Atomization: Factors Influencing Mean Drop Size," *Proceedings, 5th International Conference on Liquid Atomization and Spray Systems*, NIST, Gaithersburg, MD, pp. 49–64.

Mansour, A., and Chigier, N. A., 1990, "Disintegration of Liquid Sheets," *Physics of Fluids A*, Vol. 2, No. 5, pp. 706–719.

McDonnell, V. G., and Samuelsen, G. S., 1988, "Application of Two Component Phase Doppler Interferometry to the Measurement of Particle Size, Mass Flux and Velocities in Two-Phase Flow," *Twenty-Second International Symposium on Combustion*, The Combustion Institute, Pittsburgh, PA, pp. 1961–1971.

Rizk, N. K., and Lefebvre, A. H., 1980, "The Influence of Liquid Film Thickness on Airblast Atomization," ASME JOURNAL OF ENGINEERING FOR POWER, Vol. 102, pp. 706–710.

Stapper, B. E., and Samuelsen, G. S., 1990, "An Experimental Study of the Break-up of a Two-Dimensional Liquid Sheet in the Presence of Coflow Air Shear," AIAA Paper No. 90-0461.

Swithenbank, J., Beer, J. M., Taylor, D. S., Abbot, D., and McCreath, G. C., 1977, "A Laser Diagnostic Technique for the Measurement of Droplet and Particle Size Distribution," in: *Experimental Diagnostics in Gas Phase Combustion Systems*, B. T. Zinn and G. T. Boulman, eds., Progress in Astronautics and Aeronautics, Vol. 53, AIAA, New York, pp. 421–447.

Downloaded 02 Jun 2010 to 171.66.16.121. Redistribution subject to ASME license or copyright; see http://www.asme.org/terms/Terms_Use.cfm

Effects of Variable Liquid Properties on Multicomponent Droplet Vaporization

R. Kneer

M. Schneider

B. Noll

S. Wittig

Lehrstuhl und Institut für Thermische Strömungsmaschinen, Universität Karlsruhe (T.H.), W-7500 Karlsruhe, Federal Republic of Germany

A multicomponent droplet vaporization model, the Diffusion-Limit Model, is modified to account for the variation of liquid properties due to large temperature gradients as well as considerable concentration gradients within the droplet. The effects on the vaporization behavior are analyzed for an isolated biocomponent droplet consisting of heptane and dodecane. The results are presented for both moderate and high gas temperatures excluding combustion. During the vaporization process the liquid phase properties vary considerably. For example, the Lewis number changes by approximately one order of magnitude. The mass ratio of the liquid components seems to be rather sensitive to the variation of thermophysical property values, especially during the second half of the droplet lifetime, where about 50 percent of the droplet mass will still evaporate. The gas phase behavior is less affected by the use of constant liquid properties. For both gas temperature levels tested it was found that single component models cannot describe satisfactorily the whole vaporization process of multicomponent droplets. With regard to ignition the sharp rise of the vapor concentration in the beginning of the droplet vaporization is important. This behavior is caused by the more volatile component and cannot be achieved by the single component substitute.

Introduction

Liquid fuel combustion processes in gas turbine combustors are mainly influenced by atomization, fuel–air mixing, and evaporation. The fuel evaporation behavior is largely determined by the chemical and physical fuel properties. Typical hydrocarbon fuels consist of several hundreds or even thousands of components and show a wide boiling range due to volatility differentials, in contrast to a single component liquid marked by a distinct boiling point. Therefore realistic modeling of spray evaporation should account for the multicomponent nature of the fuel. In the present paper a bicomponent mixture is investigated. This is the simplest case where both volatility differentials and the mass diffusion within the fuel droplets become important.

In a large number of theoretical studies on drop and spray evaporation the multicomponent nature of the fuels has been neglected, assuming a single component behavior. The problems arising with simple and sophisticated single component models are addressed in a recently published paper by Abramzon and Sirignano (1989). These authors refer to the reviews of Sirignano (1983, 1988), Faeth (1977), and Law (1982) pointing out that in a detailed spray evaporation study the transient liquid heating and internal circulation should be taken into account. For practical applications this is only possible by simplifying the complex direct simulation models (Dwyer and Sanders, 1984; Haywood et al., 1989; Oliver and Chung, 1990; Huang and Ayyaswami, 1989). For this, approximated formulations are required, which will be able to handle a number of drops within a reasonable cpu-time limit (cf. Renksizbulut and Haywood, 1988; Abramzon and Sirignano, 1987; Talley and Yao, 1986).

A more accurate description of fuel spray evaporation will be possible if the fuel is considered as a multicomponent fuel, which in the simplest case will be a binary mixture. Then the volatility differences of the fuel components and the liquid diffusion process will become important as stated by Aggarwal (1987, 1988). One important result of Aggarwal's studies is the recommendation of the Diffusion-Limit Model, since in the multicomponent case internal convection initializes mass transport only along the streamlines, but not across them. Therefore the most essential feature of radial mass transport inside a droplet is the diffusion of the liquid components. This results in concentration and temperature gradients inside the droplet (Landis and Mills, 1974; Law, 1978).

Since all the physical properties, such as the diffusion coefficient or the thermal conductivity, are functions of temperature and composition, there also will be local changes of these properties. This led to the idea to account for these changes in thermophysical properties when formulating the theoretical model.

The objective of the present study is to demonstrate the transport processes inside evaporating multicomponent droplets. Thus, most of the calculations presented are related to the stagnant droplet case.

Contributed by the International Gas Turbine Institute and presented at the 37th International Gas Turbine and Aeroengine Congress and Exposition, Cologne, Germany, June 1–4, 1992. Manuscript received by the International Gas Turbine Institute February 6, 1992. Paper No. 92-GT-131. Associate Technical Editor: L. S. Langston.

Copyright © 1993 by ASME

Downloaded 02 Jun 2010 to 171.66.16.121. Redistribution subject to ASME license or copyright; see http://www.asme.org/terms/Terms_Use.cfm

Physical Model

The present model describes the evaporation of an isolated multicomponent droplet in a hot gaseous environment. In contrast to other studies, all thermophysical properties of both liquid phase and gas phase are treated as variable properties. These properties are determined as functions of temperature and composition using the presently available correlations from literature (cf. Reid et al., 1986). For more information on the particular correlations used, see Kneer et al. (1993).

Gas Phase. The gas phase is assumed to be quasi-steady applying an integral formulation of the governing equations for a stagnant environment (Hubbard et al., 1975; Abramzon and Sirignano, 1987, 1989). The droplet surface is assumed to be impermeable with respect to the ambient air, which leads to a one-way diffusion of the fuel vapor, the so-called Stefan flow. To investigate the evaporation behavior in a nonstagnant environment, convective correction factors for heat and mass transfer are employed, as suggested by Frössling (1938). The droplet motion is tracked in a Lagrangian frame of reference; see Noll (1986) and Wittig et al. (1988). To account for the effect of the Stefan flow in the convective case, the film-theory model of Abramzon and Sirignano (1987, 1989) is used.

Liquid Phase. Neglecting the internal circulation, heat conduction and mass diffusion govern the droplet evaporation process. The corresponding equations are derived for a spherical symmetric frame of reference and depend on the treatment of the thermophysical properties. Assuming these properties to be constants, the standard formulation of the liquid phase equations is obtained (cf. Landis and Mills, 1974; Law, 1978). A more accurate formulation of the problem taking the temperature and concentration dependence of the liquid properties into account is given in the present study.

The droplet diameter is subjected to a continuous change due to evaporation, hindering the solution with respect to the numerical grid. Therefore the moving boundary is fixed in using a nondimensionalized spatial coordinate,

$$\omega = \frac{r}{r_d(t)} \tag{1}$$

and an instantaneous droplet diameter,

$$\zeta = \frac{r_d}{r_{d,0}} \tag{2}$$

following Landis and Mills (1974). Thus, the governing equations can be written as

$$\frac{r_{d,0}^2}{a_d}\zeta^2\frac{\partial T_d}{\partial t} = \frac{\partial^2 T_d}{\partial \omega^2} + \left(\frac{2}{\omega} + \frac{1}{\lambda_d}\frac{\partial \lambda_d}{\partial \omega} + \frac{r_{d,0}^2}{a_d}\omega\zeta\frac{d\zeta}{dt}\right)\frac{\partial T_d}{\partial \omega} \tag{3}$$

$$\frac{r_{a,0}^2}{D_{AB}}\zeta^2\frac{\partial Y_{i,d}}{\partial t} = \frac{\partial^2 Y_{i,d}}{\partial \omega^2} + \left(\frac{2}{\omega} + \frac{1}{\rho_d}\frac{\partial \rho_d}{\partial \omega} + \frac{1}{D_{AB}}\frac{\partial D_{AB}}{\partial \omega} + \frac{r_{d,0}^2}{D_{AB}}\omega\zeta\frac{d\zeta}{dt}\right) \cdot \frac{\partial Y_{i,d}}{\partial \omega} - \frac{r_{d,0}^2}{D_{AB}}\frac{Y_{i,d}}{\rho_d}\left(\zeta^2\frac{\partial \rho_d}{\partial t} - \omega\zeta\frac{d\zeta}{dt}\frac{\partial \rho_d}{\partial \omega}\right) \tag{4}$$

The actual droplet diameter used in the boundary conditions is obtained from a liquid phase mass balance, which after differentiation and transformation leads to the final form

$$\frac{d\zeta}{dt} = -\frac{1}{r_{d,0}}\frac{\frac{\dot{m}}{4\pi r_d^2} + r_d\int_0^1 \frac{\partial \rho_d}{\partial t}\omega^2 d\omega}{\rho_d(\omega = 1,\ t) - \int_0^1 \frac{\partial \rho_d}{\partial \omega}\omega^3 d\omega} \tag{5}$$

Finally, the boundary conditions are expressed as

$\omega = 0$:

$$\frac{\partial T_d}{\partial \omega} = 0; \quad \frac{\partial Y_{i,d}}{\partial \omega} = 0,$$

$\omega = 1$:

$$\frac{\partial T}{\partial \omega} = \frac{r_d}{\lambda_a}\left(\alpha(T_{g,\infty} - T_{g,s}) - \frac{\dot{m}}{4\pi r_d^2}\sum_{i=1}^{n}\epsilon_i L_i\right) \tag{7}$$

$$\frac{\partial Y_{i,d}}{\partial \omega} = \frac{\dot{m}}{4\pi\rho_d D_{AB} r_d}(Y_{i,d,s} - \epsilon_i). \tag{8}$$

Solution Procedure. The temperature and concentration distributions within the droplet are discretized using the Crank-Nicolson scheme (Patankar, 1980). The resulting set of algebraic equations is solved by means of a suitable direct solution procedure. A uniform mesh for the nondimensional spatial (radial) coordinate ω of 100 grid points is employed. However, it was found that the number of grid points can be reduced by a factor of five, resulting only in minor deviations of the solution. Liquid and gas phase are related by the phase change at the droplet surface. Assuming ideal behavior of both liquid and ideal gas phase, with activity and fugacity coefficients equal to one, the equilibrium condition at the liquid-gas interface is determined using Raoult's law.

The numerical solution procedure executed for one time step can be described as follows: The equilibrium condition, Raoult's law, yields the molar fractions of the species in the gas phase, which are used to calculate the total and partial vaporization rates and the heat transfer coefficient. These are necessary for the evaluation of the boundary conditions at the droplet surface. Then the numerical solution of the partial differential equations, Eqs. (3) and (4), governing the liquid phase behavior will be straightforward.

Nomenclature

a = thermal diffusivity = $\lambda/\rho c_p$
c_p = specific heat, J kg^{-1} K^{-1}
d_d = droplet diameter, m
D_{AB} = binary liquid diffusion coefficient, m^2 s^{-1}
$\dot{m}$ = vaporization rate, kg s^{-1}
K_s = surface regression rate, m^2 s^{-1}
L = enthalpy of vaporization, J kg^{-1}
Le = Lewis number = $\lambda/\rho c_p D$
M = molar weight, kg kmol^{-1}
m = mass, kg
Pe = Peclet number = $K_s(t)/D$
r = radial coordinate, m
r_d = instantaneous droplet radius, m
t = time, s
T = temperature, K
u = velocity, m s^{-1}
Y = mass fraction
α = heat transfer coefficient, W m^{-2} K^{-1}
ϵ_i = partial vaporization rate = $\dot{m}_i/\dot{m}$
ζ = nondimensional actual droplet radius = $r_d/r_{d,0}$
λ = thermal conductivity , W m^{-1} K^{-1}
ρ = density, kg m^{-3}
ω = nondimensional radial coordinate = r/r_d

Subscripts

0 = initial value
∞ = free-stream condition
d = droplet
g = gas phase
i = component
ref = reference value
s = surface
tot = total
V = vapor

Downloaded 02 Jun 2010 to 171.66.16.121. Redistribution subject to ASME license or copyright; see http://www.asme.org/terms/Terms_Use.cfm

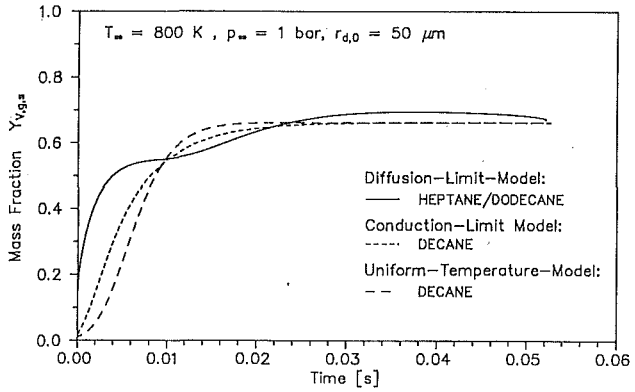

Fig. 1 Comparison of total surface vapor mass fraction obtained with two single and one multicomponent vaporization models

Results and Discussion

Results are presented for a heptane/dodecane droplet with an initial mass ratio of one and an uniform internal temperature distribution of $T_0 = 300$ K. The initial droplet diameter is $d_0 = 100$ μm. The ambient conditions chosen for the gas phase are $T_\infty = 800$ K and $T_\infty = 2000$ K at a pressure level of $p_\infty = 1$ bar. These temperature levels are selected as they are typical for prevaporization/premixing zones of combustion chambers, whereas higher-range temperatures are encountered in the primary zone of typical gas turbine combustors.

In illustrating the basic phenomena of multicomponent droplet evaporation the major part of the results is related to the stagnant droplet case. The influence of gas phase convection is shown in one case.

Features of Multicomponent Vaporization. In most cases gas turbine combustion is related to liquid fuel vaporization. Therefore, one essential aspect of existing droplet vaporization models is their ability to predict this gasification behavior. A valuable quantity to compare different droplet vaporization models is the instantaneous vaporization rate $\dot{m}$ or, as shown in Fig. 1, the surface vapor mass fraction. In this figure the vapor mass fractions calculated with the Diffusion-Limit Model as well as with two single component vaporization models are shown. The single-component models use decane as a substitute for the heptane/dodecane mixture of the multicomponent model. The Conduction-Limit Model accounts for heat conduction inside the droplet, whereas with the Uniform Temperature model the temperature inside the droplet is assumed to be homogeneous.

The Diffusion-Limit Model predicts a rapidly increasing mass fraction in the early stage of the vaporization process due to the evaporation of the more volatile heptane. With both single component models this rise in surface mass fraction is delayed compared to the multicomponent model. Due to the assumption of a uniform droplet temperature, the Uniform Temperature model is inferior also to the Conduction-Limit Model. This fact is valid also for the high-temperature case, where the droplet internal temperature gradients play an important role for the whole droplet lifetime (see Fig. 2*a*). Differences in the final levels reached with the three models are due to differences in thermophysical properties of decane and the heptane/dodecane mixture.

The further explanation of the time-dependent behavior of surface mass fraction with the multicomponent model is supported by Figs. 2 and 3, where the spatial and time-dependent distribution of droplet temperature and concentration are shown. In the moderate gas temperature case, Fig. 2(*b*), only minor internal temperature gradients are induced, whereas at high gas temperature levels the temperature distribution reveals large gradients especially during the first half

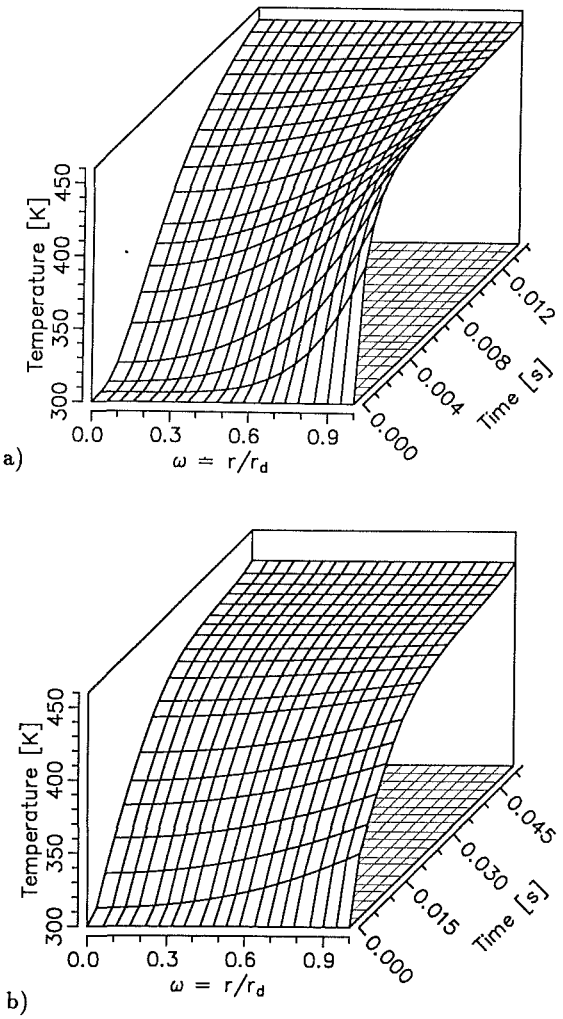

Fig. 2 Droplet internal temperature distribution: initial mass ratio: $m_{Hep}/m_{Dod} = 1$; ambient pressure: $p_\infty = 1$ bar; initial droplet radius: $r_{d,0} = 50$ μm; ambient temperature: (*a*) $T_\infty = 2000$ K; (*b*) $T_\infty = 800$ K

of the droplet lifetime (see Fig. 2*a*). Development and magnitude of internal temperature gradients depend basically both on the temperature difference between droplet surface and ambient gas phase and on the liquid thermal diffusivity.

The concentration distribution of the more volatile component (heptane) is shown in Fig. 3. Here the ω and t axes are interchanged compared to Fig. 2 for ease of representation. At high gas temperatures the center compositon ($\omega = 0$) is almost unaffected except toward the final stage of the droplet vaporization. The diffusion process is restricted to a small region close to the droplet surface ($\omega = 1$) for nearly the whole lifetime of the droplet. At moderate gas temperatures the diffusive process is visible at the center after about 40 percent of the droplet lifetime (see Fig. 3*b*). The more volatile component is depleted from the surface instantaneously after the onset of the droplet heating process. But in contrast to the high-temperature case a concentration profile inside the droplet develops due to a decreased surface regression rate providing more time for diffusive mass transport.

This corresponds to the first maximum of the vapor mass fraction in Fig. 1. The subsequent stagnation is the result of the impoverishment of the droplet surface with respect to the more volatile component, whereas the renewed rise of the vapor mass fraction level shows the increased influence of the heavier component (dodecane) as the evaporation proceeds.

Variation of Liquid Properties. As mentioned above, all thermophysical properties of the liquid mixture depend on

Downloaded 02 Jun 2010 to 171.66.16.121. Redistribution subject to ASME license or copyright; see http://www.asme.org/terms/Terms_Use.cfm

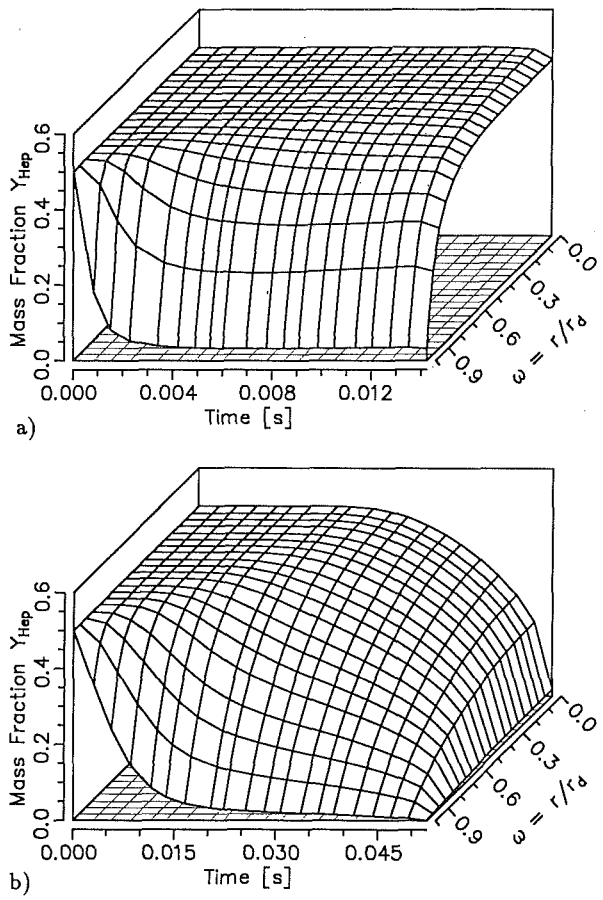

Fig. 3 Internal distribution of the more volatile component: same conditions as indicated in Fig. 2

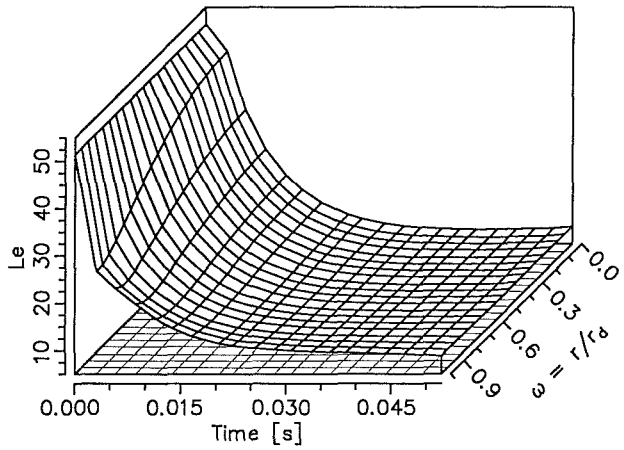

Fig. 4 Liquid Lewis number distribution, moderate temperature case

temperature and composition. Therefore, the internal temperature and concentration gradients create temporal and spatial changes of these properties, too.

Frequently the diffusional behavior of the liquid phase is characterized by the Lewis number, $\mathrm{Le} = \lambda/\rho c_p D$. The Lewis number describes the ratio of thermal to mass diffusion. For a moderate gas temperature, Fig. 4 shows the behavior of the liquid Lewis number, which decreases from the initial value of Le = 50 by one order of magnitude. These large changes result from the thermal diffusivity, which decreases by a factor of two, and from the increasing diffusion coefficient, the latter growing approximately by a factor of five. This behavior is

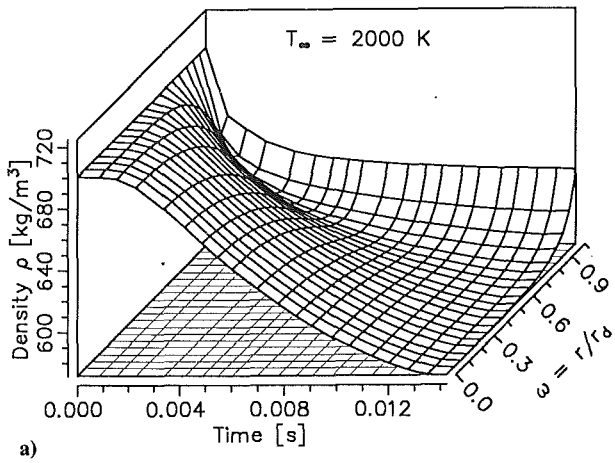

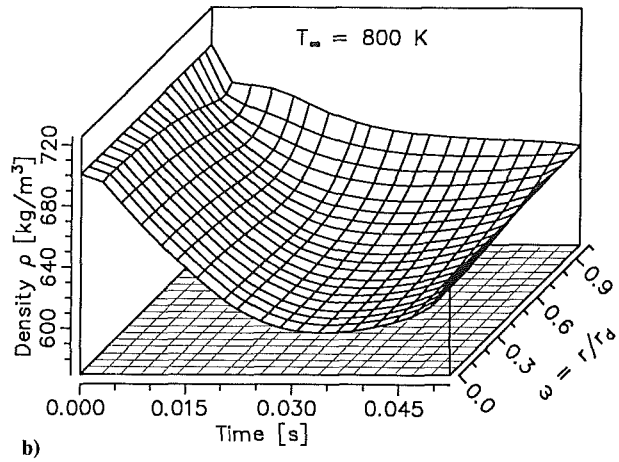

Fig. 5 Density contours for the two different ambient temperature levels

nearly the same in the high gas temperature case, indicating that the effect of composition on the liquid thermophysical properties is of minor influence compared to the effect of temperature. Therefore the Lewis number seems not to be an appropriate parameter to characterize the different vaporization behavior shown by Fig. 3. Thus, the description of diffusion-controlled vaporization should also include the time dependence of the diffusion process. Makino and Law (1988) suggest applying an instantaneous Peclet number, defined as the ratio of the surface regression rate and the diffusion coefficient ($\mathrm{Pe}_l = K_s(t)/D_l$), comprising the influence from different gas phase conditions.

The liquid density behavior is presented in Figs. 5(*a*, *b*) for the two temperature levels considered. As shown later, the density has a major influence on the droplet diameter development during vaporization. The variations of liquid density may be greater than 20 percent of the initial value $\rho_{d,0} \approx 700$ kg/m^3. It should be noted that the lower limit for the density, the critical density of the hydrocarbons considered, is $\rho_k \approx 235$ kg/m^3. Fig. 5(*a*) shows the decrease of density due to the increasing droplet temperature especially for the droplet center ($\omega = 0$), where the composition is nearly unchanged as the vaporization proceeds. At the surface of the droplet ($\omega = 1$) the density levels out after the initial sudden decrease resulting in gradients between the center and the surface. These gradients and the re-increase of the center value for the moderate gas temperature case (Fig. 5*b*) are caused by the variations in droplet composition. Here, the loss of the more volatile and lighter heptane counteracts the temperature-induced decrease of density.

Downloaded 02 Jun 2010 to 171.66.16.121. Redistribution subject to ASME license or copyright; see http://www.asme.org/terms/Terms_Use.cfm

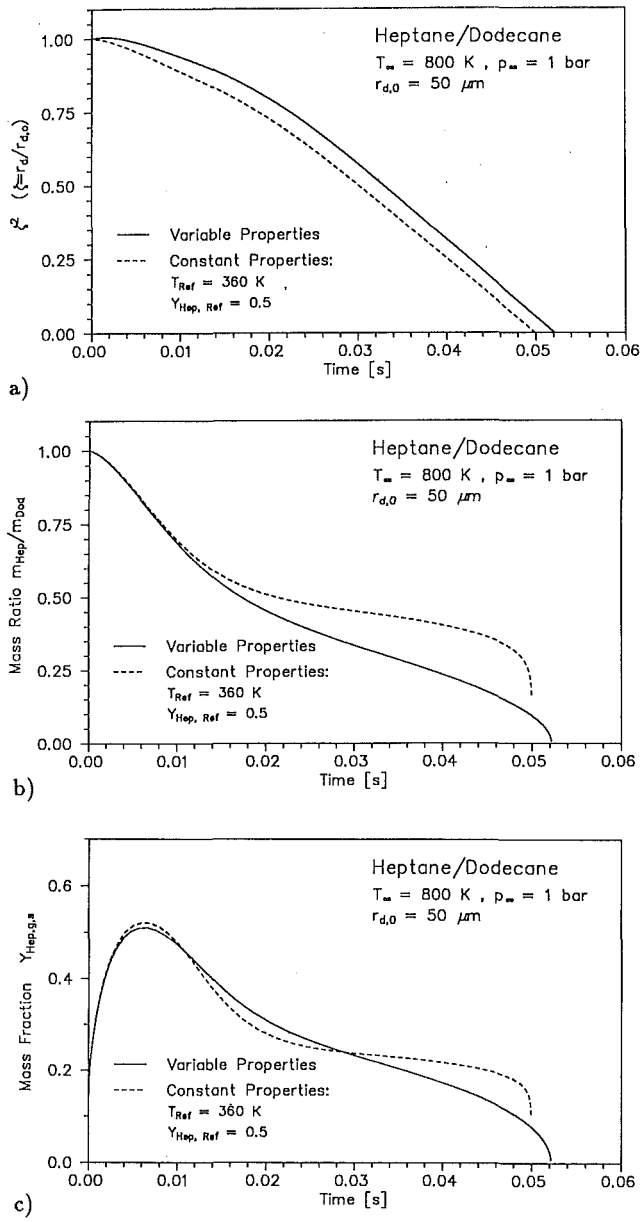

Fig. 6 Performance of the variable and constant property model with respect to histories of liquid and vapor properties: (*a*) nondimensional diameter squared; (*b*) liquid mass ratio; (*c*) heptane vapor mass fraction at droplet surface

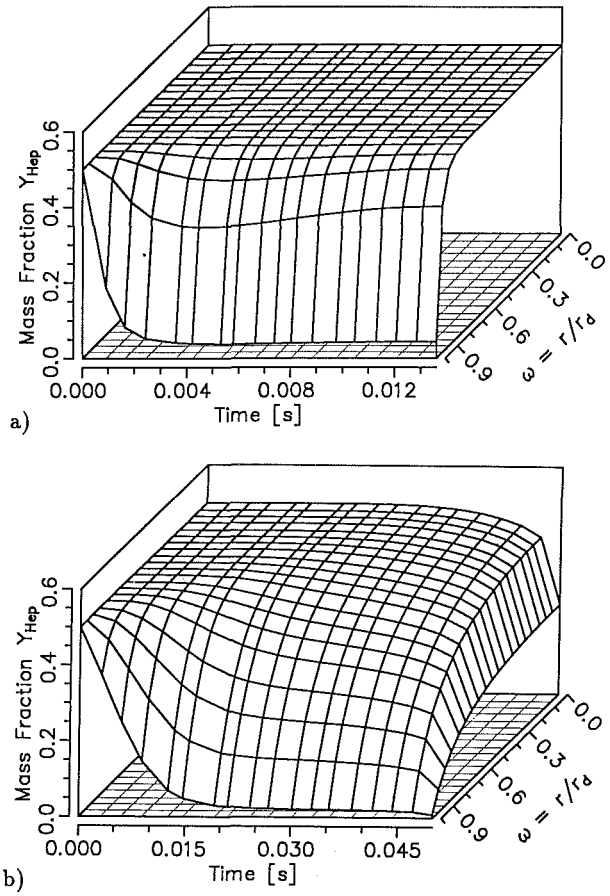

Fig. 7 Temporal and spatial distribution of heptane mass fraction; constant property formulation; same conditions as indicated in Fig. 2

Constant and Variable Property Calculations. In demonstrating the effects of liquid property variations on the vaporization process, results from the present model are compared with results from the original constant property model. The constant properties are determined for a reference temperature and droplet composition, following Abramzon and Sirignano (1989). The reference temperature, for example, is evaluated from the initial droplet temperature and the molar-averaged boiling temperature.

In Fig. 6(*a*) the nondimensional radius squared is shown, obtained from calculations with and without accounting for liquid property variations. The deviations between both curves, which can be observed immediately after the onset of the vaporization process are due to the neglection of liquid density gradients in the constant property case, inhibiting a droplet diameter increase. These gradients are related to the integrals of Eq. (5), including the temporal and spatial derivatives of density. In the case of a high-pressure environment, where the droplet is heated to a much higher temperature, the density changes will become more important. This fact is of considerable importance if comparisons between drop-size measurements and theoretical calculation are conducted.

The diagrams of the liquid mass ratio and the surface vapor mass fraction exhibit growing deviations with increasing time (Figs. 6*b*, *c*). In contrast to Fig. 6(*a*), this reveals the influence of diffusion on the vaporization behavior, which is underpredicted in the constant property formulation. Using constant properties, all liquid properties are evaluated as averaged values at the reference conditions given in Fig. 6. For the ambient conditions of Fig. 6, the thermal conductivity is lowered approximately by a factor of two and the diffusion coefficient increases to a value five times greater than its initial value due to the droplet heating. Since the droplet internal temperature gradients diminish with increasing time, the thermal conductivity is of minor influence and the diffusion coefficient variations play a major part in the variable property calculations. This is confirmed for high gas temperatures (not shown here) yielding larger deviations of mass ratio and vapor mass fractions especially in the later part of the droplet lifetime.

The underprediction of liquid diffusion applying a constant property formulation is also shown in Fig. 7, where the spatial and temporal changes of the heptane mass fraction are given. The boundary and initial conditions applied are identical to those of Fig. 2. A comparison of Figs. 7 and 3 shows that at moderate ambient temperatures, the more volatile component is not completely extracted from the droplet center as in the variable property case. Even in the high-temperature case, where diffusion does not play a major role, the diffusive influences are clearly detectable. Using the constant property formulation the droplet interior remains at a constant composition for the whole lifetime, except a small region close to the surface.

Downloaded 02 Jun 2010 to 171.66.16.121. Redistribution subject to ASME license or copyright; see http://www.asme.org/terms/Terms_Use.cfm

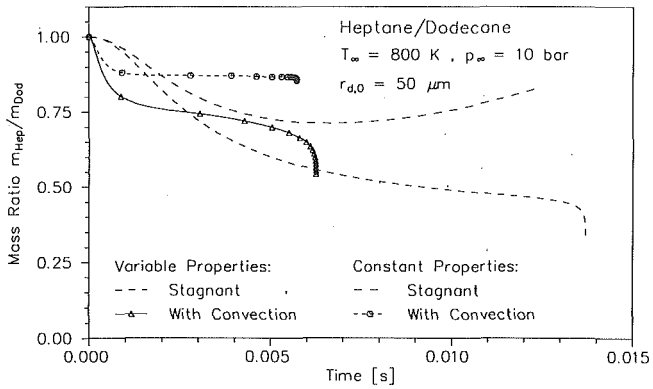

Fig. 8 Influence of increased ambient pressure and gas phase convection on the vaporization behavior: ambient temperature: T_∞ = 2000 K; ambient pressure: p_∞ = 10 bar

Conducting a variety of calculations for different liquid mixtures and different ambient conditions it was found that the mass ratio clearly reflects the deviations in variable and constant property results. The liquid mass ratio gives an averaged value for the liquid behavior, and therefore appears to be the most suitable quantity to condense the information of the three-dimensional plots.

In Fig. 8 the influence of increased ambient pressure and gas phase convection on the mass ratio history is plotted for the high-temperature case. The droplet starts its motion with an initial velocity of $u_{d,0}$ = 1 m/s in a one-dimensional gas environment moving at a constant speed of u_∞ = 20 m/s. A comparison with Fig. 6(*b*) shows larger deviations of the results from constant and variable property formulation. These are due to the increased droplet temperatures under the elevated ambient pressure, enhancing the mass diffusion. Figure 8 clearly shows that gas phase convection accelerates the vaporization. The initially large relative velocity between the droplet and the surrounding gas leads to a sudden decrease of the liquid mass ratio. This decrease slows down as the relative velocity disappears. The mass ratio curves remain at higher levels in the convective case, especially for the variable property formulation.

Conclusions

The present study is concerned with the variation of liquid properties occurring in multicomponent droplet vaporization. Internal temperature and concentration gradients cause considerable variations of the liquid properties as the vaporization proceeds. A modified multicomponent vaporization model has been developed accounting for gradients of thermophysical properties in formulating the governing equations. Numerous calculations performed for an isolated droplet regarding moderate and high gas temperatures revealed higher accuracy of the present model compared to the constant property Diffusion-Limit Model. The deviations between the present and the constant property model are due to pronounced variations of the liquid properties during the vaporization process. Thereby the diffusional resistance within the droplet mainly in the second half of the droplet lifetime is lowered.

In order to handle more complex mixtures, further work is necessary, including nonideal effects of both gas and liquid phases (cf. Kim et al., 1990). Moreover, the prediction of fuel droplet behavior under the high-pressure conditions encountered in real combustors demands replacement of the commonly used ideal gas assumption by a more accurate equation of state to describe the gas phase behavior (cf. Hsieh et al., 1991).

Acknowledgments

The present study was supported by a grant from the SFB 167 (High intensity combustors) of the Deutsche Forschungsgemeinschaft.

References

Abramzon, B., and Sirignano, W. A., 1987, "Approximate Theory of a Single Droplet Vaporization in a Convective Field: Effects of Variable Properties, Stefan Flow and Transient Liquid Heating," *Proc. 2nd ASME-JSME Thermal Engng. Joint Conf.*, Honolulu, HI, Vol. 1, pp. 11–18.

Abramzon, B., and Sirignano, W. A., 1989, "Droplet Vaporization Model for Spray Combustion Calculations," *Int. J. Heat Mass Transfer*, Vol. 32, pp. 1605–1618.

Aggarwal, S. K., 1987, "Modeling of a Dilute Vaporizing Multicomponent Fuel Spray," *Int. J. Heat Mass Transfer*, Vol. 30, pp. 1949–1961.

Aggarwal, S. K., 1988, "Further Results on Evaporating Bicomponent Fuel Sprays," *Int. J. Heat Mass Transfer*, Vol. 31, pp. 2593–2597.

Dwyer, H. A., and Sanders, B. R., 1984, "Detailed Computation of Unsteady Droplet Dynamics," *Proc. 20th Symposium (International) on Combustion*, The Combustion Institute, pp. 1743–1749.

Faeth, G. M., 1977, "Current Status of Droplet and Liquid Combustion," *Prog. Energy Combust. Sci.*, Vol. 3, pp. 191–224.

Frössling, N., 1938, "Über die Verdunstung fallender Tropfen," *Gerlands Beiträge zur Geophysik*, Vol. 52, pp. 171–216.

Hsieh, K. C., Shuen, J. S., and Yang, V., 1991, "Droplet Vaporization in High-Pressure Environments I: Near Critical Conditions," *Combust. Sci. Tech.*, Vol. 76, pp. 111–132.

Haywood, R., Nafziger, R., and Renksizbulut, M., 1989, "A Detailed Examination of Gas and Liquid Phase Transient Processes in Convective Droplet Evaporation," ASME JOURNAL OF HEAT TRANSFER, Vol. 111, pp. 495–502.

Huang, L. J., and Ayyaswamy, P. S., 1989, "Evaporation of a Moving Liquid Droplet: Solutions for Intermediate Reynolds Numbers," *National Heat Transfer Conference*, ASME HTD-Vol. 106, pp. 431–437.

Hubbard, G. L., Denny, V. E., and Mills, A. F., 1975, "Droplet Evaporation: Effects of Transients and Variable Properties," *Int. J. Heat Mass Transfer*, Vol. 18, pp. 1003–1008.

Kim, J. S., Lee, A., and Law, C. K., 1990, "On the Gasification of Droplets of Azeotropic Mixtures: Theory and Experiment," presented at the 23rd Symposium (International) on Combustion, Orleans, France, July 22–27.

Kneer, R., Schneider, M., Noll, B., and Wittig, S., 1993, "Diffusion Controlled Evaporation of a Multicomponent Droplet: Theoretical Studies on the Importance of Variable Liquid Properties," in press.

Landis, R. B., and Mills, A. F., 1974, "Effect of Internal Diffusion Resistance on the Evaporation of Binary Droplets," *Proc. 5th Int. Heat Transfer Conf. Tokyo Section B7.9*, pp. 345–349.

Law, C. K., 1978, "Internal Boiling and Superheating in Vaporization Multicomponent Droplets," *AIChE J.*, Vol. 24, pp. 626–632.

Law, C. K., 1982, "Recent Advances in Droplet Vaporization and Combustion," *Prog. Energy Combust. Sci.*, Vol. 8, pp. 171–201.

Makino, A., and Law, C. K., 1988, "On the Controlling Parameter in the Gasification Behavior of Multicomponent Droplets," *Comb. Flame*, Vol. 73, pp. 331–336.

Noll, B. E., 1986, "Numerische Berechnung brennkammertypischer Ein- und Zweiphasenströmungen," Dissertation Universität Karlsruhe, Lehrstuhl und Institut für Thermische Strömungsmaschinen.

Oliver, D. L. R., and Chung, J. N., 1990, "Unsteady Conjugate Heat Transfer From a Translating Fluid Sphere at Moderate Reynolds Numbers Liquid Droplet: Solutions for Intermediate Reynolds Numbers," *Int. J. Heat Mass Transfer*, Vol. 33, pp. 401–408.

Patankar, S. V., 1980, *Numerical Heat Transfer and Fluid Flow*, Hemisphere Publishing Corporation, Washington, DC.

Renksizbulut, M., and Haywood, R. J., 1988, "Transient Droplet Evaporation With Variable Properties and Internal Circulation at Intermediate Reynolds Numbers," *Int. J Multiphase Flow*, Vol. 14, pp. 189–202.

Reid, R. C., Prausnitz, J. M., and Poling, B. E., 1986, *The Properties of Gases and Liquids*, 4th ed., McGraw-Hill, New York.

Sirignano, W. A., 1983, "Fuel Droplet Vaporization and Spray Combustion Theory," *Prog. Energy Combust. Sci.*, Vol. 9, pp. 291–332.

Sirignano, W. A., 1988, "An Integrated Approach to Spray Combustion Model Development," *Combust. Sci. Tech.*, Vol. 58, pp. 231–251.

Talley, D. G., and Yao, S. C., 1986, "A Semi-empirical Approach to Thermal and Composition Transients Inside Vaporizing Fuel Droplets," *Proc. 21st Symposium (International) on Combustion*, The Combustion Institute, pp. 609–616.

Wittig, S., Klausmann, W., and Noll, B., 1988, "Turbulence Effects on the Droplet Distribution Behind Airblast Atomizers," *Combustion and Fuels in Gas Turbine Engines*, AGARD-CP-422, p. 5.

Downloaded 02 Jun 2010 to 171.66.16.121. Redistribution subject to ASME license or copyright; see http://www.asme.org/terms/Terms_Use.cfm

Multijet Annulus/Core-Flow Mixing—Experiments and Calculations

S. J. Baker
Department of Mechanical Engineering,
Imperial College,
London, SW7 2BX United Kingdom

J. J. McGuirk
Department of Transport Technology,
Loughborough University,
Leicestershire LE11 3TU United Kingdom

LDV measurements are reported of the flow field associated with a single row of radially injected jets penetrating a core-tube flow. Emphasis is placed on the influence of small feed-annulus height on jet entry conditions and resulting trajectories and mixing patterns. Conditions of unstable jet behavior, with strong vortex patterns in the jet holes, were observed for small annulus heights and high annulus velocities. Most measurements were, however, taken under stable conditions to allow the data to be used in a CFD validation exercise. Significant differences in the strength of backflow generated at jet impingement and in the turbulence field in the immediate hole vicinity were observed for different annulus height/core diameter ratios. These were accompanied by jet trajectory and annulus flow structure changes. Measurements of all three mean velocity components and associated normal stresses enabled the data to be utilized to assess a three-dimensional CFD calculation incorporating a k–ϵ turbulence closure. The strength of forward and back flow generated at impingement was accurately predicted when the QUICK discretization scheme was used. However, the size of upstream vortex was overpredicted. As expected using an eddy viscosity model, the turbulence field at jet impingement and in the hole vicinity was not correctly reproduced. The turbulence generation in the flow approaching the hole was greatly overestimated by the turbulence model used.

Introduction

Jets discharged into cross-flowing streams have traditionally attracted considerable interest in fluid mechanics studies due to their occurrence in environmental and engineering flows. Combined with jet impact on a solid surface, such flows have relevance to impingement cooling and V/STOL applications. Within the context of gas turbine combustors, however, it is jet-on-jet impingement in a cross-flowing stream that must be studied. Multiple radially injected jets are arranged to impinge on each other to create a suitable primary zone aerodynamic pattern and to effect rapid dilution jet mixing to control the exit temperature pattern factor. The importance of these multiple jet flow fields in combustor design has led to extensive experimental work [1, 2] and, more recently, some computational studies [3, 4].

Scant attention has been paid, however, to the effect of the annulus feed systems that are typically used in practice to supply fluid to the jet entry ports drilled in the combustor wall. (Space limitations always preclude plenum-fed jets.) This is in spite of the fact that details of the annulus flow and geometry, in combination with the port geometry, are known [5] to be influential in controlling hole discharge coefficients, jet trajectories, and the subsequent mixing patterns. One study of the effects of feed geometry on jet mixing in annular combustors has been reported in [6]; however, this only attempted to characterize such effects empirically, with no flow field measurements or other details provided. As a consequence, little is known of the important fundamental physical mechanisms that lie behind these observed effects. Furthermore, it is well documented that the turbulence field created at jet impingement has a strong impact on jet/core-flow mixing. To what extent the turbulence characteristics of the annulus/jet port flow contribute to the turbulence environment within the combustor, and to what accuracy these are predicted by current combustor models, has not been properly explored.

The work reported in the current paper aims to fill some of the gaps mentioned above. An initial experimental study to examine annulus feed effects on a single row of jet entry ports was carried out. A simple experimental configuration was chosen that allowed investigation of the interaction between jets emerging from a finite-size annulus and a cross-flowing core-flow. The simplicity of the configuration chosen was preferred to that of a realistic combustor geometry because of the consequent ease of analyzing the annulus effects in isolation. Subsequently, an existing three-dimensional CFD code, previously applied to combustor flows [7], was used to examine the ability of a k–ϵ eddy viscosity turbulence model to reproduce the observed flow and turbulence patterns. An isolated study of the jet/port flow simulation has not been carried out before, in spite of the fact that the prediction of the internal combustor flow depends to a large extent on the "boundary conditions" implied over the jet entry regions. The extent to which the k–

Contributed by the International Gas Turbine Institute and presented at the 37th International Gas Turbine and Aeroengine Congress and Exposition, Cologne, Germany, June 1–4, 1992. Manuscript received by the International Gas Turbine Institute February 6, 1992. Paper No. 92-GT-111. Associate Technical Editor: L. S. Langston.

Copyright © 1993 by ASME
Downloaded 02 Jun 2010 to 171.66.16.121. Redistribution subject to ASME license or copyright; see http://www.asme.org/terms/Terms_Use.cfm

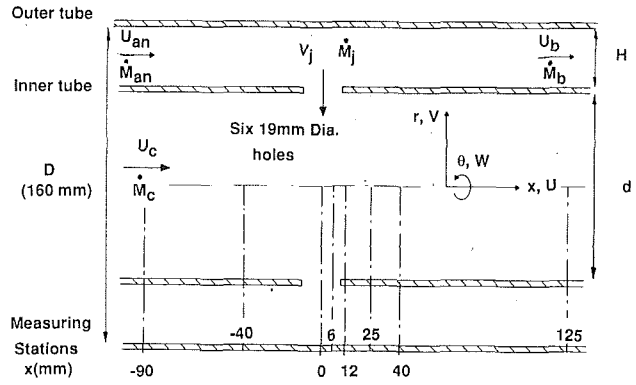

Fig. 1 Test section geometry and measurement stations

ϵ turbulence model can simulate this aspect of combustor flow is therefore an important question when assessing the adequacy, or otherwise, of combustor models.

The following sections detail the methods used, both experimental and computational, the results of the LDV measurements, their comparison with predictions, and a summary of the major conclusions drawn from the present work.

Methods

Experimental Investigation. To carry out the experiments, a water flow simulation was preferred to circumvent any seeding problems associated with LDV measurements. Care was taken to ensure that the Reynolds numbers, velocity ratios, etc., of the annulus and jet flows were sufficiently high to simulate proper flow regimes associated with air flows at typical combustor operating conditions. Two constant head tanks were used to supply co-axial core-flow and annulus flow streams. A vertical rig orientation avoided the build-up of air pockets and provided better access for the measurement system. The constant head tanks discharged, via a 1.2 m approach length, into a test section made of clear acrylic for optical access, encased in a water-filled rectangular box to minimize refraction problems when measuring radial velocities. A diagram of the test-section geometry is given in Fig. 1, together with a reference cylindrical-polar coordinate system. The rig possessed concentric inner and outer cylindrical tubes for core and annulus flows, and a single row of six equispaced 19-mm-dia holes to create the radially inflowing jets. The set of experiments carried out utilized various inner tube diameters (d) and a constant outer tube diameter (D = 160 mm) to achieve different annulus heights (H). Ideally it would have been better to change both H and d independently, but this was not possible within the constraints of available facilities and time. The measurements covered three inner tube diameters (d = 94 mm, 119 mm, and 134 mm), giving rise to (with 3 mm wall thickness tube) annulus heights H of 30 mm, 20 mm, and 10 mm, respectively. These correspond to heights of around 1.5, 1.0, and 0.5 hole diameters, which again spans values typically found in practice. As discussed below, jet instability problems curtailed the measurement program for H = 10 mm; the 20 mm height was also near the limit for stable, symmetric flow. Accordingly, the measurements reported in detail below and considered suitable as CFD validation data are only for the two larger values of H.

Figure 1 also shows the location of eight measurement planes, both upstream and downstream of the jet entry plane x = 0. Measurements were taken at fixed axial locations (and only on the plane θ = 0 containing two opposed jets) so that the measurement planes with respect to a nondimensional coordinate x/d change slightly as H is varied. Valves present in the exits from the core and annulus tubes allowed control over the mass flows. Test conditions were characterized by four mass flows: core-tube ($\dot{m}_c$), annulus supply ($\dot{m}_{an}$), jet ($\dot{m}_j$), and annulus bleed ($\dot{m}_b$), the fraction of annulus supply flow not entering the core tube via the holes. In a combustor context, primary holes near the head of the can would be characterized by significant annulus bleed flow (to feed holes farther downstream), while dilution holes would experience little or no bleed flow. Only three of these flows are of course independent ($\dot{m}_j + \dot{m}_b = \dot{m}_{an}$); the present experiments were conducted by fixing the core.flow ($\dot{m}_c$), adjusting $\dot{m}_j$ (or strictly speaking V_j, see below) to give a jet/core-flow velocity ratio typical of a combustor primary hole and ensuring that sufficient bleed flow ($\dot{m}_b$) was present to guarantee stable, symmetric jet behavior (the effect of different levels of bleed flow is discussed further below).

A single-component helium–neon LDV system with Dantex 55× transmiting optics was used for velocity measurements. A Bragg cell provided frequency shifting for negative velocity regions; downmixing of the 40 MHz shift using a Dantec 55N101 instrument allowed variable shifts between 0.001 and 10 MHz. Signal processing was via a frequency tracker and Apple microcomputer. Statistical uncertainty in measuring the mean velocity was kept below 4 percent by collecting as many as 30,000 samples in highly turbulent zones.

The approach core-flow was measured as being axisymmetric at the upstream $x = -90$ mm plane. For the tests reported here, the centerline velocity (U_c) at this station was held constant at 0.185 m/s. Core mass flow rates ($\dot{m}_c$) in the H = 30 mm and H = 20 mm tests were 1.14 and 1.61 kg/s, respectively. To retain similar overall features of the jet flow for comparison purposes, the same jet velocity (V_j = 0.85 m/s measured on the hole centerline at the inner annulus wall) was arranged in both tests; this corresponds to a velocity ratio ($R = V_j/U_c$) between jet and core-flow of 4.6. As detailed below, it was observed that annulus bleed flow was helpful in stabilizing jet behavior. Velocity and mass flow conditions at annulus inlet ($x = -90$ mm) were U_{an} = 0.16 m/s, $\dot{m}_{an}$ = 1.93 kg/s for H = 30 mm; and U_{an} = 0.3 m/s, $\dot{m}_{an}$ = 2.67 kg/s for H = 20 mm. At annulus exit, 28 percent bleed flow was used in the first case and 32 percent in the second.

Computational Investigation. The code used for the predictions reported below was a modified version of one previously applied [7] to the prediction of a can-type gas turbine combustor; accordingly only essential details are given here. The method comprised a staggered mesh finite-volume, incompressible pressure-correction algorithm, applied to the full versions of the Reynolds-averaged Navier–Stokes (RANS) equations, incorporating a standard k–ϵ model. The only modification to the code involved the ability to switch between a standard, first-order, HYBRID method and the second-order, QUICK method for convection discretization. This allowed some assessment to be made of numerical diffusion errors on a given mesh. The solution domain spanned the entire region between centerline and outer tube wall, with the internal, core-tube wall represented as a blockage to the mesh (containing, usually, just two mesh lines). High Reynolds number log-law-based wall functions were applied on all solid surfaces, internal and external. The jet hole was represented as a castellated approximation to the true circular hole shape, on the cylindrical polar mesh used. Absence of any swirl velocities in the approach flows allowed the solution domain in the circumferential direction to be restricted to a 30 deg sector. All calculations reported here were carried out on a 30,000 node mesh (40 × 40 × 16 in x, r, and θ directions, respectively).

Results

Initial tests confirmed that annulus height was important in determining the jet characteristics. Indeed, for very small an-

Downloaded 02 Jun 2010 to 171.66.16.121. Redistribution subject to ASME license or copyright; see http://www.asme.org/terms/Terms_Use.cfm

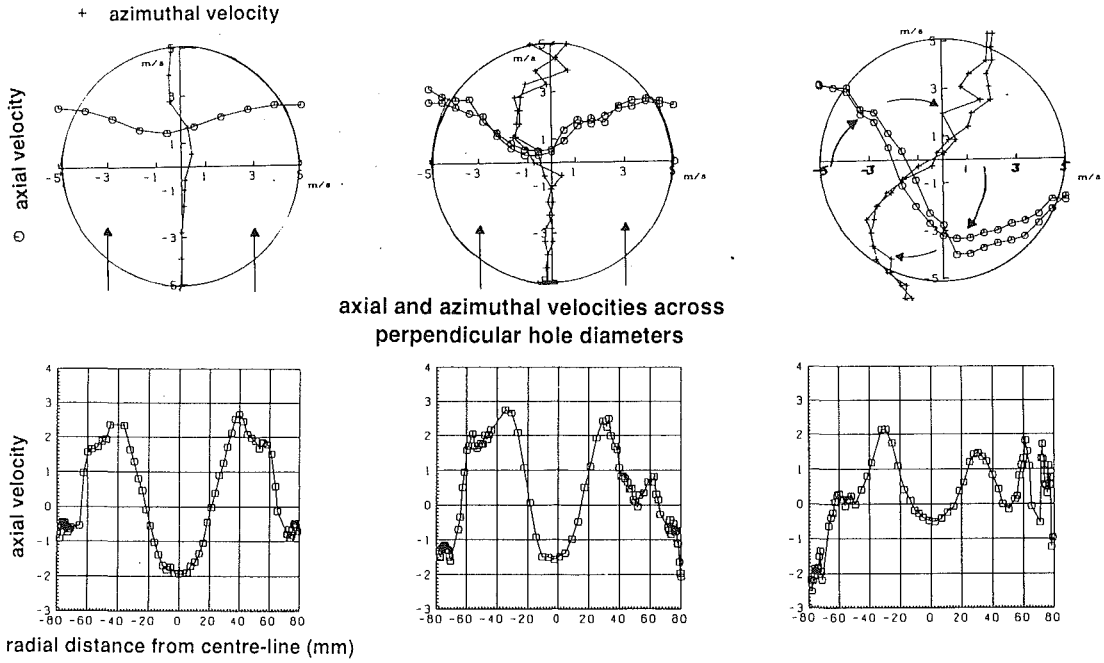

Fig. 2 10 mm annulus height, growth of vortex in hole and asymmetric flow

nulus heights, vortical instabilities were observed to form in the plane of the hole cross section (but not identically in each jet) and internal asymmetries were observed across the core-tube diameter. Figure 2 illustrates this phenomenon for a 10 mm annulus height. Measurements of axial and azimuthal velocity components across two orthogonal hole diameters are shown for various levels of annulus bleed flow. Large (35 percent) bleed flow (Fig. 2*a*) stabilizes the flow into the hole. Almost zero azimuthal velocities are measured along the vertical hole diameter (as demanded by symmetry) and the axial velocity is everywhere in the direction of the main annulus flow along the horizontal hole diameter (with a zero gradient at the center as demanded by symmetry). A measured axial velocity profile inside the core tube 12 mm downstream from the holes indicates good symmetry across the whole diameter (i.e., both opposing jets penetrating an identical amount). As the bleed flow is reduced to 25 percent (Fig. 2*b*) and 15 percent (Fig. 2*c*), the symmetric pattern over the hole breaks down and a clockwise vortex (looking down the hole from the annulus side) begins to form. This must be accompanied by vortices of opposite rotation in neighboring holes, so that opposed jets have opposite vortex rotations, leading to different penetration behavior and a breakdown of internal core-flow symmetry. The figure contains repeat measurements made for identical flow rate settings, showing that this behavior is quite deterministic and repeatable. This feature has been noted before in dilution hole geometry studies [8] and is known to require the use of splitter plates and dams in practical combustor systems to prevent its occurrence [5]. Note that the present axisymmetric geometry corresponds to a can-type combustion system, whereas [8] used a fully annular geometry. The tendency for vortex formation and jet asymmetries seems therefore to be independent of the particular combustor geometry. The origin of this phenomenon is associated with a breakdown of the flow at the rear of the hole. As the bleed flow decreases and more flow is forced through the hole, more and more of the hole flow originates from azimuthal planes removed from the hole. Some of this flow has indeed passed the hole and has to

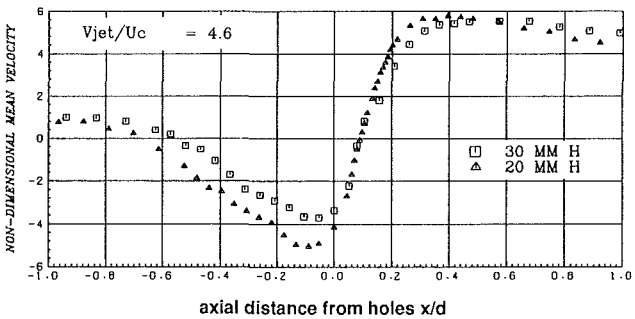

Fig. 3 Axial development of centerline velocity, R = 4.6, 30 mm and 20 mm annulus heights

approach from downstream. This leads to a left/right impingement process (as sketched in Fig. 2) about a vertical hole diameter. If this impingement process is unstable, then vortex formation can result. More measurements are clearly needed closer to the hole to clarify this important process. For the present purposes, however, a decision was made to move to a combination of annulus height and bleed flow for which stable behavior was observed, to suit the measurements to CFD calculations, which could then concentrate on a single hole and assume symmetric behavior about a longitudinal hole bisector.

Centerline axial velocity development for the two tests at a velocity ratio of 4.6 with 30 mm and 20 mm annulus heights is given in Fig. 3. These and all subsequent measurements presented here have been nondimensionalized by the constant centerline approach velocity U_c. Reducing annulus height (and thus also increasing core diameter) causes a significant increase in backflow velocity generated at impingement, and a slight increase in the forward flow velocity maximum. If the zero velocity location is taken as the jet impingement point, then little change is observed. Velocity measurements in the hole exit plane (see below) indicate a larger downstream inclination for H = 20 mm, but also a more disturbed profile as more

Downloaded 02 Jun 2010 to 171.66.16.121. Redistribution subject to ASME license or copyright; see http://www.asme.org/terms/Terms_Use.cfm

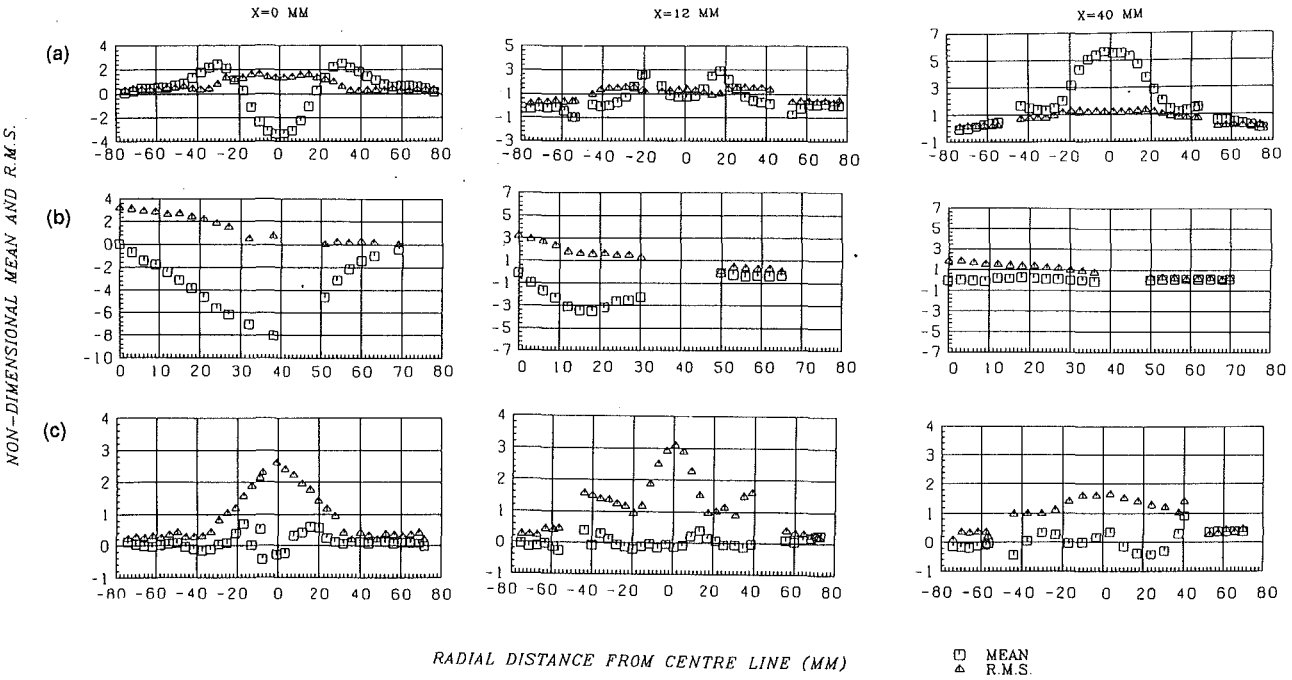

Fig. 4 Radial profiles of mean and rms velocities, H = 30 mm: (*a*) axial, (*b*) radial, (*c*) azimuthal

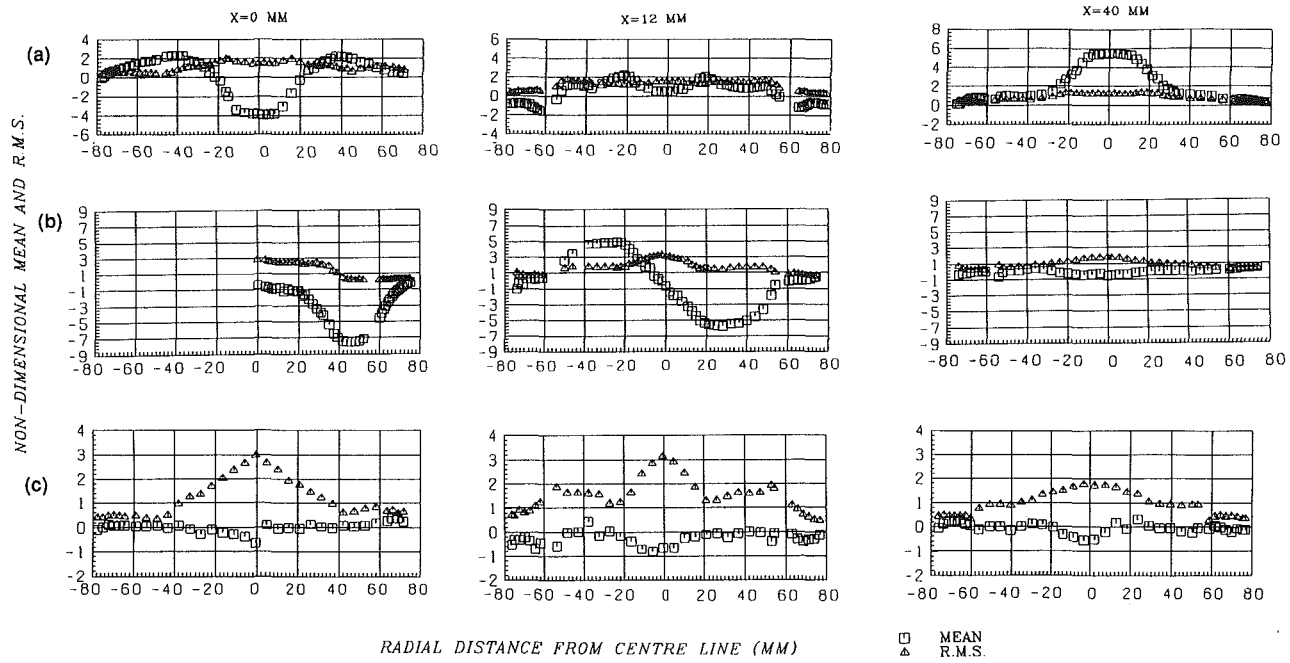

Fig. 5 Radial profiles of mean and rms velocities, H = 20 mm: (*a*) axial, (*b*) radial, (*c*) azimuthal

of the hole flow originates from the downstream annulus region. These effects seem to cancel as far as jet trajectories are concerned. The increased core diameter means that more of the upstream edge of the jet contributes to the backflow for H = 20 mm. The downstream behavior displays evidence of a slightly increased rate of mixing for the smaller annulus height, probably caused by the stronger impingement as evidenced by the larger backflow.

Radial profiles at three selected axial stations of the three mean velocity components and associated rms turbulent stresses are given in Fig. 4 for H = 30 mm and in Fig. 5 for H = 20 mm. (Gaps in the profiles occur where the tube walls interfered with laser beam passage.) Larger annulus height produces noticeably peakier axial velocity profiles just inside the core-tube wall at jet entry (x = 0). These persist until farther downstream (x = 12 mm), with final jet merging taking place at x = 40 mm. Note also the presence of negative axial velocities in the annulus at the 12 mm plane, indicating the finite annulus effect of the flow through the rear edge of the hole coming from downstream; this effect is noticeably stronger in the smaller annulus height results. The radial velocity results show an almost linear decay to zero on the centerline at jet entry for the 30 mm case, but a near-zero centerline zone for H = 20 mm; this is a result of increased core diameter. The magnitudes of the radial velocities at x = 12 mm are still of the same order for the smaller annulus height, but have been reduced by a factor of two for H = 30 mm, indicating different jet bending characteristics. Radial velocities are very small in both cases

Downloaded 02 Jun 2010 to 171.66.16.121. Redistribution subject to ASME license or copyright; see http://www.asme.org/terms/Terms_Use.cfm

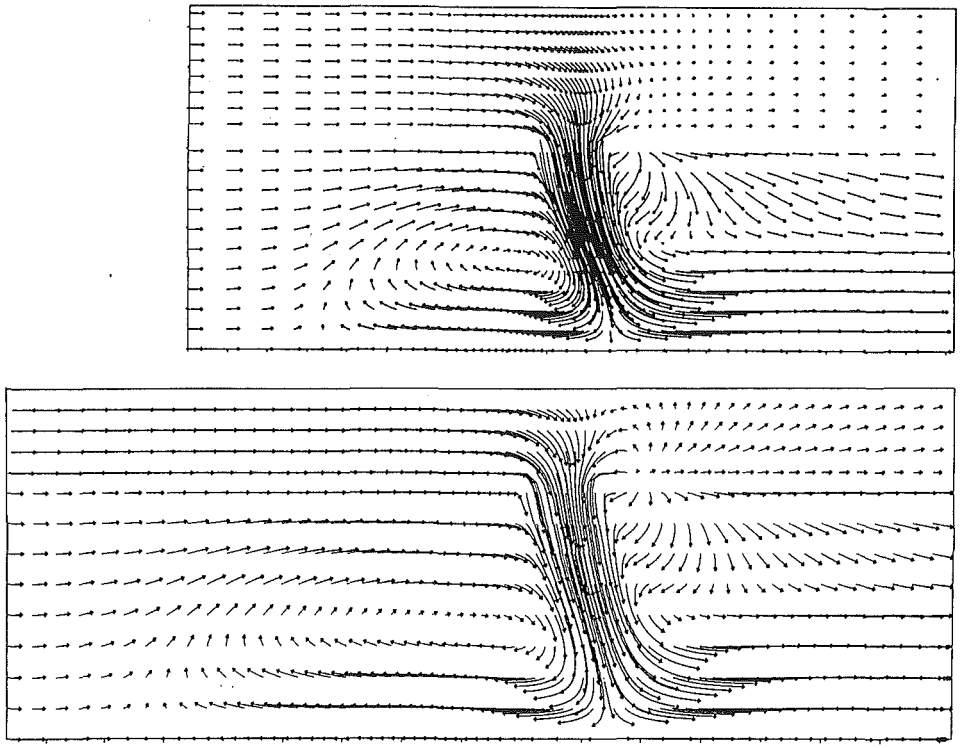

Fig. 6 Pathline visualization of predicted flow pattern on jet entry plane: H = 30 mm (top), H = 20 mm (bottom)

by x = 40 mm, implying the completion of the opposed jet merging process. Mean W velocities should of course be identically zero everywhere on the measurement plane. The data approached this true symmetry condition most of the time, but W velocities of order U_c are found near jet impingement. This is true for both annulus heights, with more apparent structure in the behavior for H = 30 mm. This is likely to be evidence of jet azimuthal "slippage" off each other at impingement, creating a locally swirling zone. The swirl velocities are very localized and disappear rapidly. The possibility should not be ignored, however, that this localized behavior at impingement is an unsteady, oscillating process, and that these oscillations have been picked up in the current long-time averaged measurements as extra "turbulence."

As far as the individual turbulent rms stresses are concerned, two aspects warrant attention. At impingement, a highly turbulent, highly anistropic zone is found, with radial and azimuthal intensities around 75 percent larger than axial (but not the comment on impingement instability above). This feature has disappeared on the centerline by 40 mm where approximate isotropy between the intensities is found over the whole core diameter. The second noteworthy feature is the appearance of peaks in the azimuthal stress intensity in the vicinity of the rear edge of the hole (see x = 12 mm profiles). The generation process leading to this increase in turbulence is associated with the strain rates caused by the strong lateral convergence of fluid from off-hole planes toward the rear of the hole. It may well be this process that eventually becomes unstable and gives rise to the vortex formation mentioned earlier.

Predictions of the above flows have been made using the CFD code described in [7] and above. A pathline visualization of the calculated velocity fields is presented in Fig. 6 for both cases. Boundary conditions in the annulus and core-tube approach flows were taken as far as possible from the measurements. The correct bleed flow was specified at annulus exit and extrapolation conditions used for the core-flow exit. The jet entry pattern, the slight downstream inclination to the trajectory, and the upstream vortex found at impingement are all plainly visible in Fig. 6. The rapid acceleration of the annulus flow as it approaches the hole and the feature mentioned above of flow entering the rear of the hole from the downstream annulus region are two aspects to note. Finally, for the smaller annulus height, it is significant that the predictions indicate a tendency for the hole to induce radial velocities over the whole annulus height. This leads to the formation of a vertical recirculation in the annulus downstream of the hole fed by laterally converging fluid as noted earlier. Instability of this vortex could be a possible cause of the behavior noted above for even smaller heights.

A quantitative comparison between predictions and experimental data is presented in Figs. 7–9. Space only permits discussion of the H = 30 mm case; a comparison of the predicted effect of annulus height will be reported in a later paper. The first two figures convey an impression of the accuracy of reproducing the mean velocity field, while Fig. 9 examines the ability to predict the turbulence energy. All three figures contain predictions made with both first-order HYBRID and second-order QUICK differencing for the convection terms. The gross features of both axial and radial mean velocities are well reproduced. The strength of backflow is larger in the QUICK predictions, as would be expected from a reduction in numerical diffusion errors; a comparison with the measured data indicates that, generally, the QUICK results lie closer to the experimental profiles than the more diffuse HYBRID results.

Discrepancies appear in four areas. First, the size of upstream vortex is predicted to be somewhat larger than is observed in the experiments (by about 40 percent in the QUICK results). Second, the negative axial velocities observed in the wake of the jet near the core-tube wall do not recover as rapidly in the predictions as in the measurements (see profile in Fig. 7*d*). The backflow velocities in the annulus feeding the rear of the holes are well predicted, however. Third, it is likely that the discharge coefficient of the hole is not well predicted, since the maximum radial velocity at hole exit is underpredicted by some 15 percent. This latter feature may be associated with the fact that the hole periphery is not precisely resolved by the

Downloaded 02 Jun 2010 to 171.66.16.121. Redistribution subject to ASME license or copyright; see http://www.asme.org/terms/Terms_Use.cfm

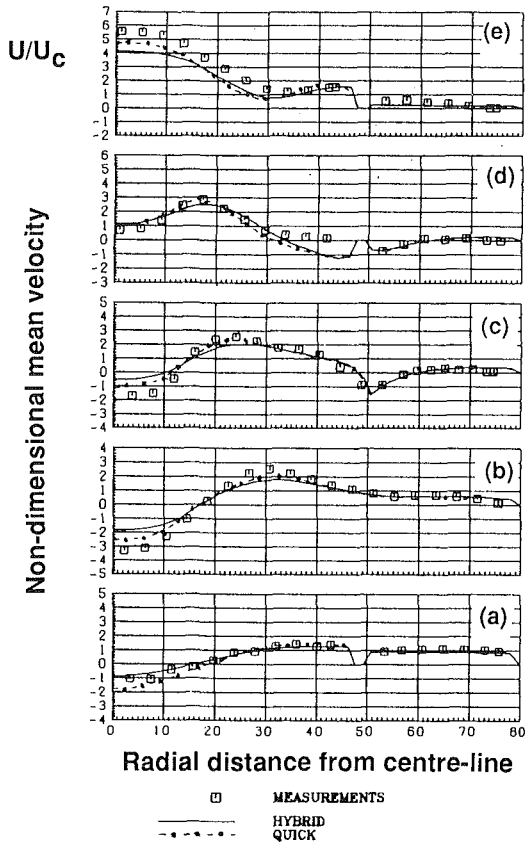

Fig. 7 Axial velocity profiles; comparison of predictions and measurements (H = 30 mm) at (*a*) x = −40 mm, (*b*) x = 0 mm, (*c*) x = 6 mm, (*d*) x = 12 mm, (*e*) x = 40 mm

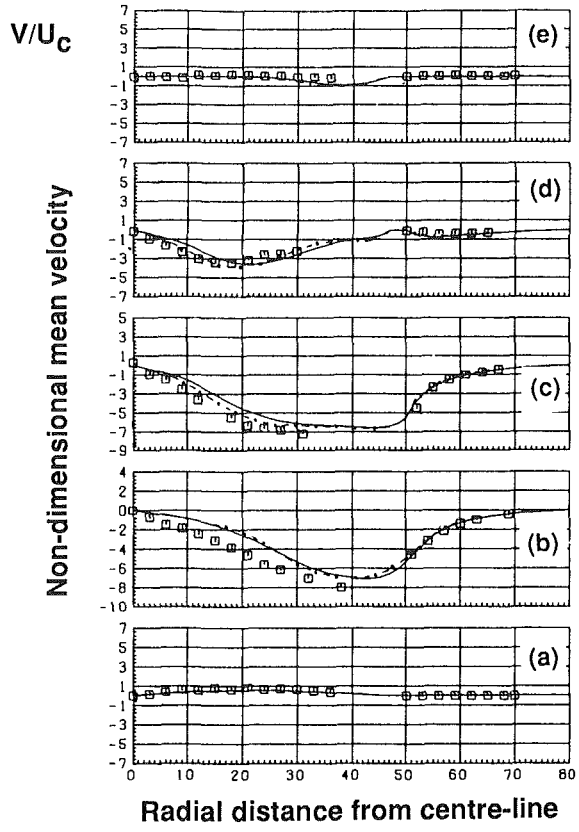

Fig. 8 Radial velocity profiles; comparison of predictions and measurements (H = 30 mm) at (*a*) x = −40 mm, (*b*) x = 0 mm, (*c*) x = 6 mm, (*d*) x = 12 mm, (*e*) x = 40 mm

cylindrical polar mesh used (a castellated approximation to the circular shape has been implemented). This point is worthy of further investigation using a mesh that can conform to the hole shape (e.g., as suggested in [9] to examine to what extent the backflow errors are a consequence of the discharge coefficient error). Finally, the centerline velocities in the downstream region imply a slower decay than observed in the experiments, indicating a too-slow mixing out of velocity maxima created by the merging jets.

The turbulence energy comparison in Fig. 9 indicates that although the turbulence field in the upstream vortex is in good agreement with experiments, jet impingement and the flow through the hole itself form two areas where the eddy viscosity model cannot simulate the measured turbulence structure. In the first case, the turbulence energy is underpredicted; this undoubtedly represents at least in part the inability of a scalar eddy viscosity model to simulate the highly anisotropic turbulence field at impingement. However, the possibility that the measured turbulence contains a contribution from large-scale flow oscillations cannot yet be discounted. For the flow through the hole, the errors are reversed; the predicted profile on the hole axis (x = 0) shows that levels of turbulence predicted are far in excess of the measured values in the hole vicinity. This is a region of high streamline curvature and flow convergence, and an eddy viscosity model is deficient at correctly representing the response of the turbulence to the complex strain rate field set up by the hole feed flow. The errors have already begun in the annulus region outside the hole as can be seen from the x = 0 profile. A switch in convection discretization treatment has only a small effect on this feature; it thus seems clearly identified as a turbulence model deficiency.

Summary and Conclusions

1 The issue of finite-height annulus feed to a row of holes drilled in a combustor wall to create radially inflowing jets

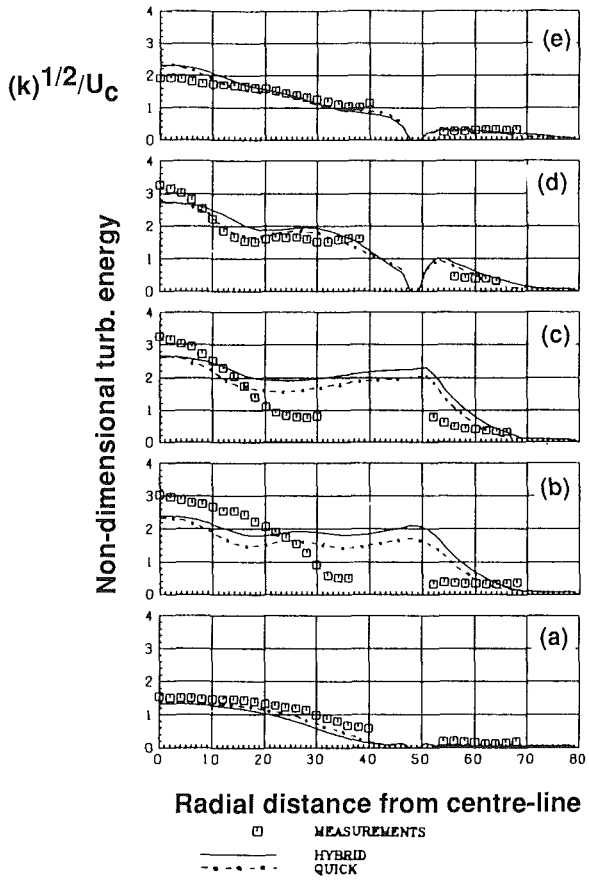

Fig. 9 Turbulence energy profiles; comparison of predictions and measurements (H = 30 mm) at (*a*) x = −40 mm, (*b*) x = 0 mm, (*c*) x = 6 mm, (*d*) x = 12 mm, (*e*) x = 40 mm

Downloaded 02 Jun 2010 to 171.66.16.121. Redistribution subject to ASME license or copyright; see http://www.asme.org/terms/Terms_Use.cfm

was identified in this paper as an aspect of combustor flow and modeling that had received scant attention in the past. The significance of the flow profiles over the hole as providing the boundary conditions for the internal combustor flow makes this a flow problem that merits closer study.

2 A generically representative but geometrically simple annulus/core flow with a single row of jets was studied experimentally using a water model and laser-Doppler velocimetry.

3 Under certain conditions unstable jet behavior and asymmetric profiles were measured. These features were identified as caused by the formation of a vortex in the jet holes originating from the instability of the impingement flow formed at the rear edge of the holes by laterally converging fluid.

4 For stable jet entry conditions, a set of experimental data suitable for use in a CFD evaluation study were obtained. All three mean velocity components and associated turbulent stresses were measured at several axial stations in the jet entry vicinity.

5 A k–ϵ calculation demonstrated good qualitative agreement with the experimental data but displayed several features at variance with the data. Size of backflow generated at impingement was overpredicted by some 40 percent and the hole discharge coefficient was obviously in error. Turbulence field discrepancies identified with limitations of an eddy viscosity based closure were also noted at both jet impingement and in the passage of the flow through the hole.

6 The castellated approximation to the hole shape adopted in the present predictions may have contributed to the above errors. A detailed study with calculations using a mesh that conforms to the hole shape is recommended.

7 Although this investigation has provided preliminary information on fluid mechanic phenomena associated with annulus-fed holes, it is felt that this topic is sufficiently important to be worthy of further study, both experimental and computational. The effect of hole shape, plunging, chamfering, etc., are some aspects that are of interest to combustor designers and should be investigated further.

Acknowledgments

This work has been carried out with the support of the Procurement Executive, Ministry of Defence. The authors would like to acknowledge many useful discussions with colleagues at Imperial College (Mech. Eng. and Chem. Eng. Depts.), at Rolls-Royce plc, and at RAE (Pyestock).

References

1 Holdeman, J. D., Srinivasan, R., and Berenfeld, A., "Experiments in Dilution Jet Mixing," *AIAA Journal*, Vol. 22, 1984, pp. 1436–1443.

2 Khan, Z. A., and Whitelaw, J. H., "Vector and Scalar Characteristics of Opposed Jets Discharging Normally Into a Cross-stream," *International Journal of Heat and Mass Transfer*, Vol. 23, 1980, pp. 1673–1677.

3 Demuren, A. O., "Modelling Turbulent Jets in Cross-flow," in: *Encyclopedia of Fluid Mechanics*, N. Cheremisinoff, ed., Gulf Publ. Co., New York, 1986, pp. 430–465.

4 Demuren, A. O., "Calculation of 3D Turbulent Jets in Crossflow With a Multigrid Method and a Second Moment Closure Model," *Proc. of International Symposium on Turbulence Modelling and Measurements*, Dubrovnik, 1990.

5 Lefebvre, A. H., *Gas Turbine Combustors*, McGraw-Hill, New York, 1983.

6 Adkins, R. C., and Gueroui, D., "An Improved Method for Accurate Prediction of Mass Flows Through Combustor Liner Holes," ASME JOURNAL OF ENGINEERING FOR GAS TURBINES AND POWER, Vol. 108, 1986, pp. 491–497.

7 Koutmos, P., and McGuirk, J. J., "Isothermal Modelling of Gas-Turbine Combustors—A Computational Study," *AIAA Journal of Propulsion and Power*, to appear, 1991.

8 Carrotte, J. F., and Stevens, S. J., "The Influence of Dilution Hole Geometry on Jet Mixing," ASME JOURNAL OF ENGINEERING FOR GAS TURBINES AND POWER, Vol. 112, 1990, pp. 73–79.

9 Shyy, W., Braaten, M. E., and Sober, J. S., "A 3D Grid Generation Method for Gas-Turbine Combustor Flow Computations," Paper No. AIAA-87-0204, 1987.

Downloaded 02 Jun 2010 to 171.66.16.121. Redistribution subject to ASME license or copyright; see http://www.asme.org/terms/Terms_Use.cfm

Studies of Jet Fuel Thermal Stability in a Flowing System

S. P. Heneghan

C. R. Martel

T. F. Williams

D. R. Ballal
Fellow ASME

University of Dayton,
Dayton, OH 45469

A flowing, single-pass heat exchanger test rig, with a fuel capacity of 189 liters, has been developed to evaluate jet fuel thermal stability. This "Phoenix Rig" is capable of supplying jet fuel to a 2.15 mm i.d. tube at a pressure up to 3.45 MPa, fuel temperature up to 900 K, and a fuel-tube Reynolds number in the range 300–11,000. Using this test rig, fuel thermal stability (carbon deposition rate), dissolved oxygen consumption, and methane production were measured for three baseline jet fuels and three fuels blended with additives. Such measurement were performed under oxygen-saturation or oxygen-starved conditions. Tests with all of the blended fuel samples showed a noticeable improvement in fuel thermal stability. Both block temperature and test duration increased the total carbon deposits in a nonlinear fashion. Interestingly, those fuels that need a higher threshold temperature to force the consumption of oxygen exhibited greater carbon deposits than those that consume oxygen at a lower temperature. These observations suggested a complicated relationship between the formation of carbon deposits and the temperature-driven consumption of oxygen. A simple analysis, based on a bimolecular reaction rate, correctly accounted for the shape of the oxygen consumption curve for various fuels. This analysis yielded estimates of global bulk parameters of oxygen consumption. The test rig yielded quantitative results, which will be very useful in evaluating fuels additives, understanding the chemistry of deposit formation, and eventually developing a global chemistry model.

Introduction

Commercial and military jet aircraft use jet fuel as a heat sink or working fluid for heat management. After absorbing heat, only a fraction of the fuel is consumed by the engines and the rest is recycled to the storage tanks. Some aircraft require ram air heat exchangers to cool the recirculated fuel to acceptable fuel tank temperatures because when jet fuel is heated above 420 K, dissolved oxygen reacts with fuel components to form gums and insoluble precipitates. These gums and precipitates can foul heat exchangers, burner feed arms, and fuel injectors.

In the future, the thermal mangement problems of advanced aircraft, including the thermal oxidative instability problems associated with heat fuels, will become increasingly severe for the following reasons:

1 Continuing demands for decreased fuel consumption will result in less fuel available for heat management.

2 Increased engine efficiency will be accomplished by higher operating temperatures further increasing the heat load on the available fuel.

3 Future aircraft will probably use powerful heat-generating hydraulic systems to increase maneuverability and/or decrease drag.

4 The development of supersonic cruise capability will result in higher airframe temperatures.

5 Ram air coolers will be dispensed with because they are both heavy and contrary to the development of efficient subsonic aircraft and also become ineffective at supersonic speeds.

6 The heat rejection rate of the avionics subsystems of military aircraft has doubled every 10 to 20 years, and can be expected to continue to increase.

In response to these problems and following the recommendations of the U.S. Air Force Thermal Management Working Group (see Harrison, 1990), the Aero Propulsion and Power Directorate of Wright Laboratories, Wright-Patterson Air Force Base, Ohio, initiated a research program aimed at increasing the thermal stability (and thus the heat sink capacity) of jet fuels. A primary objective of this program is to develop an additive package that will increase the thermal stability of JP-8 by 60 K. A secondary, long-range goal is to develop modeling techniques using global parameters to evaluate the deposition of solids in fuel system components (see Reddy and Roquemore, 1990).

This paper discusses the development of a single-pass heat exchanger system to evaluate jet fuel additives and presents numerous results on carbon deposition, oxygen consumption, and methane production that are used for global modeling studies.

Experimental Work

1 Test Rig. The experimental apparatus (known as the Phoenix rig) is a single-pass fuel-flow system that heats the

Contributed by the International Gas Turbine Institute and presented at the 37th International Gas Turbine and Aeroengine Congress and Exposition, Cologne, Germany, June 1–4, 1992. Manuscript received by the International Gas Turbine Institute February 6, 1992, Paper No. 92-GT-106. Associate Technical Editor: L. S. Langston.

Copyright © 1993 by ASME
Downloaded 02 Jun 2010 to 171.66.16.121. Redistribution subject to ASME license or copyright; see http://www.asme.org/terms/Terms_Use.cfm

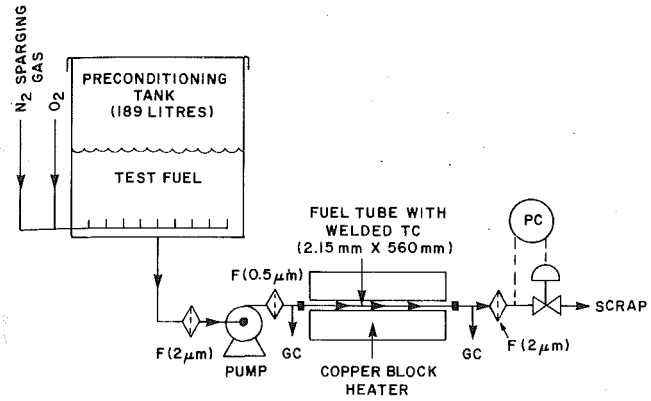

Fig. 1 Schematic diagram of the Phoenix Rig: F-filter, GC = gas chromatograph, TC = thermocouple, and PC = pressure controller

fuel in a stainless steel tube. Figure 1 is a flow schematic diagram of the Phoenix rig. A 189-liter preconditioning tank is equipped with a gas sparging system. The sparging system consists of two Brooks Model No. 5850E mass flow gas controllers and a Model 5876A indicator controller. This setup bubbles nitrogen/oxygen mixtures through the test fuel to control the dissolved oxygen content and to remove the dissolved argon.

An American Lewa Model EK-1 variable stroke, positive displacement diaphragm pump with a surge suppressor provides fuel flow in the range 1 to 100 ml/min at a pressure of 3.45 MPa. To monitor the fuel flow rate independently, a Max Machinery Model 213-310 positive displacement flow meter is employed. A manually set metering valve is located downstream of this flowmeter. This valve provides a 965 kPa pressure differential to isolate the surge suppressor from the pressure fluctuations produced by the downstream control valve.

2 Test Section. The test section through which the fuel flows is constructed of type 316 stainless steel tubing (560 mm long, 3.18 mm o.d., and 2.15 mm i.d.) heated by a copper block heater. The copper block heater is 460 mm long with a 76 mm diameter. It is capable of heating the test section to 770 K in such a way that the tube wall temperature profile remains constant during the experiment. This type of heater produces an axial fuel temperature gradient in the test section. It should be noted that the fuel heater used by Marteney and Spadaccini (1986) not only produces a temperature gradient in the test section, but also a test section wall temperature, which increases with the time duration of the experiment. A Sensotech type TJE differential pressure transducer measures the pressure drop across the test section. The fuel tubes used in our tests have an interior surface finish of 0.380 to 0.635 μm (rms value) and are tested for hydrocarbon and particulate deposits. The tubes are cut to size, cleaned using a Blue Gold alkaline metal cleaning solution in an ultrasonic bath, and then rinsed with deionized water.

Upstream of the fuel test section, a 0.5 μm sintered stainless steel filter with a bypass valve and a second Sensotech type TJE differential pressure transducer are installed. To maintain system pressure at 2.48 MPa, a Jordan MK708 6.35-mm pneumatic control valve is used. The control valve is actuated by a Micristar controller acting through a Fisher Model 546 I/P converter. A Sensotech Type TJE pressure transducer provides the pressure signal to the Micristar controller. Data are recorded using a Fluke model 2400B computer with a Model 1722A controller.

3 Gas Analyzer. We perform oxygen and methane analyses using a Hewlett Packard (HP) 5890 Series II gas chromatograph. It is equipped with a three-member tandem separation column, a thermal conductivity detector for oxygen, and a flame ionization detector for methane. This combination is capable of detecting oxygen concentrations as low as 150 parts per billion corresponding to 7500 counts. The sensitivity of this instrument to methane has not been fully determined, but it is estimated to be significantly more sensitive to methane than to oxygen. The in-line detection system is capable of sampling the fuel at the entrance to the heated test section, and at the exit of the heated section. Full details concerning the installation, construction, and calibration of the oxygen analyzer form the subject of a paper by Rubey et al. (1992).

4 Carbon Deposition Test Procedure. The test fuel passes through the tubular test section at a flow rate of 16 ml/min for 6, 12 or 24 hours. The test section is heated by the copper block heater, which is maintained at a predetermined temperature (544 K, 573 K, or 608 K). At the conclusion of the test, the test section is removed, drained, cut into 25-mm or 50-mm length segments, rinsed with hexane, dried in a vacuum oven, and analyzed for carbon deposits on a Leco RC-412 multiphase carbon analyzer. This method measures the amount of surface carbon deposit in the tube, but does not measure other deposit constituents, such as oxygen, hydrogen, sulfur, or trace metals. The amount of carbon deposit is then compared to baseline test results.

5 Temperature Measurements. A test section with welded thermocouples is used to obtain the wall temperature profile. Figure 2 shows typical measured tube wall temperatures. In this figure the bulk fuel temperature profile was calculated using a model developed by Reddy and Roquemore (1990). This model uses inlet and outlet fuel temperatures, tube wall temperature profile, fuel flow rate, and bulk fuel properties for calculations. To obtain reasonable agreement between the calculated and the measured bulk fuel discharge temperature, the model assumes turbulent pipe flow conditions, even through the Reynolds number of the fuel entering the test section was less than 100. The model also predicts high radial temperature profiles. It is possible that buoyancy effects caused by the high radial temperature gradient may produce secondary flow patterns that cause turbulent flow conditions. The measured output bulk temperature indicates that the flow is in the laminar-to-turbulent transition state.

6 Oxygen Consumption/Methane Production. The fuel flow rate is established at 16 ml/min and the copper block

Nomenclature

A = pre-exponential factor
E = activation energy
[F] = fuel concentration
f, g = functions
k, k' = reaction rate constants
[O_2] = oxygen concentration
R = universal gas constant
T = temperature
t = time
τ = fuel residence time

Abbreviations

ASTM = American Society of Testing Materials
GC = Gas Chromatograph
JFA = Jet Fuel Additive
JFTOT = Jet Fuel Thermal Oxidative Tester
JP = Jet Propellant (fuel)
JPTS = Jet Propellant Thermally Stable
MIL = Military Specifications
POSF = Propulsion Directorate—Fuels Branch

Downloaded 02 Jun 2010 to 171.66.16.121. Redistribution subject to ASME license or copyright; see http://www.asme.org/terms/Terms_Use.cfm

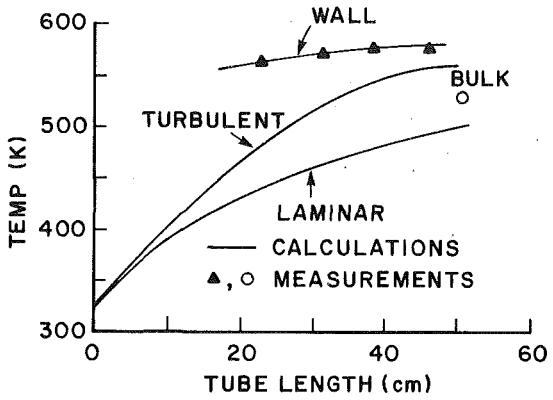

Fig. 2 Measured and calculated wall and bulk temperatures along the tube length for laminar and turbulent flow conditions

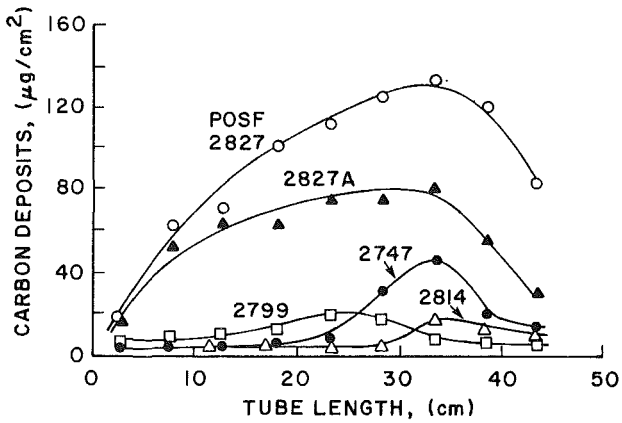

Fig. 3 Surface concentration of carbon deposits along the test section (block temperature = 573 K) for jet fuels during a 6-hour test

Table 1 Properties of baseline jet fuels

Source	ASTM Method	POSF-2747	POSF-2799	POSF-2827
JFTOT Break--point, K	D3241	605	672	539
Sulfur wt.,(%)	D3227	0	0	0.1
Aromatics (Vol %)	D1319	19	9	19
Existent Gum (mg/ml)	D381	0	0.4	0
Flash Point, K	D93	395	393	413

Table 2 Properties of blended jet fuels

Fuel Identification	JFTOT (K)	Base Fuel	Additives
POSF-2814	590	POSF-2747	Fuel system icing inhibitor Static Dissipator Corrosion Inhibitor
POSF-2827A	530	POSF-2827	JFA-5-12 mg/l
POSF-2827B		POSF-2827	JFA-5 - 50 mg/l

heater temperature is increased incrementally. The dissolved oxygen content, methane content, and temperature of the fuel are measured at the entrance to and the exit from the test section. The dissolved oxygen and methane contents of the heated fuel are then plotted versus the measured output bulk temperature and compared to baseline results. This test was performed to yield insights into the way fuel additives work, and was used to calculate global chemistry parameters for oxygen consumption.

7 Fuels Tested. Various baseline and blended jet fuels were tested. The properties of these fuels are identified in Tables 1 and 2, respectively. The initial baseline fuel (POSF-2747) was a Jet A-1 fuel. This hydrotreated product is also marketed as Super K-1 Kerosene. In our laboratory, it failed ASTM D3241 (or JFTOT) tests at a temperature of 605 K. This result was indicative of its excellent thermal oxidative stability. Fuel POSF-2799 (JPTS), an Air Force Spec. fuel (MIL-F-25524), was tested. JPTS is a known thermally stable fuel that we hope will serve as a calibration standard and thereby establish a goal for the fuel additive program. Finally, a nonhydrotreated fuel (POSF-2827) was acquired for analysis. Together, these three fuels represent the baseline fuels.

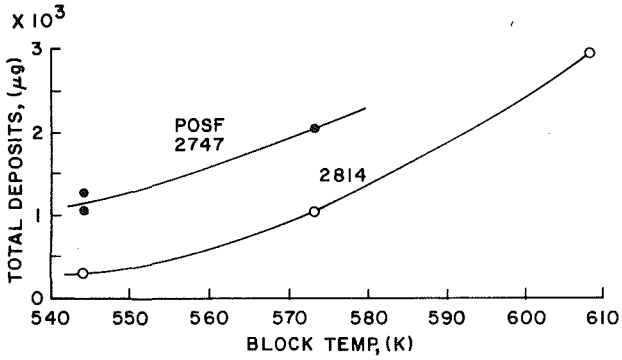

Fig. 4 Surface concentration of total carbon deposits for different block temperatures during a 12-hour test

New blends were made to test various additives using the baseline fuels. POSF-2814, was developed by mixing POSF-2747 with 22.5 ppm DuPont DCI-4A corrosion inhibitor, 1.0 ppm ASA-3 static dissipator, and 0.15 percent by volume diethylene glycol monomethyl ether. These additives, when blended with Jet A-1, produce JP-8. JFA-5 (the only currently accepted thermal stability additive package) was added to POSF-2827 in the concentration of 12 mg/l (POSF-2827A) and 50 mg/l (POSF-2827B).

Test Results

The carbon deposition test described above was used to measure the deposition characteristics of the fuels. Figure 3 shows a plot of the surface concentration of the deposition versus the axial length of the test section for various JP fuels using a copper block temperature 573 K and test durations of 6 hours. Note that the deposits increase along the length of the test section until a maximum is reached, and then decrease. It should also be noted that while our JFTOT tests indicated a decrease in the fuel thermal stability with the blending of additives to POSF-2747 (i.e., fuel POSF-2814), the flowing test here indicates that POSF-2814 has increased thermal stability. As a matter of fact, tests with all the blended fuel samples showed a noticeable improvement in fuel thermal stability.

The effects of block temperature on carbon deposition are shown in Fig. 4. The total deposit weights measured in the test section are plotted versus copper block heater temperature. As expected, carbon deposition increases with block temperature. Test duration also proved to be important. As shown in Fig. 5, carbon deposits increased by factors of 2.2 to 5.8 when the test duration was doubled to 12 hours. Further, the deposits

Downloaded 02 Jun 2010 to 171.66.16.121. Redistribution subject to ASME license or copyright; see http://www.asme.org/terms/Terms_Use.cfm

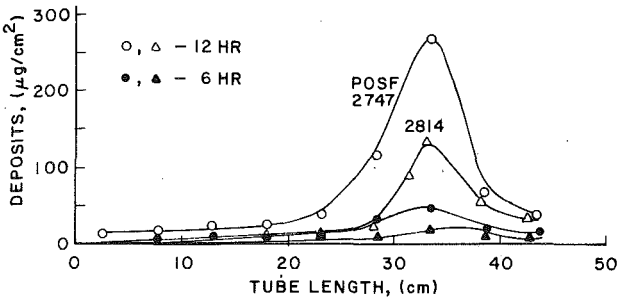

Fig. 5 Effect of test duration of the formation of carbon deposits in two representative jet fuels

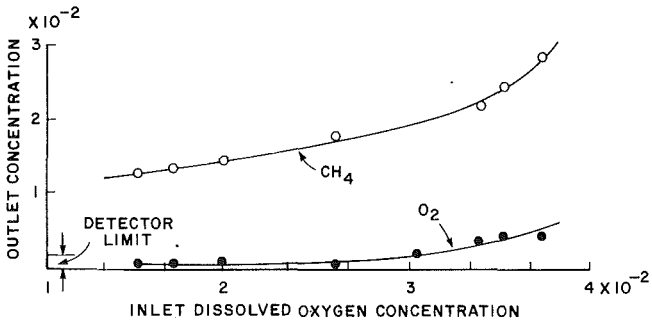

Fig. 7 Influence of inlet dissolved oxygen on the concentration of oxygen and methane at the outlet (block temperature = 573 K)

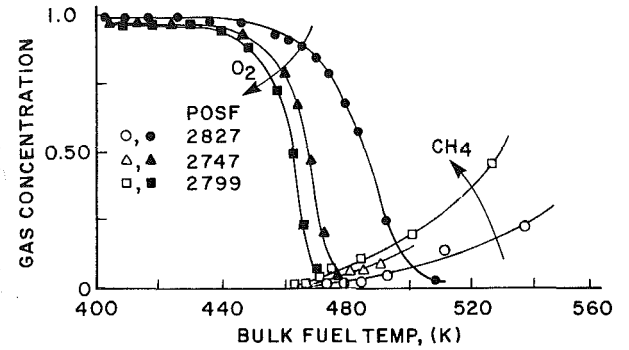

Fig. 6 Oxygen concentration and methane production versus bulk fuel temperature for baseline jet fuels

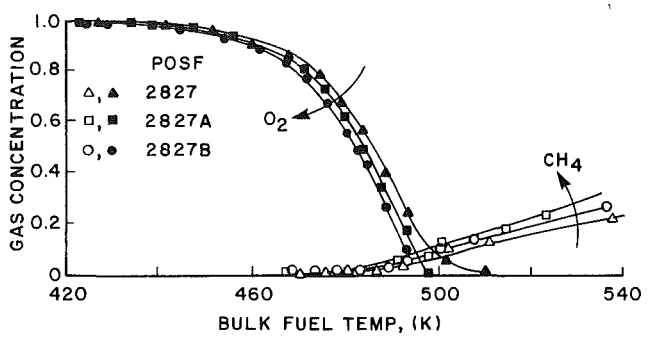

Fig. 8 Effect of fuel additives on the oxygen consumption and methane production

increased by a factor between 22 and 37 when the test duration was quadrupled to 24 hours.

The oxygen consumption and methane production curves for the three baseline fuels are shown in Fig. 6. The oxygen and methane concentrations were measured by the number of counts at the detector. The gas concentrations (corresponding to relative areas) presented in Figs. 6–8 and 10 were all normalized to the saturated oxygen level of 50 ppm (estimated) corresponding to 3×10^6 counts. Methane detection is significantly more sensitive than oxygen detection, and it is estimated to be less than 25 ppm at all times. The results of Fig. 6 suggest that at low bulk fuel temperatures, the oxygen and methane concentrations remain constant (oxygen at saturated level and methane at 0 ppm). As the temperature is increased, the oxygen concentration drops suddenly. Two fuels (POSF-2747 and POSF-2799) exhibited a drop of over 90 percent in the concentration of dissolved oxygen within a range of about 50 K change in the bulk fuel temperature. The third fuel (POSF-2827) showed a slow but measurable decrease in oxygen level over a wider temperature range. To preserve clarity in Fig. 6, results for the fuel POSF-2814 are not shown. However, it was found that presence of the additives had a minimal effect on the oxygen consumption trends. The onset of methane production occurs at a temperature that is very close to the bulk temperature at which there is a significant decrease of oxygen content. Tests of the fuels with nitrogen sparging showed a strong correlation between the initial oxygen concentration and the production of methane at 573 K block temperature.

As shown in Fig. 7, at this temperature, the available oxygen is consumed to below the detectable limit of the HP 5890-II GC and the methane production rate decreases with a decrease in the initial oxygen concentration.

Additives were tested in the Phoenix rig by measuring the oxygen consumption/methane production trends, and also by measuring the carbon deposition for 6 and 12-hour tests. Figures 8 and 9 show the results of these tests. While JFA-A acted to decrease the deposits in the test section, a 2-μm sintered metal filter located downstream (see Fig. 1) exhibited significantly increased plugging as measured by the pressure drop across the filter. This observation was made at a temperature of 400 K at the filter. Currently, testing continues to evaluate additives of four major varieties; anti-oxidants, dispersants, detergents, and metal deactivators.

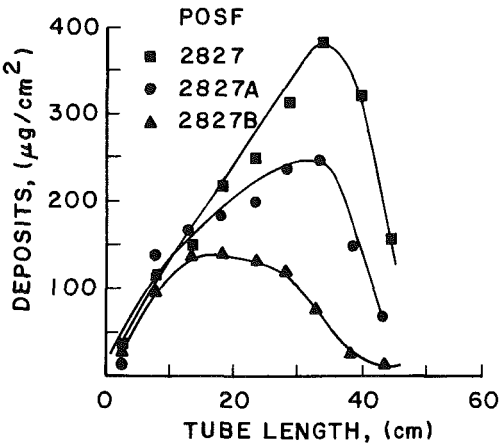

Fig. 9 Effect of fuel additives on the carbon deposition along the tube length

Discussion

The carbon deposition trends observed for the four fuels (Fig. 3) were not surprising. The best thermally stable fuel in the JFTOT tests was JPTS, while it was POSF-2814 in the Phoenix rig. The worst fuel thermal stability in either test was exhibited by POSF-2827. Fuel POSF-2827 contains 1000 ppm hetero-atoms (namely sulfur) and these atoms are known to form deposits when the fuel is oxidized. Fuel POSF-2747 was

Downloaded 02 Jun 2010 to 171.66.16.121. Redistribution subject to ASME license or copyright; see http://www.asme.org/terms/Terms_Use.cfm

expected to exhibit *good* thermal stability because it is a strongly hydrotreated fuel. It has a narrow boiling range and less than 50 ppm hetero-atoms (ASTM D3227 sensitivity). Therefore, it is not surprising that it exhibited a JFTOT breakpoint temperature higher than POSF-2827.

In Fig. 5, a decrease in deposition for fuel POSF-2814 versus fuel POSF-2747 was observed. It is hard to account for this improvement in thermal stability upon the addition of the static dissipator, anti-icing additive, and corrosion inhibitor. In fact, several other systems including the JFTOT test, microcarbon residue test, microthermal precipitation test, hot liquid process simulator test (see Pearce et al., 1992), and a multipass heat exchanger (see Lefebvre et al., 1992) indicated the contrary. Thus, the most significant conclusion is that several different tests, which may yield conflicting results, are needed to evaluate the effects of given additives on the thermal stability of a fuel.

Our other observations on the baseline fuels appear to be consistent with the observations of previous researchers. For example, the increase in carbon deposits with increasing block temperature, the decrease in deposits with decreasing oxygen, and the nonlinear increase in carbon deposit with test duration are consistent with the results obtained by Giovanetti and Szetela (1986). In general, these observations indicate that carbon deposit formation is stimulated by the temperature-driven absorption of oxygen, and catalyzed by itself.

As illustrated in Fig. 9, JFA-5 also exhibited a significant ability to decrease deposits. JFA-5 is an additive that includes an amine-type antioxidant, a dispersant, and a metal deactivator.

The carbon deposit for fuel POSF-2827 A decreased by nearly a factor of two. Fuel POSF-2827B showed a significant decrease again, indicating that JFA-5 can be effective at concentrations above that specified in MIL T-25524. However, the causes and implications of the increased plugging of the downstream filter are currently under investigation.

Figure 10 shows the depletion of oxygen versus temperature for fuels POSF-2747 and POSF-2827. In these oxygen depletion measurements, several interesting observations can be made. These observations are best explained by a simple analysis based on the following assumptions:

(*a*) For a turbulent flow, the radial fuel temperature profile is flat.
(*b*) The fuel temperature increases linearly along the tube length. This assumption is an approximation of the calculated heating curve in Fig. 2.
(*c*) The consumption of oxygen in the fuel is treated as a bimolecular reaction, i.e.;

$$d[O_2]/dt = -k'[O_2][F].$$

(*d*) $[F] \gg [O_2]$ so that $k'[F]$ can be approximated by the psuedo first-order rate constant $k = k'[F]$.
(*e*) The rate constant for the consumption of oxygen can be treated as an Arrhenius-type reaction rate constant,

$$k = A \exp(-E/RT)$$

(*f*) The chemistry pathway is independent of the temperature.

Based on these assumptions, we can evaluate the rate of oxygen disappearance, or the concentration of oxygen with time as follows:

If

$$O_2 + F \rightarrow \text{product} \quad (1)$$

then

$$d[O_2]/dt = -k'[O_2][F] \text{ and}$$
$$d[O_2]/dt = -k[O_2]$$

where

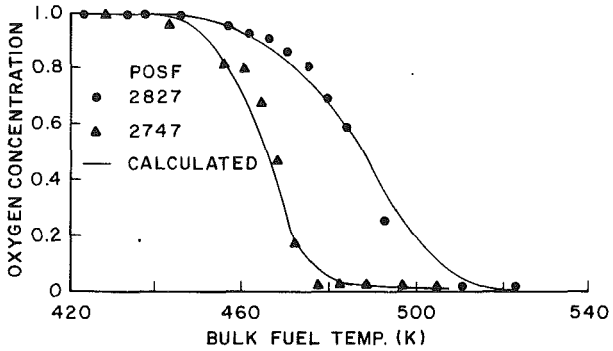

Fig. 10 A comparison of measured and calculated values for the oxygen consumption in the POSF-2747 and POSF-2827 fuels

$$k = k'[F]$$

or

$$d[O_2]/[O_2] = -k\, dt \quad (2)$$

Since $k = f(T)$ and $T = g(t)$ eq. (2) cannot be integrated easily. Hence we assumed that,

$$T = 300 + (T_{final} - 300)t/\tau \text{ or } dT = (T_{final} - 300)dt/\tau$$

Then, Eq. (2) integrates to a form

$$\ln\{[O_2]_t/[O_2]_0\} = (T_{final} - 300)(t/\tau) \times \int_{300}^{T_{final}} A \exp(-E/RT)dT. \quad (3)$$

There is no closed-form solution to Eq. (3) and therefore, a MathCad program (developed by Mathsoft Inc.) was used for integration. As shown in Fig. 10, we can predict, fairly accurately, the oxygen depletion from fuels POSF-2747 and POSF-2827 using pre-exponential values of $10^{27} s^{-1}$ and $10^{16} s^{-1}$, and activation energies of 57 kcal/mole and 35.5 kcal/mole in Eq. (3), respectively.

These measured pre-exponential factors are significantly higher than those expected from theory. A liquid-phase diffusion-limited bimolecular pre-exponential is normally about $10^{9.5}$ 1/m-s or less. The measured pre-exponential should therefore be less than the product of $10^{9.5}$ 1/mole-s and the fuel concentration of about 3 moles/1. However, jet fuel is not constituted of only one compound, and moreover we have measured the global oxygen consumption Arrhenius parameters. It remains to be seen if these measured global parameters can be somehow incorporated into the global models of fuel behavior.

Another interesting observation is that the fuel POSF-2827, which exhibits the highest temperature for oxygen consumption, also produces the largest amount of carbon deposit. This observation implies that forming carbon deposits and inhibiting some types of molecules are responsible for oxygen consumption in a jet fuel. Most probably these molecules are the hetero-atom (sulfur) compounds. Fuel POSF-2827, which is not hydrotreated, should have more of these compounds than the fuel POSF-2747. Finally, there is a difference between the present results and the data of Giovanetti and Szetela (1986). Our results show that the oxygen is nearly completely consumed at a temperature of 500 K; while Giovanetti and Szetela (1986) report that approximately 40 percent of the original oxygen remains at fuel temperatures as high as 585 K. As yet, our attempts to account for this discrepancy have not been successful.

In Fig. 8, we observe that the thermally stable fuels produce more methane than the unstable fuel. Heneghan and Zabarnick (1993) have shown that this production of methane gives additional clues to the chemical mechanisms occurring in the heated tube section. Methane production almost certainly arises

Downloaded 02 Jun 2010 to 171.66.16.121. Redistribution subject to ASME license or copyright; see http://www.asme.org/terms/Terms_Use.cfm

from the presence of methyl radicals in the system. Methyl radicals initially appear at or near the temperature at which methane first appears because these radicals react extremely quickly with oxygen to produce methyl peroxide radicals. Only after the oxygen depletion can the abstraction reaction to form methane be observed. The abstraction reaction is slower than the recombination reaction with oxygen despite the fact that methane formation is an exothermic reaction. This is because, even at 473 K, the activation energy associated with H-abstraction by methyl about 6 kcal/mole, slows the reaction down by almost three orders of magnitude. This analysis indicates that the stable fuels produce methyl radicals at lower temperatures, and that these radicals are important in the subsequent consumption of oxygen.

In the future, it will be interesting to study the oxygen and methane behavior for fuel additives to determine whether the observed trends of oxygen, methane, and deposits continue. So far, these trends clearly suggest that the consumption of oxygen at lower temperature and the more rapid production of methane indicate fewer deposits on the test section walls.

Conclusions

A single-pass flowing heat exchanger facility (Phoenix rig) was designed to test the carbon deposit forming tendencies of jet fuels in flowing systems. Three samples each of baseline JP fuels and JP fuels blended with the additives package were tested. The results, some of which were in qualitative agreement with those of other researchers, proved the design and usefulness of the Phoenix rig. Accordingly, measurements of carbon deposits, oxygen depletion, and methane production were performed for a variety of test conditions and the following conclusions emerged:

1 Tests with all the blended fuel samples showed a noticeable improvement in fuel thermal stability.
2 Both block temperature and test duration increased the total carbon deposits in a nonlinear fashion.
3 Above a threshold bulk temperature of 450 K, the fuel-dissolved oxygen concentration dropped suddenly and the onset of methane production was triggered. With nitrogen sparging, the methane production was greatly reduced. These observations suggest a complicated relationship between the formation of carbon deposits and the temperature-driven consumption of oxygen.
4 A simple analysis, based on a bimolecular reaction rate, correctly accounted for the fuel dissolved oxygen consumption rate. Such an approach proves the feasibility of developing a more rigorous model based on global kinetic parameters.

Acknowledgments

This research was supported by the U.S. Air Force Wright Laboratory, Aero Propulsion and Power Directorate, Wright-Patterson Air Force Base, Ohio, under Contract F33615-87-C-2767 with Dr. W. M. Roquemore serving as Technical Monitor.

References

Giovanetti, A. J., and Szetela, E. J., 1986, "Long Term Deposit Formation in Aviation Turbine Fuels at Elevated Temperature," AIAA Paper No. 86-0525.

Harrison, W. E., III, 1990, "Aircraft Thermal Management: Report of the Joint WRDC/ASD Aircraft Thermal Management Working Group," Report No. TR-90-2021, Wright-Patterson Air Force Base, OH.

Heneghan, S. P., and Zabarnick, S., 1993, "Oxidation of Jet Fuels and the Formation of Deposits," *Fuel*, in press.

Lefebvre, A. H., Chin, J., and Sun, F., 1992, "Experimental Techniques for the Assessment of Fuel Thermal Stability," AIAA Paper No. 92-0685.

Marteney, P. J., and Spadaccini, L. J., 1986, "Thermal Decomposition of Aircraft Fuel," ASME JOURNAL OF ENGINEERING FOR GAS TURBINES AND POWER, Vol. *108*, pp. *648-654*.

Pearce, J. A., Harrison, W. E., III, Anderson, S. D., Edwards, J. T., Byrd, R. J., Heneghan, S. P., Martel C. R., Williams, T. F., Biddle, T. B., and Edwards, W. H., 1992, "Advanced Thermally Stable Jet Fuels Development," *Aviation Fuels: Thermal Stability Requirements*, W. Kirklin and P. David, eds., ASTM STP-1138.

Reddy, K. V., and Roquemore, W. M., 1990, "A Time Dependent Model With Global Chemistry for Decomposition and Deposition of Aircraft Fuels," ACS Paper No. 90-14.

Rubey, W. A., Tissandier, M. D., Striebich, R. C., and Tirey, D., A., 1992, "In-Line Gas Chromatographic Measurement of Trace Oxygen and Other Dissolved Gases in Flowing High Pressure Thermally Stressed Jet Fuel," presented at the Symposium on Structure of Jet Fuels, American Chemical Society, San Franciso, CA, Apr.

Downloaded 02 Jun 2010 to 171.66.16.121. Redistribution subject to ASME license or copyright; see http://www.asme.org/terms/Terms_Use.cfm

G. J. Sturgess
Pratt & Whitney,
East Hartford, CT 06108

S. P. Heneghan

M. D. Vangsness

D. R. Ballal

University of Dayton,
Dayton, OH 45469

A. L. Lesmerises

D. Shouse

Wright Laboratories,
Wright-Patterson Air Force Base,
Dayton, OH 45433

Effects of Back-Pressure in a Lean Blowout Research Combustor

Experimental information is presented on the effects of back-pressure on flame-holding in a gaseous fuel research combustor. Data for wall temperatures and static pressures are used to infer behavior of the major recirculation zones, as a supplement to some velocity and temperature profile measurements using LDV and CARS systems. Observations of flame behavior are also included. Lean blowout is improved by exit blockage, with strongest sensitivity at high combustor loadings. It is concluded that exit blockage exerts its influence through effects on the jet and recirculation zone shear layers.

Introduction

Combustion stability is extremely important in gas turbine engines for aircraft use. It is becoming more difficult to ensure that adequate stability margins can be maintained because of current design trends toward airblast atomization of liquid fuel, high temperature rise, and low emissions combustors.

As part of a comprehensive research program to investigate, understand, and model lean blowouts in the combustors of aircraft gas turbine engines (Sturgess et al., 1991a), three combustors are utilized. These vehicles consist of a research combustor, a technology combustor, and a generic gas turbine combustor, which reflect the three-phase approach to the problem. The purpose of the research combustor is to yield fundamental information on the lean blowout process to assist in understanding the events taking place during blowout, and so guide in modeling them.

In gas turbine combustor design, it is generally recognized that the end of the flame-holding primary zone is determined by the transverse combustion air jets entering through the combustor liners (Lefebvre, 1983). For combustors using either pure airblast or hybrid pressure-atomizing primary/airblast secondary fuel injectors, it has been observed that dynamic interactions can occur between the axially directed jets of atomized fuel/air mixture from the injectors, and these transverse combustion air jets. Recirculation zones of the "external" (Gupta et al., 1984) or "inside-out" type (Sturgess et al., 1990) seem to be especially prone to this behavior. The interaction can be exacerbated if the airflow through the combustor dome (including the injectors) is a significant proportion of the combustor total flow, and if the transverse air jets are close to the dome.

It was therefore felt that the important back-pressure effect exerted on the flame through the presence of the combustion air jets should be included in any simulation of a gas turbine combustor primary zone.

In the research combustor, which was intended for the study of the breakdown of flame stabilization in the primary zone, the essential features of a typical primary zone of modern combustors were reproduced in simplified form (Sturgess et al., 1992a). Combustion air jets were not included directly due to the complication involved; however, the back-pressure of these jets was represented by means of exit blockage from the combustor.

Research Combustor

The research combustor consists of a central fuel jet of gaseous propane surrounded by an unheated co-axial air jet, with the confluence of the jets centrally located in a nominally circular cross-sectional duct (Sturgess et al., 1992b). The duct is closed at its forward end to give a backward-facing step. The combustor exit is open to the atmosphere; low pressure effects on lean blowout are simulated by means of dilution through injection of excess nitrogen into the air supply (Sturgess et al., 1991b). The combustor is mounted vertically on an

Contributed by the International Gas Turbine Institute and presented at the 37th International Gas Turbine and Aeroengine Congress and Exposition, Cologne, Germany, June 1–4, 1992. Manuscript received by the International Gas Turbine Institute February 6, 1992. Paper No. 92-GT-81. Associate Technical Editor: L. S. Langston.

Copyright © 1993 by ASME
Downloaded 02 Jun 2010 to 171.66.16.121. Redistribution subject to ASME license or copyright; see http://www.asme.org/terms/Terms_Use.cfm

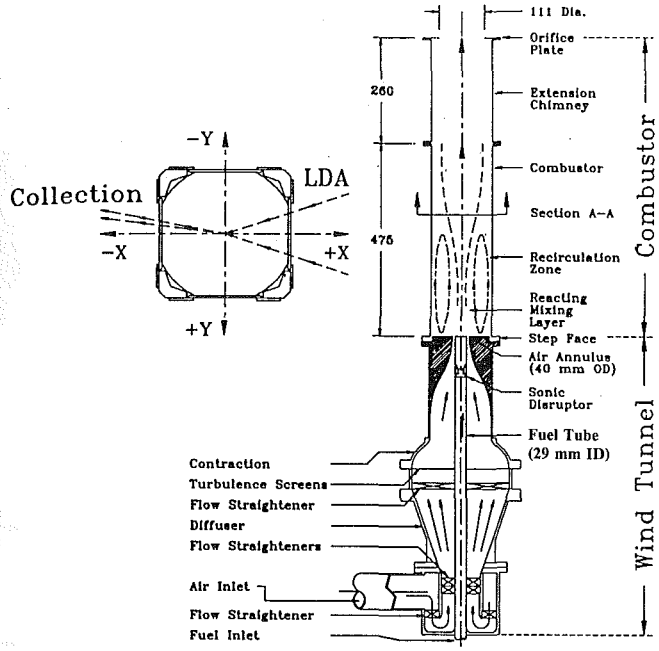

Fig. 1 Research combustor, showing axes convention

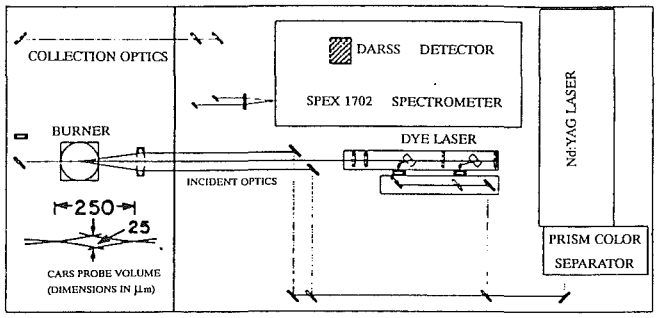

Fig. 2 Arrangement of the CARS system optics

airflow-conditioning unit, which traverses through a cutout in a fixed optical bench, Fig. 1.

The combustion tunnel was designed and constructed in two sections: a fixed upstream window section providing optical access as needed, and a replaceable downstream chimney. The chimney is available in two lengths, and the combustor can be run with either of these, or with no chimney at all. The combustor has a hydraulic diameter of 150 mm, giving length to diameter (L/D) ratios of 3.167, 4.9, and 6.513, respectively, depending on the chimney arrangement. The inner diameter of the fuel tube is 29.97 mm with a 2-deg half-angle taper over 120 mm of its length, and the outer diameter of the air passage at discharge is 40 mm.

Provision is made for combustor exit blockage. The geometric values of exit blockage are 21.0, 45.1, and 62.0 percent of the combustion cross section. These blockages are achieved by means of thin orifice plates. For the 45.1 percent geometric blockage, "top-hat" exits with tailpipe length to diameter (L/D) values of 1.0 and 2.1, respectively, are also available.

The optical windows can be replaced by metal plates containing arrays of thermocouples for wall temperature measurements, and tappings for static pressure measurements. The combustor may be run with any combination of windows and plates.

LDA Arrangement

Mean and fluctuating velocity component measurements are obtained by means of a laser-Döppler anemometer (LDA) system (Sturgess et al., 1992b), using 10-deg off-axis forward scattering. The effective probe volume is $50 \times 300 \times 750$ μm.

The combustor is mounted vertically in the facility (Sturgess et al., 1992a), and its centerline constitutes the z axis, with zero taken as the plane of the step. The x and y axes are diametral to the combustor cross section, with the x axis aligned with the LDA axis. Velocities parallel to and increasing in the direction of the z axis, and velocities normal to and directed away from the axis, are considered positive.

The effective optical window within which data may be taken is defined by: $-68.7 < x < +68.7$ mm, and $-22 < y < 33$ mm; in the downstream direction it is $+2 < z < 358$ mm. This window permits reasonable access to the major flow field features (Sturgess et al., 1992b).

For error assessments, see Sturgess et al. (1992b).

CARS Arrangement

The laser source for the coherent anti-Stokes Raman Spectroscopy (CARS) optics is a Nd:YAG pulse laser with 10 ns time resolution. The frequency-doubled source green beam (532 nm) is equally divided into four parts: two of these serve as pump beams, while the remaining two pump a dye laser oscillator and amplifier. The dye laser is tuned to provide a red broad-band Stokes beam (110 FWIIM) centered at 607 nm. The red Stokes beam and the two green pump beams are then focused together by a 25 cm focal length lens in a BOXCARS configuration. A 25×250 μm measuring spot size is achieved. The CARS signal is collected by a Spex 1702 spectrometer, 1024-element DARSS camera, and Tracor-Northern multichannel analyzer (Fig. 2). The raw data are processed by a MODCOMP minicomputer.

From the raw data the temperatures are determined by comparing the actual nitrogen spectra to the calculated spectra, using a least-squares fit. The calculation of a nitrogen CARS spectrum requires knowledge of the instrument slit function. Error problems associated with the assumption of a constant slit function when the optical path contains density and/or temperature gradients are avoided by use of a simple method of determining slit functions from the collected data at actual temperature and turbulence levels, by applying local thermodynamic equilibrium principles (Heneghan et al., 1991). This method has been shown to yield improvements in the precision of the CARS measurement (Heneghan and Vangsness, 1991).

Both fuel and air flows were monitored by separate electronic flow control units to within ± 0.5 percent and ± 1.5 percent, respectively. The combined error produced an uncertainty of ± 1.5 percent in equivalence ratio, or ± 30 K in temperature. Usually, 500 samples were taken for each CARS measurement to ensure that the error in rms temperature was less than 10 K. The rms temperature is susceptible to CARS instrument noise (Heneghan and Vangsness, 1990). However, in combusting flow the temperature fluctuations are much greater than the instrument noise, and thus the measurement precision (reproducibility) is good. It is estimated overall that the CARS mean temperature measurement accuracy is within 50 K, while the precision is well within 20 K. Unlike the LDA, CARS temperature measurements are time-averaged without density-biasing effects.

Isothermal Flow Field

Development of the isothermal flow field in the research combustor with a free outlet is fully discussed by Sturgess et al. (1992b). Briefly, at a simulated blowout condition, the

Downloaded 02 Jun 2010 to 171.66.16.121. Redistribution subject to ASME license or copyright; see http://www.asme.org/terms/Terms_Use.cfm

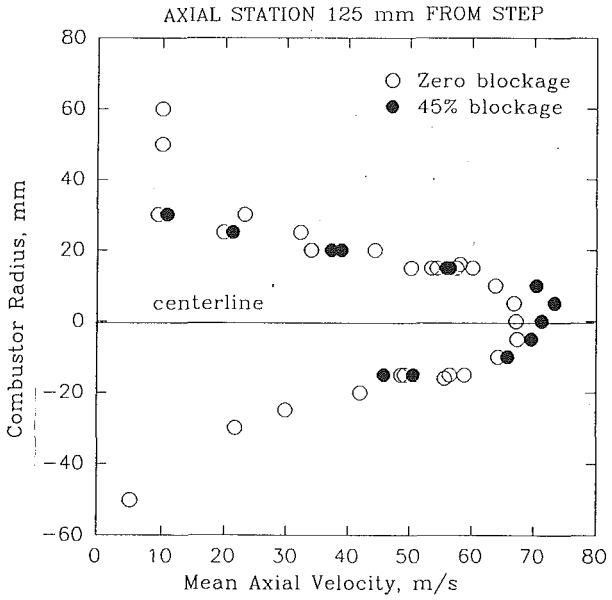

Fig. 3 Radial profiles of mean axial velocity in isothermal flow 125 mm downstream from the step-plane, showing central flow net acceleration with exit blockage

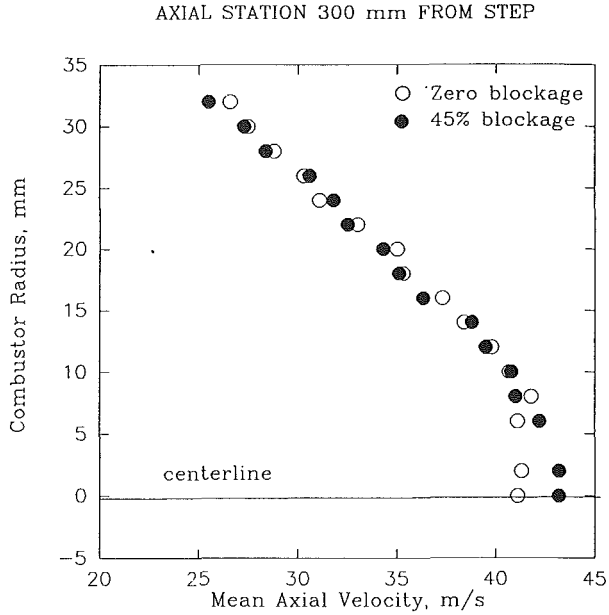

Fig. 4 Radial profiles of mean axial velocity in isothermal flow 300 mm downstream from the step-plane, showing central flow net acceleration with exit blockage

annular air jet immediately entrains the central fuel jet, generating a small central recirculation bubble of length 17 mm with a beginning about 15 mm downstream of the jet confluence. The individual jets thus quickly merge as they expand into the combustor, and soon lose their identities. This merging is complete by 138 mm from the step. The step generates a large recirculation zone of axial length 7.7 step heights, and with vortex centers about 3.1 step heights downstream.

The addition of exit blockage by orifice plate exerts an obvious effect on the radial profiles of mean axial velocity as the flow accelerates along the combustor centerline to form a vena contracta in the exit plane, with a toroidal recirculation zone forming on the forward face of the orifice plate. For the 4.9 L/D combustor the near-field is unaffected, but the centerline flow acceleration is evident as close as 125 mm downstream from the step-plane. Figures 3 and 4 demonstrate this at the 125 and 300 mm stations, respectively, for 45.1 percent blockage. Note that the acceleration effect is ameliorated to some extent by the expansion of the combined jets into the combustor.

There were no changes apparent in the fluctuating velocities with the addition of exit blockage.

The flow field with reaction present is the process of being measured. The features described under isothermal conditions are unchanged in character by the heat release.

Effects of Blockage on Flame Behavior

The research combustor operates with three basic flame conditions, depending on the equivalence ratio. For $\phi > 1.05$ approximately, a thin, sheathlike pilot flame is anchored close to the step near the outer diameter of the air passage (Sturgess et al., 1991b). The fuel source for this pilot flame is the step recirculation zone. The major heat release is then precipitated downstream in more or less distributed fashion, by the action of this pilot. Downstream flame-holding takes place in the shear layers associated with the central and step recirculation zones (Sturgess et al., 1992b). For $\phi < 1.05$ approximately, the pilot flame is highly intermittent (Roquemore et al., 1991), and the main flame is lifted (Sturgess et al., 1991b), allowing considerable premixing of reactants to take place prior to combustion. The lifted flame is positioned between 160 to 300 mm from the step-plane. When ϕ reaches 1.5 to 2.0 and before a rich blowout, a separated flame condition is again established where the pilot flame is no longer apparent to the eye, but the main flame does not lift in this case. It is located about 30 to 40 mm downstream from the step.

Lean blowout data were correlated on the basis of a combustor loading parameter (Sturgess et al., 1991b), derived from reaction rate theory as

$$LP = \dot{m}_{\text{Tot}}/(VP^nF)$$

where for gaseous fuels and with simulation of low pressures by excess nitrogen injection,

$\dot{m}_{\text{Tot}} = \dot{m}_{\text{fuel}} + \dot{m}_{\text{air}} + \dot{m}_{\text{nitrogen}}$

V = reactor volume

P = effective pressure

n = apparent global reaction order

$= 2\phi/(1 + \dot{m}_{\text{nitrogen}}/\dot{m}_{\text{air}})$

ϕ = equivalence ratio

F = temperature correction factor (to 400 K)

$= 10^{0.00143T_{in}}/3.72$

T = inlet temperature of reactants in K.

Use of LP for blowout correlations follows from the adoption of a stirred reactor modeling approach (Sturgess et al., 1992a). It also forms a useful way of characterizing the degree of "flame straining" present in the combustor.

Figure 5 provides a map of flame behavior as a lean blowout is approached, obtained by visual observation. The combustor L/D was 4.9, and the exit was a 45.1 percent blockage orifice plate. Inlet temperatures for the reactants were constant at 293 K, and no excess nitrogen was injected. The Reynolds number of the annular air jet was in the range of 24,800 to 46,000. The attached and lifted flame conditions are illustrated in Fig. 2 of Sturgess et al. (1991b).

The range of the loading parameter in Fig. 5 is such that lean blowouts were obtained close to the flammability limits for propane/air mixtures at ambient conditions (Lewis and

Downloaded 02 Jun 2010 to 171.66.16.121. Redistribution subject to ASME license or copyright; see http://www.asme.org/terms/Terms_Use.cfm

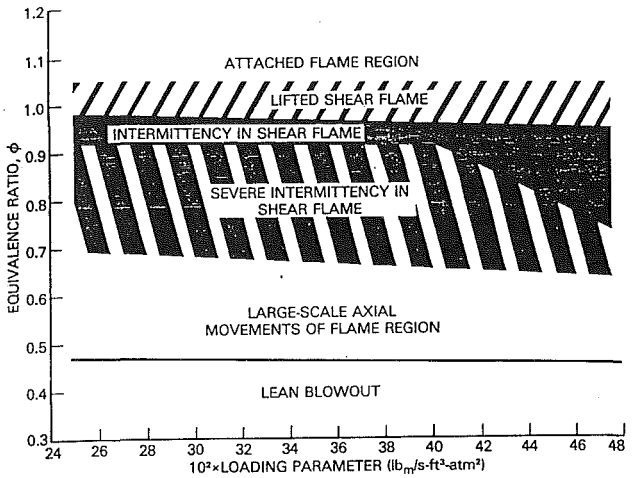

Fig. 5 Flame behavior as lean blowout is approached at low combustor loadings with 45 percent exit blockage

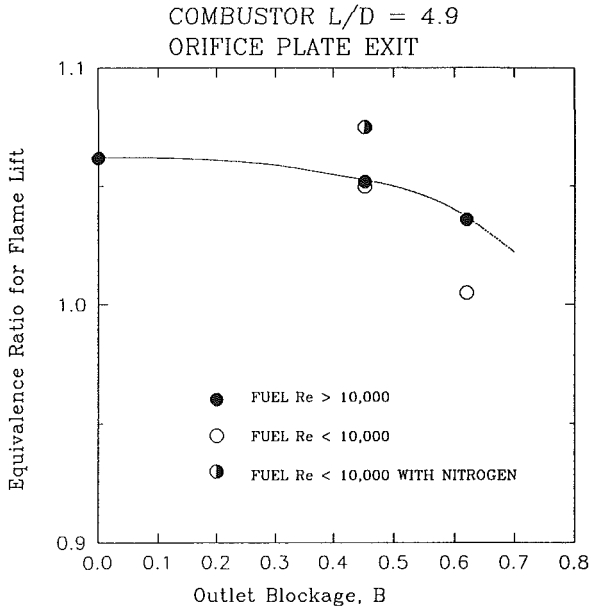

Fig. 6 Dependence of equivalence ratio for flame lift on exit blockage for low and intermediate combustor loadings

von Elbe, 1961). The flame behavior seen is both reversible and repeatable. Flame lift can be seen at about 1.05 equivalence ratio, and is insensitive to loading parameter over the limited range covered. Subsequent tests (Sturgess et al., 1991b) with injection of excess gaseous nitrogen into the air stream showed no effects on equivalence ratio for flame-lift. When the fuel flow was progressively reduced at constant airflow, or the airflow was progressively increased at constant fuel flow, the same sequence of flame events leading to a blowout took place. These events are shown in Fig. 5. Eventually, an oscillatory flow situation develops, with large-scale axial movements of the entire lifted flame about a mean position. This motion leads, in due course, to lean blowout.

The existence of the sequence of flame behaviors did not change qualitatively with differences in exit blockage. However, the equivalence ratio for flame lift was observed to decrease slightly with increase in blockage due to orifice plates (Fig. 6). Similar behavior was observed with increase in tailpipe L/D for the 45.1 percent blockage top-hat section (Fig. 7).

The significance of the 10,000 Reynolds number for the fuel jet in Figs. 6 and 7 is that this value represents a critical threshold for transition to turbulent flow for propane (Lewis and von Elbe, 1961).

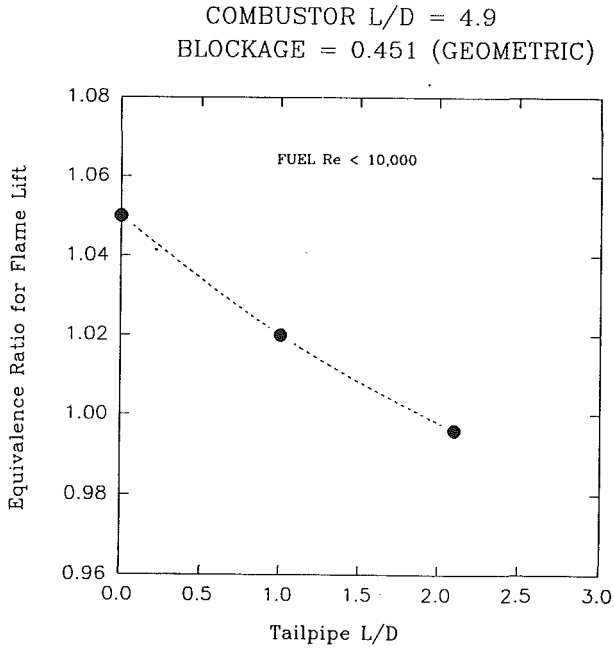

Fig. 7 Dependence of equivalence ratio for flame lift on tailpipe length for 45 percent geometric exit blockage

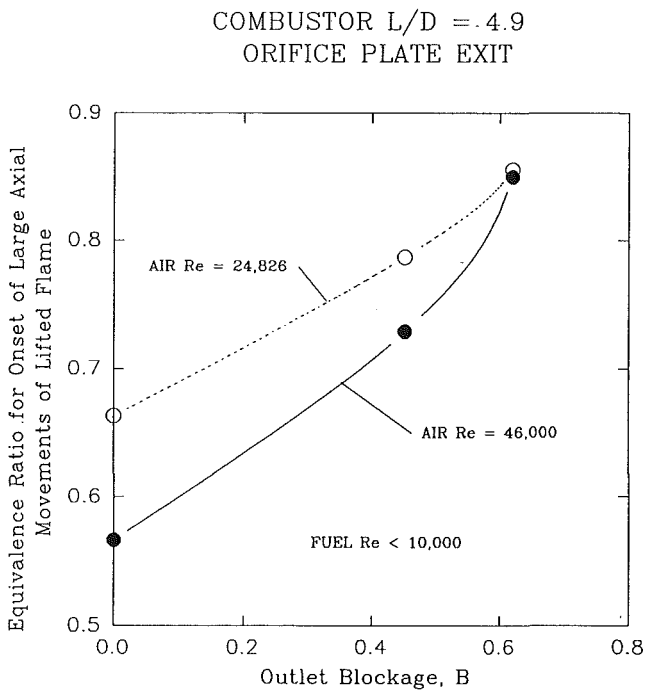

Fig. 8 Influence of exit blockage and combustor loading on equivalence ratio for onset of axial movements of the lifted flame

A fairly strong influence on the equivalence ratio for the onset of the large-scale axial oscillation of the lifted flame was observed, as shown in Fig. 8. Increased blockage raises this equivalence ratio and is therefore destabilizing, opposite to the effect on flame lift. Note the significance of air jet Reynolds numbers.

It is apparent that the loss of the important pilot flame marks the beginning of a lean blowout sequence. A similar importance of the pilot flame is observed as a rich blowout is approached. Figure 9 shows the dependence of rich equivalence ratio for loss of the pilot flame (to result in a separated main flame), on exit blockage in the 4.9 L/D combustor. Note that on the rich side, decreasing equivalence ratio denotes a maximum loss

Downloaded 02 Jun 2010 to 171.66.16.121. Redistribution subject to ASME license or copyright; see http://www.asme.org/terms/Terms_Use.cfm

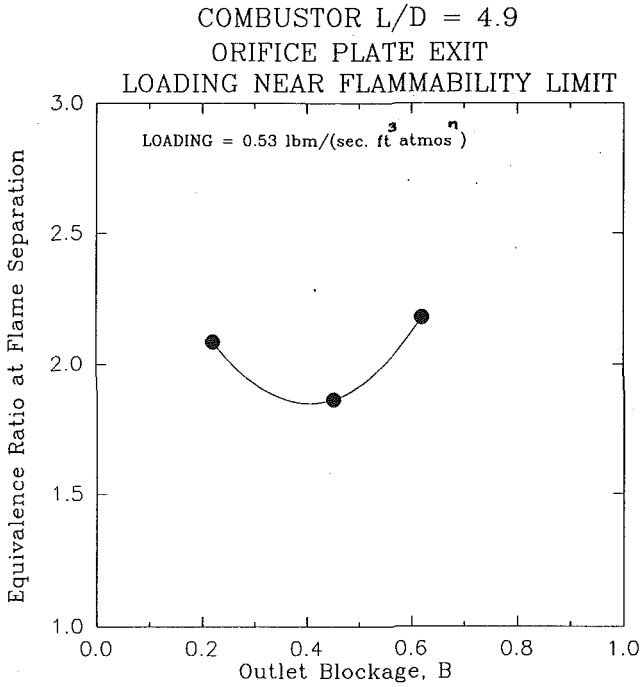

Fig. 9 Dependence of equivalence ratio for flame separation on exit blockage for low combustor loading

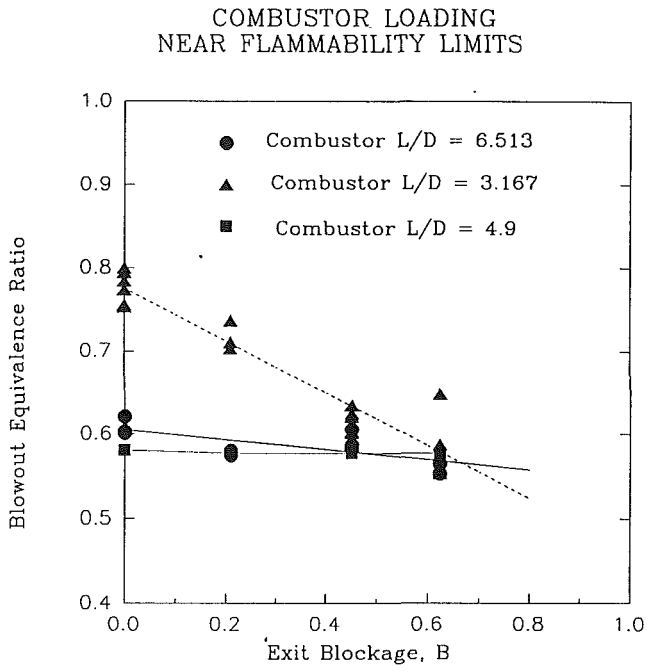

Fig. 11 Influence of exit blockage on lean blowout at low combustor loading in three combustor lengths

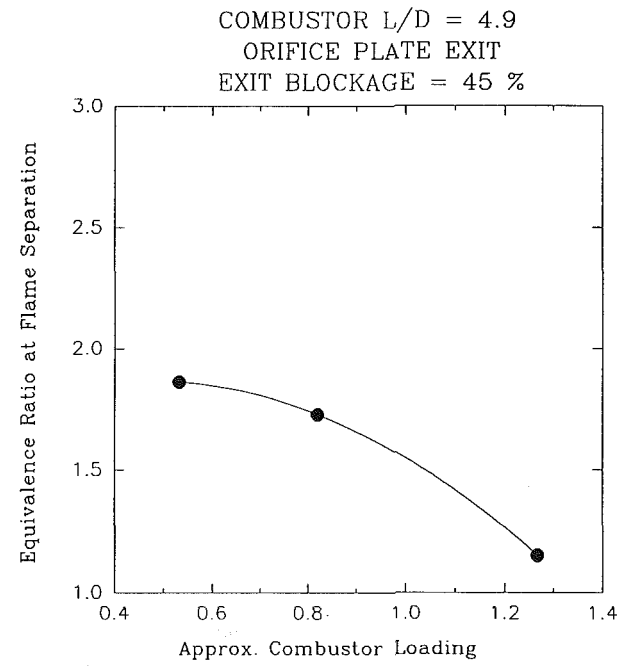

Fig. 10 Influence of combustor loading on equivalence ratio for flame separation at 45 percent exit blockage

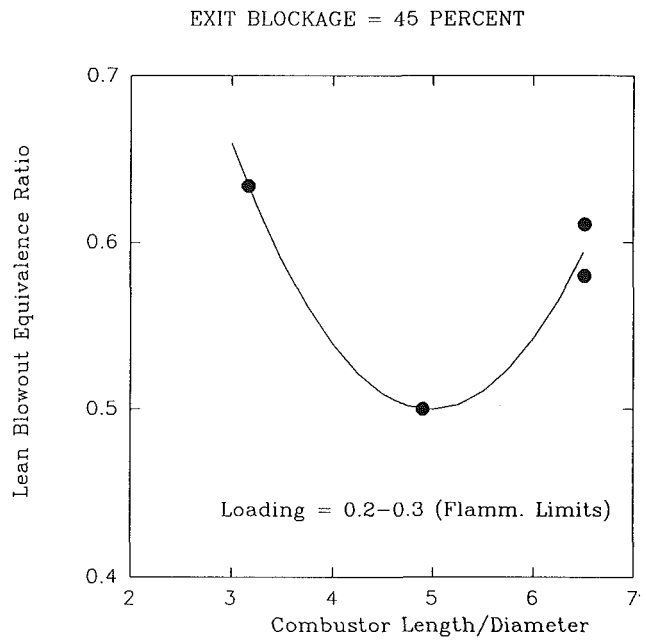

Fig. 12 Dependence of lean blowout at low loadings on combustor length with 45 percent exit blockage

of stability at 45.1 percent blockage. At given blockage this rich equivalence ratio for pilot flame loss decreases as the combustor loading is increased; Fig. 10 demonstrates this for the 4.9 L/D combustor at 45.1 percent exit blockage by orifice plate.

Direct Effects on Lean Blowout

It was observed for low values (about 0.18 lb_m/(sec.ft.^{3}atmos.^{n}) close to the flammability limits for propane/air mixtures at these conditions) of the loading parameter that the blowout equivalence ratio decreased linearly as the exit blockage by orifice plate was increased. This is shown in Fig. 11, and is somewhat surprising since the lifted flame is positioned (Roquemore et al., 1991) in the regions where the mean flow is beginning to be accelerated due to the blockage (Figs. 3 and 4), at least in isothermal flow. Heat release should increase the flow acceleration. The improvement in stability depended on the combustor L/D ratio; for a given blockage, the shorter the combustor the less stable it was and the greater its sensitivity to the exit blockage. For the 4.9 L/D combustor at this loading, the lean blowouts were virtually independent of exit blockage.

For a fixed exit orifice plate blockage of 45.1 percent at slightly higher loading parameter, the dependency on L/D is given in Fig. 12, where it can be seen that an optimum L/D

Downloaded 02 Jun 2010 to 171.66.16.121. Redistribution subject to ASME license or copyright; see http://www.asme.org/terms/Terms_Use.cfm

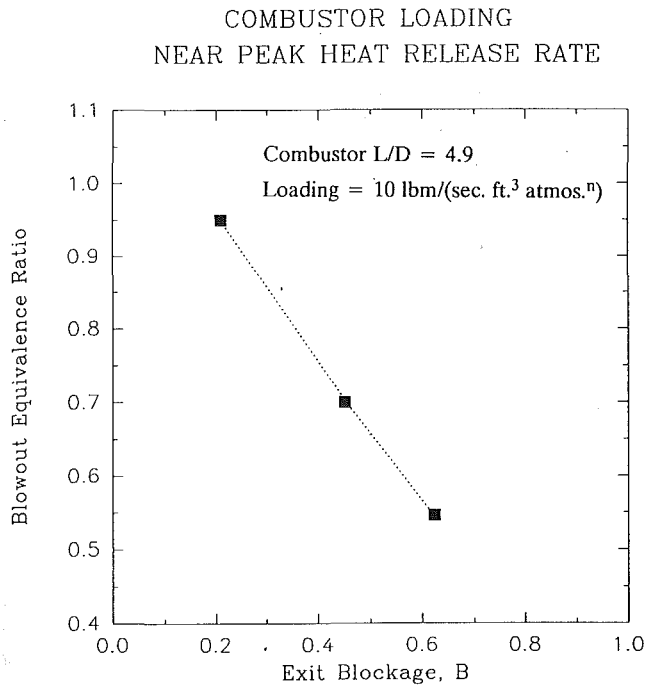

Fig. 13 Influence on lean blowout of exit blockage at high combustor loading

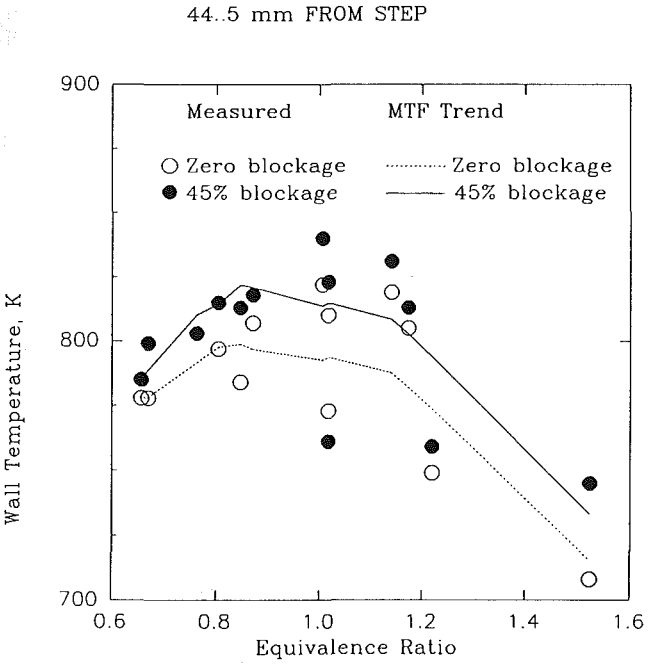

Fig. 14 Comparison of actual wall temperatures with smoothed values over a range of equivalence ratios, showing influence of exit blockage

exists. Close to the flammability limits there is also a fairly strong sensitivity of blowout equivalence ratio to combustor loading parameter. The existence of the optimum combustor length for maximum stability close to the flammability limits (Lewis and von Elbe, 1961) can be attributed to the occurrence of acoustic coupling (organ-pipe resonance driving eddy shedding off the step at 55 Hz) at large L/D (Heneghan et al., 1990), and outlet interference with flame holding at small L/D.

At 45.1 percent exit blockage the peak amplitude of the 55 Hz frequency signal measured inside the combustor by Kistler pressure transducers was increased by a factor of 5.5 when the combustor L/D was increased from 3.167 to 6.513. For the 4.9 L/D combustor with 45.1 percent exit blockage (and the acoustic treatment described by Heneghan et al., 1990), the peak-to-peak amplitudes for low-frequency oscillations (1–600 Hz) were less than 0.69 N/m^2, for high-frequency oscillations (1–5 kHz) the amplitudes were less than 6.9 N/m^2.

Figure 13 displays the sensitivity to exit blockage in the 4.9 L/D combustor operating at loadings (10 $lb_m/(sec.ft.^3 atmos.^n)$) near the peak heat release rate condition (obtained with a combination of high airflow rates and injection of excess nitrogen as a diluent). Again, the blowout equivalence ratio decreases linearly with increasing blockage. However, when contrasted with the sensitivity to blockage for this combustor near the flammability limits (Fig. 11), it is seen that blockage exerts a much more powerful influence on stability at this higher loading.

The general conclusion can be drawn that exit blockage improves the lean stability of the research combustor. The effectiveness of blockage in improving the stability in a combustor of given length depends on the loading at which the combustor is operated. Of the three combustor lengths evaluated (and for operation at low loadings at least), the 4.9 L/D combustor has the best stability at any blockage level between 0 and 62 percent. Exit blockage reduces the rich stability of the research combustor, and the extent of this also depends on the combustor loading.

Wall Temperature Behavior

The wall temperatures for the combustor are needed to provide boundary condition information for subsequent computational fluid dynamic calculations to be made in attempts to model the lean blowout process. They can also provide, by inference, additional information concerning development of major flow features in the combustor.

Wall temperatures are most conveniently expressed in nondimensional form, sometimes known as Metal Temperature Factor (MTF), and defined by

$$\text{MTF} = \frac{T_s - T_{in}}{T_{ad,fl} - T_{in}}$$

where

T_S = wall temperature
$T_{ad,fl}$ = adiabatic flame temperature.

For premixed flames, MTF represents a normalized wall temperature, and is particularly useful in the present case therefore, because of the partial premixing that takes place when the flame is lifted.

Figure 14 compares, at 44.5 mm downstream from the step and inside the step recirculation zone, actual thermocouple temperatures over a range of equivalence ratios against temperatures derived from the MTF trend with downstream distance. Data are provided for zero and 45.1 percent exit blockage in the 4.9 L/D combustor. The tests were made for a variety of jet velocity ratios and combustor flow functions. No effect of velocity ratio was apparent, and substantial increase in flow function resulted in only a negligible increase in MTF.

The figure shows that wall temperatures in the recirculation zone increase with combustor exit blockage by about 20 to 25 K for 45.1 blockage. Peak temperatures occur at equivalence ratios in the range of 0.9 to 1.1. For the attached flame condition ($\phi \geq 1.05$), temperature levels are about 820 K, and fall to about 780 K as lean blowout is approached.

The form of MTF variation with equivalence ratio is shown in Fig. 15 for a station 146 mm downstream from the step (still inside the recirculation zone). The behavior in the figure is typical of all axial stations along the combustor. MTF decreases with increasing equivalence ratio up to an equivalence ratio of about 0.95, and then becomes independent out to a

Downloaded 02 Jun 2010 to 171.66.16.121. Redistribution subject to ASME license or copyright; see http://www.asme.org/terms/Terms_Use.cfm

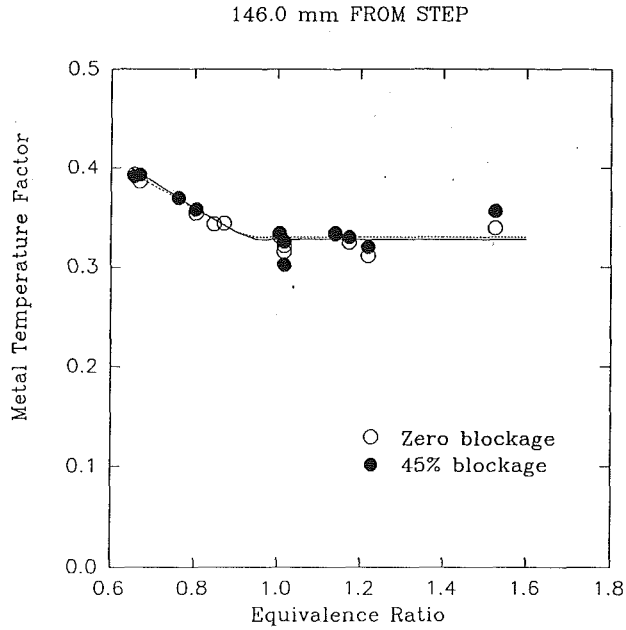

Fig. 15 Normalized wall temperatures at 126 mm from step-plane for zero and 45 percent exit blockage, showing influence of equivalence ratio

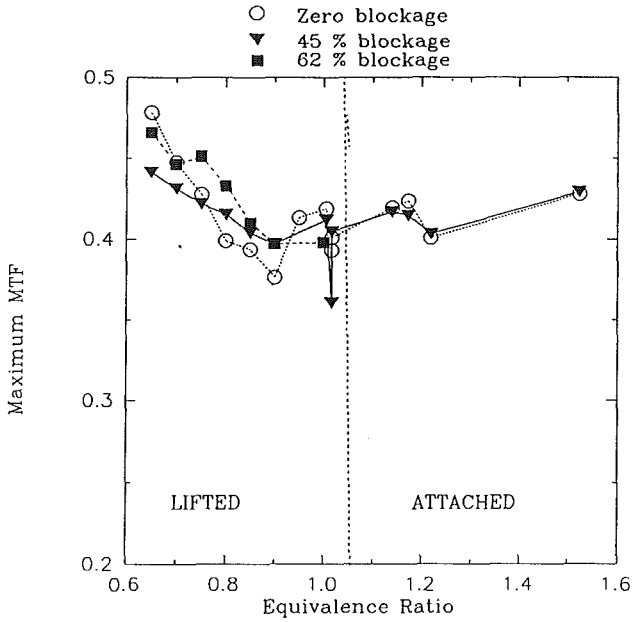

Fig. 17 Variations of maximum normalized wall temperatures for lifted and attached flames at several values of exit blockage

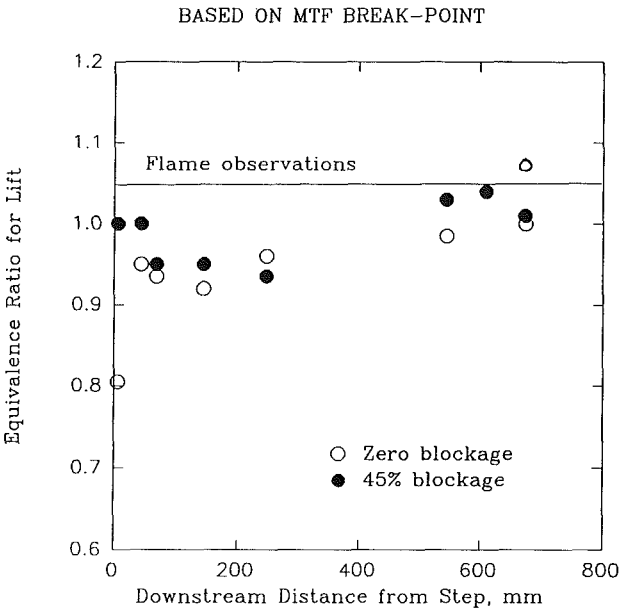

Fig. 16 Indicated equivalence ratios for flame-lift from wall temperatures, compared with direct observations

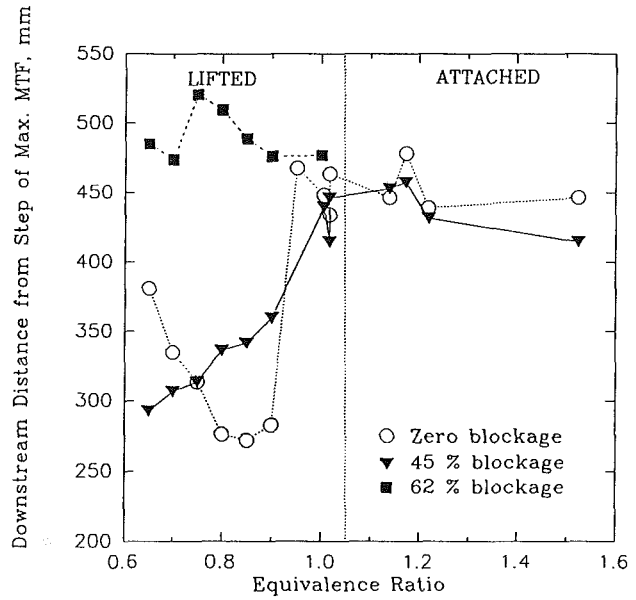

Fig. 18 Dependency of position of maximum normalized wall temperature on exit blockage for lifted and attached flames

value of 1.6. There is negligible effect of blockage on MTF at this station.

The "break" in the curve of Fig. 15 may be interpreted as representing the flame-lift condition. The inferred equivalence ratios for flame-lift based on this break for different axial locations are shown in Fig. 16 compared with the equivalence ratios for flame-lift based on direct observation (Fig. 6). As might be anticipated, inferences based on data from downstream are in better agreement with direct observations. No effect of blockage is apparent on the inferred flame-lift, which does not conflict with direct observation in Fig. 6.

The variations of the maximum value of MTF with equivalence ratio for 0, 45.1, and 62 percent geometric blockages are given in Fig. 17; the flame condition—lifted or attached—is delineated based on Fig. 6. The values of maximum MTF, and the positions at which they occur, were derived at each equivalence ratio from differentiation of curve fits to MTF versus axial distance information obtained from the curves in plots such as given in Fig. 15.

Figure 17 indicates that maximum MTF reaches its minimum value at about the equivalence ratio for flame-lift. Exit blockage does not affect the value of maximum MTF, but maximum MTF does increase as lean blowout is approached.

When the position at which maximum MTF is reached is plotted in similar fashion in Fig. 18, a strong effect of blockage is apparent for lifted flames; equivalence ratios for attached flames do not influence this position significantly. For the three blockages shown, the position of maximum MTF is roughly constant around 450 mm from the step for attached flames.

When equivalence ratio is reduced so that a lifted flame is established, an unrestricted combustor exit results in the position of maximum MTF initially moving back toward the step. However, for an equivalence ratio of 0.9, the closest position

Downloaded 02 Jun 2010 to 171.66.16.121. Redistribution subject to ASME license or copyright; see http://www.asme.org/terms/Terms_Use.cfm

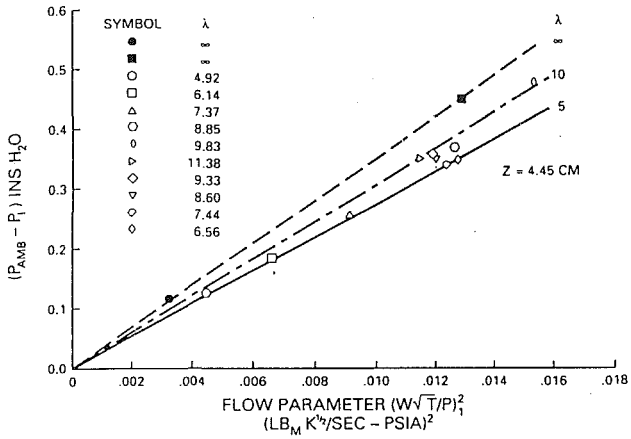

Fig. 19 Dependency of wall static pressures in the step recirculation zone on inlet flow parameter and jet velocity ratio in isothermal flow with a free exit

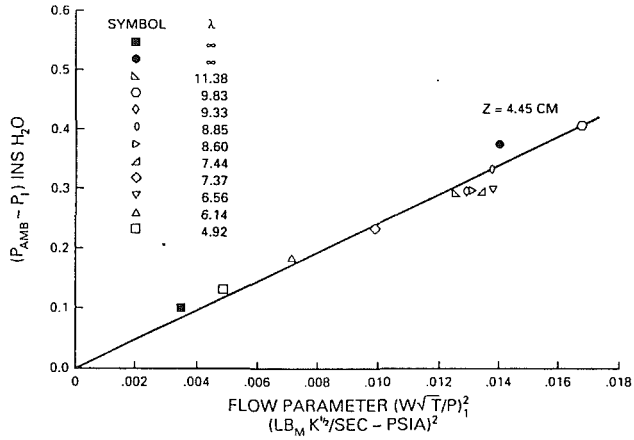

Fig. 20 Suppression of dependency of wall static pressure on jet velocity ratio by exit blockage (45 percent) in isothermal flow

to the step is reached at about 270 mm; thereafter, as equivalence ratio is further lowered toward a lean blowout, the position again moves downstream as the flame-lift increases.

The addition of exit blockage introduces an additional recirculation zone (on the orifice plate upstream face) into the combustor, and the existence of this recirculation is how blockage exerts an influence on the position of maximum MTF. The position of maximum MTF is associated with the reattachment plane of the step recirculation zone since this is where the jet shear layers reach the combustor wall (Sturgess et al., 1992b). These jet shear layers are where the majority of the heat release takes place during combustion, whether or not the pilot flame is attached (Sturgess et al., 1991a). Movements of the position of maximum MTF therefore reflect, albeit in crude fashion, movements of the reattachment plane for the step recirculation zone. The lack of blockage-effect on the value of maximum MTF (Fig. 17) indicates that heat release in the jet shear layers is not substantially changed by combustor exit blockage; however, the trajectory of these shear layers is (Fig. 18), possibly due to flow acceleration as a result of the heat release. The behavior evident in Fig. 18 for 45.1 and 62 percent blockage is the result of interactions between the step and orifice plate recirculation zones, due to heat release rate as equivalence ratio is varied, and modified by the two flame conditions.

With this flow model, the lifted-flame (partially premixed) behavior for maximum MTF in Fig. 18 at zero exit blockage is consistent with the findings of Morrison et al. (1987), Pitz and Daily (1983), and Stevenson et al. (1982) for premixed flames that a step recirculation zone at fixed (turbulent) Reynolds number decreases in size with increasing equivalence ratio. The minimum distance occurring at an equivalence ratio of 0.9 suggests that pilot flame attachment becomes evident before the directly observed equivalence ratio of 1.05 (Fig. 6). Examination of the intermittency of the pilot flame (Roquemore et al., 1991; Chen, 1991) tends to confirm this suggestion.

Wall Static Pressures

For an atmospheric pressure discharge combustor with exit blockage, wall static pressures provide means for a convenient assessment of the extent of the additional recirculation zone set up on the orifice plate upstream face. With a free exit, the difference between ambient pressure and wall static pressure in the combustor reaches zero in the exit plane. However, when the exit is restricted, this difference reaches zero at some position inside the combustor (Heneghan et al., 1990). The position where this occurs marks the stagnation plane for the aft recirculation zone on the orifice plate.

In isothermal flow the wall static pressure at a given station

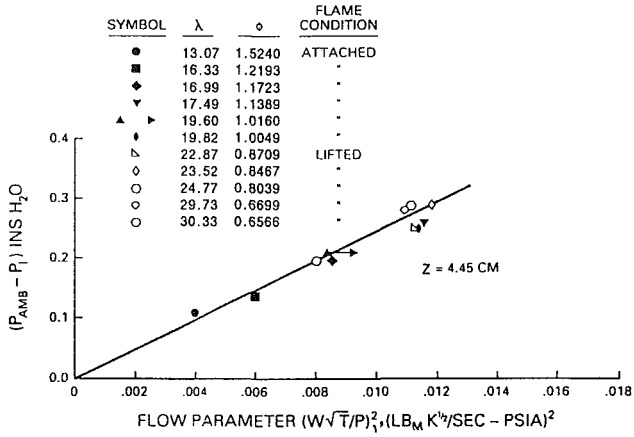

Fig. 21 Suppression of dependency of wall static pressure on jet velocity ratio by combustion with a free exit

is a function of the jet velocity ratio λ, and the inlet flow parameter, as can be seen for a station 44.5 mm downstream, in Fig. 19. As Fig. 20 demonstrates, when exit blockage is introduced, the dependency of wall static pressure on velocity ratio is suppressed. Combustion also suppresses the dependency on jet velocity ratio, even for a free exit. This is illustrated in Fig. 21, where it is also shown that the flame condition does not exert an influence.

Again using curve fits and differentiation, the axial positions along the combustor at which atmospheric pressure was attained were found. Typical wall static pressure axial distributions are given in Fig. 3 of Heneghan et al. (1990). Figure 22 shows that in isothermal flow this condition was reached at a constant 580 mm approximately, with 45.1 percent exit blockage, and was so regardless of inlet flow parameter or jet velocity ratio. With combustion and the same blockage, the position for atmospheric pressure was a strong function of equivalence ratio, as Fig. 23 shows, where the leading-edge of the aft recirculation zone moves progressively forward in the combustor as equivalence ratio is reduced, independent of flame condition.

At 62 percent blockage the position at which atmospheric pressure was attained was always greater than 600 mm from the step, and thus could not be accurately determined from the static tap positions available.

Relationship Between Recirculation Zones

The information on the end of the step recirculation zone inferred from MTF data (Fig. 18) can be combined with the

Downloaded 02 Jun 2010 to 171.66.16.121. Redistribution subject to ASME license or copyright; see http://www.asme.org/terms/Terms_Use.cfm

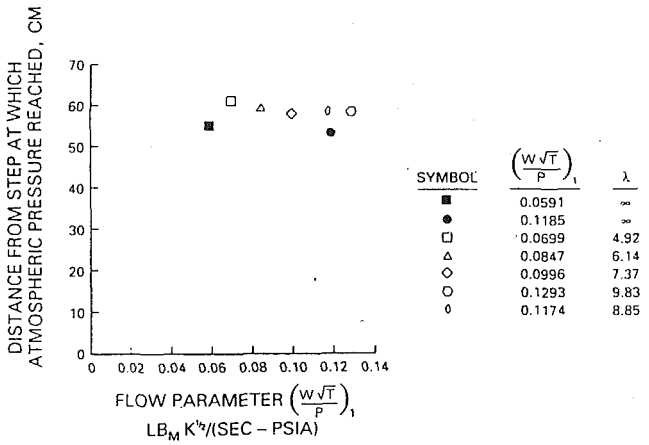

Fig. 22 Independence from inlet flow parameter and jet velocity ratio of position where atmospheric pressure is reached on the combustor wall, in isothermal flow with 45 percent exit blockage

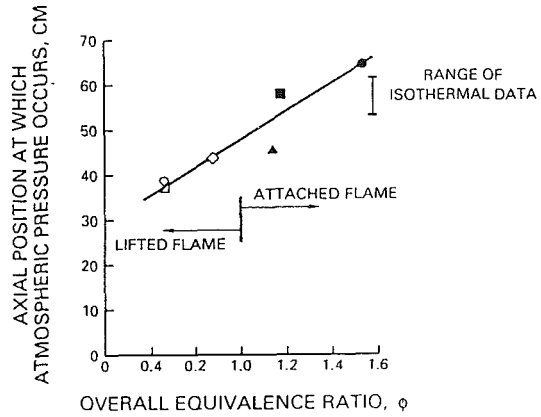

Fig. 23 Variation of downstream position where wall static pressure reaches atmospheric with equivalence ratio at 45 percent exit blockage

information on the beginning of the orifice plate recirculation zone from the static pressure data (Fig. 23) in order to examine the relationship between these two important flow features in the restricted-exit combustor.

Figure 24 shows a combination of Figs. 18 and 23 for 45.1 percent exit blockage with combusting flow. It can be deduced that there is always positive separation between the end of the step recirculation zone and the beginning of the orifice plate recirculation zone for this blockage. Furthermore, for lifted flames, this separation is maintained at a constant distance of about 80 mm, so that direct interference never happens. For attached flames, the separation distance increases, as Fig. 25 shows.

For 62 percent blockage, it appears as though direct interference between zones does not occur either, despite the fact that the inferred position of the end of the step recirculation zone is farther downstream at around 500 mm for all equivalence ratios (Fig. 18).

Gas Temperature Profiles

Limited gas temperature measurements were made using the CARS system. Profiles along the combustor centerline and, radially, close to the step, were taken at 0, 45.1, and 62 percent exit blockage by orifice plates in order to assess what blockage did to the all-important step recirculation zone. This was a quick preliminary look made prior to more extensive field-mapping of temperature to be reported separately.

The axial profiles of mean temperature along the combustor centerline at 45.1 percent exit blockage for lifted and attached

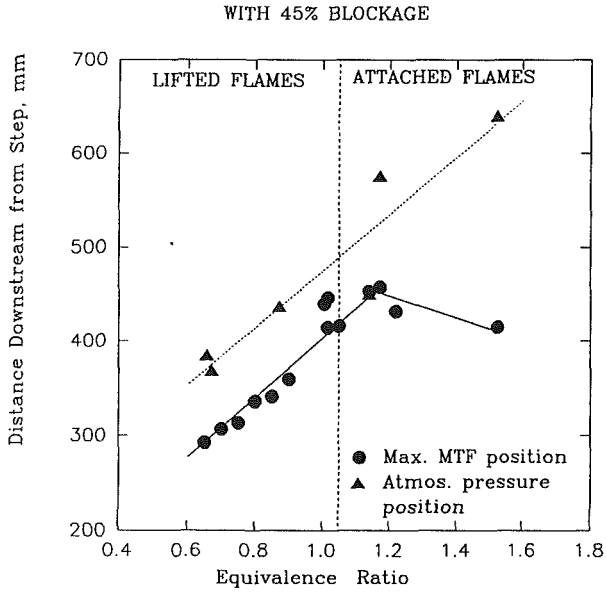

Fig. 24 Downstream positions where atmospheric pressure and maximum normalized wall temperature are attained as equivalence ratio is varied for fixed exit blockage

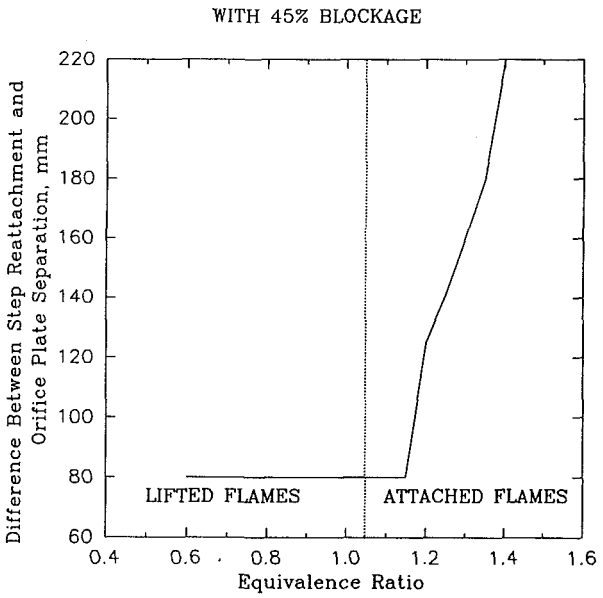

Fig. 25 Distance between recirculation zones for lifted and attached flames at fixed exit blockage

flames are given in Fig. 26, where the temperatures are presented as the ratio of actual temperature to the adiabatic flame temperature. The combustor loadings in both cases are in the range of 0.7 to 0.76 $lb_m/(sec.ft.^3 atmos.^n)$, i.e., fairly near the lean flammability limit. For both flames the temperature initially falls, and then increases again for distances greater than 100 mm from the step-plane. By consideration of Sturgess et al. (1992b), the increases in centerline mean temperature can be associated with the inner edge of the reacting jets shear layer reaching the centerline and thereby introducing sufficient oxidant for extensive chemical reaction to take place on the centerline. The initial distance in this profile can therefore be viewed as a conditional thermochemical potential core region. Note that the position of mean temperature increase is in the region where in isothermal flow the centerline mean axial velocity begins to accelerate with the 45.1 percent exit blockage (Fig. 3). Also, for the attached flame, the dimensionless mean temperature level is generally increased over that for the lifted flame.

Downloaded 02 Jun 2010 to 171.66.16.121. Redistribution subject to ASME license or copyright; see http://www.asme.org/terms/Terms_Use.cfm

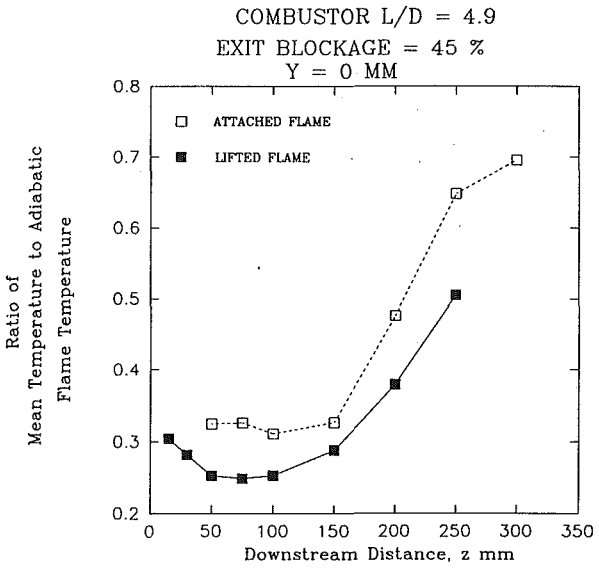

Fig. 26 Centerline profiles of dimensionless mean gas temperature for attached and lifted flames at fixed exit blockage

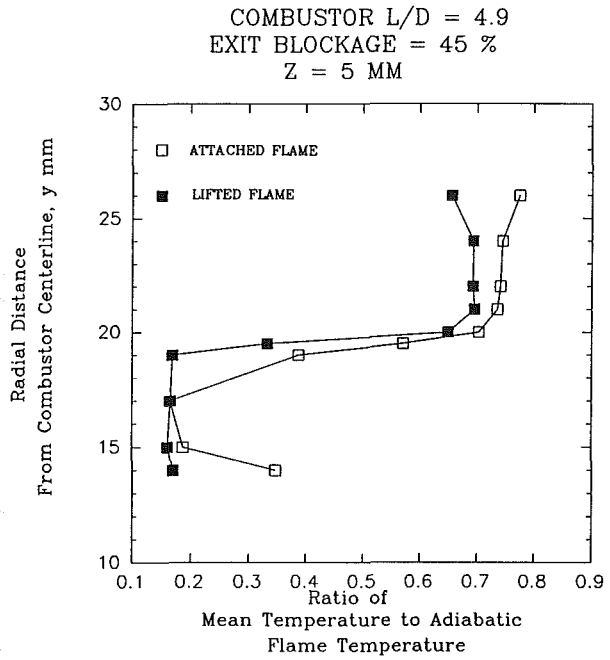

Fig. 27 Radial profiles of dimensionless mean gas temperature in the step region for attached and lifted flames at fixed exit blockage

Radial profiles of dimensionless mean temperature for the condition above are given in Fig. 27 for a downstream station 5 mm from the step. Comparison of these profiles reveals the effect of the attached flame on mean temperature, and shows the pilot flame to be located at a radius of 17 to 20 mm. The probability distribution functions (p.d.f.) confirm this definition. This is somewhat consistent with the mean position of 24 mm radius for the attached flame determined at 10 mm downstream with thin filament pyrometry (TFP) (Roquemore et al., 1991). Again, the levels of dimensionless temperature are higher at all radial positions for the attached flame condition. The p.d.f.'s for the lifted flame condition agree with the measurements of the spontaneous OH emission given by Roquemore et al. (1991), that there is a finite probability of the pilot flame being present part of the time, even though the main flame is fully lifted and an anchored pilot flame is not directly observed. For both lifted and attached flames, the step

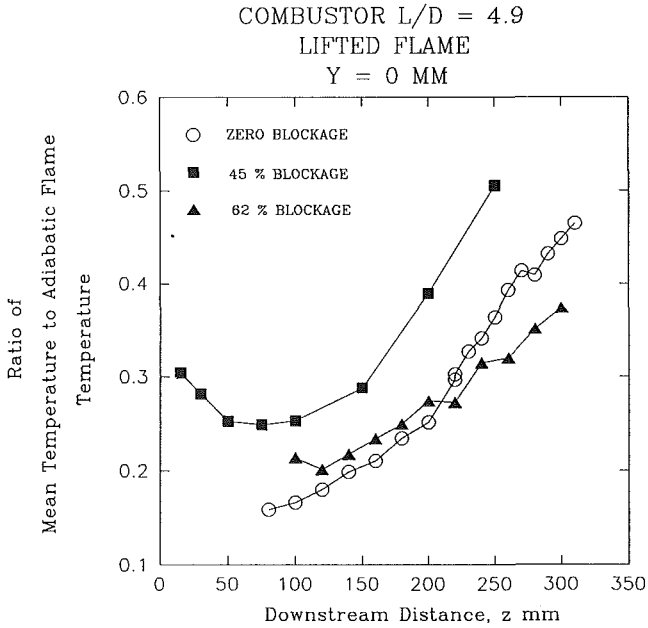

Fig. 28 Comparison of centerline profiles of dimensionless mean gas temperatures for lifted flames at various exit blockages

recirculation zone provides a significant high-temperature reservoir for the combustion processes developing in the shear layers.

Note that both Figs. 26 and 27 indicate an elevation of gas temperatures over the inlet conditions close to the confluence of the jets and around the region encompassing the small, central recirculation bubble (Sturgess et al., 1992b). Although not yet supported by strong direct evidence, it has been hypothesized (Sturgess et al., 1992a) that nonstationary flow interactions of the fuel and air jets with the central recirculation bubble result in additional radial mass transport of reactants. Such mass transport could account for early chemical reaction and hence, the observed elevated temperatures close to the orifice. The p.d.f. at a radius of 14 mm for an equivalence ratio of 1.36 at a combustor loading of 0.428 $lb_m/(sec.ft.^3 atmos.^n)$ shows that there is an equal probability of the flame being present and of fluid at inlet temperatures. This radius marks the position of the outer edge of the fuel tube. For this temperature condition to be so, either direct flame or a hot gas ignition source from the step recirculation zone must be transported completely across the annular air-jet path (see Fig. 1).

The addition of blockage increases the centerline mean temperatures for lifted flames at loadings fairly near the lean flammability limit. The effect is particularly strong for distances closer to the confluence of the jets than 100 mm as Fig. 28 shows. The radial profiles of dimensionless mean temperature indicate that blockage slightly increases the temperature in the step recirculation zone.

The centerline profiles of the ratio of the rms value of fluctuating temperature to mean temperature for 0, 45.1, and 62 percent exit blockage in the 4.9 *L/D* combustor are given in Fig. 29. The equivalence ratios are such that the flames were all lifted, and the combustor loadings were 0.7 to 0.76 $lb_m/(sec.ft.^3 atmos.^n)$. The fluctuating temperatures superimposed on the mean temperatures are not significantly affected by exit blockage. What is noteworthy, however, is the dramatic increase in the fluctuating component for distances closer than 50 mm to the jet origins. This is associated in particular with the forward stagnation point of the small, central recirculation zone, which for isothermal flow is situated at about 14 mm from the origin.

Figure 30 presents radial profiles of the ratio of rms tem-

Downloaded 02 Jun 2010 to 171.66.16.121. Redistribution subject to ASME license or copyright; see http://www.asme.org/terms/Terms_Use.cfm

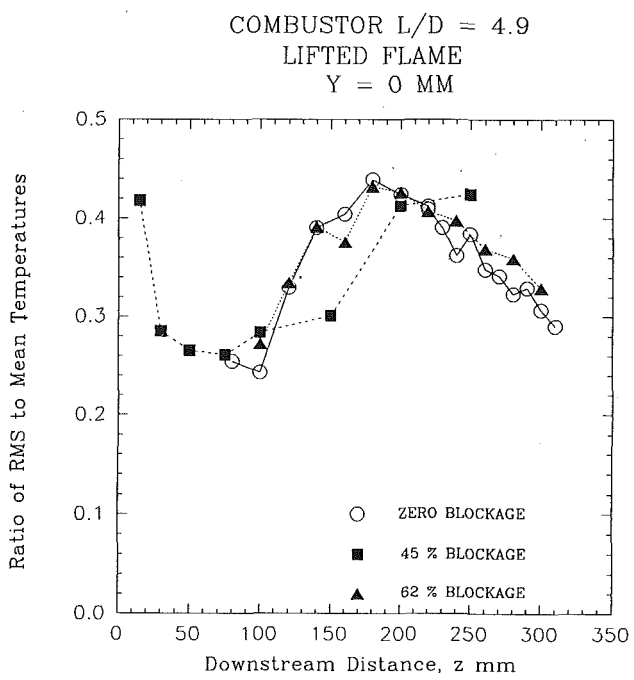

Fig. 29 Comparison of centerline profiles of dimensionless fluctuating gas temperatures for lifted flames at various exit blockages

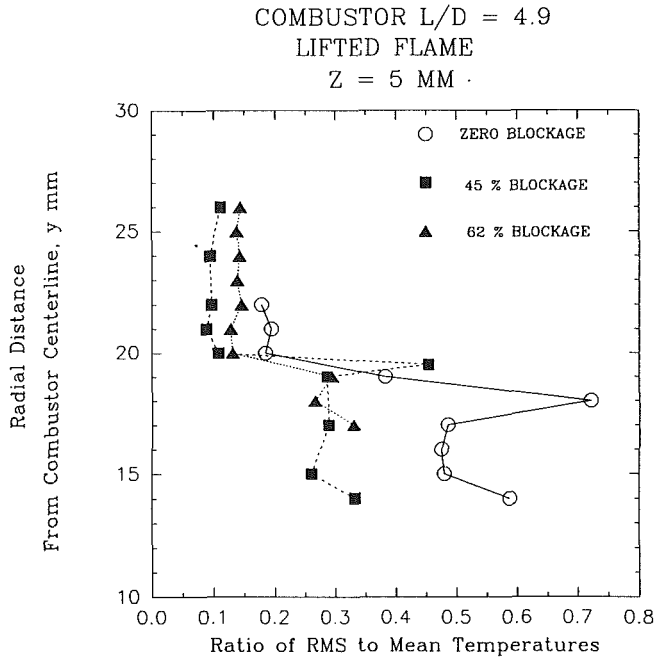

Fig. 30 Radial profiles of dimensionless fluctuating gas temperatures in the step region for lifted flames at various exit blockages

perature to mean temperature at 5 mm downstream from the step-plane for a range of exit blockage at the same operating conditions as for the previous figure, i.e., lifted flame at light loadings. Temperature fluctuations in the step recirculation zone are not much affected by the exit blockage. In sharp contrast, the existence of any blockage at all exerts a powerful suppressing effect on fluctuations in the jet shear layers.

Whether the flame is lifted or attached, there are no changes in temperature fluctuations in the step recirculation zone at 5 mm downstream with 45.1 percent exit blockage. There appear to be some differences for the two flame conditions in the shear layers (possibly the pilot flame), but the present data are not sufficient to be sure.

Discussion

The long-term intent for the research program, of which this effort is but a part, is to derive calculation procedures for lean blowout in gas turbine engine combustors. One of the calculation procedures being developed for this purpose is computational fluid dynamics (CFD). For viability, CFD should be able to provide a reasonable simulation of the real physical behavior involved in the lean blowout process. It is therefore required that significant flame events in the blowout process be experimentally identified and characterized. The attached, separated, and lifted flames, and the influence of combustor geometry on the operational conditions under which these are encountered, hence form a significant part of the data base. The ability to calculate these characteristics will form a critical test of the efficacy of any CFD modeling of lean blowout.

The research combustor exhibits a distinct and repeatable flame pattern change as it blows out on the lean side (Fig. 5). There are similarities in the flame changes for both rich and lean blowouts. A key element in these sequences of flame change is the loss of the thin, sheathlike pilot flame anchored at the outer diameter of the air jet. This pilot flame serves as a continuous ignition source for the main flame that then originates in the shear layers associated with the fuel and air jets, and the recirculation zones. For rich blowouts, loss of the pilot flame does not result in obvious changes in the main flame, either in position or character. It tends to remain concentrated in the shear layers. However, for lean blowouts, loss of the pilot flame causes the main flame to lift to a downstream position. This clearly allows significant premixing of reactants to occur, with the result that the main flame in its lifted position is more distributed across the width of the combustor. Blowout in the separated rich flame takes place suddenly; in the lifted lean flame, blowout is preceded by the onset of large-scale axial oscillations of the main flame about its mean position (Fig. 5).

The flame events described are controlled by the operating equivalence ratio of the combustor (Figs. 5 and 10). The equivalence ratios at which flame events occur are modified by the existence of back-pressure applied at the exit from the combustor (Figs. 6–9). The sensitivity of the event-equivalence ratios to the exit back-pressure depends on the combustor loading, and this sensitivity generally increases with the loading (Figs. 8 and 10).

The application of exit back-pressure to the research combustor exerts a favorable influence on the lean blowout (Fig. 11). At fixed combustor loading, the effect depends on the combustor length-to-diameter ratio. When acoustic effects and direct loss of the step recirculation zone (Fig. 12) are eliminated through use of an appropriate combustor length, the changes in blowout due to exit blockage are sensitive to combustor loading (Figs. 11 and 13). Predictably, they are strongest at high loadings approaching the peak heat release rate condition. At low combustor loadings, the improvement in stability due to blockage is consistent with a more persistent anchored flame (Figs. 6 and 7), but conflicts with an earlier onset of large-scale axial movements of the lifted flame (Fig. 8).

The presence of the outlet blockage changes the isothermal flow field in the combustor by causing acceleration of the mean axial velocities about the centerline (Figs. 3 and 4), and by introducing an additional recirculation zone on the upstream face of the orifice plate placed at the combustor exit. Acceleration of the central flow is evident as close as 125 mm downstream from the step plane (Fig. 3), or, at an L/D of 0.83 in the 4.9 L/D combustor at 45.1 percent blockage. This is upstream of the reattachment plane for the step recirculation, which is at about 2.82 L/D (Sturgess et al., 1992a). With a

Downloaded 02 Jun 2010 to 171.66.16.121. Redistribution subject to ASME license or copyright; see http://www.asme.org/terms/Terms_Use.cfm

free exit in isothermal flow, the central flow decelerates as the fuel and air jets merge and expand into the combustor around the step recirculation zone. The net acceleration that results with exit blockage represents a modification of the shear layers, and thus, flame holding in these shear layers can be expected to be changed.

The wall static pressure measurements in the step recirculation zone show that combustion suppresses a sensitivity to jet velocity ratio that is apparent in isothermal flow (Figs. 19 and 21); the addition of exit blockage in isothermal flow exercises a similar effect (Fig. 20).

With combustion, it can be inferred from wall thermocouple measurements that the position of the step recirculation zone reattachment shifts according to the equivalence ratio (Fig. 18). For lifted flames, the dependency on equivalence ratio is modified by the degree of outlet blockage (Fig. 18). From wall static pressure tap measurements, it is inferred that the size of the orifice plate recirculation is also influenced by combustion (Fig. 23). For a lifted flame at a given blockage, the movement of these two stagnation planes with equivalence ratio is such that a constant separation between them exists (Figs. 24 and 25), i.e., there is no direct interference. When the attached pilot flame condition is established, movement of the step recirculation zone attachment essentially ceases (Fig. 24). However, the orifice recirculation zone continues to decrease in size (Fig. 24), with the result that the separation between stagnation planes is increased (Fig. 25). Therefore, it is unlikely that the lean blowout improvement with exit blockage is associated with direct modification of the step recirculation zone.

The "quick-look" at mean gas temperature profiles shows the existence of the pilot flame for equivalence ratios when it is present (attached flame), and indicates slightly increased temperatures in the step recirculation zone and on the combustor centerline in the near-field. For lifted flames, exit blockage exerts its greatest effect in the near-field on the combustor centerline, particularly associated with the small, central recirculation bubble; there is little effect in the step recirculation zone. The CARS p.d.f.'s confirm earlier findings by OH emission and TFP measurements that the pilot flame is intermittently present even when direct observations indicate that it is lost and the main flame is lifted.

Fluctuating gas temperatures along the combustor centerline are insensitive to exit blockage (Fig. 29); however, they once again confirm the strong dynamic nature of the flow associated with the central recirculation bubble that is generated by entrainment of the central fuel jet by the much stronger surrounding annular air jet (Sturgess et al., 1992b). In the near-field (at 5 mm) the radial profiles of fluctuating temperature suggest that exit blockage is a dampening effect, only slightly in the step recirculation, but much more strongly in the jet shear layers (Fig. 30).

Back-pressuring the flame (by exit blockage in this case) exerts a powerful stabilizing effect on lean blowout, especially at the high combustor loadings that can represent critical operating conditions for military aircraft. Direct action of back-pressure on the step recirculation zone does not seem to take place. The back-pressure acts most strongly on the initial processes occurring in the jet shear layers by modifying their trajectories and turbulence characteristics. These initial processes emerge as being critical to the overall flame stabilization, whether the main flame is attached or lifted. Evidence is building (here and in earlier work) that dynamic behavior of the flow in the near-field can control the combustion process, perhaps through radical changes in radial mass transport.

The present results confirm that future attention should be directed at the pilot flame, the circumstances of its existence, and its contribution to the main flame. The dynamic interactions of the central recirculation bubble with the jet shear layers and of the jet shear layers with the step recirculation zone must be explored in detail, and characterized if possible. It would be desirable if such future studies could include a mass transport experiment, and time-resolved flow visualization of the combustion in the shear layers.

Conclusions

1 Back-pressure by means of exit blockage does exert an effect on the lean blowout characteristics of a combustor. The effect is weakest at low combustor loadings near the flammability limits, and strongest at high combustor loadings near the peak heat release rate. Modification of the effect occurs with changes in combustor length-to-diameter ratio.

2 Direct interference effects of exit blockage on the step recirculation zone do not occur.

3 The major effects of exit blockage on lean blowout are due to changes in the fuel and air jet shear layers, and in the interaction of this shear layer with the step recirculation zone and with the central recirculation bubble. Dynamic processes appear to play a significant part in these interactions.

4 Future experimental work should concentrate on the near-field region, the dynamic interactions taking place there, and the circumstances governing the existence and role of the anchored flame.

5 The combustor exhibits consistent and well-characterized flame behavior that depends on equivalence ratio and exit blockage. The ability to represent this behavior will provide a stringent test of the realism of any numerical modeling (CFD) of this combustor.

Acknowledgments

The authors wish to acknowledge the contributions to this work from their colleagues at Wright-Patterson Air Force Base and Pratt & Whitney, and also from Dr. P. Hedman, Brigham Young University, Provo, Utah. The University of Dayton work was supported by the U.S. Air Force Wright Laboratories, under Contract No. F33615-87-C-2767 (Contract Monitor Dr. W. M. Roquemore), and Pratt & Whitney was supported under Contract No. F33615-87-C-2822 (Contract Monitors 1st Lt. A. L. Lesmerises and Mr. D. Shouse). The authors thank the Air Force and Pratt & Whitney for permission to publish the results of this research.

References

Chen, T. H., 1991, private communication.

Gupta, A. K., Lilley, D. G., and Syred, N., 1984, *Swirl Flows*, Abacus Press.

Heneghan, S. P., and Vangsness, M. D., 1990, "Instrument Noise and Weighting Factors in Data Analysis," *Experiments in Fluids*, Vol. 9, pp. 290–294.

Heneghan, S. P., Vangsness, M. D., Ballal, D. R., Lesmerises, A. L., and Sturgess, G. J., 1990, "Acoustic Characteristics of a Research Step Combustor," AIAA Paper No. AIAA-90-1851 (to appear in *Journal of Propulsion and Power*).

Heneghan, S. P., and Vangsness, M. D., 1991, "Analysis of Slit Function Errors in Single-Shot Coherent Anti-Stokes Raman Spectroscopy (CARS) in Practical Combustors," *Reviews of Scientific Instruments*, Vol. 62, pp. 2093–2099.

Heneghan, S. P., Vangsness, M. D., and Pan, J. C., 1991, "Simple Determination of the Slit Function in Single Shot CARS Thermometry," *Journal of Applied Physics*, Vol. 69, pp. 2692–2695.

Lefebvre, A. H., 1983, *Gas Turbine Combustion*, Hemisphere Publishing Corp., McGraw-Hill, New York.

Lewis, B., and von Elbe, G., 1961, *Combustion, Flames and Explosion of Gases*, 2nd ed., Academic Press, New York.

Morrison, G. L., Tatterson, G. B., and Long, M. W., 1987, "A 3-D Laser Velocimeter Investigation of Turbulent, Incompressible Flow in an Axisymmetric Sudden Expansion," AIAA Paper No. AIAA-87-0119.

Pitz, R. W., and Daily, J. W., 1983, "Combustion in a Turbulent Mixing Layer Formed at a Rearward Facing Step," *AIAA Journal*, Vol. 21, No. 11, pp. 1565–1569.

Roquemore, W. M., Reddy, V. K., Hedman, P. O., Post, M. E., Chen, T. H., Goss, L. P., Trump, D., Vilimpoc, V., and Sturgess, G. J., 1991, "Experimental and Theoretical Studies in a Gas-Fueled Research Combustor," AIAA Paper No. AIAA-91-0639.

Stevenson, W. H., Thompson, H. D., Gold, R. D., and Craig, R. R., 1982, "Laser Velocimeter Measurements in Separated Flow With Combustion," presented at the International Symposium of Laser-Doppler Anemometry in Fluid Mechanics, Lisbon, Portugal, Paper No. 11.5.

Downloaded 02 Jun 2010 to 171.66.16.121. Redistribution subject to ASME license or copyright; see http://www.asme.org/terms/Terms_Use.cfm

Sturgess, G. J., Sloan, D. G., Roquemore, W. M., Reddy, V. K., Shouse, D., Lesmerises, A. L., Ballal, D. R., Heneghan, S. P., Vangsness, M. D., and Hedman, P. O., 1991a, "Flame Stability and Lean Blowout—A Research Program Progress Report," *Proc. 10th ISABE*, Nottingham, United Kingdom, pp. 372–384.

Sturgess, G. J., Heneghan, S. P., Vangsness, M. D., Ballal, D. R., and Lesmerises, A. L., 1991b, "Lean Blowout in a Research Combustor at Simulated Low Pressures," ASME Paper No. 91-GT-359.

Sturgess, G. J., Sloan, D. G., Lesmerises, A. L., Heneghan, S. P., and Ballal, D. R., 1992a, "Design and Development of a Research Combustor for Lean Blowout Studies," ASME JOURNAL OF ENGINEERING FOR GAS TURBINES AND POWER, Vol. 114, pp. 13–19.

Sturgess, G. J., Heneghan, S. P., Vangsness, M. D., Ballal, D. R., and Lesmerises, A. L., 1992b, "Isothermal Flow Fields in a Research Combustor for Lean Blowout Studies," ASME JOURNAL OF ENGINEERING FOR GAS TURBINES AND POWER, Vol. 114, pp. 435–444.

Downloaded 02 Jun 2010 to 171.66.16.121. Redistribution subject to ASME license or copyright; see http://www.asme.org/terms/Terms_Use.cfm

Particle Diagnostics and Turbulence Measurements in a Confined Isothermal Liquid Spray

A. Breña de la Rosa

S. V. Sankar

G. Wang

W. D. Bachalo

Aerometrics, Inc.,
Sunnyvale, CA 94086

This work reports an experimental study of the behavior and structure of a liquid spray immersed in a strong swirling field. In order to simulate some of the aerodynamic conditions experienced by a spray in a model combustor, an experimental setup using an acrylic chamber, a vane type swirler, and separate air supplies for both the secondary air and the swirl air were integrated to perform the experiments in the wind tunnel. A vane-type swirler exhibiting a high swirl number was used to produce a strong recirculation flow field downstream of a pressure swirl atomizer. Properties of the dispersed phase such as velocity, size distribution, and size-velocity correlation were measured at several locations within the swirling flow field. In addition, mean velocity and turbulence properties were obtained for the gas phase. Flow visualization was performed with a laser sheet to gain further understanding of the formation and influence of the recirculation region on the spray. A two-component PDPA system with a frequency-based Doppler signal analyzer was used throughout the measurements, and proved most valuable in the toroidal vortex region where low SNR conditions and nonuniform concentration of seed particles prevail. The results show that flow reversal of the drops is present at this swirl intensity within the recirculation region at distances up to $X/D = 2.0$. *Small variations of drop size distribution within the recirculation region are observed; however, large variations outside of it are also present. Plots of the normal Reynolds stresses and Reynolds shear stresses show double-peak radial distributions, which indicate regions in the flow where high mean velocity gradients and large shear forces are present. The decay of turbulence velocities in the axial direction was observed to be very fast, an indication of high diffusion and dissipation rates of the kinetic energy of turbulence.*

Introduction

Spray combustion encompasses the many systems that transform a liquid fuel into a useful energy output. The number of examples is impressive indeed: gas turbine engines for aircraft, for stationary power, and (in the near future) for automobiles, furnaces for space heating, utility boilers for electric power generation, and incinerators for hazardous waste incineration.

In each of those systems, swirl surrounding the fuel injector is used to promote turbulent mixing of the fuel and air, and to promote mixing of combustion products with reactants by recirculation. The mixing processes dictate the performance of these devices, including their stability, volumetric energy release, and emission of pollutants (Gupta et al., 1984; Fujii et al., 1981). In order to design combustion systems that are both economically competitive and environmentally responsible, spray combustion processes must be better understood and, as a result, refined to improve energy efficiency and to reduce the emission of pollutants.

Of major interest and importance in spray combustion systems is the effect of swirl-induced turbulent transport on the mixing and dispersion of the liquid fuel drops. Within this context, the problem is to measure drop size, drop velocity, and gas phase velocities effectively and accurately in sprays where the drops are mixing and reacting in the presence of swirl-induced turbulence. Once this hurdle is overcome, numerical models of spray combustion can be futher refined, tested, and used effectively as a powerful design tool in the new combustion systems.

The present work reports the results obtained during the first stage of a project that addresses the effect of swirl-induced turbulent transport on the mixing and dispersion of liquid fuel drops typical in gas turbine combustors and furnaces. Initial experiments consist of measurements of swirl sprays in nonreacting conditions in an environment that attempts to duplicate as much as possible the geometric similarities and aerodynamic conditions present in a small combustor. In the case of liquid sprays, the experiments conducted at isothermal

Contributed by the International Gas Turbine Institute and presented at the 37th International Gas Turbine and Aeroengine Congress and Exposition, Cologne, Germany, June 1–4, 1992. Manuscript received by the International Gas Turbine Institute February 6, 1992. Paper No. 92-GT-113. Associate Technical Editor: L. S. Langston.

Copyright © 1993 by ASME
Downloaded 02 Jun 2010 to 171.66.16.121. Redistribution subject to ASME license or copyright; see http://www.asme.org/terms/Terms_Use.cfm

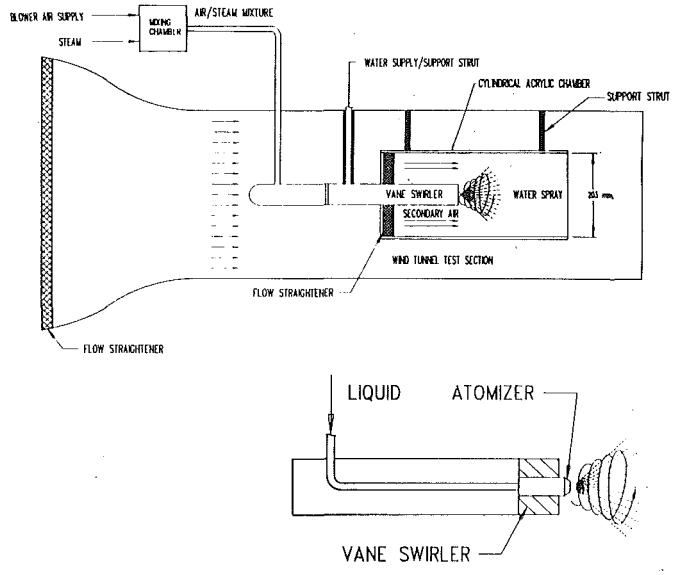

Fig. 1 Schematic of the swirl vane assembly, acrylic chamber, swirl air, and secondary air supply inside the wind tunnel test section

conditions are useful since both the aerodynamic characteristics of the flow and the atomization can be studied prior to experimental testing in the actual reactive environment.

Experimental Setup

The experiments were carried out in a 46×46 cm^2 wind tunnel using a vane-type swirler fitted to the liquid supply tube (12.5 mm i.d.) of the atomizer. An acrylic chamber of 203 mm i.d. and 3.18 mm thick was placed in the center section of the wind tunnel and surrounding the swirl-vane assembly. Upstream of the swirler, a honeycomb structure was fitted to the inside section of the acrylic chamber to dampen the turbulent fluctuations of the flow caused by routing of auxiliary piping and hence to produce a nearly isotropic flow, see Fig. 1.

The nozzle used was a Delavan 30 deg hollow cone, pressure swirl atomizer, which was operated at a pressure of $P_a = 690$ kPa and delivered a flow of 3.785 lph (1.0 gph). In the present experiments, the liquid flow rate to the nozzle was controlled by using a metering pump. In addition to the honeycomb structure upstream of the vane swirler, care was taken to place the swirler/atomizer assembly at a downstream distance where the flow conditioner and screens of the wind tunnel produced a homogeneous flow over its cross-sectional area. The wind tunnel free-stream velocity was set at $U_{fs} = 20$ m/s for all the experiments.

A radial blower was used to provide the swirl air for the experiments reported here. Both the swirl air and the steam particles were first directed to a pressure settling chamber and subsequently fed to the vane swirler, see Fig. 1. Early attempts at feeding both steam and swirl air directly into the swirler failed because the small water boiler operates at atmospheric pressure and the air blower would force the steam back into the boiler tank. As a consequence, a lower mass flow rate than that initially contemplated was used for the swirling air in order to allow for adequate seeding of the flow. The initial velocity of the swirl air going into the swirler was 3 m/s in a 76 mm i.d. pipe. The air temperature was $T_a = 298$ K and gave a mass flow rate to the swirler of $m_a = 0.016$ kg/s.

The swirler was manufactured of stainless steel and consisted of a hub with 19 mm i.d., and eight straight vanes welded equidistantly to it and forming an angle of 60 deg with the longitudinal axis of the swirler (Breña de la Rosa et al., 1992). The design of the swirlers followed the general guidelines depicted by Beer and Chigier (1983). The set of vanes and hub were placed inside a tube with 76 mm i.d. and 250 mm in length and the whole assembly fitted to the atomizer supply tube, see Fig. 1. The length of the swirl vanes blocked all the cross-sectional area of the swirl housing, such that it was not possible to see through the swirl assembly. The 60 deg vane swirler gave a nominal swirl number of $S = 1.23$. The swirl number of an annular swirler, such as the one used in the present study, with constant vane angle α can be determined from an expression given by Beer and Chigier (1983),

$$S = \frac{G_\psi}{G_x' R_s} = \frac{2}{3}\left\{\frac{1-(R_h/R_s)^2}{1-(R_h/R_s)^2}\right\} \tan \alpha \qquad (1)$$

where $G_x' = \pi \rho U_o^2 (R_s^2 - R_h^2)$ is the linear momentum, U_o is the velocity at the outer edge of the swirler, R_h and R_s are the radii of the hub and the swirl vane assembly, respectively.

The measurements were obtained with an Aerometrics two-component Phase Doppler Particle Analyzer (PDPA), whose principle of operation is described by Bachalo and Houser (1984). The system consists of a 3 W argon-ion laser; however, the power used in the present experiments was 300 mW, measured at the probe volume. This power level is a result of the power losses through the optic fibers, fiber couplers, and the transmitter unit. For comparison, a one-dimensional PDPA system typically uses a 10 mW He–Ne laser whose power is further reduced by the efficiency of the optical components in the transmitter unit. The PDPA was configured in the 30 deg off-axis forward scatter, where the scattering of light by refraction is the dominant mode and yields a linear relationship of particle size versus phase between the photodetectors over the detectable size range of the instrument. In this PDPA system, particle sizing is done with the 0.5145 μm green beams, which also give the first component of velocity, while the 0.488 μm blue beams provide the second orthogonal component of velocity.

Signal processing was performed with an Aerometrics Doppler Signal Analyzer (DSA 3000). In this system, a Bragg cell was used, which provides a maximum frequency shift of 40 MHz. The DSA 3000 signal processor determines the frequency and the phase of the Doppler signals in the frequency domain using high-speed analog to digital converters to record the signal. The accompanying software of the processor uses the discrete Fourier transform with the FFT algorithm to determine

Nomenclature

D_s = internal diameter of swirl vane assembly
D_{32} = Sauter mean diameter, μm
N_d = particle number density, cm^{-3}
R = radial position
S = degree of swirl
U_{fs} = axial free-stream velocity
u', v', w' = fluctuating axial, radial, and tangential components of velocity
$\overline{u'^2}$, $\overline{v'^2}$, $\overline{w'^2}$ = normal Reynolds stresses
$\overline{u'v'}$, $\overline{u'w'}$, $\overline{v'w'}$ = shear stresses
$\overline{u}$, $\overline{v}$, $\overline{w}$ = mean axial, radial, and tangential components of velocity
u, v, w = instantaneous axial, radial, and tangential components of velocity
X = axial distance from nozzle

Downloaded 02 Jun 2010 to 171.66.16.121. Redistribution subject to ASME license or copyright; see http://www.asme.org/terms/Terms_Use.cfm

the phase and the frequency of the signals. Since in each Doppler burst it is a single Doppler frequency that is of prime interest; the signal processing is simplified and allows the use of analog-to-digital converters (ADCs) with one-bit resolution (Ibrahim et al., 1990).

Briefly stated, the operation of the DSA 3000 consists of the following. The Doppler signal is first high-pass filtered to remove the pedestal component from it, thereby leaving a symmetric signal. A burst detection scheme is used to locate the burst signal, which is recorded digitally and stored in memory. The ADC then produces a square wave with the same frequency as the original signal and the discrete Fourier transform is subsequently applied to determine the frequency and the phase of the burst signal. The DSA 3000 uses a 160 MHz master oscillator to drive the Bragg cell, the mixer, and the ADCs. This ensures that the Bragg cell frequency is an exact binary multiple of the frequencies driving the calibration generator, the programmable mixers, and the ADC sampler.

The optical system used a fiber optic driver and single mode, polarization preserving fibers to transmit the beams to the PDPA transmitter unit. The optical components selected to obtain the turbulence data were an $f = 500$ mm transmitter lens and an $f = 300$ mm and $f = 200$ mm receiver and focusing lenses for the receiver unit. This setup gave an effective particle detection range of 0.6 to 21 μm in diameter for the turbulence data and 4 to 140 μm in diameter for the spray data.

The axial and tangential velocity components of the swirling field were evaluated for two conditions, namely, with the airflow seeded with micron size particles only and with the spray alone in the swirling field. The seed particles were generated by a small water boiler, which produced a size distribution having a linear mean of $D_{10} = 1.8$ μm and Sauter mean diameter $D_{32} = 3.9$ μm. Five or ten thousand particles (depending on data rate) were measured at each location to yield the velocity, size, and turbulence information for every experiment.

The experiments consisted of radial scans of the flow field obtained at six different axial locations, namely, $X = 10$, 20, 50, 100, 150, and 200 mm downstream from the face of the atomizer to evaluate the velocity and turbulence fields. At these same positions, measurements of drop size, drop velocity, particle number density, and size-velocity correlations were obtained for a water spray in the swirling field. At each axial position, the radial measurements were taken at 3 mm intervals from the centerline of the nozzle to the periphery of the flow field.

Results and Discussion

For all the experiments described here, the air and liquid flow rates were as described in the previous section. Figure 2 is an offset plot of the radial distribution of the mean axial air velocity (empty symbols) and of the mean axial velocity averaged over all the drop sizes (solid symbols) at five axial stations for the 60 deg vane swirler, $S = 1.23$. The reader is reminded that the mean and turbulence properties of the gaseous phase and the mean values obtained of the liquid phase constituted two separate measurements whose results have been merged in Figs. 2–5. Also shown in Fig. 2 are the boundary of the recirculation region and the boundary of the nominal 30 deg spray cone to emphasize the widening effect the swirler has on the redistribution of the spray pattern. The horizontal solid lines on the figure indicate the zero-level velocity at each axial location.

Negative axial air velocities are present for the first three radial profiles since the recirculation region extends to $X \approx 103$ mm. Notice the steep gradients of mean axial velocity present just outside the boundaries of the recirculation region. These large gradients of $\overline{u}$ are shown to have an effect on the radial profiles of the normal Reynolds stresses. The drop velocity profiles show the effect of the strong recirculation region,

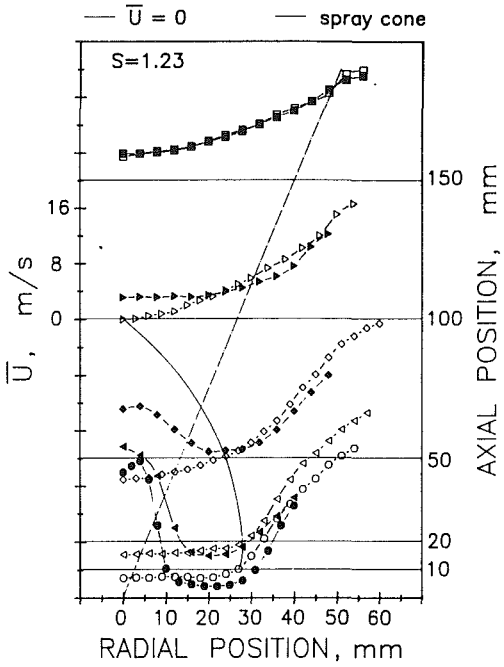

Fig. 2 Offset plots of the axial velocity (empty symbols) and of the mean velocity averaged over all the drop sizes (solid symbols.) The boundary of the recirculation region and of the 30 deg nominal spray cone are also shown.

which yields a sharp negative gradient of mean axial velocity in the core of the swirling field close to the nozzle. Outside of the recirculation region the drops are accelerated again and attain positive values of the axial velocity. The measurements indicated that the recirculation zone extended to $X \approx 103$ mm. From this location on, the drops exhibit an increase in the axial velocity from the centerline toward the periphery of the swirling field.

Preliminary measurements and visual inspection of the nozzle spraying in quiescent air confirmed a nominal spray cone angle of 30 deg. Figure 2 clearly shows the effect of the swirling air on the spray cone pattern. The swirling field yields a much wider spray and it is directly influenced by the swirl intensity, as has been shown by Breña de la Rosa et al. (1992), i.e., the stronger this parameter is, the wider the spray cone produced.

A similar plot to Fig. 2 is shown in Fig. 3 for the tangential velocity of the drops and that of the air. Due to the relatively low velocity of the swirl air $U_{sw} = 3$ m/s going into the swirler, the tangential velocity experienced by the drops is low. The rotational velocities imparted to the drops, however, were clearly visible during the laser sheet flow visualization experiments. The tangential velocity increases from zero at the center of the flow to a maximum value at the edge of the swirling field. It can be observed that the tangential velocity persists at large distances from the atomizer, i.e., $X/D = 1.97$, where $D = 76$ mm.

Figure 4 depicts the radial distributions of the mean axial velocity of discrete drop sizes and that of the air at $X = 20$ and $X = 50$ mm from the atomizer. At $X = 20$ mm, the drops are decelerated until they reach the boundary of the recirculation region $R = 27$ mm, where they accelerate again, influenced by the external air flow. Notice that the velocity profiles inside the recirculation region show steeper velocity gradients as the drop size increases, while outside of it the small drop sizes attain higher velocities much faster than the large particles. At axial distances within the boundaries of the recirculation region, i.e., $X \leq 100$ mm, the secondary air seemed to have little effect inside the vortex core. Outside of the recirculation region, however, the effect of the external air field is much

Downloaded 02 Jun 2010 to 171.66.16.121. Redistribution subject to ASME license or copyright; see http://www.asme.org/terms/Terms_Use.cfm

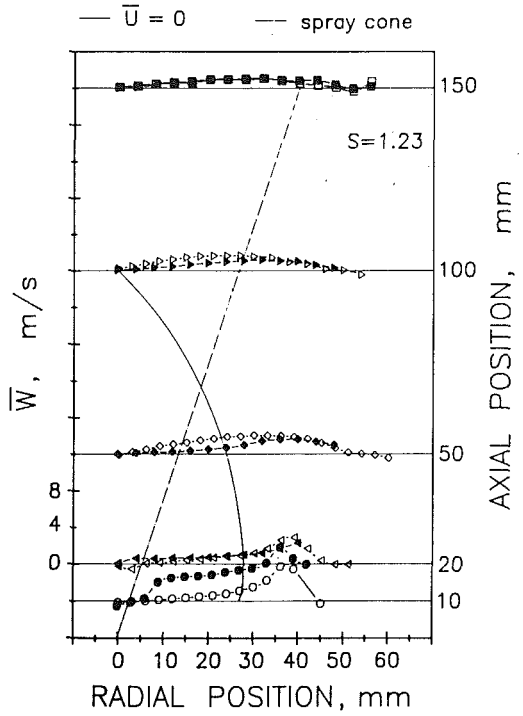

Fig. 3 Offset plots of the tangential mean air velocity (empty symbols) and of the mean velocity averaged over all the drop sizes (solid symbols). The boundary of the recirculation region and that of the spray cone are also shown.

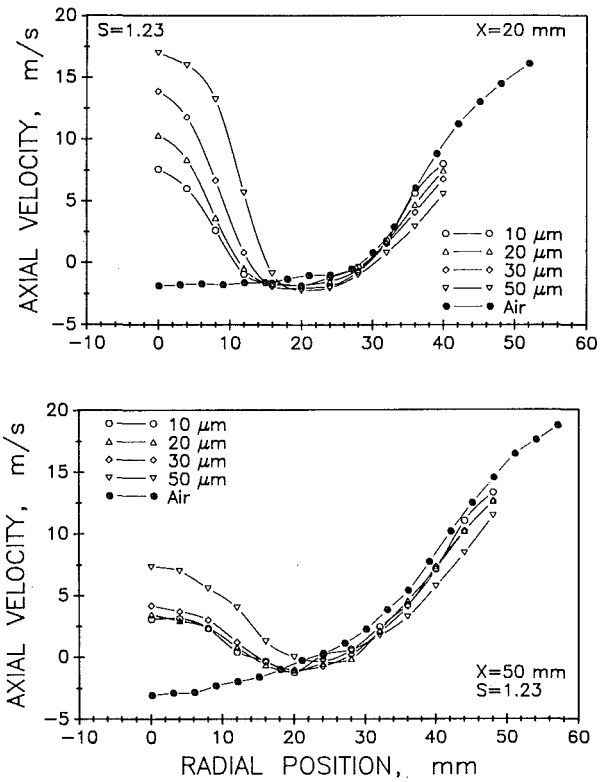

Fig. 4 Radial distributions of the mean axial velocity of the drops and of the air at $X = 20$ mm and $X = 50$ mm from the nozzle

stronger. The liquid particles that have sufficient momentum to penetrate through the vortex core are accelerated radially outward, see Figs. 2 and 4. At $X > 100$ mm the secondary air is entrained to the central region of the flow, as evidenced by flow visualization, and the liquid drops and the air show

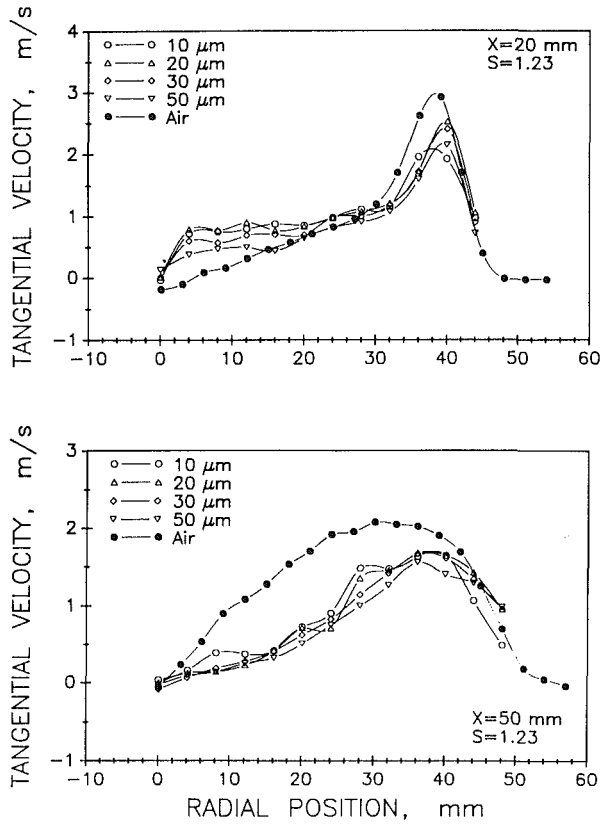

Fig. 5 Radial distributions of the mean tangential velocity of the drops and of the air at $X = 20$ mm and $X = 50$ mm from the nozzle

virtually the same axial mean velocity; see Fig. 2. The difference in the velocity profiles at $X = 50$ mm (Fig. 4) is not large among the different drop sizes at this location; however, the effect of the strong recirculation region is still felt by all the drop sizes. In the core of the spray, none of the drop sizes depicted experience negative velocities, as is shown for the case of the air.

Figure 5 is a plot of the mean tangential velocity of the drops and of the air as a function of radial position for $X = 20$ mm and $X = 50$ mm from the nozzle. The tangential air velocity increases from a value of near zero (probably caused by some asymmetry in the flow) to a maximum at the periphery of the swirling field, while the drop velocity profiles seem to follow the air velocity closely. Farther downstream, at $X = 50$ mm, the air velocity has a steeper velocity gradient than that shown by the drops. The velocity profiles of the drops do not differ greatly among themselves, with the smallest drops exhibiting velocities closest to those of the air.

Figure 6 (top) shows a radial distribution of the Sauter mean diameter, D_{32}, for the 60 deg vane swirler at four axial locations. The profiles reveal good symmetry of the flow field and the spray produced by the nozzle. It can be observed that due to the recirculating flow and intense mixing, large variations of D_{32} are present in the core at the first three axial stations. Outside of the recirculation region (see Fig. 2) the drop size distribution varies little and so does the D_{32}. A significant increase in D_{32} is observed at $X = 100$ mm, which is at the boundary of the recirculation region. The reason for this is that within the vortex core, a larger concentration of small drops is found, whereas the larger ones pass ballistically through it due to their higher momentum. As a result, it is mostly larger drops that are found at axial distances $X \geq 100$ mm, resulting in the higher values of the Sauter mean diameter. Also noticeable is a minimum value of D_{32} in the radial profiles of $X = 10$ mm and $X = 20$ mm, located at $R = 10$ mm and $R = 21$ mm, respectively. A close inspection of the drop size distri-

Downloaded 02 Jun 2010 to 171.66.16.121. Redistribution subject to ASME license or copyright; see http://www.asme.org/terms/Terms_Use.cfm

butions and their evolution in the radial direction revealed a progressive narrowing of the drop size range (and consequently a lower value of D_{32}) from the core of the flow to these radial locations; and indication that the recirculating vortex core contains predominantly small drops. However, little change was observed in the size distributions at greater radial locations for the first two axial positions.

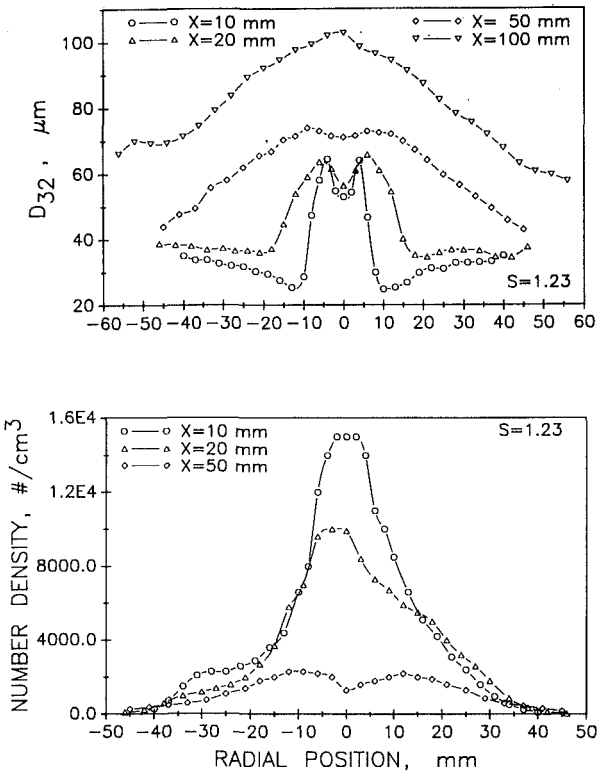

Fig. 6 Radial distribution of the Sauter mean diameter (top) and the particle number density (bottom)

Also shown on Fig. 6 (bottom) are the radial distributions of the particle number density at three axial locations. Closest to the nozzle and inside the recirculation region the concentration of particles is high; however, N_d decays quickly due to the centrifugal dispersion of the drops by the swirling motion; outside of the toroidal vortex core, N_d decreases monotonically to the edge of the swirling field. Figure 7 shows the evolution of the drop size distribution at three axial locations, namely, $X=20$ mm, $X=50$, and $X=100$ mm and at three radial positions.

The first radial location (Fig. 7 left) is at the centerline of the flow, the second is inside the recirculation region (Fig. 7 center) at $X=20$ mm and $X=50$ mm, and the third radial location is at the edge of the spray (Fig. 7 right). Two of the distributions at $X=100$ mm (which is at the boundary of the recirculation region) show bimodal behavior, probably caused by re-entrainment of large particles into the core at this axial location. The fact that the drop size distribution shows some uniformity within the recirculation region is not coincidental and is, in fact, quite relevant. For example, the reverse flow region in swirling jets has many of the characteristics of a well-stirred reactor (Kihm et al., 1990). In these jets, the temperature and gas composition are almost uniform and the fluid of this well-stirred zone is dynamically confined by the surrounding flow. Therefore, it is plausible that a fuel spray that exhibits a reasonable uniformity in the drop size distribution within this recirculation region may exhibit similar vaporization rates and air/fuel ratios. Actual measurements in the reactive case, during the second phase of this project, may confirm some of these observations.

Turbulence measurements were also obtained in the swirling field. Figure 8 depicts the radial distribution of the turbulence intensity of the gas phase at five axial locations. The intensity of turbulence was calculated using the rms values of the axial

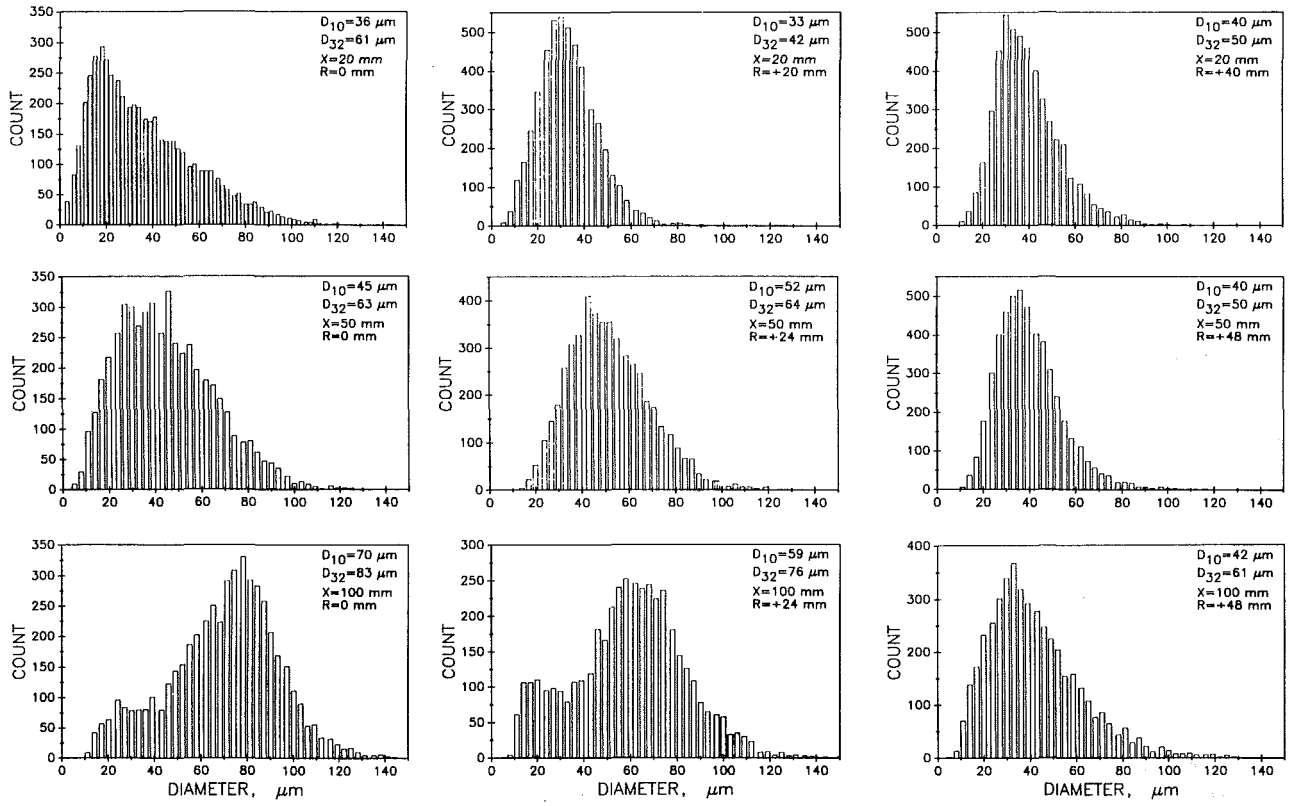

Fig. 7 Evolution of the drop size distribution from the centerline of the flow (far left) to the edge of the swirling field (far right) at $X=20$ (top), $X=50$ (center), and $X=100$ mm (bottom). In the axial direction, the edge of the recirculation region is at $x=103$ mm.

Downloaded 02 Jun 2010 to 171.66.16.121. Redistribution subject to ASME license or copyright; see http://www.asme.org/terms/Terms_Use.cfm

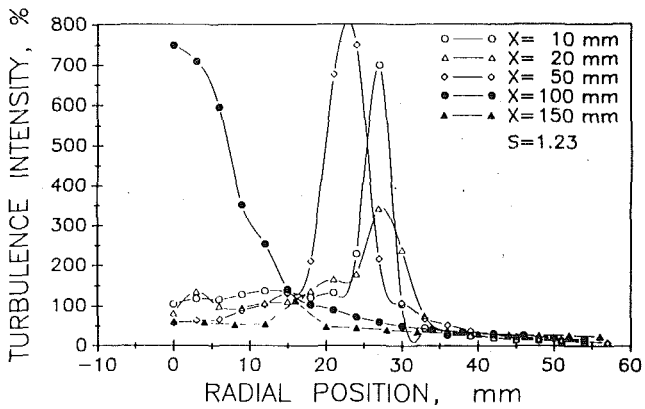

Fig. 8 Turbulence intensity of the gaseous phase for the 60 deg vane swirler

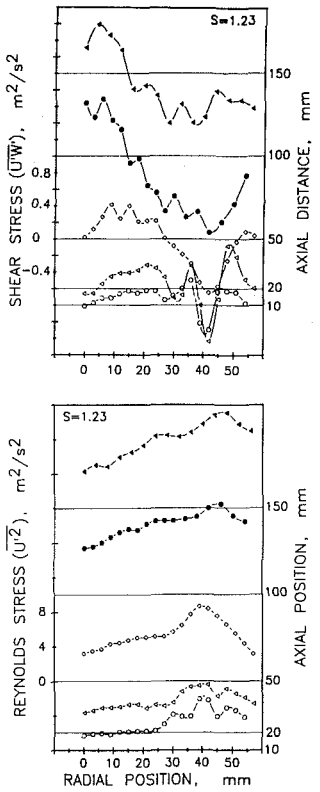

Fig. 9 Offset plots of the radial distribution of the Reynolds shear stresses $\overline{u'w'}$ (top) and of the normal Reynolds stresses u'^2 (bottom) of the gas phase for the 60 deg vane swirler

mean velocity component and with respect to the local mean velocity of the gas. Hence, it shows much higher values than it would if the values had been obtained with respect to the free-stream velocity $U_{fs} = 20$ m/s. The peaks observed in these profiles correspond to the location of the boundary of the recirculation region where the mean gas velocity is nearly zero. Note that the high value observed at $X = 100$ mm corresponds to the edge of the recirculation region in the axial direction, where the mean axial velocity is also nearly zero.

Figure 9 shows offset plots of the radial distribution of the Reynolds shear stresses $\overline{u'w'}$ and of the normal Reynolds stresses u'^2 for five axial locations. The shear stresses confirm the locations of the regions of high shear in the flow, i.e., at the boundary of the recirculation region for $X = 10$ mm, $X = 20$ mm, and $X = 50$ mm and at the boundary of the highly sheared mixing layer with the secondary air. The values of the normal Reynolds stresses are much higher than those of the shear stresses, a fact consistent with other investigators' experimental evidence (Lilley, 1988; Sislian and Cusworth, 1986). Peaks in the normal Reynolds stress profiles occur at those locations where sharp gradients of the mean velocity of the flow also occur. Figures 2 shows that the mean axial velocity gradients begin to occur at around $X = 30$ mm and are steepest at around $X = 40$ mm, which is where the profiles of the normal stresses show the highest values.

Flow Visualization

A flow visualization technique involving laser sheet illumination coupled with digital image processing and enhancement techniques was applied to gain further understanding of the structure of the spray interacting with the turbulent swirling flow. Data acquisition and data analysis were performed separately.

The laser sheet was generated with an Aerometrics laser sheet generator, Model LS-100, which uses fiber optics. The optical module of the light sheet generator is approximately 100 mm long and 20 mm in diameter and houses a system of cylindrical lenses to generate a sheet of laser light. This fiber optics based system is compact enough that it can be easily introduced into the wind tunnel through access ports located on the top wall of the tunnel.

The laser sheet was used to illuminate the swirling flow field at different vertical and horizontal cross sections to obtain a view of the toroidal vortex core, the extent of the recirculation region, and the rotational motion of the flow imparted by the swirl vanes. Three sets of images were recorded, i.e., with the seed particles in the flow, with the spray particles only, and with both the steam particles and the spray simultaneously in the flow.

The images were recorded using a Canon video camera Model E-51 for post-processing. An Imaging Technology frame grabber Model VS-100 controlled by a 486/33 AT compatible computer was used continually to grab the video images and display them on a high-resolution Electrohome monitor Model 1312. The Panasonic VCR provides the capability of analyzing the recorded images on a frame-by-frame basis with a minimum image distortion. Several video frames were also selected, digitized, and stored for further digital analysis. Each digitized images consists of 512×480 pixels.

Digital image processing and enhancement techniques were developed for this purpose. After experimenting with several image processing algorithms, a sequence of steps was identified to yield the best results for enhancing the acquired flow visualization images. The enhancement procedure consists of first applying a low-pass filter on the digitized image. This was achieved by convolving the digitized image with an approximation to a Gaussian kernel, which tends to blur the image. The next step was to generate intensity contours corresponding to the digitized image. A newly developed contouring algorithm was used for this purpose. This contouring algorithm is based on the histogram modification of the original image to yield an image possessing discrete levels and sharp discontinuities at the locations of the contours. The histogram modification was easily achieved in this study by convolving the filtered image with a 3×3 unit matrix. A fast edge-detecting filter such as the Robert cross-point edge filter was then applied to the previously convolved image. This is followed by a thresholding operation to yield the intensity contours. The final step in the image enhancement procedure was to superimpose the filtered image with the intensity contours, which was achieved by performing a logical OR operation between the filtered image and the contoured image.

The technique described above was used in the analysis of the flow visualization images obtained in this study. Thirty consecutive frames (each frame corresponds to an exposure

Downloaded 02 Jun 2010 to 171.66.16.121. Redistribution subject to ASME license or copyright; see http://www.asme.org/terms/Terms_Use.cfm

time of 1/30th of a second) were selected from the recorded video for detailed post-processing. Also because of space limitation only a few images have been presented herein. However, a sequence of a large number of images provided information of the formation process and the decay of the vortical structures in the flow.

The video camera was mounted at an angle of approximately 60 deg with respect to the horizontal plane of the laser sheet that intersected the nozzle and the swirling flow at the centerline. With the laser sheet in the horizontal midplane, the seed particles followed two recirculation bubbles. An upstream view of the flow, i.e., from the swirler to the exit of the wind tunnel, shows a right-hand side recirculation bubble having a counterclockwise motion, whereas the left-hand side shows a clockwise motion. In the central region where both flows merge and have the same upstream direction, the particles showed a slow flow reversal and subsequently bifurcated close to the nozzle to complete their recirculating motion. The limit of the recirculation region in the axial direction was accurately located on the video images at about $X \approx 100$ mm and matches the measurements obtained with the PDPA/DSA system. The articles outside the recirculation bubbles are seen flowing around them and converging downstream at the center of the flow at the boundary of the recirculation region, i.e., $X \approx 100$ mm.

Advancing the video tape frame by frame and under close scrutiny, the flow shows other features that go undetected to the naked eye when the sequence of images is averaged out and give a long-time exposure of events.

- First, the recirculation bubbles are difficult to observe and only segments of them can be seen at any one time.
- Second, and more importantly, is the observation of vortical structures that have a length scale of the same order of magnitude as the diameter of the swirler. These flow structures maintain their cohesiveness for distances that are approximately two times their diameter and subsequently dissipate into the flow. It is difficult to say at this point what effect these vortices have on the liquid drops because of the inherent difficulty in tracking a specified vortex and because of the random nature of turbulent motion. It was evident, however, that only the smallest drops get caught in these large-scale eddies.
- Third, a pulsating behavior of the flow, which was noticeable only when the spray was turned on, was observed. On a frame-by-frame analysis, the spray appeared to expand and collapse with a frequency of approximately 1/10 Hz, and this pulsation drastically changed the initial "spray cone angle" of the drops close to the nozzle. It was difficult to observe the effect the large scale eddies had on the drops since the spray virtually blurred the image of the steam particles when they were both present in the flow at the same time.

Only the small drops were observed to be entrained in the recirculation motion, while the large drops seemed to pass through the recirculation bubbles mostly unperturbed.

The images on Fig. 10 are shown here to illustrate some of the features discussed above. The pictures were shot with a Nikon FE-2 camera and a 50 mm F1.2 lens at 1/250 seconds using Kodak Plus-X-Pan ASA-125 professional film. Due to space limitations, only two are included here and, therefore, it is impossible to capture in one shot the temporal evolution and complex nature of these flows. The optimum analysis was obtained by carefully analyzing the video and the direct photographs of the flow. The top photograph, which was obtained with the seed particles and the spray, shows the presence of the recirculation region in the core of the flow. Notice also the flow reversal of the drops in the upper left corner of the flow.

The bottom photograph was obtained with the spray only in the flow. The complex flow pattern of the spray and the boundaries of the recirculation bubbles are visible on either side of the nozzle.

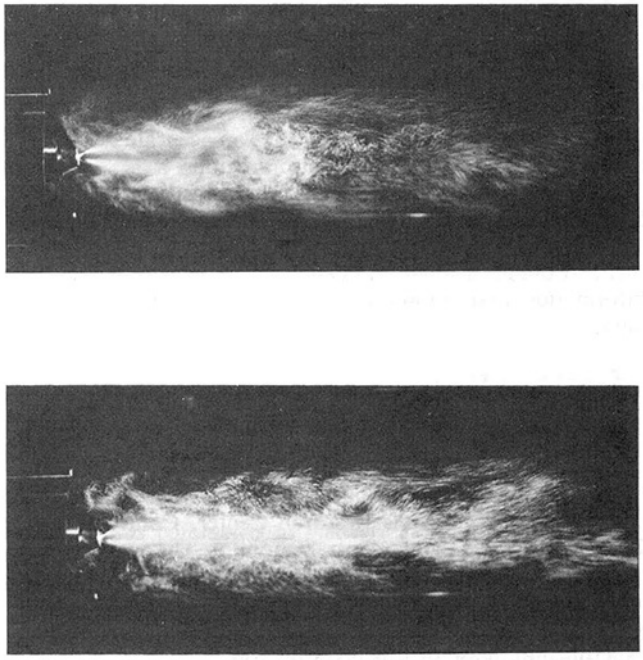

Fig. 10 Direct photographs of the flow with the spray and seed particles (top) and with the spray only (bottom) showing the recirculation region and the flow reversal of the drops on either side of the nozzle, respectively

Summary and Conclusions

The paper reported the experimental study of the structure of a liquid spray in a strong swirling field. In order to simulate some of the aerodynamic conditions experienced by a spray in a model combustor, an experimental setup using an acrylic chamber, a vane type swirler, and separate air supplies for both the secondary air and swirl air were integrated to perform the experiments in the wind tunnel. Laser sheet flow visualization coupled with digital image post-processing was performed on the flow images obtained with a video camera and has provided insight into the structure of these complex flows. The following conclusions can be drawn from the present investigation:

- The effect of the swirling flow on the original spray cone is to widen it substantially, and to provide a vortex core where intense mixing results in large changes in particle size distribution and in particle number density. Outside the recirculation region, both the D_{32} and N_d attain more uniform values.
- Inside the recirculation region, the mean axial velocity averaged over all the drop sizes (which is weighted toward the largest number of particles in the histogram) has larger values than the mean air velocity. This is consistent with both the PDPA measurements and the flow visualization images since, within the toroidal vortex core, only the smallest drops are captured in the circulating motion. Outside the recirculation region, both the particles and the air exhibit virtually the same velocities.
- The detailed plots of the axial and tangential velocities for discrete drop sizes and the air showed that in the vortex core only the smallest drops can follow the complex air recirculation motion. Careful inspection of the data revealed that within the recirculation region, $X < 100$ mm, approximately 20 percent of the drops (by number) in the spray have sizes less than 7 μm. In contrast, at axial locations $X < 50$ mm about 15 percent of the drops have $D > 40$ μm and for $50 < X < 100$ mm about 45 percent of the drops have $D > 40$ μm.
- The turbulence measurements showed regions of high turbulence intensity in the boundaries of the recirculation region. The normal stresses were found to be significantly larger than

Downloaded 02 Jun 2010 to 171.66.16.121. Redistribution subject to ASME license or copyright; see http://www.asme.org/terms/Terms_Use.cfm

the Reynolds shear stresses, indicating the need to consider the three normal stresses in any turbulence model of swirling sprays.

- Flow visualization and digital processing of the images was useful not only for gaining qualitative understanding of the structure of the flow, but for comparing the flow field with the PDPA measurements to determine an accurate location of the toroidal vortex and recirculation regions.

Future work shall be directed to the measurement of these flows in reactive conditions and to extending the flow visualization technique to acquire a set of images and averaging them to obtain a long-time exposure to provide whole field information that could be more easily compared to PDPA data.

Acknowledgments

The authors gratefully acknowledge the support of this work by the National Science Foundation, Contract ISI-8922606, and by the NASA Lewis Research Center, Contract NAS2-25204, Ms. Valerie Lyons, contract monitor. The authors would also like to express their thanks to Mr. Adam Isakovic, Mr. John Hanscom, Mr. Robert Kennedy, and Mr. Mark Yoneyama for their assistance with the design and setup during the experimental phase of this investigation.

References

Bachalo, W. D., and Houser, M. J., 1984, "Phase/Doppler Spray Analyzer for Simultaneous Measurements of Drop Size and Velocity Distributions," *Optical Engineering*, Vol. 23, No. 5, p. 583.

Beer, J. M., and Chigier, N. A., 1983, *Combustion Aerodynamics*, Robert E. Krieger Publishing Company, p. 111.

Breña de la Rosa, A., Wang, G., and Bachalo, W. D., 1992, "The Effect of Swirl on the Velocity and Turbulence Fields of a Liquid Spray," ASME JOURNAL OF ENGINEERING FOR GAS TURBINES AND POWER, Vol. 114, pp. 72–81.

Fujii, S., Eguchi, K., and Gomi, M., 1981, "Swirling Jets With and Without Combustion," *AIAA Journal*, Vol. 19, No. 11, pp. 1438–1442.

Gouldin, F. C., Depsky, J. S., and Lee, S-L., 1985, "Velocity Field Characteristics of a Swirling Flow Combustor," *AIAA Journal*, Vol. 23, No. 1, pp. 95–102.

Gupta, A. K., Lilley, D. G., and Syred, N., 1984, *Swirl Flows*, Abacus Press.

Ibrahim, K. M., Werthimer, G. D., and Bachalo, W. D., 1990, "Signal Processing Considerations for Laser Dopper and Phase Doppler Applications," presented at the Fifth International Symposium on the Application of Laser Techniques to Fluid Mechanics, Lisbon, Portugal, July 9–12.

Kihm, K. D., Chigier, N., and Sun, F., "Laser Doppler Velocimetry Investigation of Swirler Flowfields," *Journal of Propulsion*, Vol. 6, No. 4, July–Aug., pp. 364–374.

Lilley, D. G., 1988, "Lateral Jet Injection Into Swirling Combustor Flowfields," AIAA Paper No. AIAA-88-3183.

Nejad, A. S., Vanka, S. P., Favaloro, S. C., Samimy, M., and Langenfeld, C., 1989, "Application of Laser Velocimetry for Characterization of Confined Swirling Flow," ASME JOURNAL OF ENGINEERING FOR GAS TURBINES AND POWER, Vol. 111, pp. 36–45.

Sislian, J. P., and Cusworth, R. A., 1986, "Measurements of Mean Velocity and Turbulence Intensities in a Free Isothermal Swirling Jet," *AIAA Journal*, Vol. 24, No. 2, pp. 303–309.

Downloaded 02 Jun 2010 to 171.66.16.121. Redistribution subject to ASME license or copyright; see http://www.asme.org/terms/Terms_Use.cfm

Direct Measurements of Skin Friction in Supersonic Combustion Flow Fields

K. M. Chadwick
Graduate Research Assistant.

D. J. DeTurris
Graduate Research Assistant.

J. A. Schetz
Department Chairman and
W. Martin Johnson Professor.

Department of Aerospace
and Ocean Engineering,
Virginia Polytechnic Institute and
State University,
Blacksburg, VA 24061

An experimental investigation was conducted to measure skin friction along the chamber walls of supersonic combustors. A direct force measurement device was used to measure simultaneously an axial and a transverse component of the small tangential shear force passing over a nonintrusive floating element. This measurement was made possible with a sensitive piezoresistive deflection sensing unit. The floating head is mounted to a stiff cantilever beam arrangement with deflection due to the flow on the order of 0.00254 mm (0.0001 in). This allowed the instrument to be a nonnulling type. A second gage was designed with active cooling of the floating sensor head to eliminate nonuniform temperature effects between the sensor head and the surrounding wall. The key to this device is the use of a quartz tube cantilever with piezoresistive strain gages bonded directly to its surface. A symmetric fluid flow was developed inside the quartz tube to provide cooling to the backside of the floating head. Tests showed that this flow did not influence the tangential force measurement. Measurements were made in three separate combustor test facilities. Tests at NASA Langley Research center consisted of a Mach 3.0 vitiated air flow with hydrogen fuel injection at P_t = 500 psia (3466 kPa) and T_t = 3000 R (1667 K). Two separate sets of tests were conducted at the General Applied Science Laboratory (GASL) in a scramjet combustor model with hydrogen fuel injection in vitiated air at Mach = 3.3, P_t = 800 psia (5510 kPa), and T_t = 4000 R (2222 K). Skin friction coefficients between 0.001–0.005 were measured dependent on the facility and measurement location. Analysis of the measurement uncertainties indicate an accuracy to within ±10–15 percent of the streamwise component.

Introduction

Knowledge of drag resulting from skin friction is important for numerous engineering applications. Before a complete understanding of many flow fields both internal and external can be obtained, an accurate calculation or measurement of skin friction is required. In many combustor testing programs, accurate measurement of skin friction is necessary to determine combustion efficiency correctly. In addition, relatively small amounts of skin friction can seriously limit the available thrust from a scramjet combustor.

The current techniques employed in the measurement of skin friction fit into two general categories, those being either an indirect or direct method. Indirect methods involve measurement of the velocity gradient or heat transfer at the combustor wall. Reference [1] contains a review of many strategies adopted in these methods. Uncertainties with these methods can be quite large, especially in a compressible three-dimensional turbulent boundary layer, because a mathematical model or Reynolds analogy type relation is required to deduce the skin friction. For these reasons and considering that the flow types of interest in these studies are high heat flux and combusting, a direct shear force measurement technique was adopted.

A direct force measurement device is a relatively straight forward concept, but when applied to the severe testing environment of a supersonic combustor boundary layer, it can quickly become a difficult and complex engineering problem. A gage design has been developed for, but not limited to, measurement of skin friction in supersonic combustion boundary layers. This design is comparable, although somewhat improved, to the design of [2]. Also, in an attempt to optimize these gage designs further a technique was developed to match the gage sensor head thermally to the surrounding combustor wall by internal cooling.

The basic configuration of the skin friction gages consists of a cantilevered floating element. A history of early direct measurement designs which includes floating element designs is presented by Winter [3]. Skin friction balances that have been developed for supersonic flows include the efforts of Roensch and Cadwell [4], Allen [5, 6], and Voisinet [7]. The balances of these studies were primarily subject to supersonic flows with only moderate total temperatures. Reference [8] presents some limited measurements in a scramjet at the Ap-

Contributed by the International Gas Turbine Institute and presented at the 37th International Gas Turbine and Aeroengine Congress and Exposition, Cologne, Germany, June 1–4, 1992. Manuscript received by the International Gas Turbine Institute February 21, 1992. Paper No. 92-GT-320. Associate Technical Editor: L. S. Langston.

Copyright © 1993 by ASME
Downloaded 02 Jun 2010 to 171.66.16.121. Redistribution subject to ASME license or copyright; see http://www.asme.org/terms/Terms_Use.cfm

plied Physics Laboratory. DeTurris et al. [2] present skin friction measurements in scramjet combustors from several test programs.

The frictional forces that are a result of the supersonic combusting flow passing tangent to the combustion chamber walls are of a small magnitude. The shearing force must also be measured over a small area; therefore it is necessary for the skin friction gage to be very sensitive. The present designs have the ability to measure forces from a fraction of a gram to over ten grams accurately. The first of the two designs uses a deflection sensing device that was first used by Schetz and Nerney [9] and recently by DeTurris et al. [2]. This device employs piezoresistive crystal strain gages. This type of strain gage is exceedingly sensitive with gage factors in the area of 150, which is comparable to a gage factor of near 2 for common foil strain gages. This kind of sensitivity enabled the adoption of a nonnulling design. Several benefits are obtained with a nonnulling design over a self-nulling design. First, the nonnulling design is less complex in that it does not require a series of mechanical linkages, which can introduce substantial error in the measurement. Second, the time response of the nonnulling device is superior to that of the nulling device. Since the piezoresistive strain gages have a high gage factor, the cantilevered floating element of the current designs undergo extremely small deflections during a measurement. This renders insignificant any misalignment effects that could cause an errant measurement. One difficulty that is introduced by these crystal strain gages is that they are sensitive to temperature. An active cooling system near the gages was developed to minimize any error introduced by temperature gradients in the strain sensing elements.

It was determined that a temperature mismatch between the actual floating head of the skin friction gage and the surrounding wall of the combustion chamber can introduce significant error in the shearing force measurement. An optimized design has been developed that actively cools the floating head of the instrument and retains the benefits of the uncooled head design. The two designs are each capable of measuring skin friction in both axial and transverse directions, and both gage designs have been tested in unheated supersonic flow. The cooled head design is needed for high heat flux cases.

Description of Gages

General. A schematic of the skin friction gage design, which employs the displacement sensitive transducer, is shown in Fig. 1. The floating head of this instrument is mounted on a cantilevered tube, which is fit onto the sensing arm of the displacement sensor. The displacement sensor is a commercially available Deflection Sensor Cartridge (DSC) capable of sensing deflection in two orthogonal axes simultaneously. Encapsulated into the DSC are piezoresistive strain gages, making it sensitive to very small deflections. Output form the sensor is enhanced by arranging the strain gages into a half Wheatstone bridge. One gage is in tension and one in compression for each axis. Output resolution is also increased by the extension of the effective moment arm on the DSC by the cantilevered tube. Heat transfer through the instrument is a primary concern since the strain gages are temperature sensitive. The outer housing is cooled by a continuous water cooling channel and, in addition, the cantilevered beam surface area is increased

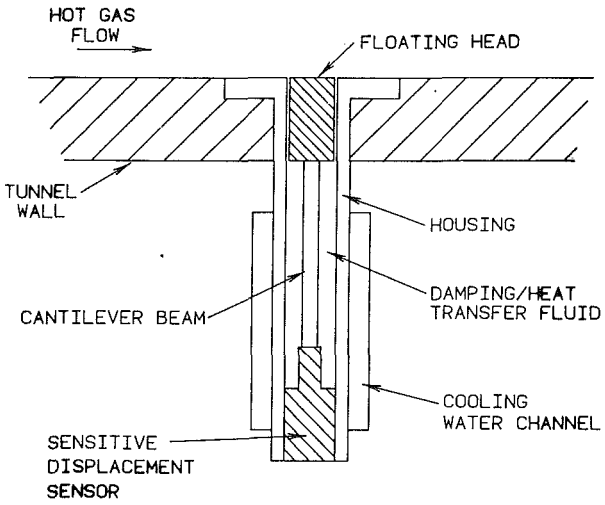

Fig. 1 Schematic of a skin friction balance

with fins. Also, the entire DSC-beam-floating head assembly is immersed in a silicon-based heat transfer fluid.

The facilities that these instruments are designed to operate in are inherently crowded on the exterior. This necessitates three basic requirements. First, the gage must be small. The current gages in use are all about three inches in length and a half an inch in diameter. Second, the instrument may be required to be mounted in any orientation dependent on the desired measurement location. Due to the presence of the internal heat transfer fluid these gages operate best when the floating head is oriented either up or on its side with respect to the duct, although inverted operation is possible. Third, these instruments must be rugged. The delicate components of these sensors are enclosed in a metal housing, which protects them from ordinary activity around the testing facilities. The strain gages are protected from thermal damage by the cooling system and the DSC cannot be overstressed since the maximum amount the floating head can move is the width of the gap between it and the housing, which is far below the maximum allowable deflection for the sensor.

It is possible to introduce misalignment effects due to the tilting of the floating heat in a nonnulling type gage. This effect has become insignificant because of the sensitivity of the piezoresistive strain gages. The gage is designed with a very stiff beam that will result in only small deflections of the sensing head, but the sensitivity of the DSC is more than adequate to detect the small deflection accurately. The expected maximum deflection of the sensing head is 0.00025 cm (0.0001 in.), which translates into a protrusion of four microinches into the flow. By itself, this small protrusion should be insignificant, but the floating head geometry is designed to eliminate this type of misalignment effect as well.

Floating head misalignment effects are always a concern with these types of instruments. Allen [5] did a systematic study to identify and minimize these effects by considering specific geometric attributes of the floating head. Those studied were the effects of gap size, lip size, misalignment with the surface by either protrusion or recession, and pressure gradient effects between the top and underside of the floating element. The results of this study were referred to extensively in the design

Nomenclature

C_f = skin friction coefficient
D = diameter of floating head
G = gap around floating head
L = lip thickness of head
P_t = total pressure
q = dynamic pressure
T_t = total temperature
V = velocity
τ_w = wall shear force
ρ = density

Subscripts

x = streamwise component
z = transverse component

Downloaded 02 Jun 2010 to 171.66.16.121. Redistribution subject to ASME license or copyright; see http://www.asme.org/terms/Terms_Use.cfm

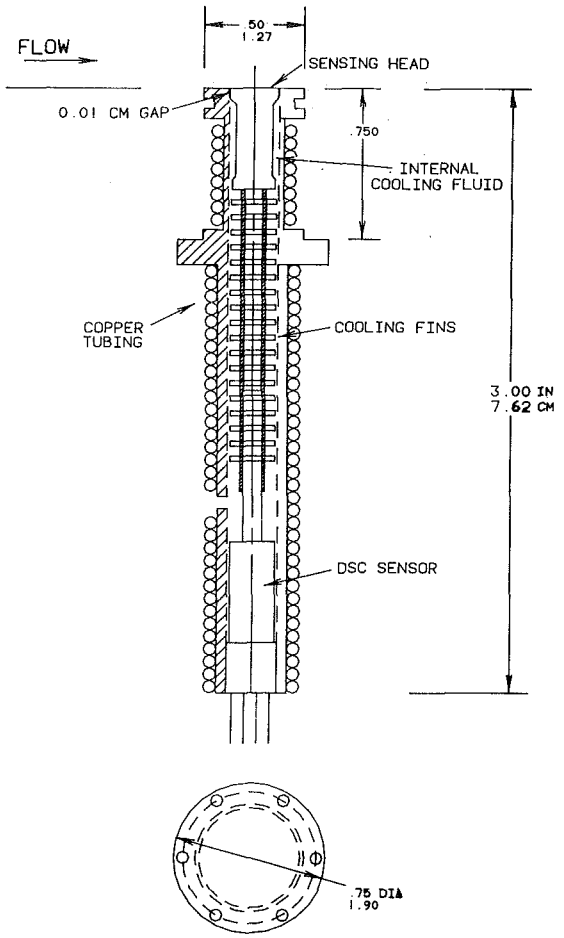

Fig. 2 Schematic of NASA Langley skin friction balance

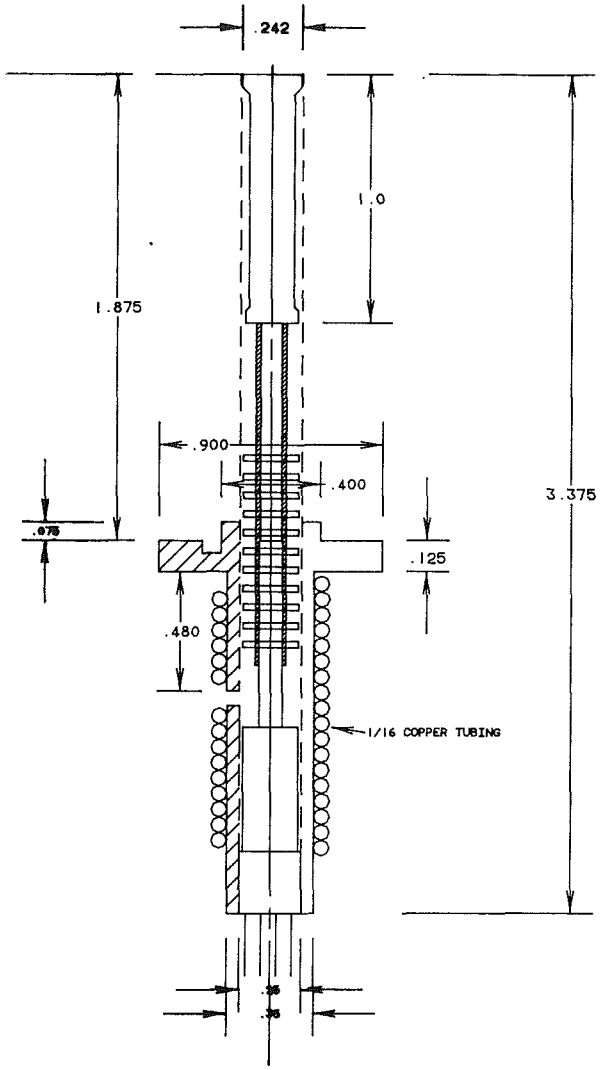

Fig. 3 Schematic of GASL skin friction balance

of the current sensor heads. The head for these gages has a diameter of 0.615 cm (0.242 in.) before tapering to a 0.462 cm (0.182 in.) diameter, leaving a thin lip at the flow surface. These dimensions were chosen to minimize the effects of the 0.01 cm (0.004 in.) gap between the head and the surrounding housing. The head also has a small lip at the lower end, leaving a 0.0153 cm (0.006) gap between it and the housing.

Allen [5] found that there was no advantage to having as small a gap size as possible. In fact, a skin friction balance is less sensitive to protrusion error with a large gap size. For the DSC gage design, the gap-to-diameter ratio (G/D) is 0.0165, which is considerably larger than the lower limit of 0.005 suggested by Allen. Effects due to the size of the floating head lip must also be considered. Again, [5] was consulted to choose a lip-to-diameter ratio (L/D) of 0.04. The gap-to-diameter ratio taken with this lip-to-diameter ratio combine to produce a design unaffected by gap size and lip protrusion effects.

The heat transfer fluid contained in the cavity between the cantilever and the outer housing serves several purposes. It not only provides thermal protection for the piezoresistive strain elements, but aids in eliminating the effects due to a possible pressure gradient acting on the top surface of the floating head [2]. Moreover, the fluid produces strong damping to limit errors introduced by facility vibrations and cantilever beam oscillations.

Design for NASA Langley Vitiated Air Tunnel. An assembly drawing for the NASA Langley gage is shown in Fig. 2. This gage is similar to that for the same facility in the study of [2], except that a cooling channel has been added to the top of the outer housing in the area that fits inside of the chamber wall. The outer housing and floating head are constructed of carbon steel to match the tunnel chamber walls. The temperature of the DSC is monitored by a type K thermocouple mounted adjacent to the DSC in the heat transfer fluid. The heat transfer fluid consists of a silicon-based oil (1000 Cs viscosity), which is filled through a small access hole on the side of the outer housing.

Designs for the GASL Test Series

DSC-Based Design. An assembly drawing for the DSC-based gage for first tests conducted at the General Applied Science Laboratory is depicted in Fig. 3. This gage is constructed of copper to match the chamber walls of the GASL facility. The tunnel walls for this test are 4.76 cm (1.875 in.); therefore, the sensor head of the balance was lengthened to 2.54 cm (1.0 in.) to aid in transferring heat from the gage. The temperature of the DSC was monitored by a thermocouple inserted through an access hole in the housing near the unit. A dummy balance was constructed for these tests, which contained a copper/constantan thermocouple on the surface of the sensor head. This dummy balance and the skin friction balance were mounted in an oblong plug which bolted into the tunnel wall. Also, the plug in which both gages were mounted was fitted with another copper/constantan thermocouple on its surface to measure chamber wall temperature. This complete package enabled the measurement of two skin friction components, sensor head temperature, and combustion chamber wall temperature.

Downloaded 02 Jun 2010 to 171.66.16.121. Redistribution subject to ASME license or copyright; see http://www.asme.org/terms/Terms_Use.cfm

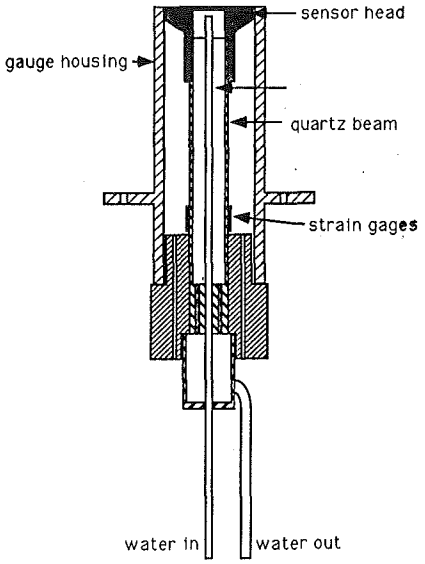

Fig. 4 Sketch of the cooled head skin friction gage

The balance used for the second series of tests at GASL is essentially the equivalent of the one for the first test series with a few exceptions. For this second test series, a balance similar to that of Fig. 3 was inserted into a housing consisting of a circular 1.27 cm (0.5 in.) diameter 4.76 cm (1.875 in.) long plug with a flange for a bolt circle to secure the unit into the chamber wall. Also, the DSC cooling system pressure was increased to approximately 150 psi (1035 kPa).

Cooled Sensor Head Design. The basic gage configuration is shown in Fig. 4. The gage is a nonnulling type similar to the previously discussed designs. The shear sensing head is supported by a quartz cantilevered tube with an outside diameter of 0.062 cm (0.238 in.) and an inside diameter of 0.40 cm (0.157 in.). Instead of using the Displacement Sensitive Cartridge to measure the sensor head deflection, piezoresistive semiconductor strain gages are mounted directly to the cantilevered quartz tube. At the location of the strain gages, the tube is machined square with an abrasive diamond wheel cutter to provide a secure smooth base to mount the strain gages and insure orthogonality of the measurement axes. This geometry was found effective in providing enough mass flow of cooling fluid to the sensor head and adequate resolution from the strain sensing elements. The sensor head is mounted to the tube, which is then mounted into the base with a ceramiclike high-temperature cement. This cement has the ability to withstand temperatures up to 2500°F (1650 K) and has a tensile strength of 425 psi (2929 kPa).

The strain gages are piezoresistive semiconductor type gages. These gages provide several advantages over conventional foil gages including higher sensitivity, resistance, and fatigue life, as well as small size. Kulite 750 ohm semiconductor strain gages are used in this instrument. These are ruggedized gages encapsulated into an epoxy/glass matrix with large solder tab terminals. Overall dimensions of each gage are 0.11 cm (0.28 in.) by 0.06 cm (0.14 in.). Four gages are mounted to the quartz cantilevered beam with a thin layer of a high-temperature strain gage cement and coated with several layers of both polyurethane and an acrylic for protection from the environment. The gages are arranged in a half Wheatstone bridge, one gage in tension and one in compression for each axis of measurement while the sensor head is displaced. This provides compensation for any axially imposed strain that may arise from an axial force on the sensor head. Bridge completion is accomplished externally with precision resistors and a potentiometer for pretest output balance. The strain gages are powered by a +5 volt regulated DC power supply.

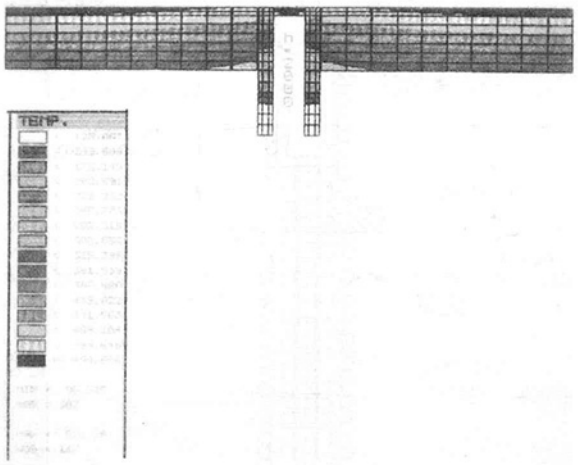

Fig. 5 Cooled head skin friction gage heat transfer contour

A flow pattern for sensor head cooling is developed through a co-axial tube arrangement. A stainless steel 0.160 cm (0.063 in.) tube is mounted along the centerline of the instrument to provide an inflow passage for the cooling fluid to the back side of the sensor head. Heat transfer calculations were made with a finite element code to determine the optimum thickness of the sensor head. In this calculation the sensor head thickness was varied to determine the thickness that would closely match the sensor head temperature with the surrounding combustion chamber wall. A heat flux that is expected from a scramjet combustor and a convection coefficient obtainable with water as the cooling fluid were prescribed as boundary conditions. A sensor head thickness of 0.083 cm (0.0325 in.) was found to be effective (see Fig. 5). The cooling fluid is exhausted from the instrument by flowing back along the outside of the stainless steel tube and inside of the quartz tube. At the base of the quartz beam, the exiting liquid passes through a manifold and out through a 0.317 cm (0.125 in.) copper line. A variable convection coefficient at the sensor head is obtainable by regulating the pressure of the incoming cooling liquid. Tests were conducted, and it was determined that the sensor head cooling system is able to withstand pressures up to 500 psi (3450 kPa). Bench tests showed that the flowing water did not influence the tangential force measurement.

The gage is enclosed by an outer housing constructed of copper as is the floating element sensor head and the cantilever beam base. The gage is mounted into the test facility with screws through a flange on the outer housing. As with all of the previously discussed designs, the cavity between the beam and the housing is filled with a silicon-based heat transfer fluid, primarily in this case for vibration damping and pressure gradient effect minimization. A calculation was performed to estimate the natural frequency of the instrument and was found to be 1.5 kHz. The overall length of the gage is 8.89 cm (3.5 in.). The sensor head was designed in a manner similar to the previous designs with a slightly larger diameter, 0.812 cm (0.320 in.), and a 0.013 cm (0.005 in.) gap. Lip size was set at 0.051 cm (0.020 in.).

Experimental Procedures

DSC Gage. Each measurement axis of the DSC forms half of a Wheatstone bridge; the crystal strain gages have a nominal resistance of 1000 ohms. Bridge completion is external to the instrument with 1000 ohm precision resistors and a 500 ohm potentiometer for pretest output balancing. The DSC is powered by a +6 volt DC power supply. For the most part, data

Downloaded 02 Jun 2010 to 171.66.16.121. Redistribution subject to ASME license or copyright; see http://www.asme.org/terms/Terms_Use.cfm

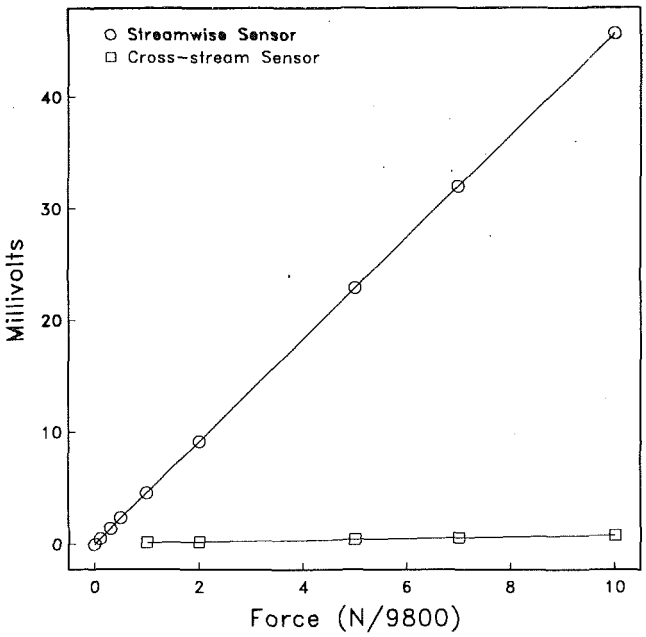

Fig. 6 DSC gage calibration

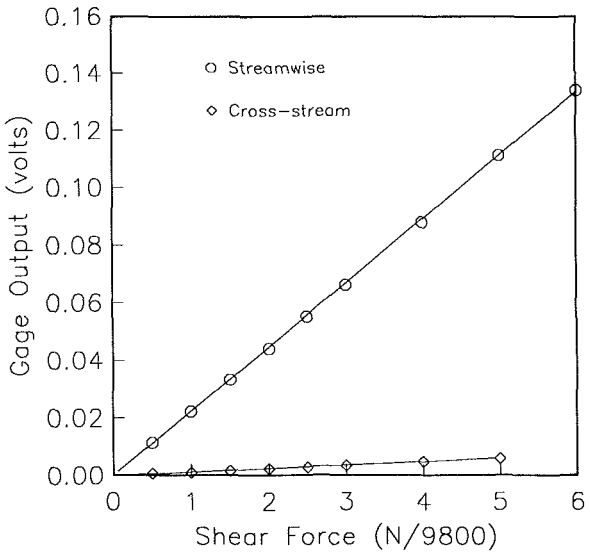

Fig. 7 Cooled heat gage calibration

are recorded with a two-channel strip chart recorder. At the NASA Langley and GASL tests, data were also recorded with a PC-AT based 12 bit, 16 channel A/D card with one multiplexed channel equipped with an electronic ice point to record up to 16 thermocouple inputs. During the second set of tests at GASL, data were also recorded on GASL hardware at a 4 Hz acquisition rate.

DSC Gage Calibration. The DSC Gage is calibrated by applying a force in the axis of measurement and recording the output voltage from the wheatstone bridge. A digital voltmeter was used to record several data points, and a least-squares linear regression was performed on the data, yielding a linear calibration curve. In order to apply the force directly to the measurement axis, the gage is clamped vertical and weight standards are hung by a thin line from the sensor head. This enables the application of the force to be "on-axis," although a slight amount of output is registered by the transverse axis. This transverse output is due to a 2 deg tolerance on the orthogonality of the DSC axes. The magnitude of transverse output is less than 5 percent of the axial output and is accounted

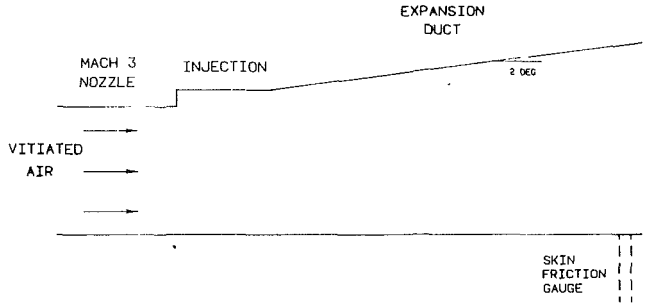

Fig. 8 NASA Langley vitiated air facility duct geometry

for in the data reduction. Figure 6 contains a sample calibration for this type of instrument.

Cooled Head Gage Calibration and Data Acquisition. This skin friction gage is calibrated in a similar manner to that of the DSC gage, that is, by directly applying a force in the measurement axis. The gage is fixed in a vertical position, which yields the desired calibration axis to be vertical. Weight standards are attached to the center of the sensor head via a thin line and allowed to hang vertically insuring that the force is applied axially. During calibration the gage is filled with the heat transfer fluid and the sensor head cooling water system is operating at 100 psi (690 kPa). Gage output is measured with a PC-AT based A/D board. An average of 100 samples over 1 second is recorded for each applied force. A sample calibration is presented in Fig. 7. As with the DSC based gage, there is a slight error in the orthogonality of the axes. This small amount of transverse axis output (less than 5 percent of axial) is recorded and accounted for in the data reduction. A least-squares regression is performed on the data to obtain the calibration curve. Calibration of the transverse axis is obtained by simply rotating the entire gage 90 deg and repeating the above procedure.

Data were recorded during the GASL test series with an IBM PC-AT equipped with a 12 bit, 8 differential channel A/D-D/A board. Data acquisition was sequenced with GASL data acquisition system and recorded for 15 seconds at 30 Hz.

NASA Langley Scramjet Test Facility and Procedures. Tests were conducted at the NASA Langley Vitiated Air Test Facility. Vitiated air was expanded to Mach 3.0, and fuel was injected through a perpendicular scheme. Skin friction measurements were recorded near the rear and on the centerline of a 2 deg, 122 cm (48 in.) long diverging duct located just downstream of the fuel injector. Figure 8 illustrates the duct geometry.

Cooling water was supplied at 100 psi (690 kPa) through a copper line immersed in a constant room temperature bath. Nominal tunnel test conditions include T_t = 3000 R (1667 K) and P_t = 500 psia (3450 kPa).

GASL Facility and Test Procedure. Tests were conducted at the General Applied Science Laboratory in two separate test series. DSC based gages were used to measure skin friction in both test series. Some results were obtained with the cooled head skin friction gage during the last test series. Measurements were acquired in a scramjet combustor model in both the constant area and diverging sections. Nominal combustor entrance conditions include M = 3.3, T_t = 4000 R (2222 K), and P_t = 800 psia (5510 kPa). The heat flux in the combustor was estimated at 400 Btu/ft^2/sec.

Experimental Results

A limited amount of results are presented here, although many test runs were conducted with the DSC based gage in all of the test facilities. The gages proved to be reliable over

Downloaded 02 Jun 2010 to 171.66.16.121. Redistribution subject to ASME license or copyright; see http://www.asme.org/terms/Terms_Use.cfm

Table 1 Summary of the DSC based skin friction gage results

Test Facility	NASA Langley Batch 5 Run 28	GASL Test 112	GASL Test 119	GASL Test 590	GASL Test 593
Mach no.	3.0	3.3	3.3	3.6	3.6
P_t (psia)	500	800	800	800	800
T_t (R)	3000	4000	4000	4000	4000
V (ft/sec)	5000	6300	6300	6300	6300
q (psf)	4100	10700	10700	7600	7600
τ_{wx} (psi)	0.122	0.11	0.092	0.2269	0.2956
τ_{wz} (psi)	0.032	0.043	-	0.0792	0.0317
C_{fx}	0.0042	0.0014	0.0012	0.0043	0.0056
C_{fz}	0.0005	0.0006	-	0.0015	0.0006

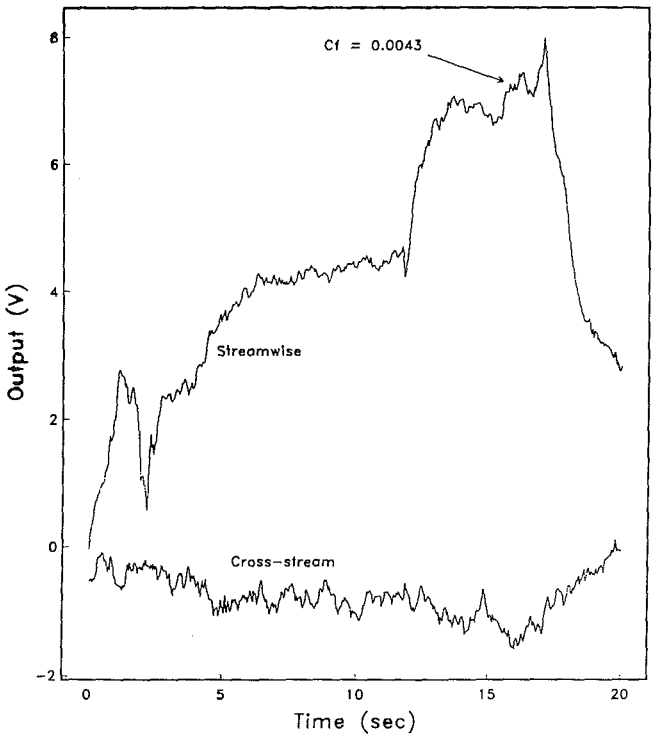

Fig. 9 NASA Langley batch 5 run 28 test results

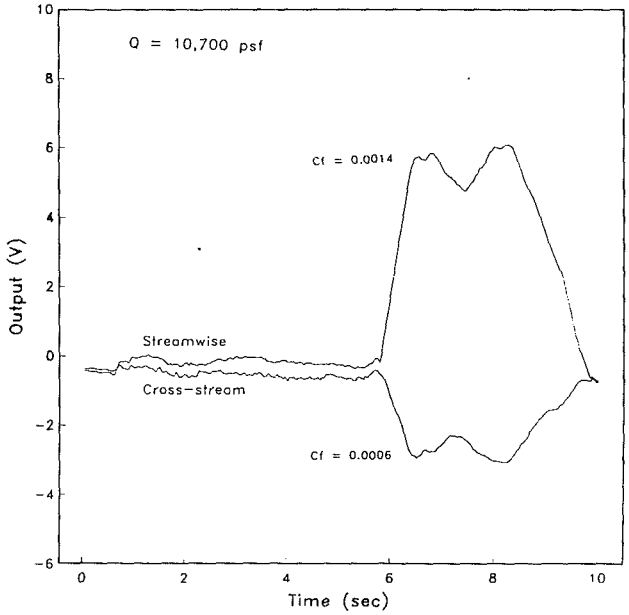

Fig. 10 GASL test 112 results

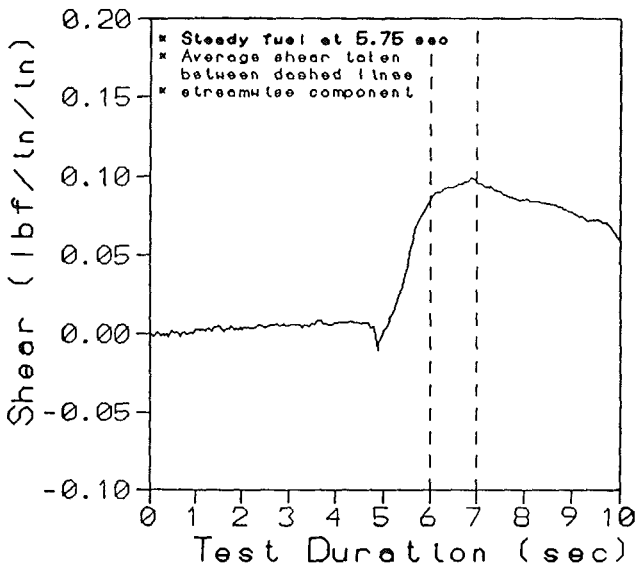

Fig. 11 GASL test 119 results

extended periods of operation. Frequency response of these gages is more than adequate to capture the frequently changing conditions exhibited by the combustors including start and finish of a fuel cycle.

A skin friction coefficient was calculated for all the tests presented here. The skin friction gage measures the tangential force due to the flow over the sensor head, which is related to the wall shear, τ_w, by the flow wetted area of the sensor head. A skin friction coefficient can be readily calculated by

$$C_f = \frac{\tau_w}{q}$$

where q is the dynamic head of the flow given as

$$q = \frac{1}{2}\rho V^2$$

Table 1 summarizes the results obtained with the DSC based gage from all three test series. The values of q used to calculate the skin friction coefficients for the GASL tests are based on flow conditions at the combustor entrance.

A sample result of the output form the NASA Langley tests is depicted in Fig. 9. A streamwise skin friction coefficient (C_f = 0.0042) was calculated from an average of the gage output between 12 and 15 seconds. The transverse or cross-stream measurement is shown to be small compared to that of the streamwise component suggesting a near two-dimensional flow field at the measurement position.

Figure 10 illustrates both the streamwise and cross-stream wall shear measured for GASL test run 112. The friction gage was located in the side wall of the constant area section of the combustion chamber downstream of a rearward-facing step. An average value of the wall shear at a point with steady fuel conditions was used to calculate a skin friction coefficient. The interval over which the average was taken is indicated on the plot as the interval between the vertical dashed lines. For test 112, τ_w = 0.11 lbf/in.^{2} (760 N/m^2) in the streamwise direction and τ_w = 0.043 lbf/in.^{2} (295 N/m^2) for the cross-stream component. The streamwise and cross-stream skin friction are listed in Table 1. Figure 11 presents the data recorded for test 119 in the streamwise direction. Shear and friction coefficient values are listed in Table 1, as well. During tests 112 and 119, the temperature of the sensor head was recorded as well as the temperature of the combustion chamber wall

Downloaded 02 Jun 2010 to 171.66.16.121. Redistribution subject to ASME license or copyright; see http://www.asme.org/terms/Terms_Use.cfm

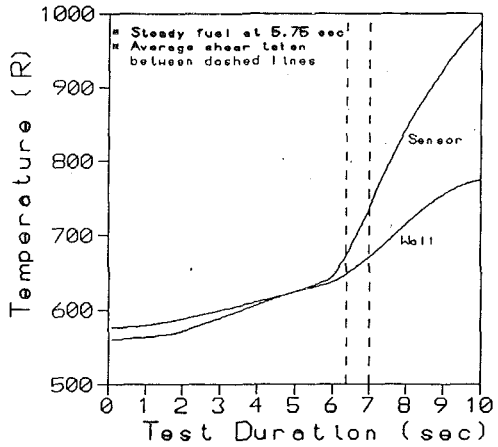

Fig. 12 GASL test 112 temperature mismatch

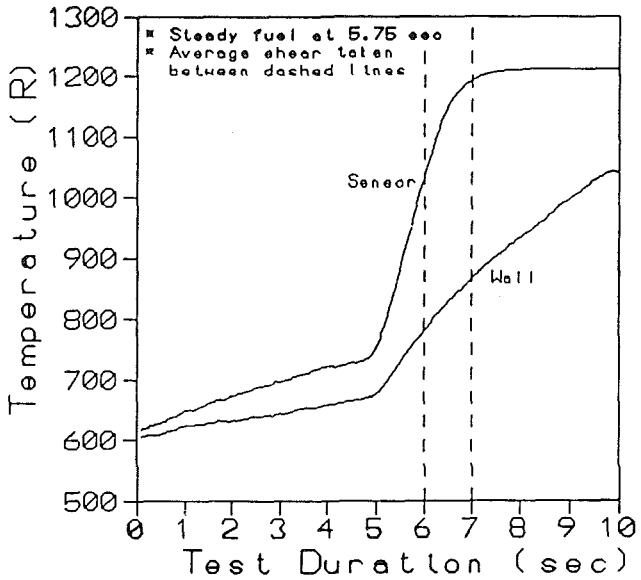

Fig. 13 GASL test 119 temperature mismatch

adjacent to the sensor head. A temperature difference of up to 400 R (222 K) was obtained during this test (see Figs. 12 and 13). A similar result was obtained for several other test runs. Considering this temperature discrepancy and its possible effects on the accuracy of the skin friction measurements was a leading factor for designing the cooled head skin friction gage.

Figures 14 and 15 present data measured for two test runs during the second test series, also conducted at GASL. Two different fuel conditions are represented in these plots. These skin friction measurements are based on a combustor inlet reference dynamic pressure. The two test runs are representative of data recorded in the constant area section of the combustor. Relatively high values of skin friction are reported for these test cases in the streamwise direction (see Table 1). Cross-stream components for this location can be as much as 35 percent of the streamwise values.

Cooled Head Skin Friction Gage Results. A first test for this type of skin friction gage was conducted in a cold Mach 3.0 supersonic flow. Output from this test is shown in Fig. 16. This result indicates that the gage has an excellent time response, apparent by its following of the start of the supersonic tunnel on the left of the figure and unstart of the tunnel on the right of the figure. Output reached a steady constant value, which translates into a skin friction of $C_f = 0.0015$. A calculation of the skin friction coefficient based on the boundary layer height measured from a nanoshadowgraph of the measurement position indicate a skin friction coefficient of $C_f = 0.0014$.

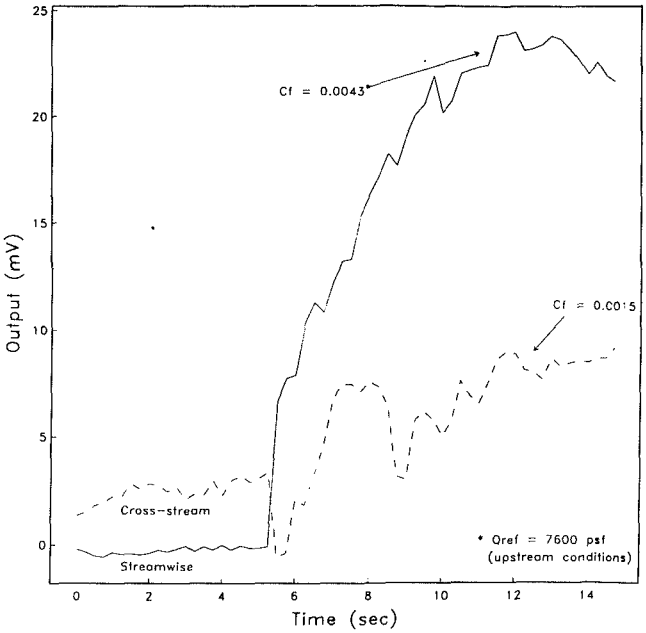

Fig. 14 GASL test 590 results

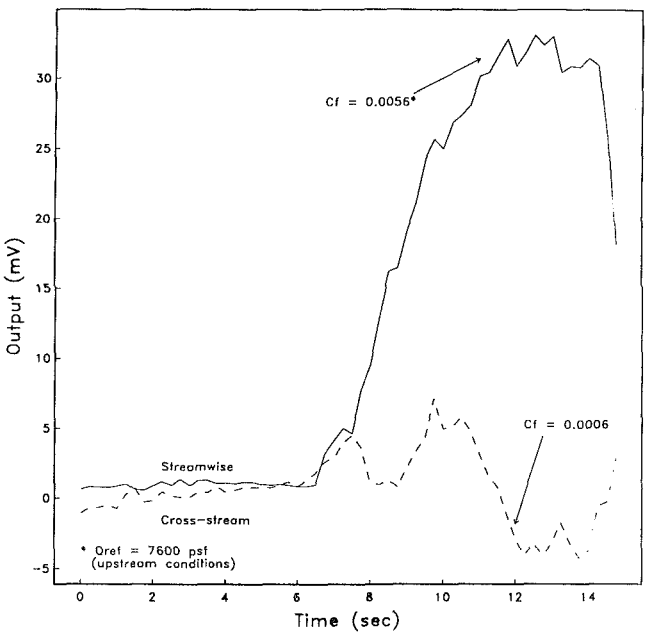

Fig. 15 GASL test 593 results

The gage was installed into the constant-area section of the combustion chamber of the last GASL test series to make a skin friction measurement. Some limited success was achieved. Figure 17 illustrates the output for the streamwise direction of Test 602. An average was taken over the range during which fuel was being injected and a skin friction coefficient was calculated to be $C_f = 0.0023$. Table 2 contains the results from this test run as well as Test 601.

Measurement Uncertainties

The largest source of error is due to heating of the DSC or, in the case of the cooled head gage, of the strain gages themselves. The manufacturer of the DSC specifies the temperature

Downloaded 02 Jun 2010 to 171.66.16.121. Redistribution subject to ASME license or copyright; see http://www.asme.org/terms/Terms_Use.cfm

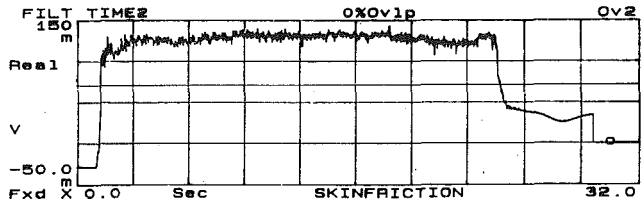

Fig. 16 Cooled heat gage cold supersonic flow results

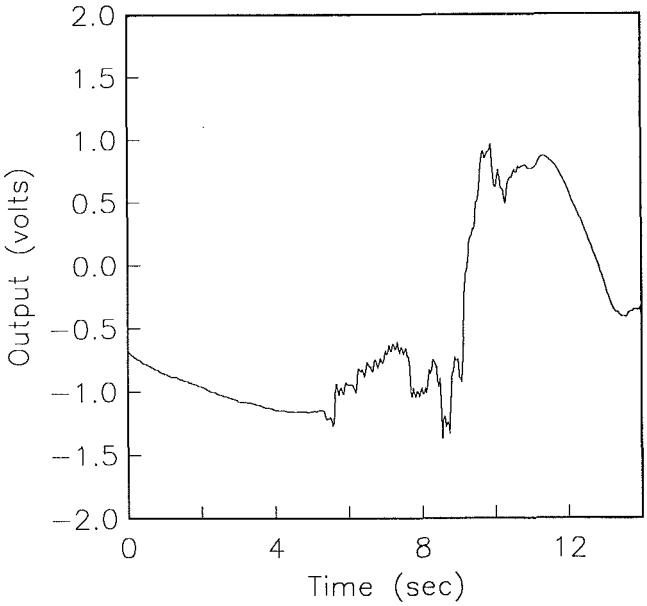

Fig. 17 GASL cooled head gage results

sensitivity to be 0.02 percent of full scale. Presently the gage operates at about 2 to 3 percent fo full scale, which would magnify this temperature error potential. This results in a requirement of keeping the DSC temperature to $\pm 2°C$. The cooling system integrated into the DSC design has been able to keep the DSC to $\pm 1°C$, which results in an uncertainty less than ± 2 percent.

Further uncertainties can be due to asymmetric heating of the crystal strain gages. A zero shift is the result of a temperature change of these elements. If the temperature change is symmetric then the output can be corrected with the known temperature sensitivity. If heating is asymmetric correction is not possible. For the DSC based gage this error is virtually eliminated by the active cooling system around the housing. In the case of the cooled head gage this type of system is not as effective. In the future, tests are planned with spray cooling on the outer housing that should reduce these errors.

Pressure gradients in the combustion chamber can result in a moment on the sensing head. Pressure drop in the duct at NASA Langley is approximately 1.5 psi/ft (34 kPa/m). This results in a negligible moment on the balance. Pressure gradients in all tests are assumed small.

Many of the measurement uncertainties with these instruments result in negligible effects. Overall uncertainty is based on the effects of the misalignment, possible zero shift, and calibration concerns. This results in an overall uncertainty of 10–15 percent.

Table 2 Cooled head friction gage results

Test Facility	GASL Test 601	GASL Test 602
Mach no.	3.3	3.3
P_t (psia)	800	800
T_t (R)	4000	4000
V (ft/sec)	6300	6300
q (psf)	7800	7800
τ_{wx} (psi)	0.160	0.181
C_{fx}	0.0029	0.0033

Conclusions

Results of these experiments confirm the validity of a floating element, nonnulling, cantilever skin friction balance design. Accurate measurements were obtained in very high heat flux supersonic environments. Measurements were improved over those previously reported by active cooling of the DSC with continuous high pressure water channels surrounding the balance.

Dual axes measurements indicate nearly two-dimensional flows in the NASA Langley facility and in the constant-area section of the combustor during the early test series at GASL. Results from the later test series at GASL show transverse shear to be up to 90 percent of the streamwise value in the diverging section of the combustion chamber indicating a highly three-dimensional turbulent flow.

The design of an active cooling system for the floating element proved to be a feasible design option to improve further the accuracy of these types of nonnulling balances. Encouraging preliminary results from both a cold and a high heat flux supersonic flow were obtained. Accuracy will be improved with better control over heating of the piezoresistive strain gages.

Acknowledgments

The invaluable assistance provided by all the involved employees of NASA Langley Research Center and the General Applied Science Laboratory is greatly appreciated.

References

1 Nitsche, W., Haberland, C., and Thunker, R., "Comparative Investigations of the Friction Drag Measuring Techniques in Experimental Aerodynamics," presented at the 14th ICAS Congress, Paper No. ICAS-84-2.4.1, Sept. 1984.

2 DeTurris, D. J., Hellbaum, R. F., and Schetz, J. A., "Direct Measurements of Skin Friction in a Scramjet Combustor," Paper No. AIAA 90-2342, 1990.

3 Winter, K. G., "An Outline of the Techniques Available for the Measurement of Skin Friction in Turbulent Boundary Layers," *Progress in Aerospace Sciences*, Vol. 18, 1977, pp. 1–57.

4 Roensch, R. L., and Cadwell, J. D., "Direct Measurements of Skin Friction in a High Reynolds Number Supersonic Blowdown Wind Tunnel," Douglas Paper No. 1728, Douglas Aircraft Company.

5 Allen, J. M., "Systematic Study of Error Sources in Supersonic Skin-Friction Balance Measurements," NASA-TN-D-8291, Oct. 1976.

6 Allen, J. M., "Improved Sensing Element for Skin-Friction Balance Measurements," *AIAA Journal*, Vol. 18, Nov. 1980, pp. 1342–1345.

7 Voisinet, R. L. P., "Combined Influence of Roughness and Mass Transfer on Turbulent Skin Friction at Mach 2.9," AIAA Paper No. 79-0003, 1979.

8 Schetz, J. A., and Nerney, B., "Turbulent Boundary Layer With Injection and Surface Roughness," *AIAA Journal*, Vol. 15, Sept. 1977, pp. 1268–1274.

Downloaded 02 Jun 2010 to 171.66.16.121. Redistribution subject to ASME license or copyright; see http://www.asme.org/terms/Terms_Use.cfm

Coherent Anti-Stokes Raman Scattering (CARS) Thermometry in a Model Gas Turbine Can Combustor

J. Y. Zhu

T. Tsuruda

W. A. Sowa

G. S. Samuelsen

UCI Combustion Laboratory,
University of California, Irvine,
Irvine, CA 92717-3550

Nonintrusive, spatially resolved instantaneous temperature measurements are presented that were obtained from a reacting spray flame in a model gas turbine can combustor using coherent anti-Stokes Raman scattering (CARS) thermometry. The results show that CARS measurements agree with thermocouple measurements at the exit of the combustor. The liquid droplet induced dielectric breakdown is not an obstacle in applying CARS to reacting sprays. The CARS measured temperature field also indicates that there is a relatively cool region ($T < 1000$ K) near the nozzle tip. Reaction occurs in the region where large numbers of droplets are present and in the interface of the swirl-induced recirculation zone. This study demonstrates that CARS is a viable diagnostic tool for nonintrusive, instantaneous temperature measurements in practical spray flames.

Introduction

In recent work at the UCI Combustion Laboratory, a wall jet model gas turbine can combustor (WJCC) has been characterized to provide information on aerodynamics, heat and mass transfer characteristics, and fuel/air mixing behavior. Previous work (e.g., Brouwer et al., 1988; Cameron et al., 1988, 1989) has employed optical techniques (i.e., Phase Doppler particle analyzer, PDPA; laser velocimetry, LV) to measure the gas phase aerodynamic field, the liquid phase droplet size, and velocity fields, and thermocouples to characterize the thermal field. Most of the critical mixing dynamics in a spray flame occurs in the primary reacting zone (upstream of the primary jets). It is difficult to correct the gas phase temperature measured from conventional thermocouple probes because of the presence of droplets. Therefore, nonintrusive temperature measurements are needed in reacting sprays. This study demonstrates nonintrusive, instantaneous, and spatially resolved temperature measurements in the WJCC combustor using nitrogen coherent anti-Stokes Raman scattering (CARS) thermometry.

Background

CARS is a nonlinear optical four-wave mixing spectroscopic technique. In the CARS process, two pump laser beams and a Stokes laser beam are phase matched and overlapped within a spatial volume to generate a coherent laserlike signal at the anti-Stokes frequency. When the frequency difference between the pump beams and the Stokes beam coincides with the frequency of a Raman-active mode of the medium (normally a vibrational-rotational transition), the CARS signal is resonantly enhanced. The use of CARS for nonintrusive temperature measurements is based on the fact that the spectral signature of a CARS signal characterizes the energy states of an ensemble of molecules. From quantum mechanics, the CARS energy spectrum is a predictable function of temperature. Therefore, the temperature can be determined by comparing the experimental CARS spectrum to a spectrum calculated using temperature as a fitting parameter. Complete reviews of the CARS process (Druet and Taran, 1981; Valentini, 1985) and a discussion of CARS as a combustion diagnostic (Eckbreth, 1988) are available in the literature.

Since the early work of Regnier and Taran (1973), CARS has been applied to many combustion flows for nonintrusive, quantitative, and spatially resolved temperature measurements. Some examples include a jet engine exhaust (Eckbreth et al., 1984), coal particle laden flows (Beiting, 1985; Alden and Wallin, 1985), internal combustion engines (Stenhouse et al., 1979; Dobbs et al., 1985; Lucht et al., 1987), sooting flames (Eckbreth and Hall, 1979; Farrow et al., 1984), and a burning droplet stream (Zhu et al., 1992).

CARS has also been used for temperature measurements in gas turbine combustors (Eckbreth, 1980; Greenhalgh et al., 1983; Bedue et al., 1984). However, little work has been done to make CARS measurements in liquid fuel fired gas turbine combustors. Eckbreth (1980) reported temperature measurements in a liquid fuel (Jet A) fired JT-12 combustor and found that turbulence has little effect on CARS signal generation efficiency. The CARS measurements agreed well with thermocouple measurements in the JT-12 combustor exhaust where droplets were not present. Bedue et al. (1984) performed single-shot CARS temperature measurements in a liquid fuel fired

Contributed by the International Gas Turbine Institute and presented at the 37th International Gas Turbine and Aeroengine Congress and Exposition, Cologne, Germany, June 1-4, 1992. Manuscript received by the International Gas Turbine Institute February 6, 1992. Paper No. 92-GT-134. Associate Technical Editor: L. S. Langston.

Copyright © 1993 by ASME
Downloaded 02 Jun 2010 to 171.66.16.121. Redistribution subject to ASME license or copyright; see http://www.asme.org/terms/Terms_Use.cfm

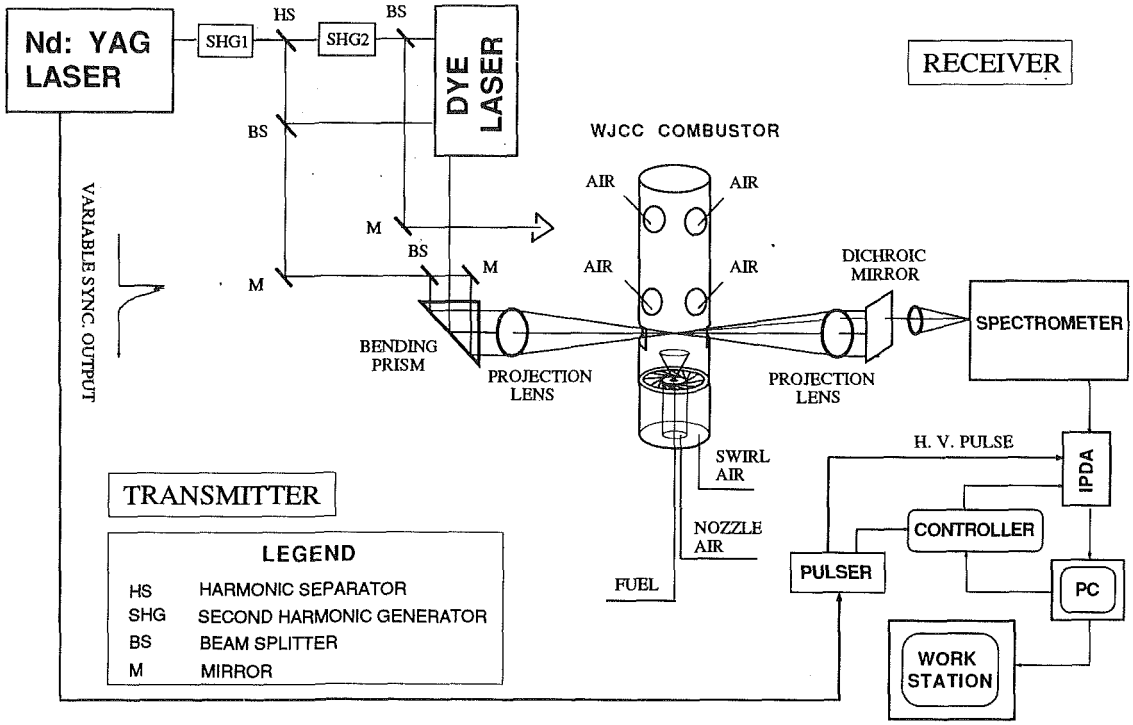

Fig. 1 Schematic of the experimental facility showing the CARS system and the WJCC combustor

model combustor. These studies demonstrated the feasibility of making CARS temperature measurements in hostile environments. Due to the signal strength, laser firing frequency, and data processing speed, detailed instantaneous temperature measurements were not performed in these studies.

The goals of this study are: (1) to demonstrate single-shot CARS temperature measurements in a liquid fuel fired model gas turbine combustor, (2) to provide detailed experimental data for numerical modeling, (3) to examine the role of fuel/air mixing and turbulence in reacting sprays using time-averaged and fluctuating temperature fields, and (4) to identify the problems encountered in applying CARS to practical liquid fuel fired combustors.

Experimental Facility

CARS System. Figure 1 shows a schematic of the experimental facility, which consists of a CARS instrument and the wall jet can combustor (WJCC). The system consists of two parts: an optical transmitter and a CARS signal receiver. The transmitter is installed on a two-level optical cart so that it can be easily moved. The optical layout on the cart can be found from Zhu et al. (1991). The CARS system employs a 10 Hz injection seeded Nd:YAG laser (Modified Spectra-Physics DCR-3) as shown in Fig. 1. The fundamental 1064 nm YAG laser beam is frequency doubled by a secondary harmonic generator (SHG1) to produce a primary 532 nm laser beam. The primary 532 nm laser beam is split 30/70 with the 30 percent leg used to pump the dye laser amplifier and with the 70 percent leg split into two pumping beams in the BOXCARS optical configuration. The remaining 1064 nm radiation is frequency doubled by another harmonic generator (SHG2) to produce a secondary 532 nm laser beam that pumps the dye laser oscillator. Both the dye laser beam (Stokes beam) and the two 532 nm pump beams are directed to a 250 mm focal length lens by a 50 mm bending prism, which forms a CARS probe volume.

In the CARS signal receiver, another 250 mm focal length lens collects the CARS signal. A dichroic mirror is used to reflect the pump and Stokes laser beams while transmitting the CARS signal. A spectrometer lens focuses the CARS beam into a spectrometer (SPEX 1702/04). An intensified photodiode array (IPDA, Princeton Instruments IRY-1024 IPDA) controlled by a ST-120 controller (Princeton Instruments) records the CARS spectrum at the exit of the spectrometer. A FG-100 pulser (Princeton Instruments) gates the IPDA detector for a signal duration of 20 ns to reduce the noise from stray light emission (e.g., flame luminescence). This gating is necessary to reduce the noise produced by laser-induced dielectric breakdown of droplets. CARS spectra are acquired by a NEC Power Mate II computer, equipped with a ST-120 control board (Princeton Instruments). CARS spectral fitting is performed on a Sun-4 workstation with an optical disk driver for data storage.

Combustor and Window Limitations. The model gas turbine combustor (WJCC) used in this study is the same as the one used in past studies (Brouwer et al., 1988; Cameron et al., 1988, 1989). The WJCC combustor is a stainless steel duct with an 80 mm diameter. The overall length of the combustor is 45.7 cm, with an operating length of 32 cm, as shown in Fig. 2. The dome region has a step expansion geometry. The primary jets are located 8 cm downstream of the fuel nozzle. The secondary jets dilute the reacting flow at a downstream distance of 16 cm from the nozzle. The swirler provides 100 percent blockage with the dimensions shown in Fig. 2. An air assist nozzle (Parker Hannifin) was used to inject JP-4 liquid fuel into the combustor. The combustor is vertically fired and is set on a three-dimensional traverse mechanism for spatial temperature mapping.

The combustor has windows for optical access. In order to determine how close to the window measurements could be made, a window failure test was conducted with the Nd:YAG laser. The test used two samples of Fused Silica Dynasil 4000 glass (Mark Optics) with two different surface qualities (Scratch/Dig: 5/10 and 40/60). During the test, neutral density filters were used to vary the laser beam energy density on the window, while keeping the laser power unchanged. Figure 3 shows the window test results. The data points represent the minimum separation distances required from the center of the

Downloaded 02 Jun 2010 to 171.66.16.121. Redistribution subject to ASME license or copyright; see http://www.asme.org/terms/Terms_Use.cfm

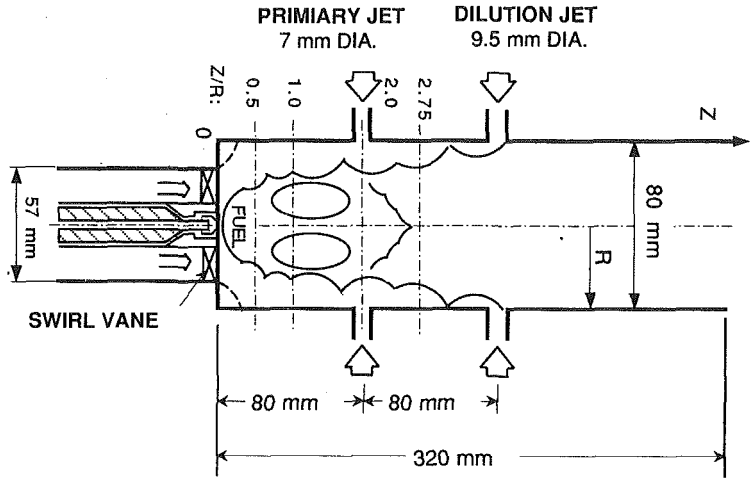

Fig. 2 Schematic of the WJCC combustor

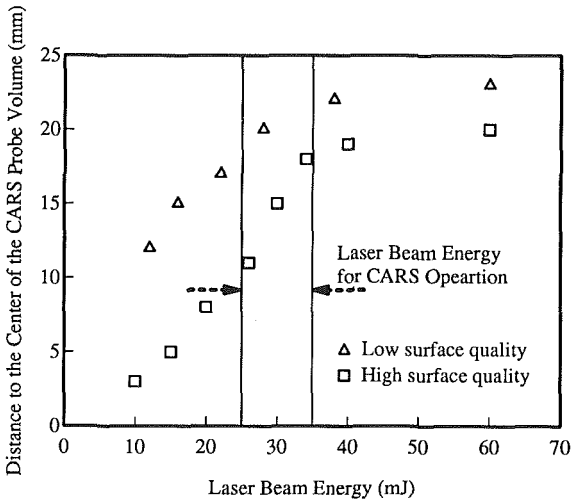

Fig. 3 Test results of optical window handling; distance from center of the CARS probe volume to window inner surface at which window damaged after 100 laser shots

CARS probe volume to the nearest window surface to avoid observable window damage after 100 laser shots. The results indicate that the window surface quality is an important factor in how close measurements can be made to the window. The results also show that even when high-quality surface finish windows (5/10) are used, it is not possible to map closer than 20 mm to the window. In order to avoid this problem, two aluminum plates were installed on the combustor that had a 10-mm-dia hole (large enough to pass the laser beams). Since the combustor is operated at 1 atm pressure, the effect of the open holes is not significant, as will be discussed later.

Experimental Summary

Experimental Conditions. The experimental conditions for the results reported in this paper are the same as the baseline testing conditions used in previous WJCC combustor experiments (Brouwer et al., 1988; Cameron et al., 1988, 1989). These baseline conditions represent a standard for comparison. Archived measurements include characterization of (1) the gas phase aerodynamic field by laser velocimetry (LV), (2) the gas phase thermal field by thermocouple, and (3) the liquid droplet size distribution and velocity by phase Doppler particle analyzer. These conditions are listed in Table 1.

To get the maximum CARS signal for reliable single-shot

Table 1 Wall jet can combustor (WJCC) operating conditions

PARAMETER	CONDITION
Swirl van size (OD)	57 mm
Nozzle air flow rate	2.50 g/s
Nozzle injection angle	60°
Fuel flow rate	0.795 g/s
Primary jet-swirl air flow rate	11.12 g/s
Dilution jet-swirl air flow rate	13.34 g/s
Swirl air flow rate	20.01 g/s
Primary jet diameter	7 mm
Dilution jet diameter	9.5 mm
Overall stoichiometry	0.3
Fuel type	JP-4
Bulk velocity	7.5 m/s
Dome geometry	step

CARS temperature measurements, the laser beam energy was set close to the threshold of air breakdown during the experiments. The dye laser beam energy was reduced to about 7 mJ to reduce the stimulated pumping effect (Snelling et al., 1989; Zhu et al., 1992), which otherwise was observed in the room air CARS spectrum.

The temperature field map within the WJCC combustor included four radial temperature profiles measured at axial distances of 20, 40, 80, and 110 mm from the nozzle tip. Each radial profile included 11 data points. At each data point 1000 measurements were made. A convergence test indicated that 200 reliable measurements were sufficient to get statistically converged mean and root mean square temperature values at a point.

Spatial Resolution. To characterize the spatial resolution, the nonresonant CARS signal generated in a piece of thin glass (0.15 mm in thickness) was collected. This method has been used by several researchers (Switzer and Goss, 1982; Boyack, 1989; Zhu, 1991). This test showed that 90 percent of the CARS signal intensity is generated in a 2-mm-long probe volume with a beam crossing angle of 3.5 deg. The diameter of the CARS probe volume is at most 150 μm (Zhu et al., 1992). Previous research suggests (Zhu and Dunn-Rankin, 1991b) that the CARS spatial averaging effects can be ignored for a 2-mm-long probe volume, if the temperature gradient is less than 250 K/mm. For the condition in a WJCC combustor, previous thermocouple measurements (Camerson et al., 1998, 1989) indicated that the steepest time-averaged temperature gradient is less than 250 mm/K. Since the flow is very turbulent, the time-averaged thermocouple measurements cannot provide information on instantaneous temperature gradients. However, since the turbulent characteristic time scale (e.g., the Taylor scale) is much longer than the CARS sampling time (10 ns), CARS can easily resolve the turbulent field.

Downloaded 02 Jun 2010 to 171.66.16.121. Redistribution subject to ASME license or copyright; see http://www.asme.org/terms/Terms_Use.cfm

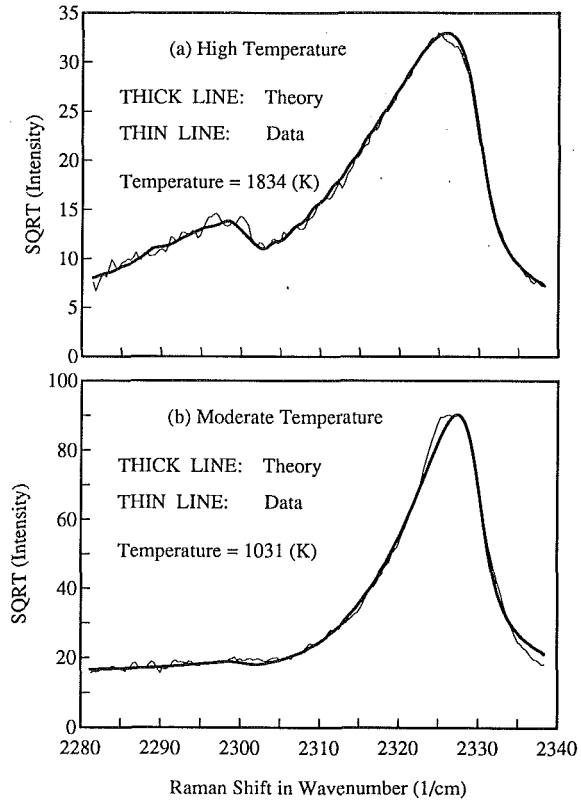

Fig. 4 Typical best library fits of measured single-shot CARS spectra

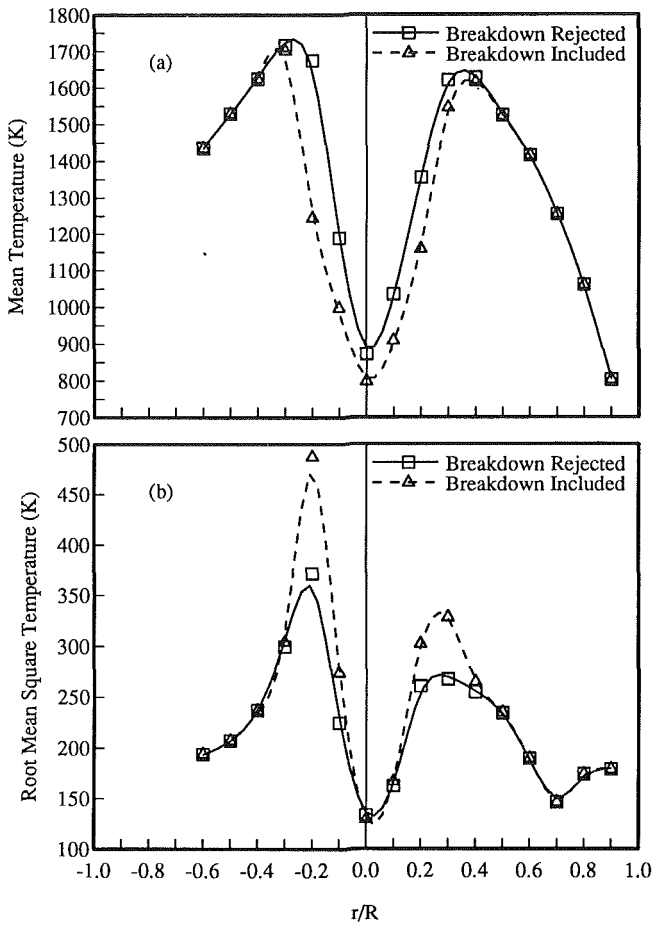

Fig. 5 A comparison of CARS measured temperature with and without rejection spectra with droplet induced breakdown: (*a*) mean temperature; (*b*) rms temperature

Error Analysis

Spectral Fitting. The temperature measured using CARS is extracted by fitting an experimental CARS spectrum to a theoretical CARS spectrum. The fitting procedure employs a library of theoretical nitrogen CARS spectra over a range from 250–3000 K in 50 K increments. The Sandia CARS code CARSFT (Palmer, 1989) generates a theoretical CARS spectra library with an instrument function deduced from a least-squares fit of the room temperature nitrogen CARS spectrum. A modified version of the Sandia quick fit code FTCARS (Palmer, 1989) linearly interpolates between temperatures represented in the spectral library to find the least-squares best fit between measured and calculated spectra. Figure 4 shows typical library quick fits of experimental single-shot CARS spectra at a high temperature (Fig. 4*a*) and at a moderate temperature (Fig. 4*b*). Both of the spectra are from the dome region in the combustor where chemical reactions occur in a highly turbulent environment. The fitting results show that the calculated theoretical CARS spectra agree well with the experimental single-shot CARS spectra. From this type of analysis, it was deduced that reliable single-shot CARS temperature measurements are achieved using the CARS system even in the liquid fuel fired reacting flows of this combustor. To ensure reliable CARS temperature results, spectra with poor signal-to-noise ratio are rejected in the spectral fitting. Further screening is done by visually checking the spectral fitting for several spectra at each measurement location. Poor spectral fits (large spectral fitting residual) are also rejected in the calculation of mean and rms temperature. With these procedures in place, the measurement uncertainty in the primary zone is less than 150 K. Outside of the primary zone, the uncertainty improves to be less than 50 K.

Droplet-Induced Dielectric Breakdown. One challenge for CARS temperature measurements in spray combustion is droplet-induced dielectric breakdown in the primary reaction zone where large numbers of fuel droplets are still present. Liquid droplets act like a lens to focus the laser beams (Chang et al., 1988; Dunn-Rankin et al., 1990) and cause dielectric breakdown at low laser beam intensity. This promotes dielectric breakdown in droplet laden flows, such as those observed in a monodisperse droplet stream flame (Zhu, 1991).

During the experiments, strong dielectric breakdown was observed within a radial distance of $r/R = 0.3$ (12 mm) from the nozzle centerline at the axial location of $Z/R = 0.5$ (20 mm). Outside of this envelope, the dielectric breakdown is insignificant. Downstream of the primary zone, dielectric breakdown was not observed, indicating quick vaporization of the spray. These observations agree with PDPA measurements taken in the WJCC combustor at the same operating conditions (Cameron et al., 1988). As suggested by Dunn-Rankin et al. (1990), breakdown spectra were rejected in the calculation of the statistical mean and root mean square temperatures. A comparison has been made to examine the effect of the rejection scheme on measured CARS temperatures as shown in Fig. 5. The results show that the temperature difference is significant only within a radial distance of $r/R = 0.3$ (12 mm) from the combustor centerline at the axial location $Z/R = 0.5$ (20 mm). The overall temperature profiles, however, are quite similar.

Nonresonant Susceptibility. In spray combustion environments, fuel droplets evaporate in the primary zone. Therefore, fuel vapor concentration can be high in the wake of a droplet

Downloaded 02 Jun 2010 to 171.66.16.121. Redistribution subject to ASME license or copyright; see http://www.asme.org/terms/Terms_Use.cfm

or in a droplet cloud. In addition, the nonresonant susceptibility of most hydrocarbon fuels is orders of magnitude higher than that of nitrogen (Farrow et al., 1987). This can cause CARS temperature measurement errors in spray flames such as the one examined in this study. The errors result from the nonresonant third-order susceptibility being kept constant during spectral fitting as explained by Zhu (1991). By varying the nonresonant susceptibility in the quick fitting procedure as proposed by Hall and Boedeker (1984), Zhu (1991) estimated that the nonresonant susceptibility near the surface of a combusting droplet with a size of 120 μm is about 2.5 times the value of nitrogen. The error in the mean temperature due to using constant nonresonant susceptibility is about 3 percent (50 K). The same analysis was applied for several measurement points near the fuel nozzle (Z = 20 mm) where droplets are present as indicated by PDPA measurements (Cameron et al., 1988). The error due to nonresonant susceptibility was found to be less than 3 percent.

Results and Discussion

Comparison Between CARS and Thermocouple Measurements. To verify the CARS temperature measurements, CARS measurements are compared with previous thermocouple measurements taken at the axial location Z/R = 2.5 (Cameron et al., 1988) in the WJCC using the same operating conditions. However, the combustor was horizontally fired in the early studies. At this axial distance a thermocouple gives fairly accurate temperature measurements. Figure 6 shows that the difference between the CARS and the thermocouple data are within 100 K, except at the radial location close to the wall. This 100 K difference is likely due to thermocouple measurement error (the thermocouple data were not corrected for heat losses). The difference may also be due to the difference in measurement locations (Z/R = 2.75 for CARS; Z/R = 2.5 for T/C). Thermocouple data measured at a closer axial location to the primary jets show a slightly steeper temperature profile compared to CARS measurements, indicating a less expanded cool region at the center of the combustor. This is consistently observed when comparing previous thermocouple measurements (Cameron et al., 1988) and the CARS measurements. At a radial location close to the wall, the effect of the open hole in the aluminum window can be seen. At these radial locations, the CARS measurements give lower temperatures than the thermocouple. The comparison shown in Fig. 6 suggests that CARS measurements are consistent in trend to thermocouple measurements and close in magnitude. The open hole in the aluminum window does not appear to affect most of the measurement region significantly near the combustor centerline.

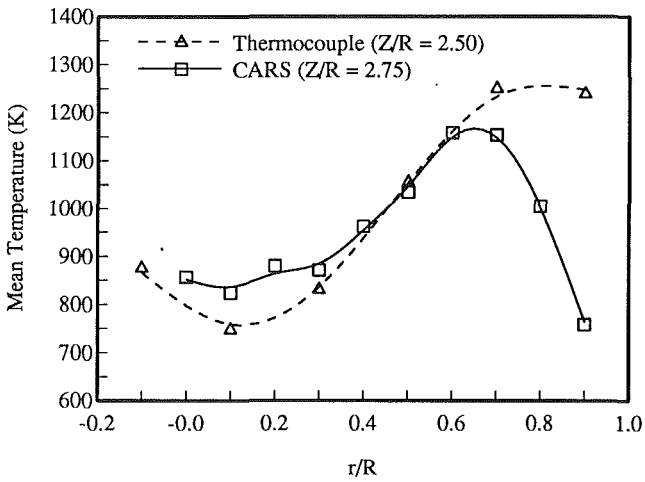

Fig. 6 Comparison between CARS measurements and thermocouple data in the dilution zone

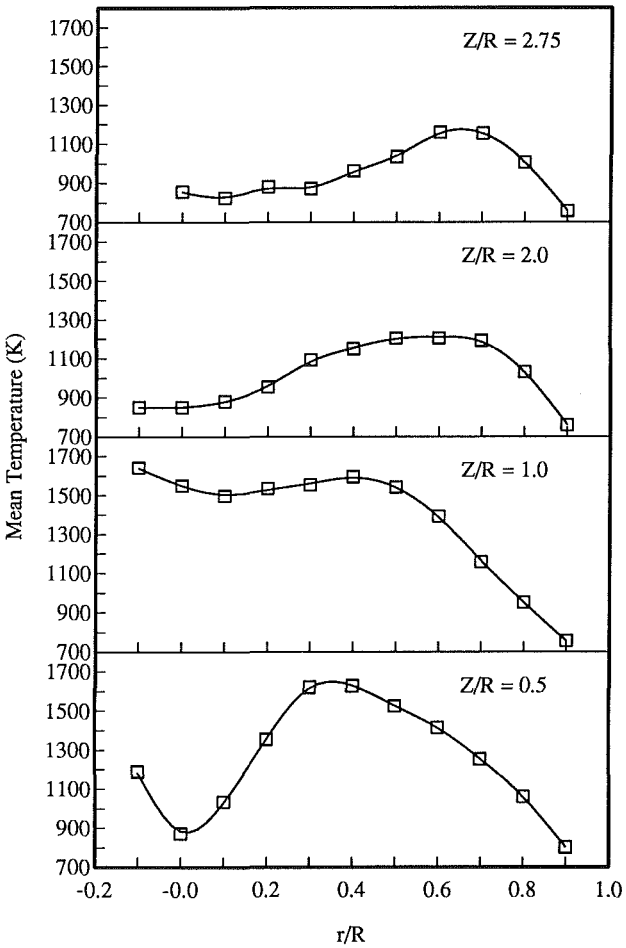

Fig. 7 CARS measured mean temperature field in the WJCC combustor

Mean Temperature Field. Figure 7 presents CARS measured mean temperatures within the WJCC combustor. At the axial location of Z/R = 0.5 (20 mm), the mean temperature is low at the combustor centerline. At this location the gas temperature is less than 1000 K within a radius 4 mm (r/R = 0.1) from the centerline. A strong on-axis recirculation zone is not present in this region to carry the hot combustion gas back from downstream regions and little turbulent heat convection is present due to small azimuthal velocities as indicated by previous aerodynamic measurements (Cameron et al., 1989). The mean temperature rises to a maximum value at a radial location of r/R = 0.35 (14 mm) and then decreases near the wall due, in large part, to the open hole in the window. When interpreting results with spatially resolved droplet data rate (Cameron et al., 1988), it is interesting to find that high temperatures are measured where large numbers of droplets are still present. Droplet measurements taken in the reacting hollow cone spray indicate that liquid droplets are present in this combustor up to Z/R = 1.5. Consistent with the hollow cone spray results, the mean temperature profiles clearly show that reactions are taking place in the cone region of the spray and not along the centerline of the combustor. The maximum temperature is around 1600 K.

The center cool region disappears at an axial location of Z/R = 1.0 (40 mm). The centerline mean temperature is close to the maximum temperature 1600 K with a slight outward movement to a radial location of r/R = 0.4 (16 mm). This flat high-temperature profile reveals a well-mixed region occurring at this axial location due to swirl-induced recirculation

Downloaded 02 Jun 2010 to 171.66.16.121. Redistribution subject to ASME license or copyright; see http://www.asme.org/terms/Terms_Use.cfm

as indicated by LV measurements in a previous study (Cameron et al., 1989).

Farther downstream at $Z/R = 2.0$ (80 mm), the primary sidewall jets depress the mean temperature at the centerline. Here again, the maximum mean temperature peak has moved radially outward to a radial location $r/R = 0.6$ (24 mm). The broader flat temperature distribution of 1200 K in a radius of $r/R = 0.4$ to 0.7 indicates that the upstream reaction products are in this region.

At the axial location $Z/R = 2.75$, the CARS measurements agree with the thermocouple data as discussed in the beginning of this section. The center cool region expands due to the influence of the primary jets. Therefore, the maximum mean temperature continues to move outward to $r/R = 0.7$ (28 mm).

The rms Temperature Field. The mean temperature data provide the time-averaged information about the reaction thermal field. In most practical applications, the mean information is not sufficient and may be misleading. The temperature of hot gas packets can be as high as the adiabatic flame temperature. The measured mean temperature may be 30–40 percent lower than this value. Furthermore, turbulence plays a significant role in heat transfer, fuel/air mixing, and combustion in reacting flows. Therefore, characterization of the instantaneous temperature is also important. Unfortunately, a conventional thermocouple can not measure the instantaneous temperatures due to its slow response. With a 10 ns laser pulse, CARS can resolve the turbulent thermal field. The CARS measured rms temperature field reveals the dynamic behavior of the thermal field. It also represents how much the temperature field fluctuates due to flow structure, combustion heat release, and heat transfer in the region of interest.

Figure 8 presents the root mean square temperature field measured using CARS. For the $Z/R = 0.5$ (20 mm) axial location, the maximum temperature fluctuation occurs at a radial location $r/R = 0.25$ (10 mm), which is between the mean temperature peak ($r/R = 0.35$) and the cool region ($r/R = 0$). The maximum rms temperature is about 275 K. The maximum temperature fluctuation was found around a mean temperature of 800–900 K. At this location strong turbulent mixing is taking place due to the swirling axial air flow and high radial and axial temperature gradients. The rms temperature increases near the wall due to the cooling effects of the open window.

The peak rms temperature moves radially outward as axial distance increases. The magnitude of the peak values does not decrease significantly with axial distance. Like the mean temperature profile, the rms temperature profile shown in Fig. 8 at $Z/R = 1.0$ is also flat, indicating a well-mixed region induced by flow recirculation at this axial location. Intense turbulent mixing is experienced at this axial location due to reaction heat release and on-axis flow recirculation as indicated by previous velocity measurements (Cameron et al., 1989). Notice the maximum rms temperature appears at $r/R = 0.6$, corresponding to the interface of the recirculation zone. At $Z/R = 2.0$, the penetration of the primary jets depresses the rms temperature at the centerline. Due to jet expansion and turbulent heat transfer, the rms temperature profile becomes uniform farther downstream.

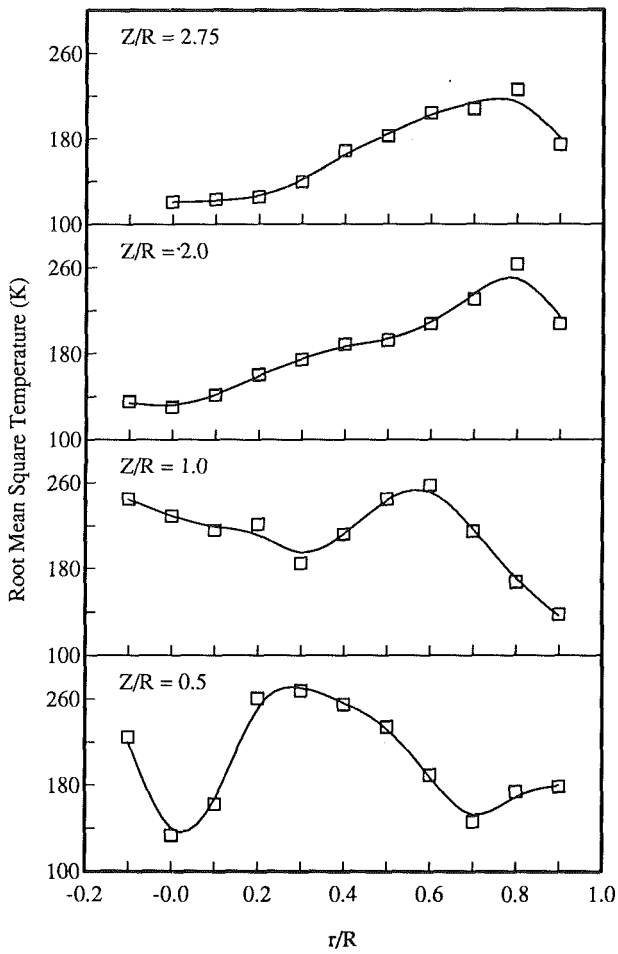

Fig. 8 CARS measured rms temperature field in the WJCC combustor

Conclusions

This study demonstrated detailed single-shot CARS temperature measurements in a liquid fuel fired model gas turbine combustor. The experiments reveal:

1 The interaction of the laser beams with optical windows is an important factor to be considered in near-wall CARS measurements. Aerodynamic windows like those used in this study or extended windows are necessary for this kind of application.

2 Droplet-induced dielectric breakdown can cause serious problems in CARS temperature measurements in the region where large numbers of liquid droplets are present. Rejecting experimental CARS spectra that display breakdown characteristics in the data processing procedure is an effective approach. The absolute difference between the CARS measured temperature resulting from rejecting and including breakdown data processing schemes is significant. However, the trends in the temperature profiles are similar. Further study on droplet-induced breakdown is needed.

3 In the WJCC combustor, the measured CARS temperatures reveal a cool region ($T < 1000$ K) at the center of the combustor near the fuel nozzle tip. In this region, there is no mean reverse axial flow to carry the hot combustion gas from downstream locations back upstream and little turbulent mixing as evidenced by the small azimuthal velocities. The results also indicated that most of the heat release occurs where large numbers of droplets are still present.

4 The CARS measured mean and rms temperature fields are consistent with previously measured aerodynamic, droplet size, and droplet number density fields. The CARS measured temperatures agree with previous thermocouple data in the region away from the primary combustion zone, suggesting that reliable instantaneous temperature measurements were achieved.

Acknowledgments

This research is sponsored by the US Air Force Environics Laboratory (Contract No. F08635-90-6-0100) with complementary funding from the Allison Gas Turbine Division of General Motors. The authors also like to thank Dr. Alan Eck-

Downloaded 02 Jun 2010 to 171.66.16.121. Redistribution subject to ASME license or copyright; see http://www.asme.org/terms/Terms_Use.cfm

breth of United Technology Research Center for his initial guidance on the CARS instrument design and Professor Paul Hedman of Brigham Young University (BYU) for his assistance.

References

Alden, M., and Wallin, S., 1985, "CARS Experiments in a Full-Scale (10 × 10 m) Industrial Coal Furnace," *Appl. Opt.*, Vol. 24, pp. 3434–3437.

Beiting, E. J., 1985, "Coherent Interference in Multiplex CARS Measurements: Nonresonant Susceptibility Enhancement Due to Laser Breakdown," *Appl. Opt.*, Vol. 24, pp. 3010–3017.

Bedue, R., Gastebois, P., Bailly, P., Pealat, M., and Taran, J. P. E., 1984, "CARS Measurements in a Simulated Turbomachinery Combustor," *Combust. and Flame*, Vol. 57, pp. 141–153.

Boyack, K. W., 1989, "A Study of Turbulent Nonpremixed Jet Flame of CO/N_2 Using Coherent Anti-Stokes Raman Spectroscopy," Ph.D. dissertation, Brigham Young University, Provo, UT.

Brouwer, J., Cameron, C. D., and Samuelsen, G. S., 1988, "A Parametric Investigation of a Model Gas Turbine Can Combustor," AIAA Paper No. 88-2859.

Cameron, C. D., Brouwer, J., and Samuelsen, G. S., 1988, "A Comparison of Spray Characterization in an Isothermal Chamber and in a Model Gas Turbine Combustor," *Proceedings of the 4th International Conference on Liquid Atomization and Spray Systems (ICLASS)*, Sendai, Japan, pp. 145–152.

Camerson, C. D., Brouwer, J., Wood, C. P., and Samuelsen, G. S., 1989, "A Detailed Characterization of the Velocity and Thermal Fields in a Model Can Combustor With Wall Jet Injection," ASME JOURNAL OF ENGINEERING FOR GAS TURBINES AND POWER, Vol. 111, pp. 31–39.

Chang, R. K., Eickmans, J. H., Hsieh, W.-F., Wood, C. F., Zhang, J.-Z., and Zheng, J.-B., 1988, "Laser Induced Breakdown in Large Transparent Water Droplets," *Appl. Opt.*, Vol. 27, pp. 2377–2385.

Dobbs, G. M., Sangiovanni, J. J., Anderson, T. J., Boedeker, L. R., Eckbretch, A. C., and Hall, R. J., 1985, "Optical Diagnostics for Diesel Engine Applications," R 85-957012-F, UTRC Report.

Druet, S. A. J., and Taran, J. P. E., 1981, "CARS Spectroscopy," *Prog. Quan. Electr.*, Vol. 7, pp. 1–72.

Dunn-Rankin, D., Switzer, G. L., Obringer, C. A., and Jackson, T. A., 1990, "Effect of Droplet Induced Breakdown on CARS Temperature Measurements," *Appl. Opt.*, Vol. 29, pp. 3150–3159.

Eckbreth, A. C., and Hall, R. J., 1979, "CARS Thermometry in a Sooting Flame," *Combust. and Flame*, Vol. 36, pp. 87–98.

Eckbreth, A. C., 1980, "CARS Thermometry in Practical Combustors," *Combust. and Flame*, Vol. 39, pp. 133–147.

Eckbreth, A. C., Dobbs, G. M., Stufflebeam, J. H., and Tellex, P. A., 1984, "CARS Temperature and Species Measurements in Augmented Jet Engine Exhausts," *Appl. Opt.*, Vol. 23, pp. 1328–1339.

Eckbreth, A. C., 1988, *Laser Diagnostics for Combustion Temperature and Species*, Abacus Press, Cambridge, MA.

Farrow, R. L., Lucht, R. P., Flower, W. L., and Palmer, R. E., 1984, "Coherent Anti-Stokes Raman Spectroscopic Measurements of Temperature and Acetylene Spectra in a Sooting Diffusion Flame," *20th Symp. (Int.) on Combust.*, The Combustion Institute, pp. 1307–1312.

Farrow, R. L., Lucht, R. P., and Rahn, L. A., 1987, "Measurements of the Nonresonant Third-Order Susceptibility of Gases Using Coherent Anti-Stokes Raman Spectroscopy," *J. Opt. Soc. Am. B*, Vol. 4, pp. 1241–1246.

Greenhalgh, D. A., Porter, F. M., and England, W. A., 1983, "The Application of Coherent Anti-Stokes Raman Scattering to Turbulent Combustion Thermometry," *Combust. and Flame*, Vol. 49, pp. 171–187.

Hall, R. J., and Boedeker, L. R., 1984, "CARS Thermometry in Fuel-Rich Combustion Zones;" *Appl. Opt.*, Vol. 23, pp. 1340–1346.

Lucht, R. P., Teets, R. E., Green, R. M. Palmer, R. E., and Ferguson, C. R., 1987, "Unburned Gas Temperatures in an Internal Combustion Engine, I, CARS Temperature Measurements," *Combust. Sci. Tech.*, Vol. 55, pp. 41–61.

Klick, D., Marko, K. M., and Rimai, L., 1981, "Broadband Single-Pulse CARS Spectra in a Fired Internal Combustion Engine," *Appl. Opt.*, Vol. 20, pp. 1178–1181.

Palmer, R. E., 1989, "The CARSFT Computer Code for Calculating Coherent Anti-Stokes Raman Spectra: User and Programmer Information," Sandia Report SAND 89-8206 UC-13, Sandia National Laboratories, Livermore, CA.

Regnier, P. R., and Taran, J. P. E., 1973, "On the Possibility of Measuring Gas Concentrations by Stimulated Anti-Stokes Raman Scattering," *Appl. Phys. Lett.*, Vol. 23, pp. 240–242.

Snelling, D. R., and Smallwood, G. J., and Parameswaran, T., 1989, "Effect of Detector on Nonlinearity and Image Persistences on CARS Derived Temperature," *Appl. Opt.*, Vol. 28, pp. 3233–3241.

Stenhouse, I. A., Williams, D. R., Cole, J. B., and Swords, M. D., 1979, "CARS Measurements in an Internal Combustion Engine," *Appl. Opt.*, Vol. 18, pp. 3819–3825.

Switzer, G. L., and Goss, L. P., 1982, *Temperature: Its Measurements and Control in Science and Industry*, Vol. 5, J. F. Schooley, ed., AIP Pub., New York, pp. 583–586.

Switzer, G. L., Goss, L. P., Trump, D. D., Reeves, C. M., Stutrud, J. S., Bradley, R. P., and Roquemore, W. M., 1986, "CARS Measurements in the Near-Wake Region of an Axisymmetric Bluff-Body Combustor," *AIAA J.*, Vol. 24, pp. 1155–1162.

Taylor, D. J., 1983, "CARS Concentration and Temperature Measurements in Coal Gasifiers," Los Alamos Scientific Lab Report, LA-UR 83-1840.

Valentini, J. J., 1985, "Coherent Anti-Stokes Raman Spectroscopy," in: *Spectrometric Techniques*, IV, Academic Press, New York, pp. 1–59.

Zhu, J. Y., 1991, "Coherent Anti-Stokes Raman Spectroscopy (CARS) Gas Temperature Measurements in a Monodisperse Combusting Droplet Stream," Ph.D. dissertation, University of California, Irvine, CA.

Zhu, J. Y., and Dunn-Rankin, D., 1991a, "Using Coherent Anti-Stokes Raman Spectroscopy to Probe the Temperature Field of a Combusting Droplet Stream," *Appl. Opt.*, Vol. 30, pp. 2672–2674.

Zhu, J. Y., and Dunn-Rankin, D., 1991b, "Effect of Spatial Averaging in CARS Thermometry," presented at the Fall Meeting of the Western States Section/The Combust. Inst., WSS/CI 91-69, Los Angeles, CA, Oct. 14–15.

Zhu, J. Y., Dunn-Rankin, D., and Samuelsen, G. S., 1992, "CARS Temperature Measurements in a Combusting Droplet Stream Flame," *Combust. Sci. Tech.*, Vol. 83, pp. 97–114.

Downloaded 02 Jun 2010 to 171.66.16.121. Redistribution subject to ASME license or copyright; see http://www.asme.org/terms/Terms_Use.cfm

The Combustion of Droplets Within Gas Turbine Combustors: Some Recent Observations on Combustion Efficiency

J. Odgers

D. Kretschmer

Department of Mechanical Engineering,
Université Laval Québec,
Quebec, Canada

G. F. Pearce

Aeronautical Research Laboratories,
Melbourne, Australia

For many years investigators studying the combustion behavior within gas turbines have presumed droplet size to play a very important role in defining combustion efficiency. Recently a very large number of experiments have been conducted jointly by Laval University and the Aeronautical Research Laboratory in Melbourne. In the course of these investigations, over a wide range of operating conditions, a single combustor has been investigated using three different Simplex atomizers at each of the conditions for three fuels. In addition, the same combustor has been used to investigate a very wide range of fuels (87) at ambient inlet conditions. The measured combustion efficiencies show no measurable effects due to droplet size, although volatility effects have been noted (measured as T_{AV}). It is thought that these effects are reflected in terms of a transfer number and related to diffusional phenomena, rather than evaporative phenomena. A great number of experimental data are reviewed, and in addition to showing the absence of effects of droplets, a small section deals with the precision of experimental values of combustion efficiency and how it might influence models predicting combustion efficiency, especially with respect to possible future pollution requirements.

Introduction

For many years droplet size has been considered to be a major factor in determining the combustion efficiency within gas turbine combustors. This observation is in accord with both theoretical and practical observations made with respect to the evaporation of single droplets. Recent experiments suggest that a new interpretation is possible, which, within the range of droplet sizes examined, shows little or no effect upon the exhaust combustion efficiency. The object of these notes is to present support for these practical observations by considering the reacting flow regimes within the combustor and their effects upon the combustion processes.

The Traditional Viewpoint

The total time of combustion of a droplet may be written in the form

$$\tau_c - \tau_e + \Delta\tau_d + \Delta\tau_r \qquad (1)$$

The delta terms are introduced since diffusion and reaction processes begin immediately after the initial formation of vapor. If any one of the individual times is much longer than the others, then the total burning time will be essentially that of this individual process. In a real combustor it should be possible to forecast the combustion efficiency providing that the limiting process can be estimated. For example, at ambient inlet temperatures Brzustowski [1] attempted to define the areas of control as indicated in Fig. 1 for single droplets in a

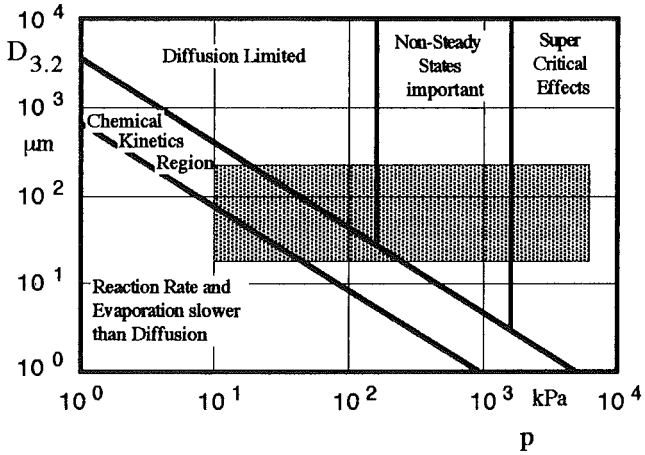

Fig. 1 Physical and chemical control of combustion processes (after Brzustowski [1]); shaded portion is typical gas turbine pressure and droplet range ($T_3 = 300$ K)

Contributed by the International Gas Turbine Institute and presented at the 37th International Gas Turbine and Aeroengine Congress and Exposition, Cologne, Germany, June 1–4, 1992. Manuscript received by the International Gas Turbine Institute February 6, 1992. Paper No. 92-GT-135. Associate Technical Editor: L. S. Langston.

Copyright © 1993 by ASME
Downloaded 02 Jun 2010 to 171.66.16.121. Redistribution subject to ASME license or copyright; see http://www.asme.org/terms/Terms_Use.cfm

quiescent atmosphere. The added shaded portion represents the range of typical gas turbine operating conditions.

The application of Fig. 1 to real combustors is somewhat doubtful. The assumptions of an isolated droplet in a quiescent atmosphere are obviously not applicable. However, if it is assumed that small droplets are rapidly entrained, the local surroundings would then appear to be quiescent to the droplet. With this assumption Fig. 1 might give some indication of control in practical combustors. The area of droplet evaporation control is remarkably small, even at this low air temperature. Any increase in the latter would reduce even more the area of evaporative control. It seems likely that diffusion plays the most significant role, since it must be a factor in the regions of nonsteady states and super critical effects. The implications are that a critical look should be cast at the accepted role of droplets in gas turbine combustors.

Much of the work on droplet evaporation has been done for single droplets, and a useful review of this type of work is given by Beér and Chigier [2]. Although the many cited formulae for droplet evaporation are superficially different, most of them can be considered as variants of a more general formula for steady-state evaporation:

$$\tau_e = \frac{d_0^2}{\beta} \tag{2}$$

where

$$\beta = \frac{8\frac{\lambda}{c_{p,g}}\ln(1+B)}{\rho_f} \tag{3}$$

and

$$B = \frac{f \times q_n + c_{p,g}(T_g - T_B)}{h_{fg} + c_l(T_B - T_f)} \tag{4}$$

Various workers have suggested somewhat similar equations to those above (e.g., Frössling [3]):

$$-\frac{dm}{d\tau} = \frac{4\pi r D M_f p_v}{RT} \times [1 + 0.276\ Sc^{1/3} Re^{1/2}] \tag{5}$$

The significance of droplet Reynolds number is doubtful. In the first place, the value of Reynolds number is too small for the local flow to appear turbulent to the droplet. Also, most authorities are of the opinion that small droplets very rapidly assuming the high velocity of the air stream in the combustor. In this case even enhancement of the heat and mass transfer by relative motion becomes small or disappears. Therefore, these effects will not be considered any further.

All of the formulae are based upon single droplet experiments and assume a steady state. Neither of these conditions are met in a real combustor. In particular, the value of β (burning constant in Eq.(3)) seems to be very sensitive to both the number of drops and their size. To some extent, this has been demonstrated by Beér and Chigier [2] using the results of various workers. Thus for normal heptane, single drop $\beta = 0.96$; two-drop array $\beta = 0.88$; monosize stream $\beta = 0.529$; uniform spray $\beta = 0.47$. This implies that the closer the droplets are to each other, the longer they take to burn. The following explanation is suggested in [2]. As the droplets become nearer to each other, the burning region becomes depleted of oxygen. This in turn increases the distance of the flame from the drop and reduces the temperature gradients between the drop and the flame, hence a decrease in β. It is uncertain whether this effect could possibly exist in the presence of the strong mixing patterns in a gas turbine combustor. Even though the surroundings might appear quiescent to a single droplet, this does not obviously apply to the whole spray. Similar results were observed for other fuels, but even these tests were not performed at conditions typical of those in a real combustor.

Nomenclature

A = const
a = const
a = thermal diffusivity $= \lambda/(c_p \cdot \rho)$, m^2/s
B = transfer number (fuel)
c_p = specific heat at constant pressure, J/(kg•K)
c_l = specific heat of liquid fuel, J/(kg•K)
d_o = initial droplet diameter, m
D = diffusion coefficient, m^2/s
d = droplet diameter, m
$D_{3,2}$ = Sauter Mean Diameter (SMD), m
$-dm/d\tau$ = mass rate of evaporation of a fuel drop, kg/s
FN = flow number of an atomizer, imp. gal/h $psid^{0.5}$
f = fuel/air ratio (by mass)
h_{fg} = latent heat of evaporation, J/kg
M = molar mass, kg/mol
Ma = Mach number
$\dot{m}_a$ = air mass flow, kg/s
$\dot{m}_f$ = fuel mass flow, kg/s
n = pressure exponent (pseudoreaction order, $n = 2y^2/\Phi$)
p = pressure, Pa
p_c = critical pressure, Pa
p_r = reduced pressure $= p/p_c$
p_3 = combustor inlet pressure, Pa
Pr = Prandtl number $= \nu/a$
q_n = calorific value of fuel (nett), J/kg
R = gas constant, J/(mol•K)
Re = Reynolds number
r = radius of droplet, m
S_L = laminar flame speed (Eq. (11)), m/s
S = flame speed (Eq. (11)), m/s
Sc = Schmidt number $= \nu/D$
SMD = Sauter Mean Diameter (droplet) $= D_{3,2}$, m
T = temperature, K
T_{avg} = average boiling point $= (T_{10} + T_{30} + T_{50} + T_{70} + T_{90})/5$, K
T_B = boiling temperature at any pressure, K
T_3 = combustor inlet temperature, K
T_{stoic} = stoichiometric flame temperature, K
V = volume, m^3
β = evaporation constant (Eq. (3)), m^2/s
η = combustion efficiency
η_c = combustion efficiency
$\eta_{c,e}$ = combustion efficiency due to evaporation
$\eta_{c,\theta}$ = combustion efficiency due to reaction loading
Θ = theta parameter (Eq. (8))
λ = thermal conductivity, W/(m•K)
ν = kinematic viscosity, m^2/s
ρ = density, kg/m^3
τ = time, s
τ_c = total combustion time, s
τ_d = diffusion time, s
τ_e = evaporative time, s
τ_r = reaction rate time, s
Φ = equivalence ratio $= f_{actual}/f_{stoic}$
Ω = fraction of total fuel in form of vapor

Subscripts

1 = at droplet surface
3 = combustor inlet
3.2 = Sauter mean
a = air
B = at boiling point
bz = burning zone
c = combustion
eff = effective
f = fuel
g = gas (or vapor)
l = liquid
v = vapor

Downloaded 02 Jun 2010 to 171.66.16.121. Redistribution subject to ASME license or copyright; see http://www.asme.org/terms/Terms_Use.cfm

Table 1 Combustion efficiency and spray evaporation at various engine speeds [12]

Engine Speed	$d_{90\%}$ *	Evaporation Time			Recorded Combustion Efficiency	% of droplets evaporated
		Heat Transfer Theory	Diffusion Theory	actually available		
%	μm	ms	ms	ms	%	
40	333	40	21	13	91,2	94,7
50	313	29	18	12	96,7	95,8
60	276	19	14	10	96,4	96,3
70	227	12	9	9	100	98,8
80	177	10	6	9	100	99.8
90	144	9	4	8	100	99,9
100	110	4	2	7	100	100

* The stated diameter represents the maximum diameter of the lower 90% of all droplets.

Nuruzzaman et al. [4] investigated monosized droplet stream combustion and, for kerosine, their results may be expressed, approximately (ambient inlet conditions), as

$$\tau_c = 2.5 \times 10^6 d^2 \tag{6}$$

Thus for droplets of 100 μm an burning time of 25 ms is indicated. Priem and Heidman [5] suggested that for a real combustor the so-called square law for droplet evaporation should be modified to the power 1.45. Therefore, there is some confusion as to which formula to apply to describe droplet evaporation, especially cloud evaporation.

Kadota and Hiroyasu [6] considered the combustion of single droplets under supercritical conditions. They concluded that the final temperature of the droplet was close to its critical temperature and independent of the pressure. The lifetime of the droplet correlated well with the reduced pressure. For the fuels tested and for $p_r \leq 0.3$, the droplets of the several fuels had a lifetime given by $\tau = kp_r^a$ (a from -0.17 to -0.21). Above $p_r = 0.3$ the power law no longer applied, and the droplet lifetime decreased abruptly with increasing pressure. Miyasaka and Law [7] also found that the d^2"law" did not apply to linear drop arrays. Other workers [8–11] suggest that the combustion length is proportional to the evaporation time, which is a function of the initial droplet diameter and any preheating of the fuel.

The interesting thing about much of the above work is that for a typical fuel (kerosine) the apparent value of evaporation/burning time is considerably larger than the mean time available in real gas turbine equipment. As an illustration, assume an idling condition with $T_3 = 300$ K, $p_3 = 0.1$ MPa. For a combustor operating at a reference Mach number of 0.03, the "cold" residence times are about 4 to 6 ms (depending upon the combustion zone considered) with corresponding "hot" residence times of the order of 1 to 4 ms. These times are short compared with those indicated from classical droplet studies and would imply that to be commensurate with observed high combustion efficiencies in gas turbine combustors the actual droplet evaporation times are much smaller than those indicated by the classical studies outlined above. Several explanations are possible:

1 The droplets are broken up into finer droplets with a much smaller evaporation time.

2 The droplets are entrained into the recirculation for a time sufficient for evaporation.

3 The rates of evaporation are faster than the individual droplet studies indicate, due either to the actual conditions (not replicated by the fundamental experiments) or to the cloud effects.

Some 35 years ago Clarke [12] considered the theoretical fuel-burning capacity of an aerogas turbine vortex and its effect upon combustion efficiency at various engine speeds. His results (Table 1) suggest that even very large droplets are very largely evaporated.

While Clarke's work shows a size effect on combustion efficiency, it also suggests that the size of droplets at which the effects become noticeable is normally larger than any likely to be experienced in a real combustor. There are one or two other pointers that suggest that droplet size may not be quite as important as is usually assumed:

1 The relatively easy substitution of a high calorific value gas for a liquid fuel in an industrial gas turbine. Normally the changeover is met by substituting a gas injector having a similar geometric placement of the fuel to that of the liquid spray.

2 The dispute between those combustion engineers who consider "vaporizers" to be more efficient than (say) air-blast atomizers. Many years ago, one of us (J.O.) was involved in a comparison of a vaporizer combustor (Mamba) with a liquid fuel-fired version of the same combustor. Efficiency-wise, at the same operating conditions, the two were very similar.

Some Other Published Observations of Spray Combustion

The work of Borgoyne and Cheon [13] involved the measurement of flame speeds of monodispersed tetralin sprays in air. The results indicated that for droplets less than 10 μm the flames behaved as if they were gaseous premixed ones. Above about 40 μm they concluded that the droplets burned individually in their own envelope, ignition proceeding upstream from one burning droplet to another. At intermediate sizes the behavior was transitional. As a result of this transformation, the weak limit of the mixtures was reduced and the flame speed decreased as the initial droplet size was increased. The burning time approximated to the d^2 law.

Onuma et al. [14, 15] found that their kerosine spray flame (axial jet, low turbulence) was very similar to that obtained by a diffusion propane flame in the same apparatus. The similarity was found with respect to the reacting gas components and to temperature distribution. A second series of tests was specifically aimed at the measurement of the NO distribution within the flame. In this latter experiment as well as the kerosine and the propane flames, a heavy oil flame was also examined. Despite the larger droplet size of the heavier oil, the shapes and measured profiles of NO were almost the same.

Khalil and Whitelaw's [16] experiments consisted of burning, in unconfined flow, four different spray configurations and comparing the results with a simulated gaseous flame. The measurements consisted of velocity, turbulence intensity, temperature, temperature fluctuations, and droplet concentration. The flames were found to be generally similar, but with significant changes in details. The flames of smaller droplets (45 μm) had a shorter length than those of the large droplets (100 μm) but a longer length than the simulated gas flame.

Lefebvre et al. [17–22] found that droplets had a considerable effect on most combustion processes. Their expressions for efficiency are derived from the general theory of droplet evaporation modified by the influence of reaction rate. Like most workers in the field their formulae are somewhat empirical and it is sometimes possible to obtain quite unrealistic values. Some typical formulae from Lefebvre et al. are given below:

Combustion Efficiency

$$\eta_c = \eta_{c,e} \times \eta_{c,\theta} \tag{7}$$

$$\eta_{c,\theta} = 1 - \exp\left[\frac{-0.022 p_3^{1.3} V_c \exp(T_c/400)}{f_c \dot{m}_a}\right] \tag{8}$$

$$\eta_{c,e} = 1 - \exp\left[\frac{-36 \times 10^6 p_3 V_c \beta_{eff}}{T_c d_0^2 f_c \dot{m}_a}\right] \tag{9}$$

Downloaded 02 Jun 2010 to 171.66.16.121. Redistribution subject to ASME license or copyright; see http://www.asme.org/terms/Terms_Use.cfm

Table 2 Summary of available fuels and test data

Item	Range	Units
Molar mass	0,078 - 0,191	kg/mol
Hydrogen content by mass	7,74 - 16,4	%
No. of C atoms	6 - 13,7	
No. of H atoms	6 - 26	
Saturation Value S_h	0,429 - 1,000	
c/h ratio (mass)	5,11 - 11,92	
H/C ratio atomic	2,67 - 1,00	
Density @ 288 K	679 - 1022	kg/m^3
API gravity	6,95 - 76,9	API°
Aniline point	-54,9 - 183,1	°F
Net calorific value	40,14 - 44,74	MJ/kg
Freezing point	146 - 280	K
Critical temperature	513 - 748	K
Critical pressure	1,80 - 4,90	MPa
ASTM distillation D-86		
IBP	317 - 478	K
FBP	355 - 598	K
T_{av}	339 - 525	K
Flash point	245 - 351	K
Smoke point	7,1 - >55	mm
Surface tension @ 298 K	17,4 - 35,7	dyne/cm
Kinematic viscosity @ 303 K	0,442 - 6,61	mm^2/s
Parachor	207 - 508	cgs units
Stoichiometric A/F (mass)	13,2 - 15,2	
T_{stoich} @ T_3 = 350 K	2332 - 2442	K

$$\beta_{\text{eff}} = \left[\frac{8\left(\frac{\lambda}{c_p}\right)_g \ln(1+B)(1+0.22\,\text{Re}_{d_0}^{0.5})}{\rho_f} \right] \tag{10}$$

Flame Speed

$$S = a_g \left[\frac{C_3(1-\Omega)\rho_f D_{3,2}^2}{8C_1\rho_g \ln(1+B)} + \frac{a_g^2}{S_L^2} \right] \tag{11}$$

For Eqs. (7)–(11), the nomenclature is that of Lefebvre. T_c is the combustion temperature, and C_3 and C_1 are constants. Other terms are as defined in the nomenclature.

From all of the above, it is obvious that the predominant opinion is that droplets influence the combustion phenomena observed in gas turbines and allied equipment. In a review paper, Peters [23] concurs with this. Faeth [24] conceded that in some practical systems spray combustion can be modeled as a gaseous diffusion system, but he warns that in many instances such simplifications are unwarranted. In a review such as this, it is not possible to cite all of the work that has been done with respect to droplet combustion, and the above must be regarded as only being typical examples of the enormous amount of data available. With such a welter of opinion taking the view that droplet size is all-important in influencing the combustion behavior in gas turbines, it is with some trepidation that the authors present the following observations based upon measurements and observations made at Laval University (Quebec) and the Australian Department of Defence Aeronautical Research Laboratory at Melbourne.

Present Experimental Data

The following data were (and are being) obtained during the course of a comprehensive program that is ongoing at the Laval University (Quebec) and the Aeronautical Research Laboratory (Melbourne) of the Australian Defence Department. The major variables appertaining to this program are:

1 Preparation and physical testing of over 100 fuels. The exact chemical composition is known for most of these fuels, although several commercial fuels have been included so as to obtain representative results. The range of variables examined is given in Table 2. All of the fuels have been tested at atmospheric pressure in one or other of the several combustors. Several fuels have been tested over a wide range of inlet conditions in one or more of the combustors outlined below.

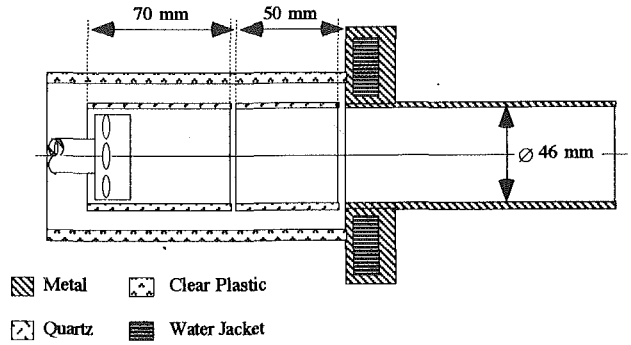

Fig. 2 Schematic of transparent combustor

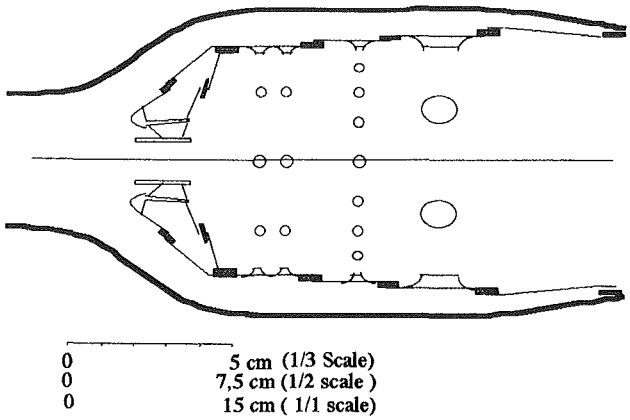

Fig. 3 Schematic of conventional combustors

2 To date three combustion chambers have been tested, a small transparent combustor (transparent or plexi, see Fig. 2), a small (95 mm diameter) conventional can-type combustor (1/3, Fig. 3) and a (142 mm diameter) geometrically similar combustor (1/2, Fig. 3). The appellations 1/2 and 1/3 represent the geometric scale relative to a so-called full-scale combustor (286 mm diameter) yet to be tested. The results from these latter three chambers will form the basis of the size scaling portion of the program.

3 For the scaled combustors the effects of operating conditions are determined by independently varying the following:

(*a*) inlet temperature (350 to 550 K)
(*b*) inlet pressure (100 to 900 kPa)
(*c*) reference casing Mach number (0.019–0.062)

At each of these separate conditions a range of operating air fuel ratios was examined (A/F = 50/1–100/1). The transparent combustor was operated solely at ambient atmospheric conditions.

4 Each of the three scaled combustors is tested using three different Simplex injectors of varying flow number (but the same injection angle). In addition, the 1/2-scale combustor has been tested with an air-assist atomizer. The transparent combustor used only an air-assist atomizer. With reference to droplet size the results from the above program are the ones most pertinent to the present considerations.

One of the major objectives of the combustion studies was to isolate which fuel characteristics were of the most importance in defining the various combustion phenomena. Many of the fuels used were synthesized using two or more pure compounds. Table 3 lists these compounds. In addition, JP-4, JP-10, and (transparent combustor only) RJ-6 fuels were also used.

Downloaded 02 Jun 2010 to 171.66.16.121. Redistribution subject to ASME license or copyright; see http://www.asme.org/terms/Terms_Use.cfm

Table 3 List of compounds used to synthesize fuels for testing all Laval combustors

Fuel No.	Name	Fuel No.	Name
22	tert-amyl-benzene	23	benzene
24	butyl-benzene	25	cyclo-hexane
26	cyclo-hexene	27	decalin
28	decane	30	dicyclo-pentadiene
31	dodecane	32	heptane
33	iso-hexanes (mixture)	34	methyl- cyclo-hexane
35	*iso*-octane	36	1-octene
37	iso-propyl-benzene	38	tetralin
39	toluene	40	o-xylene

A base fuel was synthesized from a mixture of paraffins such that the viscosity and boiling point characteristics were roughly the same as those of a typical JP-4. The composition of the base fuel was (by volume) hexanes 10 percent, *n*-heptane 20 percent, iso-octane 50 percent, *n*-decane 10 percent, *n*-dodecane 10 percent. All other fuels are addressed to the base fuel, and it was hoped to be able to differentiate between the physical and chemical effects of the fuels and relate these to the combustion phenomena. Most of the other fuel mixtures were made by blending other compounds with the base fuel. When using mixtures of the compounds listed below and the base fuel, it was decided that the purity of the substances was such that the resultant chemical composition could be calculated, without the need for chemical analysis. Properties directly dependent upon the chemical composition were similarly calculated for the mixtures (e.g., calorific value, Parachor); other properties (e.g., viscosities, surface tension, ASTM distillation) were measured.

Observed Droplet Behavior

Transparent Combustor. Full details of the various tests carried out using this combustor may be found in [25–30]. The combustor is illustrated in Fig. 2, and it was fitted with an air-assist atomizer (Parker-Hannifin) calibrated using a Malvern Spray Analyser. Based upon this calibration, for the test conditions cited below, the range of droplet size was 15–18 μm SMD. At all conditions the comparison between test rig measurement of the air/fuel ratio and gas analysis measurement was within ± 5 percent. For each of the fuel flows chosen, the following items were measured:

(*a*) Gas analysis: CO_2, CO, HC, O_2, NO_x, NO
(*b*) Exhaust carbon content
(*c*) Flame radiation at a single station
(*d*) Flame color and photograph
(*e*) Exhaust temperature distribution
(*f*) Fuel and air flows
(*g*) Inlet temperature and humidity

Eighty different fuels were tested in this combustor over a range of equivalence ratios. The inlet conditions were:

$T_3 = 324$ K, $p_3 = 0.1$ MPa, $\dot{m}_a = 26.4$ g/s (main),
$\dot{m}_a = 1.6$ g/s (injector), $\dot{m}_f = 0.2$ to 0.8 g/s, Ma = 0.019.

The reproducibility of the combustion efficiency for a single fuel (base fuel) is illustrated in Fig. 4. It is considered to be satisfactory. The two tests were separated by a time interval of several months and included several rebuilds of the test rig. An interesting feature is the form of combustion efficiency curve. The combustor is cylindrical in character with a reaction zone (primary zone) largely generated by a centrally located primary baffle plus secondary effects due to the penetration of the air (introduced annularly at the end of the zone). Observations of the transition from weak to rich mixtures (within the reaction zone) showed the following effects:

1 At weak conditions ($\Phi_{overall} \leq 0.1$) combustion was limited to a region within the boundaries of the shroud.

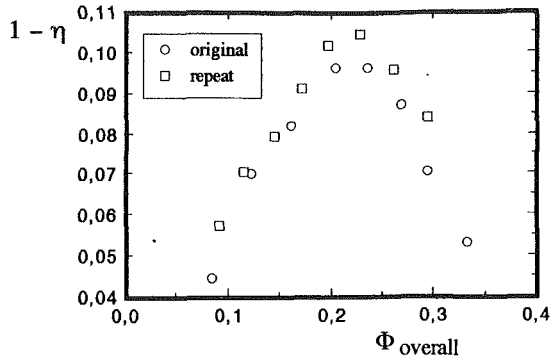

Fig. 4 Repeatability of combustion efficiency: transparent combustor

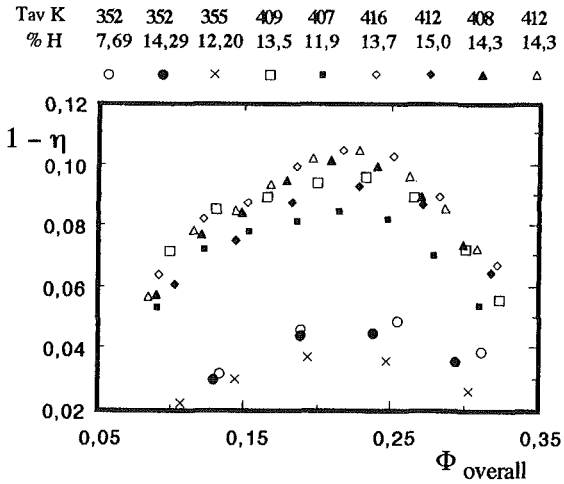

Fig. 5 Combustion efficiencies of "constant" boiling mixtures (plexi)

2 As the mixture richened, the shroud of the baffle became dull red and the flame began to burn downstream of the shroud ($\Phi_{overall} = 0.1$–0.2).
3 Further richening produced bright red heat at the shroud, and the flame appeared to occupy the whole of the primary zone and to penetrate into the secondary zone.

Based upon these observations, and ignoring any droplet effects, the combustion efficiency characteristics may be explained as:

4 At the weak overall conditions, the reaction zone is burning at $\Phi < 1$, and hence the flame is within an oxygen-rich region. Due to the intimate mixing of fine droplets and air, the reaction rate is sufficiently high to yield a high overall efficiency.
5 As the mixture richens ($\Phi_{overall} = 0.1$–0.2) the baffle reaction zone becomes overloaded and burns inefficiently. At this stage the fuel/temperature combination in the secondary zone is insufficient to burn this fuel and the efficiency decreases at the combustor outlet.
6 Further richening of the overall mixture pushes more fuel into the secondary zone, but at the same time the temperature is increased such that the fuel continues to burn downstream of the main reaction zone, thereby augmenting the overall efficiency.

The net result of all this is to yield a curve of efficiency such as that illustrated in Fig. 4. The hydrocarbons and carbon monoxide reflect this behavior in the form of their respective curves, as also the oxides of nitrogen and the flame radiation. All the fuels yielded the same form of curve, although the levels could differ. With such a small span of droplet size variation it would not be expected that any significant changes in combustion behavior could be attributed to size variation.

Downloaded 02 Jun 2010 to 171.66.16.121. Redistribution subject to ASME license or copyright; see http://www.asme.org/terms/Terms_Use.cfm

Table 4 Combustor operating conditions

Test Series	Inlet Conditions T3 K	p3 kPa	Reference Mach Number	Air/Fuel Mass Ratio	Atomizer Flow Number
A1	350	105	0,040		0,33
B1	302	154	0,033		
B2	314	220	0,048		
B3	318	268	0,062	50	0,33
B4	320	403	0,053		
B5	333	712	0,053	to	0,67
B6	338	896	0,054		
C1	320	403	0,053	100	and
C2	450	410	0,054		
C3	550	410	0,054		1,1
D1	550	410	0,054		
D2	550	700	0,055		
D3	550	906	0,055		

1/3 Combustor, Base Fuel, Tetralin and JP10, Wide range of Conditions

Table 5 Gas analysis equipment limits of accuracy for combustion efficiency measurement

Overall A/F	CO ppm	EI_{CO} g/kg fuel	EI_{HC} g/kg fuel	$(1-\eta)$ %	η %
40	100	4,1	0,9	0,18	99,82
60	100	6,1	1,3	0,28	99,72
75	100	7,6	1,7	0,34	99,66
100	100	10,1	2,2	0,46	99,54
200	100	20,1	4,4	0,92	99,08

Further, the smallness of the droplets, based upon the findings of Burgoyne et al. [13] and Faeth [24], indicates that it would be reasonable to expect the combustion to ape a gaseous diffusion flame. With this in mind a fuel property was sought that might be representative of diffusion processes. The simplest measured property seemed to be the boiling point of the fuel (T_{avg} for mixtures or real fuels). This property represents both fuel volatility and diffusion. The results are shown in Fig. 5. This shows that the most volatile fuels yield the higher combustion efficiencies. At the same time it suggests that the hydrogen content has little significance in determining the level of combustion efficiency. The strong dependence upon T_{AV} is very significant, especially since here there is an absence of droplet size effects. It will be seen that a similar dependence will be found for a conventional spray-fed system.

The experimental part of this program [31–33] was carried out in Australia using the 1/3 combustor (Fig. 3) and operating it over a wide range of conditions (Table 4) using the fuels shown. The unit employed any one of three different atomizers having flow numbers 0.33, 0.67, 1.10 imp. gal./(h$\sqrt{\text{psid}}$). Wall and exhaust temperatures were measured using chromel/alumel thermocouples. The gases analysed were CO_2, CO, HC, NO/NO_x.

Accuracy of Gas Analysis. The two measurements of greatest importance in determining the combustion efficiency are CO and HC. It was estimated that for accurate measurement it was required to have a minimum of 100 ppm CO and 2 ppm HC. Since the amount of CO is so much greater than the HC, the CO (100 ppm) was used to define the limiting combustion loss, below which accuracy would be doubtful. This of course, varies with the overall air/fuel ratio. For Table 5 a value of 100 ppm was assumed and the hydrocarbon content was based upon experimental ratios as described in [32, 34].

The values listed in Table 5 may be a little conservative, but they do give an appreciation of possible errors. Since most of the work was done within the range of A/F from 40/1 to 100/1, it is felt that values of combustion efficiency above 99.8 percent should be treated circumspectly, though not ignored. It also means that at any condition, regardless of other losses of accuracy, the likely error in repeatability or reproducibility will not be better than ±0.1 percent. This value is (as will be shown) less than other inaccuracies due to test rig measurements and rebuild effects, etc.

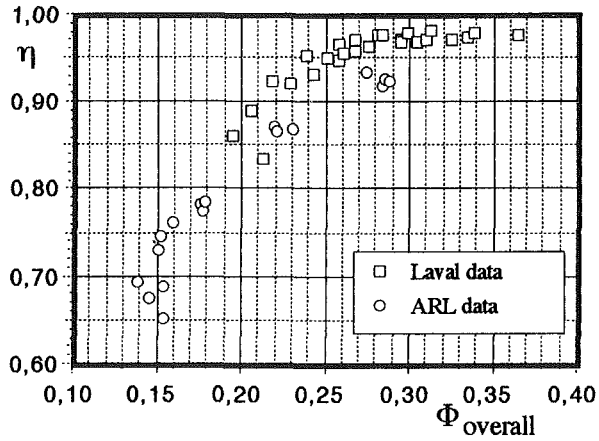

Fig. 6 Combustion efficiency

Test Repeatability and Reproducibility. No attempt will be made here to analyze the separate effects of these latter variables. Instead, the overall effects will be demonstrated by comparing the reproducibility of the test rigs and combustor as operated at Laval and at the ARL. Figure 6 plots both sets of data on the same curve, and although the conditions are not identical, there is a strong suggestion that the reproducibility at high efficiencies (>96 percent) is about ±0.5 percent, between 90 and 96 percent it is about ±1.5 percent, and below this value (to 83 percent), about ±3 percent. Expressed in terms of combustion inefficiency, the scatter is much more constant at about ±15 percent of the actual inefficiency.

The significance of the above findings is that it suggests the possible accuracy required for *any model* of combustion efficiency. Also, the consistency of the repeatability of the combustion loss suggests that model predictions should be in terms of inefficiency. On this basis, based upon the above, a model accuracy of ±20 percent of the combustion loss *at any value of inefficiency* would be commensurate with the experimental accuracy of determination, at least down to a loss of 0.2 percent.

The Effects of Droplet Size on Combustion Efficiency

In this section a number of results are presented in diagram form. Because of publication restrictions only samples of the data are used. If all the data were to be represented here, at least 50 diagrams would be required for this section alone.

Test Using Base Fuel, No. 41 (1/3 Combustor). If droplet size has a significant role in determining the level of the combustion efficiency, one would anticipate a measurable difference if the same combustor were run at the same conditions but with differently sized atomizers.

Figures 7–9 illustrate the performance of the 1/3 combustor using three atomizers of different size. For many points, droplet sizes are indicated in the figures. The data are typical for the range of operating conditions investigated. Arbitrarily three ranges of combustion efficiency have been identified: (1) high efficiencies (>98 percent), (2) medium efficiencies (98–90 percent), (3) low efficiencies (<90 percent).

It is obvious that at none of the conditions examined is there

Downloaded 02 Jun 2010 to 171.66.16.121. Redistribution subject to ASME license or copyright; see http://www.asme.org/terms/Terms_Use.cfm

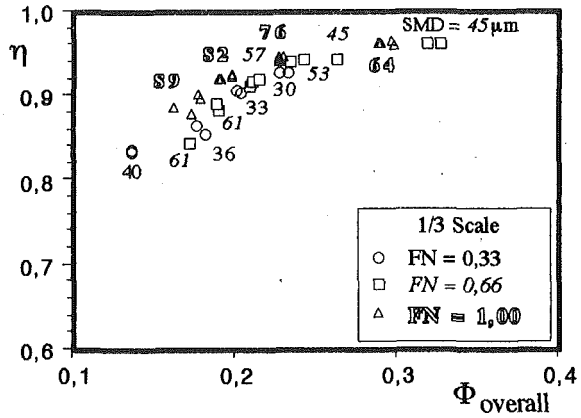

Fig. 7 Droplet size effects at low combustion efficiencies, fuel 41, $T_3 = 325$ K, $p_3 = 400$ kPa, Ma = 0.054; numbers indicate droplet size in μm

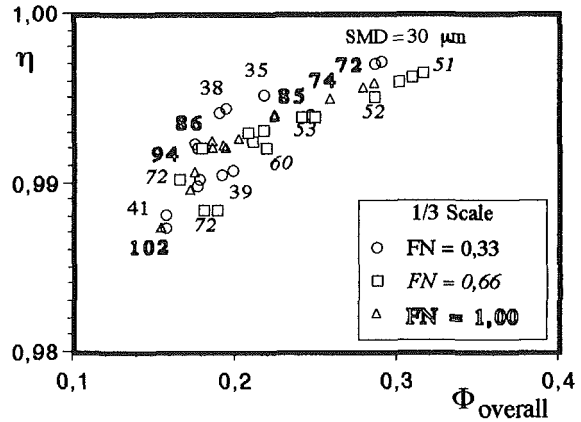

Fig. 8 Droplet size effects at high combustion efficiencies; fuel 41, $T_3 = 550$ K, $p_3 = 400$ kPa, Ma = 0.055; numbers indicate droplet size in μm

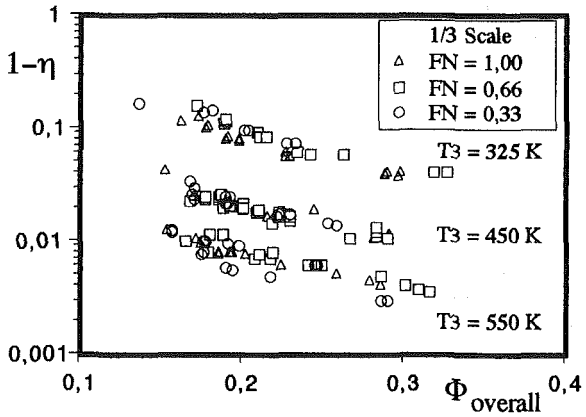

Fig. 9 Effects of droplet size and air inlet temperature; fuel 41, $p_3 = 400$ kPa, Ma = 0.055; numbers indicate droplet size in μm

a significant effect of droplet size upon combustion efficiency. If there is any trend at all to be observed, it is that at some conditions the larger droplets show a marginal increase in combustion efficiency, which is contrary to what might be expected based upon traditional thinking. An explanation of this trend might be that the larger droplets, in these particular experiments, give a better penetration and mixing.

The failure to discover any significant effects of droplet size also suggests that the developed air flow pattern is predominant in defining the mixing (diffusion) process. About the only contradictory note was a few points where the SMD was greater than 150 μm, where there might be indications contrary to

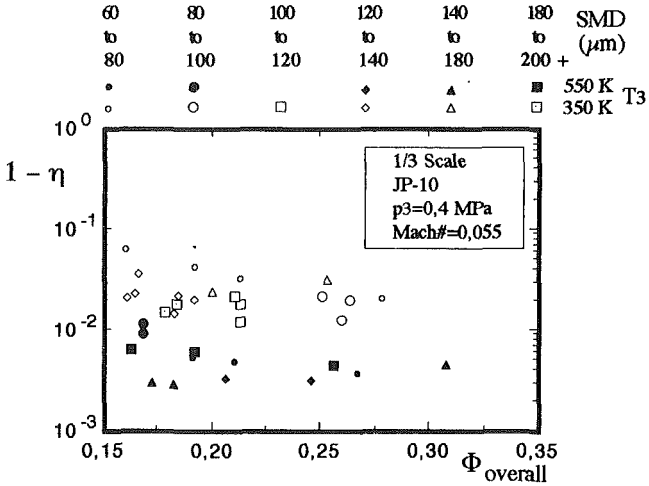

Fig. 10 Droplet effects upon efficiency loss, fuel JP-10

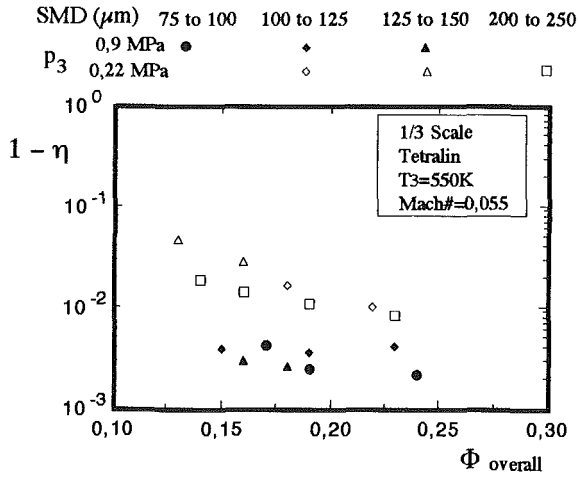

Fig. 11 Droplet effects upon efficiency loss, fuel tetralin

those above. The number of points was too small to enable any conclusions to be drawn.

The droplet sizes were calculated using a well-developed formula for Simplex Atomizers, following calibration on a Malvern instrument. Even should the droplet sizes be not accurately defined, the changes in the atomizer flow numbers are such as to ensure a considerable difference in the droplet size for the same fuel flow and operating condition.

Tests Using JP-10 Fuel No. 42 (1/3 Combustor). Using the same test rig, a fair amount of data has been obtained using JP-10 as the fuel [35]. Typical results from this work are illustrated in Fig. 10. Again, droplet effects are negligible.

Tests Using Tetralin, Fuel No. 38 (1/3 Combustor). Some of the results from this work are illustrated in Fig. 11 and once again, droplet effects are negligible.

Tests Using the 1/2 Combustor. In an attempt to achieve confirmatory evidence, results from a larger version of the combustor (but same geometry-hereafter referred to as the 1/2 scale combustor) were examined. This latter combustor utilized two atomizers, the one a Simplex, the other an Air-Assist. Nine different fuels were tested at atmospheric conditions. Typical results are given in Fig. 12. Overall, the results suggest that the Air-Assist gives marginally better efficiencies than the Simplex, but the differences, in most instances, are within the experimental accuracy defined above.

Downloaded 02 Jun 2010 to 171.66.16.121. Redistribution subject to ASME license or copyright; see http://www.asme.org/terms/Terms_Use.cfm

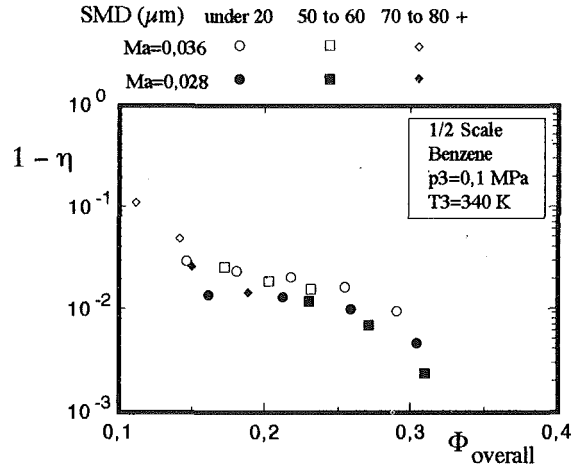

Fig. 12 Effects of droplet size upon combustion efficiency; simplex and air-assist atomizers

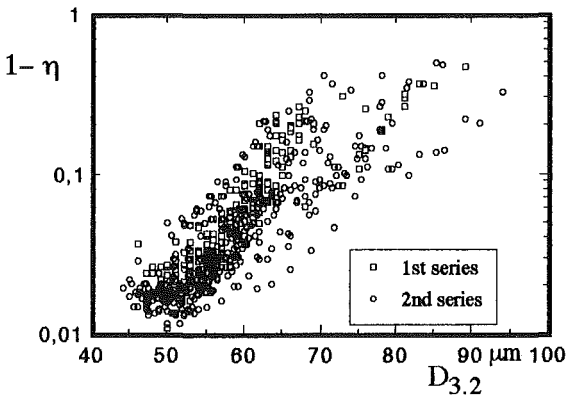

Fig. 13 Droplet size and combustion efficiency—a wide range of fuels

Summarizing the above results, it would appear that for the two combustors used, over a wide range of operation conditions, for any single fuel, and for droplets within the range of about 10 to 200 μm, there is little or no influence of droplet size upon combustion efficiency. The question now remains as to whether these results are peculiar to this type of combustor, or similar phenomena exist for other combustors. Unfortunately data are very sparse, since, in most of the published literature, a change of droplet size is nearly always accompanied by a change in some other variable. The assessment of combustion efficiency has always been considered a very important step in performance description. It was, therefore, decided to attempt a correlation parameter having no dependence upon droplet size. If this could be done using the present data, then it should also be applicable to data from other published sources. If this latter were verified then it would do much to substantiate the absence of droplet effects.

Combustion Efficiency Correlations

For a long time the "theta" parameter [17] was used to describe combustion efficiency performance, and it proved to be a very useful development tool. Basically it was a form of simple reaction loading parameter. Its deficiencies were:

(*a*) It had to be established experimentally.
(*b*) Each air/fuel ratio gave a different curve.
(*c*) Each combustor gave a unique curve.
(*d*) Its accuracy at the high combustion efficiency region is not sufficient to be helpful with pollution measurements or requirements.

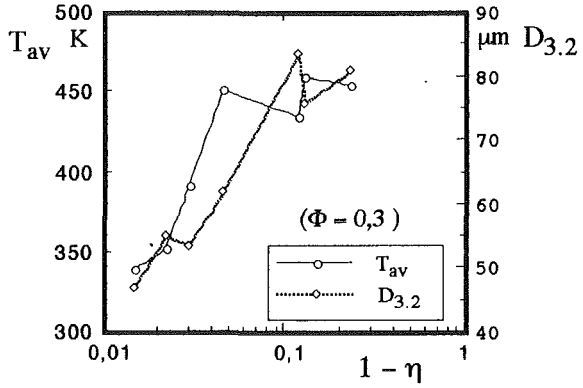

Fig. 14 Effects of droplet size and volatility upon combustion efficiency (1/3 scale combustor)

(*e*) There is no indication of the type of pollutant producing the combustion loss.
(*f*) It does not take droplet effects into account.

1/3 Combustor—Wide Range of Fuels-Atmospheric Conditions. As indicated earlier, the 1/3 combustor [36] was tested in the Laval Laboratories using a wide range of fuels, but only at ambient inlet conditions and with only a single pressure atomizer ($FN = 0.33$: British Units—imp. gal/(h$\sqrt{\text{psid}}$)). In total over 600 experimental points were obtained and their results analysed in various ways. Figure 13 illustrates a simple plot of all the data in the form of efficiency loss 1-η versus SMD. There would appear to be a distinct relationship, but is must be remembered that in this case, for any individual fuel, the droplet size was reduced by increasing the fuel flow. Thus, the performance is not influenced by droplet size alone, but also by the effects of increased fuel loading and equivalence ratio (reaction temperature), plus any other "unknown" effects.

Alternative effects may be illustrated by cross plotting data so as to obtain the behavior at a single equivalence ratio. Such a curve is illustrated for a representative range of fuels in Fig. 14. The overall equivalence ratio (selected at $\Phi = 0.3$) ensures that reaction temperatures are fairly similar, and since the fuel densities are not very different, then the changes in fuel loading will be small. Thus it might well be thought that the droplet relationship (right-hand scale in Fig. 14) would describe truly a droplet effect. However, a very similar correlation exists in terms of the average boiling point of the fuels (left-hand scale in Fig. 14). Thus it becomes important to identify which of the two fuel characteristics (if either) is the more satisfactory. Data for other equivalence ratios showed very similar behavior.

Similar effects of boiling characteristics of the fuels have been noted elsewhere [37–39] by Gleason et al. on the J-79 and F-101 engines. The work recorded here on the transparent combustor (droplet size near uniform) suggests that T_{avg} has a considerable effect upon the combustion efficiency of a wide range of fuels. The work done in Australia suggests that for a single fuel there is little or no effect of droplet size on combustion efficiency (this has been shown for three fuels). In view of these facts, it would seem logical to give more credence to volatility effects than to droplet size, at least for small droplets in the range obtained in practical combustors, say below 150 μm. In an attempt to find the "best" fuel property to describe the combustion efficiency, some 20 other properties were substituted for the boiling point, but the latter was always found to yield the least scatter. Eventually, a combination of properties might have to be found.

A full discussion of what is summarized below has been given elsewhere [32, 33]. In an attempt to substantiate the present findings a correlation parameter was developed using

Downloaded 02 Jun 2010 to 171.66.16.121. Redistribution subject to ASME license or copyright; see http://www.asme.org/terms/Terms_Use.cfm

Table 6

Combustor	Fuels Examined	p_3 MPa	T_3 K	Expt. points	Std.Dev % loss	A	B
1/3 ghost	80	0,1 to 0,9	300 to 550	987	42,6	0,885	6,08
F 101	13	0,4 to 1,3	460 to 850	105	63,0	0,674	5,81
J79-17A	13	0,25 to 1,4	410 to 790	126	90,3	0,874	6,09
J79-17C	13	0,25 to 1,4	420 to 800	112	73,0	0,932	6,93
T 56-A-14	1	0,1 to 1,0	440 to 600	127	56,0	0,745	4,98
PT6A-65	10	0,2 to 1,1	400 to 640	182	54,9	0,706	5,90

the data from the Australian ARL and the Laval University sources. This took the general form

$$\lg\lg\frac{1}{\eta}=A\times\left[0.911\ \lg\frac{\dot{m}_{f,\ 300K}}{V_{bz}p_3^n}+4.01n+\frac{558}{T_3}-1.42\Phi_{bz}+0.00934\ T_{avg}+2.35\lg p_C\right]-B \quad (12)$$

The results pertaining to this form of correlation were quite promising, so it was decided to apply the form of correlation to the performance of other combustors in the published literature. Data from five sources were used; data for the J79-17A, J79-17C and the F101 engines from Gleason et al. [38–40], for the T-56-A-14 from Reider et al. [41] and for the PT6A-65 engine from Gratton et al. [42]. Table 6 summarizes the findings.

The standard deviation for Table 6 appears to be high, but it must be remembered that it refers to the combustion loss. Thus, in the regions of greatest importance, at high efficiencies, the table infers that one can predict a loss of 0.2 percent with a general accuracy of about ±0.1 percent. In terms of the overall efficiency this becomes 99.8±0.1, a very acceptable limit compared with most other predictions.

General Discussion

It is held that droplet size has a pronounced influence on the value of combustion efficiency, especially in those regions where the combustion efficiency is only moderate or poor. There are theoretical grounds for this assumption based upon the well known d_2 law and measured times of droplet evaporation/combustion. This law has required modification (power varying between 1 and 2) for cloud burning of droplets, but there seem to be no publications pertinent to real conditions within gas turbines.

At conditions where the droplets are very small (less than 20 μm) it has been shown experimentally that the droplet combustion apes that of a gas flame. At these conditions the air flows were quite modest.

In a real gas turbine, correlations have been used that show, apparently, that the droplets have a significant effect upon the level of combustion efficiency. In particular, the small size of droplets has been claimed as being one of the major features why air-blast and air-assist fuel injectors improve the performance of combustors, which, previously, used pressure-jet atomizers. However, based upon the published literature available to the authors almost all, if not all of the data show that in addition to changing droplet size some other parameter has also been changed (e.g., equivalence ratio, fuel loading or air loading), besides the obvious very intimate mixing of the droplets with the air used for atomization. Under such circumstances it becomes very difficult to isolate the droplet effects.

The introduction of alternative fuels, at first glance, seems to substantiate the influence of droplet size, but much of the change in combustion efficiency may be equally well correlated against a boiling point function of the fuels.

During the course of the program on alternative fuels and scaling (described above) a large quantity of test data were obtained for which the combustor was operated at conditions that were identical except for the change of atomizer. The combustor was operated with each of three atomizers, the sole difference between the atomizers being a change by a factor of three in flow number. These changes were such that a factor of two (or more) was obtained in the droplet sizes. The differences in flow number were such that, if droplet size had any significant effect upon the combustion efficiency (at a stable operating condition) it should have been obvious. No effect was discovered, or if there was any trend at all, it was that the larger droplets gave a marginally higher combustion efficiency, exactly contrary to what would be anticipated. This was possibly due to a less rapid entrainment of these larger droplets and, therefore, some increase in heat and mass transfer by relative movement. This was found to be true for each of three different fuels tested over a wide range of conditions.

Data were also available for a large number of fuels (about 80) tested in two different types of combustor. Both units had small dimensions (flame tubes 2 in. and 3 in.). One was conventional and had a Simplex injection system; the other was a baffle-type combustor and operated with a very efficient air-assist injector in which (over all of this latter test series; 372 points) the SMD of the droplets varied only from 15 to 18 μm. This is considered to be of negligible significance. Despite this, there were considerable differences in combustion efficiency between the different fuels and these were shown to be related to the boiling points of the fuels. Fuels having the same boiling point exhibited the same efficiency regardless of hydrogen content, or other properties.

In an attempt to assess the significance of all of the above observations, a series of correlations have been obtained between the combustion efficiency and the operating conditions of individual combustors. The correlation takes the general form

$$\lg\lg\frac{1}{\eta}=A\times\left[0.911\lg\frac{\dot{m}_{f,\,300K}}{V_{bz}p_3^n}+4.01n+\frac{558}{T_3}-1.42\Phi_{bz}+0.00934\ T_{avg}+2.35\lg p_c\right]-B$$

The form of this equation has also been shown to be adequate for the published data for three other combustors.

Obviously this investigation has limitations insofar as:

(*a*) The range of droplet sizes investigated were from 14 to 150+ μm, with a few points extending to 200+ μm.

(*b*) Only eight combustors have been examined to date, but they are significantly different in the type of design, the type of fuel injection system, and, particularly, in size. They are:

- (*i*) Small plexi (2.0 in. diameter) combustor; air-assist; shrouded baffle.
- (*ii*) 1/3 (3.0 in. diameter) combustor; Simplex injector; conventional pipe chamber.
- (*iii*) 1/2 (4.5 in. diameter) combustor; Simplex and air-assist injectors; conventional pipe chamber.
- (*iv*) J 79-17 A combustor (5.6 in. diameter); dual orifice injector; cannular.
- (*v*) J 79-17 C combustor (5.6 in. diameter); air blast injector; cannular.
- (*vi*) F101 combustor (dome height 3.4 in.); fuel atomi-

Downloaded 02 Jun 2010 to 171.66.16.121. Redistribution subject to ASME license or copyright; see http://www.asme.org/terms/Terms_Use.cfm

zation by two swirlers; counterrotating, with low-pressure fuel injection.

(*vii*) T56-A-14 combustor, can-annular combustor using dual-orifice injectors.

(*viii*) PT6A-65 combustor, small reverse annular, 14 single orifice pressure atomizers.

(*c*) Range of inlet temperatures from 320 K to 851 K.

(*d*) Range of inlet pressures from 0.1 to 1.4 MPa.

Taking cognizance of the above limitations, it is inferred that droplet size plays little, if any, role in determining the combustion efficiency.

The work contained in this report is specific to steady-state operating conditions. No claims are made for the effects of droplet size on any other aspect of combustion. It is the authors' opinion that the effect of droplet size on ignition and relight might be substantial. However, other combustion features, such as wall temperatures and weak extinctions, also suggest that little or no drop size effects will be remarked.

One other aspect that tends to support the idea that drop size is not especially important in defining the combustion efficiency is the relative ease by which one can transform a liquid-fired combustor into a gaseous one, specifically if the fuel is a gas such as propane or butane. Even methane can generally be used with only minor changes to the injection system, and the problems with low calorific gases are much more associated with their volume flow than with their actual combustion behavior.

This leads to the following as a scenario within the combustor at steady-state condition. The flame is an agglomeration of burning fuel droplets and vapor so intimately mixed that individual flamelets behave as though they are a single turbulent, confined diffusion flame. The droplets, being relatively small, are thought to assume the same velocity as the air very quickly after injection. The situation is further reinforced by the presence of a strong recirculatory air flow, which predominates in "shaping" the flame. This pattern is maintained at any steady-state operating conditions and helps to ensure only gradual changes in the combustion behavior. At such conditions the influence of fuels of differing composition is limited to those properties that effect the diffusional processes rather than the evaporative ones. Thus, the transfer number may be more representative than the overall evaporation equation, which would include droplet diameter effects. At the present stage the boiling point of the fuels has been inserted into the correlation as being the simplest way of representing such diffusional considerations. It is hoped that this approach may become more refined as more results become available. The necessity of including a term involving critical pressure in the final form of efficiency correlation again supports the idea of a diffusional process due to the effect of the critical pressure on the boiling point of the fuel and its transfer number.

Finally, it is important to stress that the authors do not imply that droplet size is never of consequence. Especially at unsteady conditions, such as ignition or relight, it seems highly likely that droplet size is of great importance due to the low temperatures, which make for long evaporation times. Even at high temperatures, if there are very large droplets (e.g., larger diameters than those investigated here) then they could begin to play a significant part in the combustion process. The present work does not define these boundaries.

References

1 Brzustowski, T. A., "Chemical and Physical Limits on Vapor-Phase Diffusion Flames of Droplets," *Can. J. Chem. Engrg.*, Vol. 43, 1965, pp. 30–35.

2 Beér, J. M., and Chigier, N. A., *Combustion Aerodynamics*, Chap. 6, Fuel and Energy Science Monographs, J. M. Beér, ed., Applied Science, London, 1972.

3 Frössling, N., "Gerlands Beiträge zur Geophysik," Vol. 52, 1938, p. 170; AERE, Harwell, translation, Aug. 1963.

4 Nuruzzaman, A. S. M., Hedley, A. B., and Beér, J. M., "Combustion of Monosized Droplet Streams in Stationary Self-Supporting Flames," *Thirteenth Symposium (International) on Combustion*, The Combustion Institute, Pittsburgh, 1971, p. 787.

5 Priem, R. J., and Heidman, X. X., NASA Tech. Report, R-67, 1960.

6 Kadota, T., and Hiroyasu, H., "Combustion of a Fuel Droplet in Supercritical Gaseous Environments," *Eighteenth Symposium (International) on Combustion*, The Combustion Institute, Pittsburgh, 1981, p. 275.

7 Miyasaka, K., and Law, C. K., "Combustion of Strongly Interacting Linear Droplet Arrays," *Eighteenth Symposium (International) on Combustion*, The Combustion Institute, Pittsburgh, 1981, p. 283.

8 Spalding, D. B., *Aeronaut*, Vol. 10, 1959, p. 1.

9 Adler, J., ARC Tech. Report, No. 20, 1959, p. 189.

10 Williams, F. A., Penner, S. S., Gill, G. and Eckel, E. F., *Combustion and Flame*, Vol. 3, 1959, p. 355.

11 Il'Yashenko, S. M., *Jour. AIAA*, Vol. 1, 1963, p. 267.

12 Clarke, J. S., "The Relation of Specific Heat Release to Pressure Drop in Aero-gas-turbine Combustion Chambers," presented at the Joint Conference on Combustion, Section 5, Gas Turbines, IMechE-ASME, Boston, June 15–17, 1955, and London, Oct. 25–27, 1955.

13 Burgoyne, J. H., and Cohen, L., "The Effect of Droplet Size on Flame Propagation in Liquid Aerosols," *Proc. Roy. Soc. London*, Vol. A 225, 1954, p. 375.

14 Onuma, Y., and Ogasawara, M., "Studies of the Structure of a Spray Combustion Flame," *Fifteenth Symposium (International) on Combustion*, The Combustion Institute, Pittsburgh, 1974, p. 453.

15 Onuma, Y., Ogasawara, M., and Inoue, T., "Further Experiments on the Structure of a Spray Combustion Flame," *Sixteenth Symposium (International) on Combustion*, The Combustion Institute, Pittsburgh, 1976, p. 561.

16 Khalil, E. E., and Whitelaw, J. H., "Aerodynamic and Thermodynamic Characteristics of Kerosene—Spray Flames," *Sixteenth Symposium (International) on Combustion*, The Combustion Institute, Pittsburgh, 1976, p. 569.

17 Lefebvre, A. H., *Gas Turbine Combustion*, Chaps. 5–11, McGraw-Hill Series in Energy, Combustion and Environment, N. Chigier, consulting ed., Hemisphere Pub. Co., 1983.

18 Ballal, D. R., and Lefebvre, A. H., "Flame Propagation in Heterogeneous Mixtures of Fuel Droplets, Fuel Vapor and Air," *Eighteenth Symposium International on Combustion*, The Combustion Institute, Pittsburgh, 1981, p. 321.

19 Lefebvre, A. H., "Fuel Effects on Gas Turbine Combustion-Liner Temperature, Pattern Factor, and Pollutant Emissions," *AIAA J. of Aircraft*, Vol. 21, No. 11, Nov. 1984, p. 887.

20 Lefebvre, A. H., "Fuel Effects on Gas Turbine Combustion—Ignition, Stability, and Combustion Efficiency," ASME JOURNAL OF ENGINEERING FOR GAS TURBINES AND POWER, Vol. 107, pp. 24–37.

21 Lefebvre, A. H., "Influence of Fuel Properties on Gas Turbine Combustor Performance," AFWAL-TR-84-2104, 1985.

22 Lefebvre, A. H., "Fuel Effects on Gas Turbine Combustion," AFWAL-TR-81-2081, 1983.

23 Peters, J. E., "Current Gas Turbine Combustion and Fuels Research and Development," *J. of Propulsion*, Vol. 4, No. 3, May–June 1988, p. 193.

24 Faeth, G. M., *Progress in Energy and Combustion Science*, Vol. 3, Pergamon Press, Oxford, New York, 1977.

25 Kretschmer, D., and Odgers, J., "The Behaviour of Synthetic Fuels in a Small Transparent Combustor," Paper 41, AGARD Conference Proceedings No. 422, Combustion and Fuels in Gas Turbine Engines, PEP 70th Symposium, Crete, Oct. 19–23, 1987.

26 Kretschmer, D., and Odgers, J., "On the Weak Extinction of Gas Turbine Combustors," presented at the 9th International Symposium on Air Breathing Engines, Athens, Greece, Sept. 4–9, 1989.

27 Kretschmer, D., and Odgers, J., "Alternative Fuels for Gas Turbines, A Review of Work Done for the Canadian DND at the Laval University Combustion Laboratories," *Proc. 23rd Automotive Technology Development Contractors' Coordination Meeting (ATD/CCM)*, Dearborn, MI, Oct. 21–24, 1985; SAE P-165, pp. 377–384.

28 Kretschmer, D., Odgers, J., and Daigle, G., "A Small Transparent Combustor for Alternative Fuel Characterisation," AIAA Paper No. 86-0368, 1986.

29 Kretschmer, D., and Odgers, J., "The Characterisation of Combustion by Fuel Composition. Measurements in a Small Transparent Combustor," Report No. jo 159, Laval University, Combustion Laboratories, 1986.

30 Wang, G., Kretschmer, D., and Odgers, J., "On the Combustion Efficiency of a Small Unconventional Combustor for Research Into Alternative Fuels," Paper No. 91-Yokohama-IGTC-47, 1991.

31 Odgers, J., Kretschmer, D., Pearce, G., and Repacholi, N., "Alternative Fuels, Atomizer Scaling, and Combustor Scaling at Laval University, Québec and the Aeronautical Research Laboratory, Melbourne—A Review of Work to-date and Projections for the Future," Report No. jo 189, Laval University, Combustion Laboratories, 1990.

32 Odgers, J., Kretchmer, D., and Pearce, G., "The Combustion of Droplets Within Gas Turbine Combustors, Some Recent Observations on Combustion Efficiency," Report No. jo 194 Laval University, Combustion Laboratories, 1991.

33 Kretschmer, D., Wang, G., Odgers, J., and Pearce, G., "On the Performance of a Small Conventional Combustor Burning a Variety of Fuels," presented at the Tenth International Symposium on Air Breathing Engines, Nottingham, United Kingdom, Sept. 1–6, 1991.

34 Odgers, J., "Air Pollution by Gas Turbines—Is Control Possible?" *Canadian Aeronautics and Space Journal*, Oct. 1970, pp. 339–344.

Downloaded 02 Jun 2010 to 171.66.16.121. Redistribution subject to ASME license or copyright; see http://www.asme.org/terms/Terms_Use.cfm

35 Kretschmer, D., "Final Report on the Testing of a 1/3 Scale Combustor on JP-10; Tests Performed in Australia," Report No. jo191, Laval University, Combustion Laboratories, 1990.

36 Odgers, J., and Kretschmer, D., "Final Report on the Atmospheric Testing of the 1/3 Scale Combustor—Part 1—Combustion Efficiency and Pollutants, Report No. jo181, Laval University, Combustion Laboratories, 1988.

37 Gleason, C. C., and Martone, J. A., "Fuel Character Effects on J 79 and F101 Engine Combustion Emissions," ASME Paper No. 80-GT-70, 1980.

38 Gleason, C. C., Oller, T. L., Shayerson, M. W., and Bahr, D. W., "Evaluation of Fuel Character Effects on J79 Engine Combustion System," AFAPL-TR-79-2015, June 1979.

39 Gleason, C. C., Oller, T. L., Shayerson, M. W., and Bahr, D. W., "Evaluation of Fuel Character Effects on F101 Engine Combustion System," AFAPL-TR-79-2018, June 1979.

40 Gleason, C. C., Oller, T. L., Shayerson, M. W., and Kenworthy, M. J., "Evaluation of Fuel Character Effects on J79 Smokeless Combustor," AFAPL-TR-80-2092, June 1980.

41 Reider, S. B., Vogel, R. E., and Weaver, W. E., "Effect of Fuel Composition on Navy T56 Aircraft Engine Hot Section Components," NAPC-PE-88C, Nov. 1983.

42 Gratton, M., Critchley, I., and Sampath, P., "Alternate Fuels Combustion Research," AFWAL-TR-84-2042, July 1984.

Downloaded 02 Jun 2010 to 171.66.16.121. Redistribution subject to ASME license or copyright; see http://www.asme.org/terms/Terms_Use.cfm

Second-Generation Low-Emission Combustors for ABB Gas Turbines: Field Measurements With GT11N-EV

M. Aigner

G. Müller

ABB Power Generation Ltd.,
Ch-5400 Baden, Switzerland

In February 1991, a type GT11N gas turbine (Midland, USA) was retrofitted with ABB's new EV-Silo-Combustor. Tests were then carried out to examine the operation concept, to demonstrate the technical reliability, and to confirm the low emission performance of this new technology. This paper will describe: the combustor design—one single silo combustor mounted on the turbine and equipped with 37 Ev burners; and the results of the extensive field measurements—the operation concept (lean premix combustion without any pilot diffusion flames, 7 burner groups) is simple and reliable. The emission targets—$NO_x < 25$ ppmv (15 percent O_2, natural gas), $CO < 8$ ppmv, $UHC < 5$ ppmv—were reached. NO_x values are even lower than 15 ppmv at base load. The NO_x predictions for the GT11N-EV, based on the results of high-pressure tests in Cologne (ASME Paper No. 90-GT-308), compared very well with the results of field measurements.

Introduction

Numerous programs to develop low-emission gas turbine combustion chambers have led to the conclusion that premix burners and combustors exhibit the most potential with respect to primary emission control. Based on this fundamental doctrine and on the experience of ABB's first-generation DRY-NOX-burner (refer to Koch et al., 1985) a development program was started with the goal of improving the performance of ABB's Silo combustors by replacing the present burner, including the premixing tube. This development program was carried out in five phases (refer to Aigner et al., 1990):

Phase 1: Examination of the basic phenomena led to the invention of the double cone burner (EV burner).

Phase 2: Atmospheric tests in combustion laboratories were used to define the optimal burner geometry (Sattelmayer et al., 1992).

Phase 3: The results of high-pressure tests of a single burner showed the influence of pressure on the burner characteristics and the emissions (Aigner et al., 1990).

Phase 4: Tests in a model combustor with 37 burners led to the definition of the optimal burner swirl directions in a silo combustor.

Phase 5: Installation and commissioning of an EV Silo combustor on a gas turbine. The results of these studies are discussed in this paper.

ABB found in the Midland Cogeneration Venture facility an ideal partner for the engine tests of phase 5. During spring 1991 one of the existing Midland type GT11N gas turbines was retrofitted with a new silo combustor comprising of 37 EV burners (see Fig. 1). The following commissioning and testing period was used to gain experience on different operation concepts, to optimize the emissions, and to study the global operation behavior. On the basis of this knowledge an optimal operation concept regarding emissions and reliability was chosen and installed.

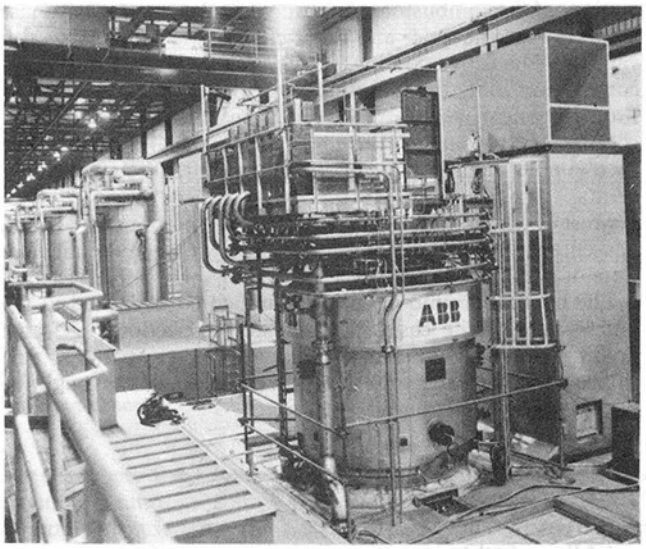

Fig. 1 View of the GT11N-EV combustor in Midland

Contributed by the International Gas Turbine Institute and presented at the 37th International Gas Turbine and Aeroengine Congress and Exposition, Cologne, Germany, June 1-4, 1992. Manuscript received by the International Gas Turbine Institute February 21, 1992. Paper No. 92-GT-322. Associate Technical Editor: L. S. Langston.

Copyright © 1993 by ASME
Downloaded 02 Jun 2010 to 171.66.16.121. Redistribution subject to ASME license or copyright; see http://www.asme.org/terms/Terms_Use.cfm

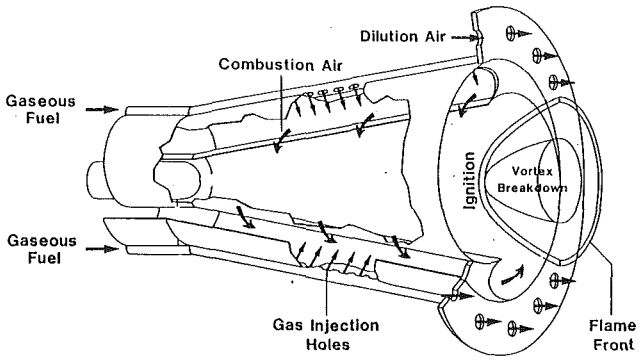

Fig. 2 Operating principle of the EV burner

GT11N EV Retrofit: The EV Burner

The EV burner consists of two halves of a hollow cone, which are shifted to form two air inlet slots of constant width. The inflowing combustion air produces a vortex breakdown structure, which acts as a flame stabilizing element (Sattelmayer et al., 1992). The gaseous fuel is injected into the combustion air by two fuel distribution tubes, comprising two rows of small holes, which are arranged parallel to the air inlet slots [see Fig. 2]. This design leads to complete mixing shortly after injection and provides the basis for a perfect lean premix burner in which mixing and combustion occur in the same chamber. Because of the high velocity and swirl number in the cone itself, ignition can only take place near the flow stagnation point of the recirculation zone and the flame is stabilized in free space. There is no flame holder body exposed to ignitable mixtures and no danger of any flashback damaging the burner.

Combustion Chamber

The first application of the EV burner on an operating gas turbine is the retrofit of a GT11N combustor. The design of the new combustor had to meet the following requirements:

The convection flange between the combustor and the hot gas casing had to keep the original size of the standard combustor. The main design principles had to be derived from the proven Dry-NO_x technology to minimize the risk of failures of combustor components.

These requirements led to the silo combustor shown in Figs. 1 and 3. The combustor is a double-shell silo combustor with counterflow cooling, mounted vertically on the turbine housing.

The air from the compressor flows upward between the inner, intermediate, and outer liners, cooling the hot internal sections of the combustor. Changing the relation of the airmass flow between the inner and outer channels is a simple way to vary the convective cooling in this region. Near the primary combustion zone, the inner liner is formed from two rows of finned segments with a combination of convective and film cooling. The amount of film cooling air in the GT11N is varied by a simple modification of the entrance to the finned segments.

Most of the combustor air flows into the combustor plenum and enters the primary combustion zone through the air inlet slots of the 37 EV burners.

The burners are mounted in an arched cover bolted to the outer liner. In the case of combustor inspections, a frame holding the seven EV burners that form the innermost ring can easily be removed and the combustor entered through the opening thereby produced.

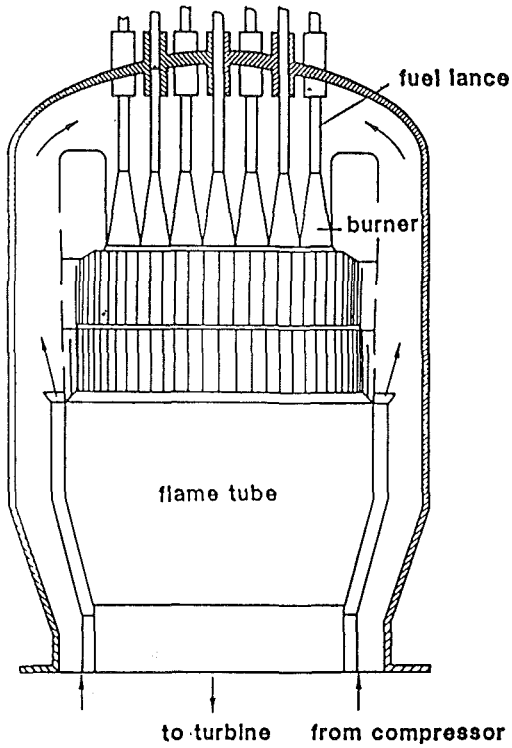

Fig. 3 GT11N Silo Combustor equipped with EV burners

The central burner is equipped with a spark plug and functions as an igniter. Three flame out detectors are installed at even intervals around the circumference of a single plane in the lower section of the combustor. These have additional optical equipment so that the combustion zone can be observed visually.

Fuel Distribution System

All 37 EV burners installed in the combustor operate in a pure premix mode. For part-load operation, the number of burners in operation is reduced in order to optimize combustion performance. The lean blow-off limit of a premix burner and the fact of the nearly constant air mass flow to the burners preclude the operation of all burners over the whole load range.

In Midland the gaseous fuel is supplied through the original emergency shut-off and the main control valve up to the combustor. Then the gas is distributed to the burners using six control valves (group valves, see Fig. 1) and seven ring pipes. The group valves allow individual regulation of the fuel mass flow to each group of burners and can function in staging or piloting operating concepts.

Instrumentation

The test combustor in Midland was equipped with extensive instrumentation to observe the behavior of the new components. Approximately 150 thermocouples measured the following temperatures: material temperatures at selected points of the burners, burner rings, lances, and inner liner; air temperature at the diffuser outlet and the burner inlet.

Eighteen static pressure probes provided information about fuel and air distribution and various pressure losses. Piezoelectric pressure probes were used to monitor pressure pul-

Nomenclature

ETA = combustion efficiency
FAR = fuel-to-air ratio
ma = air mass flow
mf = fuel mass flow
$mf100$ = fuel mass flow at base load
P = pressure
ppmv = parts per million by volume
T = temperature

Downloaded 02 Jun 2010 to 171.66.16.121. Redistribution subject to ASME license or copyright; see http://www.asme.org/terms/Terms_Use.cfm

sations. Three optical probes allowed observation of almost all the burners during machine operation. Three standard sample probes installed at the end of the turbine diffuser are used for the measurement of emissions (CO, CO_2, UHC, O_2, NO, and NO_2).

Operation Concepts

After the installation of the combustor was finished, the commissioning and testing period started. This time was used to pursue the following objectives:

- test of staging and piloting operation concepts
- definition of the final operation concept
- demonstration of the operating safety of the burner
- demonstration of the emission performance
- establishment of the commissioning procedure for subsequent EV combustors

From the beginning a staging operating concept using seven burner groups was examined. As developed for the Dry-NO_x combustor, all operating burners have the same fuel-to-air ratio. From idle the fuel-to-air ratio of the pilot burners is increased over the load up to the first switching point. At this stable load point the group 1 valve opens, the number of burners in operation increases from six to nine, and the fuel-to-air ratio of the burners drops by 33.3 percent (see Fig. 4). Between idle and base load this procedure is repeated six times. This concept is very simple; however, the large fluctuations in the burner fuel-to-air ratio over the load lead to swings in emissions.

The second operation concept, called the piloting concept, is based on the fact that in a cluster of EV burners complete reaction of the fuel can be obtained even if a small number of burners is operated below their blow-off limit (Sattelmayer et al., 1990). To achieve this, an ideal arrangement of the burners in the combustor and the optimal mixing of the hot gases between the pilot and the group burners is required. If the arrangement of the burners in the combustor is correct, it is possible to run most of the burners under constant conditions and to handle load changes through a small number of burners operating very lean (see Fig. 5).

The tests in Midland have shown that the piloting concept works very well between 25 percent load and base load and over this load range leads to NO_x emissions below 25 ppmv.

In the low-load range the staging of the first two groups leads to better combustion efficiency than the piloting variant. For the final operation concept a compromise was reached in staging the first two groups and piloting the last four groups of burners.

Emissions With the Actual Operation Concept

The actual operation program (groups 1, 2, staged; groups 3–6 piloted) leads to the emissions shown in Figs. 6–8.

The NO_x values between idle and 20 percent load fluctuate depending on the fuel-to-air ratio of the burners. From 20 percent load to base load the NO_x is maintained nearly constant below 25 ppmv, with the change from the staging to the piloting operation. The small decrease from 25 ppmv at 20 percent load to 13 ppmv at full load is due to the optimization of the piloted concept to achieve good combustion efficiency at part load.

The unburned hydrocarbons (UHC) decrease sharply between 40 and 65 percent load and reach less then 3 ppmv at full load. The arrow in the diagram (Fig. 7) shows a prediction of UHC-emissions, attainable if the burner air could be regulated by 20 percent over the load using variable inlet guide vanes or variable combustor geometry.

The CO emissions show the same behavior over the load as the UHCs and reach values of well under the 8 ppm target at base load. The good quality of the combustion is shown in Fig. 8 where the combustion efficiency is plotted against the load of the gas turbine. The efficiency is more then 99.99 percent at base load and never drops below 96 percent over the whole load range.

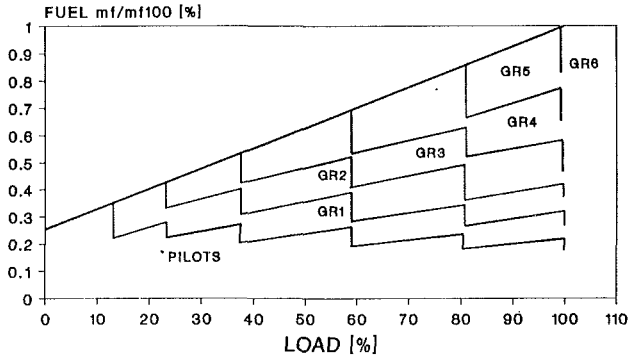

Fig. 4 GT11N EV fuel distribution with burner staging concept

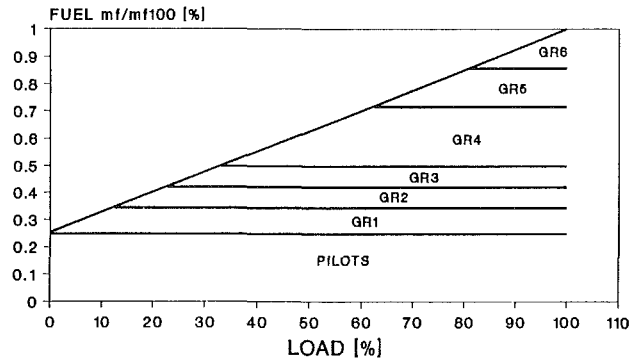

Fig. 5 GT11N fuel distribution with burner piloting concept

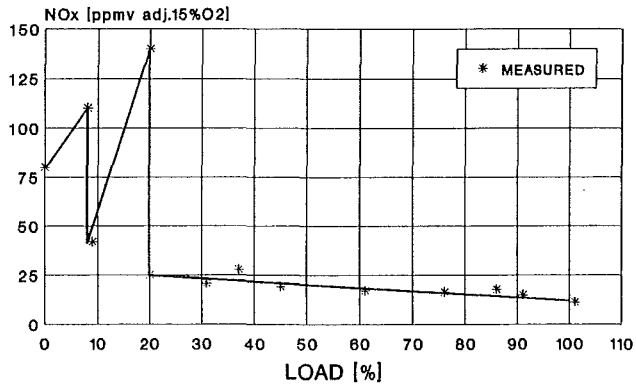

Fig. 6 GT11N EV NO_x emissions using a combination of staging and piloting concept

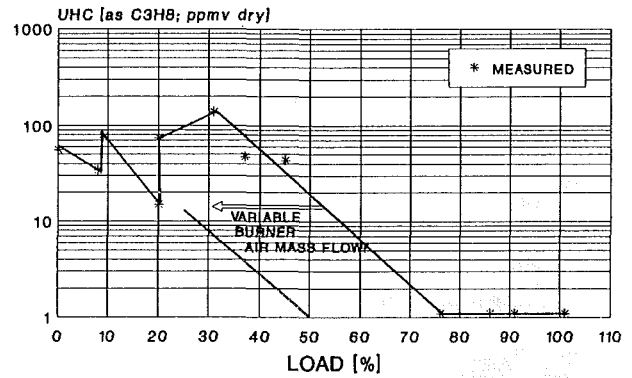

Fig. 7 GT11N EV UHC emissions using a combination of staging and piloting concept

Downloaded 02 Jun 2010 to 171.66.16.121. Redistribution subject to ASME license or copyright; see http://www.asme.org/terms/Terms_Use.cfm

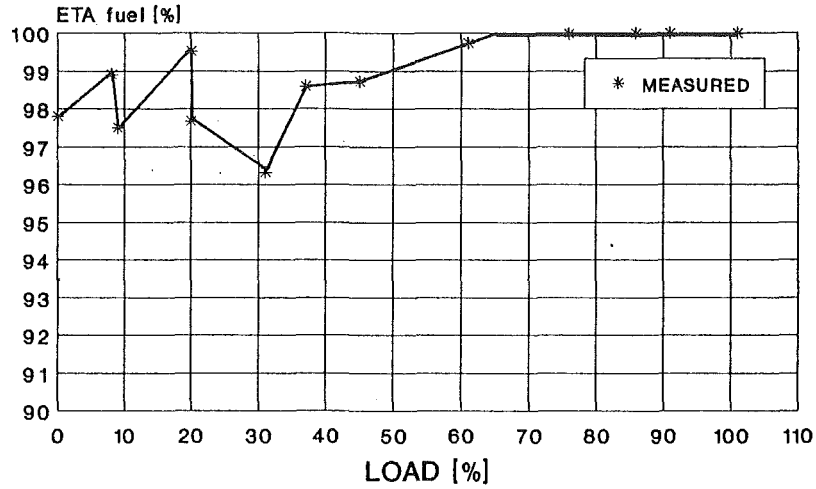

Fig. 8 GT11N EV combustion efficiency using a combination of staging and piloting concept

Comparison of the Machine Values With High-Pressure Test Results

One question of high interest was the comparison of the NO_x values of the gas turbine with the results of the high-pressure tests in Cologne (Aigner et al., 1990). Tests were carried out where the number of burners in operation and the amount of cooling air to the finned segments were changed at base load. This allowed the burner fuel-to-air ratio to be varied over a wide range and gave information about the behavior of the EV burner, if the combustor design and regulation was altered.

Figure 9 shows measured NO_x emissions of the GT11N EV versus the fuel-to-air ratio of the burners. All measurement points are taken under or near base load conditions ($T = 370$ °C; $P = 12.5$ bar). The gas turbine attained with the original design ($PHI/PHI_o = 1$) corrected NO_x-values of 13 ppmv at 15 percent O_2. The diagram also demonstrates that a GT11N equipped with EV burners can reach base load NO_x emissions of 9 ppmv under optimal conditions.

The comparison of these emissions with this results of the high-pressure tests shows a good correspondence and confirms ABB's ability to predict emissions accurately on the basis of high-pressure tests.

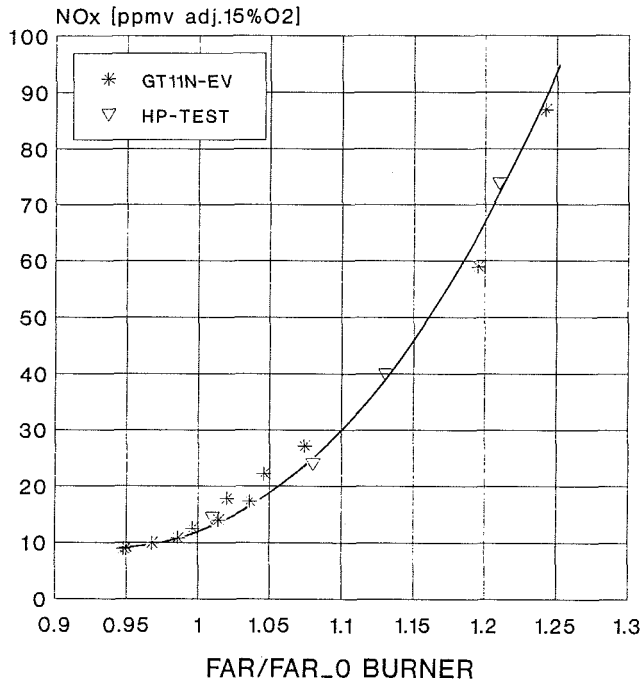

Fig. 9 GT11N EV NO_x emissions at base load against fuel-to-air ratio: comparison with results from the high-pressure tests (Aigner et al., 1990)

Operation Experience

Temperature measurements at 10 points of the burner surface showed a maximum material temperature of only 26°C above the air inlet temperature. This demonstrates that there is no danger of overheating the EV burner.

The GT11N EV in Midland has been in commercial operation since the end of the commissioning and testing period for more then 3500 hours. In this period no combustor problems have occurred and the unit was always available with the exception of routine inspections.

Conclusion

The extensive tests of the EV-burner technology on an GT11N confirmed:

- The EV burner, an advanced second-generation premix burner, is simple and reliable. The absence of any mechanical flame holder removes the danger of flashback.
- Reliable operation of the burners over the whole load range without any diffusion flame is possible.
- Both staging and piloting operations of the EV-burner were tested. The staging concept is very simple and leads to alternating NO_x emissions. The piloting concept allows constant NO_x emissions over a wide range of load without regulation of the burner air. In the GT11N EV a combination of burner staging and burner piloting concepts guarantees the optimum in operating safety and low-emissions performance.
- Emissions are below the target:
  $NO_x < 25$ ppm [15 percent O_2]
  UHC < 5 ppm
  CO < 8 ppm
- NO_x values are even lower than 15 ppmv at base load.
- After 3500 operation hours no combustor or burner wear appeared and all emission values were unchanged.

References

Aigner, M., Mayer, A., Schiessel, P., and Strittmatter, W., 1990, "Second Generation Low Emission Combustors for ABB Gas Turbines: Tests at Full Engine Conditions," ASME Paper No. 90-GT-308.

Koch, H., Brühwiler, E., Strittmatter, W., and Sponholz, H. M., 1985, "Dry-NO_x Brennkammer, Entwicklung und erreichte Resultate," presented at CIMAG, Oslo, Norway.

Sattelmeyer, T., Felchlin, M. P., Haumann, J., Hellat, J., and Styner, D., 1992, "Second-Generation Low-Emission Combustors for ABB Gas Turbines: Burner Development and Tests at Atmospheric Pressure," ASME JOURNAL OF ENGINEERING FOR GAS TURBINES AND POWER, Vol. 114, pp. 118–125.

Downloaded 02 Jun 2010 to 171.66.16.121. Redistribution subject to ASME license or copyright; see http://www.asme.org/terms/Terms_Use.cfm

J. P. Claeys

K. M. Elward

W. J. Mick

R. A. Symonds

Gas Turbine Design and Development Engineering, General Electric Company, Schenectady, NY 12345

Combustion System Performance and Field Test Results of the MS7001F Gas Turbine

This paper presents the results of the combustion system test of the MS7001F installed at the Virginia Power Chesterfield station. Tests of water and steam injection for NO_x control were performed. Results of emissions, combustor dynamics, and combustor hardware performance are presented. Emissions test results include NO_x, CO, unburned hydrocarbons, VOC, and formaldehyde levels. Combustor dynamic activity over a range of diluent injection ratios, and the performance of an actively cooled transition duct are also discussed. Combustion system mechanical performance is described following the first combustion system inspection.

Introduction

The MS7001F is the first 2300°F (1533 K) heavy-duty gas turbine designed, tested, and commissioned. This step-change in firing temperature for the new machine presented design challenges for most of the gas turbine components including the combustion system (Brandt, 1988). Component testing and development of the combustion system were accomplished, in large part, on single combustor test stands at GE's turbine test laboratories. The first 7F machine was no-load and load tested at the Greenville, SC, test facility in 1988 and 1989, shipped and installed at its Chesterfield, VA, site (Virginia Power), and instrumented and tested during the spring of 1990. The amount of instrumentation and the detail embodied in the test plan are greater than in any previous machine test. The success of this field test is due to the attention to detail and the extensive component testing that occurred prior to machine assembly. The results obtained confirm the quality of the system design, and allow for quick response to changing market needs such as upgraded output or improved emissions guarantees.

System Description

The combustion system for the GE MS7001F gas turbine is illustrated in Fig. 1, which shows one of the 14 combustion chambers of the machine in cross section. The use of multiple, reverse flow combustion chambers is typical of the GE heavy-duty, industrial gas turbine design. The 13 deg cant of the combustors allows for a more compact combustor and gas turbine design. The combustion system consists of a fuel nozzle assembly, a flow sleeve, a cap and liner assembly, and a transition piece. The combustion system incorporates advanced cooling technology to permit firing temperatures of 2350°F (1561 K). Ignition is achieved with a spark plug in 2 of the 14 chambers with cross firing connections to ignite the balance of the chambers. Successful ignition is sensed with four ultraviolet flame detectors located nearly opposite to the location of the spark plugs.

The air flow paths for the combustion system are also shown in Fig. 1. After leaving the diffuser area of the compressor, air flows past the transition pieces and forward toward the head end of the liner. The air splits between two parallel paths before entering the liner. Some of the air flows through the holes provided in the impingement sleeve of the transition piece for cooling; the balance of the air passes through an array of multiple holes in the flow sleeve. The air, now outside the liner, experiences dilution, mixing, cooling, and enters holes in the liner sleeve and passes through the cap of the liner, where the air and fuel mix. Inside the liner, the air and fuel react and flow downstream through the transition piece before entering the turbine section.

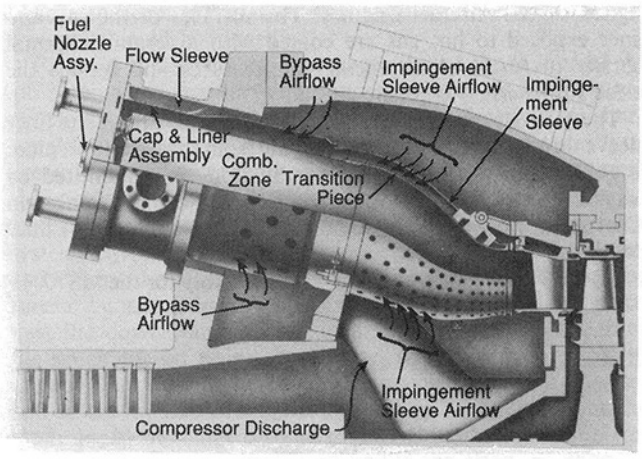

Fig. 1 MS7001F combustion system

Contributed by the International Gas Turbine Institute and presented at the 37th International Gas Turbine and Aeroengine Congress and Exposition, Cologne, Germany, June 1–4, 1992. Manuscript received by the International Gas Turbine Institute February 24, 1992. Paper No. 92-GT-314. Associate Technical Editor: L. S. Langston.

Copyright © 1993 by ASME

Downloaded 02 Jun 2010 to 171.66.16.121. Redistribution subject to ASME license or copyright; see http://www.asme.org/terms/Terms_Use.cfm

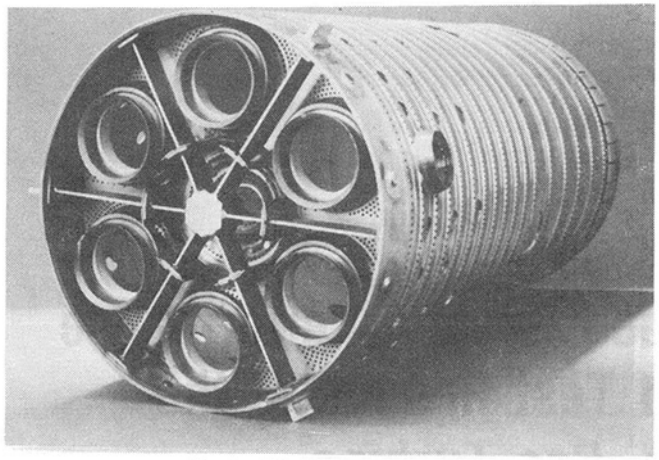

Fig. 2 MS7001F cap and liner

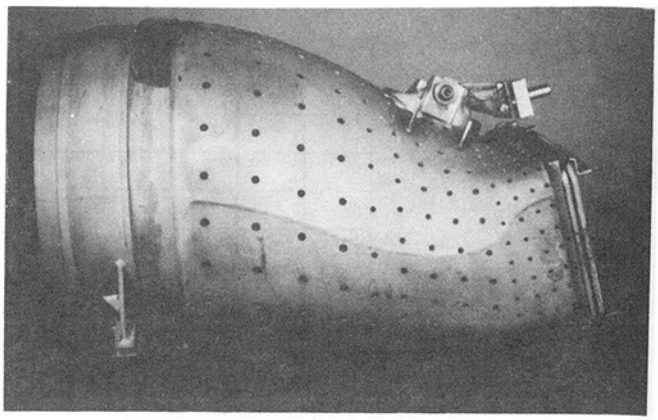

Fig. 3 MS7001F transition piece assembly

The fuel nozzle assembly is designed to allow use of either gas or distillate fuel and to transfer from one fuel to the other during operation. Six individual, dual-fuel nozzles are attached to an internally manifolded cover. Each fuel nozzle consists of a swirl tip, an atomizing air tip, and a distillate spray nozzle. Gas fuel is injected through metering holes in the swirler. Continuous atomizing air is used with the distillate fuel spray. Water or steam for NO_x control also enter through the combustion cover. The multinozzle design offers two significant advantages over single-nozzle designs. First, it allows more thorough mixing and control of the fuel and air in the reaction zone, resulting in a shorter flame length and improved combustor performance. Second, it produces significantly lower noise levels than single-nozzle combustors and thereby improves combustor component wear. The low noise benefits of the multinozzle configuration were first realized on the GE MS7001E multinozzle quiet combustor (EPRI, 1985; Fitts et al., 1990).

The cap and liner assembly, shown in Fig. 2, consists of a slot film cooled, 14 in. (0.35 m) diameter, 30 in. (0.76 m) long liner sleeve and a multinozzle cap assembly. The slot cooling design employed has evolved from earlier applications on other GE gas turbine liners. The relatively short liner length is another benefit of the multinozzle design, which produces a shorter reaction zone than single-nozzle combustors. The shorter liner has less surface area to cool. Thus, in spite of the higher firing temperature, the MS7001F liner operates at temperatures less than or equal to those of earlier designs. The cap is film cooled in the center and impingement cooled in the region surrounding the fuel nozzles. The impingement/splash plate design employed on the MS7001F cap is similar to that currently employed on the domes of annular combustors designed by GE Aircraft Engines. The surfaces of the cap and liner exposed to hot gas are coated with a ceramic thermal barrier to further limit metal temperatures and reduce the effects of thermal gradients.

The flow sleeve forms an annular air space about the liner sleeve through which spent cooling air from the transition piece is guided and the balance of combustion air is admitted by way of the array of holes. The flow sleeve also acts to maintain a sufficient flow velocity on the back side of the liner for liner cooling.

Figure 3 shows the transition piece assembly for the MS7001F gas turbine. The transition piece assembly employs an innovative cooling design, which has allowed the increases in compression ratio and firing temperature that are required in an advanced gas turbine.

The transition piece directs the hot gases from the exit of the liner sleeve to the inlet of the turbine. Such a transition duct is typical of GE gas turbines and has been successfully employed on thousands of gas turbines in various configurations. All earlier designs, however, are convectively cooled by the passive flow of compressor discharge air around the transition piece. Good heat transfer is effected on the inner radial and side surfaces of the transition piece by virtue of the high-velocity air flow and correspondingly high heat transfer coefficients over these surfaces. However, the outer radial panel, particularly toward the aft end of the transition piece, is in a shadow where the air is relatively stagnant and the heat transfer coefficient is low. As a result, the outer radial panel toward the aft end of the transition piece experiences the highest temperatures which are thus design limiting.

In contrast, the MS7001F transition piece is surrounded by a sleeve in which an array of holes is provided. Air flows through the holes and impinges on the back side of the transition piece, thereby providing an effective impingement-type cooling of the surface. The shape of this "impingement" sleeve roughly parallels that of the transition piece with the gap between the two increasing from the aft end to the forward end to accommodate the increase in air flow from each of the consecutive rows of cooling holes. The use of impingement cooling allows more precise control of the cooling of the transition piece while having only a small, adverse effect on the combustion system's overall pressure drop.

The cooling of the transition piece provided by the impingement sleeve results in significantly more uniform metal temperatures on the transition piece, thereby lowering thermal stresses and allowing higher hot gas and compressor discharge temperatures to be accommodated while maintaining metal temperatures consistent with GE experience. The internal surfaces of the transition piece, those exposed to the hot gas, have a ceramic thermal barrier coating applied to limit the maximum metal temperature further.

Test Plan and Objectives

The test plan for the field test of the MS7001F was quite

Nomenclature

IGV = inlet guide vane
ppbv = parts per billion by volume
ppmvd = parts per million by volume, dry
ppmvw = parts per million by volume, wet
TF = firing temperature

Downloaded 02 Jun 2010 to 171.66.16.121. Redistribution subject to ASME license or copyright; see http://www.asme.org/terms/Terms_Use.cfm

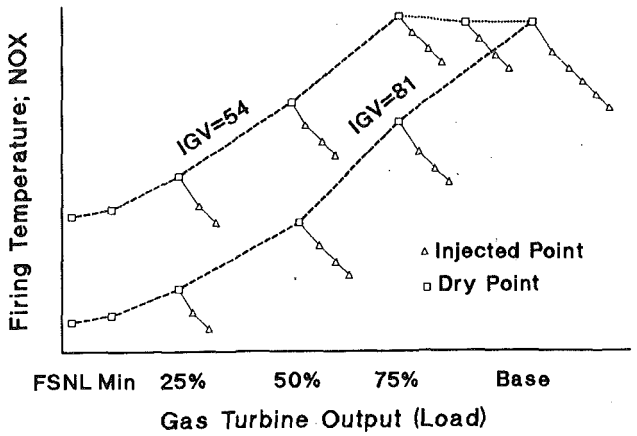

Fig. 4 MS7001F field test emissions plan

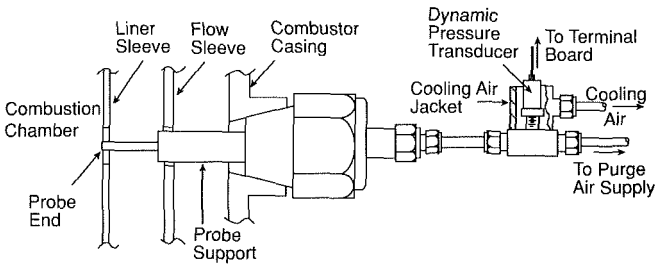

Fig. 5 Schematic arrangement of combustion chamber dynamic pressure probe

comprehensive as described briefly by Cincotta (1990). A large portion of this test plan was specifically for measurement and evaluation of the performance of the combustion system. Previous testing at the Greenville factory test had evaluated ignition capability and part-load performance as well as full temperature performance (albeit at reduced air flow due to the load absorbing limits at the factory test site). The overall field tests involved synchronization on oil and gas, full load, mechanical design, various configurations of water and steam injection, aeroperformance, modulated inlet guide vanes (IGV), and operating performance. The combustion emissions test plan was detailed enough that nearly all combustion requirements were investigated as part of the emissions test plan. Figure 4 presents the emissions test points in schematic fashion. For each fuel, gas or oil, points were run at various combinations of firing temperature and inlet guide van angle, which corresponded to load points of approximately 0, 25, 50, 75, and 100 percent of base load. On most of these test points diluent injection was also tested; these points are shown as branches off the main lines of constant IGV angle.

The noninjected points were run to give emissions values for the dry case. The injected points were run to determine required diluent flow for NO_x control and the performance of the combustion system, injection control systems, and the 7F machine itself. Firing temperatures above base load and guide vane angle greater than 81 deg were also explored. Diluent/fuel ratios were selected to straddle the ratios required for NSPS (New Source Performance Standard), and 42/65 (42 ppm @ 15 percent O_2 with natural gas, 65 ppm @ 15 percent O_2 with distillate). NSPS and 42/65 were required to check the lab data for NO_x abatement with water and steam and to provide data for the control curves for the customer whose permit required operation at 42/65. In addition to the emissions measurements, the fully array of combustion data was taken for each test point. Water injection and steam injection were both evaluated. A special water injection skid and associated

Table 1 Combustion system instrumentation

	MEASURED QUANTITIES OR SENSORS (TOTAL SENSOR COUNT = 524)						
COMPONENT	METAL TEMP.	DYNAMIC PRESS.	DIFF'L PRESS.	STATIC PRESS.	HOT GAS TEMP.	HOT GAS PRESS.	STRAIN GAGES
FUEL NOZZLE ASSEMBLY	20	7	7				
FLOW SLEEVE ASSEMBLY				36			
CAP & LINER ASSEMBLY	92	14					20
TRANSITION PC. ASSEMBLY	136			116	48	8	20
TOTALS	248	21	7	152	48	8	40

hardware and piping were installed for the water injection points; afterwards the machine was configured and tested in the steam injection mode which the customer had purchased. At the completion of the testing and prior to commissioning the machine, a complete combustion system inspection was performed to ensure GE and the customer of the integrity of the hardware.

Instrumentation Description

Four combustion chambers were instrumented, in various combinations, with thermocouples to measure metal temperatures on the liner and transition piece, thermocouples to measure combustor exit profile, pressure taps to monitor air flow distribution, and strain gages to quantify the dynamic response of the liner and transition piece. In addition, all chambers were instrumented with dynamic pressure transducers to measure combustion chamber pressure oscillations and static pressure taps to assess uniformity of air flow among the chambers. In total, the combustion system was instrumented with more than 520 sensors. Table 1 illustrates the distribution of the various sensors among the combustor's component parts. The data collected by these sensors were in addition to the data typically captured by the gas turbine's control system, such as fuel flow, water or steam injection flow, exhaust temperatures, etc.

Dynamic pressure oscillations within the combustion chamber are measured with a radial probe that is approximately flush with the inside wall surface of the liner sleeve. The probe penetrates the outer casing of the unit's pressure vessel. Once outside the machine, a dynamic pressure transducer is affixed to the probe. Figure 5 is a schematic illustration of the dynamic pressure probe. Each of the gas turbine's 14 combustors was outfitted with a dynamic pressure probe to ensure that worst chamber behavior could be monitored. Dynamic pressures in each of the fuel, diluent, and atomizing air supply manifolds were also recorded so that any coupling to the combustor dynamics could be identified.

Figure 6 is a schematic representation of the layout of the gas turbine and auxiliary equipment as well as the location and proximity of the control and data rooms. Steady-state data, consisting of gas and metal temperatures and static and total pressures, were recorded periodically on a digital data acquisition system. Control system data relevant to the combustion system were also accessed and recorded by the data acquisition system. Dynamic data from piezo-electric pressure transducers and electrical resistance strain gages were recorded in analog format on magnetic tape. Data were recorded during all start-ups, shutdowns, and loading transients, as well as at each of the specified test points once steady-state operation was attained. Data were gathered for dry operation as well as water and steam injection for both gas and distillate fuels over the load range of the gas turbine to characterize the behavior of the combustor.

Downloaded 02 Jun 2010 to 171.66.16.121. Redistribution subject to ASME license or copyright; see http://www.asme.org/terms/Terms_Use.cfm

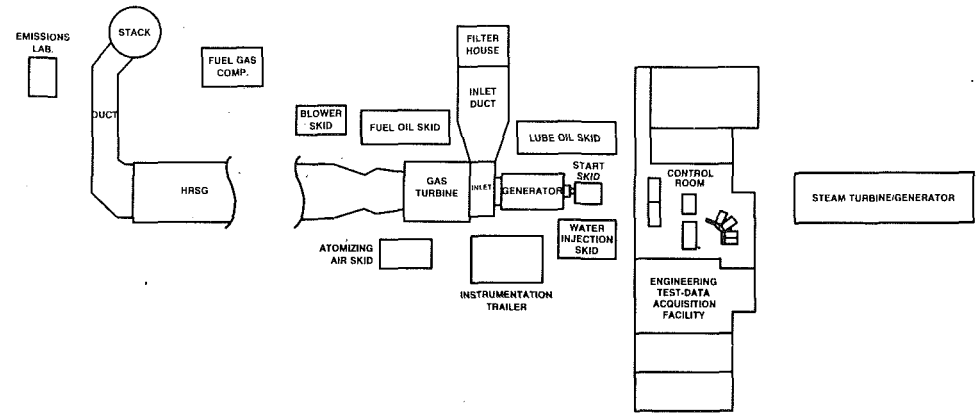

Fig. 6 Plant layout

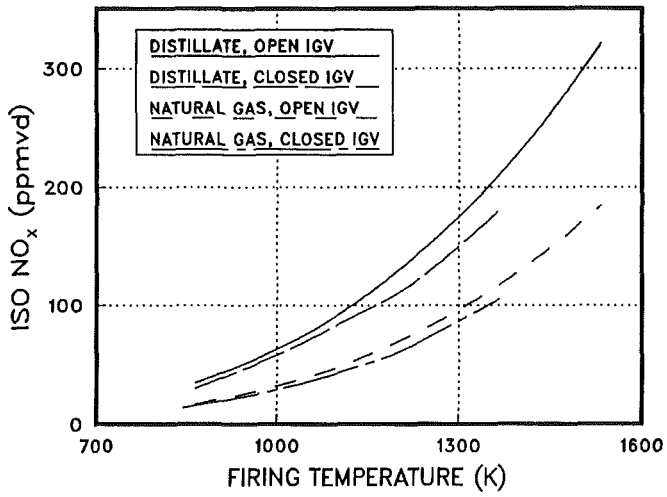

Fig. 7 NO_x at ISO conditions as a function of firing temperature

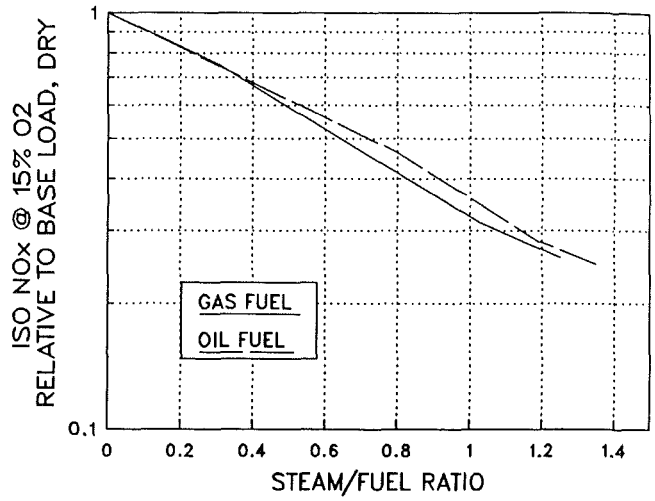

Fig. 8 Effect of water injection on NO_x emissions

Test Results

Emissions. Throughout the testing of the MS7001F, GE had a contracted vendor on site measuring exhaust emissions. The exhaust was sampled for oxides of nitrogen (NO_x), carbon monoxide (CO), unburned hydrocarbons (UHC's), volatile organic compounds (VOC's), aldehydes, particulates, and nitrous oxide (N_2O). In addition visible emissions were recorded. Emissions were measured without diluent injection and with water and steam for NO_x control.

Oxygen Traverse. Before emissions sampling began, a duct traverse was done to measure oxygen. The traverse was done in the ducting between the HRSG and the stack. As expected, the O_2 variation was very small and the balance of the testing was carried out using only a single point sample. Samples for particulates, aldehydes, etc., were also single point samples but were taken at a different point.

NO_x. NO_x results, without steam or water injection, are shown in Fig. 7 corrected to ISO humidity, temperature, and pressure. The pressure corrections are based on ambient pressures rather than compressor discharge pressures as suggested by EPA. This figure shows NO_x for minimum and maximum IGV angle for both gas and distillate fuels.

The machine was tested with both steam and water for NO_x abatement. The base load levels of NO_x corrected to ISO conditions and 15 percent oxygen relative to base load, without water or steam injection, are shown in Figs. 8 and 9, respectively, for both fuels. From these figures, approximate diluent/fuel ratios at base load required for NO_x reduction to various

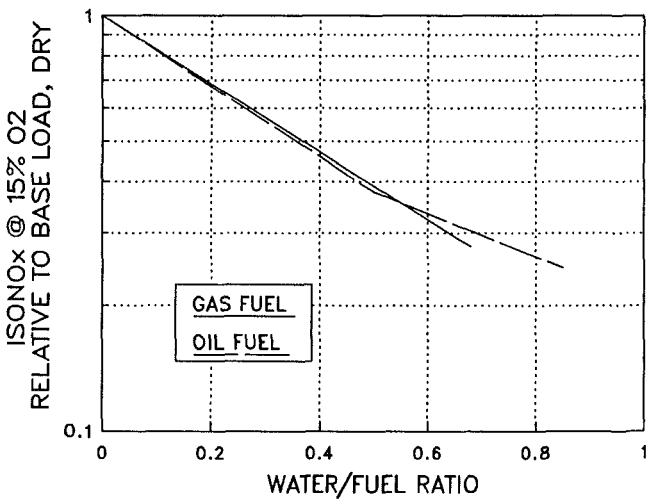

Fig. 9 Effect of steam injection on NO_x emissions

NO_x control codes can be determined (these are given in Tables 2 and 3).

NO_2. In addition to total NO_x, NO_2 was also measured at each data point. Normally, the emissions sample is run through a converter, which changes all NO_x to NO. Thus, total NO_x is measured as NO. To measure NO_2, the sample bypassed the converter and was fed directly into a NO_x meter, measuring

Downloaded 02 Jun 2010 to 171.66.16.121. Redistribution subject to ASME license or copyright; see http://www.asme.org/terms/Terms_Use.cfm

Table 2 Water/fuel ratios required for various NO_x emissions levels

FUEL	NOx level	W/F
Natural Gas	NSPS	.16
Natural Gas	42 ppmvd	.68
Distillate	NSPS	.47
Distillate	65 ppmvd	.85

Table 3 Steam/fuel ratios required for various NO_x emission levels

FUEL	NOx level	S/F
Natural Gas	NSPS	.40
Natural Gas	42 ppmvd	1.25
Distillate	NSPS	.85
Distillate	65 ppmvd	1.35

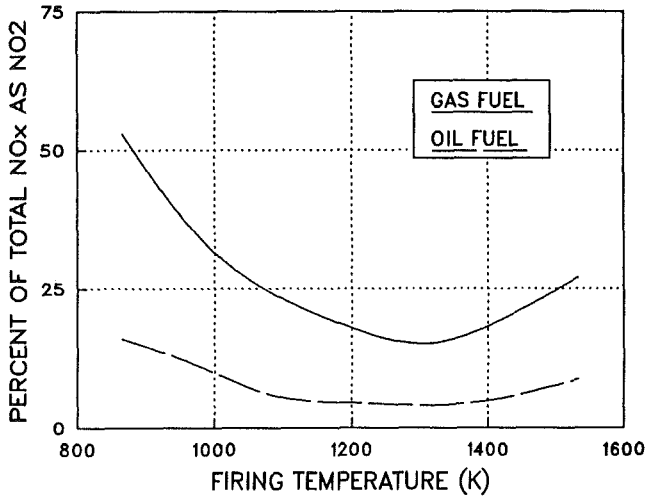

Fig. 10 NO_2 emissions as a function of firing temperature

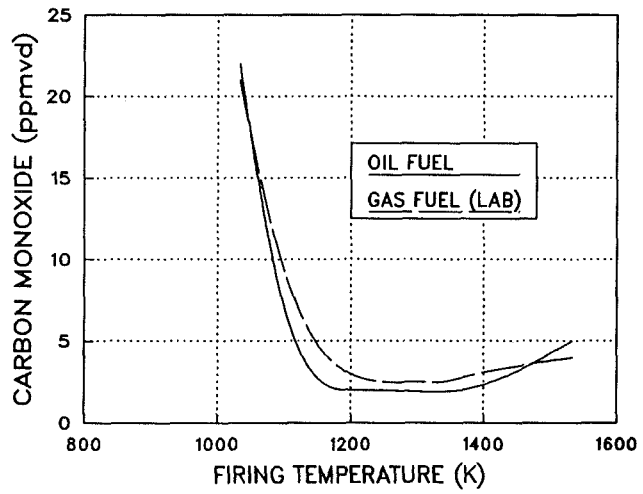

Fig. 11 Carbon monoxide emissions as a function of firing temperature

actual NO in the exhaust. By subtracting this number from the total NO_x number, the concentration of NO_2 is obtained. Figure 10 summarizes the results, showing percent of total NO_x as NO_2 for both fuels at 81 deg IGV.

Note that for gas fuel, the percentage of total NO_x present as NO_2 is higher than for distillate. This is probably due to high unburned hydrocarbon levels present during all natural gas testing. During natural gas testing, a valve between the gas manifold purge and gas supply was not functioning properly.

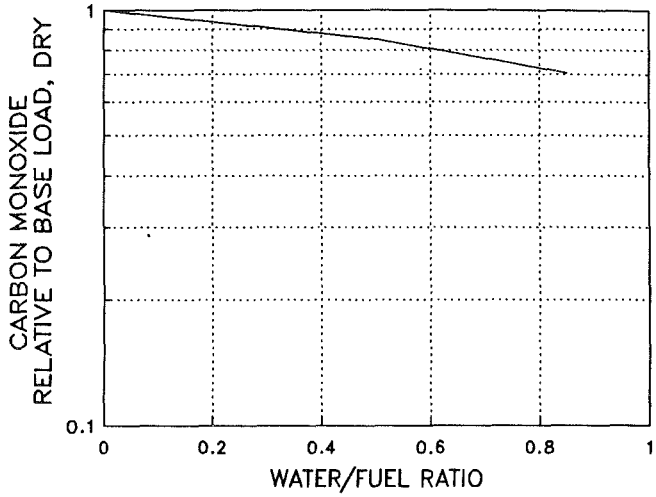

Fig. 12 Effect of water injection on carbon monoxide emissions

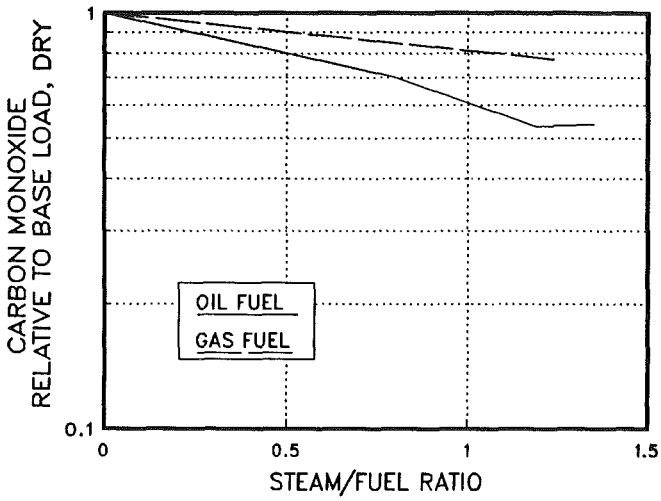

Fig. 13 Effect of steam injection on carbon monoxide emissions

As a result, some natural gas was vented to the atmosphere near the inlet filters of the gas turbine. Some of this gas was ingested into the turbine and bypassed the combustion system. This gas showed up as unburned hydrocarbons in the exhaust. Evidence exists to suggest that high levels of unburned hydrocarbons accelerate the conversion of NO to NO_2, with little or no effect on total NO_x (Hori, 1988).

Carbon Monoxide. Carbon monoxide emissions as a function of firing temperature without water or steam injection are presented in Fig. 11 for distillate oil and natural gas. The gas data are based on laboratory observations. Due to the leaking gas manifold purge valve, CO data gathered while burning natural gas are not accurate. Based on the agreement between laboratory and field CO data gathered on distillate fuel, the CO curve for gas from the laboratory data is used here.

The effect of water and steam injection on CO emissions at base load is shown in Figs. 12 and 13. Because of the leak in the purge valve, CO data on gas fuel are limited to those gathered during the compliance test that was performed after the engineering testing and after the leak was corrected. The base load compliance test data are limited to the single point at a steam fuel ratio of 1.25 shown in Fig. 13. Since the machine was only compliance tested in the steam injection configuration, no water-injected data are shown for gas fuel.

Unburned Hydrocarbons. Figure 14 shows the total un-

Downloaded 02 Jun 2010 to 171.66.16.121. Redistribution subject to ASME license or copyright; see http://www.asme.org/terms/Terms_Use.cfm

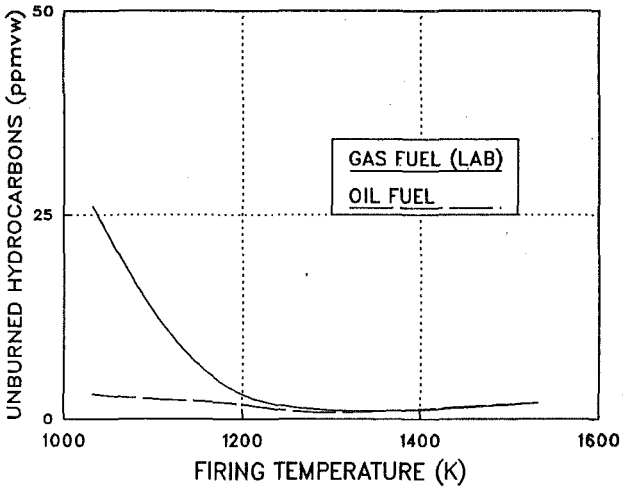

Fig. 14 Unburned hydrocarbon emissions as a function of firing temperature

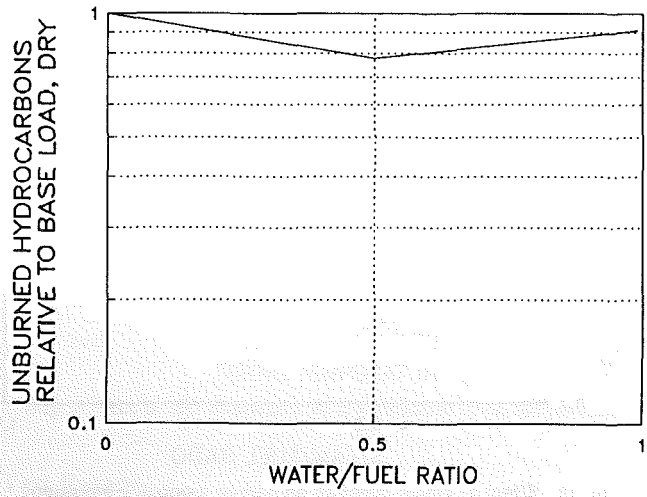

Fig. 15 Effect of water injection on unburned hydrocarbon emissions

burned hydrocarbon emissions for distillate and gas fuels with no diluent injection as a function of firing temperature. As with the CO data, the gas-fired data shown in the figure are based on laboratory results.

The effect of water injection on total unburned hydrocarbons at base load is shown in Fig. 15. Once again, because of the unreliable natural gas data, no gas curve is shown for water injection. No figure is shown for steam injection because unburned hydrocarbon emissions showed no change with steam injection for either fuel at base load.

VOC's. Volatile Organic Compounds have been defined as all unburned hydrocarbons excluding methane and ethane. The levels measured were all in the range of one ppm or less and therefore are not shown in figure form.

Visible Emissions. Visible emissions were measured by a certified visible emissions observer (VEO). Opacity as determined by the VEO was measured on distillate fuel at base load both with no water injection and with a water/fuel ratio of about 1.0 and again at no load on distillate. No VEO readings were taken while burning natural gas; however, the worst case for smoke usually occurs when burning distillate. All opacity readings taken for these points were either zero or 5 percent.

Particulates. One particulate sample was taken for each fuel at base load. For distillate the sample was taken with a water/fuel injection ratio of about 1.0. The gas sample was taken with steam injection at a steam/fuel of about 1.1. For both samples the particulate emissions rate was less than the guaranteed values of 7 and 14 pounds per hour for the 7F on gas and distillate, respectively.

Table 4 Summary of aldehyde emissions (all values ppbv)

FUEL	DIST	DIST	DIST	GAS	GAS	GAS
LOAD (MW)	0.0	140.5	150	10.7	14.5	154
w/f	0.0	0.0	0.99	N/A	N/A	N/A
s/f	N/A	N/A	N/A	0.0	0.0	1.07
Acetaldehyde	1270	37.8	21.3	47	15.5	17.4
Acetone	308	210	144	96.8	723	723
Acrolein	530	<3.30	<2.42	<2.16	<2.56	<2.38
Benzaldehyde	89.7	<1.75	<1.28	<1.14	<1.35	<1.25
Butyraldehyde	123	<2.57	<1.88	<1.68	<1.99	<1.85
Formaldehyde	6970	946	485	10800	93.6	1130
Hexaldehyde	132	<1.85	<1.35	<1.21	<1.43	<13.1
Isovaleraldehyde	18	61.0	38.3	1.55	<1.84	<13.1
Veraldehyde	309	24.0	18.2	12.7	1.84	503

Aldehydes. Six exhaust samples were collected in an impinger train to check for aldehyde emissions; three for distillate and three for natural gas fuel. The impingers contained acidified 2,4-dinitrophenylhydrazine. Probe and impingers were recovered with methylene chloride. Each sample was analyzed with high-performance liquid chromatography for nine different aldehydes. The results appear in Table 4. Formaldehyde was the most prevalent specie detected with a maximum value of about 7 ppmv on distillate and 11 ppmv on gas. All other readings were on the order of 1 ppmv or less. The high readings on gas fuel may have been effected by the leaking gas purge valve. The highest reading on distillate occurred at minimum load with no water injection. The oil nozzles at this point were configured to runs with a mix of oil and water and as such were sized larger than conventional oil nozzles. The low fuel flow through this nozzle having a higher flow number probably resulted in poor atomization of the fuel. This would be supported by the higher hydrocarbon readings: 82 ppmvd versus 21 ppmvd for a similar minimum load point with conventional oil nozzles.

N_2O. For 11 of the test points, samples of the exhaust were drawn into tedlar bags and sampled for nitrous oxide (N_2O). The results appear in Table 5. For all of the points no N_2O was detected with the detection limit set at 500 ppb for some points and 260 ppb for others.

Combustor Dynamic Pressures. Figure 16 illustrates typical frequency spectra of the MS7001F combustor at base load, dry, and at a water-to-fuel ratio of 1.0. In both cases the dynamic activity is broad band with no significant discrete peaks. The effect of water injection is seen here to shift the entire spectrum to a higher overall level. At even higher injection rates, there is an enhanced response around the combustor's lowest longitudinal mode. This enhancement, however, is still fairly broad in nature. A distributed noise signature provides a minimal stimulus to the combustion system components. GE's experience with such a low and broad band signature shows a strong relationship between such dynamic behavior and the wear behavior of the combustor. That is, with low dynamic levels, the wear of the combustion system is correspondingly low. This is important as the combustor is subjected to increasing levels of diluent injection for NO_x control or power augmentation.

Downloaded 02 Jun 2010 to 171.66.16.121. Redistribution subject to ASME license or copyright; see http://www.asme.org/terms/Terms_Use.cfm

Table 5 Summary of N_2O emissions

FUEL	LOAD (MW)	W/F	S/F	N_2O (ppbv)
OIL	0.0	0.0	N/A	ND*
OIL	9.6	0.0	N/A	ND*
OIL	10.6	0.0	N/A	ND*
OIL	140.5	0.0	N/A	ND*
OIL	147.5	0.0	N/A	ND*
OIL	150.0	0.99	N/A	ND*
OIL	150.0	1.42	N/A	ND+
GAS	10.7	N/A	0.0	ND+
GAS	12.8	0.0	N/A	ND+
GAS	144.5	N/A	0.0	ND+
GAS	155.0	N/A	1.07	ND+

* not detected at <500 ppb
\+ not detected at <260 ppb

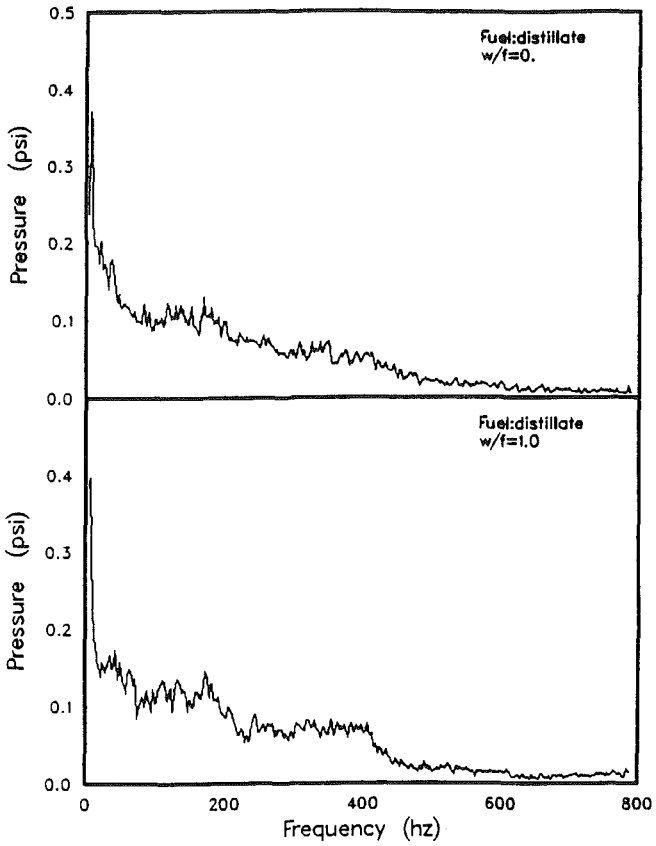

Fig. 16 Combustion dynamic pressure spectra

The remainder of the combustor dynamic pressure data is presented as overall (rms) levels of the signal from 0–800 Hz. The 0–800 Hz range captures all relevant combustion acoustic information, which generally drops off quickly above 400–500 Hz in these large combustors. For reference, the lowest acoustic resonant mode of this combustor is a longitudinal standing wave, which varies in frequency from about 200 Hz at zero load to about 300 Hz at base load. All combustor dynamic pressure plots have been normalized to base load, dry on distillate fuel.

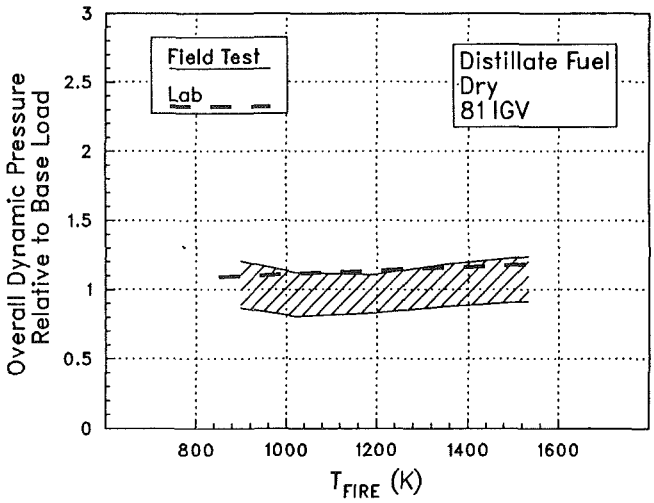

Fig. 17 Combustor dynamic pressure as a function of firing temperature for distillate fuel

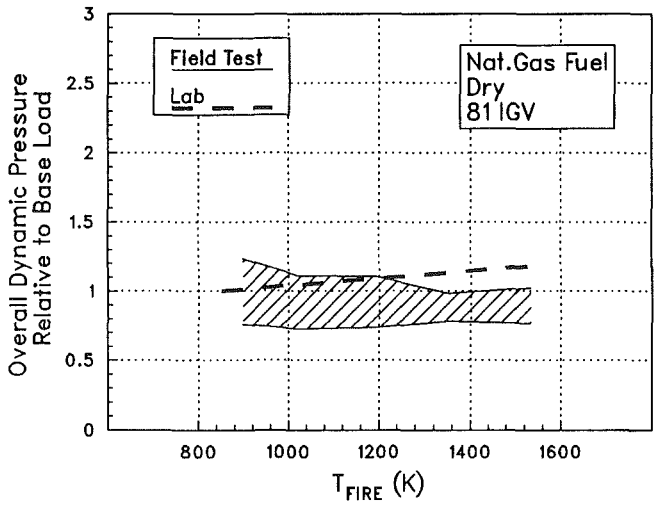

Fig. 18 Combustor dynamic pressure as a function of firing temperature for gas fuel

Figure 17 is a plot of the overall combustor dynamic pressure as a function of firing temperature on distillate fuel dry. The curve is an average of all 14 chambers while the shaded region shows the maximum to minimum range. All shown are the dynamic pressure levels seen during laboratory single chamber tests. As seen, the laboratory data fall near the high end of what is seen in the machine. The relative flatness of the curve as load increases is a measure of the inherent quietness of the multinozzle combustor design. Figure 18 illustrates the same data but for gas fuel operation. The same comments regarding the dynamic pressure activity apply to gas fuel as for distillate fuel.

To illustrate the effect of diluent injection on the dynamic pressure oscillations, the dynamic pressure is plotted as a function of the diluent to fuel ratio. Figures 19–22 show these plots for both fuels, for both diluents and for both base load (100 percent) and part load (50 percent). The field test data are compared to laboratory data in each figure. In addition, each figure contains lines corresponding to the diluent to fuel ratios required for various levels of NO_x control. The increase attributable to water injection can be determined by referring to the point of zero water to fuel ratio (dry).

The results for distillate fuel show that as diluent injection is increased, the dynamic pressure level increases only slightly.

Downloaded 02 Jun 2010 to 171.66.16.121. Redistribution subject to ASME license or copyright; see http://www.asme.org/terms/Terms_Use.cfm

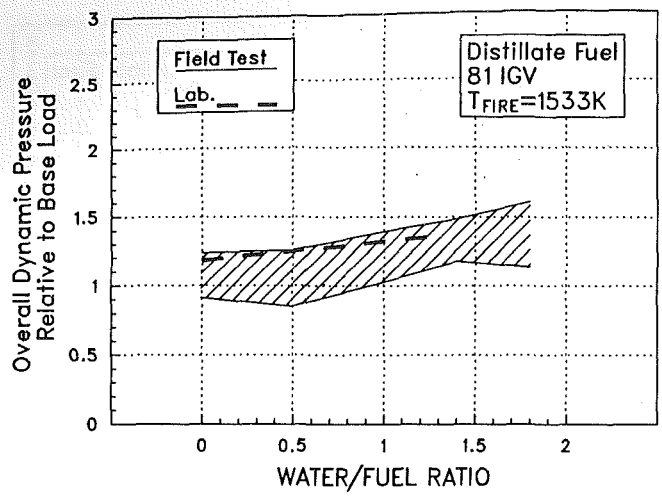

Fig. 19 Effect of water injection on combustor dynamic pressure for distillate fuel

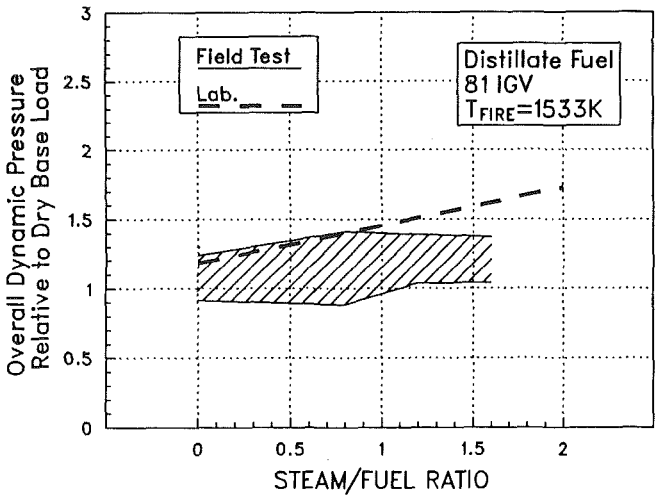

Fig. 21 Effect of steam injection on combustor dynamic pressure for distillate fuel

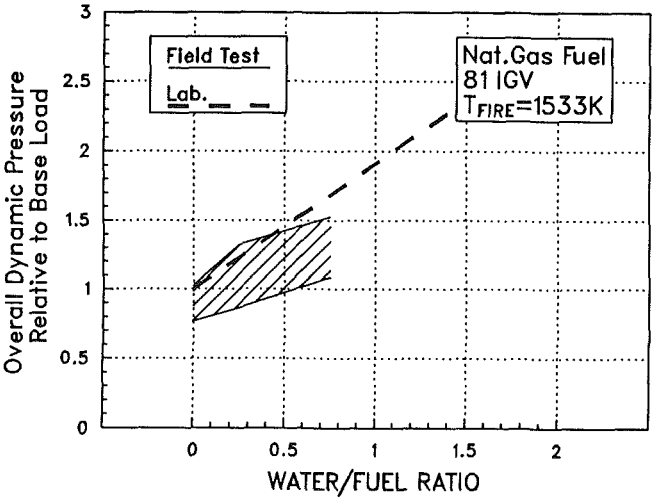

Fig. 20 Effect of water injection on combustor dynamic pressure for gas fuel

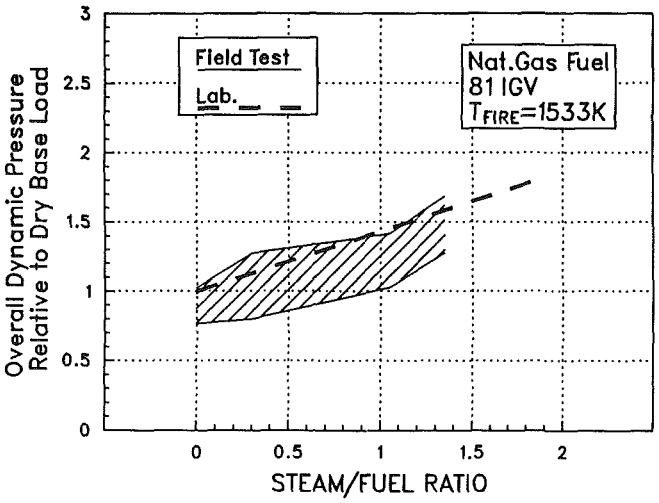

Fig. 22 Effect of steam injection on combustor dynamic pressure for gas fuel

With water injection, the increase is about 0.25 psi or about 20 percent as the water-to-fuel ratio approaches 2:1. With steam injection, an increase of about 15 percent is seen at a steam/fuel ratio of about 1.6.

On gas fuel, the increase in dynamic pressure levels with increasing diluent injection is more pronounced than that seen for distillate fuel. This is probably attributable to the interaction of the gas fuel and water flows, which are both injected into the reaction zone as discrete jets in close proximity to one another. Although this injection scheme produces higher dynamic levels, it does yield good emissions performance. These levels are still well within the range of experience of other GE combustors.

Overall, the dynamic pressure behavior of the GE MS7001F gas turbine combustor was very good. The level of dynamic pressure oscillations was at the low end of GE's experience. The quiet behavior should prove to be beneficial in promoting hardware longevity. The low levels are an inherent result of the combustor's design features, which were developed specifically to reduce the level of dynamic pressure activity.

Combustor Dynamic Strains. The liner and transition piece were instrumented with several dynamic strain transducers. These gages were located at points of high stress such as near the hardware support points or near stress concentrators such as liner holes. The measured strain levels were quite low and subject to a poor signal-to-noise ratio; therefore, a detailed quantitative assessment of the strain data was not made. The maximum peak-to-peak dynamic strains observed were about 50 μin./in. and occurred during base load operation on the liner.

Combustor Metal Temperatures. The combustor metal temperatures for base load, dry operation are shown in Figs. 23 and 24. Figure 23 shows the axial distribution of liner metal temperature. The liner thermocouples were installed on the back side of the liner wall. There is one thermocouple for each of the 16 film-cooled panels located at the point on each panel where the highest metal temperatures are expected. The temperatures are uniform over the first 80 percent of liner length but rise about 200°F (110 K) in the last 20 percent. Because of the hotter tail end, the liner material changes from Hastelloy-X to Haynes-188 over the last 35 percent of the liner. The Haynes-188 alloy has 100–200°F (55–110 K) better temperature capability than the Hastelloy-X.

Figure 24 compares the circumferential temperature distributions typical of the MS7001F impingement-cooled transition piece with those of a passively cooled transition piece from an

Downloaded 02 Jun 2010 to 171.66.16.121. Redistribution subject to ASME license or copyright; see http://www.asme.org/terms/Terms_Use.cfm

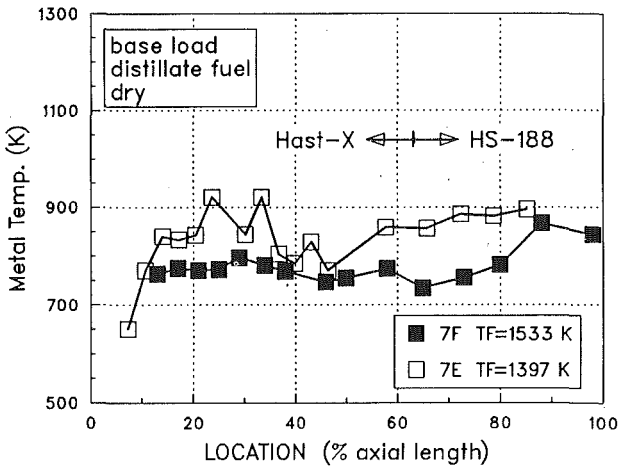

Fig. 23 Liner metal temperature distribution

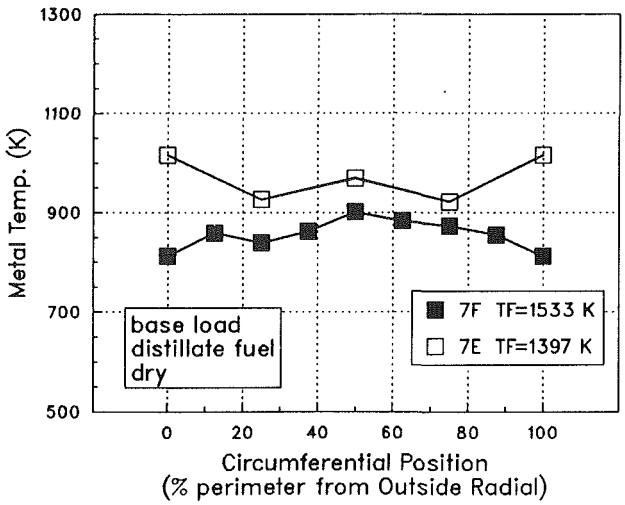

Fig. 24 Transition piece circumferential temperature distribution

MS7001E machine. The passively cooled, MS7001E transition piece shows a decided temperature rise on the outer radial panel, which coincides with the location of the mounting features. Higher stresses in proximity to the mounting feature in combination with temperature level therefore limit the capability of the transition piece when the bulk of the part has not approached the maximum operating temperature limit. The side walls of the MS7001F design show a moderate rise in metal temperature; however, as the stress levels in the side wall are relatively low, the metal temperature can be allowed to rise without creating a concern. Not only is the temperature more uniform as a result of the impingement cooling, but overall the temperatures are lower for the MS7001F design. Therefore, as a direct result of the impingement-cooled design and the consequent uniformity of temperature, the transition piece should exhibit improved longevity from enhanced low cycle fatigue and creep behavior.

The circumferentially averaged axial temperature distribution on the transition piece is shown in Fig. 25. Each temperature in the figure is the average of eight thermocouples located around the circumference of the transition piece. The thermocouples were positioned so as not to be directly in line with the impingement cooling jets, to ensure a temperature measurement that was not overly optimistic. The temperature distribution is seen to be fairly flat and is below the imposed temperature limit for the transition piece material.

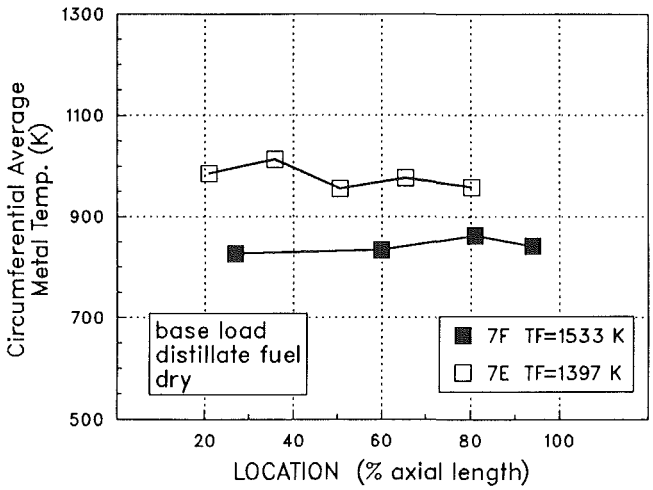

Fig. 25 Transition piece axial temperature distribution

Inspection Results

The combustion system inspection performed at the completion of the engineering test showed no operationally related hardware distress. One liner was inadvertently damaged during disassembly but was readily repaired. The combustion system was reassembled and the unit commissioned. During the engineering test, the unit accumulated 209 fired hours and 37 fired starts. It was recommended that the next inspection be performed after 3000 hours of operation.

At the first combustion inspection after commercial operation of the unit, an additional 3,965 fired hours and 96 fired starts had accumulated. The unit had operated primarily on gas fuel. The unit had operated for approximately six hours on distillate fuel prior to the planned shutdown for the inspection. The unit was brought down on a fired shutdown with distillate fuel.

The overall condition of the combustion system was very good. The inspection results indicate that the hardware is capable of at least 8000 hour inspection intervals. While some unexpected conditions were noted, they will not adversely affect the 8000 hour inspection interval.

Approximately half of the gas swirl tips were cracked to the point that reuse was not recommended. Since the inspection, a failure analysis and flow study were completed to understand better the cause of the swirl tip cracking. The work showed that the swirl tip is subject to large thermal gradients, causing thermomechanical fatigue. A modification that significantly reduces the magnitude of the stresses was developed and will be installed at the next scheduled outage.

The fuel nozzles also exhibited a buildup of hard carbon on the face. The carbon buildup only occurs with distillate fuel operation and is worst at low loads and during a fired shutdown. Since the inspection, flow studies and laboratory tests have identified design changes that will significantly reduce, if not eliminate, the buildup. Improved design fuel nozzles will be installed at the next scheduled outage.

Two liners exhibited a small perforation, approximately 0.5 in.^{2} (3.2 cm^2) of the splash plate and impingement plate. The carbon buildup on the gas tip face caused the perforation by blocking the gas fuel injection passage such that the fuel was forced around the back of the cap. Except for the perforation, no other area of the liner cap exhibited overly high temperatures based on metallurgical examination of the parts. Elimination of the fuel nozzle carbon buildup will prevent recurrence of this problem.

To some degree, all transition pieces had spalled regions of thermal barrier coating. The spalling is attributed to a greater

Downloaded 02 Jun 2010 to 171.66.16.121. Redistribution subject to ASME license or copyright; see http://www.asme.org/terms/Terms_Use.cfm

than desired coating thickness, as determined by chip samples. The excessive thickness of the coating is detrimental to the adhesion of the coating. Until recently, the coating was applied to the transition piece with a hand operation, resulting in poor control of the coating thickness. To improve the process control of this operation, a robotic operation was developed, producing a more uniform, correct thickness coating. Subsequent visual inspections made in December 1991 showed the coating to be in excellent condition.

Closing

As stated, this was the most detailed engineering test of a new gas turbine. Combustion component evaluation was a major portion of this field test. Test results verified the results from individual component and single chamber development testing. These results confirm the basic soundness of the mechanical design and the ability of the combustor to meet emissions requirements. Finally, the causes underlying the areas of minor hardware distress seen at the first combustion inspection are understood and changes to address these findings will be implemented at the next scheduled machine outage.

References

Brandt, D. E., 1988, "The Design and Development of an Advanced Heavy-Duty Gas Turbine," ASME JOURNAL OF ENGINEERING FOR GAS TURBINES AND POWER, Vol. 110, pp. 243–250.

Cincotta, G. A., 1990, "MS7001F Gas Turbine Test and Performance Evaluation," General Electric Report 3645, Schenectady, NY.

EPRI, 1985, "High Reliability Gas Turbine Combustor Project," EPRI AP-3885, Project 1801-1, Final Report.

Fitts, D. O., Symonds, R. A., and Western, E. R., 1990, "Combustion System Performance of a Water Injected MS7001E Gas Turbine Operating at a NO_x Emission Level of 25 ppmvd," ASME Paper No. 90-GT-71.

Hori, M., 1988, "Nitrogen Dioxide Formation by the Mixing of the Hot Combustion Gas With Cold Air," *Twenty-Second (International) Symposium on Combustion*, The Combustion Institute, pp. 1175–1181.

Downloaded 02 Jun 2010 to 171.66.16.121. Redistribution subject to ASME license or copyright; see http://www.asme.org/terms/Terms_Use.cfm

H. Kumakura

M. Sasaki

D. Suzuki

Central Engineering Laboratories,
Nissan Motor Co., Ltd.,
Yokosuka, Japan

Low NO_x Combustor for Automotive Ceramic Gas Turbine—Reliability Assurance

Two aspects of reliability assurance are discussed. First, this paper deals with the reliability design of emissions under transient conditions. The optimization was made from the simulation results of the relationship between the response of the variable combustor geometry to follow load changes and the resulting exhaust emission levels. The load variation pattern used in this investigation was that of the Japanese ten-mode regulation. Second, this paper describes the validity of the reliability design prepared for the ceramic liner of the combustor. A service life prediction was made for the liner on the basis of stress analysis results and fatigue parameters.

Introduction

The ceramic gas turbine engine is seen as being a promising alternative automotive engine because of its potentialities for meeting social and environmental requirements in the 21st century. The first report [1] dealt with the basic design of a prevaporization-premixing lean combustor capable of meeting Japan's ten-mode exhaust emission regulations for gasoline engine passenger cars. Several observations were presented in that report based on the results of combustion experiments conducted with the prevaporization system and a uniformly premixed fuel. It was shown that the uniformly premixed fuel. It was shown that the exhaust emission performance of this combustor, particularly its low NO_x level, is dependent on the premixed state of the liquid fuel, and that a uniform mixture must be formed in order to obtain low emissions while suppressing autoignition and backfire.

In the present work, ten-mode driving simulations were conducted to examine the functions and performance required of the combustor and associated devices in order to meet the sharp and frequent load changes demanded of cars. The simulations clarified the conditions needed to satisfy Japan's ten-mode exhaust emission standards. An investigation was then made of the structural reliability of the ceramic combustor liner. Ceramics are thought to be the most promising materials for various gas turbine components because of the high combustor inlet temperatures in a range of 1200 ~ 1300 K. Based on the results obtained, a method was devised for designing and selecting the material properties needed to meet the service life requirements. In addition, a test was conducted to evaluate the performance of a reaction-bonded SiC (RBSC) liner and a study was made of a method for predicting the service life of ceramic components.

Contributed by the International Gas Turbine Institute and presented at the 37th International Gas Turbine and Aeroengine Congress and Exposition, Cologne, Germany, June 1-4, 1992. Manuscript received by the International Gas Turbine Institute February 6, 1992. Paper No. 92-GT-109. Associate Technical Editor: L. S. Langston.

Modeling Emissions for the Ten-Mode Cycle

Figure 1 shows a cross-sectional side view of a two-shaft 75 kW regenerative ceramic gas turbine with variable stator vanes. In this TR-100V model gas turbine, the combustor is inserted vertically into the scroll. The specifications of the engine are given in Table 1.

Passenger cars in industrial countries around the world are required by statutory regulations to provide good exhaust emissions performance in certain prescribed model driving modes that simulate the sharp and frequent load changes of city driving. In this work, an investigation was made of the issues that must be considered in order to assure acceptable emissions performance under transient operating conditions, using Japan's ten-mode test as an example.

Ten-Mode Driving Simulation. In order to conduct driving simulations, it was necessary to prepare models of the engine dynamic characteristics, transmission, and vehicle. The numerical model of the engine was represented using a nine-dimensional model [2]. These equations took into account the

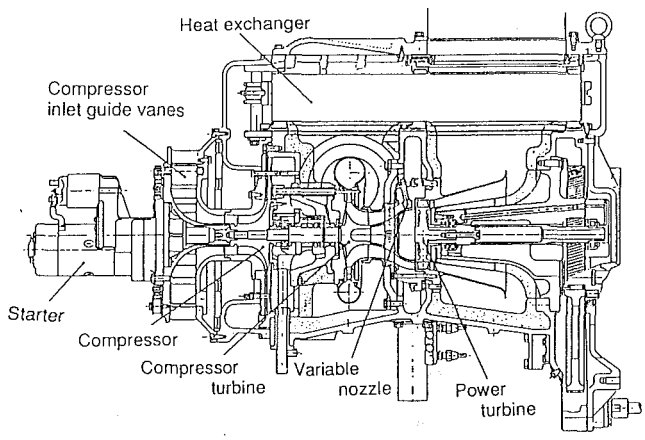

Fig. 1 Construction of TR-100V ceramic gas turbine

Copyright © 1993 by ASME
Downloaded 02 Jun 2010 to 171.66.16.121. Redistribution subject to ASME license or copyright; see http://www.asme.org/terms/Terms_Use.cfm

Table 1 Specifications of TR-100V engine

Type	2-shaft regenerative
Design power	75kW
Comperssor	single-stage cetrifugal compressor with inlet guide vanes
Compressor turbine	single-stage radial-flow turbine
Power turbine	single-stage axial-flow turbine with variable nozzle
Gasifier turbine speed	100,000rpm
Power turbine speed	75,000rpm
Heat exchanger	rotating heat exchanger (1 unit)

Table 2 Rotating heat exchanger specifications

Core dimensions	480mm in dia. x 71mm	Colburn factor	2.65 / Re
Hydraulic diameter	0.635mm	Density	1.92 x 10^{-6}(kg/mm^3)
Surface area/volume	3.28 (mm^2 /mm^3)	Design temperature efficiency	94 %
Specific heat	1.13 (kJ / kgK)		

design performance of the aerodynamic components and heat exchanger (HE) used in the TR-100V, the leakage and losses of each section, and the moment of inertia of each shaft. The TR-100V engine has been designed to improve fuel efficiency through the use of a rotating heat exchanger, which regenerates exhaust gas heat for preheating the air at the combustor inlet. But the HE must have a large thermal capacity, which can cause a response delay due to thermal inertia during transient operation. In conducting the driving simulations, it was recognized that the response delay originating in the large heat capacity of the HE would have a large governing influence on the required fuel flow rate and combustor inlet temperature. Consequently, the first task was to model the HE.

Conventional models of the dynamic characteristics of heat exchangers have usually had a matrix core that is finely divided in the circumferential and axial directions. With these models, differential equations have been formulated by concentrating the divided elements [3]. While this type of model can accurately approximate actual phenomena, a great deal of computer time is needed in order to improve calculation accuracy. As a result, incorporating this type of model directly into the engine model would have an undesirable effect on analysis efficiency. To avoid that problem a simplified HE model was created in this work by substituting low-order transfer functions for the conventional finely divided model. Table 2 gives the HE specifications used in the divided model.

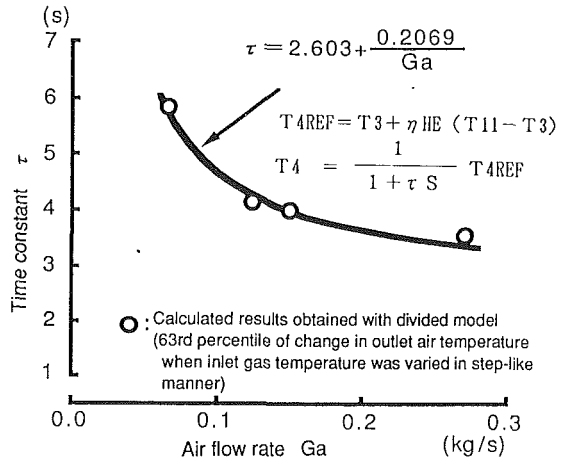

Fig. 2 Heat exchanger model

Indentification calculations were made with a model having a one-order delay. It provided accurate approximations of the changes in the time constant. At the point where the time constant became double, the temperature changes obtained with the first-order delay model were approximately 10 percent larger than the results of the calculations made with the divided model. It was decided, therefore, that the first-order delay model would be more suitable for modeling the gas turbine engine, since under mode driving the inlet gas temperature would vary frequently in response to load changes. Figure 2 shows a model of the time constant, which varies according to the airflow rate, and the calculation procedure. As indicated in the figure, the time constant, τ, was modeled only as a function of the airflow rate, Ga.

Results of Ten-Mode Driving Simulation. An actual ten-mode test is conducted under a hot engine condition after the test vehicle has been driven through several cycles of the mode. In order to simulate this test process, the engine condition at the start of driving in the simulations was set to coincide with the condition in the 135th second following ten-mode driving. The gross vehicle weight was calculated as 1100 kg plus the weight of five passengers.

The turbine inlet temperature (TIT) limit of the TR-100V is 1623 K. The gas temperature limit at the HE inlet, which is determined by the heat resistance capability, was set at 1323 K in the simulations. Generally, as the engine load decreases, the TIT shows a smaller drop and the gas temperature at the HE inlet rises. Consequently, the TIT must be lowered in order to keep the inlet gas temperature within the allowable limit. The ten-mode driving simulations were all conducted within this restricted temperature range. The results of ten-mode sim-

Nomenclature

A, B = areas
b = width of a disk, mm
F = failure probability after service life
Ga = air flow rate, kg/s
h = thickness of a disk, mm
KIc = stress intensity factor
k = experimental constant
m = Weibull modulus
N = crack growth parameter
n = experimental constant
P = combustion pressure, MPa
R = neutral plane radius of a disk, mm
T = temperature K
T_3 = heat exchanger air inlet temperature, K
T_4 = heat exchanger gas inlet temperature, K
T_{4REF} = target outlet air temperature, K
T_{11} = heat exchanger gas inlet temperature, K
T_{IN} = combustor inlet temperature, K
t_{LIFE} = service life
V_{ER} = effective volume
δ = weight gain due to oxidation, mg/cm^2
η_{HE} = heat exchanger efficiency
κ = section modulus
λ = excess air ratio
λ_{pp} = excess air ratio in lean combustion zone
$\Delta\lambda_{pp}$ = change in λ_{pp} for 1 percent change in maximum hole area
σ = stress
τ, T_c = time constant s

Subscripts

ref = reference condition
$< >_{EI}$ = emission index
4_{PB} = four-point bending

Downloaded 02 Jun 2010 to 171.66.16.121. Redistribution subject to ASME license or copyright; see http://www.asme.org/terms/Terms_Use.cfm

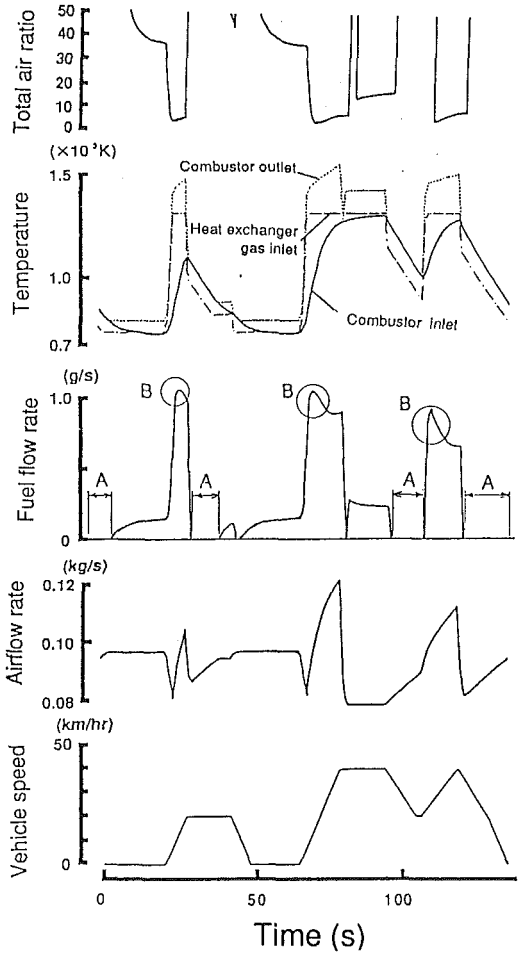

Fig. 3 Ten-mode simulation results

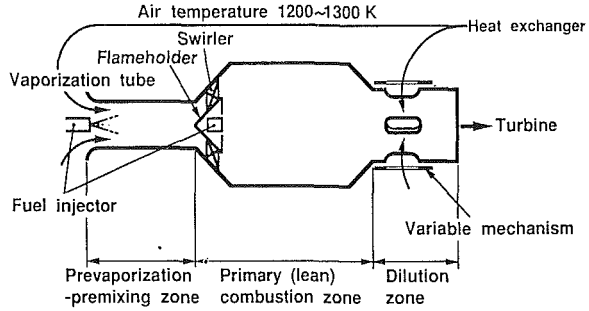

Fig. 4 Construction of prevaporization-premixing lean combustor

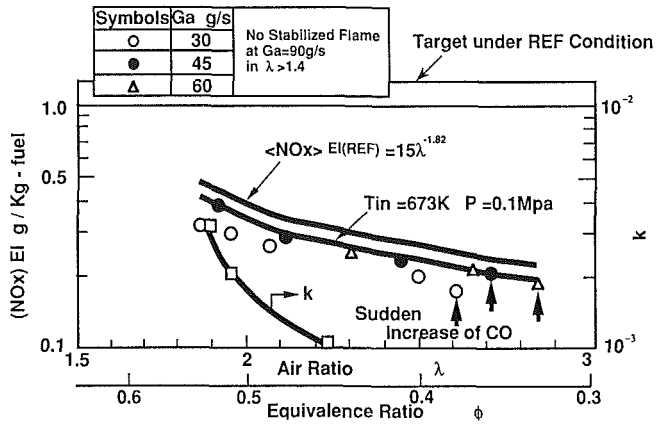

Fig. 5 NO_x emission characteristics of premixing lean combustion of diesel fuel

ulations, which incorporated the abovementioned HE model are given in Fig. 3.

During Acceleration. When the fuel supply is increased to accelerate a vehicle from an idling condition, the HE is still at a relatively low temperature. As a result, in addition to supplying the fuel needed to generate the power output for net acceleration, it is also necessary to supply fuel for heating the large-thermal-capacity HE. The fuel injection pattern needed for acceleration, therefore, must show a rapid rise in the quantity of fuel injected initially. (This is indicated in Fig. 3 as the portion of the fuel flow rate designated as *B*.) Accordingly, in order to obtain a richer mixture, the total air ratio at the onset of acceleration should be made smaller than the excess air ratio corresponding to the power output for steady-state operation. This measure is needed in order to assure a low NO_x level.

During Steady-State Driving and Deceleration. When a vehicle resumes steady speed operation following the completion of acceleration or during deceleration, the thermal inertia of the HE gives rise to the opposite phenomenon of what occurs during acceleration. In either of these situations, a region is momentarily maintained in which a certain level of engine output is provided by the stored enthalpy of the HE alone even though the fuel supply has been sharply reduced. In this case, the total excess air ratio must be greatly increased to obtain a leaner mixture and thereby prevent an increase in CO emissions and extinguishing of the combustion flame. A fuel cutoff control was provided in this work to cut the fuel supply in this region (indicated as portion *A* of the fuel flow rate). As a result, this improved fuel efficiency by approximately 15 percent compared with the level obtained when the minimum fuel quantity was limited to the fuel flow rate for idling in all speed ranges. On the negative side, there is also the concern that large amounts of unburned HC and CO could be generated when re-ignition occurs. Consequently, the re-ignition conditions and ignition mechanism need to be optimized.

Because of the response delay that occurs during acceleration and deceleration, it was found that the primary fuel injector for prevaporization should have a turn-down ratio of at least 10 even when operation is limited to the region of ten-mode driving.

Emissions. The general structure of the prevaporization-premixing lean combustor is shown schematically in Fig. 4. Under ten-mode driving, all fuel is supplied by the primary injector at the most upstream position. After prevaporization and premixing, the fuel is supplied to the main combustion zone where lean combustion takes place. In this lean combustion zone, it is necessary to maintain a λ_{pp} (excess air ratio in lean combustion zone) that provides a sufficiently low NO_x level and sufficiently stable combustion regardless of changes in the total excess air ratio.

A prediction was made of the NO_x level using the emission index noted in the previous report [1]. Experimental NO_x emission equations were obtained by varying air ratio, inlet air temperature and pressure. Figure 5 shows one of those experimental results. This index is given by the following expression, based on data for lean combustion of a uniformly premixed fuel (JIS No. 2 light fuel).

$$<NO_x>_{EI} = <NO_x>_{EI_{REF}} (P/P_{REF})^n \exp\{k(T_{IN} - T_{IN_{REF}})\}$$

$$<NO_x>_{EI_{REF}} = 1.5\lambda_{pp}^{-1.82} \quad (1)$$

where $T_{IN_{REF}}$ = 773 K, P_{REF} = 0.1MPa, n = 0.3, k = 1.8 × 10^{-3} (at λ_{pp} = 2) and the effective range is $1.9 < \lambda_{pp} < 2.6$.

A time history profile of the NO_x level calculated with Eq. (1) is shown in Fig. 6 in relation to T_{IN} and P. Integrating

Downloaded 02 Jun 2010 to 171.66.16.121. Redistribution subject to ASME license or copyright; see http://www.asme.org/terms/Terms_Use.cfm

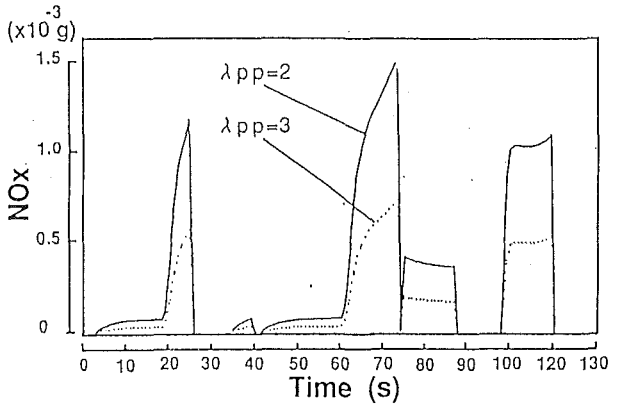

Fig. 6 NO_x simulation results for effect of λ_{pp}

these predicted NO_x values yields the total NO_x level for ten-mode driving. As seen in the figure, the predicted values for $\lambda_{pp} = 2$ and 3 both clear the current standard of 0.25 g/km.

However, these predictions were based on experimental data for combustion of a completely uniform premixed light fuel. As mentioned in the previous report [1], the required condition for uniform premixing is complete vaporization of over 90 percent of the initial fuel spray. The atomization performance required of the injector to attain that level of vaporization is an exceptionally rigorous value of d0.9 V (maximum droplet diameter in 90 percent of the fuel volume) $< 60\ \mu$m. Under real-world conditions, it is necessary to take into account fuel droplets that are not completely vaporized and the presence of a residual nonuniform mixture. In the basic experiment that was conducted to find Eq. (1), the stable combustion range at $T_{IN} = 673$ K was set at $\lambda_{pp} < 2.6$. However, in places where T_{IN} is higher than 673 K, it should be possible to obtain stable combustion in a higher λ_{pp} region (i.e., lean mixture). To assure stable combustion in a lean mixture region of $\lambda_{pp} = 3$ as shown in Fig. 6, a larger margin must be allowed for clearing the NO_x emission standard.

On the other hand, the CO level tends to be strongly influenced by the total excess air ratio, unlike NO_x emissions, which are governed only by the excess air ratio λ_{pp} in the lean combustion zone. As seen in Fig. 3, there was a lack of systematic data for total excess air ratios above 20, which made it impossible to predict emissions behavior in an ultralean region, such as what occurs during deceleration.

One effective way to assure stable combustion under a condition of a very small fuel flow rate is to raise the combustor inlet temperature, which can generate beneficial effects in many other areas as well. For instance, it promotes the formation of a leaner mixture (e.g., λ_{pp} 2 —> 3) than the air ratio λ_{pp} set for the premixed lean combustion zone. It also serves as a countermeasure against an increase in unburned HC and CO emissions at the time of re-ignition following a fuel cutoff, as mentioned in the previous section. Specific measures that can be adopted here to raise the inlet temperature include reducing the idle speed of the gasifier turbine and raising the matching engine temperature through the use of variable inlet guide vanes at the compressor inlet.

Simulations were carried out in which it was assumed that these control methods were adopted. The combustor inlet air temperature was raised from the original level of approximately 750 K to 973 K and 1173 K and predictions were made of the respective NO_x emission level. The results shown in Table 3 indicate that NO_x emissions could be maintained at a sufficiently low level in ten-mode driving so long as the inlet temperature is in this high-temperature range.

Table 3 NO_x simulation results for effect of temperature

Minimum air temperature at combustor inlet (K)	Predicted NOx level (g/km)
Apporx. 750 (original)	0.061
973	0.064
1173	0.073

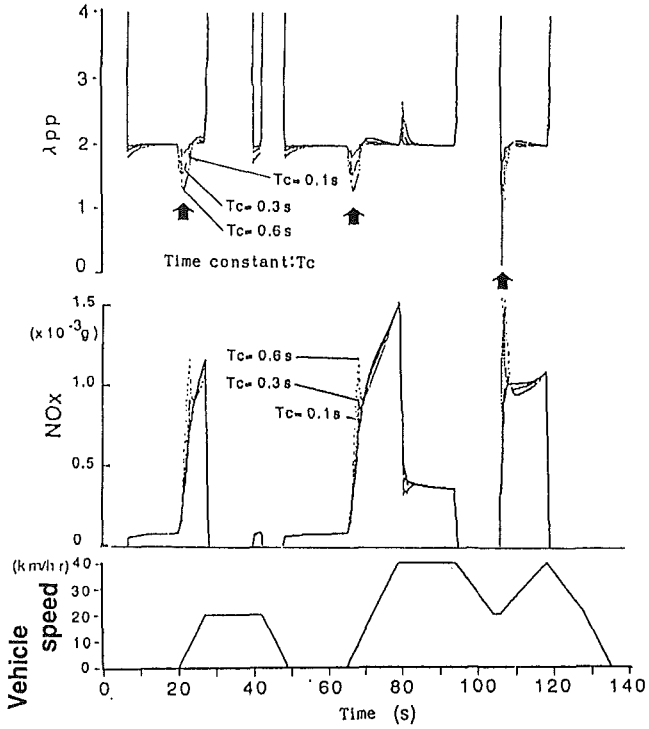

Fig. 7 Effect of response delay of variable mechanism (ten-mode)

A Proposed Variable Geometry Mechanism

The variable mechanism is intended to control the amount of air inducted into the main (lean) combustion zone in order to maintain the λ_{pp} in the zone in a suitable range regardless of changes in vehicle operating conditions. The variable mechanism must be able to assure a wide range of air distribution ratios. Further, it must also respond sensitively to changes in the fuel flow rate and adjust the air distribution ratio accordingly in order to maintain the λ_{pp} in the lean combustion zone at the optimum value at all times.

Figure 7 shows the effect of the responsiveness of the variable mechanism on the set λ_{pp} value and NO_x level. (Responsiveness here means the ability to follow the indicated control value.) For the sake of simplicity, it was assumed that a linear relationship existed between the control value of the variable mechanism and the air distribution ratio. The effects of the responsiveness of the variable mechanism were calculated assuming that it had a time constant of 0.1 ~ 0.6 s as indicated in Fig. 7. The effect of the delay by the variable mechanism in following the control value caused the air ratio to shift to the rich side during acceleration and to the lean side during deceleration in relation to the set λ_{pp} value in the lean combustion zone. The difference from the set λ_{pp} value became more pronounced as the time constant increased. However, when control was performed with λ_{pp} set at 2, the shift to the lean side was not so large as to extinguish the flame; the critical issue was the shift to the rich side (indicated by the downward arrow in Fig. 7). When re-accelerating from 20 to 40 km/h in particular, there was a brief interval when λ_{pp} dropped to nearly

Downloaded 02 Jun 2010 to 171.66.16.121. Redistribution subject to ASME license or copyright; see http://www.asme.org/terms/Terms_Use.cfm

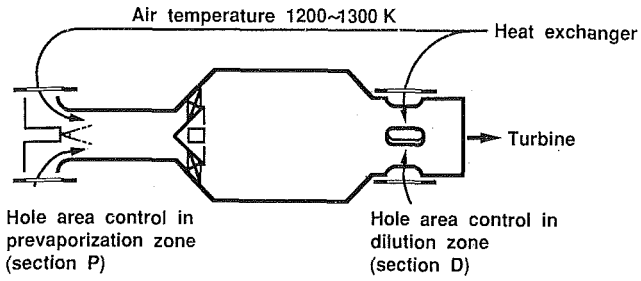

Fig. 8 Locations for installing variable mechanism

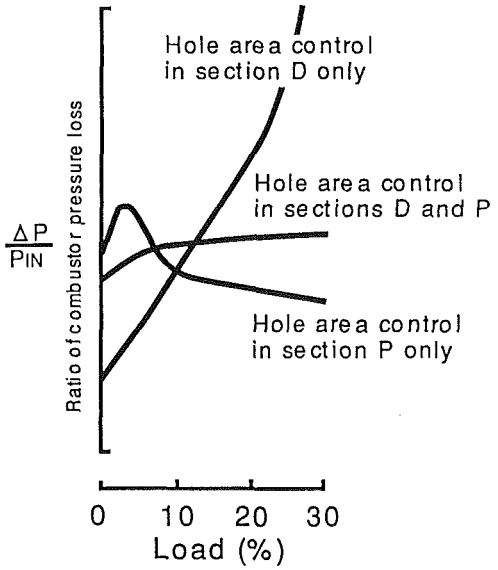

Fig. 9 Ratio of combustor pressure loss versus engine load rate

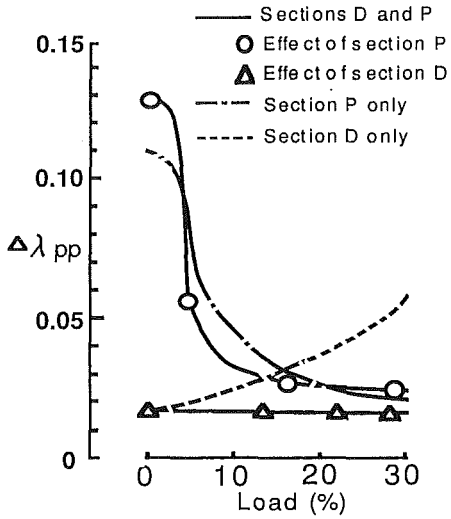

Fig. 10 Effect of hole are a control error on set λ_{pp} value

Table 4 Advantages and disadvantages of different locations for installing variable mechanism

	Hole area control in section P only	Hole area control in section D only	Hole area control in section D and P
Pressure loss	Fair	Poor	Good
Control sensitivity	Fair	Good	Fair
Simplicity of construction	Good	Fair	Fair

1.0 even though the time constant was 0.1 s. With a time constant of 0.3 s or 0.6 s, there were even regions where λ_{pp} fell below 1.0, indicating an excessively rich mixture. In the range of applicability of the NO_x model in Eq. (1), λ_{pp} was greater than 1.9 and so there was no clear indication of the sharp increase that actually occurred in the NO_x level. It is estimated that when $\lambda_{pp} = 1.0$, the NO_x level would increase by more than one order of magnitude.

Consequently, in order to shorten the interval in which the NO_x level rises during the initial period of acceleration, it is thought that a time constant of less than 0.1 s should be assured for the response performance of the variable mechanism. Even that time constant will not be able to prevent λ_{pp} from shifting to the rich side when accelerating from a cruising speed or during fast start-off acceleration. Therefore, the fuel supply rate should also be controlled in concert with the operation of the variable mechanism.

As shown in Fig. 8, there are two conceivable places where the variable mechanism could be installed to control the hole area through which air is inducted. One location is in the prevaporization zone (section *P*) and the other is in the dilution zone (section *D*). Three different variable control approaches are possible: (1) apply control only in section *P*; (2) apply control only in section *D*; (3) apply control in both sections. Figure 9 shows the general pressure loss characteristics obtained with each method. With the first approach, combustor pressure loss increases in the low-load region. With the second approach, assuming that the minimum allowable pressure loss is determined by the flow velocity required in the prevaporization zone under a low load, the pressure loss rises sharply with increasing load. In addition, with this approach it would be necessary to ensure that the variable mechanism operates reliably in the hot section at a relatively far distance from the engine surface. The third approach would basically allow the pressure loss characteristic to be determined freely and a flexible characteristic could be selected. Naturally, this approach would involve the installation of two variable mechanisms, which would make the engine construction more complicated.

Figure 10 shows the effect of error in hole area control on the set λ_{pp} value. When control is applied in the *P* section or in both the *P* and *D* sections, λ_{pp} shows high sensitivity to variation in the hole area in the low-load region near idle speed. As a result, it is apt to deviate from its set value. This indicates that the variable mechanism components would require high machining accuracy and a high level of control accuracy would have to be assured. On the other hand, when control is applied only in the *D* section, the sensitivity of λ_{pp} to hole area variation increases in the high load region, but the degree of sensitivity is smaller than that seen with the other two methods. As a result, λ_{pp} is less likely to deviate from its set value. The advantages and disadvantages of each variable control approach are summarized in Table 4 with respect to the foregoing observations. These are points that designers should take into consideration when selecting the optimum system.

Strength of the Ceramic Liner

Analysis of Ceramic Liner Reliability. Finite element analysis was used to calculate the stress distribution of a ceramic liner for a diffusion flame combustor under conditions equivalent to the design power output. The calculated results are shown in Fig. 11 and the material properties used in the calculations are given in Table 5. With this liner, the maximum tensile stress occurred around the secondary air holes and that value was the greatest under design power output conditions for both steady-state and transient operations. The maximum transient thermal stress at the time of ignition was lower than the maximum thermal stress seen in Fig. 11, which suggests

Downloaded 02 Jun 2010 to 171.66.16.121. Redistribution subject to ASME license or copyright; see http://www.asme.org/terms/Terms_Use.cfm

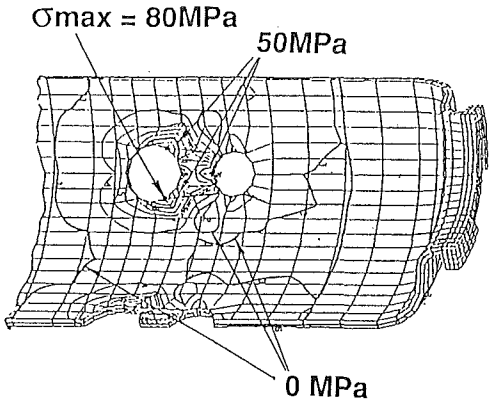

Fig. 11 Thermal stress distribution (for operation at design power output)

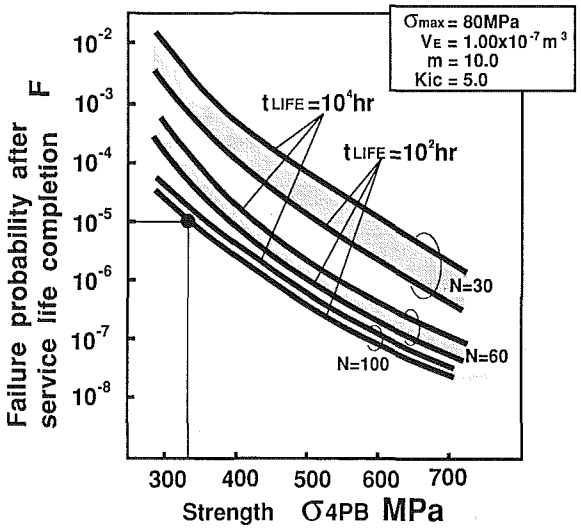

Fig. 12 Failure probability after service life completion versus material strength

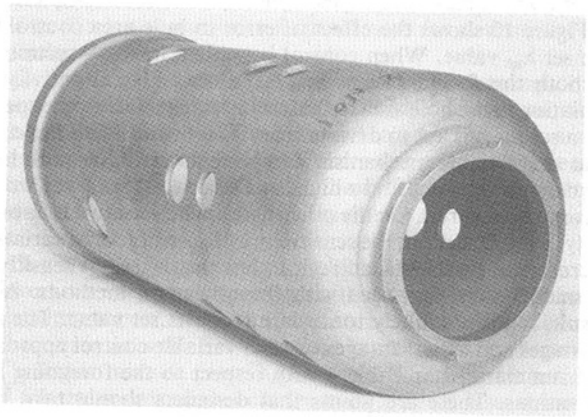

Fig. 13 Test ceramic liner

that transient thermal stress did not contribute significantly to a decline in service life.

Estimates were made of static fatigue, i.e., slow crack growth, based on the stress analysis results. Reliable data of crack growth parameter (N) were not obtained. Consequently, the possibility that N would have a value in a range of 30 ~ 100 was considered. We will assume that the load frequency distribution of a vehicle during its lifetime can be estimated roughly as indicated in Table 6. Then, the static fatigue after 150,000 km of operation (including 1.5×10^4 starts) can be calculated in terms of a comparable period of time under conditions equivalent to the design power output. Under a condition where the load is less than 40 percent, it does not contribute significantly to a decline in service life. The service life, t_{LIFE}, calculated under design power output conditions is less than 200 hours.

Table 5 Material properties of RBSC

Young's modulus	3.1×10^4 MPa
Coefficient of thermal expansion	4.4×10^{-6} 1/K
Thermal conductivity	50.24 W/mK
Specific heat	3.2×10^{-3} J/mm^3 K
Poisson ratio	0.26
3-point bending strength	286 MPa *
Weibull distribution factor	9.4

* Following surface polishing and oxidation at 1493K for 100hr

Table 6 Load fluctuation frequency and service life of passenger cars

Load range(%)	Frequency ratio
0~10	0.1
10~20	0.2
20~40	0.55
40~80	0.1
80~100	0.05

Predictions were made of the failure probability in relation to the service life under conditions equivalent to the design power output when $N = 30 \sim 100$ and the expected Weibull modulus was $m = 10$. The results are given in Fig. 12. The failure probability at around a design life of 200 h was found to be on the order of 10^{-4} for the strength level given in Table 5, which would not be sufficient performance for an automotive component. The failure probability required after the completion of the design service life is less than 10^{-5}. Reducing the failure probability to that level would require material strength of approximately $\sigma_{4PB} \geq 350$ MPa in terms of four-point bending strength. This indicates that either the strength of the material will have to be improved or a reduced stress design will have to be adopted.

Based on the results of the foregoing investigations, a test was conducted to evaluate a ceramic (RBSC) liner for use in a diffusion flame combustor. The test liner had an inner diameter of 85 mm and an average thickness of 1.8 mm (Fig 13). The properties of the RBSC material are given in Table 5. The ceramic liner was fabricated by cold isostatic pressing (CIP). A typical test piece showed a weight gain due to oxidation, δ, of approximately 2 mg/cm^2 after exposure to the atmosphere and the combustion gas stream for 100 h at 1623 K. A weight gain on this order does not show any significant correlation with material strength [4]. The combustion test of the linear was carried out at atmospheric pressure and under temperature and volumetric airflow rate conditions matching those of actual gas turbine operation. The maximum thermal stresses recorded under design power output and under cyclic operation were 36 MPa and 39 MPa, respectively. An ignition experiment was also conducted while constantly maintaining the combustor inlet temperature below 323 K. The maximum transient thermal stress measured in that experiment was 41 MPa after 120 s of operation.

The experimental apparatus was constructed such that the combustion air stream could be heated directly by the precombustor as well as by the rotating HE in order to simulate

Downloaded 02 Jun 2010 to 171.66.16.121. Redistribution subject to ASME license or copyright; see http://www.asme.org/terms/Terms_Use.cfm

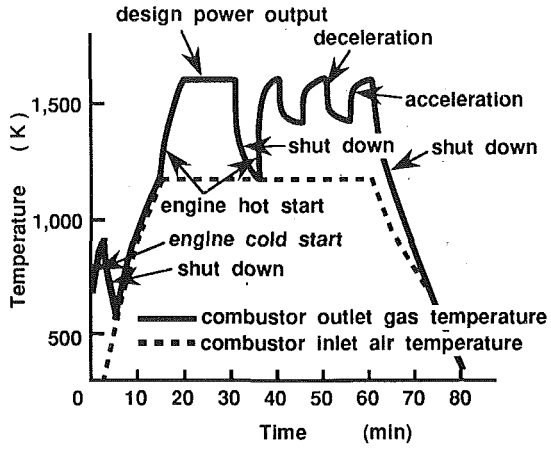

Fig. 14 Cyclic test pattern

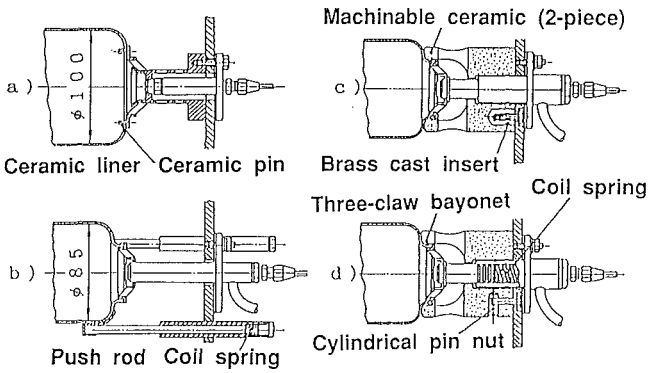

Fig. 15 Changes in ceramic liner support design

the combustor inlet temperature conditions of an actual gas turbine. The cyclic operation pattern is shown in Fig. 14. The failure probability of the liner following cumulative testing for a total of approximately 300 h was estimated from a static fatigue analysis to be less than 6×10^{-5}. Similarly, disk-shaped pieces were also cut from a new liner and measurements were made of the radial crushing strength. A comparison of liner strength values before and after use is given in Table 7. Calculations made with a static fatigue model ($m = 6.4$) indicated that the degree of strength degradation attributable to the test evaluation would be approximately 17 percent. The values in Table 7 show that the liner strength following the test evaluation was about 10 percent lower than that of a new liner, although the Weibull modulus was higher. Much more testing will have to be done in order to confirm whether there is any significant difference in strength before and after use.

This radial crushing strength test procedure offers a number of excellent advantages. The level of strength degradation that occurs prior to liner failure can be identified. The radial crushing strength of a disk is a relatively easy-to-manage parameter, which facilitates ready application of the test method. It is also possible to maintain the surface condition of the product under test. This procedure is seen as being a valuable tool for conducting systematic evaluations of the service life of products. In addition, comparisons of disk-shaped test pieces having different diameters revealed that the test procedure provides an excellent description of the dimensional effects obtained according to the effective volume [4]. Although the radial stress distribution of a disk is relatively complex, the following expression provides an accurate approximation of effective

Table 7 Comparison of radial crushing strength of used and new ceramic liners

Use history	Number of Test piece	Radial crushing strength	Weibull distribution factor
New liner	10	244 MPa	6.4
After 300hr of testing	6	221 MPa	10.3

volume, V_{ER}, in cases where the diameter of a disk is sufficiently larger than its thickness:

$$V_{ER} = 2bhR(\pi/2 - \phi 0)/(m+1)^2 \quad (3)$$

where $\phi 0 = \cos^{-1}\{2[1+\kappa(1-2R/h)]/(1+\kappa)/\pi\}$, $\kappa = (R/h) \ln\{(R+h/2)/R-h/2)\} - 1$.

Based on the results of a three-point bending test (Table 7), the concept of effective volume was applied to estimate the strength of a new liner and a significant difference was found. Therefore, in addition to evaluating actual components, it is felt that the radial crushing strength test procedure for ceramic disks having an as-fired surface is a valid test method for standard test pieces.

Investigation of Liner Support Construction. In the initial period of the combustion test evaluation described above, there were numerous instances where the liner was damaged because of changes that occurred in the alignment of the liner support structure. The support went through several design changes and improvements as shown in Fig. 15(*a*)-(*d*). The design was changed from a simple pin support to a flexible rod support and finally to a flexible bayonet support. The final specification featured a three-claw bayonet (Fig. 13 and Fig. 15(*d*)) combined with a flexible lever, which eliminated the problems stemming from the support structure. As this example illustrates, careful attention must also be paid to the structural design of associated components in order to bring out the maximum benefits offered by the excellent properties of ceramics.

Conclusion

The results of the present work are summarized below:

1 The thermal inertia inherent in a high-efficiency heat exchanger gives rise to thermal delay under transient operation. As a result, the total air ratio, fuel supply rate, and other combustion conditions show markedly large changes compared with quasi-steady-state changes.

2 The response delay of the variable mechanism has an adverse effect on the NO_x level, especially during acceleration. To prevent the NO_x level from increasing, a small time constant of around 0.1 s is required.

3 Service life can be treated in terms of static fatigue life even when consideration is given to non-steady-state conditions such as starts.

4 Conducting radial crushing strength tests on disk-shaped pieces is a suitable method for assessing standard test pieces, evaluating material strength, and assessing the strength of actual components.

References

1 Sasaki, M., Kumakura, H., and Suzuki, D., "Low NO_x Combustor for Automotive Ceramic Gas Turbine—Conceptual Design," ASME Paper No. 91-GT-369, 1991.

2 Kumakura, H., et al., "A Control System for a High-Quality Generating Set Equipped With a Two-Shaft Gas Turbine," ASME JOURNAL OF ENGINEERING FOR GAS TURBINES AND POWER, Vol. 113, 1991, pp. 290-295.

3 Itoh, T., et al., "Analytical Consideration of Fuel Economy and Dynamic Response of a Regenerative High Temperature Automobile Gas Turbine," ASME Paper No. 79-GT-127, 1979.

4 Sasaki, M., et al., "Development of a Reaction Sintered SiC Combustor Liner and Issues Remaining to be Solved," *Gas Turbine Society of Japan* [in Japanese], Vol. 16-63, 1988.

Downloaded 02 Jun 2010 to 171.66.16.121. Redistribution subject to ASME license or copyright; see http://www.asme.org/terms/Terms_Use.cfm

Development of a Liquid-Fueled, Lean-Premixed Gas Turbine Combustor

L. H. Cowell

K. O. Smith

Solar Turbines Inc.,
San Diego, CA 92101

Development of a lean-premixed, liquid-fueled combustor is in progress to achieve ultra-low No_x emissions at typical gas turbine operating conditions. A filming fuel injector design was tested on a bench scale can combustor to evaluate critical design and operating parameters for low-emissions performance. Testing was completed using No. 2 diesel. Key design variables tested include premixing length, swirler angle, injector centerbody diameter, and reduced liner cooling. NO_x emissions below 12 ppmv at 9 bar pressure were measured. Corresponding CO levels were 50 ppmv. An optimized injector design was fabricated for testing in a three injector sector of an annular combustor. Operating parameters and test results are discussed in the paper.

Introduction

Stationary gas turbine manufacturers are being driven to control NO_x emissions to greater extents. For midsize industrial gas turbines, NO_x emissions levels below 25 ppmv are being sought in some areas in the near term with below 10 ppmv desired in the 5 to 10 year frame. Presently, NO_x emissions are controlled to the 25-to-50 ppmv level through the use of water or steam injection. To reduce emissions to the 10 ppmv level, Selective Catalytic Reduction (SCR) is the only commercially available technology. Recent advancements in lean-premixed combustion technology to control NO_x emissions to 25 ppmv and below have been significant and suggest that this control technology can be an alternative to water injection and SCR. The use of lean-premixed combustion for "dry" NO_x control avoids the technical problems and high costs associated with these control methods. The majority of lean-premixed combustor development to date has been completed using natural gas fuel.

The development of lean-premixed combustion technology using liquid fuels has trailed the work being completed using natural gas, but has been demonstrated as a viable approach (Smith and Cowell, 1989a; Smith, 1987, 1983). The combustor concept being developed uses lean-premixed/prevaporized combustion to limit NO_x emissions. Emissions are reduced by operating the burner primary zone at a leaner fuel/air ratio than is conventional. In addition, premixing reduces fuel/air mixture inhomogeneities that can cause locally high gas temperatures that can contribute significantly to NO_x emissions.

Program Overview

Solar Turbines, with co-sponsorship from the California Energy Commission's Energy Technology Advancement Program, has been engaged in advancing the lean-premixed combustion technology for liquid fuels toward engine readiness. The study described in this paper is an intermediate step in this process to define the key design variables of lean-premixed, liquid-fuel injector through experimental rig testing and evaluation. The program used No. 2 diesel fuel for firing the test cylindrical can combustor. This information has been used to scale and design injectors for testing in a sector of an annular combustor. Sector testing is in progress.

Combustion System Description

The ultralow NO_x injector and can combustor assembly is illustrated in Fig. 1. Key features of the combustor and injector assemblies are presented below, which include the primary air swirler, fuel injector, and combustor liner.

Primary Air Swirler. A 16-vane, axial flow swirler is used to impart a high degree of swirl to the primary combustion air. This swirl serves two purposes. First, the swirl aids in fuel/air premixing as described in detail below. More importantly, the swirling flow acts to stabilize the combustion process in the burner primary zone. The vortex motion in the primary zone recirculates hot combustion products back upstream along the combustor axis toward the swirler. The recirculated hot products act as an ignition source for the incoming fuel/air mixture, thus providing a stable flame.

In earlier development of the filming injector (Smith and Cowell, 1989b), a radial swirler was used. An axial swirler was employed for the second-generation design because of its more compact size and its use as standard engine hardware. The radial swirler was also retested in an effort to replicate data and to investigate the influence of swirler blade angle on combustor performance. The radial swirler design has provisions for changing the blade angle, where the axial swirler does not.

Fuel Injector. The key to obtaining low NO_x emissions with clean liquid fuels (very low fuel-bound nitrogen levels) is va-

Contributed by the International Gas Turbine Institute and presented at the 37th International Gas Turbine and Aeroengine Congress and Exposition, Cologne, Germany, June 1–4, 1992. Manuscript received by the International Gas Turbine Institute February 6, 1992. Paper No. 92-GT-112. Associate Technical Editor: L. S. Langston.

Copyright © 1993 by ASME
Downloaded 02 Jun 2010 to 171.66.16.121. Redistribution subject to ASME license or copyright; see http://www.asme.org/terms/Terms_Use.cfm

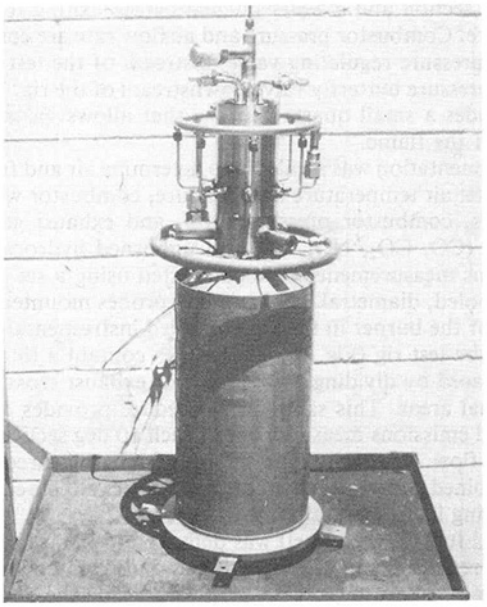

Fig. 1 Ultralow NO_x injector and can combustor assembly

porization of the fuel and effective mixing of the fuel and air flow prior to combustion. The vaporization and premixing processes must be completed in a relatively short time to avoid autoignition in the fuel/air mixing passage. In addition, the mixing must involve reasonably smooth flows so as to avoid wakes and recirculating flows in the mixing region. Such low velocity zones increase the likelihood of "flashback" from the primary zone.

The injector design concept consists of an air swirler, an injector centerbody, filming injector orifices, a premixing passage, and a pilot fuel burner assembly. The injector design is shown in Fig. 2. Air enters the injector through a passageway between the injector centerbody and the outer injector sleeves. Air passes through the swirler and into the premixing passage. The premixing passage is where the fuel film is created, the fuel vaporizes, and the fuel and air mix. Fuel is filmed onto one or two surfaces. Typically, the majority of the fuel is filmed on the centerbody (designated "inner filming") with the remaining fuel filming on the outer wall of the premixing passage ("outer filming"). The pilot fuel burner is located at the downstream end of the injector. Fuel is filmed on both inner and outer surfaces through 32 discrete orifices. The pilot injector does not include fuel premixing and does not operate in the lean premixed mode. The pilot burner is used at light-off only and is then extinguished.

The fuel injection concept employs filming of the liquid fuel on the cylindrical surface of the centerbody and the outer walls of the premixing passage. The fuel film is carried downstream to the primary zone by the shear stresses imposed by the swirling primary airflow. The fuel vaporizes and then premixes as the film progresses along the centerbody. The injector is functioning correctly when the fuel is fully vaporized and premixed with the air at the downstream end of the injector attached to the combustor liner. In practice at certain operating conditions, insufficient residence time exists in the swirler channel to allow fuels with low vapor pressure fractions such as No. 2 diesel to vaporize completely. To augment fuel vaporization, an air-assist capability is incorporated in the centerbody and outer premixing passage wall designs. These secondary airstreams exit from the downstream ends of both the centerbody and outer wall through an annular gap just inside the centerbody lip and just outside the outer wall termination. The air-assist stream acts to atomize any remaining fuel film as it flows off the centerbody and into the primary zone.

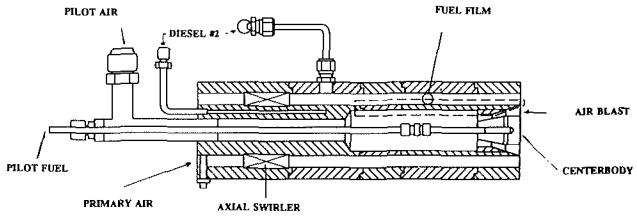

Fig. 2 Ultralow NO_x injector concept

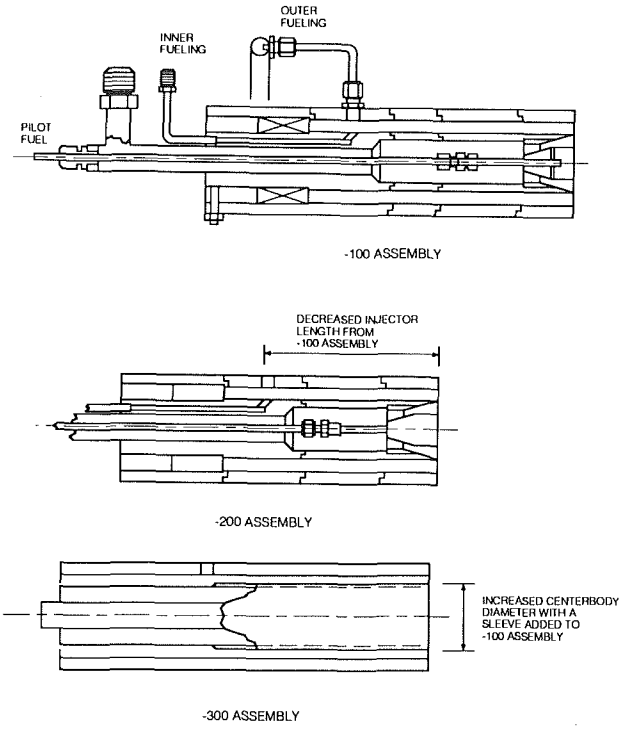

Fig. 3 Three liquid-fueled low NO_x injector assemblies

A total of four different assemblies of the liquid filming injector concept have been tested. A schematic of three of these assemblies is included as Fig. 3. The assembly not illustrated includes a radial swirler. This assembly was tested in the feasibility study. Tests have been completed with these assemblies to study the influence of an axial swirler versus a radial swirler, premixing length, and centerbody diameter.

The Radial Swirler Assembly. The prototype assembly described by Smith and Cowell (1989b) was used to evaluate the feasibility of the filming, premixing injector concept. The injector was operated demonstrating superior emissions characteristics. This assembly has the baseline premixing passage dimensions. Axial swirlers are typically used in gas turbines with annular combustors due to space constraints in the engine casing. A radial swirler was used in the feasibility study because the vane blade angle is easily changed and the aerodynamic characteristics of this swirler had been established in earlier lean-premixed injector development using natural gas as the fuel.

The −200 Assembly. As a means of verifying that the injector with the axial swirler performs with the same emissions characteristics as the injector with the radial swirler, the −200 assembly was fabricated and tested. This assembly, shown in Fig. 3, is basically the same injector as the radial swirler assembly with the exception of an axial swirler replacing the radial swirler. The blade angle of both types of swirlers was set the same with the goal of establishing the same swirl angle

Downloaded 02 Jun 2010 to 171.66.16.121. Redistribution subject to ASME license or copyright; see http://www.asme.org/terms/Terms_Use.cfm

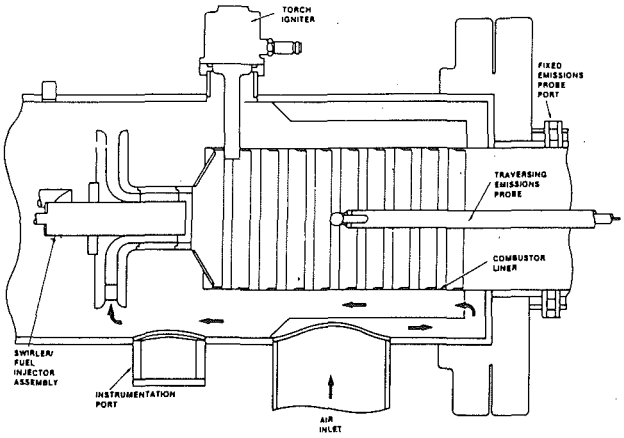

Fig. 4 Combustor test rig schematic

with both assemblies. The length of the air/fuel vaporizing and premixing passage is identical to that of the radial swirler assembly.

The −100 Assembly. For this assembly the same injector as the −200 assembly was modified by increasing the premixing passage by 2 centerbody diameters. The added length to the premixing passage provides additional residence time for fuel vaporization and air/fuel mixing.

The −300 Assembly. The −300 differs from the other assemblies by the addition of a sleeve on the centerbody to decrease the flow area of the premixing passage by 30 percent. The −300 assembly can be operated in two modes. First, at a constant combustor pressure drop ratio of 4 percent, the air velocity through the premixing passage will be the same as in the other two assemblies, but the total airflow will be reduced by 30 percent with a reduction of combustor loading by that amount. Secondly, the combustor can be operated at the same combustor loading of the other assemblies, but with a corresponding increase of air velocity through the premixing passage.

Can Combustor Liner. The combustor liner used for the liquid-fueled combustor development comprised only a primary zone. No secondary or dilution air was used because the test facility was limited in airflow capacity. The primary zone is a 20-cm-dia can with a total length-to-diameter ratio of 2.25. Primary zone length was intentionally overized during the original hardware design to permit an assessment of burner emissions as a function of primary zone length. Construction is of Hastelloy X sheet metal of 1.0-mm thickness.

To maintain acceptable low combustor wall temperatures, the primary zone was film cooled. The combustor dome incorporates eight radial cooling strips. A total of 10 circumferential cooling strips is located at equally spaced intervals along the combustor axis. The baseline can combustor employs 43 percent of the total air for liner cooling.

Test Rig Description

The combustor test rig is illustrated in Fig. 4. Preheated combustion air enters the test section after being measured with an ASME sharp-edged orifice run. Within the combustor casing, the airflow is initially in a reverse flow direction around the outside of the combustor liner. This reverse flow configuration simulates the flow pattern in a multiple, canted can, gas turbine combustion system. The canted burner geometry was originally selected to provide a high degree of flexibility in integrating an advanced combustor into the existing gas turbine.

Combustor exhaust gases flow through a water-cooled diagnostic section and a water quench before exiting to the atmosphere. Combustor pressure and airflow rate are controlled using a pressure regulating valve upstream of the test rig and a back-pressure butterfly valve downstream of the rig. The test rig includes a small quartz window that allows visual monitoring of the flame.

Instrumentation was available to determine air and fuel flow rates, inlet air temperature and pressure, combustor wall temperatures, combustor pressure drop, and exhaust gas composition (CO, CO_2, NO_x, O_2, and unburned hydrocarbons). Emissions measurements were conducted using a set of three water-cooled, diametral, gas sampling probes mounted downstream of the burner in the water-cooled instrumentation section of the test rig (Fig. 4). The probes contain a total of 36 holes spaced by dividing the combustor exhaust cross section into equal areas. This sampling procedure provides an area-averaged emissions measurement in each 60 deg section of the exhaust flow. The emissions samples from the three probes are combined and analyzed in commercially available emissions monitoring instrumentation.

Liquid fuel (No. 2 diesel) was delivered to the test rig from a high-pressure pump after filtering and metering with a mass flow meter. Fuel flowed to a manifold inside the combustor casing where it was distributed to the various fuel delivery passages through same-diameter tubing. An equal flow of fuel to each of the injector elements was achieved by incorporating a high pressure drop orifice in each of the discharge lines of the fuel manifold. The large uniform pressure drop in each line assured that the fuel flows in the lines were equal to within a few percent.

Test Procedure

A typical test run of the ultralow NO_x can combustor involves combustor rig and emissions system warm-up, combustor light-off, and combustor performance testing. Once air is preheated to the desired operating temperature, the combustor pilot burning natural gas is ignited with a torch. After a stable pilot flame is achieved, the torch is extinguished. At this point, a gradual transfer from pilot fuel injection to main fuel injection (No. 2 diesel) is effected manually while maintaining roughly constant combustor operating conditions. Once the burner is fully operational on the main liquid fuel injector, the pilot fuel flow is terminated. Combustor pressure and fuel and airflows are set to the desired test conditions.

At the desired combustor test point, the burner is allowed to reach a stable operating condition before data are recorded. This requires approximately 5 minutes. During this stabilization period, the flame is inspected visually and gaseous emissions levels are monitored using a continuous strip chart recorder. When stable operation is achieved, test data are recorded by an automated data acquisition system. Subsequently, the combustor operating conditions are altered to the next test point and the process is repeated.

Data Analysis

The data are analyzed to determine the combustor equivalence ratio. In general, the overall equivalence ratio is calculated in three ways from independent measurements of O_2 concentration, CO_2 concentration, and measured air and fuel flow rates. These calculated values agree to within 2 percent for the data to be regarded as valid. The equivalence ratio data reported in this paper are based on measured O_2 concentration.

The equivalence ratio is also determined based on the airflow split throughout the combustor. The airflow in the test combustor can with the liquid-fueled, low-NO_x injector is divided into 49 percent for swirler air, 43 percent for liner cooling, 5 percent for inner assist, and 3 percent for outer assist.

Downloaded 02 Jun 2010 to 171.66.16.121. Redistribution subject to ASME license or copyright; see http://www.asme.org/terms/Terms_Use.cfm

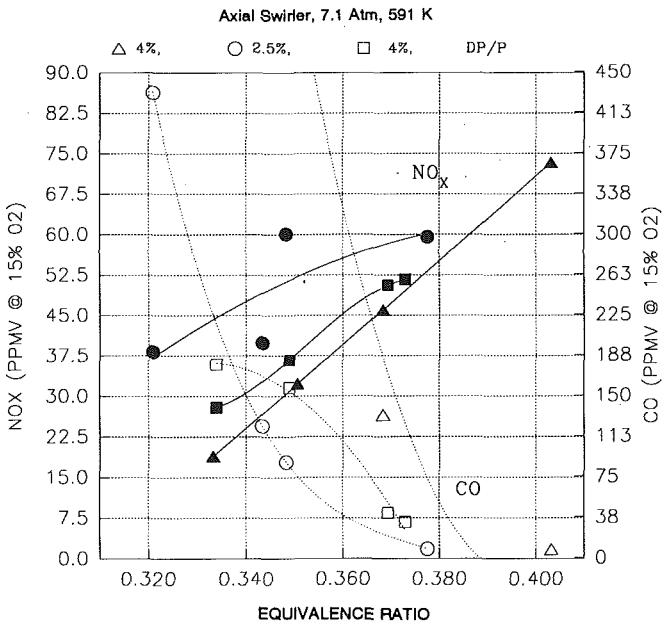

Fig. 5 Emissions signature of −200 injector assembly

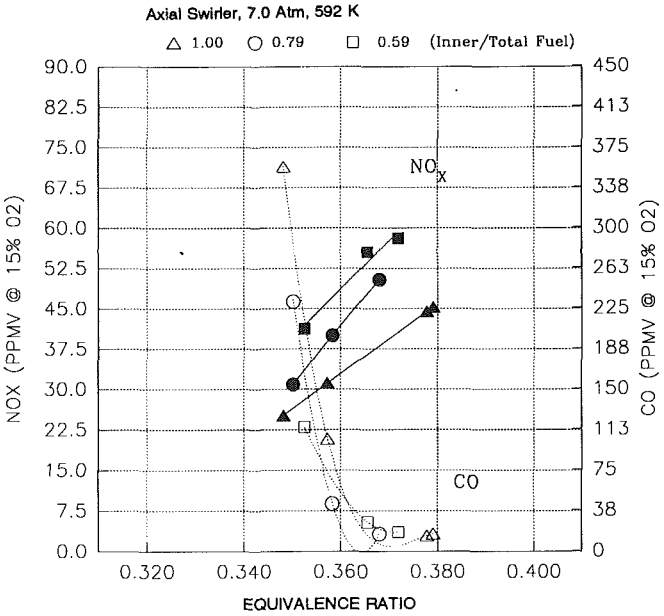

Fig. 6 Test result of −100 injector assembly at varying inner/total fuel ratios

Test Results

To characterize the impact of combustor design and combustor operating conditions on burner performance, tests under both combusting and noncombusting flow conditions were conducted. Noncombusting, cold flow tests were used to determine the pressure drop and flow split characteristics of the ultralow NO_x combustor assembly. In addition, noncombusting flow visualization studies were conducted to examine qualitatively the performance of the filming fuel injector concept under varying operating conditions. These results are discussed by Smith and Cowell (1989b).

Can combustor test activities were completed over a series of 15 tests. Tests are described below in a chronological order with emphasis on the injector assembly configuration tested.

Axial Swirler Performance. The operation of the filming injector was initially assessed in the −200 assembly. In these tests, the emissions signature of the axial swirler with the standard premixing length was established. The results of these tests are summarized in Fig. 5. Testing was completed at 5.1 and 7.1 atm combustor pressure with a constant inlet air temperature of 591 K. The combustor pressure drop ratio was held at 4 percent for all the data except for a short series at 2.5 percent. The data shown in Fig. 5 were taken at 7.1 atm. All the diesel fuel was fed in through the inner fueling passages on the injector centerbody. The amount of air introduced to the injector tip as air blast was varied from none to 6.4 percent of the total air input. Air blast to the centerbody is used to atomize fuel at the downstream end of the centerbody.

Figure 5 is a graph of NO_x and CO emissions versus combustor equivalence ratio. The classic relation between these pollutants and equivalence ratio is clearly illustrated. The figure shows that as equivalence ratio is increased, NO_x emissions increase while CO emissions decrease. The key to designing combustors with low emissions characteristics is to find the balance between the NO_x and CO relation with air/fuel ratio. In general, NO_x levels will be referenced at 50 ppmv CO emissions.The results in Fig. 5 indicate a general decline in the NO_x control capabilities of the filming injector when compared to results obtained with the radial swirler. In that testing, NO_x levels of 9–19 ppmv were obtained; whereas in Fig. 5 the lowest result is 44 ppmv. Data included in Fig. 5 were taken with varying amounts of inner air blast. The best results were obtained with no air blast. The combustor pressure drop ratio was lowered to 2.5 percent and the NO_x emissions increased significantly to 67 ppmv.

Increased Premixing Length. The −100 injector assembly was installed to see if an improvement in combustor emissions performance could be realized by increasing the injector premixing length by two centerbody diameters. The results of these tests are summarized in Fig. 6. Testing was completed at 7.0 atm combustor pressure with a constant inlet air temperature of 592 K. The combustor pressure drop ratio was held at 4 percent for all testing. These tests have been conducted with capabilities for both inner and outer fueling. Inner fueling denotes fuel introduced on the injector centerbody, while outer fueling indicates fuel injected through ports on the outer walls of the premixing passage.

The NO_x and CO emissions signatures shown in Fig. 6 indicate that the lowest emissions were obtained with all the fuel delivered to the centerbody (inner/total = 1.00). With CO concentrations of 50 ppmv, the NO_x emissions were 39 ppmv. NO_x emissions increase as more fuel is delivered to the outer fueling port. CO emissions are lowest at an inner/total fuel ratio of 0.8. The trend for CO emissions with fuel delivery location is not as clear. The increased premixing length had only a slight benefit on the emissions signature compared to tests completed with the −200 assembly. Results were still worse in terms of pollutant emissions than obtained in tests with the radial swirler. In order to verify the past performance of the radial swirler, that injector was again installed for combustion testing.

Radial Swirler Tests. Testing of the radial swirler combustor hardware was accomplished at three blade angles; 52.2, 54.4, and 62.8 deg. The radial swirler hardware was installed in the test rig with a goal of replicating the results of the past study and completing more tests with various swirl angles. The swirl patterns of the axial and radial designs have been compared on the flow visualization bench with no noticeable difference in fluid flow patterns and only a 3 deg difference in swirl angle.

Data taken with the radial swirler hardware operating at several air inlet temperatures (Fig. 7) show NO_x and CO emis-

Downloaded 02 Jun 2010 to 171.66.16.121. Redistribution subject to ASME license or copyright; see http://www.asme.org/terms/Terms_Use.cfm

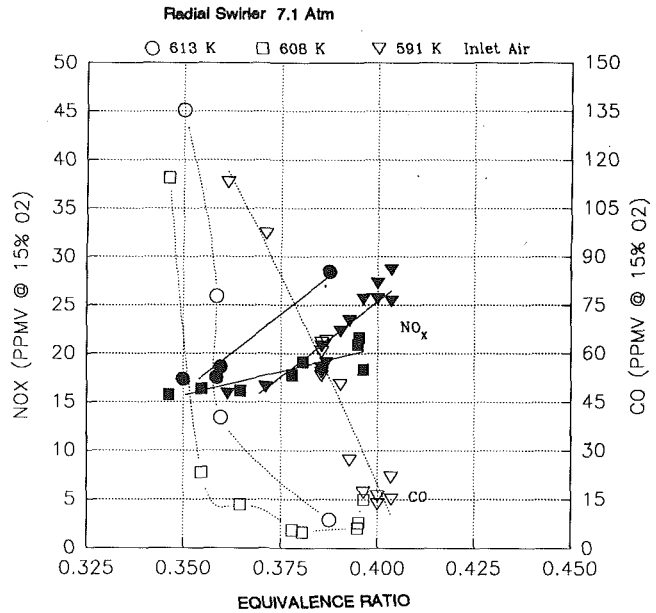

Fig. 7 Emissions signature of radial swirler injector assembly at varying air inlet temperatures

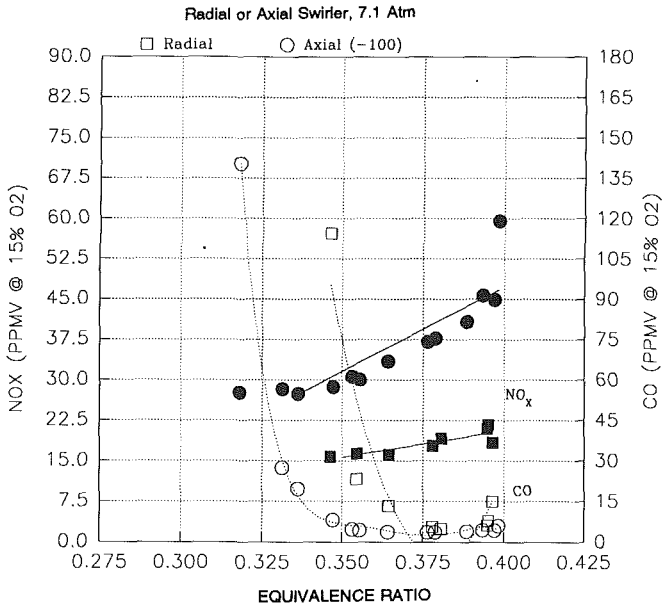

Fig. 9 Comparison of emissions characteristics of injectors featuring axial and radial swirler

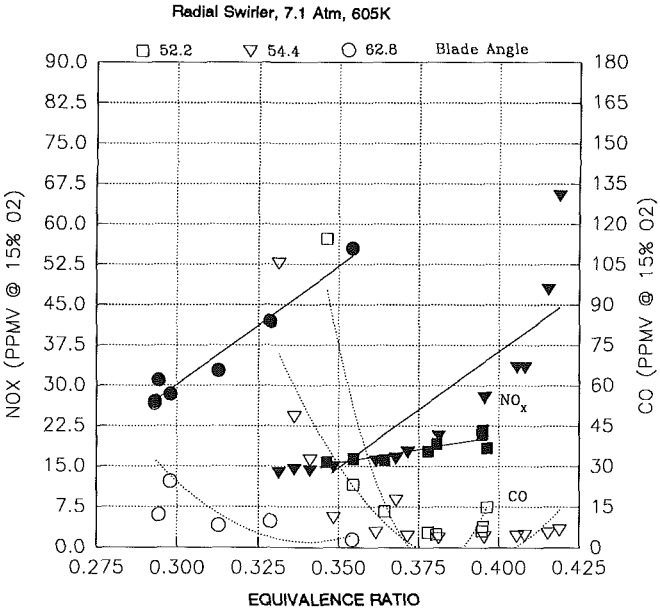

Fig. 8 Influence of radial swirler blade angle on emissions characteristics of liquid-filming injector

sions versus equivalence ratio. The radial swirler injector was operated with all fuel being admitted through the centerbody. The combustor was operated at a pressure of 7.1 atm. NO_x emissions as low as 15.5 ppmv @ 15 percent O_2 while maintaining CO emissions below 50 ppmv were obtained. Figure 7 shows that this condition is obtained at an air inlet temperature of 608 K. Emissions rise substantially as the temperature is lowered below 600 K. This is attributed to incomplete fuel vaporization in the premixing passage. As inlet air temperatures increase to 613 K, emissions also increase slightly due to higher flame temperatures. The data suggest that air inlet temperature must be sufficiently high to vaporize all the diesel fuel fully in the premixing passage, but not substantially higher because flame temperature (and NO_x emissions) is increased with increased inlet air temperature.

The radial swirler injector hardware was operated at various swirler blade angles. Results from these tests are included in Fig. 8. In these tests the blade angle was held at three points: 52.2; 54.4, and 62.8 deg. The combustor was operated at similar conditions for all three tests with inlet air at 605 K, combustor pressure of 7.1 atm, and inner fueling only. The data presented in Fig. 8 indicate that the lowest emissions are obtained at a blade angle of 54.4 deg. At this angle, NO_x emissions down to 14 ppmv were measured. As the blade angle is increased, the NO_x emissions rise substantially. The difference in emissions as the angle is increased between 52.2 and 54.4 deg is a slight improvement from 15.5 to 14 ppmv. In past tests, the blade angle has always been set at 52.2 deg for both the radial and axial swirlers.

Retest of the −100 Assembly. The axial swirler (−100 assembly) injector with the increased premixing length was reinstalled for another evaluation. NO_x emissions as low as 28 ppmv were recorded in this test. These tests were completed at 7.1 atm, 4 percent combustor pressure drop ratio, combustor air inlet temperature of 605 K, and all inner fueling. Included in Fig. 9 are those data and the data taken with the radial swirler. As clearly illustrated, the radial swirler still performs better than the axial swirler despite an increased premixing length.

Increased Centerbody Diameter Performance. Testing of the −300 assembly, which includes an axial swirler and increased centerbody diameter, was completed in two tests. These tests were run to investigate whether an increased centerbody diameter as illustrated in Fig. 3 (−300 assembly) would improve the emissions characteristics of the combustor. The −300 assembly, like the −100 assembly, has an increased premixing length of two centerbody diameters over the −200 assembly and the radial swirler injector assembly. The combustor was operated at 7.0 atm, 4 percent combustor pressure drop ratio, and combustor air inlet temperature of 604 K.

Emissions results are summarized in Fig. 10 as NO_x and CO versus equivalence ratio. Included in the graph are data taken with the radial swirler hardware and the axial swirler in the −100 assembly. The graph shows clearly that the best results are obtained with an axial swirler in the −300 assembly and inner and outer ("dual") fueling. With that arrangement, referencing to a CO emission level of 50 ppmv, NO_x levels as low

Downloaded 02 Jun 2010 to 171.66.16.121. Redistribution subject to ASME license or copyright; see http://www.asme.org/terms/Terms_Use.cfm

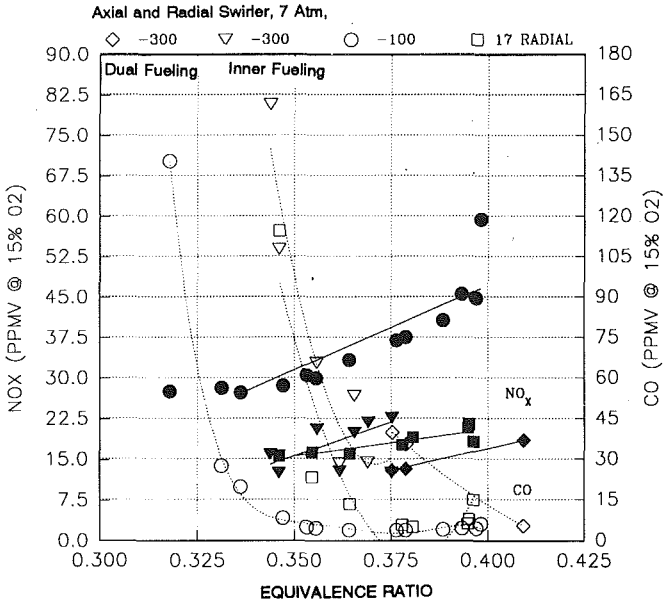

Fig. 10 Comparison of test results of −300 injector assembly with increased centerbody diameter with other injector configurations

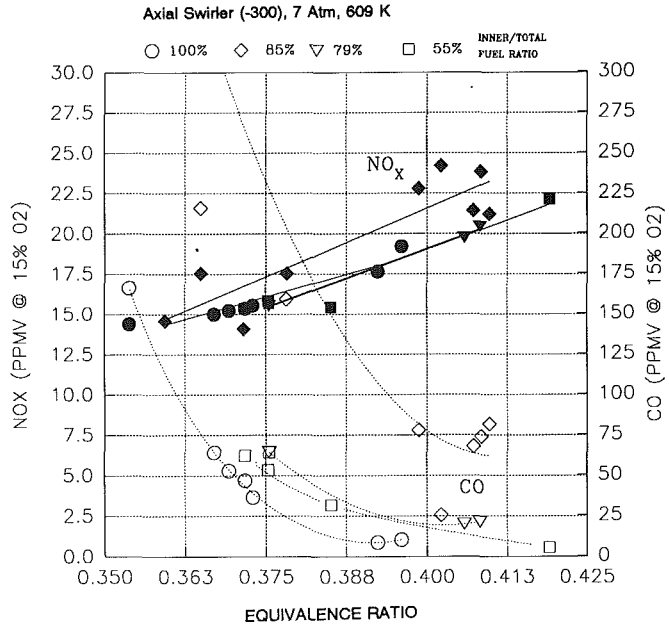

Fig. 11 Emissions signature of −300 assembly at varying inner/total fuel ratios

as 12 ppmv are recorded. It should be noted that the inner/total fuel ratio is not known for these data due to faulty instrumentation. The improved results of the −100 to −300 assemblies are attributed to the increased filming surface area as well as the decreased combustor throughput.

The −300 assembly was run in a second test in the combustion rig for a total of 4.5 hours with goals of broadening the data base and determining on a first cut the impact of coke deposits on performance. Data were taken at two combustor pressures of 7 and 9 atms. Emissions results at both pressures are shown in Figs. 11 and 12. At 7 atm, the combustor was operated at an average air inlet temperature of 609 K and combustor pressure drop of 4 percent. The fueling location was varied from all inner fueling to inner and outer fueling. Figure 11 delineates data taken at different fueling location ratios as inner/total fueling ratio. At the reference CO emissions level of 50 ppmv and inner/total fueling ratios varying from 55, 79, 85, and 100 percent, the corresponding NO_x levels are 15.5, 15.8, 23, and 15.0 ppmv, respectively. The data taken at an 85 percent level show increased scatter due to testing difficulties. The remaining data indicate a very slight influence of inner/total fueling ratio on emissions characteristics.

More data taken at 7 atm with an increased combustor pressure drop ratio of 5.25 percent show an increase in emissions levels with a NO_x concentration of 21 ppmv. The increased $\Delta P/P$ had the strongest impact on the CO emissions curve, shifting it toward higher equivalence ratios. This result is attributed to an increased combustor throughput.

In Fig. 12, data taken at 9 atm were plotted. The combustor was operated at an inlet air temperature of 614 K and a combustor pressure drop ratio of 4 percent. This plot shows the emissions signatures as a function of inner/total fuel ratio. At inner/total fueling ratios of 74, 83, and 87 percent, corresponding NO_x emissions of 17.9, 15.9,and 15.5 are shown, respectively. The most striking observation is that when compared to the data taken at 7 atm, included in Fig. 11, the NO_x emissions are virtually unchanged. Closer comparison does indicate a slight increase in NO_x emissions with pressure, but the CO curves shift toward lower equivalence ratios. Thus, the increased pressure over this range is decreasing CO emissions more than it is increasing NO_x emissions. At varying fueling ratio, the lowest NO_x emissions are recorded at the highest

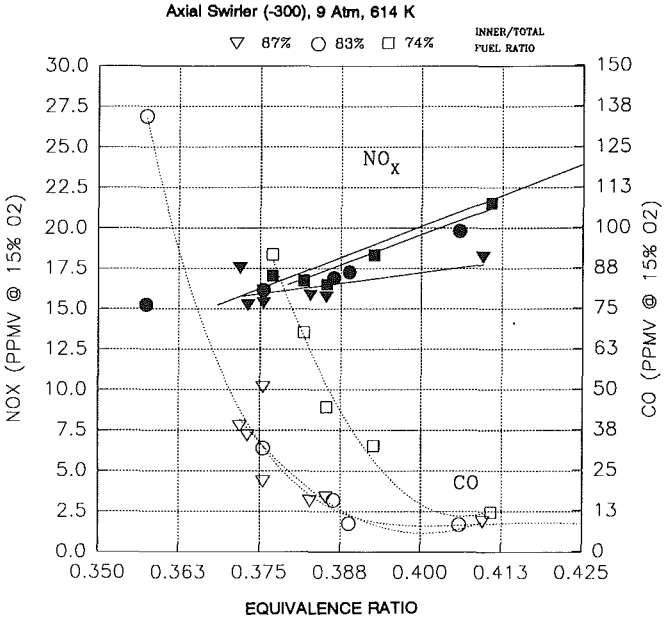

Fig. 12 Emissions signature of −300 assembly at full engine pressure

inner/total fuel ratio. At 7 atm, the influence is not strong. The flame appeared steadier at 9 than at 7 atms.

Throughout the test, no degradation in combustor performance was detected. Following this test the injector was inspected for coking. Pictured in Fig. 13 is the inner filming surface as it appeared following the test. Diesel residue in the form of coke is seen clearly on the filming surfaces. The injector centerbody shows deposits located near the downstream end of the injector. The deposits are up to 0.2 mm thick. Evidence of the coke shedding is indicated by the texture of the deposit on the metal surface and supported by observations of the flame. During operation, the flame was largely blue in color, indicating a high level of premixing. At points during the test and particularly during the final hour of the test, yellow

Downloaded 02 Jun 2010 to 171.66.16.121. Redistribution subject to ASME license or copyright; see http://www.asme.org/terms/Terms_Use.cfm

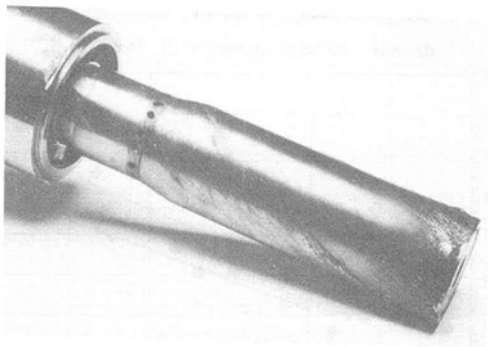

Fig. 13 Deposits on injector centerbody after 4.5 hour diesel run

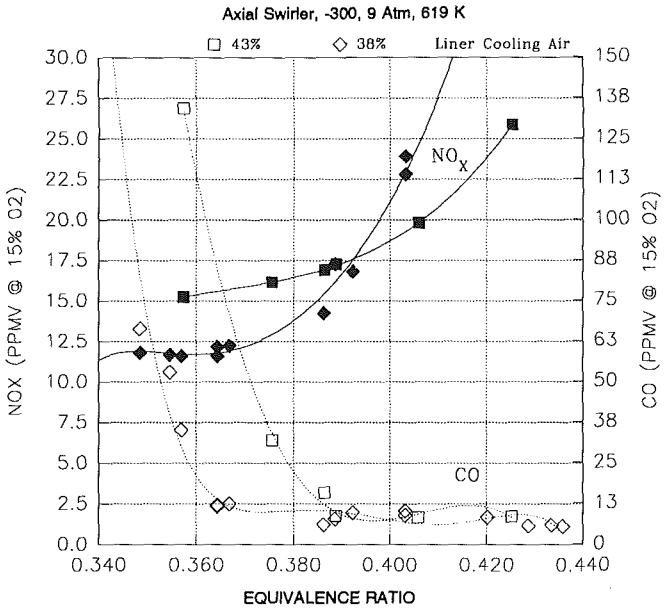

Fig. 14 Influence of liner cooling on emissions signature of −300 injector assembly

"sparks" in the flow field were observed. These "sparks" were most likely coke deposits shedding and burning in the combustor free stream.

Reduced Liner Cooling. The −300 injector assembly was operated in two tests using reduced cooling in the combustor liner. Approximately 5 percent of the liner cooling holes was blocked off with pieces of metal foil. The liner was installed on the air bench to determine the exact airflow split. The results from the cold flow test indicate a 15 percent reduction in the cooling hole flow area with a corresponding 5 percent reduction in the amount of air distributed to liner cooling.

The combustor was run at typical test conditions of 9 atm, 619 K inlet, 4 percent drop, and inner/total fuel ratio of 81 percent. The emissions signature for this test is included in Fig. 14 with data taken at higher cooling airflow rates. The combustor operated with good emissions characteristics with NO_x emissions of 11.8 ppmv recorded at a corresponding CO level of 50 ppmv. A comparison of the data included in Fig. 14 indicates the influence of liner cooling on emissions characteristics. The data suggest that reduced liner cooling extends the range of operation with low CO emissions. The NO_x emissions are also decreased significantly at leaner operation. Thus, decreasing liner cooling improves the emissions characteristics of the combustor. The liner operated at maximum temperatures up to 994 K at the richest conditions with reduced cooling. Combustor liner temperatures are usually maintained below 1144 K as a conventional design criterion for industrial gas turbines to ensure adequate liner durability. It is unknown whether further reductions in liner cooling would improve upon these emissions characteristics.

Discussion and Summary

The primary technical goal of the program is to minimize NO_x emissions, with 10 ppmv (corrected to 15 percent O_2) being a specific target. At the same time, CO emissions are to be maintained below 50 ppmv. The 10 ppmv NO_x goal reflects the NO_x reduction capabilities being claimed by suppliers of current SCR systems. The goal of can combustor testing was to determine the critical injector design parameters that have the greatest impact on emissions characteristics. The concept was evaluated through testing of four injector assemblies. The injectors featured variable swirler design, premixing length, and centerbody diameter. In addition, the radial swirler blade angle, the inlet air temperature, combustor pressure, and fuel distribution were varied.

Swirler Design. Testing completed with an axial swirler and a radial swirler mounted on filming injectors with nearly identical physical dimensions yielded results indicating substantial changes in the emissions characteristics. While the reason for this change in emissions is not fully resolved, a contributing factor is the characteristics of the recirculation zone generated with each swirler type. Flow visualization of the premixing passage with both swirler types indicated a 3 deg difference in angle of the fuel film on the centerbody. The size and shape of the recirculation zone have a strong influence on combustor performance. The recirculation zone is the region in the combustor where the flame is stabilized.

The recirculation zone may have a different shape with one swirler versus the other. If the recirculation zone is too large and flat, some of the "fresh" fuel/air mixture is quenched by the liner cooling air. This would tend to generate higher CO emissions at a given equivalence ratio. The swirler type should not have an impact on the fuel filming and vaporization rate in the injector premixing passage. To comprehend fully the aerodynamic changes resulting from the different swirler designs, the velocity profile through the premixing passage and in the combustor dome would have to be measured.

Swirler Blade Angle. The NO_x emissions signature was lowest at a blade angle of 54.4 deg. The worst results were obtained with the blade angle set at 62.8 deg. The axial swirler was designed with a 52.2 deg blade angle. The blade angle of the radial swirler was changed and tested at 52.2, 54.4, and 62.8 deg. As described in the previous section, the swirl angle has a direct and strong impact on the size and shape of the recirculation zone. The swirl angle refers to the angle of the aerodynamic gas streamlines relative to the combustor centerline. The blade angle is the angle of the tangent to the trailing edge of the vane. In general, the swirl angle is slightly less than the blade angle. Radial and axial swirlers typically generate the same swirl for a given blade angle. For the hardware tested in this program, the radial and axial swirlers had the same blade angle, but a small difference in swirl angle may have existed. This observation was supported by the flow visualization tests where a 3 deg difference in swirl angle was measured. A slight change in swirl angle can make a substantial difference in combustor emissions performance.

Premixing Length. The premixing length was varied by two centerbody diameters using the axial swirler in the −100 and −200 injector assemblies. A reduction of NO_x emissions of 55 percent to 28 ppmv was recorded as the premixing length was increased. Increased premixing length allows for more complete fuel vaporization and premixing. Combustion of a lean, well-mixed fuel/air mixture reduces NO_x emissions by

Downloaded 02 Jun 2010 to 171.66.16.121. Redistribution subject to ASME license or copyright; see http://www.asme.org/terms/Terms_Use.cfm

avoiding high temperatures within the primary combustion zone. In a conventional combustor, liquid fuel is atomized into the primary combustion zone, mixing with air and burning in a diffusion mode. Under these conditions, "hot spots" can develop where local fuel concentrations can significantly exceed overall concentrations. Premixing and homogenizing the fuel/air mixture is a well-documented method for emissions control and the basis for the technology being used in this program. There is a degree of fuel/air premixing beyond which no significant improvement in NO_x emissions will result. Clearly, with the standard premixing length in the -200 assembly, this "critical" premixing length has not been met. The -100 assembly with the increased premixing length generated both a yellow diffusion flame and blue premixed flame depending on the operating conditions. The -300 assembly had an increased premixing length with an increased centerbody diameter. With this assembly, the flame was blue, burning in the premixed mode under a wider range of operating conditions.

An indication of the degree of fuel vaporization with premixing length is the "coke" deposits on the injector centerbody. The deposits are typically found to be light or nonexistent except at the far downstream end of the injector centerbody. Therefore, the band of deposits on the centerbody marks the location of final fuel vaporization. In the -100 assembly, these deposits were located at 90 percent of the premixing length downstream of the fuel inlet holes. The -200 assembly had coke deposits located at greater than 95 percent of the premixing length. This suggests that the potential for unvaporized fuel passing through the premixing passage is greater with the -200 assembly than the -100 assembly. In summary, premixing length appears to have an influence on combustor emissions performance only up to the point that the fuel is fully vaporized and premixed. As will be detailed in the next section, vaporization and premixing can be accomplished over shorter distances, if the injector centerbody diameter is increased.

Centerbody Diameter. The lowest emissions results were obtained with the axial swirler in the -300 assembly. The centerbody of the injector was increased by 14 percent while maintaining a constant premixing annulus outer diameter. This change has two important impacts on the operation of the injector/combustor assembly. First, the increased diameter provides a greater surface area for fuel filming and vaporization. The greater the surface area for the fuel to film over, the thinner the film. The fuel vaporizes and premixes more rapidly with a thinner fuel film. Secondly, the increased diameter decreases the swirler/premixing passage effective area, reducing the total combustor air throughput. The combustor loading is an important design criterion that impacts combustion emissions characteristics and efficiency. The combustor loading versus efficiency is a dome-shaped curve. For high combustion efficiency, the loading must be high enough to ensure rapid and complete fuel/air mixing and low enough to allow sufficient residence time for complete reaction. Typically, in gas turbine combustors, incomplete combustion is most characterized by CO and unburned hydrocarbons (UHC) emissions measurements. At low or high combustor loadings, these emissions tend to be high regardless of the stoichiometry of the fuel/air mixture. The changes made in combustor loading by changing the centerbody diameter did not result in higher emissions of CO and UHC. Therefore, it appears unlikely that combustor loading had as strong an influence as fuel vaporization at these test conditions.

Reduced Liner Cooling. Cooling air tends to quench the combustion process near the liner. The quenched mixture is high in CO and UHC. In general, the greater the amount of combustion air used for liner cooling, the higher the pollutant

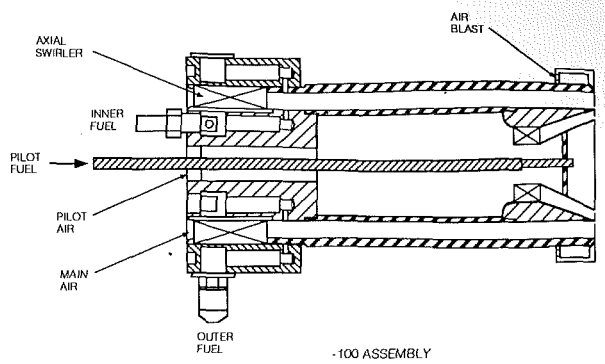

Fig. 15 Liquid-fueled low NO_x injector design for sector testing

emissions. The design goal is to employ just enough air to maintain liner temperatures between 1145 K and 922 K. Testing has confirmed that as liner cooling air was decreased by 5 percent, NO_x emissions dropped from 15.5 to 11.8 ppmv. The liner temperatures were maintained below 978 K. A further reduction in liner cooling could yield lower emissions, but this has not been confirmed through testing.

Injector Coking. Coke deposits have been observed on the injector following four hours of operation. The coke deposits are of sufficient magnitude to limit engine operation between overhaul and injector cleaning. Coke is the heavier fractions of diesel fuel that remain on the filming surfaces after vaporization has been completed. These deposits build in thickness, eventually impeding the operation of the combustor. Work completed did not address this issue, but rather aimed at determining whether injector coking was a serious design constraint. The testing has confirmed that a solution to this problem should be sought if this technology is going to reach the production engine level.

Injector coking has been identified as the sole development issue for the filming injector. Coke deposits formed during testing may limit engine operation to an unacceptably short interval. Several injector design solutions have been identified to correct this problem. The most promising is moving the air blast location from the injector tip upstream on the injector centerbody in the premixing passage. At this position, sufficient fuel filming distance for vaporization is provided for all but the heaviest fractions of the diesel fuel. The heavy fuel is finely atomized by the air blast and carried airborne into the combustion zone where it is consumed. This design modification is undergoing testing.

Sector Rig Injector Design. The results of can combustor testing have been used to design the injector that is going to be used in an annular sector rig as this technology nears engine demonstration. The design is shown schematically in Fig. 15. The injector features an increased premixing length, axial swirler, large centerbody diameter, pilot burner, integrated fuel distribution plugs, and lightweight nonmodular construction. The sector rig uses three injectors and the target gas turbine uses twelve.

The injector premixing length will allow adequate time for fuel vaporization while still being sufficiently short to fit into the sector rig casing. The injector tested in the can combustor had a variable premixing length. The emissions performance of the combustor did improve as the premixing length was increased. The position in the injector of final fuel vaporization is marked by coke deposits. With the -300 assembly, the coke deposits were located 2.6 centerbody diameters from the fuel injection locations. The sector design premixing length allows sufficient residence time for fuel vaporization over a broad range of operating conditions. The overall length of the injector

Downloaded 02 Jun 2010 to 171.66.16.121. Redistribution subject to ASME license or copyright; see http://www.asme.org/terms/Terms_Use.cfm

could be constrained in the engine, which means that limiting the injector length, if possible, is important.

An axial swirler with a blade angle of 54 deg has been designed for the sector injectors. The axial swirler exhibited worse performance than the radial swirler design. However, in the −300 assembly with an increased premixing length and larger centerbody diameter, excellent emissions characteristics were recorded. An annual combustor geometry generally requires axial swirlers because they are more compact than radial swirlers. It would be difficult to fit twelve radial swirlers around the annular combustor used for the gas turbine. The blade angle of 54 deg provided the lowest emissions characteristics in can combustor testing.

Increased injector centerbody diameter was found to improve emissions significantly when used in tandem with an axial swirler and an increased premixing length. The centerbody diameter has been increased by 20 percent over the baseline design. The increased centerbody improves combustor performance by allowing a greater surface area for filming and reducing combustor loading.

The pilot burner design is copied from that used on the subscale can combustor injector. Main fuel distribution is controlled by fuel restricting orifices, which are an integral part of the injector. Each of the 16 plugs has a 0.064 cm ±0.003 orifice that should provide consisently uniform fuel distribution. The injector is made as a one-piece assembly. The sector injector design can be fabricated for one-third the cost of the −300 assembly used for can combustor testing.

The sector combustor liner has been used for development of natural gas fired low-NO_x technologies. The liner cooling holes are in place and can be blocked as needed. Varying the amount of cooling air to the liner is one of a few test variables that will be examined through sector testing. Other test variables include equivalence ratio, inner/total fuel ratio, combustor pressure drop ratio, and inlet air temperature and pressure.

Acknowledgments

The work presented in this paper was supported by the California Energy Commission under Contract No. 500-88-022 with Mr. David Hatfield as Program Manager.

References

Smith, K. O., 1983, "Ultra-low NO_x Combustor Concept for Methanol Firing," ASME Paper No. 83-GT-29.

Smith, K. O., 1987, "Experimental Evaluation of Fuel Injector Configurations for a Lean-Premixed Low NO_x Gas Turbine Combustor," ASME Paper No. 87-GT-141.

Smith, K. O., and Cowell, L. H., 1989a, "Cost Effective NO_x Emissions Reduction for Cogeneration Gas Turbines—Final Report," California Energy Commission Contract No. 500-85-025.

Smith, K. O., and Cowell, L. H., 1989b, "Experimental Evaluation of a Liquid-Fueled, Lean-Premixed Gas Turbine Combustor," ASME Paper 89-GT-264.

Downloaded 02 Jun 2010 to 171.66.16.121. Redistribution subject to ASME license or copyright; see http://www.asme.org/terms/Terms_Use.cfm

G. J. Micklow
Director,
Computational Fluid Dynamics Laboratory,
Mechanical Engineering Department.

S. Roychoudhury
Graduate Research Assistant.

University of Florida,
Gainesville, FL 32601

H. L. Nguyen
Senior Research Engineer,
Combustion Technology,
NASA Lewis Research Center,
Cleveland, OH 44155

M. C. Cline
Los Alamos National Laboratory,
Los Alamos, NM 88888

Emissions Reduction by Varying the Swirler Airflow Split in Advanced Gas Turbine Combustors

A staged combustor concept for reducing pollutant emissions is currently under investigation. A numerical study was performed to investigate the chemically reactive flow with liquid spray injection for staged combustion. The staged combustor consists of an airblast atomizer fuel injector, a rich burn section, a converging connecting pipe, a quick mix zone, a diverging connecting pipe and a lean combustion zone. For computational efficiency, the combustor was split into two subsystems, i.e., the fuel nozzle/rich burn section and the quick mix/lean burn section. The current study investigates the effect of varying the mass flow rate split between the swirler passages for an equivalence ratio of 2.0 on fuel distribution, temperature distribution, and emissions for the fuel nozzle/rich burn section of a staged combustor. It is seen that optimizing these parameters can substantially improve combustor performance and reduce combustor emissions. The optimal mass flow rate split for reducing NO_x emissions based on the numerical study was the same as found by experiment.

Introduction

One of the key aspects in the development of advanced combustor concepts is the emissions requirement associated with advanced cycle gas turbine engines. Of particular importance are the oxides of nitrogen, carbon monoxide, and unburned hydrocarbons that are formed in these cycles. The increases in combustor inlet pressure and temperature found in these cycles can cause substantial increases in NO_x emissions. The NO_x production can be reduced to environmentally acceptable levels only by designing advanced, innovative low-emission combustors. One promising concept for achieving low NO_x production is staged combustion.

Combustion is initiated in a fuel-rich zone with an equivalence ratio in the range of 1.2 to 2.4. This reduces the flame temperature, thereby reducing NO_x formation. The hydrocarbon reactions proceed rapidly, depleting the available oxygen, further inhibiting NO_x formation. Additional air is then added and combustion is completed under excess air conditions, holding the flame temperature down and reducing NO_x emissions. The staged combustion concept offers wide stability limits and range of operation.

For staged combustion to be effective, the fuel must be well atomized and well distributed in the rich zone. Otherwise, localized regions at near-stoichiometric conditions can form, causing high temperatures. Also the size and the position of recirculation regions in the combustor can be important. Recirculation regions in undesirable locations, such as the primary zone corners, can increase residence time and increase NO_x production. Therefore the design of an effective fuel injector nozzle is of paramount importance.

The superior combustion and reduced emissions of the high shear airblast atomizer relative to the conventional pressure atomizer are well established [1]. The airblast atomizer has better spray uniformity, multifuel capability, higher combustor efficiency, low smoke production, and low pattern and radial profile factor in comparison to the pressure atomizer. This superior performance has led to the widespread adoption of the airblast fuel injector in modern high pressure ratio gas turbine engines. The airblast fuel injector produces a finer spray because of the more thorough mixing of the fuel and air. Such mixing yields a flame of low luminosity and soot, thus resulting in relatively cooler liner walls, a minimum of exhaust smoke, and lower NO_x emissions. Furthermore, the placement of the fuel droplets in the burning zone is mainly dictated by the airflow pattern, being almost insensitive to fuel flow variations. Thus airblast fuel injectors exhibit lower pattern factors.

For the advanced high-pressure ratio aircraft engines, the aforementioned advantages of the airblast atomizer become even more important. For these cycles more air is supplied to the primary zone via the combustor front end to be used for combustion. Therefore the amount of air available for liner cooling will decrease, and the lower liner temperature asso-

Contributed by the International Gas Turbine Institute and presented at the 37th International Gas Turbine and Aeroengine Congress and Exposition, Cologne, Germany, June 1-4, 1992. Manuscript received by the International Gas Turbine Institute February 6, 1992. Paper No. 92-GT-110. Associate Technical Editor: L. S. Langston.

Copyright © 1993 by ASME
Downloaded 02 Jun 2010 to 171.66.16.121. Redistribution subject to ASME license or copyright; see http://www.asme.org/terms/Terms_Use.cfm

ciated with airblast atomizers is more important. Also, the increased fuel flow of advanced cycles will increase the airflow through the fuel nozzles and dome swirlers. This will possibly make the nozzle assembly one of the most important combustor subcomponents, responsible for an optimally designed primary zone of these high temperature rise, short L/D, advanced cycle combustors. The importance of optimizing these nozzles and swirler designs becomes very critical [2–6].

Considerable work has been done in recent years to gain a fundamental understanding of fuel spray, air swirler fluid mechanics, and droplet–airflow interaction [7–9]. Particular emphasis has been placed on the atomization process. Spray and airflow characteristics have been predicted using empirical techniques with varying degrees of success [10–12], and with more complex and accurate models involving numerical multidimensional computations of spray and airflow dynamics [13–18]. One of the major shortcomings of the empirical approach is that it is only applicable for a limited number of nozzle geometric parameters and operating conditions. Extrapolation or deviation from those conditions could result in substantial error. Recently the more complex numerical approach has shown promise with the inclusion of more accurate physics, providing a better prediction of mean drop size and droplet size distribution.

The object of the current study is to investigate the effect of mass flow rate split between the swirler passages on the fuel atomization process, temperature distribution, and emissions production in a rich-burn section of a typical RQL combustor. Detailed spray and airflow characterization is performed using a multidimensional full Navier–Stokes calculation routine, which has the capability to model liquid spray injection and finite rate chemistry.

Computational Technique. The program used in the current study was the KIVA-II code [19] developed by Los Alamos National Laboratory. The code has its primary application for investigation of the complex combustion processes in internal combustion engines. These processes include transient three-dimensional dynamics of evaporating fuel sprays interacting with multicomponent gases undergoing mixing, ignition, chemical reactions, and heat transfer. KIVA and KIVA-II have been widely used by the automobile industry for a number of years and have been thoroughly tested under a wide range of operating conditions. The modular structure of KIVA-II is general and most of the major options can be activated or deactivated through the input data file. Due to the fact that complex geometry can be modeled with inflow-outflow boundary conditions, the code can be applied to gas turbine combustors.

The KIVA-II computer code solves the compressible, turbulent, three-dimensional transient equations of reacting multicomponent gas mixtures with the flow dynamics of an evaporating liquid spray. The conservation laws for vapor-gas mass, momentum, and energy are solved by an arbitrary Lagrangian–Eulerian finite volume approach, when the initial and boundary conditions are specified, by using a time-marching technique. The spatial differencing is made conservative. The cells are hexahedrons and the mesh does not need to be orthogonal. Coupled implicit differencing is used for the diffusion terms and terms associated with pressure wave propagation. The coupled implicit equations are solved by a method similar to the SIMPLE [20] algorithm, with individual equations being solved by the conjugate residual method. KIVA-II uses an explicit quasi-second-order upwind (QSOU) scheme for convection. This scheme is monotone and approaches second-order accuracy when convecting smooth profiles. Turbulence is modeled using a k–ϵ model. The Monte Carlo-based particle fluid spray model allows the prediction of droplet sizes, lifetimes, velocities, and trajectories of fuel droplets emanating from air-blast nozzles. This allows the prediction of the fuel vapor distribution in the combustor. For combustion, the number of species and chemical reactions that can be included is arbitrary. The code distinguishes between slow reactions, which proceed kinetically, and fast reactions, which are assumed to be in equilibrium. Chemical rate expressions, which are Arrhenius in form, are evaluated by a partially implicit procedure. A fast implicit algebraic solver is used to compute chemical equilibria. The prediction of NO_x formation is accomplished through an extended Zeldovich mechanism. This is the most predominant NO_x mechanism at high temperatures.

An initial prediction with KIVA-II of the swirling fuel spray of an advanced gas turbine nozzle showed good agreement between predicted and measured air velocity profiles [21].

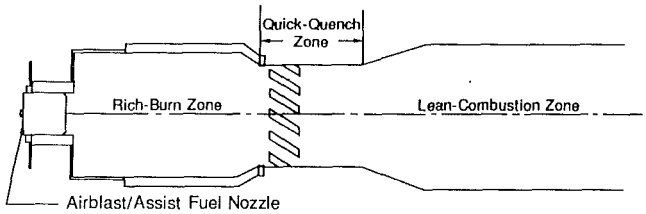

Fig. 1 Combustor geometry

Table 1 Mass flow rate split percentages

Case	Inner	Outer	Dome
1	35	35	30
2	23	47	30
3	18	52	30
4	9	67	24

Problem Description. For the current investigation the problem was assumed to be axisymmetric. The overall combustor is shown in Fig. 1. For this study only the fuel nozzle/rich burn section was analyzed. The combustor rich-burn section diameter was 0.1524 m and the length from the fuel nozzle exit to the start of the quick quench zone was 0.2032 m. The dimensions of the fuel injector cannot be given as the information is restricted. The mesh extended into the converging connecting pipe and the outlet boundary condition was to specify the static pressure. The angle of the connecting pipe was 30 deg with respect to the axial direction.

The following inlet conditions were prescribed for all cases:

Temperature = 811 K
Pressure = 620.5 kPa
Air mass flow rate = 0.494 kg/s
Equivalence ratio = 2.0
Turbulent length scale = 0.25 of the respective passage width
Turbulent kinetic energy = 1 percent of the respective 0.5 w^2

where w is the inlet axial velocity.

The fuel was injected at 293.0 K. The fuel was considered to be Jet-A in liquid phase and propane in the gaseous phase according to Nguyen and Ying [22]. The inlet swirl profile was modeled as a wheel flow with 60 deg turning at the tip of each swirl vane in the inner, outer, and dome air passages, respectively. The flow was rotating clockwise in all three swirlers when viewed from upstream. The exit pressure for the rich-burn section was set to 620.5 kPa. The boundary conditions at the walls utilized the law of the wall with adiabatic walls.

Results

A parametric study was performed to investigate the effect of varying the mass flow rate split between the inner, outer

Downloaded 02 Jun 2010 to 171.66.16.121. Redistribution subject to ASME license or copyright; see http://www.asme.org/terms/Terms_Use.cfm

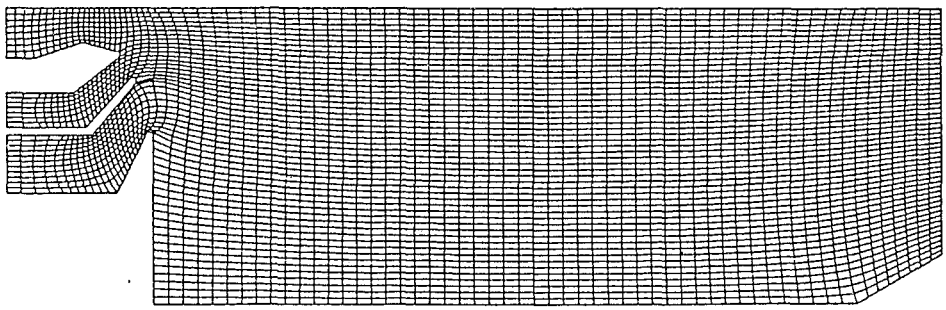

Fig. 2 Axisymmetric grid

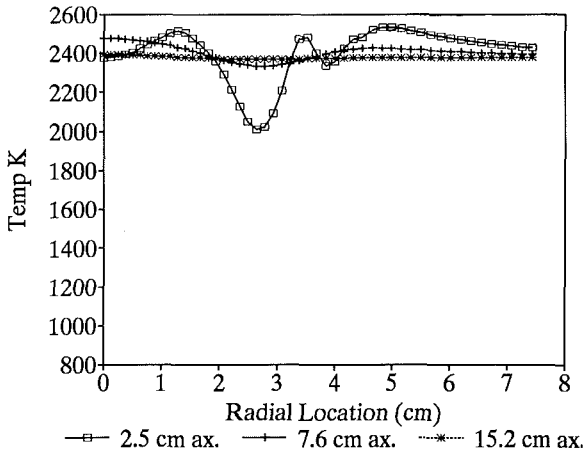

Fig. 3 Case 1 temperature distribution

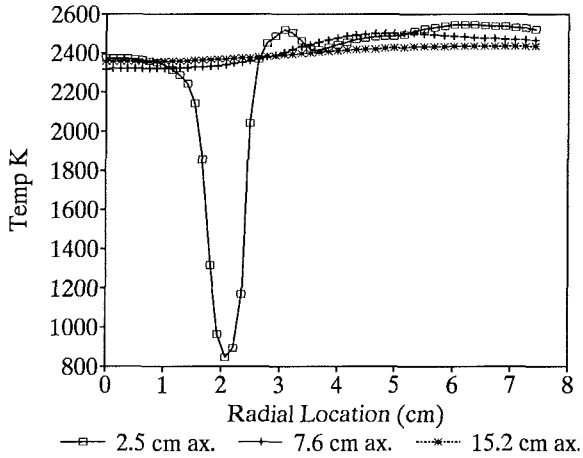

Fig. 5 Case 3 temperature distribution

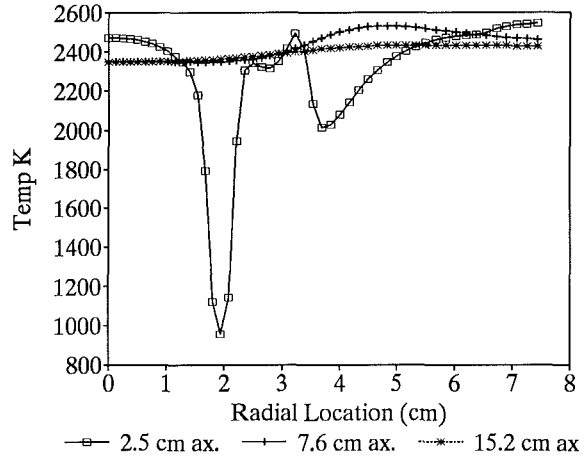

Fig. 4 Case 2 temperature distribution

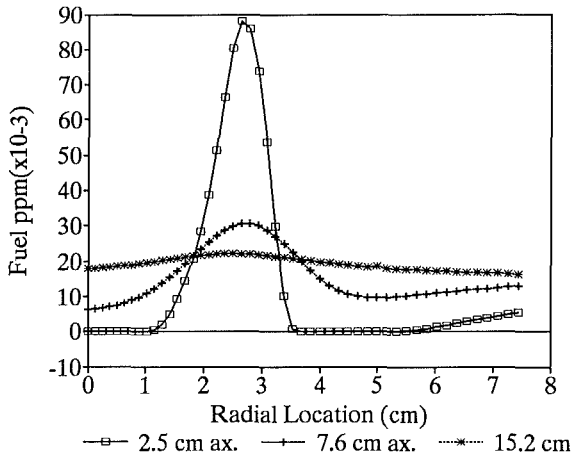

Fig. 6 Case 1 fuel distribution

and dome swirler passages. The total mass flow rate was held constant. Table 1 gives the corresponding flow splits for the four cases investigated.

The grid (81 × 51) for the two-dimensional axisymmetric calculation is presented in Fig. 2. The temperature distributions for cases 1–3 are presented in Figs. 3–5, at various axial distances downstream of the nozzle exit. The profiles are presented at axial locations 2.5, 7.6, and 15.2 cm from the nozzle exit. The 15.2 cm case is approximately at the exit of the rich-burn section. It is seen from the figures that case 1 (Fig. 3) has the most uniform temperature profiles at all locations. This is of importance as the generation of NO is directly related to the temperature distribution and any localized hot spots will lead to substantial NO production. The uniformity in the temperature distribution is directly related to the fuel distribution in the combustor. The fuel concentration is shown in Figs. 6–8 for cases 1, 2, and 3. It is seen that case 1 has the most uniform distribution, particularly at the rich-burn section exit. It is well established that better fuel atomization and more uniform fuel distributions lead to reductions in both NO and CO emissions. The spray patterns for cases 1–3 are found in Figs. 9–11. The fuel is injected from the lip of the inner passage. Once again, it is seen that case 1 has both the widest cone angle and the most uniform fuel distribution through the entire combustor. The scale on the plot ranges from violet signifying a low density to red representing a high fuel density. For case 1, the maximum fuel density is 5.33×10^{-4} g/cm^3, while for cases 2 and 3 the maximum densities are 9.31×10^{-4} and 9.34

Downloaded 02 Jun 2010 to 171.66.16.121. Redistribution subject to ASME license or copyright; see http://www.asme.org/terms/Terms_Use.cfm

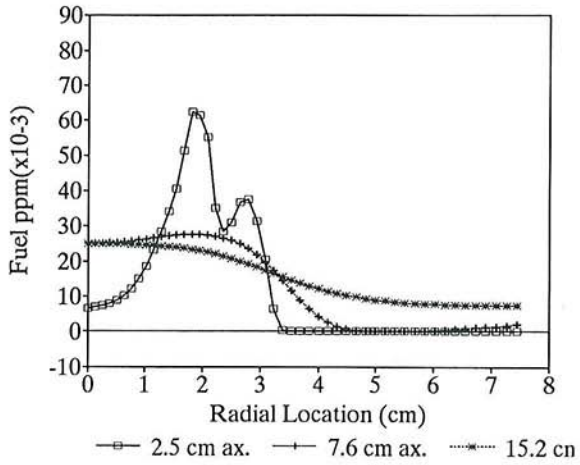

Fig. 7 Case 2 fuel distribution

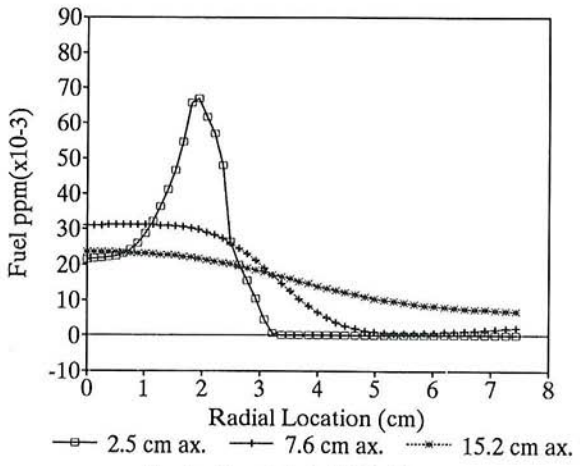

Fig. 8 Case 3 fuel distribution

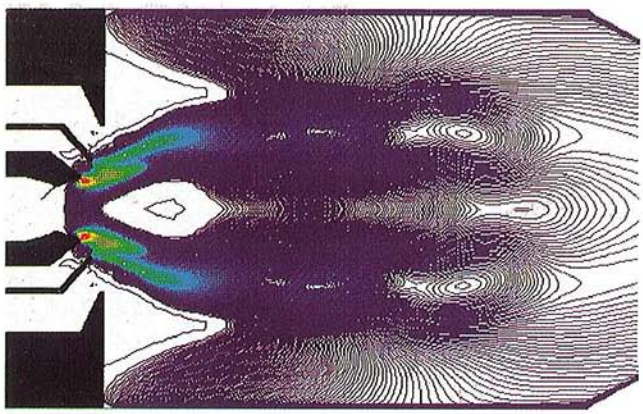

Fig. 9 Case 1 fuel concentration

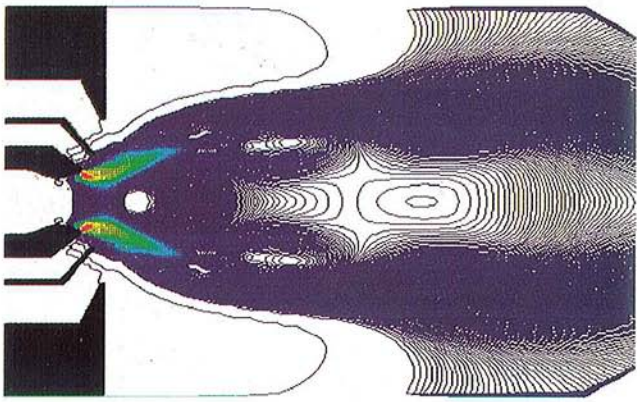

Fig. 10 Case 2 fuel concentration

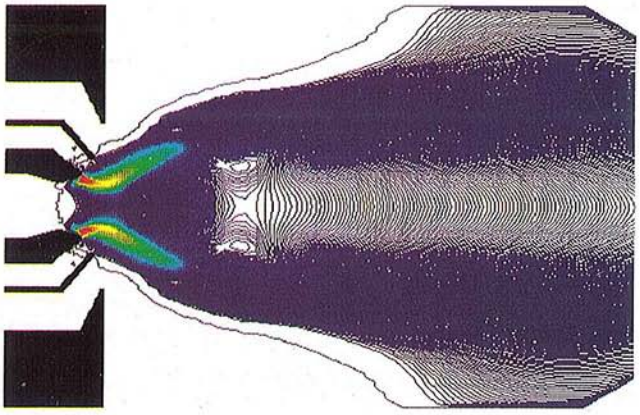

Fig. 11 Case 3 fuel concentration

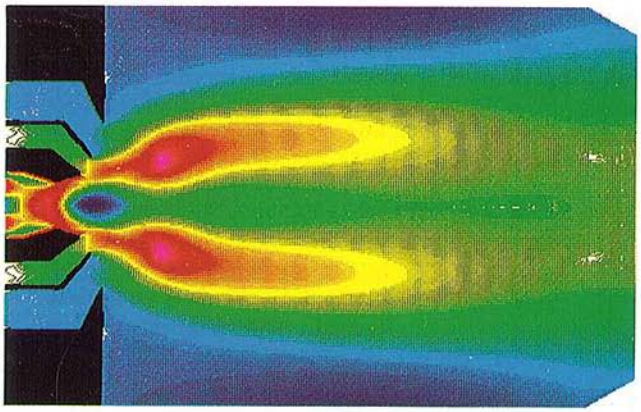

Fig. 12 Case 1 axial velocity distribution

$\times 10^{-4}$ g/cm^3, respectively. Since the fuel flow rate is the same for all cases, it is clearly seen that case 1 has the most uniform fuel distribution. The fuel distribution is directly related to the flow pattern set up by the swirling air profiles from each of the inner, outer, and dome air passages.

The axial velocity profiles are presented in Figs. 12–14. The blue on the figure represents negative or low-velocity and the red represents high-velocity fluid. From Fig. 12, for case 1 it is seen that a strong recirculation zone is formed immediately downstream of the fuel injection point and the air flares out around this recirculation zone. The maximum reverse flow velocity (dark blue zone) for this zone is approximately -60 m/s (-200 ft/s). This is the reason for the wide spray angle for the fuel for this case. High-velocity gas is found surrounding the central recirculation zone, which dissipates substantially midway through the rich-burn section. The maximum axial velocity (red zone) is approximately 260 m/s (850 ft/s). The high-velocity gas is important to provide the high shear forces required for good fuel atomization. It is known that the main transport of the fuel from an airblast nozzle is from the momentum of the swirler air. Case 1 has the same mass flow rate through the inner and outer passages. In Fig. 13, with the

Downloaded 02 Jun 2010 to 171.66.16.121. Redistribution subject to ASME license or copyright; see http://www.asme.org/terms/Terms_Use.cfm

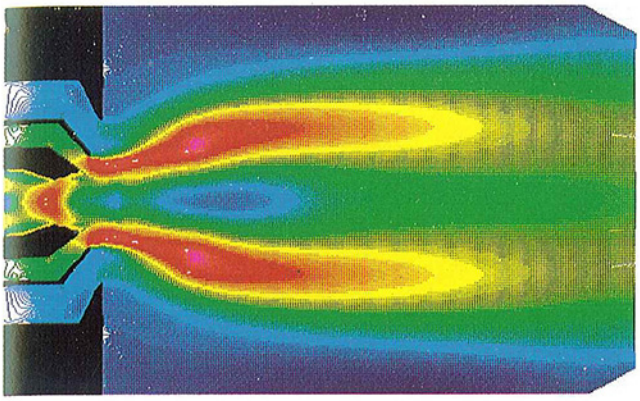

Fig. 13 Case 2 axial velocity distribution

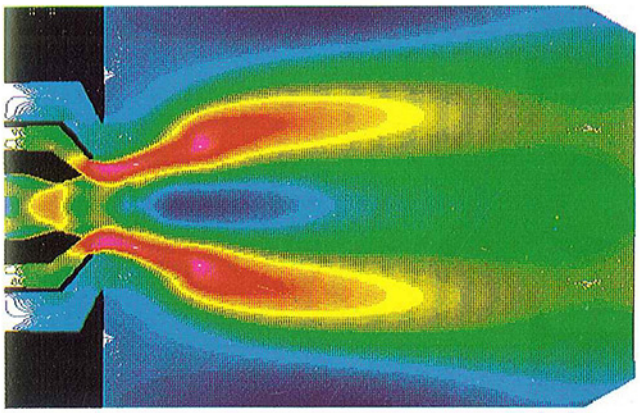

Fig. 14 Case 3 axial velocity distribution

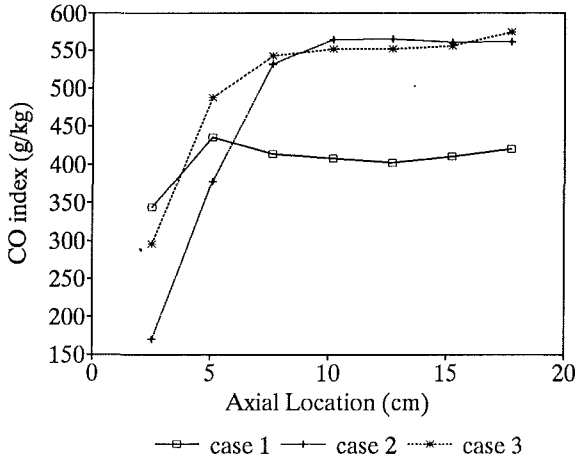

Fig. 15 CO emissions index

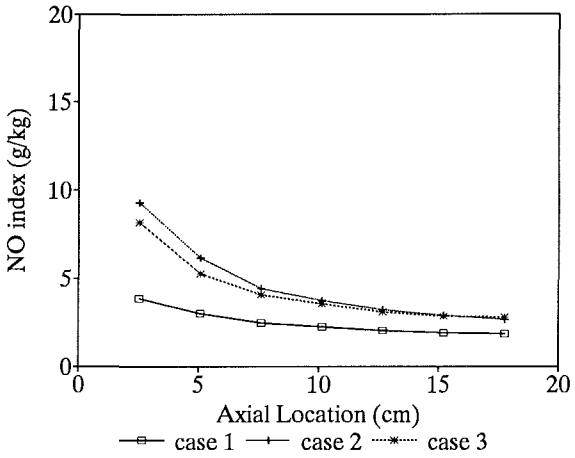

Fig. 16 NO emissions index

higher air mass flow through the outer swirler, the central recirculation zone has become thin and elongated as the high-velocity air extends farther downstream on the sides of the recirculation zone carrying the fuel along with it. The strength of the recirculation zone has decreased. The maximum reverse flow velocity is now approximately -46 m/s (150 ft/s).

The magnitude of the high-velocity streams surrounding the recirculation zone has decreased with a maximum axial velocity of approximately 244 m/s (800 ft/s). Thus the quality of fuel atomization will diminish in comparison to case 1. This leads to a higher fuel concentration in this area as was seen previously in Fig. 10. For case 3 the outer swirler mass flow rate was further increased at the expense of the inner passage. A flow pattern similar to case 2 was produced and is seen in Fig. 14. The magnitude of the velocity of the gas surrounding the central recirculation zone has decreased further in comparison to cases 1 and 2. The maximum axial velocity is now 229 m/s (750 ft/s). This will further decrease the fuel atomization quality.

The CO emissions index is presented in Fig. 15. At the combustor exit the emissions index is the lowest for case 1. This is directly related to the more uniform fuel distribution in the combustor. In Fig. 16 the NO emissions index is found. It should be noted that the extended Zeldovich mechanism used here accounts only for the thermal NO_x production. However, it is believed to be the major source of NO_x production. Because of the low sensitivity of prompt NO_x formation to temperature and stoichiometry within this range of local equivalence ratio, the prompt NO_x formation will be essentially constant for all three cases [23]. Therefore the predicted trends should be correct. A rough estimate based on [23] is that the magnitude of the prompt NO_x should be between 10–20 percent of the thermal NO_x. Once again case 1 has the lowest value for the NO emissions index. It is seen that higher NO_x production at the dome leads to a higher value of NO_x at the combustor exit. Thus a more uniform temperature and fuel distribution at the dome leads to lower NO_x production in that region and also at the rich-burn exit. Another significant factor in NO generation is residence time. The size of the corner recirculation zones in the combustor front end is important. The air in the corner recirculation zones has a large residence time and is subjected to high temperatures, causing substantial NO generation. NO concentration contours are found in Figs. 17–19. In Fig. 17, for case 1 a high concentration of NO is found in the corner recirculation zones. The violet in Fig. 17 indicates a low NO concentration while the red represents a high concentration. The maximum NO concentration for case 1 was 8.17×10^{-7} g/cm^3. In Figs. 18 and 19 for cases 2 and 3, respectively, the recirculation zones are larger and therefore the NO generation is higher. Also the maximum NO concentration is higher. The values are 1.25×10^{-6} and 1.33×10^{-6} g/cm^3 for cases 2 and 3, respectively. This is seen directly in the NO emissions index previously presented in Fig. 16. The trends found for CO and NO emissions index have been substantiated in testing of an overall RQL combustor [24].

Finally, case 4 will be discussed. Case 4 was investigated to explain further a low value of NO emissions index found in testing of the overall RQL combustor. Case 4 had the lowest percentage of air through the inner swirler of all the cases investigated. From Fig. 20 it is seen that a large recirculation zone (dark blue) is formed downstream of the nozzle. With

Downloaded 02 Jun 2010 to 171.66.16.121. Redistribution subject to ASME license or copyright; see http://www.asme.org/terms/Terms_Use.cfm

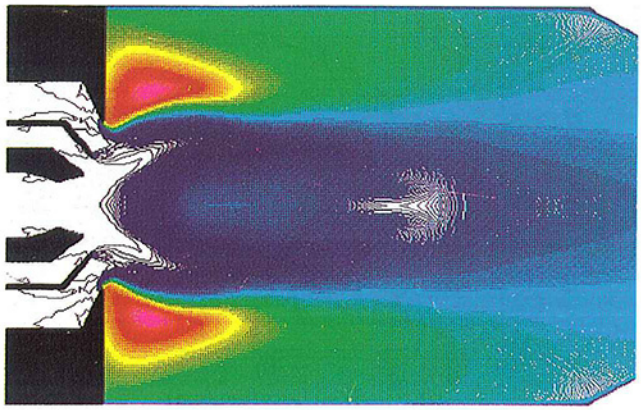

Fig. 17 Case 1 NO distribution

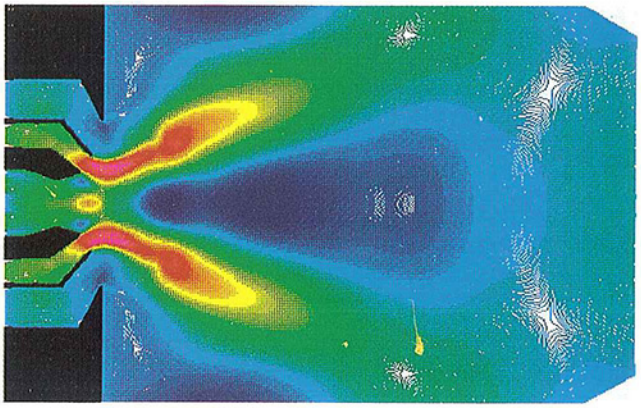

Fig. 20 Case 4 axial velocity distribution

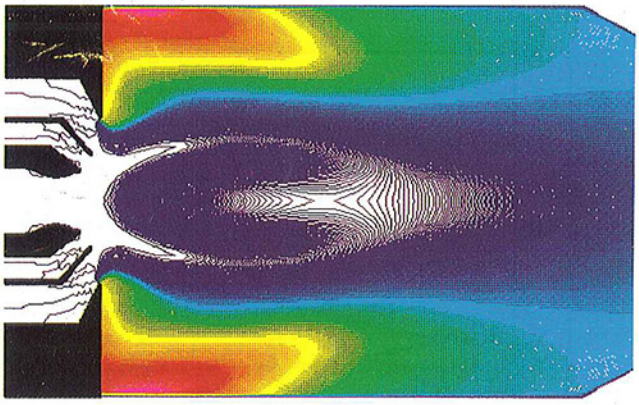

Fig. 18 Case 2 NO concentration

Fig. 21 Case 4 fuel concentration

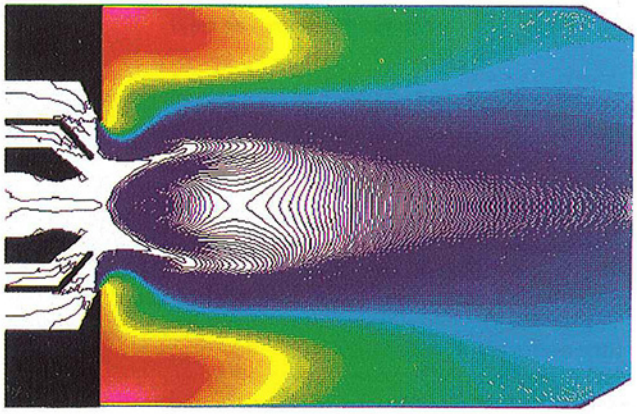

Fig. 19 Case 2 NO concentration

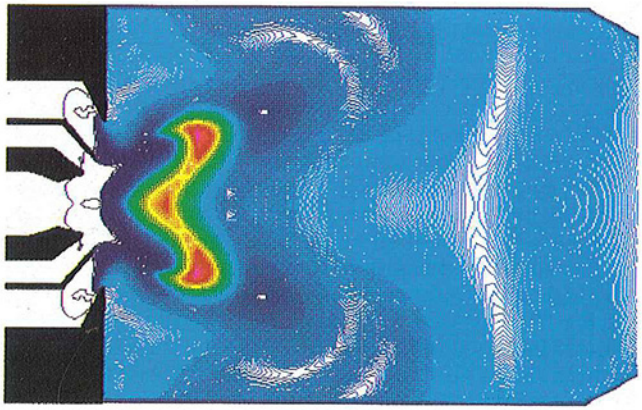

Fig. 22 Case 4 NO concentration

the low air flow rate through the inner swirler, the fuel atomization was poor and the fuel spray remained in the immediate vicinity of the nozzle (Fig. 21), causing inefficient combustion, low flame temperatures, and low NO production (Fig. 22). This was observed directly in the test as coking of the nozzle and a low emissions index was recorded [24].

Conclusions

A parametric study was performed to investigate the effect of varying the air mass flow splits between the inner, outer, and dome swirler passages and fuel distribution and emissions. It was found that optimizing these parameters can substantially improve combustor performance and reduce combustor emissions. The case for which the mass flow rate was balanced between the inner and outer flow passages gave the best fuel distribution, most uniform temperature distribution, and lowest CO and NO emissions index of the configurations studied.

It was seen that lowering the inner swirler mass flow rate while increasing the flow rate in the outer passage led to progressively poorer fuel atomization and in the worst case to the pooling of the fuel in the immediate vicinity of the nozzle exit. This was substantiated by test data where coking of the nozzle and low inefficient combustion was observed.

Finally, it was seen that the corner recirculation zones at the combustor front end could cause substantial NO generation. Reducing the size of the zones reduced the NO production.

Downloaded 02 Jun 2010 to 171.66.16.121. Redistribution subject to ASME license or copyright; see http://www.asme.org/terms/Terms_Use.cfm

The trends found from the KIVA II calculations were in direct accordance with test data, making it a valuable tool for investigation of design parameters affecting combustor emissions.

References

1 Norsten, E. R., and Lefebvre, A. H., "Effect of Fuel Injector Method on Gas Turbine Combustion," *Emissions From Continuous Combustion Systems*, W. Correlius and W. G. Agnew, eds., Plenum Press, New York, 1972, pp. 255–278.

2 Micklow, G. J., and Nguyen, H. L., "The Design and Performance of Dome Swirlers for Gas Turbine Airblast Atomizers," 1989 Fall Meeting Western State Section, The Combustion Institute, Paper No. 89-88.

3 Micklow, G. J., Dogra, A. S., and Nguyen, H. L., "Effect of Vane Twist on the Performance of Dome Swirlers for Gas Turbine Airblast Atomizers," AIAA Paper No. 90-1955.

4 Micklow, G. J., Roychoudhury, S., and Nguyen, H. L., "Effect of Nozzle Lip Geometry an Spray Atomization and Emissions of Advanced Gas Turbine Combusters," AIAA Paper No. 91-2201, 1991.

5 Gupta, A. K., Lilley, D. G., and Syred, N., *Swirl Flows*, Abacus Press, Tunbridge Wells, United Kingdom, 1984.

6 Ramavajjala, M., and Gupta, A., "Swirl Effect on NO and NO_2 Emissions in a Variable Geometry Combustion," AIAA Paper No. 91-0643, 1991.

7 Lefebvre, A. H., *Gas Turbine Combustion*, Hemisphere Publishing Corp., Washington, DC, 1983.

8 Gupta, A. K., and Lilley, D. G., "Combustion and Environmental Challenges for Gas Turbines in the 1990's," AIAA Paper No. 91-1964, 1991.

9 Lilley, D. G., "Investigations of Flowfields Found in Typical Combustor Geometries," NASA Contractor Report 3869, Feb. 1985.

10 Simmons, H. C., "The Prediction of Sauter Mean Diameter for Gas Turbine Fuel Nozzles of Different Types," ASME Paper No. 79-WA/GT-5.

11 Yang, G. X., and Chin, J. S., "Experimental Study on Atomization of Plain Jet Injector Under High Pressure Co-axial Airflow," ASME Paper No. 87-GT-56.

12 Reitz, R. D., and Bracco, F. V., "Mechanism of Atomization of a Liquid Jet," *Phys. Fluids*, Vol. 25, No. 10, Oct. 1982, pp. 1730–1742.

13 Nguyen, H. L., Carpenter, M. H., and Ramas, J. I., "The Effects of Engine Speed and Injection Characteristics on the Flow Field and Fuel/Air Mixing in a Motored Two-Stroke Diesel Engine," AIAA Paper No. 87-0227, 1987.

14 Sturgess, S. A., Syed, S. A., and McManus, K. R., "Calculation of a Hollow-Cone Spray in a Uniform Air Stream," *J. Propulsion and Power*, Vol. 1, No. 5, 1984, pp. 360–368.

15 Rizk, N. K., and Mongia, H. C., "A Model for Airblast Atomization," AIAA Paper No. 89-2321, 1989.

16 Wu, R. J., Reitz, R. O., and Bracco, F. V., "Measurements of Drop Size at the Spray Edge Near the Nozzle in Atomizing Liquid Jets," *Phys. Fluids*, Vol. 29, 1986, pp. 941–951.

17 Nguyen, H. L., Carpenter, M. H., Ramos, J. R., and Stegeman, J. D., "Numerical Simulation of the Flow Field and Fuel Sprays in an IC Engine," SAE Paper No. 87-0599, 1987.

18 Bower, G., Chang, S. K., Corradini, M. L., El-Beshbeeshy, M., Martin, J. K., and Krueger, J., "Physical Mechanisms for Atomization of a Jet Spray: A Comparison of Models and Experiments," SAE Paper No. 881318, 1988.

19 Amsden, A. A., O'Rourke, P. J., and Butler, T. D., "KIVA-II: A Computer Program for Chemically Reactive Flows With Sprays," Los Alamos National Laboratory, LA-11560-MS, May 1989.

20 Patankar, S. V., *Numerical Heat Transfer and Fluid Flow*, Hemisphere Publishing Corporation, Washington, DC, 1980.

21 Butler, T. D., "Analysis of an Air-Assist Atomizer," Los Alamos National Laboratory, private communications, May 1990.

22 Ying, S. J., and Nguyen, H. L., "Numerical Simulation of Jet Combustion Approximated by Improved Propane Chemical Kinetics," Paper No. AIAA-91-1859, 1991.

23 Hayhurst, A. N., and Vince, I. M., "The Origin and Nature of Prompt Nitric Oxide in Flames," *Combustion and Flame*, Vol. 50, 1983, pp. 41–57.

24 Nguyen, H. L., NASA Lewis Research Center, private communications, restricted test data, Aug. 1991.

Downloaded 02 Jun 2010 to 171.66.16.121. Redistribution subject to ASME license or copyright; see http://www.asme.org/terms/Terms_Use.cfm

Modification of Combustor Stoichiometry Distribution for Reduced NO_x Emission From Aircraft Engines

G. J. Sturgess

R. G. McKinney

S. A. Morford

United Technology Corporation,
Pratt & Whitney,
East Hartford, CT 06108

Measurements of the emissions from an experimental engine were analyzed to construct a design chart for the reduction of oxides of nitrogen (NO_X) in conventional combustors. The design chart was used to reconfigure the stoichiometry distribution of the combustor of a production engine so as to reduce NO_X while holding the emissions of carbon monoxide, unburned hydrocarbons, and smoke well below existing regulations. Combustion section pressure loss and combustor outlet temperature distributions were substantially unchanged. The modified design was refined with the aid of computational fluid dynamics calculations to optimize the emissions reduction. Worthwhile reductions in NO_x were obtained with combustor modifications that are transparent to the engine user.

Introduction

Concerns over the environment are again becoming matters of public and political discussion throughout the world, and especially in Europe. Of particular interest is the direction and magnitude of possible climatic changes arising through acceleration of global warming and ozone depletion due to man-made pollutants. Although aircraft operations are only small contributors to the overall annual emission of pollutants, aircraft are the only direct source of these pollutants in the upper atmosphere. There is speculation that persistent concentrations of pollutants can exist along busy air corridors, such as the western approaches to Europe and North–South routes along the Eastern seaboard of the United States.

European airlines appear to be especially aware of environmental pressures, and do not wish to see their future growth and/or operations perhaps curtailed by "green" legislation. In their desire to be "good neighbors," these airlines are requesting the assistance of engine manufacturers with near-term but worthwhile reductions in emissions, and more substantial reductions for the longer term. For the first time, consideration is being given to reduction of emissions at cruising altitude, in addition to the landing and takeoff cycle covered by existing Internal Civil Aviation Organization (ICAO) regulations.

Engine manufacturers are responding to the concerns and needs of their customers. In order to achieve worthwhile reductions in engine emissions in the near term, changes to the engine, its systems, and the combustor can only be minor, and must not introduce any deteriorations in reliability, safety, repairability, operating costs, and overhaul lives. Ideally, the changes should be transparent to the user. With these caveats, changes to the fuel injectors and combustor liner hole patterns are virtually the only feasible candidates for achieving the sought-for reductions in emissions. More radical and expensive solutions might be considered for the long term, but the same caveats will apply.

Emissions Concerns

The exhaust from the aircraft gas turbine engine is composed of: carbon dioxide (CO_2), water vapor, unburned (lower) hydrocarbons (UHC), carbon monoxide (CO), oxides of nitrogen (NO_x), particulate matter (soot), and excess atmospheric oxygen and nitrogen. The carbon dioxide and water vapor (both greenhouse gases) are a natural consequence of the complete burning of a hydrocarbon fuel, and they can only be reduced by burning less fuel. The unburned hydrocarbons (such as methane, which is a greenhouse gas), carbon monoxide, and soot are a consequence of combustion inefficiency. The oxides of nitrogen (mostly nitric oxide {NO} with a few percent of nitrogen dioxide {NO_2} and a little nitrous oxide {N_2O}, also a greenhouse gas) arise in two ways: from so-called "prompt NO_x" where in fuel-rich regions of the combustor, fuel fragments react preferentially with atmospheric nitrogen to form cyanogen, which is subsequently reacted via the radical pool to NO via NH_2; and from thermal fixation of atmospheric nitrogen due to the high temperatures present in the combustor.

Rather obviously, the proportions of these various constituents vary according to the power level of the engine, such that most of the UHC and CO are produced at low-temperature, low-power operation, and most of the NO_x and soot are produced at high-temperature, high-power operation.

At sea level and in the lower atmosphere, the CO, UHC, and NO_x can contribute to photochemical smog. NO_x can result

Contributed by the International Gas Turbine Institute and presented at the 37th International Gas Turbine and Aeroengine Congress and Exposition, Cologne, Germany, June 1–4, 1992. Manuscript received by the International Gas Turbine Institute February 6, 1992. Paper No. 92-GT-108. Associate Technical Editor: L. S. Langston.

Copyright © 1993 by ASME
Downloaded 02 Jun 2010 to 171.66.16.121. Redistribution subject to ASME license or copyright; see http://www.asme.org/terms/Terms_Use.cfm

in damage to plant life, as well as adding to the acid rain problem. These are mostly local effects confined to airport environs. At altitude, the particulate matter and water vapor can result in local modifications to cloud cover, while the greenhouse gases can trap infrared radiation from the earth. In the stratosphere under the influence of ultraviolet radiation from the sun, photodissociation and photolysis of ozone and water vapor can produce the hydroxyl radical (OH), and this as well as NO can destroy atmospheric ozone by catalytic scavenging. However, these reactions take place at altitudes greater than where the subsonic commercial transport fleet operates. In the troposphere, where the subsonic fleet does operate, NO can create ozone. However, it should be appreciated that these critical altitudes are not fixed but fluctuate during the day, with latitude and with the seasons. In addition, once introduced into the atmosphere these persistent pollutants can migrate to higher altitudes.

Background

Although the direct correspondence of aircraft emissions, climate, and health is not precise, engine manufacturers have, in the past, responded positively to the environmental concerns of their customers. In the 1960s, heavy exhaust smoke trails were reduced to near-invisibility by modifications to the combustor. In the 1970s, emissions of UHC and CO at idle power were reduced to extremely low levels by changes to the fuel injectors. Noise pollution has also been much reduced with the introduction of high bypass ratio engines, exhaust mixers, acoustic treatment of nacelles, and by optimizing blade/vane relationships in the rotating machinery.

The output of CO_2 and H_2O is reduced by burning less fuel. The modern, high-bypass, high-pressure, high-temperature aircraft gas turbine engine has a cruise-specific fuel consumption that is about 60 percent of that of the engines used on the first generation of transports. These improved efficiency engines, used in aircraft that are themselves more efficient, mean that on a seat-mile basis, modern transports only burn about 40 percent of the fuel used by the first Boeing 707 (Koff, 1991). These improvements in fuel-burn are expected to continue in the future. Not only does reduced fuel-burn reduce direct operating costs, it also reduces pollution.

It was quickly realized that the large amounts of UHC produced at engine idle powers were the result of unreacted and partially reacted fuel reaching the vicinity of the combustor walls where the relatively cool film cooling air chilled chemical reactions and froze constituents. Pratt & Whitney's solution to this problem was to invert the conventional recirculation zone of the combustor (Lefebvre, 1983) so that the dwell time before fuel reached the combustor walls was maximized (Sturgess et al., 1992, Fig. 1). Output of CO at idle power was reduced through raising the temperature of the combustion zone. This was achieved by increasing the combustion zone equivalence ratio. Production of excess smoke at high power due to slight over-richness (Bahr, 1985) was minimized by utilizing the improved atomization and mixing offered by airblast fuel injectors.

Unfortunately, the very design features that produced these performance gains and significant reductions in selected exhaust emissions resulted in increased operating temperatures in the reaction zones of the combustor at all engine power levels. These higher temperatures have tended to exacerbate the formation of NO_x. The current focus is on reducing NO_x without giving up on the reductions achieved in the emission of the other pollutants.

Near-Term Strategy

The strategy adopted for achieving worthwhile reductions in exhaust NO_x in the near term was to confine modifications to the distribution of stoichiometry along the combustor length in order to achieve an optimum arrangement, giving at least a 15 percent reduction compared to engines currently in service. The reduction goal was to apply to altitude cruise as well as around the landing takeoff cycle. The initial application was to the International Aero-Engines (IAE) V2500-A5 engine, so that the NO_x reduction was relative to the V2500-A1 model. This engine was selected because of its small geometric size.

Approach for Emissions Reduction

It was assumed that the majority of the oxides of nitrogen produced by aircraft gas turbine engines results from the thermal fixation of atmospheric nitrogen due to the exposure to the high temperatures present in the combustor.

"Prompt-NO_x" was neglected. It then follows that reduction in the emission of NO_x can be achieved by minimizing exposure of the working fluid to excessive temperatures.

Low flame temperatures can be achieved by avoiding stoichiometric burning. However, this is difficult to attain in non-

Nomenclature

B = transfer number
c_p = specific heat at constant pressure
D_{32} = Sauter mean diameter of liquid fuel spray
d_{IBZ} = IBZ axial length
EI = emission index
k = thermal conductivity
M = momentum
$\dot{m}$ = mass flow rate
$\overline{m}_{NOX}$ = time-averaged mass fraction of NO_X
NRF = NO_X reduction factor
OFAR = overall fuel-to-air ratio by mass
R = universal gas constant
S = source term, mixedness
t = time
$\overline{u}_j$ = mean velocity component in j direction
V = one-dimensional, mass-averaged, mean axial velocity in IBZ
Γ = exchange coefficient
ΔP = pressure drop
ν = kinematic viscosity
ρ = density
σ = Schmidt number, standard deviation
τ = characteristic time
ϕ = equivalence ratio

Subscripts

B = burned gas
CO = carbon monoxide
delay = ignition delay for fuel/air mixture
evap = evaporation of liquid fuel spray
f = fuel
g = combustion gas
HC = hydrocarbons
in = inlet
inj = fuel injector
mix = mixing, mixture
react = reaction
recirc = recirculation zone
spray = liquid fuel spray
stoich = stoichiometric
t = turbulent
Tot = total (sum of)

Downloaded 02 Jun 2010 to 171.66.16.121. Redistribution subject to ASME license or copyright; see http://www.asme.org/terms/Terms_Use.cfm

premixed combustion, especially with liquid fuels. A promising compromise is initially to burn fuel-rich so that there is insufficient oxygen to produce much NO_x, but any unreacted fuel is gasified, and then to add excess air rapidly so that this gasified fuel is reacted fuel-lean. This is the so-called "rich-burn/quick-quench/lean-burn" (RBQQLB) approach.

When applied to conventional combustors with minimum modification, the RBQQLB approach is limited in how rich it may be, and in the effectiveness of the quench provided through standard air addition by transverse jets.

Implementation of Strategy

In order to fulfill the near-term strategy, it was necessary to be able to determine, in some manner, the balance of CO and NO_x emissions produced in a combustor. An experimental approach was used. However, calculation of emissions was also necessary to check assumptions and to order the measurements.

Calculations of the quantities of pollutants produced in a combustor is an involved procedure. It first requires the formulation of a chemical reaction mechanism, with appropriate reaction rate expressions and suitable rate constants. This kinetic scheme can then provide the source terms of the transport equations needed for each species involved in the reaction mechanism. The species transport equation of the time-averaged mass fraction of NO_x, $\overline{m}_{NOX}$, for example, written in Cartesian tensor notation, is:

$$\frac{\partial}{\partial x_j}\left(\overline{\rho u_j}\overline{m}_{NOX} - \Gamma_{\text{eff},j}\frac{\partial \overline{m}_{NOX}}{\partial x_j}\right) = S_{NOX} \tag{1}$$

where the exchange coefficient is the sum of its laminar and turbulent values,

$$\Gamma_{\text{eff}} = \Gamma + \Gamma_t \tag{2}$$

and the turbulent exchange coefficient can be found from a specified or calculated turbulent Schmidt number, together with the turbulent kinematic viscosity, provided via turbulence modeling:

$$\sigma_t = \nu_t/\Gamma_t \tag{3}$$

S_{NOX} is a source term for NO_x. Similar transport equations can be written for each chemical species of interest.

Solution of the species transport equations, together with the Reynolds- or Favre-averaged Navier–Stokes equations and the enthalpy equation in a computational fluid dynamics (CFD) computer code, yields in principle, the complete three-dimensional fields of all relevant quantities. For liquid fuels, the CFD code should include spray and droplet evaporation models, together with all the associated refinements.

Unfortunately, when applied to the complexity of practical combustors with adequate grid resolution and with realistic kinetic mechanisms, such all-encompassing codes present a nonviable computational burden even to the most capable of modern computers.

There are several pragmatic ways of circumventing these difficulties. Two approaches were utilized in the work presented in this paper. The first is phenomenological modeling, based on one-dimensional descriptions of the combustor. This approach is used for data analysis. The second approach involves postprocessing a conventional CFD solution for a combustor to estimate emissions from the number and volumes of gas pockets above and below the critical temperatures for excess NO_x and CO formation, respectively (Morton and Marshall, 1974). This was used for refining a low-emissions design.

There are other possible approaches; the two used represent the simplest of the choices.

Development Vehicles

Initial experimental development work was carried out in a JT9D-70A experimental test engine. The baseline combustor configuration was common for the JT9D-59/-70/-7Q engine models, but the 20 fuel injectors used were of ExCello D-23 hybrid design, using a pressure-atomizing primary and an airblast-atomizing secondary. Exhaust duct measurement of CO, NO_x, UHC, and smoke were made with EPA-approved sampling rakes. The directly measured emissions data were adjusted to conditions appropriate to standard day, steady-state engine operating points for a takeoff thrust of 227 kN (an installed thrust of 51,153 lb_f) using the corrections of Sarli et al. (1975); NO_x was also corrected to 60 percent relative humidity on a standard 15°C (59°F) day. These data were analyzed by means of one-dimensional, phenomenological modeling, and an emissions reduction methodology was developed.

The NO_x reduction methodology established in the experimental engine was applied to the V2500 combustor, which utilizes 20 pure airblast fuel injectors of Parker-Hannifin design. Proving tests of the modified combustor, mounted in an engine diffuser case, were made in the Pratt & Whitney High-Pressure Combustion Laboratory (HPCL), using a traversing multiheaded gas-sampling probe mounted in the combustor outlet plane for emissions measurements. These tests were conducted at correct V2500 engine conditions using unvitiated high-pressure air. A baseline V2500-A1 engine model combustor was tested in the same rig and facility.

A CFD computer code was used to refine the detailed air port pattern of the most promising configuration from the proving tests. The objective of the optimization was to maximize the NO_x reduction achieved while maintaining the quality of the exit temperature distribution, and keeping the other emissions within current regulations. The refined combustor was then tested in the HPCL.

Confirmation of the refined combustor performance was established in a V2500 experimental test engine.

Phenomenological Modeling

For implementation of the simplified RBQQLB approach in the JT9D-70A combustor, chemical reaction of the fuel with compressor delivery air was assumed to take place in two distinct zones existing axially displaced from one another. For local equivalence ratios less than and up to unity, combustion would be confined to an initial burning zone (IBZ); for local bulk equivalence ratios greater than unity, unburned, and now gaseous, fuel exiting the IBZ due to insufficient oxygen for complete combustion, would be consumed in a secondary burning zone (SBZ). The dilution zone of the combustor would not contribute to the reaction process, but serves merely to tailor the exhaust gas temperature distribution to suit the turbine.

For engine idle conditions, it was postulated that minimum CO and maximum NO_x would be produced simultaneously in the IBZ for unity equivalence ratio in this zone. Together with the assumption of 100 percent oxygen consumption efficiency in the IBZ when it is at unity equivalence ratio, this postulate can be used to define the quantity of air participating in the IBZ.

The postulate can be examined through use of simple reaction kinetics appropriate for lean mixtures; for example, the partial equilibrium theory for CO (Westenberg, 1971) and a simple rate equation for NO_x (Quan et al., 1972). However, these expressions apply for prevaporized fuel premixed with combustion air. In the gas turbine combustor, the fuel is introduced in liquid form from discrete sources separate from the discrete sources of combustion air. Therefore, chemical reaction has to be preceded by liquid fuel atomization, fuel spray evaporation, mixing of vaporized fuel with combustion air, and ignition delay. When it does take place, the chemical reaction consists of a hydrocarbon reaction producing most

Downloaded 02 Jun 2010 to 171.66.16.121. Redistribution subject to ASME license or copyright; see http://www.asme.org/terms/Terms_Use.cfm

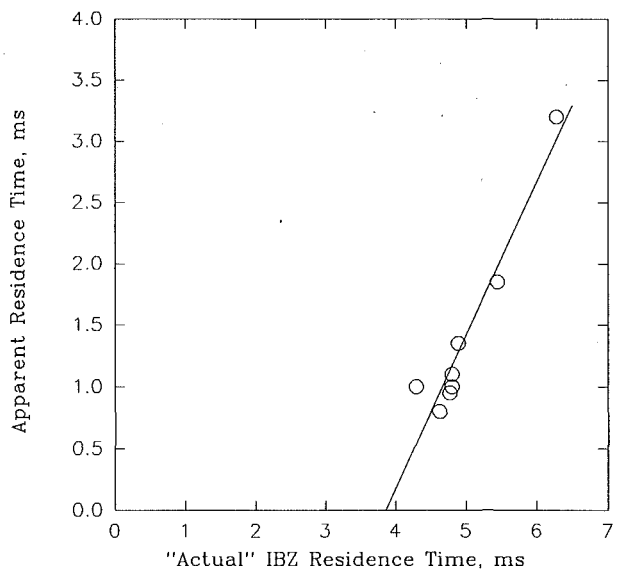

Fig. 1 Experimental engine: comparison of IBZ residence times from NO_x and from one-dimensional flow

of the heat release, reaction of CO produced during the hydrocarbon reaction, and under the influence of high temperatures, thermal fixation of atmospheric nitrogen to mostly NO.

Each of the processes described has a characteristic time associated with it, and these times can be estimated. However, the processes will be taking place concurrently to greater or lesser extent, depending on the fluid dynamics. Hence, the total times for CO elimination and NO production cannot be obtained by subtraction from the total residence time of a simple summation of the individual process times.

Since the bulk of the NO formation will take place last of all, an estimate of the effective time for all of the preceding processes can be made from NO information.

Quan et al. (1972) present a convenient expression for the formation of NO, based on the simplified Zeldovich et al. (1947) mechanism. The expression is suitable for lean mixtures, but given its simple form, is easily calibrated for a range of equivalence ratios. The rate constants of this expression were adjusted so that the calculated NO matched the measurements of Cooper's (1980) data for fully vaporized Jet A fuel premixed with air at 0.3 MPa pressure and with inlet temperatures of 600 to 800 K. The modified expression is:

$$\frac{d[\mathrm{NO}]}{dt} = 1.2\times 10^{8}[\mathrm{N_2}]_e[\mathrm{O_2}]_e^{1/2}\exp(-64{,}000/RT) \qquad (4)$$

where $[N_2]_e$ and $[O_2]_e$ are the equilibrium concentrations of nitrogen and oxygen in moles/cc, T is the adiabatic flame temperature of the mixture in K, and R is 1.987 cal/mole K. The equilibrium values were obtained from the CREK program of Pratt and Pratt (1984). The expression was also satisfactorily checked against the measurements of Semerjian and Ball (1977) for vaporized Jet A fuel premixed with atmospheric pressure air at 756 K inlet temperature.

At idle power conditions of the experimental engine, this expression was used to calculate the emission indices of NO as NO_2 g/kg of fuel burned, for a range of equivalence ratios up to unity at several residence times. Measured values of NO_x (as gm/kg NO_2) were then overplotted on this figure for their appropriate values of IBZ equivalence ratio, found on the basis of the postulate (procedure described below). If it is now assumed that the calibrated expression for NO gives the correct idle power NO_x in the IBZ for premixed, prevaporized fuel and air, the apparent residence times to generate the measured NO_x values can be found from the overlay. These apparent times represent only the effective NO_x formation times. (The procedure may be understood by reference to Fig. 4, which is a similar plot, but for carbon monoxide.)

The apparent residence times may be plotted against the actual residence times in an IBZ of fixed length, where the actual residence time is the total time spent by the complete mixture in the IBZ, i.e.,

$$\tau_{\mathrm{Tot}} = V/d_{\mathrm{IBZ}} \qquad (5)$$

where

d_{IBZ} = axial length of IBZ
V = One dimensional mass-averaged axial velocity in IBZ at IBZ conditions, for the mean cross-sectional area of IBZ

Such a plot is shown in Fig. 1, where a straight line is fitted through the data points. The intercept of this line on the abscissa represents the effective time taken by all of the other physical and chemical processes proceeding concurrently. From Fig. 1, this represents 3.863 ms for d_{IBZ} of 12.7 cm (5 in.).

Methodologies exist for calculating the individual process times. These are as follows: atomization was assumed to take place instantaneously, and spray evaporation was obtained from Ballal and Lefebvre (1981), where

$$\tau_{\mathrm{evap}} = \frac{C_3^3\rho_f\, c_{p_g} D_{32}^2}{8C_1 k_g \ln(1+B)} \qquad (6)$$

and $C_3 = 0.46$; $C_1 = 0.31$ for polydisperse sprays, $B = 3.7$ for kerosine (Spalding, 1955), and D_{32} is the Sauter mean diameter, which was obtained from Simmons (1971) as

$$D_{32} = \frac{225\dot{m}_f^{0.205}}{\Delta P_f}\ \mu\mathrm{m} \qquad (7)$$

$\dot{m}_f$ being the fuel flow in pph, ΔP_f is fuel pressure drop across atomizer in psi, since the hybrid fuel injector at idle operated on its pressure-atomizing primary, which had a flow number of 4.3 pph/(psi)$^{1/2}$.

Mixing time depends on the recirculation zone size and shape, and the momentum ratio of the recirculating flow to that of the fuel spray. When the length of the IBZ is varied, the shape of the recirculation zone will not change, but its size will. Mixing will take place across the surface area of the fuel spray. For the "inside-out" recirculation, this surface across which mixing occurs is the surface of a frustum of a cone determined by the size of the fuel injector, the spray angle, and the position of the first row of transverse combustion air jets that terminate the recirculation around the spray. For hybrid injectors the central, nominally conical, spray of primary fuel is quickly pulled radially outward by the surrounding swirling atomizing air, so that it has an apparent origin upstream of the fuel source plane. (See Sturgess et al., 1992, Fig. 1, for a visual representation of these flow patterns.)

For the injector dimensions and spray angle in the experimental engine,

$$\text{Surface area} \propto d_{\mathrm{IBZ}}(2.0 + 0.637 d_{\mathrm{IBZ}})\ \text{in.}^2 \qquad (8)$$

The momentum ratio is evaluated at the mid-distance of the IBZ, i.e., $d_{\mathrm{IbZ}}/2$. With the assumption of constant pressure mixing and introduction of the area expressions for the spray and recirculation zones at $d_{\mathrm{IBZ}}/2$ into the momentum expressions,

$$\frac{M_{\mathrm{recirc}}}{M_{\mathrm{spray}}} \propto \left[\frac{0.5\dot{m}_{\mathrm{Tot}}}{(\dot{m}_f + \dot{m}_{a,\mathrm{inj}})}\right]^2 \times \frac{T_{\mathrm{recirc}}}{T_{\mathrm{spray}}}\left[\frac{(1.0+0.3185 d_{\mathrm{IBZ}})^2}{148.4 - 20(1.0+0.318 d_{\mathrm{IBZ}})^2}\right] \qquad (9)$$

where

Downloaded 02 Jun 2010 to 171.66.16.121. Redistribution subject to ASME license or copyright; see http://www.asme.org/terms/Terms_Use.cfm

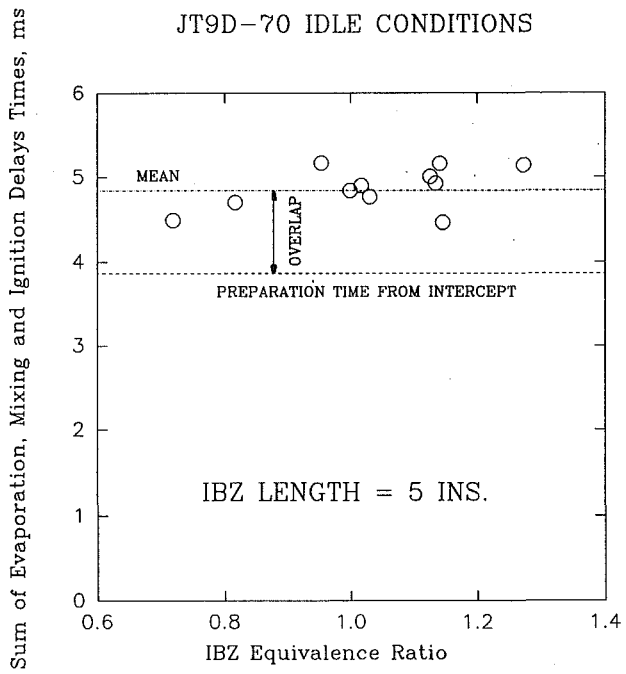

Fig. 2 Experimental engine: comparison of IBZ residence time from sum of individual process times with intercept from Fig. 1

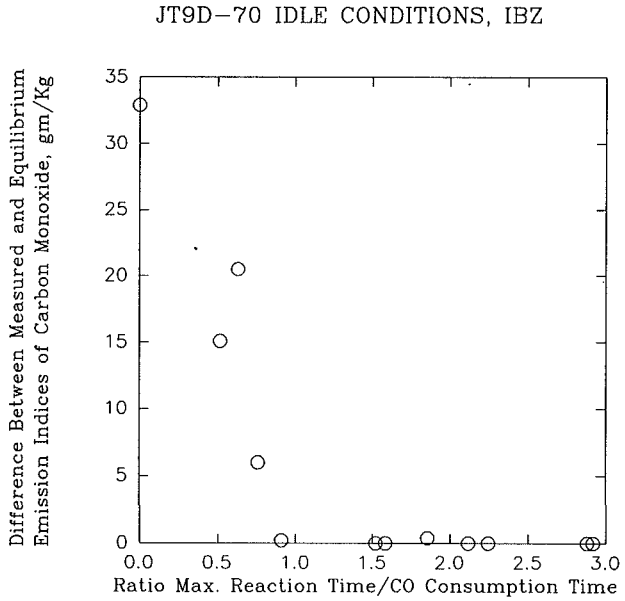

Fig. 3 Experimental engine: demonstration of real residence time for reaction from CO consumption

$\dot{m}_{\text{Tot}}$ = total mass flow in IBZ
$\dot{m}_f$ = fuel mass flow rate
$\dot{m}_{a,\text{inj}}$ = airflow introduced in fuel injector
T_{recirc} = recirculation zone bulk temperature
T_{spray} = mean temperature of fuel spray

Usually, entrainment depends on the square root of momentum ratio (Beer and Chigier, 1972), so combining Eqs. (8) and (9),

$$\tau_{\text{mix}} = C\left(\frac{M_{\text{recirc}}}{M_{\text{spray}}}\right)^{1/2} d_{\text{IBZ}}(2.0 + 0.637 d_{\text{IBZ}}) \tag{10}$$

where the constant C has been determined empirically to be 0.106 for this combustor. The value of C probably does not vary much for other combustors using this type of primary zone design; however, it could be, and almost certainly is, different for alternative primary zone designs. It was obtained presently by fitting the data to a single operating point; the value so obtained was then held constant for all other operating conditions.

The ignition delay time was determined from a data correlation in Arrhenius form (Sturgess, 1979). The fuel and air mixture at a mixed mean temperature T_{mix}, is taken as traveling in association with reacted gases of the recirculation zone at the burned gas temperature, T_B, such that the effective temperature for ignition is $T_{\text{mix}} + 0.25\ (T_B - T_{\text{mix}})$.

The characteristic time for hydrocarbon reaction is taken from Plee and Mellor (1979) as

$$\tau_{\text{HC}} = \frac{10^{-4}}{\phi_{\text{IBZ}}} \exp\ (21{,}000/RT_{\text{stoich}})\ \text{ms} \tag{11}$$

Generally, the values of τ_{HC} are so small (around 0.007 ms) that the heat release was assumed to take place instantaneously.

The time for CO consumption was also taken from Plee and Mellor (1979) as,

$$\tau_{\text{CO}} = 10^{-1} \exp\ (3100/RT_{\text{CO}}) \tag{12}$$

where

$$T_{\text{CO}} = 0.85T_{in} + 0.15T_B$$

If there were no concurrency of processes, chemical reactions would begin after time τ where,

$$\tau = \tau_{\text{evap}} + \tau_{\text{mix}} + \tau_{\text{delay}} \tag{13}$$

The values of τ were calculated using Eqs. (6)–(12), and are plotted against IBZ equivalence ratio in Fig. 2; a mean line through the data is indicated, at a value of 4.842 ms. If it is assumed that NO formation begins immediately after the HC reaction releases most of the calorific value of the fuel, the difference between this mean value and the intercept value from Fig. 1 represents a characteristic "process overlap time" due to concurrency of processes. It can be seen from Fig. 2 that τ_{overlap} has a value of 0.979 ms.

Hence, the maximum time for reaction, τ_{react}, is then given by,

$$\tau_{\text{react}} = \tau_{\text{Tot}} - (\tau - \tau_{\text{overlap}}) \tag{14}$$

When τ_{react} is equal to τ_{CO}, there is sufficient residence time left in the IBZ for the CO generated there to be reduced to the equilibrium value appropriate for the thermodynamic conditions existing in the IBZ. If $\tau_{\text{react}} < \tau_{\text{CO}}$, super-equilibrium values of CO will appear in the exhaust. This is illustrated in Fig. 3, where it can be seen that these conditions are satisfied remarkably well.

When the measured emission indices of CO are overplotted on the Westenberg plot, Fig. 4, it can be seen that for $\phi_{\text{IBZ}} > 0.98$ equilibrium values of CO exist; for $\phi_{\text{IBZ}} < 0.95$, the CO levels are greater than equilibrium, and correspond to indicated effective residence times around 0.1 ms. Again, these times are just for the conversion of CO to CO_2.

The effective time indicated by Fig. 4 is not in exact accord with the previous accounting of times, as may be realized by comparing Figs. 4 and 5. Figure 5 shows nonequilibrium levels of CO for available reaction times between 0 and 0.6 ms, so there is at least consistency with Fig. 4, but disagreement on level of reaction time. Given that the difference between measured and equilibrium values of CO is shown correctly to fall to zero for a unity ratio of calculated and required CO reaction times in Fig. 3, the doubt must fall on Fig. 4 rather than Fig. 5, and on the rate constants used in the Westenberg partial equilibrium calculation. Unlike the rate constants used for NO in Eq. (4), the CO rate constants were not pre-adjusted to other experimental data.

Reference to the calculations shows that for the experimental

Downloaded 02 Jun 2010 to 171.66.16.121. Redistribution subject to ASME license or copyright; see http://www.asme.org/terms/Terms_Use.cfm

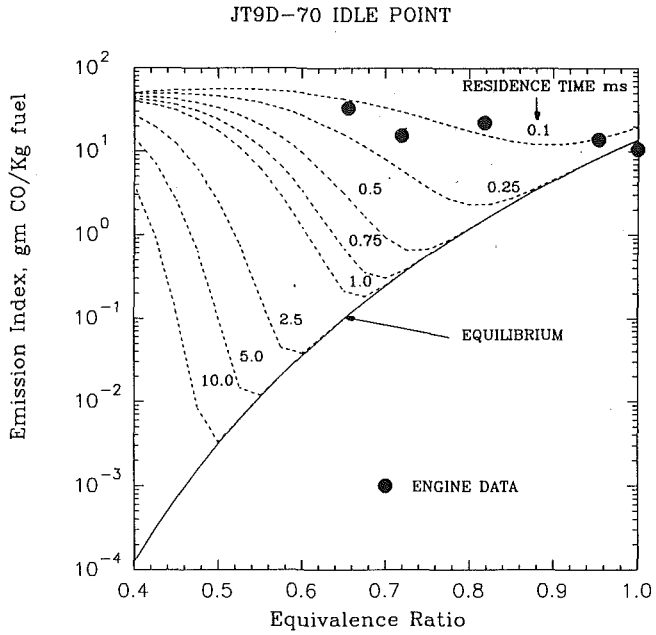

Fig. 4 Experimental engine: estimation of IBZ reaction residence time from Westenberg's partial equilibrium theory

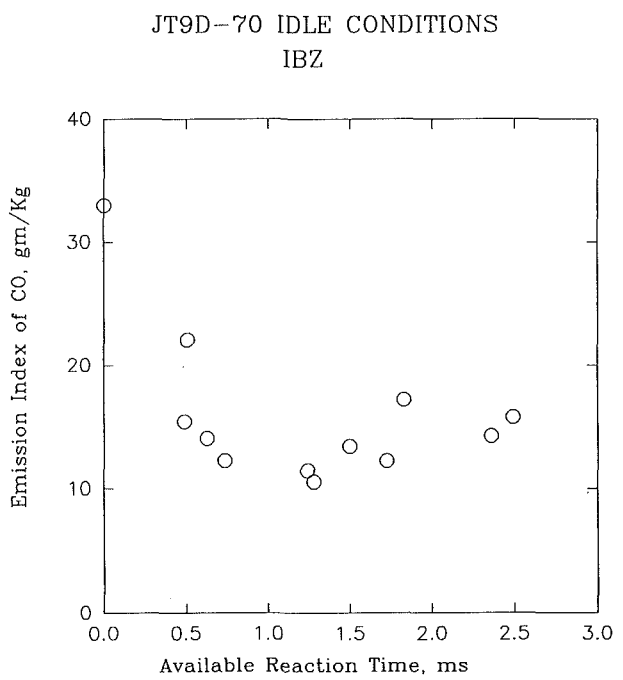

Fig. 5 Experimental engine: absolute reaction residence time from characteristic times

engine idle conditions, the calculated CO reaches a minimum for an equivalence ratio of 0.9 (Fig. 4), and the calculated NO_x reaches a maximum at an equivalence ratio of 0.95. Thus, the postulate for determining the IBZ equivalence ratio is not exactly correct. However, given the uncertainties in both the measurements and the calculations, it remains a good working hypothesis upon which to base airflow bookkeeping.

JT9D-70A Engine Data

The equivalence ratio of the IBZ is defined by

$$\phi_{IBZ} = \frac{OFAR \times 100}{\%Air_{IBZ} \times 0.068} \tag{15}$$

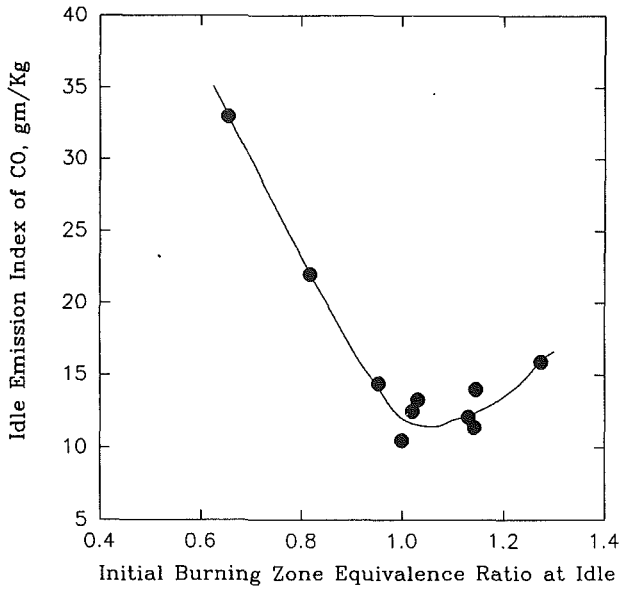

Fig. 6 Experimental engine: equivalence ratio for minimum CO at idle power

for Jet A fuel. If the minimum CO is attained with unity equivalence ratio (as postulated) at an overall fuel-to-air ratio (OFAR) of 0.0126 for JT9D-70A idle power, then the fraction of total combustor airflow that is active in the IBZ is found from Eq. (15) as 18.53 percent.

The airflow introduced through the combustor dome can fairly be considered to supply most of this active air. The dome airflow consists of the injector air, injector-guide leakage air, air provided for a small smoke-control swirler (insert swirler) mounted around the injector guide, and the dome cooling air. The remainder of the air will be recirculated from the transverse air jets used to terminate the IBZ. For a single row of opposed jets introduced through equal size, round, flush ports in the liners, this recirculated air was found by difference to be 27.9 percent of the jet air. It was found for a given dome flow that the amount of jet air recirculated depended on the number of rows of jets used, whether or not the air ports were of a uniform size, whether or not the jet rows were opposed or staggered, flush or plunged, etc., as might be expected.

The correlated idle-point data measured in the JT9D-70A engine were plotted against the IBZ equivalence ratio for different combustor geometries. These geometric variations covered different IBZ lengths, changes to the air port arrangements, and changes to the insert swirler; blockage rings were also used to vary the injector airflow. Figures 6 and 7 show the CO and NO_x results, with mean lines drawn through the data points. With the airflow accounting described above, it can be seen that the actual minimum CO was found at an IBZ equivalence ratio of 1.05, and the actual maximum NO_x was at unity equivalence ratio. However, the scatter is such that these differences from the postulate are not of great significance. The precision of the NO_x measurement is around ± 2 gm/kg.

For brevity, UHC results are not presented, but the idle combustion efficiency (involving both CO and UHC) reaches a maximum greater than 99.5 percent for 0.9 IBZ equivalence ratio. This is in accord with Fig. 4.

Figure 7 also shows the NO_x variation with IBZ equivalence ratio at engine approach conditions; at this higher-power point the maximum NO_x is again found around unity equivalence ratio. The trade that exists between idle power CO, and NO_x, as influenced by fuel-rich or lean burning, is illustrated for idle and approach powers in Fig. 8.

When the design is set for maximum combustion efficiency and minimum CO at idle, the IBZ is very rich at higher engine

Downloaded 02 Jun 2010 to 171.66.16.121. Redistribution subject to ASME license or copyright; see http://www.asme.org/terms/Terms_Use.cfm

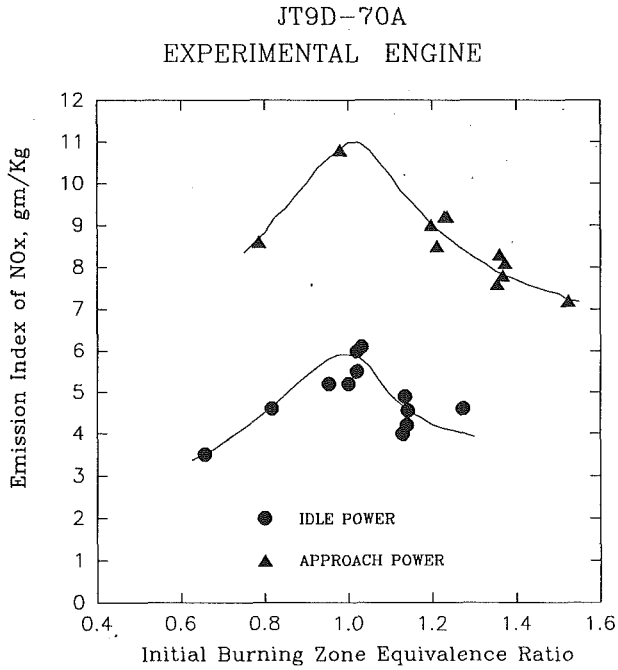

Fig. 7 Experimental engine: IBZ equivalence ratio for maximun NO_x at low power levels

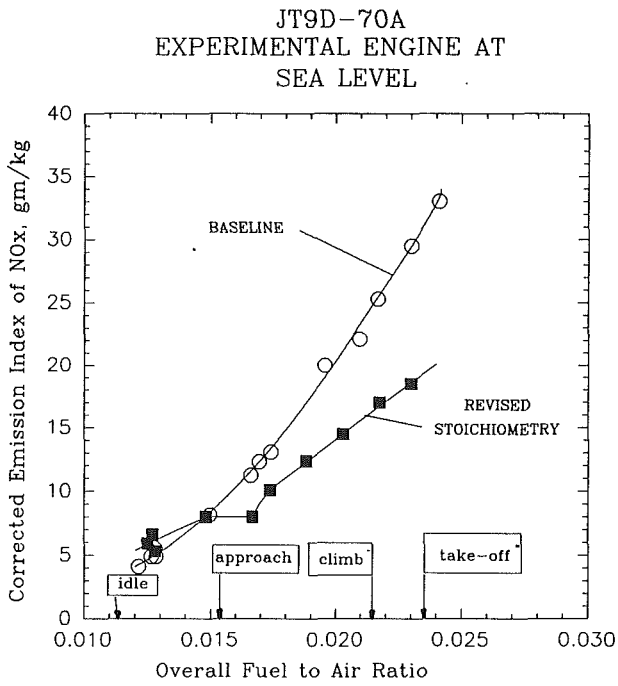

Fig. 9 Experimental engine: demonstration of NO_x characteristic with engine power, illustrating "quasi-staging"

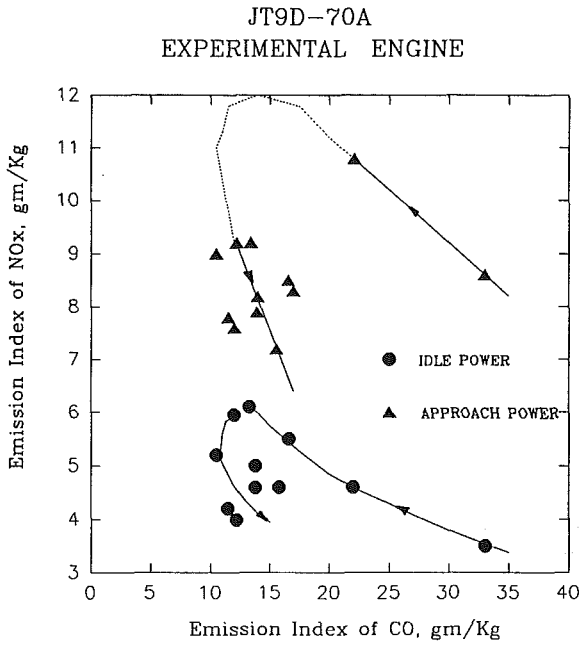

Fig. 8 Experimental engine: CO versus NO_x trade-off at low power levels

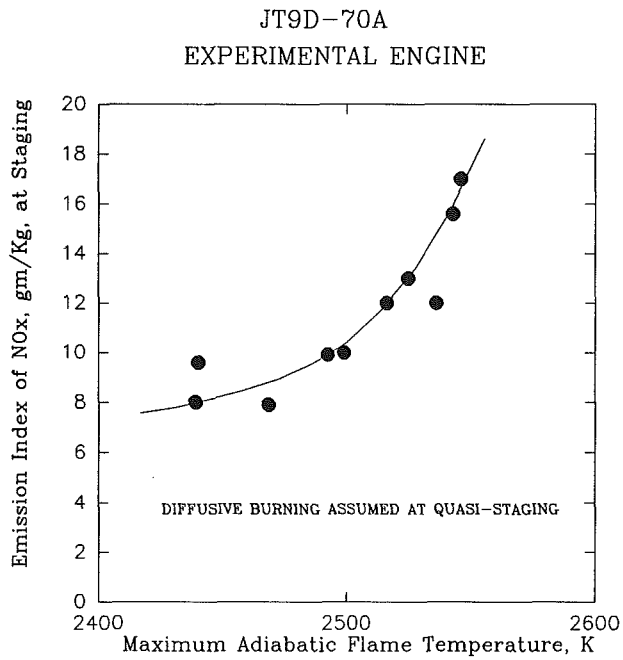

Fig. 10 Experimental engine: demonstration that "quasi-staging" takes place when IBZ is stoichiometric

power levels and the excess fuel burns lean in the secondary burning zone (SBZ). NO_x is therefore reduced over more conventional designs. Figure 9 compares NO_x up a sea level power line for the JT9D-70A original combustor and the modified combustor. The "hesitation" region of the RBQQLB NO_x curve represents ultralean burning in the SBZ with almost zero additional NO_x generation. Thus, at higher power levels the total NO_x produced is the sum of the rich IBZ and the lean SBZ.

The discontinuous character of the curve can be interpreted as being "aerothermochemical staging" of the combustor. The NO_x level at aerothermochemical staging is related to purely diffusive burning in the IBZ, as shown in Fig. 10.

The exhaust smoke increases with engine power to a maximum value at some intermediate power, and then decreases as takeoff power is approached. This characteristic arises because the total exhaust smoke is the result of two competing processes—soot generation in the rich and relatively cool IBZ, and soot burn-up in the lean and increasingly hot SBZ. The level of exhaust smoke is best controlled at the soot source, through the airblast fuel injector and the fine control of the insert swirler. This is demonstrated in Fig. 11.

The levels of all emissions are also powerfully influenced by the mixing achieved in the combustor. All conventional and stoichiometry-modified combustors represent a certain level of mixedness set up by the pressure drop across the combustor. If a well-stirred reactor represents the practical limit attainable for mixing, the level of mixing in gas turbine combustors can

Downloaded 02 Jun 2010 to 171.66.16.121. Redistribution subject to ASME license or copyright; see http://www.asme.org/terms/Terms_Use.cfm

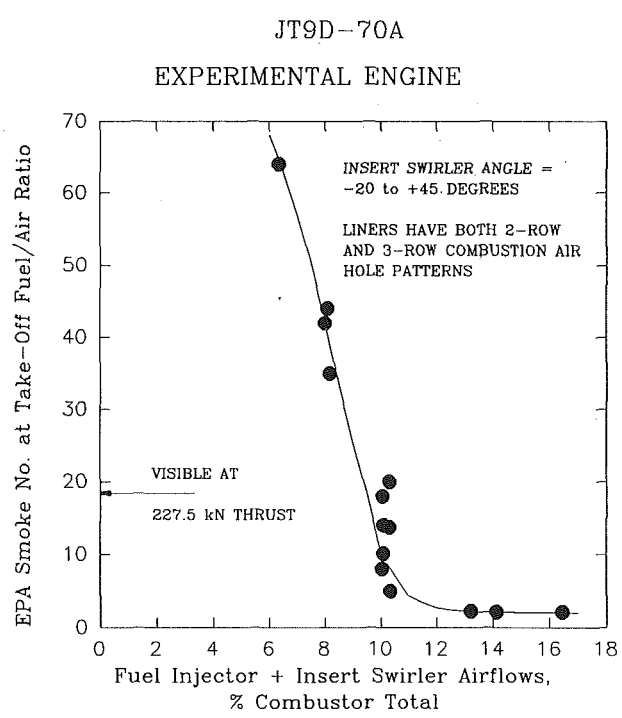

Fig. 11 Experimental engine: control of takeoff exhaust smoke through fuel injector and insert swirler airflows

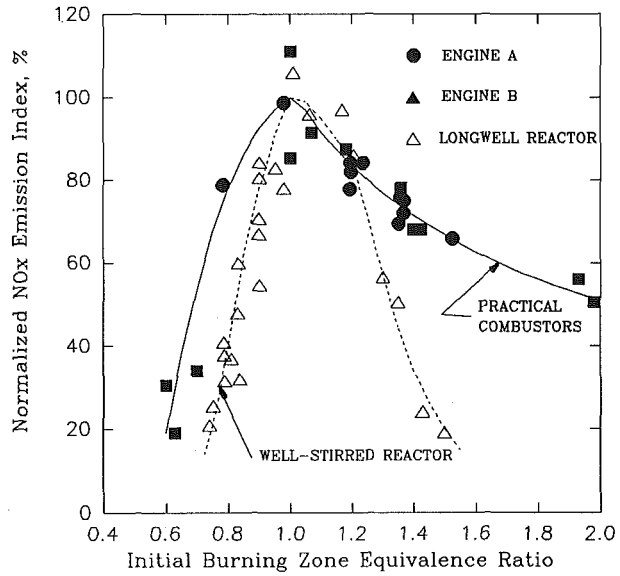

Fig. 12 Comparison of practical combustor NO_x emission behavior against the ideal of the well-stirred reactor

be gauged by comparing engine NO_x results against those obtained in a well-stirred reactor (WSR) burning gaseous fuel. Such a comparison is presented in Fig. 12, where the WSR is that of Longwell (1972) burning methane, and the liner pressure drop for the engine is 3.0 percent of the combustor inlet total pressure.

Low NO_x Methodology

The SBZ equivalence ratio can be defined as follows:

$$\phi_{SBZ} = \text{OFAR}\,(1-\phi_{SBZ}^{-1})\,\frac{100}{\%\ \text{Air}_{SBZ}\times 0.068} \tag{16}$$

The active air in the SBZ will involve the remainder of the jet air from the IBZ, any additional jet air specifically introduced into the SBZ, and some of the IBZ film cooling air, but none of the dilution zone air.

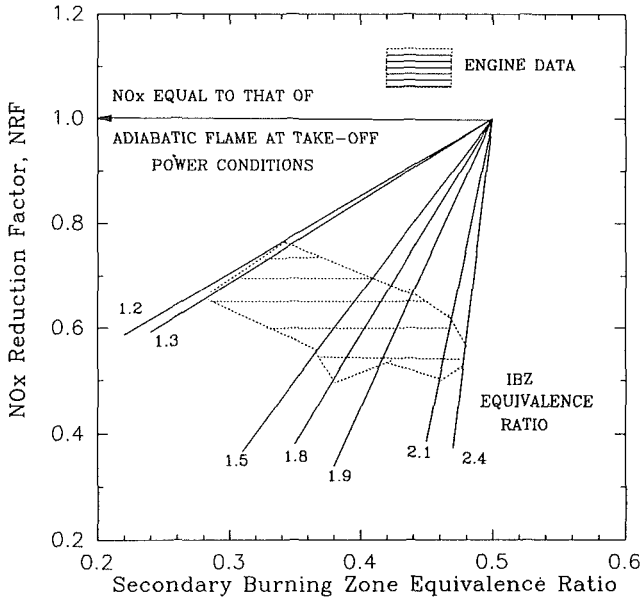

Fig. 13 NO_x control design chart for "quasi-staging"

When the measured NO_x values were plotted against SBZ equivalence ratio, the data were ordered by lines of constant IBZ equivalence ratio. The gradients of these lines were such that they were observed to converge for an SBZ equivalence ratio of 0.5. Referencing to the NO_x at this convergence point (base) enabled a NO_x reduction factor (NRF) to be defined where

$$\text{NRF} = EI_{\text{NOX}}/(EI_{\text{NOX}})_{\text{base}} \tag{17}$$

The engine results, replotted in the form of NRF's, are given in Fig. 13, where the hatched area represents the region of data points. The intersection point of the IBZ equivalence ratio lines, for which the NRF is unity, was found to represent a NO_x emission index value appropriate for the maximum adiabatic flame temperature representing the JT9D-70A takeoff power conditions. This was obtained from the engine data correlation of Kretschmer and Odgers (1973). The data used in this correlation were collected from older engines of conventional combustor design where the assumption of diffusive burning at stoichiometric conditions was entirely appropriate.

Figure 13 represents a low-NO_x design chart that is appropriate for the JT9D-70A engine. Since engine combustors all tend to have about the same liner pressure drop and specific residence time, the chart can be used as a guide for other engines, provided that they use either hybrid or pure airblast fuel injectors. Note that the figure indicates the NO_x advantages of operating the IBZ as rich as possible. This must be balanced against the limited exhaust smoke control achievable with fixed geometry combustors. Experience suggests a limit of 1.8 for the IBZ equivalence ratio when airblast injectors are used.

Direct Application to V2500 Combustor

The low NO_x design methodology embodied in the NRF chart of Fig. 13 was applied to the V2500 combustor, shown in Fig. 14. The assumption was that changes in emissions sensitivity due to differences in residence time and liner pressure drop between the JT9D-70A experimental combustor and

Downloaded 02 Jun 2010 to 171.66.16.121. Redistribution subject to ASME license or copyright; see http://www.asme.org/terms/Terms_Use.cfm

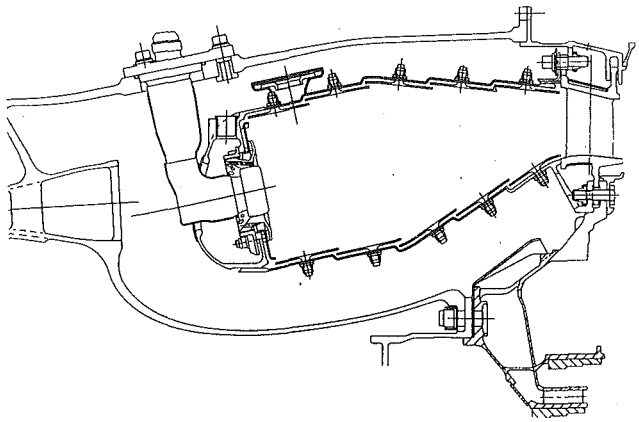

Fig. 14 Cross section of IAE V2500 combustor

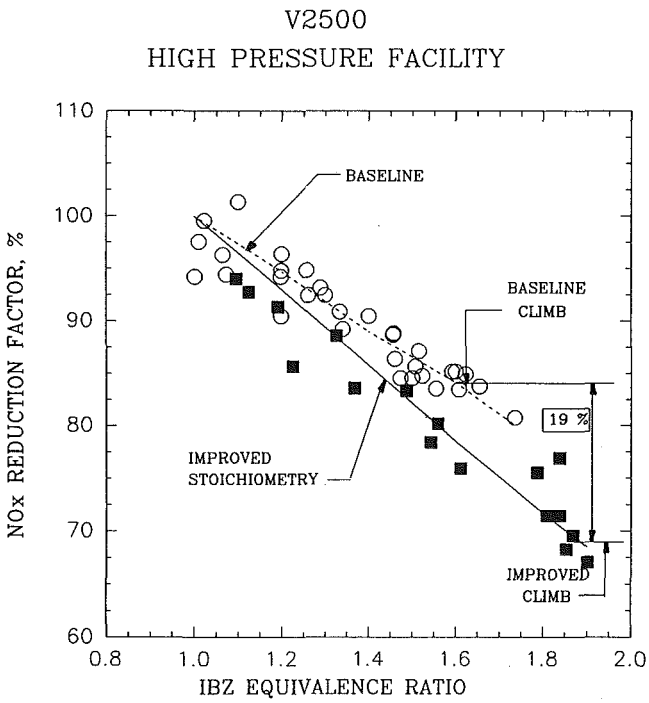

Fig. 15 V2500 in HPCL: NO_x reduction due to initial application of Fig. 13 design chart

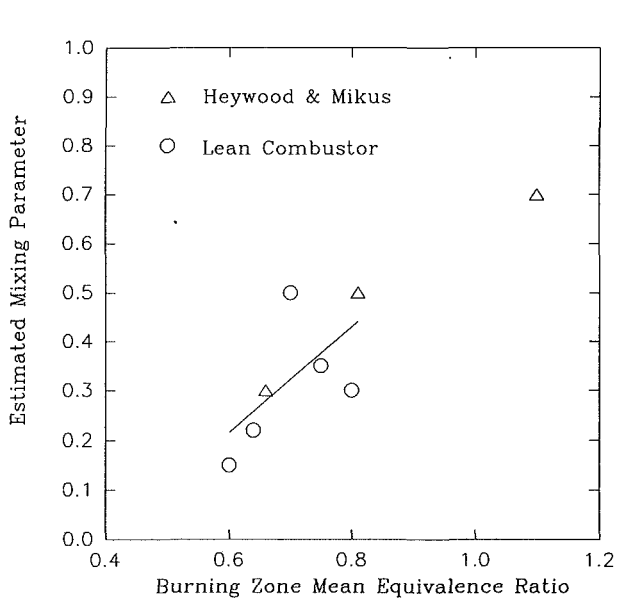

Fig. 16 Estimates of the mixedness of practical combustors

that of the V2500 would be small. This is a justifiable first step. However, the application was made in several increments to try to find an optimum split between IBZ and SBZ equivalence ratios for the V2500 combustor.

It was found that compared to the baseline-A1 combustor stoichiometry distribution, the minimum NO_x emissions were achieved by increasing the IBZ equivalence ratio 17 percent, while that of the SBZ was reduced 29 percent. Figure 15 indicates that at climb power conditions with this stoichiometry distribution, the emission of NO_x was reduced by 19 percent. Similar evaluations of the NO_x reductions at other power conditions, and calculation of the mission-weighted EPAP, showed that the revised configuration reduced it by 14 percent.

CFD Refinement

The axial distribution of bulk equivalence ratio along a combustor represents only a rough guide to the emissions reductions that are achievable. The actual values attained will really depend on the effective equivalence ratios at which most of the fuel is burned, i.e., on the fuel/air "mixedness" achieved.

If it is taken that in any non-premixed system the fuel really burns with a Gaussian distribution of equivalence ratios about the mean (Morton and Marshall, 1974), the mixing can be represented through the mixedness, S, where

$$S = \sigma/\bar{\phi} \tag{18}$$

and σ represents the standard deviation and $\bar{\phi}$ the mean equivalence ratio, such that $S=0$ represents a perfectly stirred reactor. Figure 16 gives some estimates for mixedness achieved in practical combustors by Heywood and Mikus (1973), and presently for a lean burning combustor. The uncertainties on each estimated mixedness are high (± 0.1), and the curve-fit is only for the limited range of lean equivalence ratios since S would not be expected to increase monotonically with mean equivalence ratio over both lean and rich conditions. The effect of $S>0$ is apparent in Fig. 12.

Significant changes in mixedness require combustor changes beyond the scope of the present guidelines. However, worthwhile improvements in macrolevel mixing might be achieved by careful positioning of the air ports in the liner that form the SBZ, so as to minimize NO_x-forming pockets of high-temperature gas. To this end, the NASTAR (Navier–Stokes Analysis for Arbitrary Regimes) CFD computer code (Rhie and Stowers, 1989) was utilized to gain an understanding of the reacting flow field in the modified combustor, and to examine the effects of circumferential redistributions of the various liner airflows.

The code was applied to the modified stoichiometry combustor operating at high-power conditions. The computational domain consisted of a single fuel injector segment of the combustor, with periodic boundary conditions. The grid employed consisted of 199,280 nodes, and a longitudinal cross-section is shown in Fig. 17. Liquid fuel was simulated by means of an appropriate gaseous fuel. Solution was made on a CRAY XM-P computer, and 19.6 CPU hours were required to reach convergence. Convergence was judged on the basis of the overall residuals, achieved temperature rise, and stability of major flow features. Grid-independent solutions are not claimed, but the bounding geometries are well represented. The solutions can be considered as being of engineering pragmatism, rather than of scientific exactitude.

Post-processing was accomplished on a Silicon Graphics IRIS workstation using the FAST and PLOT3D visualization software developed by NASA Ames. Combustion gas isotherms, an example of which is shown in Fig. 18, and isosur-

Downloaded 02 Jun 2010 to 171.66.16.121. Redistribution subject to ASME license or copyright; see http://www.asme.org/terms/Terms_Use.cfm

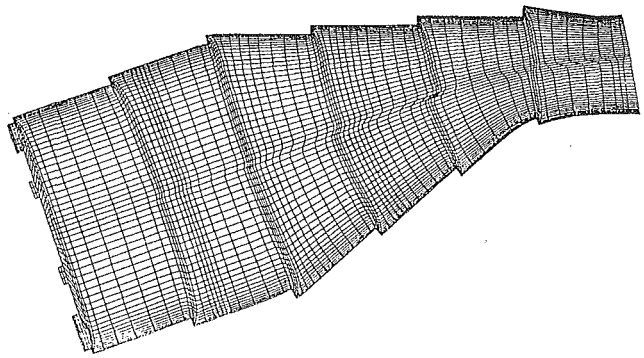

Fig. 17 Cross section of computational grid used for V2500 combustor CFD calculations

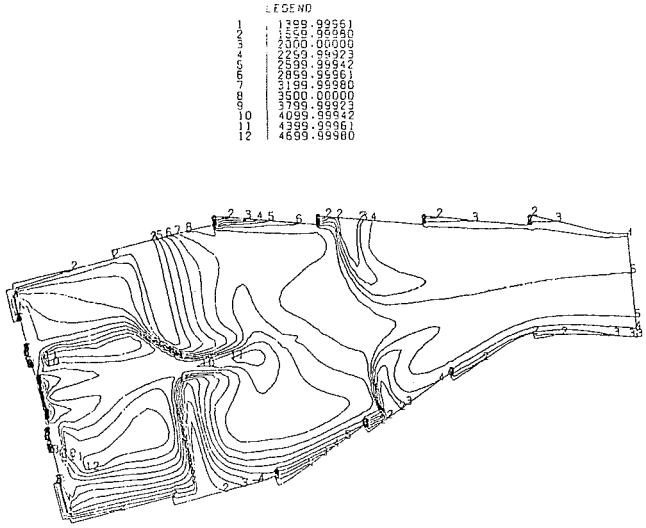

Fig. 18 Example of calculated isotherms in V2500 combustor

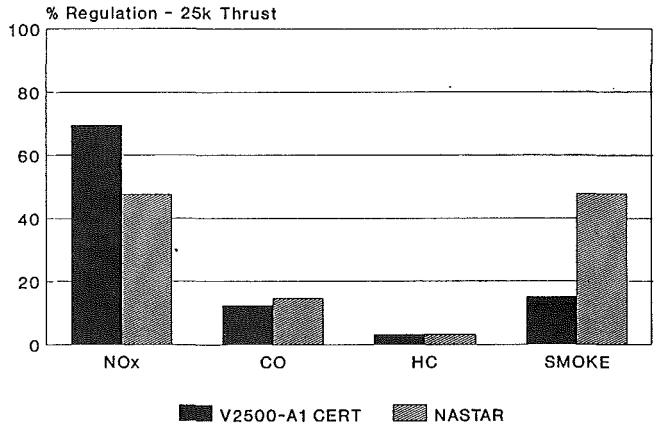

Fig. 19 V2500 engine: comparison of emissions from baseline combustor and the redistributed stoichiometry combustor after CFD refinement, at V2500-A1 conditions

faces, were examined to determine the volumes of thermal NO_x-producing hot gases. The aerodynamics of the flow field were assessed via tracers introduced from the fuel injector and combustion and dilution air jets.

The aim of the study was to minimize the extent of gaseous hotspots in the combustor flow field, and so reduce NO_x generation. Guided by the CFD results, the positions of the airports in the SBZ were adjusted to match the calculated flow from the IBZ better. Here, the intent was to increase macromixing by maximizing interaction of the air jets with the excess gasified and partially reacted fuel leaving the IBZ.

When the refined design was tested, the NO_x emission index at climb was reduced by 23 percent compared to the Bill-of-Materials (B/M) -A1 configuration, and the EPAP was reduced by 19 percent. Figure 19 compares the emissions as a percentage of the ICAO regulation for the B/M combustor and the NASTAR-refined, adjusted stoichiometry combustor. These are engine results. The slight NO_x–CO and more significant NO_x–smoke trades are evident; however, the values of these pollutants remain well below the regulation levels.

Discussion

With some convenient assumptions, emissions test data from an experimental engine using a combustor modified to have a fuel-rich front end at high power levels, have been analyzed phenomenologically in terms of axially displaced, two-stage burning.

Since a combustor is shown to behave as though fuel-staged at intermediate powers (Fig. 9), "staging" takes place automatically when the initial burning zone reaches stoichiometric conditions (Fig. 10), and unreacted fuel then spills over into a secondary burning zone where it is burned fuel-lean. The attained emissions levels represent a trade-off between NO_x and CO (Figs. 7–9). The use of airblast atomization for preparation of most or all of the injected fuel, together with smoke control air introduced intimately with the fuel sources (Fig. 11), enables IBZ equivalence ratios as high as 1.8 to be used without generating excessive smoke. The mixing of fuel and air controls the effectiveness of the stoichiometry distribution in reducing NO_x (Fig. 12).

The analyzed data were presented in terms of a NO_x reduction factor (NRF), relating the achieved NO_x to the maximum NO_x, as a function of IBZ and SBZ equivalence ratios (Fig. 13). This plot indicates that lowest NO_x is obtained with IBZ equivalence ratios as high as possible, and SBZ equivalence ratios as low as possible. This is expected since these conditions represent minimum bulk flame temperatures in each zone. However, the NRF plot also indicates that reductions in SBZ equivalence ratio are more effective at higher IBZ equivalence ratios than lower ones.

At idle power levels in the experimental engine, actual available residence time in the IBZ for reduction of CO to equilibrium levels was found to be quite small (less than 0.8 ms) in relation to the one-dimensional bulk residence time (4.5 to 6.0 ms). This is because most of the residence time is taken up with mixture preparation (fuel evaporation, mixing, and ignition delay). Concurrency of the processes in mixture preparation is equivalent to about 1 ms residence time. Mixing is the limiting time.

The NO_x control methodology embodied in the NRF chart was successfully applied to an entirely different combustor for the V2500 engine (Fig. 15). The successful transfer between engines was because specific residence time and liner pressure drop do not differ much from combustor to combustor designed to a common design system. However, mixing is still important, even on the macrolevel. This explains the further success (Fig. 19) achieved at the same pressure drop, by refining the modified combustor via the CFD calculations to provide optimum circumferential locations of the SBZ air ports in the liners, for mixing air with the IBZ discharge flow. The value of CFD when used in this fashion is well demonstrated.

The present success demonstrates that considerably greater NO_x reduction potential is available in the RBQQLB approach if the restraining caveats existing for this generation of the V2500 combustor are lifted. Stoichiometric interfaces at interior cooling films in the IBZ, responsible for most of the IBZ NO_x, could be eliminated with use of improved liner materials and external cooling, for example. Mixing in the SBZ could be dramatically improved with redesign of the combustor

Downloaded 02 Jun 2010 to 171.66.16.121. Redistribution subject to ASME license or copyright; see http://www.asme.org/terms/Terms_Use.cfm

cross section to present SBZ combustion air better to the unburned gasified fuel exiting from the IBZ. Both of these improvements would lower NO_x production, while the latter could also enhance soot burn-up to minimize exhaust smoke. Flexibility of the RBQQLB approach could be further amplified with the addition of variable geometry to break the trade between low NO_x at high power and higher CO at lower power.

Conclusions

1 Modification of the axial distribution of fuel/air stoichiometry in a conventional combustor to provide at high engine powers a rich initial burning zone followed by a lean secondary burning zone, has been shown to result in a favorable NO_x–CO trade; the use of airblast atomization for liquid fuel results in adequate exhaust smoke control for operation to equivalence ratios as high as 1.8.

2 The rich/lean combustor results in a NO_x versus engine power curve that simulates axial fuel staging behavior.

3 A design methodology for NO_x reduction factor has been devised. This methodology indicates leaner secondary burning zones are more effective at richer initial burning zones, for lower overall NO_x.

4 Application of the NO_x reduction methodology was successfully made to a separate existing engine combustor, and worthwhile reductions in NO_x were achieved without loss of control of CO or smoke.

5 CFD was used to refine the modified combustor, and a further improvement in emissions was gained. Pressure loss was unaffected, and exit temperature distributions were acceptable to the turbine.

6 Mixing of fuel and air limits the effectiveness of emissions control by stoichiometry modification. Improvements in mixing at even the macrolevel can result in significant changes in the efficacy of stoichiometry modification.

Acknowledgments

The authors wish to thank United Technologies Corporation, Pratt & Whitney, for permission to publish this paper. Thanks also to members of the International Aero-Engines team for their encouragement and assistance. Appreciation is expressed to our customers for their useful input.

References

Bahr, D. W., 1985, "Technology for the Design of High Temperature Rise Combustors," AIAA Paper No. AIAA-85-1292.

Ballal, D. R., and Lefebvre, A. H., 1981, "Flame Propagation in Heterogeneous Mixtures of Fuel Droplets, Fuel Vapor and Air," *Proc. 18th Symposium (International) on Combustion*, The Combustion Institute, pp. 321–328.

Beer, J. M., and Chigier, N. A., 1972, *Combustion Aerodynamics*, Halstead Press Div., Wiley, New York.

Cooper, L. P., 1980, "Effects of Degree of Fuel Vaporization Upon Emissions for a Premixed, Partially Vaporized Combustion System," NASA Tech. Paper No. 1582.

Heywood, J. B., and Mikus, T., 1973, "Parameters Controlling Nitric Oxide Emissions From Gas Turbine Combustors," presented at AGARD Propulsion & Energetics Panels 41st Meeting on Atmospheric Pollution by Aircraft Engines, London, United Kingdom.

Koff, B., 1991, "Spanning the Globe With Jet Propulsion," AIAA/SAE William Littlewood Memorial Lecture, AIAA Paper No. 2987.

Kretschmer, D., and Odgers, J., 1973, "Modeling of Combustors: The Effects of Ambient Conditions on Performance," ASME Paper No. 73-WA/GT-6.

Lefebvre, A. H., 1983, *Gas Turbine Combustion*, Hemisphere Publishing Corp., McGraw-Hill Book Co.

Longwell, J. P., 1972, *Proc. Emissions From Continuous Combustion Systems*, W. Cornelius and W. G. Agnew, eds., Plenum Press, New York, pp. 91–94.

Morton, H. L., and Marshall, R. L., 1974, "Impact of Emission Regulations on Gas Turbine Combustor Design," *Canadian Aeronautics and Space Journal*, Vol. 20, No. 3, pp. 101–109.

Plee, S. L., and Mellor, A. M., 1979, "Characteristic Time Correlation for Lean Blowoff of Bluff-Body-Stabilized Flames," *Comb. Flame*, Vol. 35, pp. 61–80.

Pratt, B. S., and Pratt, D. T., 1984, "An Interactive Code for Calculation of Gas-Phase Chemical Equilibrium," NASA Report No. CR-168337.

Quan, V., Marble, F. E., and Kliegel, J. R., 1972, "Nitric Oxide Formation in Turbulent Diffusion Flames," *Proc. 14th Symposium (International) on Combustion*, The Combustion Institute, pp. 851–860.

Rhie, C. M., and Stowers, S. T., 1989, "Numerical Analysis of Reacting Flows Using Finite Rate Chemistry Models," Paper No. AIAA-89-0459.

Sarli, V. J., Eiler, D. C., and Marshall, R. L., 1975, "Effects of Operating Variables on Gaseous Emissions," presented to Air Pollution Control Association (APCA) Specialty Conference on Air Pollution Measurement Accuracy as It Relates to Regulation Compliance, New Orleans, LA.

Semerjian, H. G., and Ball, I. C., 1977, "Potential Reduction of NO_x Emissions With Premixed Combustion," presented at the Spring Technical Meeting of The Combustion Institute—Central States Section, NASA-Lewis Research Center.

Simmons, H. C., 1971, Parker-Hannifin Corp., private communication.

Spalding, D. B., 1955, *Some Fundamentals of Combustion*, Butterworths Scientific Publications, London.

Sturgess, G. J., 1979, "Advanced Low Emissions Catalytic Combustor Program," *Proc. Premixed, Prevaporized Combustor Technology Forum*, NASA Rept. CP-2078.

Sturgess, G. J., Sloan, D. G., Lesmerises, A. L., Heneghan, S. P., and Ballal, D. R., 1992, "Design and Development of a Research Combustor for Lean Blow-Out Studies," ASME JOURNAL OF ENGINEERING FOR GAS TURBINES AND POWER, Vol. 114, pp. 13–19.

Westenberg, A. A., 1971, "Kinetics of NO and CO in Lean, Premixed Hydrocarbon–Air Flames," *Combustion Science and Technology*, Vol. 4, pp. 59–64.

Zeldovich, Y. B., Sadovinikov, P. Y., and Frank-Kamenetskii, D. A., 1947, "Oxides of Nitrogen in Combustion," *Proc. Acad. Sci. USSR*, Inst. Chem. Phys., Moscow–Leningrad, M. Shelef, translator.

Downloaded 02 Jun 2010 to 171.66.16.121. Redistribution subject to ASME license or copyright; see http://www.asme.org/terms/Terms_Use.cfm

J. B. McVey

F. C. Padget

T. J. Rosfjord

United Technologies Research Center,
East Hartford, CT 06108

A. S. Hu

A. A. Peracchio[1]

B. Schlein

D. R. Tegel[2]

Pratt and Whitney,
Commercial Engine Business,
East Hartford, CT 06108

Evaluation of Low-NO_x Combustor Concepts for Aeroderivative Gas Turbine Engines

An experimental program was conducted to evaluate low-NO_x combustor concepts applicable to natural-gas-burning aeroderivative gas turbine engines operating at a nominal pressure ratio of 20:1. Gas sampling measurements at the exit of the primary zone of high-shear and lean premixed burners were acquired under elevated entrance pressure and temperature conditions over a range of primary zone equivalence ratios. Piloting systems were incorporated in most of the burner designs to achieve satisfactory burner operability. Both swirl stabilized and perforated-plate (grid) stabilized burners were found to produce NO_x levels lower than the current engine goal of 25 ppm (15 percent O_2).

Introduction

The commonly used method of reducing the amount of oxides of nitrogen from the exhaust of gas turbines by use of water or steam injection, although effective, presents several problems. Water, when available, needs to be demineralized whether injected as a liquid or as steam and therefore increases operating costs. Carbon monoxide is increased. Water injection may contribute to combustion noise that leads to durability problems.

Dry low-NO_x operation, while providing a significant commercial advantage, involves more complex combustion and fuel systems. Such systems have been successfully demonstrated in industrial gas turbines, especially those with large silo burners (Becker et al., 1986) where physical space is not a major consideration. Implementation is more difficult in aeroderivative gas turbines. In order to achieve the high power to weight output in the small spaces required for aviation applications, the combustors of aeroderivative engines operate at pressures of 20 to 30 atmospheres, inlet temperatures of 800 to 1100°F and volumetric heat release rates of 5 to 6 million Btu/h-cu ft-atm. The increased temperature and pressure cause higher rates of formation of NO_x while the reduced volume available leaves little physical room for alternative chamber designs.

The principles for minimizing NO_x formation in a gas turbine combustor primary zone are well established. Either the combustor is operated with a very fuel-rich front end and the reaction is rapidly quenched, or it is operated with a lean primary zone and special steps are taken (variable geometry, fuel staging, enriched pilot zones, etc.) to ensure stable part-power operation. Industrial engines applied to operations where clean gaseous fuels are available are focusing on the lean approach. These low-pressure-ratio systems are free from autoignition and flashback, and the large chamber volumes available permit individual burners to be isolated from one another so that burner staging can be implemented without the inactive burners quenching the products output by the active burners.

In high-pressure-ratio aeroderivative engines, premixing must be performed rapidly due to the decreased autoignition times associated with elevated compressor discharge temperature and pressure. Isolated burners cannot be accommodated in the compact burner envelope. Some other form of staging must be effected to ensure stable operation. Air staging in which primary zone stoichiometry is maintained at a high level at part power has generally been found to be impractical due to the projected unreliability of variable geometry air-handling devices. Fuel staging by the use of pilot zones that locally enrich an otherwise uniform mixture appears promising in light

[1]Current address: United Technologies Research Center, East Hartford, CT.
[2]Current address: General Electric Company, Schenectady, NY 12345.

Contributed by the International Gas Turbine Institute and presented at the 37th International Gas Turbine and Aeroengine Congress and Exposition, Cologne, Germany, June 1-4, 1992. Manuscript received by the International Gas Turbine Institute February 6, 1992. Paper No. 92-GT-133. Associate Technical Editor: L. S. Langston.

Copyright © 1993 by ASME
Downloaded 02 Jun 2010 to 171.66.16.121. Redistribution subject to ASME license or copyright; see http://www.asme.org/terms/Terms_Use.cfm

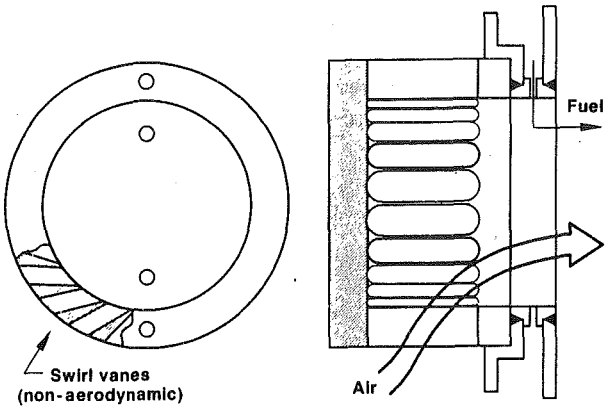

Fig. 1 High-shear injector configuration

of the development of sophisticated electronic fuel control systems. The compact nature of aeroderivative engine combustors also places a further burden on the designer due to the requirement that a commercially viable engine must be equipped with a fuel injection system that can also operate on liquid fuels and that then requires water or steam injection to provide NO_x control.

This program was undertaken as part of a Turbo Power and Marine (TPM) and Pratt & Whitney (PW) effort to evaluate the potential of lean primary zone low-NO_x combustion concepts applicable to the TPM FT-8 engine, a moderate pressure ratio (20:1) aeroderivative engine.

Approach

A review of the recent literature and our own in-house work identified two approaches that could have applicability to a 20:1 aeroderivative engine. One approach is the high-shear combustion system, which has been under investigation at the University of Leeds for a number of years (Al Kabie and Andrews, 1990). In that approach fuel is injected into the high-shear region produced by an air swirler; rapid combustion ensues. Very low NO_x levels have been reported for tests conducted under atmospheric pressure test conditions.

The second approach is lean premixed combustion. The challenges here are to achieve adequate premixing and adequate flame stability. Two different strategies to achieving the necessary flame stability are in use. Swirl stabilized systems are being employed in heavyweight industrial engines by both Siemens Kraftwerke Union (Becker et al., 1986; Maghon et al., 1990) and by ABB (Sattelmayer et al., 1992; Aigner et al., 1990). Those implementations differ in the nature of the air swirlers and fuel injection methods employed.

The second flame stabilization strategy is the use of a perforated plate or grid, which can provide a relatively quiescent wake stabilization region. This region should have different stability characteristics compared to the vigorously stirred vortex breakdown region, which serves as the stabilization site in swirl-stabilized devices. This approach was investigated using fully premixed and prevaporized liquid fuels for aircraft engine application at United Technologies (McVey and Kennedy, 1980) as well as in other studies conducted as part of the NASA-sponsored activity to suppress NO_x emissions in the stratosphere (Tacina, 1990). Advantages of the bluff-body stabilized systems are that no residual swirl, which can affect turbine aerodynamics and heat transfer, is introduced in the burner flow, and the size of the recirculation regions, where NO_x can be expected to be formed in significant quantities, will be smaller than in the case of the swirl-stabilized devices.

To evaluate these concepts, burner modules were fabricated and tested in an apparatus having a characteristic dimension of 5 in. (This is approximately the annulus height of the FT-8 aeroderivative engine.) The modules replicated the primary zone of the burner and were based on the specification that the primary zone equivalence ratio would range from 0.5 to 0.6 at rated power. Evaluation of the merits of a given configuration was based on sampling and analyses of the primary zone gas output. In practice, additional air (approximately one-third of the total burner air) would be introduced into the burner at the primary zone exit to further oxidize the CO and to provide temperature pattern control. For this lean-primary-zone burner, the additional air would be expected to have no impact on NO_x output (dilution effects are accounted for by the conventional practice of reporting NO_x on the "corrected to 15 percent O_2 basis"). The burner modules tested are characteristic of the concept as it would be implemented on engines except certain modules were equipped with more than one piloting source for purposes of exploring piloting effectiveness. The design procedure utilized both CFD and flow visualization techniques (not reported here) to establish module characteristics such as swirler angles, and the size, location, and number of injection sites. Final combustor module design descriptions and the results of combustion test program are described hereunder. The objective of this program was to screen the three described fuel injectors with regard to low-NO_x potential and burner operability when employing natural gas fuel.

Table 1 High-shear injector fuel orifice patterns

Number of Orifices	Orifice Diameter (in.)	Injection Angle
42	0.047	Normal to Flow
18	0.047	Normal to Flow
8	0.078	30 deg Upstream
4	0.078	30 deg Upstream

Combustor Concept Description

Three different fuel–air preparation concepts were evaluated in this program. Each device was attached to the same tubular combustion chamber for the evaluation. All the air entering the combustion chamber passed through the fuel–air preparation devices consisting of appropriately sized air swirlers, mixing tubes, and gas injection passages. Descriptions of the hardware (referred to hereafter as "injectors") embodying these concepts follow.

High-Shear Fuel Injector. The high-shear module (Fig. 1) was designed to provide for the injection of gaseous fuel into a highly turbulent region created by an intense tangential shear flow; this is to result in rapid mixing, burning, and quenching of the gases. The turbulent region is generated at the periphery of the swirling jet exiting the swirler, where the highly swirled air contacts the quiescent region formed by the sudden expansion of the passage diameter from the swirler diameter to the burner diameter. Fuel is injected into this turbulent region at locations immediately upstream of the injector discharge.

The tested high shear injector consisted of a radial inflow swirler composed of 22 equally spaced slots 0.25 in (0.64 cm) wide by 0.65 in. (1.65 cm) long set at a 45 deg angle to the radius. The slots are formed by wedge-shaped vanes. The number, size, and inclination of the metering holes through which the gaseous fuel was injected were varied to achieve a variety of fuel penetration levels (Table 1). There was no provision for pilot fuel injection in this device.

Aero-Vane Injector. The aero-vane injector (Fig. 2) was designed to achieve the highest possible level of fuel–air premixing prior to the introduction of the mixture into the combustor. This device provided two flow paths: a primary flow and a pilot flow. An annular array of 32 airfoil-shaped vanes admitted the premixed airflow in a radial-inflow manner. The airfoils were 0.9 in. tall, positioned within a 4.0-in.-dia circle,

Downloaded 02 Jun 2010 to 171.66.16.121. Redistribution subject to ASME license or copyright; see http://www.asme.org/terms/Terms_Use.cfm

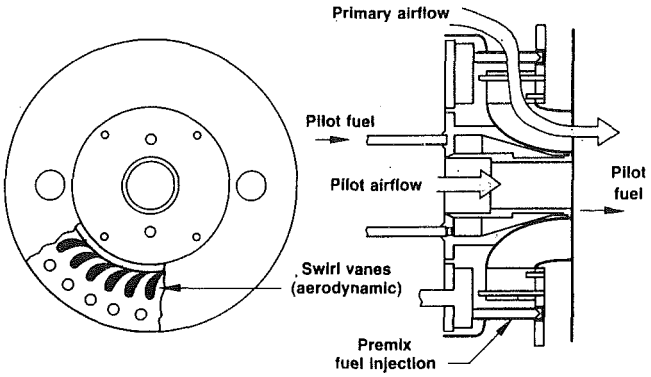

Fig. 2 Aero-vane injector configuration

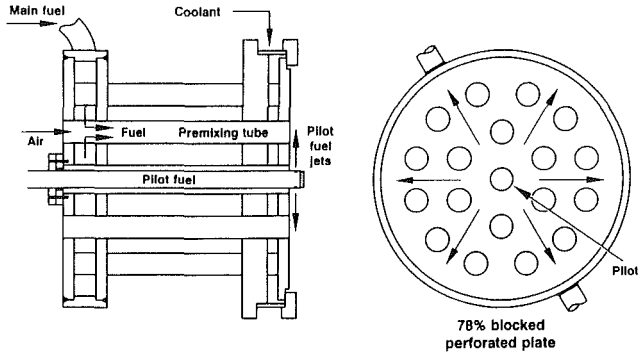

Fig. 3 Piloted perforated plate injector configuration

and imposed swirl with a vane turning angle of 60 deg. Fuel injection tubes were located upstream of and between each pair of vanes. Each tube had two rows of five equally spaced fuel injection orifices of 0.015 in. diameter providing a total of 320 fuel injection locations for the device. The two orifice rows were on opposite sides of each fuel tube and oriented to inject gas normal to the approaching airflow. The multiplicity of fuel injection sites, long mixing path length, and the use of airfoil vanes were design features felt necessary to achieve a high degree of fuel–air premixing, minimum pressure loss, and separation-free flow compatible with preignition margin. Small-diameter injection tubes were selected to minimize the extent of wake regions. Quarter-ellipsoid wall contours turned and accelerated the premixed flow toward the annular exit defined by outer and inner diameters of 2.7 in. and 1.1 in., respectively. The pilot airflow passage was cylindrical with a diameter of 0.9 in. During the course of the test program, flow restrictors were placed within this passage to alter the percentage of the total airflow that passed through the pilot. For the data presented here, a circular flow restrictor, 0.505 in. diameter, was used to establish the pilot airflow as 10 percent of the total airflow. Pilot fuel was injected in the axial direction through 18 equally spaced, 0.015-in.-dia orifices located on a 0.99 in. layout diameter on the exit end of the pilot.

Piloted Perforated Plate Injector. The piloted perforated plate injector used multiple fuel–air premixing tubes extending upstream from a combustion stabilization plate (Fig. 3). Eighteen premixing tubes were arranged in two circular arrays, with six tubes equally spaced on a 2.09-in.-dia circle and twelve tubes equally spaced on a 4.02-in.-dia circle. Each tube had an inside diameter of 0.555 in. Together, the 18 flow paths represented 22 percent of the cross-sectional area of the 5-in.-dia combustor. This open area percentage was specified in order to achieve a nominal 3.5 percent pressure loss at the high power test condition. The tubes had an overall length of 5.0 in., with fuel injected into each tube 0.63 in. from the tube inlet through three equally spaced 0.031-in.-dia orifices. A welded manifold supplied all tubes. The combustion stabilization plate was constructed from 0.25-in.-thick, type T-304 stainless steel, which was electron-beam welded onto the tube array. This plate had an outer diameter of 5.5 in. to permit the assembly to be held in a mounting flange. A backing plate was located upstream of the stabilization plate to form a 0.25 in. wide gap for backside cooling airflow. The air coolant flow was supplied to this gap from the mounting flange. The coolant was injected over a 100 deg arc of the circumference, convected across the plates, captured over a similar 100 deg arc, and fed into the combustor downstream of the gas sampling location. The total coolant flow rate, nominally 0.2 lb/s, was adequate to maintain backside stabilization plate temperatures to less than 1200°F; no other thermal protection was used. A pilot fuel injector was positioned on the centerline of the stabilization plate. This injector consisted of a separate tube with six equally spaced, 0.038-in.-dia orifices oriented to inject fuel 0.1 in. downstream of, and parallel to, the plate face. The mounting holes that held the pilot were slotted to permit a rotation of the pilot jet orientation with respect to the premix tube array.

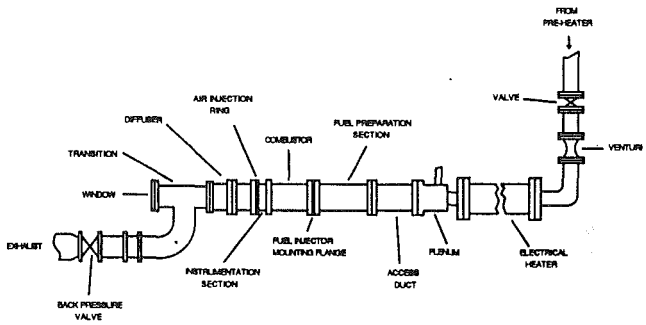

Fig. 4 Schematic diagram of single-injector test apparatus with a nominal 5-in.-diameter

Test Apparatus

The test facility and related systems permitted independent control of airflow, fuel flow, inlet temperature, and combustor pressure. The test apparatus (Fig. 4) was essentially a series of components of circular cross section flanged together. The facility air delivered to the test cell was initially heated to about 300°F using a remote, nonvitiated natural-gas-fired heater, was metered by a venturi, and additionally heated to the desired combustor entrance temperature by an electrical resistance-type heater located immediately upstream of the test facility. The air was delivered to an access spool, located upstream of the test section, where static pressure and stagnation temperature profiles were acquired. The access spool fed the airflow to the fuel preparation section which housed the fuel injector. The fuel injector was secured to a 0.5-in.-thick water-cooled mounting flange, which comprised the combustor bulkhead. Gaseous fuel was delivered to the main fuel injector and piloting sites using three independently regulated and metered supplies. Commercial grade methane, having the characteristics of natural gas, was supplied by tube trailers.

The combustion chamber (Fig. 5) was a 13-in.-long cylindrical section of jacketed steel pipe containing a 1.5-in.-thick castable ceramic liner, which provided a 5-in. ID. The insulating liner was cast from a commercially available ceramic consisting mostly of alumina. The outer jacket was fed with water coolant at a nominal coolant flowrate of 10 gpm; this provided a usable test apparatus pressure rating of 265 psia. The combustor housing contained a passage in which a 20-joule spark ignitor was located.

Downloaded 02 Jun 2010 to 171.66.16.121. Redistribution subject to ASME license or copyright; see http://www.asme.org/terms/Terms_Use.cfm

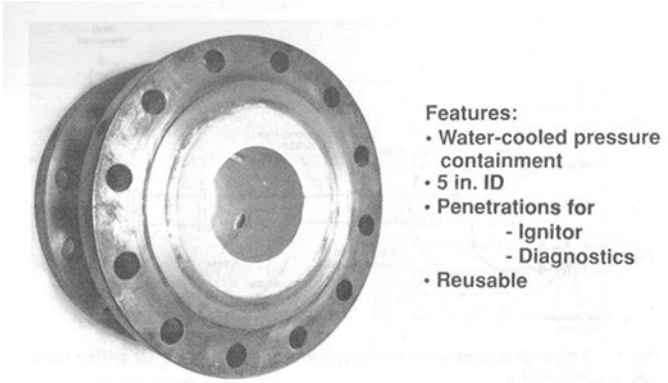

Fig. 5 View of combustor test section showing ceramic liner with a 5-in. diameter

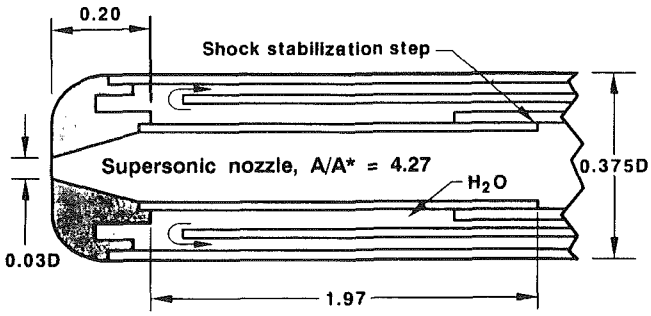

Fig. 6 Aerodynamic-quenching gas sampling probe tip details

A water-cooled instrumentation section incorporating seven emissions probes and two static pressure taps was located immediately downstream of the combustor exit. A description of the probe design is given in the following section. The probe tips extended upstream into the combustion chamber such that the distance from the fuel injector exit to the sampling location was 10 in. This distance provided a residence time of 15 ms at a baseline reference velocity of 54 ft/sec based on non-combusting flow conditions (7 ms based on hot flow conditions). These values are comparable to those existing in the FT-8 engine.

Downstream of the instrumentation section, the combustor exhaust passed through an air injection ring (intended to terminate any extended vortex breakdown region produced by the swirl-stabilized fuel preparation devices), a diffuser, and then into a transition section. The transition section diverted the flow through two 90 deg turns prior to encountering exhaust coolant water sprays and the back-pressure valve. A window was located in the transition section along the combustion centerline in order to permit observation of the flame patterns.

Temperatures, pressures, airflow rates, and fuel flows were measured by conventional transducers, scanners, and flowmeters; data were processed by an automatic data acquisition and recording system.

Combustor emissions levels were determined from a seven-probe gas sampling array installed in the instrumentation section. Six of the probes were positioned at different radii based on equal area segments and the seventh probe was located on the centerline. The probe inlets were designed (Chiappetta and Colket, 1984) to provide a combination of aerodynamic and thermodynamic quenching in order to freeze the chemical reactions of CO and NO rapidly (Fig. 6). Calculations of the heat transfer within the supersonic flow portion of the probe indicated that the stagnation temperature would be reduced by approximately 800°F in a 1.97-in.-long water-cooled passage. At the same time, the stagnation pressure would decrease from 200 psia to 40 psia. The flow would then be reduced to subsonic conditions at a shock stabilization step; this would yield a static temperature sufficiently low to prevent significant CO oxidation and NO_x formation.

Table 2 Test matrix in the 5-in.-dia. combustor rig

	Equivalence Ratio							
	LBO	0.35	0.40	0.45	0.50	0.55	0.6	0.65
High Shear Injector								
42 Fuel Orifices	x		x		x		x	
18 Fuel Orifices	x		x		x		x	
8 Fuel Orifices								
@ 30 deg	x				x		x	
4 Fuel Orifices								
@ 30 deg	x		x			x	x	
Aero Vane Injector								
0% Pilot Fuel	x				x	x		x
5% Pilot Fuel	x				x	x		x
10% Pilot Fuel	x			x	x	x		x
10% Pilot/Swirl					x			
3.4% dP/P					x			
Perforated Plate Injector								
0% Pilot Fuel	x				x	x	x	x
5% Pilot Fuel	x			x	x	x	x	x
10% Pilot Fuel	x				x	x		x

Emissions samples were transferred through electrically heated lines to a valving system, where the samples could either be combined or extracted individually, and then delivered to the gas analyzers. The emissions sampling and analysis system employed is capable of continuous monitoring of emissions of carbon monoxide, oxygen, carbon dioxide, unburned hydrocarbons, and oxides of nitrogen.

Test Matrix

The operating condition used in the screening of the fuel preparation concepts was the 100 percent rated power condition. The test facility was capable of providing inlet airflow at the engine compressor discharge temperature, but optimum utilization of the facility air heating capability dictated a compromise be reached relative to combustor reference velocity or pressure level. Because pressure-scaling criteria were felt to be relatively well established, reference velocity was fixed at the engine level and pressure was reduced by 25 percent. The test conditions were then as follows: $P_o = 200$ psia, $T_o = 850$ F, $U_{ref} = 54$ ft/sec.

Tests were conducted for primary zone equivalence ratios that ranged about the nominal design value of $\phi = 0.5$. Tests in which fuel flow was ramped downward were conducted to evaluate the lean blowout limit. The matrix of tests conducted is presented in Table 2.

Results

Exit Plane Uniformity. Gas sample measurements were acquired using samples delivered from individual probes and from groups of probes. Experience gained during the course of the program indicated that the probe-to-probe variations in the samples were small compared to the difference in level associated with the design concept. Data showing NO_x level as a function of radius for the seven probes are given for each of the combustor design concepts in Fig. 7. The small observed variation led to the practice of ganging the inner three probe samples and the outer four probe samples such that a characterization was obtained by analyzing just two samples. For purposes of this paper, the levels obtained from these samples have been combined (using area-weighting) such that a single average value is presented.

Downloaded 02 Jun 2010 to 171.66.16.121. Redistribution subject to ASME license or copyright; see http://www.asme.org/terms/Terms_Use.cfm

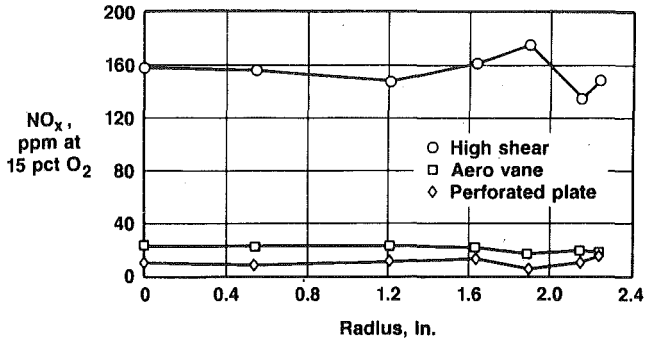

Fig. 7 Radial variation of NO_x for various injector configurations

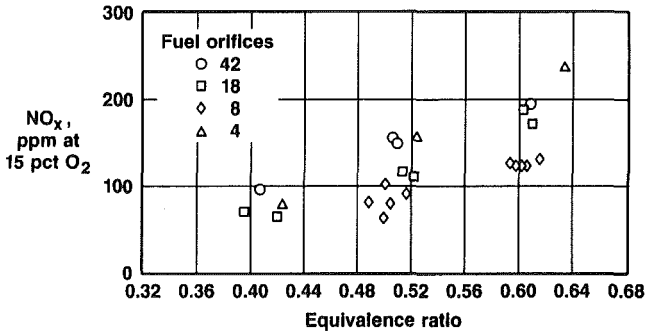

Fig. 8 High-shear injector NO_x signature

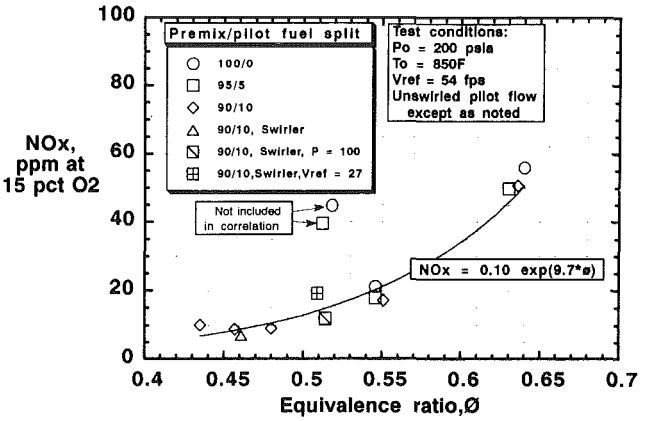

Fig. 9 Aero-vane injector NO_x signature

NO_x Emissions. The measured NO_x emissions are presented for each of the concepts in Figs. 8–10 as corrected NO_x concentration as a function of primary zone equivalence ratio. The equivalence ratio is based on the metered total (pilot plus main) fuel flow and measured airflow. In all cases, this equivalence ratio, determined from the metered fuel and air flows, compared favorably with the value determined from the gas samples. An interpretation of the data included in these plots is presented in the Discussion of Results section.

CO Emissions. For all data points presented, the levels of CO and unburned hydrocarbons were sufficiently low such that no primary zone flame temperature depression due to inefficient operation could bias the reported NO_x levels. CO levels for selected configurations (those that produced the lowest NO_x levels for each concept) are given in Fig. 11. Several points at the lower equivalence ratio levels show the expected increase, which indicates that inefficient operation would ensue if fuel flow were further reduced. It should be emphasized that this CO level is that which would issue from the primary zone.

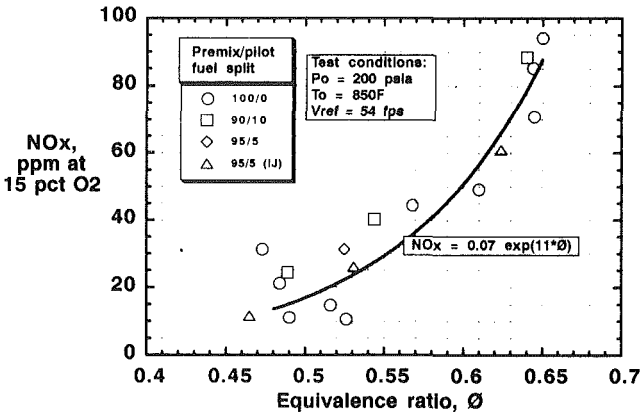

Fig. 10 Piloted perforated plate injector NO_x signature

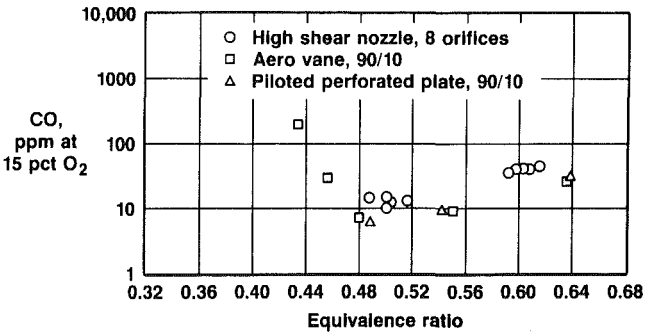

Fig. 11 CO signature for various injector configurations

Although the levels shown in the figure are low, even further CO burn-up would occur in the downstream regions of the actual FT-8 combustor.

Pressure Loss. The injector pressure loss for the high shear and perforated plate devices was approximately 3 percent of P_o. The aero-vane injector demonstrated a pressure loss of 9 percent, which was greater than intended due to an unexpected adverse interaction of the vanes with the fuel injection rods. Further testing with a halved reference velocity and a pressure loss of 3.4 percent showed only a 5 ppm increase in NO_x production at the baseline condition, probably due in part to the increased residence time. Except where otherwise noted, the data presented for the aero-vane device are for pressure loss of approximately 9 percent.

Blowout Limits. Blowout limits were determined by slowly ramping the fuel flow downward until either of two events occurred: (1) The flame pattern showed evidence of oscillations indicative of incipient blowout; (2) CO and UHC emissions showed a dramatic rise. The results of these tests (at FT8 high-power conditions) are given in Table 3, where it is seen that the non-premixed high-shear device produced the lowest level when unpiloted—a result that was anticipated. Piloting was effective in providing a satisfactory stability margin at the high power condition.

Discussion of Results

General Observations. The following observations regarding the operating characteristics of the test apparatus were made:

- Neither pre-ignition nor flashback occurred during any of the approximately 30 test sessions. No precautions such as limitations on the rate of change of chamber

Downloaded 02 Jun 2010 to 171.66.16.121. Redistribution subject to ASME license or copyright; see http://www.asme.org/terms/Terms_Use.cfm

Table 3 Lean extinction characteristics

Nozzle Design	LBO Equivalence Ratio	Data Type
High Shear Injector		
42 Fuel Orifices	0.30	Observation
18 Fuel Orifices	0.32	"
8 Fuel Orifices at 30 deg	0.36	"
4 Fuel Orifices at 30 deg	0.40	"
Aero Vane Injector		
0% Pilot Fuel	0.52	Low Efficiency
5% Pilot Fuel	0.50	"
10% Pilot Fuel	0.43	"
Perforated Plate Injector		
0% Pilot Fuel	0.49	Low Efficiency
5% Pilot Fuel	0.44	"
10% Pilot Fuel	0.39	"

pressure or rate of change of fuel flow were required to avoid flashback.

- No thermal discoloration indicative of high thermal loads was found in any of the premixing passages.
- The piloted perforated plate concept demonstrated high noise levels at equivalence ratios above 0.5. This noise is most likely due to coupling of the concentrated, combustion zone with the chamber acoustic modes. The aero-vane device exhibited relatively quiet and stable operation throughout the range of equivalence ratios tested.

High-Shear Injector NO_x Results. The data of Fig. 8 indicate that there is a correlation between level of NO_x formation and the extent to which the fuel penetrated the combustor entrance air stream. By decreasing the number of gas jets and/or increasing the size of individual jets, the penetration of the fuel was increased and NO_x was reduced. A reversal of the trend occurred when the number of jets was reduced from eight to four. When the number of jets was reduced to four, the circumferential nonuniformity associated with the discrete jets could have produced local concentrations leading to increased NO_x.

Water flow visualization tests indicated that at the lowest value of jet penetration, much of the fuel was delivered to the corner recirculation region formed by the sudden expansion at the injector discharge. As penetration increased, more of the fuel entered the high-shear flow region between the corner recirculation region and the central vortex core. Also, as penetration was increased, the fuel was more uniformly distributed throughout the airflow. It is not possible to establish whether the reduction in NO_x is due to better premixing or to the effects of high shear on the combustion process.

The levels of NO_x produced by the various fuel injector configurations tested gave no indication that NO_x levels in the desired range could be achieved. In particular, the levels were higher than were projected by scaling the results reported by the University of Leeds. As a consequence, the high-shear approach was set aside and evaluations of the premixed concepts were conducted.

Aero-Vane Injector NO_x Results. Results of tests performed using three different splits between pilot and main flow with the aero-vane injector show the anticipated decrease in NO_x with decreased primary zone equivalence ratio (Fig. 9). For the case where no pilot flow was employed, blowout occurred at an equivalence ratio of 0.52. As blowout was approached, rough combustion was experienced; the rise in NO_x levels shown is attributed to temporal variations in fuel flow,

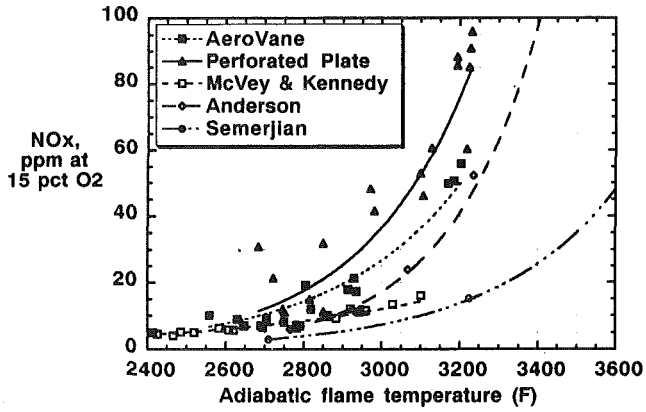

Fig. 12 Comparison of results with published data on aero-engine lean premixed combustor emissions

which resulted as the chamber pressure varied. The use of 10 percent pilot flow resulted in extension of the blowout limit to $\phi = 0.44$ with no attendant increase in NO_x. (The NO_x production associated with the stratified pilot flow was offset by decreased NO_x production in the leaner main flow.)

Tests conducted using 10 percent pilot flow with a reduced reference velocity (boxed-plus symbol in Fig. 9) and with a swirler inserted in the pilot flow passage (triangle) indicated no significant influences of NO_x levels.

Piloted Perforated Plate Injector NO_x Results. This premixed system achieves wide operability limits without the use of swirl stabilization (and the aforementioned residual swirl question). The characteristic strong dependence of NO_x emissions on primary zone equivalence ratio (Fig. 10) is characteristic of premixed systems. The scatter in the data is larger than observed in the aero-vane injector data; also, the average NO_x levels are higher. These characteristics are indicative of a lack of complete mixing of fuel and air. It was also observed, however, that significant discrete-tone noise at equivalence ratios greater than 0.5 was generated when testing this device; whether temporal variations in mixture ratio contributed to the high NO_x levels is uncertain.

In the unpiloted mode, quiet and stable operation was achieved at equivalence ratios down to $\phi = 0.48$ where NO_x levels were in the 10–15 ppm range. Unpiloted operation at somewhat lower equivalence ratios was possible, but flame oscillations and rough combustion occurred.

Injection of a small percentage (5 percent) of the fuel by direct injection of gas into the base recirculation was effective in permitting smooth combustion to occur while not substantially increasing NO_x. Orientation of the pilot injector such that the gas jets did (triangular symbol, Fig.10, labeled *IJ* for intersecting jets) or did not (diamonds) intersect the main fuel–air streams issuing from the holes in the perforated plate stabilizer did not have an observable effect on stability or emissions. It was demonstrated in part-power tests (not documented here) that, by injection of increasing amounts of pilot fuel into the base recirculation region, combustion could be sustained at all levels of engine burner air pressure, entrance temperature, and fuel flows that would be experienced in the engine when going from idle to full power. This is significant in terms of the ability of this type of device to be implemented in an engine in which fuel staging is employed to achieve adequate operability and low NO_x emissions simultaneously.

Comparison With Published Data. In Fig. 12, the results achieved with the aero-vane and perforated plate configurations are compared with data compiled for lean premixed concepts applicable to aircraft engines. Extensive testing of lean, premixed, prevaporized combustor concepts was carried out

Downloaded 02 Jun 2010 to 171.66.16.121. Redistribution subject to ASME license or copyright; see http://www.asme.org/terms/Terms_Use.cfm

in the 1970s under conditions representing a variety of engine cycles (fuel type, combustor residence time, and air entrance conditions). Tacina (1990) presented a compilation in which the results reported by Anderson (1975) using gaseous propane fuel at inlet temperatures of 980°F and a pressure of 5.5 atm was representative of the upper bound of NO_x results and the results reported by Semerjian et al. (1979) for vaporized Jet-A at an inlet temperature of 672°F and a pressure of 1 atm was representative of the lower bound. The data of McVey and Kennedy (1980), which extend to somewhat lower flame temperatures, are also shown. These data are all reported to have been acquired for a nominal residence time (hot) of 2 ms.

The acquired NO_x levels measured in this program for the perforated plate concept are clearly higher than the other reported data. As previously stated, the most likely explanation is imperfect premixing of the fuel and air. The data analyzed by Tacina do not indicate that residence time has a strong effect, particularly at low flame temperatures, where the prompt NO_x mechanism is believed to play a major role. The fact that the residence time is three times higher in the current test series is probably not a significant factor in explaining the higher levels.

The NO_x level measured for the aero-vane device lies above the upper bounds of these published data but is of a comparable level at the low flame temperature. The NO_x level increases with flame temperature at approximately the same rate as do the published data of Anderson (1975). At the lowest flame temperatures for which the combustor was stable (2600–2700°F), the levels measured in these 13.6 atm tests were approximately three times those of the 1 atm data included in the Tacina compilation.

Concluding Remarks

The results of this program show that both the piloted-perforated-plate and the swirl-stabilized lean-premixed combustion concepts hold promise for the achievement of NO_x emission levels of less than 25 ppm at 15 percent O_2. Applying a pressure scaling exponent of 0.5 to extrapolate these data from 13.6 atm to an engine with a 20:1 pressure ratio rating, and selecting the conditions at which the burners operated in a stable and efficient mode, the minimum NO_x potential is estimated to be

Piloted perforated plate (5 percent pilot):	16 ppm
Aero vane (10 percent pilot):	12 ppm

Conclusions

- Lean premixed combustion can be applied to aeroderivative engines having compressor discharge temperatures and residence times characteristics of 20:1 pressure ratio engines. The total absence of pre-ignition or auto-ignition experienced in these tests (at 13.6 atm) suggests that operation at 20 atm using these systems is practical and that low NO_x and high efficiency can be achieved in burners compatible with the combustion chamber volumes available in aeroderivative engines.
- Lean premixed combustion systems have a higher potential for achieving low-NO_x emissions that do high-shear combustion systems.
- Piloted combustors can provide efficient and stable operation over an adequate range of primary zone stoichiometrics without the piloting fuel producing a significant increase in NO_x emissions.
- Swirl-stabilized premixed combustors can produce NO_x levels that are equal to or lower than levels achieved with bluff-body (grid) stabilized systems; the high residence time associated with the large vortex-breakdown recirculation regions associated with swirl-stabilized devices does not adversely impact NO_x formation.
- Swirl-stabilized premixed combustion systems provide wide stability limits; the rapid mixing associated with a vortex breakdown region does not result in premature flame quenching.

Recommendations

Based on the experience gained in this effort and problems anticipated in the implementation of the concepts in an engine, the following activities should be undertaken:

- The relative sensitivity of NO_x emissions produced by swirl-stabilized and bluff-body (grid) stabilized combustion systems to combustor approach flow nonuniformities should be assessed.
- The ability to use piloting fuel systems to achieve efficient operation at low power conditions should be assessed.
- The impact of the presence of high swirl in the combustor discharge flow on turbine durability and performance should be assessed.
- The amplitudes of combustion-driven pressure oscillations (noise) developed by premixed combustion systems should be documented under conditions where the combustor acoustic boundaries simulate those of an engine.
- Efforts should be undertaken to quantify the extent of premixing achieved in the injector/mixing tubes used in piloted-perforated plate designs and to develop devices for producing improved flow homogeneity.

References

Aigner, M., Mayer, A., Schiessel, P., and Strittmatter, W., 1990, "Second-Generation Low-Emission Combustors for ABB Gas Turbines: Tests Under Full Engine Conditions," ASME Paper No. 90-GT-308.

Al Kabie, H. S., and Andrews, G. E., 1990, "Radial Swirlers With Peripheral Fuel Injection for Ultra-low NO_x Emissions," ASME Paper No. 90-GT-102.

Anderson, D., 1975, "Effect of Equivalence Ratio and Dwell Time on Exhaust Emissions From an Experimental Prevaporizing Burner," NASA TMX-71592, Mar.

Becker, B., Berenbrink, P., and Brandner, H., 1986, "Premixing Gas and Air to Reduce NO_x Emissions With Existing Proven Gas Turbine Combustion Chambers," ASME Paper No. 86-GT-157.

Chiappetta, L., and Colket, M. B., III, 1984, "Design Considerations for Aerodynamically Quenching Gas Sampling Probes," ASME *Journal of Heat Transfer*, Vol. 106, p. 460.

Maghon, H., Berenbrink, P., Termuehlen, H., and Gartner, G., 1990, "Progress in NO_x and CO Emission Reduction of Gas Turbines," ASME Paper No. 90-JPGC/GT-4.

McVey, J. B., and Kennedy, J. B., 1980, "Lean Stability Augmentation Study," *Journal of Energy*, Vol. 4, pp. 32–38.

Sattelmayer, T., Felchlin, M. P., Haumann, J., Hellat, J., and Styner, D., 1992, "Second-Generation Low-Emission Combustors for ABB Gas Turbines: Burner Development and Tests at Atmospheric Pressure," ASME JOURNAL OF ENGINEERING FOR GAS TURBINES AND POWER, Vol. 114, pp. 118–125.

Semerjian, H. G., Ball, I. C., and Vranos, A., 1979, "Pollutant Emissions From 'Partially' Mixed Turbulent Flames," *17th Symposium (International) on Combustion*, The Combustion Institute, Pittsburgh, PA, pp. 679–887.

Tacina, R., 1990, "Low NO_x Potential of Gas Turbine Engines," NASA TM 102452; Paper No. AIAA-90-0550.

Downloaded 02 Jun 2010 to 171.66.16.121. Redistribution subject to ASME license or copyright; see http://www.asme.org/terms/Terms_Use.cfm

Carbon Monoxide Emissions From Gas Turbines as Influenced by Ambient Temperature and Turbine Load

W. S. Y. Hung
Combustion Engineering,
Solar Turbines Incorporated,
San Diego, CA 92186

The emissions of carbon monoxide (CO) from gas turbines are typically below 100 ppmvd at 15 percent O_2 at design full-load operating conditions. The use of water/steam to reduce NO_x emissions from gas turbines results in an increase in CO emissions from gas turbines. This is particularly true when increased rates of water/steam injection are used to meet stringent NO_x limits. Regulations limiting CO emissions from stationary gas turbines were first initiated in the late 1980s by the Federal Republic of Germany and the state of New Jersey in the United States. Since these regulations are silent on ambient and load corrections, these CO limits could be the limiting factor in the current development of dry low-NO_x combustion systems by gas turbine manufacturers. In addition, since manufacturers are usually quite specific regarding the conditions for CO guarantees, a conflict for the gas turbine user, who is responsible for the permit application, is readily apparent. This paper attempts to characterize the CO emissions from gas turbines as a function of ambient temperature and turbine load. An ambient temperature correction equation for CO emissions, based on previous work, is presented. The intent is to provide more extensive information on CO emissions such that better defined CO limits can be adopted. Ultimately, this should help the combustion design engineers in developing improved dry low-emissions combustion systems for the gas turbine industry.

Introduction

In practical combustion systems, such as the gas turbine combustion system, much of the carbon monoxide (CO) emissions are attributed to the incomplete combustion of the hydrocarbon fuel. As suggested by Lefebvre (1983), this may be caused by one or more of the following:

- Inadequate burning rates in the primary combustion zone
- Inadequate mixing of fuel and air
- Quenching of products before completion of combustion

In view of these complicated processes that affect CO emissions, the ability to predict CO emissions from gas turbines has been rather limited in accuracy (Fletcher, 1980) compared to the ability to predict NO_x emissions using the diffusion-limited mixing model by Hung (1991). Any attempt to develop a universal CO correction equation independent of combustor design, fuel injector design, and operating conditions would be impossible in a practical sense.

In the design of a combustor for industrial gas turbines, specific criteria must be met to ensure a long life of satisfactory and reliable operation under a wide range of ambient temperatures, environmental conditions, and fuels. Typical combustor design requirements were presented by Meier et al. (1986). One of these requirements is to achieve more than 99.9 percent combustion efficiency at design operating conditions to optimize the thermal efficiency of the gas turbine cycle. In order to meet the above requirement, CO emissions have to be less than 100 parts per million by volume, dry sample basis (ppmvd) at 15 percent O_2.

Although the current state-of-the-art knowledge does not allow combustion engineers to predict CO emissions from gas turbines accurately, the various known approaches to reduce CO as listed by Lefebvre (1983) can help the designers to achieve the 99.9 percent combustion efficiency goal. CO emissions from gas turbines are typically below this 100 ppmvd design limit. This may explain why Ketterer and Dibelius (1974) did not find any stationary gas turbine specific CO emissions limit after a review of air pollution regulations in 80 nations in the early 1970s. The field measured data reported by Ambrose and Obidinski (1972), Carl et al. (1975), and Hanson and Felix (1975) provided additional evidence that CO emissions from stationary gas turbines were insignificant. As a consequence, the U.S. Environmental Protection Agency (EPA) found it unnecessary to set a control technology-based CO standard in terms of the emission index when the standards of performance for stationary gas turbines were promulgated in 1979 (EPA, 1989a). Instead, CO emissions from stationary

Contributed by the International Gas Turbine Institute and presented at the 37th International Gas Turbine and Aeroengine Congress and Exposition, Cologne, Germany, June 1-4, 1992. Manuscript received by the International Gas Turbine Institute February 6, 1992. Paper No. 92-GT-105. Associate Technical Editor: L. S. Langston.

Copyright © 1993 by ASME
Downloaded 02 Jun 2010 to 171.66.16.121. Redistribution subject to ASME license or copyright; see http://www.asme.org/terms/Terms_Use.cfm

gas turbines are controlled through an air quality-based standard (EPA, 1989b) in terms of the mass emission rate.

In order to meet stringent NO_x limits in California, Europe, and Japan, stationary gas turbines for cogeneration applications typically utilize water or steam injection to reduce NO_x emissions. Some of the test results were reported by Ambrose and Obidinski (1972), Farrell and Thomas (1981), Bahr and Lyon (1984), Touchton (1984), Hung and Agan (1985), and Burnham et al. (1987). The use of water or steam to reduce NO_x emissions, particularly at high rates of injection, can significantly increase CO emissions (Farrell and Thomas, 1981; Hung and Agan, 1985; Burnham et al. 1987). Consequently, control technology-based CO limits have been adopted by the Federal Republic of Germany (FRG, 1986) and the New Jersey Department of Environmental Protection (NJDEP, 1987) limiting CO emissions from stationary gas turbines to 100 mg/m^3 at 15 percent O_2 and 50 ppmvd, at 15 percent O_2, respectively. Since both of these regulations make no reference to any standard ambient and/or operating conditions for compliance, all possible site ambient and operating conditions are implied.

Lipfert (1972) was the first to attempt to correlate gas turbine emissions data. Subsequently, many turbine-specific NO_x correlation equations have been published, which are compared and evaluated by Rubins and Marchionna (1976). In recognition of the effect of ambient conditions on emissions, the EPA has developed an ambient correction equation based on data available from conventional combustion systems at the time to correct measured NO_x emissions to ISO standard ambient conditions (EPA, 1989a) for stationary gas turbines. For control technology-based emissions limits, a definition of the standard test ambient and operating conditions similar to EPA's New Source Performance Standards is essential, if a common benchmark is called for during the site or factory acceptance test.

Correlations of CO emissions data from aircraft and aero-derivative industrial gas turbines were reported by many, including Vaught (1975), Marzeski and Blazowski (1976), Mellor (1977), Donovan and Cackette (1978), Platt and Norster (1979), Lyon et al. (1979), and Farrell and Thomas (1981). In this paper, the author attempts to establish CO correlation equations for small and medium-sized industrial gas turbines. The information developed may help regulators to define control technology-based CO limits better such that any CO limit will not impede the current dry low-NO_x combustion system developments by gas turbine manufacturers.

Review of Previous Work

McAdams (1971) was the first to perform a statistical analysis of then-available emissions data from aircraft gas turbines. This EPA-sponsored attempt to derive correction factors from random emissions data was unsuccessful. The need for a large engine-specific sample size and the importance of controlled variations in ambient conditions became evident.

In analyzing emissions data from three different aircraft gas turbine models, Lipfert (1972) observed a correlation between CO and unburned hydrocarbon (UHC) emissions at CO emissions above 100 ppmvd. From this, Lipfert proposed a means to predict CO and UHC emissions from an empirically derived combustion efficiency. This type of approach was reported by Kretschmer and Odgers (1973) for order of magnitude estimates. It has very limited practical usage, particularly for stationary gas turbines, which typically operate at conditions with CO emissions below 100 ppmvd.

Testing in a controlled environment test cell, Vaught (1975) measured and reported the effect of ambient inlet air temperature on CO emissions from an aero-derivative industrial gas turbine (3300 kW) burning JP-5 and DF-2 liquid fuels. The

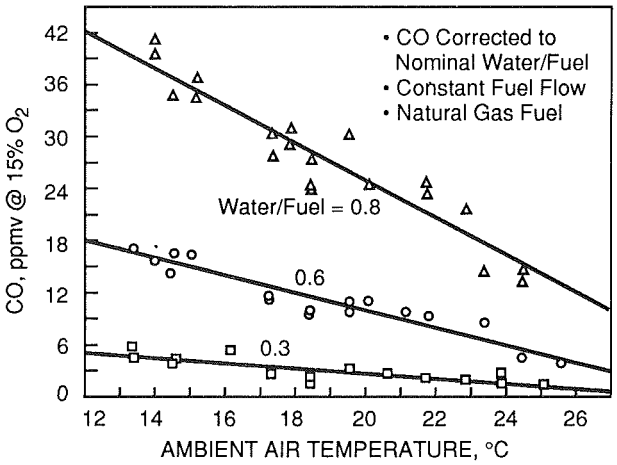

Fig. 1 Ambient temperature effect on CO

proposed correlation equations are unique to the turbine model and fuels tested.

Based on combustor rig tests, Marzeski and Blazowski (1976) presented empirically determined ambient temperature and pressure correction factors for idle CO emissions from the C-130 transport aircraft gas turbine, including the effect of fuel type and combustor design.

Based on a characteristic time model of the spray combustion process of liquid fuel, Mellor (1977) developed a semi-empirical CO correlation equation for geometrically similar automotive gas turbine combustors.

In an EPA-sponsored program to develop ambient correction factors for aircraft gas turbines, Donovan and Cackette (1978) presented CO correction factors as a function of combustor inlet air temperature and engine idle pressure ratio. Approximately 2000 test data sets from 30 engines were used in this correlation.

Platt and Norster (1979) developed and reported CO correlation equations for a number of aircraft gas turbines as a function of combustor inlet pressure and temperature. These equations can be used to predict ambient effects on CO emissions from these gas turbines as combustor inlet pressure and temperature are varied due to changes in ambient conditions.

Concentrating on engine idle conditions where CO is highest, Lyon et al. (1979) developed and reported a CO correlation for the CFM56 aircraft gas turbine. This correlation equation was found unsatisfactory by Farrell and Thomas (1981) when it was applied to data from a 5600-hp industrial gas turbine. Consequently, Farrell and Thomas (1981) developed and reported another custom CO correlation equation.

The effect of ambient humidity on CO emissions from an aircraft gas turbine combustor was measured and reported by Kauffman (1980). Kauffman observed that an increase in humidity causes an increase in CO emissions. It is clear, however, that emissions are more sensitive to changes in ambient temperature than in humidity.

Ambient Temperature Correction

Hung and Agan (1985) presented the measured effect of ambient temperature on CO emissions from a 7-MW industrial gas turbine burning natural gas fuel at 0.3, 0.6 and 0.8 water/fuel mass flow ratios as shown in Fig. 1. The fuel flow was held constant with an uncertainty of ±2 percent throughout the tests. A strong ambient temperature effect on measured CO emissions was observed. At each constant water/fuel ratio, the measured CO emissions at an ambient temperature of about 14°C, as shown in Fig. 1, were three to four times the corresponding values at about 25°C. A correlation of these data

Downloaded 02 Jun 2010 to 171.66.16.121. Redistribution subject to ASME license or copyright; see http://www.asme.org/terms/Terms_Use.cfm

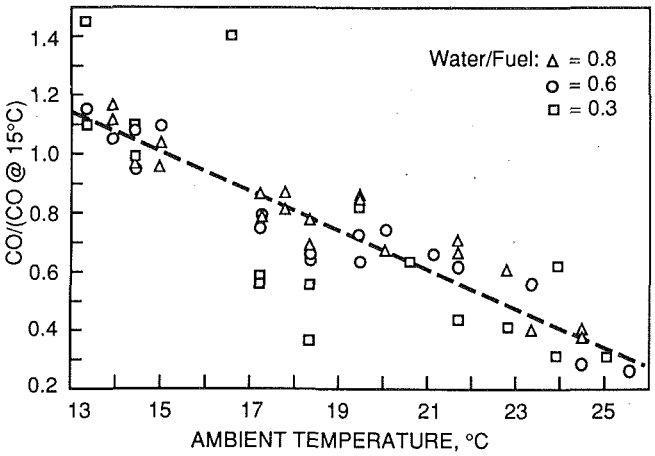

Fig. 2 Normalized CO versus ambient temperature

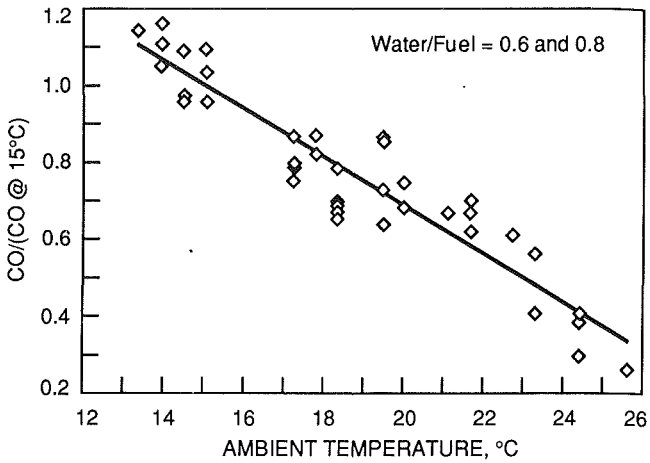

Fig. 3 Normalized CO versus ambient temperature (*W/F* = 0.6 and 0.8)

was not performed because CO emissions from stationary gas turbines were not required to meet any control technology-based limit at that time.

In view of recent interest in ambient effects on CO emissions from stationary gas turbines, a correlation of these data was recently performed. The straight lines in Fig. 1 are the least-square curve-fit of the three sets of data. The CO values at 15°C as determined by these lines were used to normalize each of the three data sets. The normalized CO data were plotted as a function of ambient temperature as shown in Fig. 2 (Hung and Agan, 1985). The linear regression line was also determined and presented (Fig. 2). Upon further review of the data (same symbol definition) in Figs. 1 and 2, it became obvious that the CO emissions at 0.3 water/fuel mass flow ratio were so small that the measurement uncertainties were amplified when the data were normalized. Eliminating this set of normalized data (water/fuel = 0.3) gives a much better linear correlation of normalized CO emissions as a function of ambient air temperature (Fig. 3). The linear regression line has been adjusted slightly such that it will calculate unity exactly at 15°C. This adjusted equation is as follows:

$$CO_T/CO_{15} = 1 - 0.0634(T - 15) \quad \text{for } T < 30 \qquad (1)$$

where:

CO_T = emissions of CO in ppmvd at 15 percent O_2 at ambient temperature, T

CO_{15} = emissions of CO in ppmvd at 15 percent O_2 at 15°C

T = ambient air temperature in °C

Although these data only covered ambient temperatures ranging from 13 to 26°C, Eq. (1) may be used to estimate CO emissions at ambient temperatures below 13°C. As indicated above, Eq. (1) is not valid for estimating CO emissions at ambient temperature above 30°C. Since testing at high ambient temperatures produces low levels of CO and UHC, which are difficult to measure, Marzeski and Blazowski suggested that an upper limit on ambient temperature be set for CO and UHC emissions testing. To extend this suggestion, the author proposes that a normal ambient temperature of 10–25°C be specified for CO or UHC emissions compliance testing either in the field or in the factory prior to shipment to the field. This would eliminate many of the weather-related problems, such as sample conditioning and human factors, encountered during emissions compliance testing in extreme weather conditions.

Equation (1) was developed from data taken from a 7-MW industrial gas turbine that was uprated to 8.8 MW. The combustion system technology for a 3.9-MW gas turbine is very similar to that of the 8.8-MW gas turbine. It is expected, therefore, that Eq. (1) will be applicable to a 3.9-MW gas turbine as well, based on limited cold ambient data available with water injection applications. There are, however, insufficient data from two other industrial gas turbines (rated at 1.1 MW and 3.1 MW) to make similar determinations.

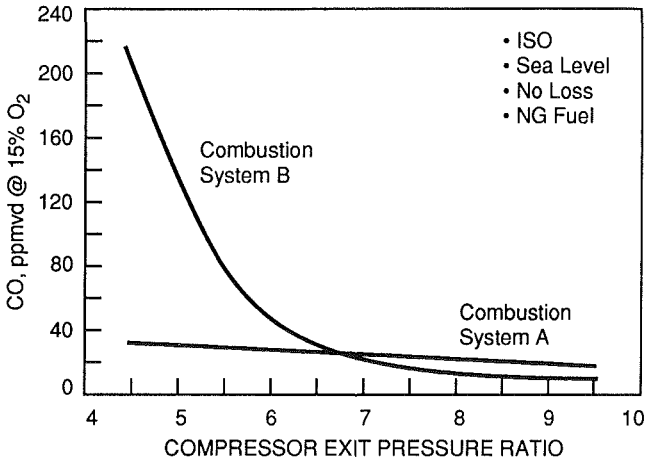

Fig. 4 CO emissions versus pressure ratio

Load Correction

Since CO emissions from gas turbines at any given load (specific combustor inlet conditions) can be caused by one or more of at least three known processes (Lefebvre, 1983), the amount of emissions for a given fuel depends on these same three processes:

- Combustor design technology (Donovan and Cackette, 1978)
- Fuel injector design (Bahr, 1982)
- Combustor inlet conditions (Platt and Norster, 1979)

Therefore, it is not surprising to learn that the engine idle CO correlation equation developed by Lyon et al. (1979) was found unsatisfactory by Farrell and Thomas (1981) when it was applied to another turbine of a different design.

Through changes in combustor and fuel injector technology in the same family of industrial gas turbines (Davis, 1989), the CO emissions from the two-shaft turbine versions of these two combustion systems burning natural gas at similar combustor inlet conditions display significantly different characteristics (Fig. 4). This suggests the need to develop a custom load correction equation for CO emissions for each gas turbine model.

The CO emissions from four industrial gas turbines, rated

Downloaded 02 Jun 2010 to 171.66.16.121. Redistribution subject to ASME license or copyright; see http://www.asme.org/terms/Terms_Use.cfm

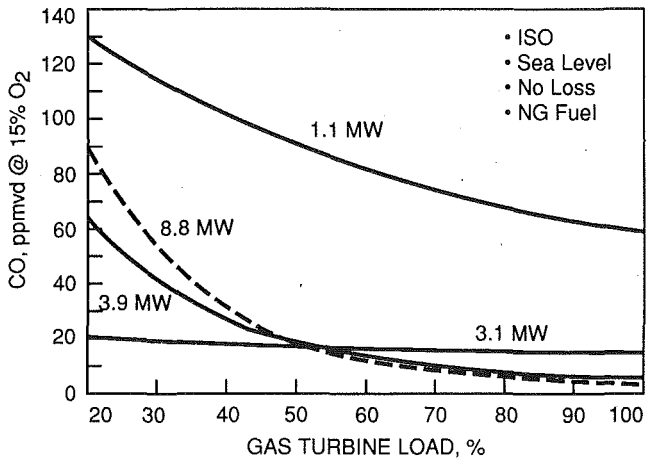

Fig. 5 CO emissions versus turbine load

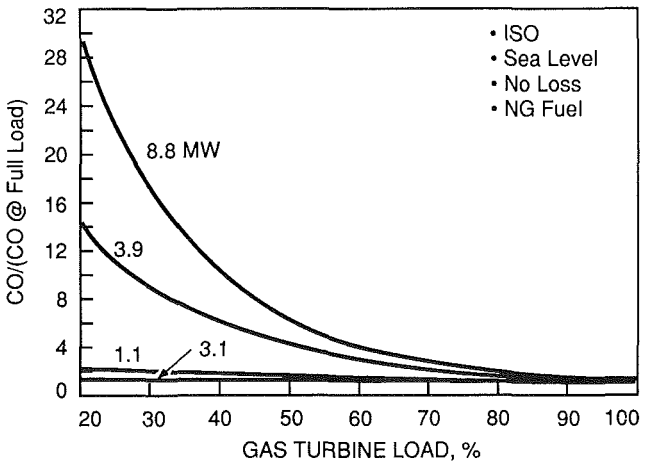

Fig. 6 Normalized CO versus turbine load

at 1.1, 3.1, 3.9, and 8.8 MW, as a function of turbine load at ISO, sea level, no loss conditions burning natural gas fuel are compared in Fig. 5. These represent the average emissions from 12, 21, 30, and 15 of the above gas turbine models, respectively. The results of normalizing the CO emissions by the corresponding emissions at full (100 percent) load are presented in Fig. 6. From curve-fitting these normalized data with exponential functions, a custom CO load correction equation has been developed as follows:

$$CO_{FL} = C_1 \times CO_L \times \exp[C_2 \times (L/FL)] \quad (2)$$

where:

CO_{FL} = emissions of CO at design full load in ppmvd at 15 percent O_2
C_1, C_2 = custom constants for each turbine model (Table 1)
CO_L = emissions of CO at operating load, L, in ppmvd at 15 percent O_2
exp = transcendental constant = 2.718
L = operating load in MW
FL = design full load in MW

Figure 6 shows that significantly different CO load correction characteristics are displayed by different turbine models. In addition, there is large variation (over 100 percent) from turbine to turbine within the same model, particularly near idle or no load, conditions, or when the CO emissions are low (< than 5 ppmvd at 15 percent O_2).

Combustion Efficiency

The combustion efficiency of stationary sources can be more accurately determined today through a measurement of the combustion inefficiency—the measured emissions of UHC and CO. For pipeline quality natural gas, the relationship between combustion efficiency, UHC, and CO emissions is as follows:

$$\eta_c = 1 - (UHC_{EI} + 0.211\ CO_{EI})\ 10^{-3} \quad (3)$$

where:

η_c = combustion efficiency, ratio
UHC_{EI} = emissions index of UHC, g/kg fuel
CO_{EI} = emissions index of CO, g/kg fuel

The relationships between emissions index and emissions expressed as ppmvd at 15 percent O_2 for UHC and CO at ISO conditions are as follows:

$$UHC_{EI} = 0.0288\ UHC \quad (4)$$

$$CO_{EI} = 0.0503\ CO \quad (5)$$

where

UHC = emissions of UHC in ppmvd at 15 percent O_2
CO = emissions of CO in ppmvd at 15 percent O_2

Using Eqs. (3), (4), and (5), the combustion efficiencies of four natural gas fired industrial gas turbines were determined from measured UHC and CO emissions at design full-load conditions (Table 2). The combustion efficiencies are over 99.9 percent because 99.9 percent combustion efficiency at design point is one of the gas turbine combustor design requirements (Meier et al., 1986).

Table 1 Custom CO load correction constants for Eq. (2)

Turbine Rating, MW	C_1	C_2
1.1	0.3503	1.049
3.1	0.5839	0.538
3.9	0.0306	3.486
8.8	0.0126	4.371

Table 2 Typical emissions-derived combustion efficiencies for natural gas-fired industrial gas turbines at design full-load conditions

Turbine Rating, MW	Emissions (ppmvd @ 15% O_2)		Combustion Efficiency
	UHC	CO	
1.1	2.91	57.90	0.9993
3.1	1.67	14.50	0.9998
3.9	2.80	4.46	0.9999
8.8	2.45	2.95	0.9999

Mass Emission Rate

When emissions are expressed in ppmvd at 15 percent O_2, which is proportional to the emissions index, the values are indicative of the levels of technology achieved. In order to assess the amount of pollutants emitted into the atmosphere, however, the mass emission rate is the unit of interest. The CO mass emission rate from the 3.1-MW and the 3.9-MW gas turbines as a function of turbine load at ISO, sea level, no loss conditions, burning natural gas fuel are plotted in Fig. 7. Although the CO emissions from the 3.1-MW gas turbine increase as load decreases (Fig. 5), the CO mass emission rate decreases as load decreases (Fig. 7) from 100 to 20 percent load. This is due to the more rapid rate of decrease in the fuel consumption compared to the rate of increase in CO emissions as load decreases.

Low Emissions Combustor

The research and development of dry low-emissions com-

Downloaded 02 Jun 2010 to 171.66.16.121. Redistribution subject to ASME license or copyright; see http://www.asme.org/terms/Terms_Use.cfm

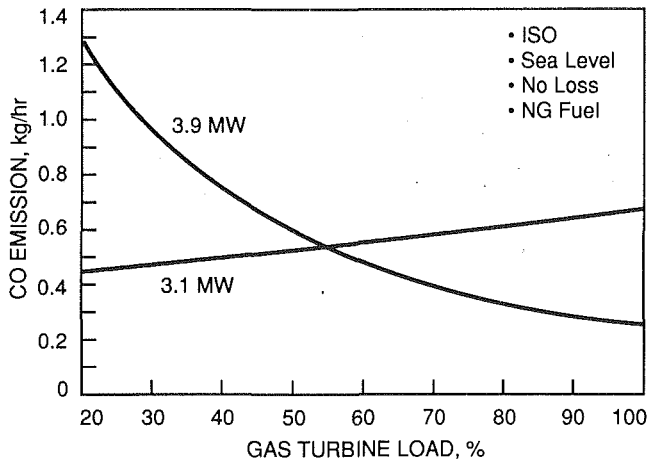

Fig. 7 CO mass emission rate versus load

bustors for industrial gas turbines by gas turbine manufacturers was initiated in the early 1970s. The basic research and preliminary development work on a hybrid combustor that uses features of both conventional and premixed combustors were reported by Mumford et al. (1977). This led to the first successful development of a dry low-emissions combustor for an 120-MW industrial gas turbine (Aoyama and Mandai, 1984). The emissions levels achieved are $NO_x < 75$ ppmvd at 15 percent O_2 and CO < 50 ppmvd at 15 percent O_2. With this same NO_x goal, the successful development of a dry low-NO_x combustor for an 80-MW gas turbine was reported by Kuroda and Ishibashi (1989). The CO emissions at part load are apparently not acceptable (Angello and Lowe, 1989).

Since NO_x levels below 42 ppmvd at 15 percent O_2 have been achieved by water/steam injection, the development of dry low-emissions combustors, using the hybrid combustion concept, to meet NO_x levels below 42 ppmvd at 15 percent O_2 were reported by Davis and Washam (1989), Becker et al. (1990), Aigner et al. (1990), and Smith and Roberts (1991). Meeting a NO_x goal below 42 ppmvd at 15 percent O_2 is in itself a sufficient challenge. To meet simultaneously a NO_x goal below 42 ppmvd and a CO goal below 50 ppmvd at 15 percent O_2 at near-design conditions is more of a challenge. If ambient and load corrections for CO are not allowed and the ambient and load conditions for emissions compliance test are undefined, CO limits could impede the success of dry low-emissions combustor development currently in progress.

Conclusion

The emissions of CO from gas turbines are a strong function of the combustor and fuel injector design. For a given combustion system, CO emissions are strongly affected by the ambient temperature and, to a lesser extent, the ambient humidity. An ambient temperature correction equation for CO has been developed, although the full extent of its applicability has yet to be verified.

CO emissions from gas turbines typically decrease with increasing load, reaching a minimum at design full-load conditions. The emissions characteristics as a function of load vary significantly from one turbine design to another. A custom equation has to be developed for each turbine model. Since significant variation from turbine to turbine has been observed for a given turbine model, a significant number of turbine tests is required to develop a custom equation.

In view of the high variability of CO emissions data, it is suggested that a technology-based CO limit should only be required at design full-load and standard ambient conditions, and compliance tests should be conducted at near-design full-load and standard ambient conditions. Custom or specified ambient and load correction equations must be allowed to correct measured data to design standard conditions. This should help resolve the current regulatory/manufacturer conflict over the development of dry low-emissions combustors to benefit the gas turbine user and, most importantly, our environment.

References

Aigner, M., Mayer, A., Schiessel, P., and Strittmatter, W., 1990, "Second Generation Low-Emission Combustors for ABB Gas Turbines: Tests Under Full-Engine Conditions," ASME Paper No. 90-GT-308.

Ambrose, M. J., and Obidinski, E. S., 1972, "Recent Field Tests for Control of Exhaust Emissions From a 35-MW Gas Turbine," ASME Paper No. 72-JPG-GT-2.

Angello, L., and Lowe, P., 1989, "Dry Low NO_x Combustion Development for Electric Utility Gas Turbine Applications, A Status Report," ASME Paper No. 89-GT-254.

Aoyama, K., and Mandai, S., 1984, "Development of a Dry Low NO_x Combustor for a 120-MW Gas Turbine," ASME JOURNAL OF ENGINEERING FOR GAS TURBINES AND POWER, Vol. 106, pp. 795–800.

Bahr, D. W., 1982, "HC and CO Emission Abatement via Selective Fuel Injection," ASME Paper No. 82-GT-178.

Bahr, D. W., and Lyon, T. F., 1984, "NO_x Abatement via Water Injection in Aircraft-Derivative Turbine Engines," ASME Paper No. 84-GT-103.

Becker, B., Bonsen, F., and Simon, G., 1990, "A Simple and Reliable Combustion Control System," ASME Paper No. 90-GT-173.

Burnham, J. B., Giuliani, M. H., and Moeller, D. J., 1987, "Development, Installation, and Operating Results of a Steam Injection System (STIG) in a General Electric LM5000 Gas Generator," ASME JOURNAL OF ENGINEERING FOR GAS TURBINES AND POWER, Vol. 109, pp. 257–262.

Carl, D. E., Obidinski, E. S., and Jersey, C. A., 1975, "Exhaust Emissions From a 25-MW Gas Turbine Firing Heavy and Light Distillate Fuel Oils and Natural Gas," ASME Paper No. 75-GT-68.

Davis, L. B., and Washam, R. M., 1989, "Development of a Dry Low NO_x Combustor," ASME Paper No. 89-GT-255.

Davis, W. W., 1989, "Centaur Gas Turbine Technology," presented at TTS30, Turbomachinery Technology Seminar, Solar Turbines Incorporated, San Diego, CA.

Donovan, P., and Cackette, T., 1978, "The Effects of Ambient Conditions on Gas Turbine Emissions—Generalized Correction Factors," ASME JOURNAL OF ENGINEERING FOR POWER, Vol. 100, pp. 640–646.

EPA, 1989a, "Standards of Performance for Stationary Gas Turbines," *Code of Federal Regulations*, Chap. I, Title 40, Part 60, Subpart GG, Section 335.

EPA, 1989b, "Prevention of Significant Deterioration of Air Quality," *Code of Federal Regulations*, Chap. I, Title 40, Part 52, Subpart A, Section 21.

Farrell, R. A., and Thomas, M. E., 1981, "Effects of Inlet Conditions and Water Injection on Emissions From a Dual-Fuel Industrial Gas Turbine," ASME Paper No. 81-GT-47.

Fletcher, R. S., 1980, "Emissions," *The Design and Development of Gas Turbine Combustors*, Northern Research and Engineering Corporation, Woburn, MA, Vol. I, Chap. 7.

FRG, 1986, "Technical Instructions on Air Quality control—TA Luft," *First General Administrative Regulation Pertaining to the Federal Emission Control Law* (GMBI, p. 95, 202).

Hanson, K. A., and Felix, P. C., 1975, "Emissions Characteristics of a Gas Turbine Combustor for High Nitrogen Content Fuels," ASME Paper No. 75-Pwr-28.

Hung, W. S. Y., 1991, "A Predictive NO_x Monitoring System for Gas Turbines," ASME Paper No. 91-GT-306.

Hung, W. S. Y., and Agan, D. D., 1985, "The Control of NO_x and CO Emissions From 7-MW Gas Turbines With Water Injection as Influenced by Ambient Conditions," ASME Paper No. 85-GT-50.

Kauffman, C. W., 1980, "Effect of Ambient Conditions on the Emissions From a Gas Turbine Combustor," NASA Contractor Report 3355.

Ketterer, R. J., and Dibelius, N. R., 1974, "Status of Air Pollution Regulations Affecting Gas Turbines in 80 Nations," ASME Paper No. 74-WA/GT-8.

Kretschmer, D., and Odgers, J., 1973, "Modelling of Combustors: The Effects of Ambient Conditions upon Performance," ASME Paper No. 73-WA/GT-6.

Kuroda, M., and Ishibashi, Y., 1989, "Development of a Low-NO_x Combustor," *Hitachi Review*, Vol. 38, No. 3.

Lefebvre, A. H., 1983, *Gas Turbine Combustion*, Hemisphere Publishing Corporation, New York.

Lipfert, F. W., 1972, "Correlation of Gas Turbine Emissions Data," ASME Paper No. 72-GT-60.

Lyon, T. F., Dodds, W. J., and Bahr, D. W., 1979, "Determination of the Effects of Ambient Conditions on CFM56 Aircraft Engine Emissions," EPA-460/3-79/011, Environmental Protection Agency, Ann Arbor, MI.

Marzeski, J. W., and Blazowski, W. S., 1976, "Ambient Temperature and

Downloaded 02 Jun 2010 to 171.66.16.121. Redistribution subject to ASME license or copyright; see http://www.asme.org/terms/Terms_Use.cfm

Pressure Corrections for Aircraft Gas Turbine Idle Pollutant Emissions," ASME Paper No. 76-GT-130.

McAdams, H. T., 1971, "Analysis of Aircraft Exhaust Emission Measurements: Statistics," EPA Contract Report No. NA-5007-K-2, Cornell Aeronautical Laboratory, Inc., Cornell University, Buffalo, NY.

Meier, J. G., Hung, W. S. Y., and Sood, V. M., 1986, "Development and Application of Industrial Gas Turbines for Medium-Btu Gaseous Fuels," ASME JOURNAL OF ENGINEERING FOR GAS TURBINES AND POWER, Vol. 108, pp. 182–190.

Mellor, A. M., 1977, "Characteristic Time Emissions Corrections and Sample Optimization: GT-309 Gas Turbine Combustor," *Journal of Energy*, Vol. 1, No. 4, pp. 244–249.

Mumford, S. E., Hung, W. S. Y., and Singh, P. P., 1977, "A Potential Low NO_x Emission Combustor for Gas Turbines Using the Concept of Hybrid Combustion," ASME JOURNAL OF ENGINEERING FOR POWER, Vol. 99, pp. 631–637.

NJDEP, 1987, "April 21, 1987 Cogeneration and Electric Generation Gas *Turbine Nitrogen Oxides Control Strategy,*" *New Jersey Department of Environmental Protection.*

Platt, M., and Norster, E. R., 1979, "Time Degradation Factors for Turbine Engine Emissions," FAA-RD-79-8, Vol. 1, NREC 1238, U.S. Department of Transportation, Washington, DC.

Rubins, P. M., and Marchionna, N. R., 1976, "Evaluation of NO_x Prediction-Correlation Equations for Small Gas Turbines," AIAA Paper No. 76-612.

Smith, K. O., and Roberts, P. B., 1991, "Development of a Low NO_x, Industrial Gas Turbine Combustor," presented at the Canadian Gas Association Symposium on Industrial Application of Gas Turbines, Banff, Alberta.

Touchton, G. L., 1984, "Influence of Gas Turbine Combustor Design and Operating Parameters on Effectiveness of NO_x Suppression by Injected Steam or Water," ASME Paper No. 84-JPGC-GT-3.

Vaught, J. M., 1975, "The Effect of Inlet Temperature and Pressure on an Industrial Turbine Engine Exhaust Emission," ASME Paper No. 75-WA/GT-11.

Downloaded 02 Jun 2010 to 171.66.16.121. Redistribution subject to ASME license or copyright; see http://www.asme.org/terms/Terms_Use.cfm

The Flow Inside a Model Gas Turbine Combustor: Calculations

J. J. McGuirk[1]
Professor of Aerodynamics.

J. M. L. M. Palma[2]
Assistant Professor.

Imperial College of Science, Technology and Medicine, Mechanical Engineering Department, London SW7 2BX, United Kingdom

The present study assesses the ability of the k–ϵ turbulence model to calculate the flow inside gas turbine combustors. Results of calculations using a cylindrical system of coordinates, hybrid differencing, and a mesh with about 40,000 nodes are compared with velocity measurements of the flow inside a perspex model of can-type gas turbine combustor. The larger discrepancies between measurements and predictions were found in the primary region. The complexity of the flow near the primary jet impingement led to underprediction of the maximum negative axial velocity and turbulence kinetic energy by about 35 and 20 percent, respectively. The calculated results exhibited higher levels of momentum diffusion compared to the experiments and did not show the two contrarotating vortices created between the primary jets; no qualitative agreement with the azimuthal velocity downstream of the primary jets could be achieved. Despite these deficiencies, the model gave acceptable results in other regions of the combustor and correct prediction of the main features of the combustor flow was possible.

1 Introduction

The development of numerical models, during the seventies, and the larger capacity of today's computers have led to an increased use of computational fluid dynamics (CFD) in the design of gas turbine combustors, a trend that has been followed by the major gas turbine engine manufacturers (e.g., Correa and Shyy, 1987; Priddin and Coupland, 1986; Sturgess, 1986) and whose origin can be traced back to the pioneer works of, for instance, Jones et al. (1977) and Serag-Eldin and Spalding (1979).

The main physical models and numerical techniques used nowadays were already incorporated in the computer codes presented in these early works. The development of fluid modeling during the last decade was relatively slow. It was soon realized that the major drawbacks of CFD were the need for large computer systems and the unavailability of flexible grid systems (Jones and Priddin, 1978) enabling the exact simulation of complicated shapes and geometric details such as those available in real combustors (Lefebvre, 1983). The concentration of efforts to overcome the above difficulties (Coupland and Priddin, 1987; Shyy et al., 1987), the shortage of experimental data in a detailed form appropriate for physical model validation, and the argument that the turbulence model was not so important in this type of flow (at least for velocity field prediction, since the flow is driven in a large proportion by the pressure gradient, Green and Whitelaw, 1983; Coupland and Priddin, 1987) have prevented the appraisal of currently available turbulence models in the calculation of the flow inside real gas turbine combustor geometries. However, great attention (e.g., Bruce et al., 1979; Srinivasan et al., 1983) has been given to the development and assessment of CFD models in simpler flow constituents of the gas turbine combustor flow, as for instance, swirling flows, jets in crossflow, etc., and this has been the methodology followed by many authors.

Most of the numerical studies on realistic gas turbine combustor flows available used the standard k–ϵ model. Examples of calculations with improved versions of the k–ϵ model (e.g., Wild et al., 1987; Ikeda et al., 1987) were not conclusive in terms of showing their advantages, although they seem to be necessary, at least in the light of previous experience based on calculations of simpler flows (e.g., Sloan et al., 1986).

There are two main requisites for a correct evaluation of CFD models: the availability of a set of experimental data accurate and detailed enough to enable the specification of the boundary conditions, and a comparison between experimental and numerical values. In geometries of this complexity, due to incomplete experimental information and limitations of the numerical models, simplifications have to be made for specification of the boundary conditions and their effect assessed prior to CFD appraisal. To facilitate this and because no correct prediction of combusting flows is possible without a preliminary evaluation of the physical models embedded in the computer codes under less demanding conditions, the study of noncombusting gas turbine combustor flows becomes a task of great importance in this route toward a greater reliability and confidence on the numerical models and their use in combustor design.

The requirements above have been fulfilled in previous pub-

[1]Present address: Loughborough University of Technology, Department of Transport Technology, Loughborough, Leiscestershire LE11 3TU, United Kingdom.

[2]Present address: Faculdade de Engenharia da Universidade do Porto, Department of Mechanical Engineering and Industrial Management, 4099 Porto Codex, Portugal.

Contributed by the International Gas Turbine Institute for publication in the JOURNAL OF ENGINEERING FOR GAS TURBINES AND POWER. Manuscript received by the International Gas Turbine Institute April 1, 1992. Associate Technical Editor: L. S. Langston.

Copyright © 1993 by ASME
Downloaded 02 Jun 2010 to 171.66.16.121. Redistribution subject to ASME license or copyright; see http://www.asme.org/terms/Terms_Use.cfm

lications by the authors. The works by Bicen et al. (1989) and Palma (1989) provide a set of detailed velocity measurements obtained in a realistic combustor geometry by laser-Doppler velocimetry. The assessment of the numerical accuracy and effect of using different boundary conditions has been previously evaluated too (McGuirk and Palma, 1992) and the objective here is to present the results obtained from the calculation of the flow inside a model can-type gas turbine combustor under isothermal conditions.

The work is presented in three sections. Section 2 introduces the governing equations, the calculation procedure, the domain of integration, and the boundary conditions used in the present calculations. The actual validation of the k–ϵ turbulence model is made in Section 3. Section 4 is a summary of the main conclusions.

2 Mathematical Model

2.1 Governing Equations. The Reynolds-averaged equations governing the fluid motion of an incompressible, constant property, Newtonian fluid, and the transport of a scalar are, in an Eulerian description (cf. Hinze, 1975):

$$\frac{\partial U_i}{\partial x_i}=0$$

$$\rho\frac{DU_i}{Dt}=-\frac{\partial P}{\partial x_i}+\frac{\partial}{\partial x_j}\left[\mu\left(\frac{\partial U_i}{\partial x_j}+\frac{\partial U_j}{\partial x_i}\right)-\rho\,\overline{u_i\,u_j}\right]+F_i$$

$$\rho\frac{DC}{Dt}=\frac{\partial}{\partial x_i}\left(\Gamma\frac{\partial C}{\partial x_i}-\rho\,\overline{u_i\,c}\right)+F_C$$

The Reynolds stresses, $\rho\overline{u_i\,u_j}$, are related to the local strain through the Boussinesq eddy viscosity concept:

$$\rho\,\overline{u_i\,u_j}=\frac{2}{3}\rho k\delta_{ij}-\mu_t\left(\frac{\partial U_i}{\partial x_j}+\frac{\partial U_j}{\partial x_i}\right)$$

The turbulent eddy viscosity, μ_t, a scalar, is defined according to:

$$\mu_t=C_\mu\,\rho\,\frac{k^2}{\epsilon}$$

The double correlation $\rho\,\overline{u_i\,c}$ is approximated:

$$-\rho\,\overline{u_i\,c}=\Gamma_t\frac{\partial C}{\partial x_i}$$

where Γ_t, the eddy diffusivity, is given by:

$$\Gamma_t=\frac{\mu_t}{\sigma_t}$$

and σ_t is designated as the turbulent Prandtl number. The equations for the transport of momentum and scalar quantities then revert to:

$$\rho\frac{DU_i}{Dt}=-\frac{\partial P}{\partial x_i}+\frac{\partial}{\partial x_j}\left[\mu_{\text{eff}}\left(\frac{\partial U_i}{\partial x_j}+\frac{\partial U_j}{\partial x_i}\right)\right]+F_i$$

$$\rho\frac{DC}{Dt}=\frac{\partial}{\partial x_i}\left(\Gamma_{\text{eff}}\frac{\partial C}{\partial x_i}\right)+F_C$$

where $\mu_{\text{eff}}=\mu+\mu_t$ and $\Gamma_{\text{eff}}=\Gamma+\Gamma_t$.

The turbulence kinetic energy, k, and its rate of dissipation, ϵ, are determined from the modeled equations below (cf. Jones and Launder, 1972):

$$\rho\frac{Dk}{Dt}=\frac{\partial}{\partial x_i}\left(\frac{\mu_t}{\sigma_k}\frac{\partial k}{\partial x_i}\right)-\rho\,\overline{u_i\,u_j}\frac{\partial U_i}{\partial x_j}-\rho\,\epsilon$$

$$\rho\frac{D\epsilon}{Dt}=\frac{\partial}{\partial x_i}\left(\frac{\mu_t}{\sigma_\epsilon}\frac{\partial \epsilon}{\partial x_i}\right)-\frac{\epsilon}{k}C_1\rho\,\overline{u_i\,u_j}\frac{\partial U_i}{\partial x_j}-C_2\rho\frac{\epsilon^2}{k}$$

These equations and the set of constants ($C_\mu=0.99$, $C_1=1.44$, $C_2=1.92$, $\sigma_k=1.00$, $\sigma_\epsilon=1.3$) constitute the standard k–ϵ turbulence model.

2.2 Calculation Procedure. A methodology for numerical solution of the governing equations, similar to that described in detail by Patankar (1980), has been incorporated into a computer program originally written by Jones (1975). Finite difference techniques were used for discretization of the transport equations above with velocity and scalar cells located in different locations in the grid. The diffusion and convection terms were approximated by central and hybrid differencing schemes, respectively.

The coupling between pressure and velocity was accomplished using the AVPI algorithm (Jones, 1984; McGuirk and Palma, 1993). The iterative calculation procedure was considered as converged only when the integrated flux of the passive scalar was the same (within 2 percent) at every transverse cross section; this is a very stringent criterion, found necessary due to the slower convergence of the scalar field.

Nomenclature

C = passive scalar
C_μ, C_1, C_2 = constants of k–ϵ turbulence model
F_i = source term
k = turbulence kinetic energy
$\dot{m}$ = mass flow rate
P = static pressure
r, R = cylindrical polar coordinate
R_c = internal diameter of combustor
t = time
U = axial component of velocity
U_b = bulk velocity (0.741 m/s)
V = radial component of velocity
x_i = spatial coordinates in tensor notation
$\rho\,\overline{u_i\,u_j}$ = Reynolds stresses
$\rho\,\overline{u_i\,c}$ = double correlation
W = azimuthal component of velocity
Z = cylindrical polar coordinate
Γ = diffusivity
ϵ = rate of dissipation of turbulence kinetic energy
θ = swirler vane angle
Θ = cylindrical polar coordinate
μ = dynamic viscosity
ρ = density
σ_k, σ_ϵ, σ_ϕ = constants of k–ϵ turbulence model
σ_t = turbulent Prandtl number

Operators

$D/Dt=\partial/\partial t+U_i\,\partial/\partial x_i$ = substantial derivative
$\overline{}$ = time-averaged quantity
δ_{ij} = Kronecker delta
$\partial/\partial x_i$, $\partial/\partial t$ = partial derivatives

Subscripts

cross = crossflow
fuel = fuel
i, j, k, l = indices of the tensorial notation
p = pressure
pr = primary
sw = swirler
u, v, w = velocities

Downloaded 02 Jun 2010 to 171.66.16.121. Redistribution subject to ASME license or copyright; see http://www.asme.org/terms/Terms_Use.cfm

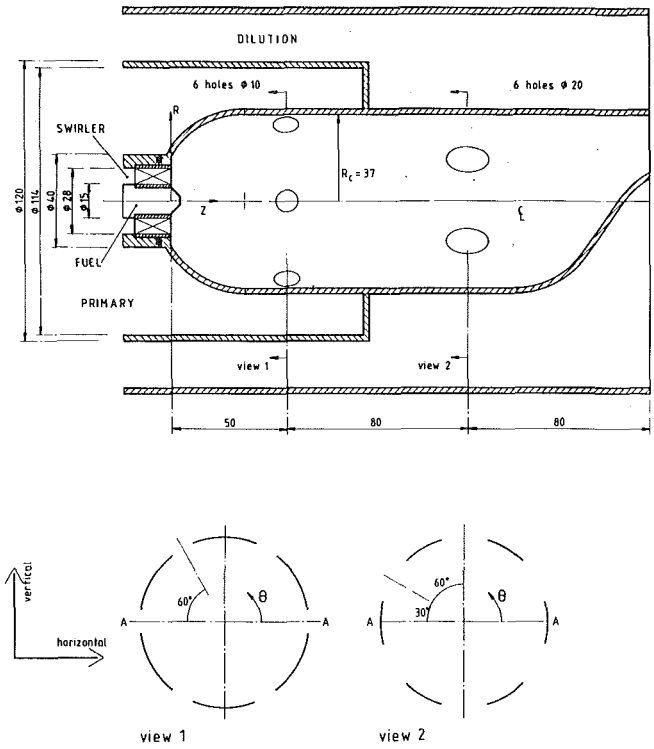

Fig. 1 Combustor model

Table 1 Combustor flow splits

N	θ	$\dot{m}_{sw}$	$\dot{m}_{pr}$	$\dot{m}_{dil}$	$\dot{m}_{tot}$	$\frac{\dot{m}_{pr}}{\dot{m}_{sw}}$	$\frac{\dot{m}_d}{\dot{m}_{cross}}$
1	45°	0.543 [17]	1.04 [33]	1.60 [50]	3.19	1.92	1.01
2	30°	0.797 [23]	1.04 [30]	1.60 [47]	3.44	1.31	0.87
		higher swirler flow					
3A	–	-	1.04 [40]	1.60 [60]	2.64	∞	1.53
		without swirler flow					
3B	–	0.543 [17]	1.04 [33]	1.60 [50]	3.19	1.92	1.01
		flow through the swirler, but without tangential component					

$\dot{m}$ = kg/s

mass flow rate as percentage of the total within brackets

$\dot{m}_{cross} = \dot{m}_{sw} + \dot{m}_{pr}$

θ – swirler vane angle

2.3 Domain of Integration: Numerical Mesh. Figure 1 shows the combustor model as in the experiments by Palma (1989). This was a perspex replica of a metal model used for combusting studies by Bicen et al. (1990). This metal model had been designed to simulate the primary zone configuration of modern can combustors, operating with a relatively low swirler flow and a low air-fuel ratio in the primary zone. Operating conditions in the water rig experiments were tailored (Bicen et al., 1989) in such a way that the velocity measurements and flow visualization were consistent with the temperature distribution in the combusting flow. Measurements (Palma, 1989) by laser-Doppler velocimetry of the three velocity components included spectral analysis, distributions of probability density functions (pdfs), and moments up to the fourth order. A flow visualization study using a fluorescent dye and both still and high-speed photography was also made to observe the mixing phenomena and the dynamic behavior of the jets.

The calculations were restricted to a 60 deg sector of the flow inside the combustor and the length of the domain was set about one combustor radius downstream of the dilution holes. A cylindrical polar system of coordinates with the longitudinal direction aligned with the axis of the combustor was used. The annulus and the nozzle were not included, and the hemispherical head, the primary, and the dilution holes were approximated by rectangular castellations. The exclusion of the turbine nozzle was partially because there was no interest in the flow at the combustor outlet in the present work, but also because it was known from the experiments (Palma, 1989) that the presence of the nozzle was not felt upstream of the dilution holes. Furthermore, calculations with the nozzle would have had to cover the entire 360 deg of the combustor, regardless of the existence of the swirler flow, whereas neglecting the nozzle meant that a 60 deg sector could be used. When there was no swirler flow a smaller sector (only 30 deg) was used.

A numerical mesh of $60 \times 32 \times 22$ (axial, radial, circumferential) grid nodes with memory requirements of about 3 Mbytes was used. The grid spacing in the axial and radial directions (see Table 2) was changed smoothly (according to Sundqvist and Veronis, 1970) to minimize the deterioration of the formal accuracy of the finite difference scheme due to variable grid spacing and in such a way that a higher concentration of nodes occurred near the holes and the swirler. In the azimuthal direction, the grid was regular except around the primary hole axis and on the edges of the domain. An average spacing of 3 deg between vertical planes was found acceptable. The mesh used in the present work resulted from a previous study by McGuirk and Palma (1992). It was concluded that for this flow and using the boundary conditions described below there was no need of either finer or higher order finite difference approximations of the convection terms, because of the high turbulence viscosity generated in this flow.

2.4 Boundary Conditions. The set of boundary conditions used in the present work emerged from the preliminary study by McGuirk and Palma (1992). This assessed the validity of the boundary conditions by comparison between the measurements and results of calculations with various options of the velocity profiles in the combustor entries.

The swirler was simulated by an annular gap with the outer radius identical to the swirler outer radius, and the inner radius increased in order to cause an area reduction similar to that caused by the vanes in the real swirler. The dimensions of this gap and the swirler flow rate, together with plug flow assumptions, set the axial velocity (1.25 ms^{-1}, case 1). Assuming solid body rotation and using the swirl number (0.46 and 0.56, for 30 and 45 deg swirlers, respectively) previously evaluated experimentally (Palma, 1989), the swirl velocity was then found from the integration of the swirl number definition (Beer and Chigier, 1972); this guaranteed that experiments and calculations had the same swirl number. The radial velocity was set to zero. The turbulence kinetic energy (1.50×10^{-2} m^2s^{-2}) and the dissipation rate (3.06×10^{-1} m^2s^{-3}) were found by assuming isotropic turbulence with an axial turbulence intensity of 0.10 ms^{-1}, based on the measurements, and a typical eddy length equal to the height of the annular gap.

The axial and swirl velocities in the plane of both primary ($U = 0\ ms^{-1}$; $W = 0.03\ ms^{-1}$) and dilution holes ($U = 0.15\ ms^{-1}$;

Downloaded 02 Jun 2010 to 171.66.16.121. Redistribution subject to ASME license or copyright; see http://www.asme.org/terms/Terms_Use.cfm

Table 2 Numerical grid

N.	Z [m]	R [m]	T [deg.]	N	Z(m)
1	0.0000	0.0000	0.000	31	0.0707
2	0.0010	0.0011	1.875	32	0.0739
3	0.0025	0.0024	3.750	33	0.0772
4	0.0045	0.0036	7.500	34	0.0805
5	0.0071	0.0048	11.250	35	0.0845
6	0.0100	0.0060	15.000	36	0.0885
7	0.0130	0.0070	18.750	37	0.0924
8	0.0160	0.0080	22.500	38	0.0962
9	0.0190	0.0090	26.250	39	0.1000
10	0.0220	0.0102	28.125	40	0.1035
11	0.0250	0.0113	30.000	41	0.1068
12	0.0280	0.0125	31.875	42	0.1100
13	0.0310	0.0135	33.750	43	0.1131
14	0.0340	0.0145	37.500	44	0.1160
15	0.0370	0.0150	41.250	45	0.1187
16	0.0400	0.0165	45.000	46	0.1212
17	0.0430	0.0173	48.750	47	0.1236
18	0.0455	0.0186	52.500	48	0.1259
19	0.0490	0.0201	56.250	49	0.1280
20	0.0500	0.0217	58.125	50	0.1300
21	0.0510	0.0235	60.000	51	0.1320
22	0.0521	0.0255	61.875	52	0.1342
23	0.0534	0.0275		53	0.1368
24	0.0548	0.0293		54	0.1397
25	0.0563	0.0309		55	0.1430
26	0.0581	0.0324		56	0.1469
27	0.0601	0.0349		57	0.1514
28	0.0624	0.0360		58	0.1568
29	0.0649	0.0370		59	0.1630
30	0.0677			60	0.1700

$W = 0.10\,\text{ms} - 1$), and radial velocity in the plane of the dilution holes ($V = 0.85\ \text{ms}^{-1}$) were assumed constant over the hole. The radial velocity in the plane of the primary holes resulted from a piecewise approximation of the measurements of radial velocity (Palma, 1989) 3 mm outside the combustor. Turbulence kinetic energy and dissipation (primary hole: $k = 7.66 \times 10^{-2}\ \text{m}^2\text{s}^{-2}$; $\epsilon = 2.12\ \text{m}^2\text{s}^{-3}$; dilution hole: $k = 7.50 \times 10^{-3}\ \text{m}^2\text{s}^{-2}$; $\epsilon = 3.25 \times 10^{-2}\ \text{m}^2\text{s}^{-3}$) were again determined as above. The turbulence kinetic energy was made up of the individual contributions along the three main directions obtained experimentally (axial, radial, and azimuthal turbulence intensities 0.3, 0.06, and 0.244, respectively, for the primary holes and 0.10, 0.05, and 0.05 ms^{-1} for the dilution holes). The eddy length was assumed equal to the hole diameter. The velocity values given above, in parentheses, correspond to flow split n.1, as in Table 1; for different flow splits, velocity will be changed accordingly.

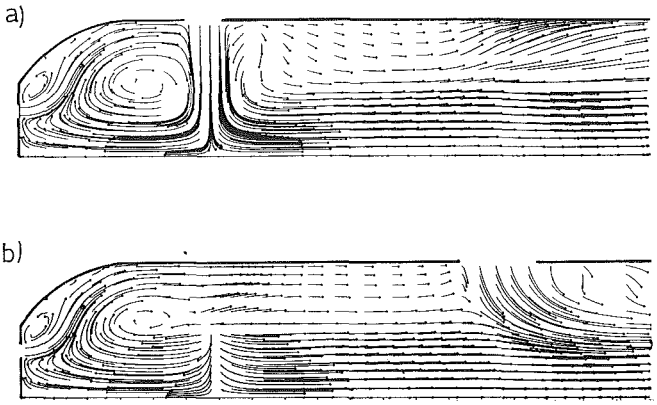

Fig. 2 Streakline plots corresponding to case 1: views in the longitudinal planes containing the axes of the holes

A zero axial gradient was prescribed at the outlet section for all the variables.

The longitudinal side boundaries were planes of cyclic (periodic) or symmetry boundary conditions for swirling and no swirling flow, respectively. The wall regions were treated using the wall function approach (Launder and Spalding, 1974).

The fuel injector (Fig. 1) was a cone with 10 equally spaced holes of 1.7 mm diameter through which an extra flow rate of 0.083 kgs^{-1} was injected. The fuel injection was simulated by point sources located in the first column of the grid. These cells were split into two annular rings of 15 deg angular aperture each, located on the edges of the calculation domain and at the same radial location as the holes in the real injector. The sources of axial and radial momentum were similar, to guarantee a 45 deg injection, as in the experiments. The azimuthal momentum source was set to zero. A value of $1.50 \times 10^{-2}\ \text{m}^2\text{s}^{-2}$ (identical to the swirler) was assumed for the turbulence kinetic energy, and the dissipation was calculated by assuming an eddy size of the diameter of the fuel injector holes.

3 Discussion of Results

Calculations were performed for four different flow conditions (Table 1). The results of the calculations are shown together with the experimental results when available. Experimental data from measurements along the combustor diameter are included in order to show the degree of flow repeatability achieved in the experiment. The discussion of results is split into calculations of combustor flow with and without swirler (subsections 3.1 and 3.2, respectively).

3.1 Combustor Flow With Swirl

Standard Case (45 deg Swirler). The results corresponding to case 1 are presented in Figs. 2–11. The streakline plots in Figs. 2 and 3 give a global picture of the mean flow pattern inside the combustor under the present conditions. The salient features are: (*i*) in Fig. 2, the toroidal vortex in the combustor head (caused by the joint effect of the primary jet impingement and shearing, at the upstream side of the jet, between the jet and the crossflow) and (*ii*) in Fig. 3 (*b*), the two contrarotating vortices in the cross section containing the dilution holes axes caused by spanwise deflection. These vortices are typical of jets in crossflow geometries (e.g., Andreopoulos and Rodi, 1984) and probably do not appear at the plane of the primary jets (Fig. 3*a*) because of the strong jet impingement.

The results of velocity and turbulence kinetic energy, Figs. 4–11, show that the largest discrepancies between numerical and experimental results occur in the region around primary jet impingement (Figs. 5–8); lower recirculated mass flow, i.e., lower axial velocities, and lower turbulence levels compared with the measurements are features of this region, which ex-

Downloaded 02 Jun 2010 to 171.66.16.121. Redistribution subject to ASME license or copyright; see http://www.asme.org/terms/Terms_Use.cfm

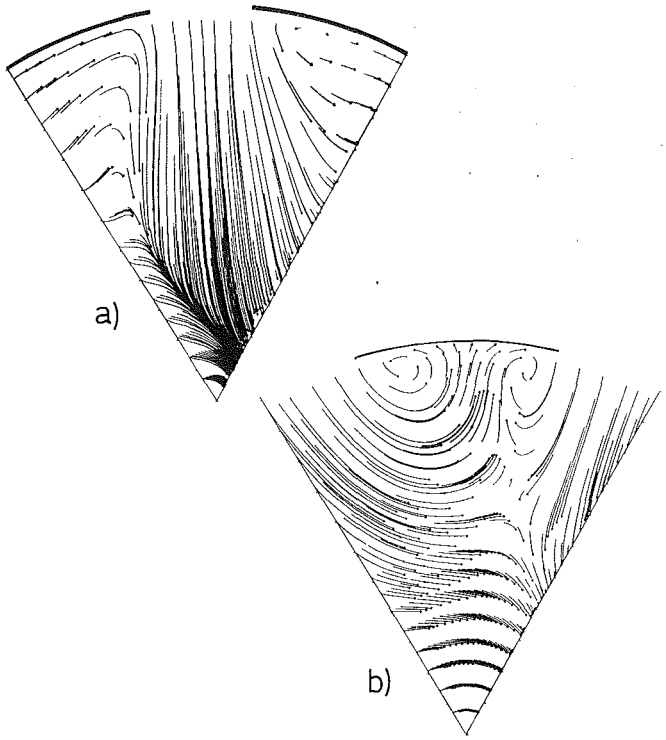

Fig. 3 As in Fig. 2, but views in the cross-sectional planes containing the axes of the primary and dilution holes: (*a*) $z = 50$ mm; (*b*) $z = 130$ mm

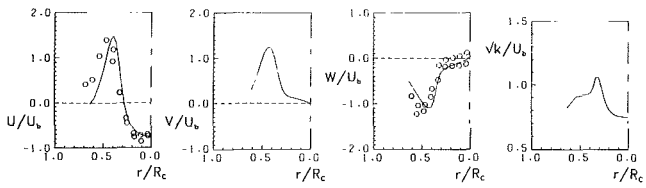

Fig. 4 Results corresponding to case 1 at $z = 8$ mm, $\theta = 0$ deg (experimental results from Palma, 1989)

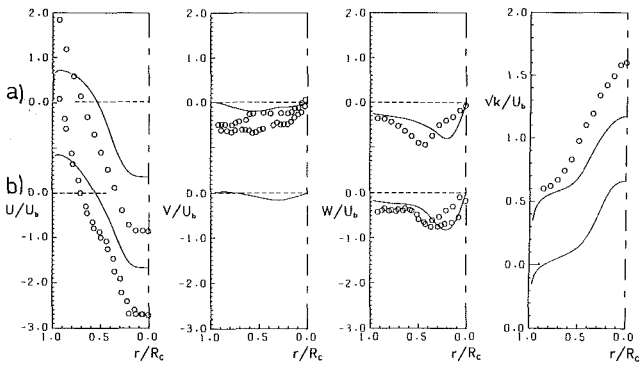

Fig. 5 Results corresponding to case 1: (*a*) $z = 40$ mm, $\theta = 0$ deg; (*b*) $z = 40$ mm, $\theta = 30$ deg

tends to about 10 mm downstream of the primary holes. The agreement in the farthest downstream and upstream stations (Figs. 4 and 11, at $z = 8$ and 130 mm, respectively) is excellent. Only after using the type of radial velocity boundary condition described above, was the good agreement of the radial velocity along the axis of the primary holes (Fig. 7*a*) achieved. Nevertheless, the calculations still show a weaker toroidal vortex in the combustor head (Fig. 5) and lower values of turbulence kinetic energy. The centerline plot in Fig. 6 displays a difference of about 35 and 20 percent between the maximum numerical

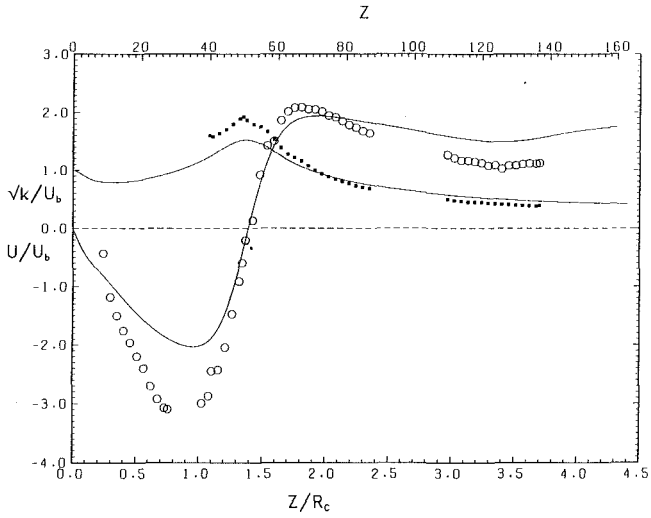

Fig. 6 Axial velocity and turbulence kinetic energy along the combustor centerline

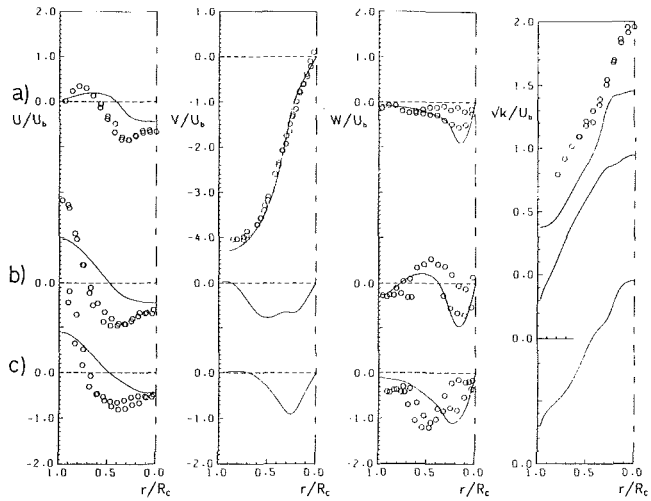

Fig. 7 Results corresponding to case 1: (*a*) $z = 50$ mm, $\theta = 0$ deg; (*b*) $z = 50$ mm, $\theta = 15$ deg; (*c*) $z = 50$ mm, $\theta = 30$ deg

and experimental values of the axial velocity and turbulence kinetic energy, respectively.

Near the walls at $z = 40$ mm, Fig. 5, there is an underprediction of the axial velocity, which is most likely simply a consequence of the reduced backflow rate predicted by the calculations. Although there is a strong link between the axial velocities near the wall and on the centerline, as has been shown in preliminary calculations of the present flow (McGuirk and Palma, 1992), the possibility that this behavior is also a consequence of either the castellated approximation of the combustor head or an inefficient treatment of the flow near the combustor walls cannot be fully discarded. The underprediction of the axial velocity near the walls is a characteristic of all the downstream stations up to $z = 85$ mm, in particular the ones not aligned with the primary hole axis.

At $z = 50$ mm and at angular locations between the hole axis (Figs. 7*b* and 7*c*) the minimum value of the axial velocity at midradius is not predicted, and this then affects the shape of the profile downstream of the jets (Figs. 8*b* and 8*c*). In the $\theta = 0$ deg plane, the agreement improves as the distance from the primary holes increases (Figs. 8*a*, 9*a*, and 10). However, this good agreement in the intermediate locations $z = 70$ mm and $z = 85$ mm is fortuitous partly since it corresponds to the region where, in the centerline plots (Fig. 6) the experimental

Downloaded 02 Jun 2010 to 171.66.16.121. Redistribution subject to ASME license or copyright; see http://www.asme.org/terms/Terms_Use.cfm

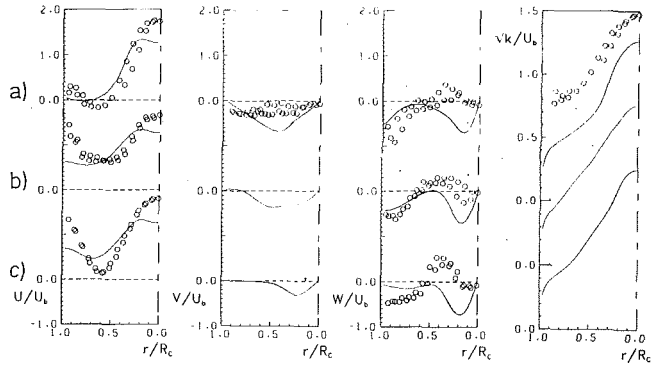

Fig. 8 Results corresponding to case 1: (*a*) $z = 60$ mm, $\theta = 0$ deg; (*b*) $z = 60$ mm, $\theta = 15$ deg, (*c*) $z = 60$ mm, $\theta = 30$ deg

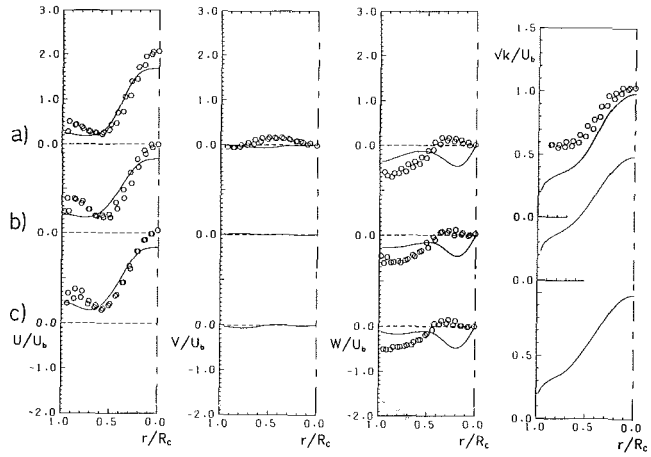

Fig. 9 Results corresponding to case 1: (*a*) $z = 70$ mm, $\theta = 0$ deg; (*b*) $z = 70$ mm, $\theta = 15$ deg; (*c*) $z = 70$ mm, $\theta = 30$ deg

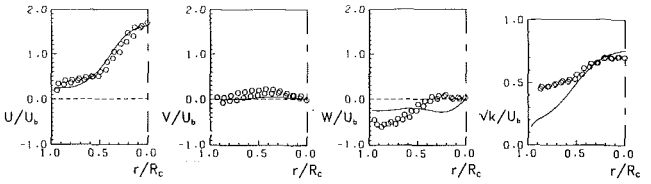

Fig. 10 Results corresponding to case 1 at $z = 85$ mm, $\theta = 0$ deg

and numerical curves for the centerline axial velocity cross each other. Nevertheless, this level of agreement is never obtained in the azimuthal component of velocity.

The correct shape of the turbulence kinetic energy distribution is shown across the combustor. The maximum values exist around the primary jet, especially near the impingement point (Figs. 6–8). Downstream of the primary jets (Figs. 6, 9, and 10) there is a good agreement between experimental and numerical values in the central region around the centerline. The calculations consistently show lower values of turbulence kinetic energy near the walls, even in regions where good agreement of the axial velocity is obtained (for instance, $z = 85$ mm, Fig. 10), which suggests that the lower values may be a consequence of the radial gradient of the azimuthal velocity whose magnitude near the walls is also underpredicted.

The flow inside the first half of the combustor can be viewed as a result of the relative strengths of the swirler and primary jet flow. The calculations, by underpredicting the strength of the toroidal vortex in the combustor head, which is mainly set by the primary jet impingement, overpredict the strength of

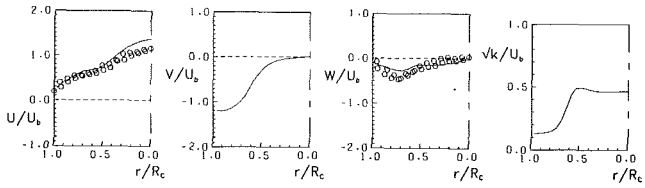

Fig. 11 Results corresponding to case 1 at $z = 130$ mm, $\theta = 30$ deg

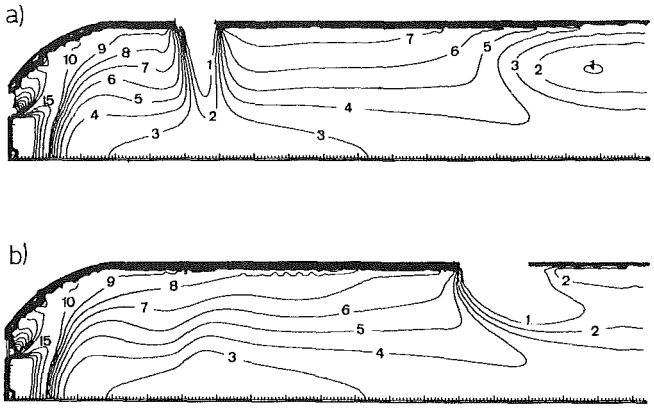

Fig. 12 Fuel fraction (values in percent) field in the longitudinal planes

the swirler flow and show the central core usually rotating as the swirling flow. Therefore, features exhibited in the measurements and strongly associated with the primary jets are not shown so obviously by the calculations; this becomes clear in the azimuthal velocity around the centerline and in the intermediate angular locations. Only at $z = 50$ mm, Fig. 7(*b*), do the calculations show the positive values of the azimuthal velocity. The downstream stations fail to show the correct shape of the azimuthal velocity profile (Figs. 8–10) and evidence higher levels of radial diffusion compared with the measurements.

In the present case, the dominance of the swirler relative to the primary jet flow partly explains why lower levels of turbulence are predicted in the impingement region; because as Palma's (1989) measurements showed, higher levels of swirl reduce the turbulence intensity in the center of the combustor. Calculations without swirler flow (see subsection 3.2) predicted higher values of turbulence kinetic energy and stronger backflow but never as high as the measured values with swirler flow. The boundary conditions tests showed that better results could be obtained as the distribution of the radial velocity along the axis of the primary holes approached the measured values (McGuirk and Palma, 1992); this dependence of the turbulence kinetic energy on the radial gradient of the radial velocity is expected to be extended to a dependence also on the axial gradient of the axial velocity along the centerline, which the calculations largely underpredict and may explain the lower levels of turbulence. In addition, the calculations show in general a higher level of diffusion compared with the measurements, which is known to be a typical feature of the k–ϵ model in recirculating flows, in particular in regions of destabilizing curvature. Variants of the k–ϵ model to remedy this deficiency in two-dimensional flows are available (e.g., Leschziner and Rodi, 1981), which usually involve a reduction of the eddy viscosity either through the alteration of the constant C_μ or the inclusion of extra terms in the equation for the dissipation rate.

The transport of fuel is illustrated by the contour plots of fuel fraction in Fig. 12. Values above 10 percent occur only within the first 10 mm of the combustor. The fuel jet, unable

Downloaded 02 Jun 2010 to 171.66.16.121. Redistribution subject to ASME license or copyright; see http://www.asme.org/terms/Terms_Use.cfm

to penetrate the toroidal vortex prevailing in the combustor head, mixes with the swirler flow and escapes between the primary jets, being transported near the wall with reduced mixing with the central core of the flow, formed mainly by primary jet fluid. In the dilution region, the jets, because of their weaker penetration drive the fuel toward the centerline. This was also the picture built on the basis of the flow visualization study in Palma (1989), which fully supports the present calculations.

Predictions have also been performed with various values of turbulent Prandtl number (Palma, 1989). Calculations with a value of 0.4 showed smoother distributions. In the plane of the primary jets, the calculations showed, due to the increased diffusion, that the penetration of the primary jet had been reduced, leading to higher values of the fuel fraction on the centerline. This agreed with the restricted set of measurements made with an intrusive concentration probe by Palma (1989) and may support the use of a constant turbulent Prandtl number lower than 0.9, as has been suggested by various authors (e.g., Coupland and Priddin, 1987). The need to increase the diffusion of a passive scalar for better agreement with the measurements contrasts with the suggestion to lower the value of the constant C_μ in the model to reduce the diffusion of momentum. It appears that when the structure parameters tuned for two-dimensional flows are used in three-dimensional flows, they tend to overpredict the diffusion of momentum and underpredict the diffusion of a passive scalar. The difficulty of selecting the appropriate Prandtl number is merely the evidence of the deficiency of the scalar flux model, which might be overcome (only) by using higher order scalar flux models, in order to take into account the strong flow anisotropy.

Heitor and Whitelaw (1986) anticipated the failure of turbulence viscosity models in the prediction of the flow in the primary region, based on the argument that turbulence is mainly generated by the interaction between the fluctuating density and velocity field, and the mean pressure gradient. Although this argument is valid only for combusting flow, the present results tend to agree with it, since the poor performance of the k–ϵ model in the intermediate region appears to be a consequence of the poor results upstream in the combustor. It follows that the use of higher order closure turbulence models, though perhaps necessary to improve the predictions in the primary region, may not be needed for the downstream regions.

The existence of other mechanisms contributing to the high experimental values of turbulence, and not accounted for by the present turbulence model, should not be fully discarded, as for instance, the contribution that may have occurred due to the low frequencies attributed to the jet instability, as discussed by Palma (1989). The characteristic time (1/60 Hz, i.e., 0.017 s) and length scale of the phenomenon above are higher than the time step ($\Delta t = 0.004$ s) and the average dimensions of the grid cells at the primary jet impingement (about 2 mm), and the present mathematical model should be able to predict such a phenomenon in principle. This, however, may have been precluded by the symmetry (cyclic) boundary conditions of the present calculations; full three-dimensional calculations, covering the whole 360 deg of the combustor, may be needed since instantaneously the assumptions of cyclic symmetry are not valid. These calculations will increase the memory requirements by a factor of six, for a similar numerical accuracy.

Calculations obtained with a 30 deg swirler under similar experimental conditions (Palma, 1989) evidenced features identical to those discussed above. Results with the 30 deg swirler, but a higher swirler flow rate, are shown below.

Combustor Flow With a Higher Swirler Flow Rate (30 deg Swirler). Calculations with an increased swirler flow rate were made (primary to swirler flow ratio of 1.31, case 2 in Table 1). The axial velocity through the swirler was changed from 1.25 ms^{-1}, as in case 1, to 1.83 ms^{-1}; no other boundary condition was changed. Figures 13 and 14 show the flow pattern, which is topologically more complex than in the previous case. These, and Figs. 2 and 3, provide a good example of the complexity of the flow inside a gas turbine combustor and variety of new features that can appear by slight changes of the combustor operating conditions. The swirler flow pentrates axially deeper into the primary zone (Fig. 13), rather than being restricted to the region near the wall (as in Fig. 2, corresponding to a higher primary to swirler flow ratio of 1.92). Three vortices can be identified in the combustor head: a large one with a counterclockwise rotation and two smaller vortices trapped below the swirler flow stream, one in the wake of the swirler hub and the other closer to the primary hole axis. Two interesting aspects appear in this region: First, the two smaller vortices seem to be part of the larger vortex limited by the swirler flow stream and the combustor centerline; second, the connection between these two vortices appears to be made by a dislocated saddle point (Perry and Chong, 1987). (An extra

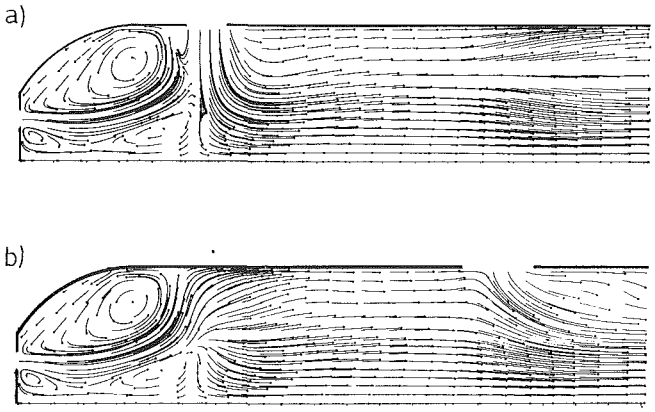

Fig. 13 Streakline plots corresponding to case 2: views in the longitudinal planes containing the axes of the holes

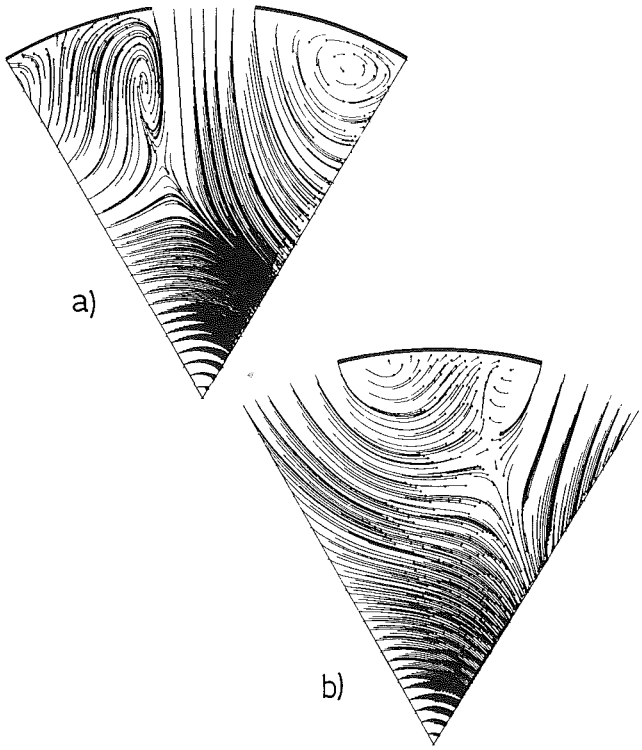

Fig. 14 As in Fig. 13 but views in the cross-sectional planes: (*a*) $z = 50$ mm; (*b*) $z = 130$ mm

Downloaded 02 Jun 2010 to 171.66.16.121. Redistribution subject to ASME license or copyright; see http://www.asme.org/terms/Terms_Use.cfm

vortex structure seems to exist on the upstream edge of the primary hole near the wall but the number of streaklines in this region is not enough to resolve it.) The longitudinal views (Fig. 13) evidence a stronger axisymmetry of the flow relative to the previous case (Fig. 2) in much of the combustor head, implying that the flow is now dominated by the swirler instead of the primary jet flow.

Cross-sectional views in the plane of the primary hole axis, viewing the flow from the downstream end toward the swirler, are shown in Fig. 14(*a*); two vortices can be seen, one on each side of the jet. The swirler flow rotates clockwise and the vortex on the right-hand side, being on the low-pressure side of the jet, is larger and can even rotate in a direction opposite to the swirler flow; compare this with Fig. 3(*a*), corresponding to case 1. In the plane of the dilution hole axis (Fig. 14*b*), there is a structure similar to the one observed in the plane of the primary holes, which is not so clear because of the increased bending of the jets.

The restricted measurements of axial and azimuthal velocities, at only one station between the primary jets (Palma, 1989) were not enough to confirm or deny the existence of this flow pattern. However, given the level of agreement between the calculated and experimental results in the previous subsection, the pattern shown above is believed to be generally correct. The swirler flow rate in this case was 23 percent of the total flow, i.e., similar to the experimental conditions of Heitor and Whitelaw (1986) and Bicen and Jones (1986) and the pattern predicted here is likely to be similar to that in existence in their experiments; note, for instance, the radial distribution of turbulence kinetic energy in the work of Heitor and Whitelaw with a peak at midradius, which, according to the present calculations, is likely to be associated with the stagnation point caused by the merging of the swirler flow stream and the primary jet flow (Fig. 13*a*). Also, the striking and unexplained strong influence of the fuel flow rate upon the axial velocity along the axis of the primary hole noted by Bicen and Jones (1986) may be explained through the contribution of the fuel to an increase of the swirler flow rate and the vortex near the centerline in the plane of the primary holes.

3.2 Combustor Flow Without Swirl. Calculations were also made to assess the performance of the turbulence model in the absence of swirler flow. Two calculations were made: case 3A, with no flow through the swirler (both the azimuthal and axial velocities were set to zero) and case 3B, with only the azimuthal velocity set to zero. The domain of integration was halved; a 30 deg sector limited by longitudinal planes of symmetry was used. The number of nodes in the azimuthal direction was also halved to maintain a similar grid resolution.

Figures 15 and 16 show the longitudinal streakline plots for the two flow conditions mentioned above. In case 3A, Fig. 15, there is a single vortex in the head, whereas with flow through the annular gap simulating the swirler (Fig. 16) a recirculating region, in the upper left corner, can be seen; the size of this region is larger than in case of swirling flow (Fig. 3). In the intermediate region there is another toroidal vortex (Fig. 15), which is eliminated if there is flow through the swirler, either without (Fig. 16) or with swirl component (Fig. 2). This is simply because the swirler flow increases the axial momentum near the walls, downstream of the primary jets. The measurements, although confirming the existence of this structure, showed (Palma, 1989) that it was actually smaller, and this is a consequence of a lower predicted recirculated flow rate. In realistic combustor geometries, the probability of this structure occurring is reduced by including extra holes (smaller) between the primary and dilution holes. Farther downstream, in the wake of the dilution jets (Figs. 15), there is a tendency for this phenomenon to reappear.

Quantitative differences between the flow conditions 3A and 3B have been discussed by Palma (1989). Here, it is sufficient to say that the main differences occur either near the wall, where the extra swirler flow shows by increasing the axial velocity upstream of the dilution jets, or near the centerline downstream of the dilution jets. In general, the level of agreement between the experimental and numerical results is the same as in the previous situation with swirling flow, as for instance, the underprediction of the axial velocity and turbulence kinetic energy on the centerline. The comments made in subsection 3.1 are also valid for this condition and show that the deficiencies of the turbulence model are associated with the prediction of the impingement region irrespective of the existence of swirler flow.

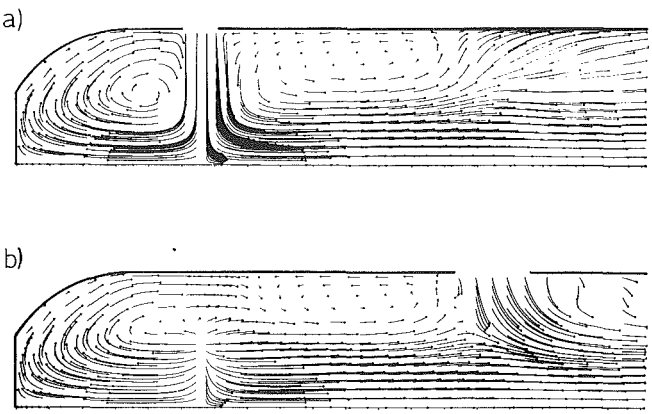

Fig. 15 Streakline plots corresponding to case 3A (without swirler flow): views in the longitudinal planes containing the axis of the holes

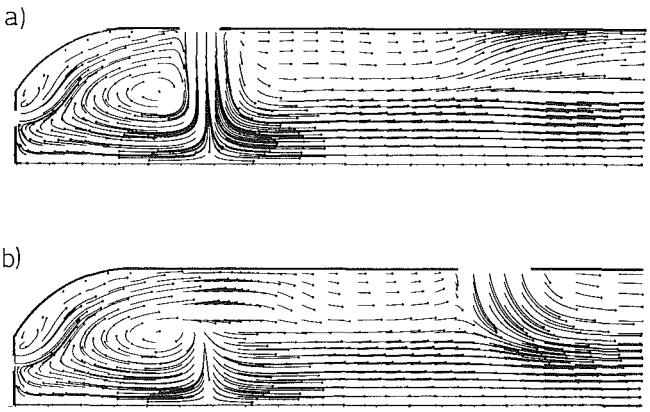

Fig. 16 Streakline plots from calculations with flow through the swirler gap without a swirl component of velocity (case 3B): views in the longitudinal planes containing the axes of the holes

4 Conclusions

Numerical prediction of the flow inside a gas turbine combustor was performed. The main conclusions of this work are:

1 The calculated results exhibit, in general, higher levels of momentum diffusion compared to the measurements. This showed, for instance, in the axial centerline velocity through the underprediction (35 percent) of the maximum negative value and a decay rate lower than measured.

2 The maximum turbulence kinetic energy, at the primary jet impingement, was underpredicted by about 20 percent.

3 No qualitative agreement with the experimental azimuthal velocity in the region downstream of the primary jets could be achieved. The model does not show the two contrarotating vortices created between the primary jets and due to their strong impingement.

Downloaded 02 Jun 2010 to 171.66.16.121. Redistribution subject to ASME license or copyright; see http://www.asme.org/terms/Terms_Use.cfm

4 The model gives acceptably good results and proved to be a powerful design tool. However, for higher confidence on the results under flow conditions differing from the present ones a cautious use of the model is recommended.

Acknowledgments

The present work was financed by Rolls-Royce plc and the Ministry of Defence (United Kingdom). It gives us great pleasure to acknowledge their support and the assistance of staff of the Imperial College Computer Centre, mainly through Mr. T.-S. Dau.

References

Andreopoulos, J., and Rodi, W., 1984, "Experimental Investigation of Jets in Crossflow," *Journal of Fluid Mechanics*, Vol. 138, pp. 93–127.

Beer, J. M., and Chigier, N. A., 1972, *Combustion Aerodynamics*, Applied Science Publishers, London, United Kingdom.

Bicen, A. F., and Jones, W. P., 1986, "Velocity Characteristics of Isothermal and Combusting Flows," *Combustion Science and Technology*, Vol. 49, pp. 1–15.

Bicen, A. F., McGuirk, J. J., and Palma, J. M. L. M., 1989, "Modelling Gas Turbine Combustor Flow Fields in Isothermal Flow Experiments," *Proceedings of the Institution of Mechanical Engineers. Part A: Journal of Power Engineering*, Vol. 203, pp. 113–122.

Bicen, A. F., Tse, D. G. N., and Whitelaw, J. H., 1990, "Combustion Characteristics of a Model Can-Type Combustor," *Combustion and Flame*, Vol. 80, pp. 111–126.

Bruce, T. W., Mongia, H. C., and Reynolds, R. S., 1979, *Combustor Design Criteria Validation. Vol. 1—Element Tests and Model Validation*, USARTL-TR-78-55A.

Correa, S. M., and Shyy, W., 1987, "Computational Models and Methods for Continuous Gaseous Turbulent Combustion," *Progress in Energy and Combustion Science*, Vol. 13, pp. 249–292.

Coupland, J., and Priddin, C. H., 1987, "Modelling the Flow and Combustion in a Production Gas Turbine Combustor," *Turbulent Shear Flows V*, F. Durst, B. E. Launder, and J. H. Whitelaw, eds., Springer-Verlag, pp. 310–323.

Green, A. S., and Whitelaw, J. H., 1983, "Isothermal Models of Gas-Turbine Combustors," *Journal of Fluid Mechanics*, Vol. 126, pp. 399–412.

Heitor, M. V., and Whitelaw, J. H., 1986, "Velocity, Temperature, and Species Characteristics of the Flow in a Gas-Turbine Combustor," *Combustion and Flame*, Vol. 64, pp. 1–32.

Hinze, J. O., 1975, *Turbulence*, 2nd ed., McGraw-Hill, New York.

Ikeda, Y., et al., 1987, "Flow Characteristics of Mixing Process of Dilution Air in a Premixing Gas Turbine Combustor," *International Gas Turbine Congress*, pp. III33–III39.

Jones, W. P., and Launder, B. E., 1972, "The Prediction of Laminarisation With a Two-Equation Turbulence Model," *International Journal of Heat and Mass Transfer*, Vol. 15, pp. 301–314.

Jones, W. P., 1975, "PACE: A Computer Program for Solving Three-Dimensional Flow Problems," Rolls-Royce Internal Report.

Jones, W. P., Clifford, W. C., Priddin, C. H., and Chair, R., 1977, "A Comparison Between Predicted and Measured Species Concentration and Velocities in a Research Combustor," AGARD-CP229 Paper No. 40.

Jones, W. P., and Priddin, C. H., 1978, "Predictions of the Flow Field and Local Gas Composition in Gas Turbine Combustors," *Proceedings of the 17th International Symposium on Combustion*, The Combustion Institute, Pittsburgh, PA, pp. 399–409.

Jones, W. P., 1984, private communication.

Launder, B. E., and Spalding, D. B., 1974, "The Numerical Computation of Turbulent Flows," *Computer Methods in Applied Mechanics and Engineering*, Vol. 3, pp. 269–289.

Launder, B. E., 1978, "Heat and Mass Transport," *Turbulence*, 2nd ed., P. Bradshaw, ed., Springer-Verlag, Berlin, pp. 231–287.

Lefebvre, A. H., 1983, *Gas Turbine Combustion*, McGraw-Hill, New York.

Leschziner, M. A., and Rodi, W., 1981, "Calculation of Annular and Twin Parallel Jets Using Various Discretization Schemes and Turbulence Model Variations," ASME *Journal of Fluids Engineering*, Vol. 103, pp. 352–360.

McGuirk, J. J., and Palma, J. M. L. M., 1992, "The Influence of Numerical Parameters in the Calculation of Gas Turbine Combustor Flows," *Computer Methods in Applied Mechanics and Engineering*, Vol. 96, pp. 65–92.

McGuirk, J. J., and Palma, J. M. L. M., 1993, "The Efficiency of Alternative Pressure-Correction Formulations for Incompressible Turbulent Flow Problems," *Computers & Fluids*, Vol. 22, No. 1, pp. 77–87.

Palma, J. M. L. M., 1989, "Mixing in Non-reacting Gas Turbine Combustor Flows," Ph.D. Thesis, University of London, United Kingdom.

Patankar, S. V., 1980, *Numerical Heat Transfer and Fluid Flow*, Hemisphere Publishing, New York.

Perry, A. E., and Chong, M. S., 1987, "A Description of Eddying Motion and Flow Patterns Using Critical Point Concepts," *Annual Review of Fluid Mechanics*, Vol. 19, pp. 125–155.

Priddin, C. H., and Coupland, J., 1986, "Impact of Numerical Methods on Gas Turbine Combustor Design and Development," in: *Calculations of Turbulent Reactive Flows*, R. M. C. So, J. H. Whitelaw, and H. C. Mongia, eds., ASME AMD-Vol. 81, pp. 335–348.

Serag-Eldin, M. A., and Spalding, D. B., 1979, "Computations of Three-Dimensional Gas-Turbine Combustion Chamber Flows," ASME JOURNAL OF ENGINEERING FOR POWER, Vol. 101, pp. 326–336.

Shyy, W., Braaten, M. E., and Sober, J. S., 1987, "A Three-Dimensional Grid Generation Method for Gas-Turbine Combustor Flow Computations," AIAA Paper No. 87-0204.

Sloan, D. G., Smith, P. J., and Smoot, L. D., 1986, "Modelling of Swirl in Turbulent Flow Systems," *Progress in Energy and Combustion Science*, Vol. 12, pp. 163–250.

Srinivasan, R., Reynolds, R., Ball, I., Berry, R., Johnson, K., and Mongia, H. C., 1983, "Aerothermal Modelling Program. Phase I—Final Report," NASA CR-168243, GARRET 21-4742-2.

Sturgess, G. J., 1986, "Calculations of Aerospace Propulsion Combustors: A View From Industry," in: *Calculation of Turbulent Reactive Flows*, R. M. C. So, J. H. Whitelaw, and H. C. Mongia, eds., ASME AMD-Vol. 81, pp. 185–231.

Sundqvist, H., and Veronis, G., 1970, "A Simple Finite-Difference Grid With Non-constant Intervals," *Tellus*, Vol. 22, pp. 26–31.

Wild, P. N., et al., 1987, "Three-Dimensional Gas Turbine Combustor Modelling," AGARD-CP422, Paper 27.

Downloaded 02 Jun 2010 to 171.66.16.121. Redistribution subject to ASME license or copyright; see http://www.asme.org/terms/Terms_Use.cfm

Three-Dimensional Gas Turbine Combustor Emissions Modeling

N. K. Rizk

H. C. Mongia

Allison Gas Turbine Division,
General Motors Corporation,
Indianapolis, IN 46206

An emission model that combines the analytical capabilities of three-dimensional combustor performance codes with mathematical expressions based on detailed chemical kinetic scheme is formulated. The expressions provide the trends of formation and/or the consumption of No_x, CO, and UHC in various regions of the combustor utilizing the details of the flow and combustion characteristics given by the three-dimensional analysis. By this means, the optimization of the combustor design to minimize pollutant formation and maintain satisfactory stability and performance could be achieved. The developed model was used to calculate the emissions produced by several engine combustors that varied significantly in design and concept, and operated on both conventional and high-density fuels. The calculated emissions agreed well with the measurements. The model also provided insight into the regions in the combustor where excessive emissions were formed, and helped to understand the influence of the combustor details and air admissions arrangement on reaction rates and pollutant concentrations.

I Introduction

Emissions from conventional gas turbine combustors are significantly affected by the details of the front end of the combustor and the subsequent admittance of air into various combustion and dilution zones. The design of the combustor is, therefore, required to be optimized in order to meet the expected trends of the lowering emissions levels while maintaining satisfactory peformance over a wide operating envelope. For instance, minor changes in liner air distribution can create sizable variations in such parameters as lean blowout and ignition, exit gas temperature profile, and nitric oxide emissions. Sufficient cooling air would be required to maintain low wall temperature levels and gradients for enhanced structural durability of the combustor components.

It is realized that the development of the combustor requires better knowledge of the flow characteristics within the combustor and of the important processes of fuel injection, evaporation, mixing, hydrocarbon combustion chemistry, and convective and radiative heat transfer. Over the years, empirical and semiempirical tools have been used to evaluate the emissions and performance of the combustor through the estimation of a number of parameters, including spray quality, droplet combustion, and characteristics dimension and time of the combustion zone (Ballal and Lefebvre, 1981; Lefebvre, 1984, 1985; Washam and Mellor, 1979; Plee and Mellor, 1979). Effects of fuel properties and operating parameters on the combustor performance are usually addressed in these approaches.

In order to achieve significant reduction in the pollutant emissions produced by the combustor, it is essential to obtain a better understanding of the processes for formation of various species of interest within the combustor. By this means, the conditions favorable for the excessive formation of such pollutants as NO_x, CO, and UHC could be avoided. A detailed representation of the combustor flow field made available through numerical methods has been used to provide some insight into the interaction of the swirling flow with fuel injection and spray and the impact of this interaction of fuel evaporation, mixing, and turbulent combustion. In light of such information, many useful modifications to the details of the combustor could be performed.

It is recognized, however, that due to the incomplete understanding of the various combustion processes and numerical diffusion, analytical calculations, of practical gas turbine combustors cannot yet be considered quantitatively accurate (Mongia et al., 1986; Sturgess, 1983). Significant advances are needed in physical submodels, numerics, and in the simulation of the actual hardware in order to enhance the predictive capability of the model. In recent years, an approach that combines the capabilities of the three-dimensional finite volume calculations with empirical expressions has been formulated to provide various performance parameters. This approach was successfully applied to conventional diffusion flame combustors as well as to other concepts of rich-lean and premixed/prevaporized combustion (Rizk and Mongia, 1986, 1990a, 1991a, 1991b).

In the present investigation, a detailed finite rate reaction scheme was used to provide the trends of pollutant formation in various combustor regions. The results were utilized as a fundamental basis for the developememt of an emission model. The model simulates the large number of reactions involved in the kinetic scheme by mathematical expressions for NO_x, CO, and unburned hydrocarbon concentrations. The combination of these expressions with multidimensional calculations has provided a useful tool for the evaluation of pollutant formation history inside the combustor. In the following sec-

Contributed by the International Gas Turbine Institute and presented at the 37th International Gas Turbine and Aeroengine Congress and Exposition, Cologne, Germany, June 1-4, 1992. Manuscript received by the International Gas Turbine Institute February 6, 1992. Paper No. 92-GT-129. Associate Technical Editor: L. S. Langston.

Copyright © 1993 by ASME
Downloaded 02 Jun 2010 to 171.66.16.121. Redistribution subject to ASME license or copyright; see http://www.asme.org/terms/Terms_Use.cfm

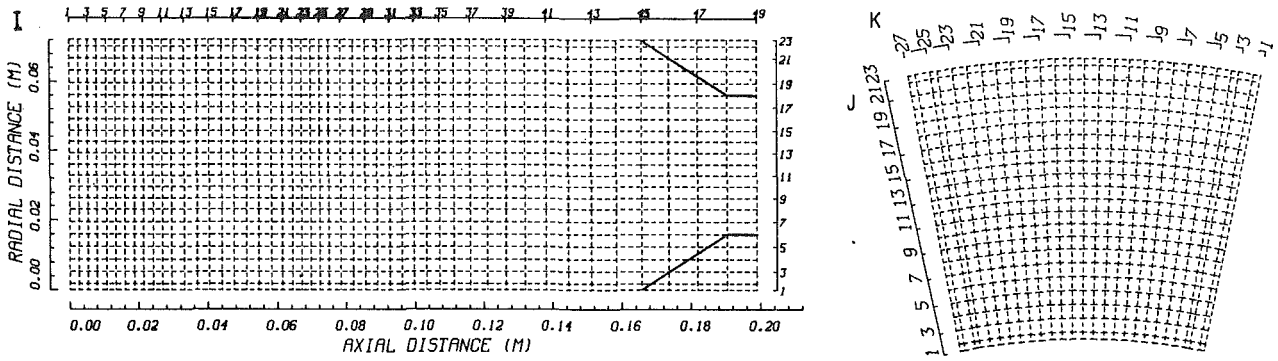

Fig. 1 Grid network used in the three-dimensional analysis

tions, a description of the three-dimensional model and the calculation procedure is given. The application of the developed emissions model to a large number of combustor configurations is addressed in later sections of this paper.

II Three-Dimensional Combustor Model

In this section, a description is given for the three-dimensional model that has been used to provide the details of the flow field of several gas turbine combustors. Examples of the results are also included in this section to illustrate the capability of the model to capture the main features of the flow within the combustor. The next section addresses the development effort of the emissions model that utilizes the flow parameters offered by the three-dimensional analysis.

1 Numerical Model. The combustor model used in the present approach is a three-dimensional, finite-volume method that solves the Navier–Stokes equations for a reacting flow field (Patankar, 1980). The program simulates turbulence by the two-equation k–ϵ model (Launder and Spalding, 1974), and combustion following vaporization is determined by a four-step chemical reaction model based on Arrhenius and eddy breakup concepts (Hautman et al., 1981; Mongia and Reynolds, 1979).

The transport equations for all dependent variables are of the following form:

$$\text{div}[\rho u\phi - (\mu_{\text{eff}}/\text{Pr})\text{grad}\phi] = S_\phi \tag{1}$$

where ρ is mixture density, u is the velocity, μ_{eff} is effective turbulent viscosity, Pr is the effective Prandtl/Schmidt number, and S_ϕ is the source term for variable ϕ. The reaction model is given by the following four-step scheme:

$$C_xH_y \rightarrow C_xH_{y-2} + H_2 \tag{2}$$

$$C_xH_{y-2} + \frac{x}{2}O_2 \rightarrow xCO + \frac{y-2}{2}H_2 \tag{3}$$

$$CO + \frac{1}{2}O_2 \rightarrow CO_2 \tag{4}$$

$$H_2 + \frac{1}{2}O_2 \rightarrow H_2O \tag{5}$$

A modified form of the Rosin–Rammler spray drop size distribution that has been found to fit experimental data is used in the model to express the spread in the drop size range in the spray (Rizk and Lefebvre, 1985; Custer, and Rizk, 1988). The distribution is given by:

$$v = 1 - \exp - (\log_e d/\log_e x)^q \tag{6}$$

where v is volume fraction of droplets having diameter less than d, x is a parameter related to spray mean size, and q defines the spread in drop sizes. The evaporation calculation is based on the vapor concentration gradient concept that estimates the gas properties at reference temperature using the one-third rule (Faeth, 1977). The calculation takes into account both heat-up and steady-state stages, and the effect of the forced convection is included in the calculation of the evaporation constant λ as follows:

$$\lambda = \frac{8kg}{C_{pg}\rho_F}\log_e(1+B_M)(1+0.3\text{Re}^{0.5}\text{Pr}^{0.33}) \tag{7}$$

Re and Pr are the Reynolds and Prandtl numbers based on gas properties at film temperature, relative velocity, and instantaneous drop diameter. kg, C_{pg}, and ρ_F are thermal conductivity, specific heat of gas, and fuel density. B_M is the mass transfer number.

An iterative finite-difference solution procedure is used to solve the resulting system of nonlinear partial differential equations. The variables computed by the code include the three velocity components, temperature, turbulence characteristics (k–ϵ), composite fuel fraction, unburned fuel, intermediate fuel, CO, and H_2.

The three-dimensional code was used in the present investigation to provide the details of the flow characteristics of a large number of configurations that encompass can, straight throughflow, and reverse flow combustors. These combustors were tested with conventional fuels such as JP-4, JP-5, and DF-2, and one combustor was also tested with four high-density fuels. The results of the three-dimensional analysis are required for the development of the emissions model as described in the next section. The measurements obtained for all combustors are used for model validation purposes.

2 Combustor Analysis. The modeling of the combustors involved the selection of representative sectors that included the details of the front end and the radial injection features. The methods adopted in cooling the combustor wall were also simulated in the combustor sector. Typically, the sector was divided into a large number of finite difference nodes along axial, radial, and circumferential directions, in the order of 30,000 to 50,000 total nodes, as shown in Fig. 1. Provisions were made to block parts of the dome and exit sections to match the geometry details of the combustor.

The results of the three-dimensional analysis were investigated using computer-drawn plots of selected longitudinal and

Nomenclature

B_M = mass transfer number
d = droplet diameter, m
F = fraction of total fuel flow
F_B = fraction of total fuel burned
P_3 = system pressure, Pa
Pr = Prandtl number
q = distribution parameter
Re = Reynolds number
T = temperature, K
v = volume fraction of droplets
x = mean drop size parameter, m
λ = evaporation constant, m^2/s
τ = residence time, ms
ϕ = equivalence ratio

Downloaded 02 Jun 2010 to 171.66.16.121. Redistribution subject to ASME license or copyright; see http://www.asme.org/terms/Terms_Use.cfm

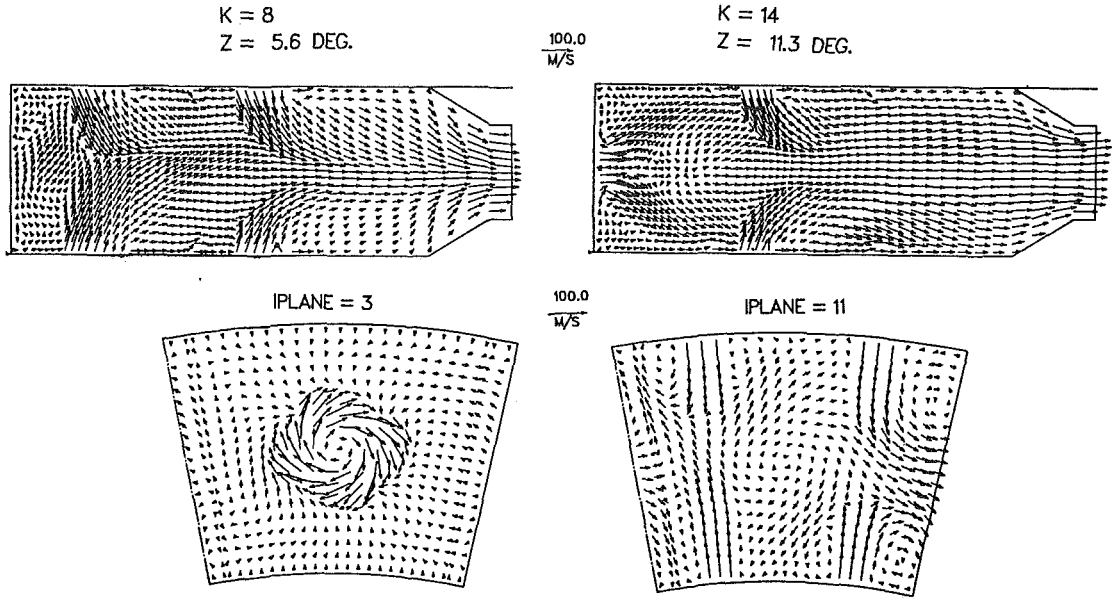

Fig. 2 Velocity vectors in annular combustor

transversal sections of the combustor sector. Figure 2 shows the velocity vectors for an annular combustor at two planes: straddled and in-line with the fuel injector, and at cross-sectional planes; immediately downstream of the swirler and the one that contains the primary jets.

The main features of the flow field, such as flow reversal in the primary zone, the jet penetration, and the flow acceleration toward the exit of the combustor, are all illustrated in Fig. 2. Information on the size of the recirculation zone, balance between opposed jets in various combustor zones, and regions in the combustor that may contain near-stagnant flow provides valuable assistance during the developmental phases of the combustor.

The contours of the fuel/air ratio of the two longitudinal planes are given in Fig. 3. The figure shows the existence of a fuel-rich core downstream of the fuel nozzle, and near-stoichiometric regions occur behind the primary jets. The drop in fuel concentration in the vicinity of the radial air jets is also illustrated in the figure. The cross-sectional view at the primary and intermediate hole planes is also given in Fig. 3 to show more details of the fuel distributions in the combustor. It is observed that rich regions are concentrated near the center of the primary jet plane while lower concentrations of the fuel are present near the walls. The mixing with the primary jet air results in a drop in fuel/air ratio levels at the intermediate jet plane with few pockets of rich mixture, behind and almost in line with the primary jets. Any effort to reduce the emissions levels of this combustor should focus on possible changes in design that can eliminate regions of potential pollutant formation.

The gas temperature contours for the two longitudinal and the two transverse planes are illustrated in Fig. 4. The fuel-rich mixture prevailing in the primary zone of the combustor results in relatively low gas temperature in this zone. The subsequent admission of air downstream brings the mixture closer to the stoichiometric conditions resulting in hotter regions, in particular near the walls. This information indicates the need to adjust the cooling arrangement in the liner to handle the heat transmitted to the wall in various zones. The transvere section at the primary jet plane shows higher temperatures to the sides of the sector than those in the core. At the intermediate jet plane, regions of hot gases exist near both walls.

It has been illustrated in the above discussion that the simulation of the combustor hardware by using the three-dimensional code can aid the effort to reduce emissions produced by the combustor through subtle changes to the details of the combustor. As mentioned earlier, a hybrid approach has been formulated to give an estimate of the emissions and performance by combining the analytical capability of the three-dimensional model with empirical correlations (Rizk and Mongia, 1986, 1990c). To use the output data of the model in this approach, the modeled combustor sector is divided into a relatively large number of subvolumes. A typical number of around 1000 subvolumes is considered sufficient to represent the whole combustor sector in the calculations. By this means, sophisticated reacting flow models are brought closer in representing actual combustor hardware with significantly less computation.

The relevant combustion and flow characteristics within each subvolume are evaluated and prepared for use as an input to the empirical correlations. The input data include gas flow rate, flow-averaged temperature, fuel/air ratio, fractions of fuel evaporated and burned, in addition to the turbulence characteristics in each subvolume. The overall performance of the combustor in this approach is obtained by the summation of the contributions of various subvolumes according to fraction of fuel burned or volume fraction of each subvolume, whichever applies to the performance parameter under consideration.

In the present investigation, a model for pollutant formation and/or consumption within various regions of the combustor has been developed to replace the empirical expressions used in the hybrid approach. As described in the next sections, the history of pollutant concentrations in the combustor is evaluated using a calculation procedure that is based on a detailed chemical kinetic scheme for the reaction of hydrocarbon fuels.

III Emissions Model

1 Emissions Evaluation Methods. Several empirical and analytical emissions models have been proposed in the literature to provide estimates of the exhaust emissions of No_x, CO, and unburned hydrocarbons. The calculation procedures, followed in most of these models are based on the concept that the concentrations of various species are governed by rection rate, mean residence time, and the mixing process. It is recognized that factors that inhibit the formation of one pollutant may enhance the formation of the others. For instance, oxides of nitrogen are produced in the hot region of the combustor, while the presence of CO and UHC in the

Downloaded 02 Jun 2010 to 171.66.16.121. Redistribution subject to ASME license or copyright; see http://www.asme.org/terms/Terms_Use.cfm

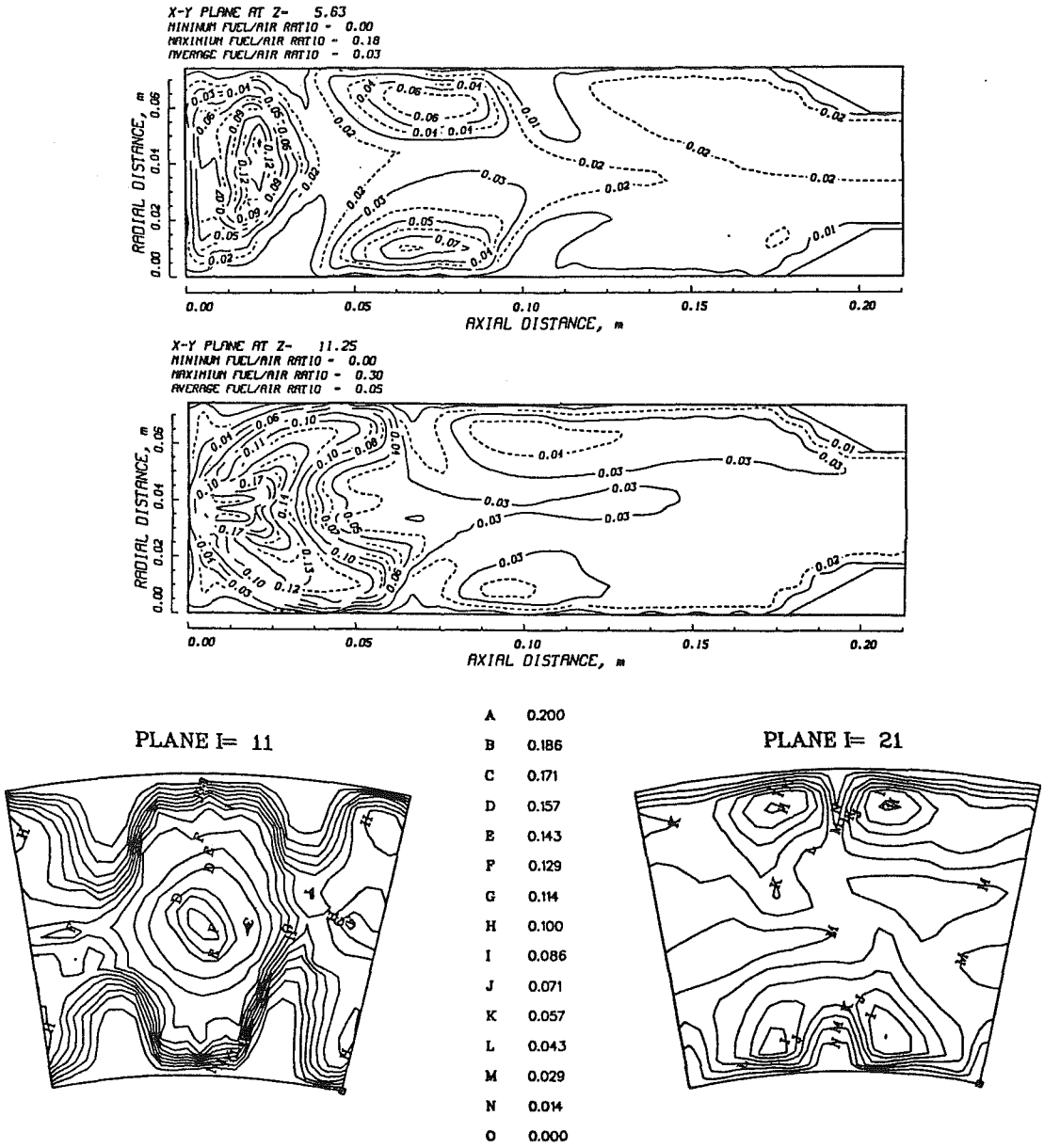

Fig. 3 Fuel/air contours in combustor

exhaust is an indication of incomplete combustion of fuel due to inadequate burning rate in the primary zone or to the chilling effects of the liner coolant. The residence time also has an opposite effect of the NO_x production on one side and the CO and UHC concentrations on the other.

The empirical approaches have considered these factors directly in the form of simple correlations (Lefebvre, 1984, 1985). In the analytical models, the effects of the system pressure, temperature, and residence time are already accounted for through their roles in controlling the reactions. Hammond and Mellor (1973) proposed a combination of perfectly stirred reactors to simulate various regions of the combustor and used a global finite rate mechanism for hydrocarbon combustion. They concluded that the poor predictions of the emissions variation with combustor loading were due to neglecting the heterogeneous effects and to the concept used to simulate the primary zone.

Other analytical models offered in the literature include the simulation of the combustor by streamtubes that surround a central recirculation zone (Mosier et al., 1973) or the use of various appropriate arrangements of separate reactors (Fletcher and Heywood, 1971). Rizk and Mongia (1991b) proposed a flow model that simulates a combustor operating on a rich/lean combustion concept. It consists of a number of reactors that represent the combustion in the rich zone, the mixing process in the quench zone, and the continuation of the reaction in the lean zone. A chemical kinetic mechanism was used to provide the trends of variation of NO_x formation with various operating parameters. The results of this effort were utilized to derive a number of expressions that simulate the kinetic mechanism in simpler forms. Satisfactory agreement with the data was achieved using this approach.

A similar model has been formulated to estimate the concentrations of NO_x, CO, and UHC in conventional types of combustors (Rizk and Mongia, 1993). The model considers the primary zone to consist of two central reactors in series that define a lean blowout zone followed by main primary zone reaction. The near-wall region in the primary zone is simulated by two other reactors to account for the reaction of the fuel that escapes the central recirculation zone of the com-

Downloaded 02 Jun 2010 to 171.66.16.121. Redistribution subject to ASME license or copyright; see http://www.asme.org/terms/Terms_Use.cfm

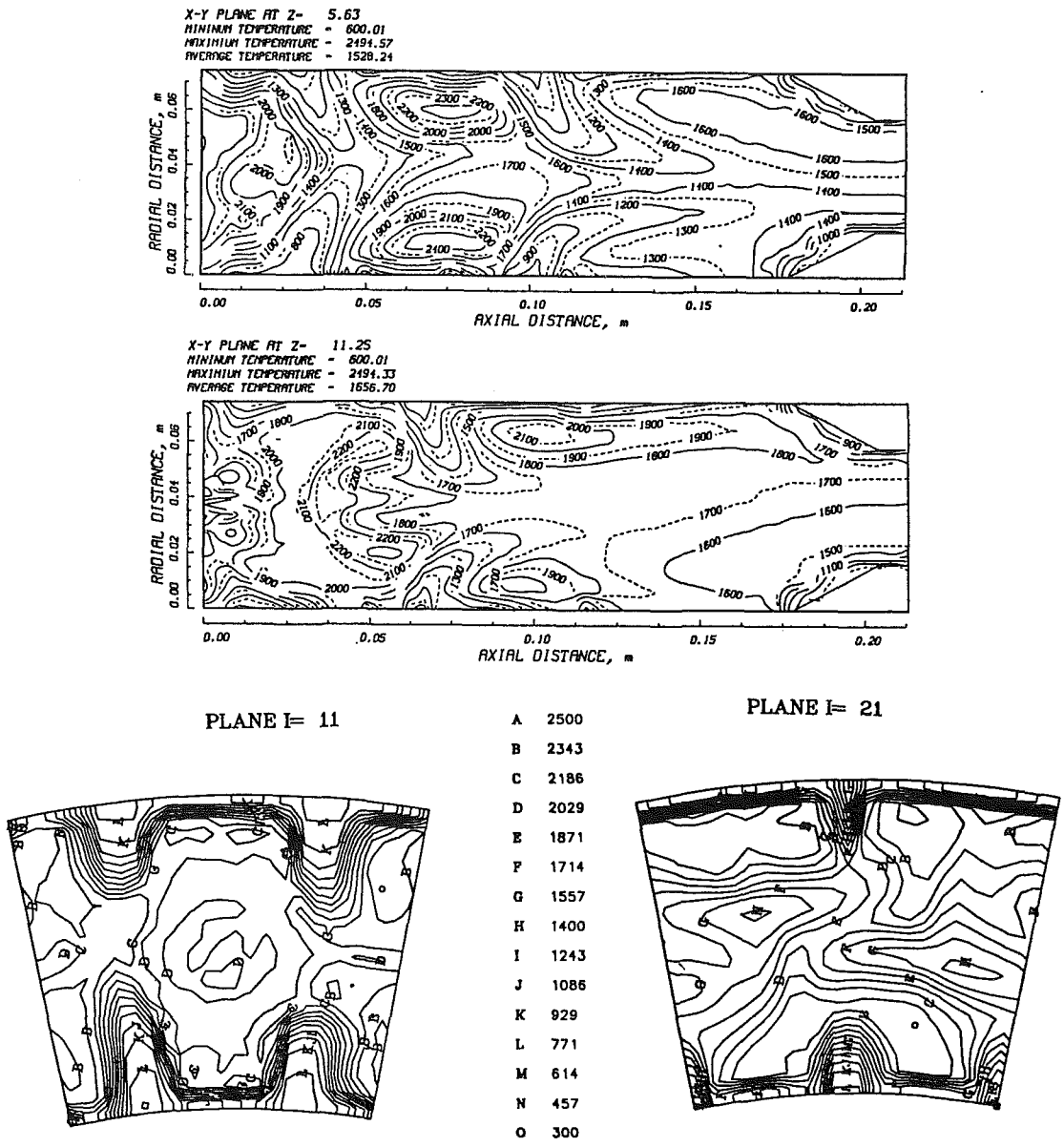

Fig. 4 Gas temperature contours in combustor

bustor. The intermediate and dilution zones are also represented by a number of individual reactors. The formation of NO_x and CO, the conversion of CO to CO_2, and the reaction of the hydrocarbons in various zones are evaluated in the model using equations that are based on the chemical reaction calculations. A number of parameters that define distribution of fuel and air, and the flow of the hot gases between the reactors need to be estimated in this approach. Corrections for the evaporation delay time and mixing processes are included in the procedure.

In the present investigation, a concept has been formulated to combine the vast information offered by the three-dimensional analysis on the details of the combustor flow field with the equations that simulate the chemical kinetic scheme. The flow pattern and fuel distribution provided by the three-dimensional analysis eliminate the need to make the engineering estimates required for the emissions model. Also, the use of a detailed reaction mechanism to provide the data needed for the model development improves the accuracy of the prediction of pollutant formation in the combustor. The calculation of the emissions using the developed model is made through a number of steps. Once the three-dimensional analysis is completed, the combustor sector is divided into a large number of subvolumes. The average flow and combustion parameters within each subvolume are then prepared for use in the equations.

2 Emissions Model Development. The reaction mechanism proposed by Westbrook and Pitz (1984) for the pyrolysis and oxidation of propane was used to establish the key elements controlling the emissions concentrations. The mechanism involves 163 elementary reactions for the combustion of propane that has combustion properties similar to those of more complex practical fuels. An extended Zeldovich mechanism was added to the kinetic model to enable calculating the NO_x formation. It is described by Glassman (1977) as follows:

$$O + N_2 \rightarrow NO + N \quad (8)$$

$$N + O_2 \rightarrow NO + O \quad (9)$$

$$N + OH \rightarrow NO + H \quad (10)$$

A numerical study was conducted to determine the separate effects of such parameters as reaction temperature, residence

Downloaded 02 Jun 2010 to 171.66.16.121. Redistribution subject to ASME license or copyright; see http://www.asme.org/terms/Terms_Use.cfm

time, system pressure, and fuel/air mixture strength on pollutant characteristics. Based on the results of these calculations, a number of expressions were derived to simulate the reaction mechanism. The NO_x formation early in the primary zone is expressed by the following equation:

$$NO_{xi}(g/kg) = 1E13(P_3/1.4E6)^{aa}\exp(-71{,}4421/T_i)(7.56\phi_i^{-7.2} - 1.6)\tau_i^{0.64}F_i \quad (11)$$

The subscript i refers to the parameters provided by the three-dimensional calculations for subvolume i, P_3 is system pressure, Pa, T is gas temperature, K, ϕ is equivalence ratio, τ is residence time, ms, and F is the fraction of total fuel flow in subvolume. At equivalence ratio higher than 1.08, the NO_x equation is given by:

$$NO_{xi} = 1E13(P_3/1.4E6)^{aa}\exp(-71{,}442/T_i)(5.212\phi^{-2.99} - 1.6)\tau_i^{0.64}F_i \quad (12)$$

The exponent of the pressure term (aa) varies with the equivalence ratio as follows:

$$aa = 11.95\exp(-\phi/5.76) - 10 \quad (13)$$

The parametric investigation has also shown that the NO_x concentration increases in downstream regions of the primary and intermediate zones, at a lower rate, if temperatures are high enough. The concentration levels in these regions are controlled by the additional formation of NO_x and the possible reduction of NO_x formed earlier in the primary zone. The same approach given by Rizk and Mongia (1992) to divide the primary zone equally into two reactors in series, defining lean blowout and main reaction regions, is followed here. The NO_x formation in downstream regions is given by:

$$NO_{xi} = 1E14(P_3/1.4E6)^{aa}\exp(-71{,}442/T_i)(1.172\phi^{-4.56} - 0.6)\tau_i^{0.876}F_i \quad (14)$$

The total NO_x produced by the combustor is the summation of the contributions from all subvolumes.

The simulation of the various combustion zones by a series of reactors has indicated that CO is formed in large quantities early in the primary zone. A significant proportion of the CO is however, converted to CO_2 in downstream regions of the primary and intermediate zones. Additional formation of CO may also occur if the reaction temperature is sufficiently high in these regions. Following the same concept of equally dividing the primary zone into two reactors in series used in NO_x calculation, the CO formation early in the primary zone is given by:

$$CO_i(g/kg) = \exp(-CE/T_i)\,Cph\,(P_3/1.4E6)^{a1}(\tau_i/0.5)^{a2}F_{Bi} \quad (15)$$

The parameter CE varies with ϕ according to the following relationship:

$$CE = 6.23E14\phi_i^{3.8}\exp(-\phi_i/0.56)^{1.75} \quad (16)$$

and the function Cph is given by:

$$Cph = 4.54E3\phi_i^4\exp(-\phi_i/1.02)^{2.23} \quad (17)$$

F_b is the fraction of fuel burned in the subvolume i, and the exponents of the pressure and residence time are calculated by:

$$a1 = -0.447\phi_i^{-1.87} + 0.2 \quad (18)$$

$$a2 = -0.362\phi_i^{-1.9} + 0.2 \quad (19)$$

The reaction model has also shown that when the conditions dictate fairly low temperature, partial combustion occurs. A threshold temperature of about 1370 K is found to be the least temperature for near-complete combustion. Below this temperature level, the expression for CO formation based on the chemical kinetic calculations is given by:

$$CO_i = (7.E-15\exp(T_{Ii}/36.1) + 140)(P_3/4.3E5)^{-0.62}F_{Bi} \quad (20)$$

T_i is reaction temperature corrected for the residence time as follows:

$$T_I = T\tau^{0.057} \quad (21)$$

The total CO formed is the summation of the individual contributions from various subvolumes in this first region of the primary zone. Large proportion of CO formed early in the primary zone is converted to CO_2 reducing the CO concentration according to the following expression:

$$CO_i = 2.52\exp(-5000/T_i)(0.00017\exp(\phi_i/0.126) + 0.05)CO_{IN}(P_3/1.4E6)^{a3}\tau_i^{a4}F_i \quad (22)$$

This equation describes the trend of variation of CO with reaction temperature in the temperature range higher than 2000 K according to the chemical reaction calculation. F is fraction of total fuel flowing through subvolume i, and CO_{IN} is the inlet value of CO to the second region of the primary zone. The exponents $a3$ and $a4$ are given by:

$$a3 = 3.79\exp(-1.56/\phi_i) - 0.8 \quad (23)$$

$$a4 = 0.875\phi_i^{0.94} - 1.0 \quad (24)$$

The CO concentration at temperatures below 2000 K is described by:

$$CO_i = 0.122T_i^{-0.2}\phi_i^{-2.45}(P_3/4.34E5)^{a3}CO_{IN}F_i \quad (25)$$

The CO concentration in each axial plane of the combustor is calculated by the summation of the contributions from the subvolumes of the net CO after allowing conversion to CO_2 to take place. In addition, any extra CO formed under the conditions prevailing in these subvolumes is calculated using Eq. (17) or (20) and added to the CO concentration at this plane. The calculation of the CO concentration proceeds downstream of the combustor following the same procedure and using the concentration for the previous plane as an inlet value for next plane.

The calculation of the UHC using the chemical kinetic scheme has shown that the presence of most of the unburned fuel in the combustor exhaust is due to incomplete combustion in low-temperature regions. The results of the reaction modeling indicate that significant quantities of UHC exist in near-wall regions if the reaction temperature is below about 1370 K. The expression derived utilizing these results is used in the proposed emission model in the following form:

$$BHC = 0.144\exp(TT_i^{5.1}/5.43E15)(1 - Brn)(P_3/8E5)F_i \quad (26)$$

BHC is the fraction of total fuel burned in subvolume i, Brn is total fuel burned in upstream regions, F is fraction of fuel flow, and TT is temperature corrected for residence time using the following expression:

$$TT_i = T_i\tau_i^{0.2} \quad (27)$$

At reaction temperatures above 1370 K, the following equation is used for fraction of fuel burned in subvolume:

$$BHC = 1.239\exp(-539.2/TT_i)(1 - Brn)(P_3/8E5)\tau_i^{0.5}F_i \quad (28)$$

The summation of the fractions of fuel burned in all subvolumes yields the overall fraction of fuel burned in the combustor (BHC_T). The unburned hydrocarbons concentration is, therefore, calculated by this equation:

$$UHC(g/kg) = 1000 - 1000BHC_T \quad (29)$$

The next section addresses the application of the developed approach to a number of production combustors to estimate their emissions characteristics and evaluate the model capability to match the measurements.

IV Combustor Emissions Evaluation

The emissions produced by gas turbine combustors are governed by operating conditions as well as the details of the combustor front end and radial air admission into various

Downloaded 02 Jun 2010 to 171.66.16.121. Redistribution subject to ASME license or copyright; see http://www.asme.org/terms/Terms_Use.cfm

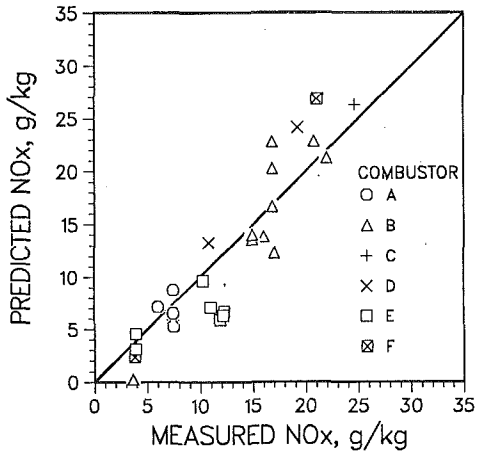

Fig. 5 Comparison between calculated and measured NO_x

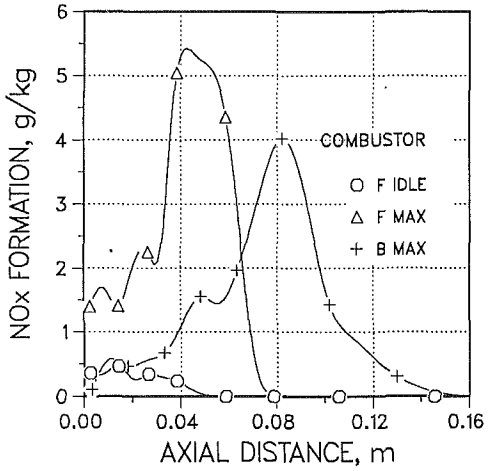

Fig. 6 NO_x formation at different axial locations

zones. Different types of combustors can have significantly different emissions characteristics. Chemical and physical properties of fuel can alter levels of pollutant concentration within the combustor through their effects on reaction rates, atomization, and evaporation processes. In the present effort, the data obtained for six groups of combustors are compared with the calculated values of NO_x, CO, and UHC computed by the emissions model.

As described earlier, the calculation procedure involves conducting a three-dimensional analysis of the combustor and using the results as input to the emissions expressions that are based on chemical kinetic calculations. Pollutant formation and/or destruction are estimated for the combustor, which is divided into large numbers of subvolumes representing various regions of the combustor. Following this approach, the emissions for all the combustors under investigation were calculated and compared with the measured data. It is worth mentioning that the developed calculation approach does not involve any empirical input or require engineering estimates of certain combustor flow parameters. Description of the combustors and the fuel types tests in these combustors are given in the following subsection.

1 Combustors Descriptions. Five different configurations of the annular combustor *A* were used in the analysis. The baseline combustor had no dome swirlers, and the other four modified combustors had dome swirlers, different primary zone features, and air distributions. Combustor *A* only operated on a DF-2 fuel. Combustor *B* was also an annular type of comparable size to combustor *A*. The combustor *B*, however, operated at much higher pressures and temperatures and the fuel used was JP-5. Modifications of combustor *B* included fully and partially blocked dome swirlers, and size and location variations of primary jets.

Combustors *C*, *D*, and *E* were all of the can-annular type and of similar sizes. The common features in liners *C* and *E* were the absence of dome swirlers and the arrangement of radial air injection in the primary zone. The fuel injectors used in the two designs were completely different. A piloted airblast atomizer was utilized in combustor *C* while a dual-orifice pressure atomizer was used in combustor *E*. Combustor *D* has a dome swirler, and the primary jet configuration was different from the one used in the other two liners. The fuels burned in combustors *C* and *D* were DF-2 and JP-5, respectively, while combustor *E* was tested with JP-4 and four high-density fuels.

The last combustor included in this investigation (combustor *F*) was a reverse flow annular type. Combustor *F* was considerably smaller in size than the first two annular combustors *A* and *B*. The liner had no intermediate air jets and the combustor operated on both JP-4 and JP-5 fuels. The data utilized in the emissions model calculations included those obtained at maximum power conditions in addition to a number of idle and part-load measurements.

The wide variety of combustor configurations, fuel types, and power modes included in this investigation has provided a broad data base needed for testing and demonstrating the model.

2 Emissions Calculations. Figure 5 shows a comparison between the calculations and the measurements of NO_x for all combustor configurations. The agreement is quite satisfactory, indicating that the three-dimensional combustor emissions model provides reasonable accurate estimates of NO_x. The model, in addition to giving the total NO_x produced by the combustor, provides insight into the process of formation of the NO_x within the combustor. Examples of the local contributions of various combustor zones to the total NO_x are given in Fig. 6 for two combustors of the annular type. The figure shows that significant amounts of NO_x start to form at a distance of about 0.04 m, which is downstream of the primary jets in both designs. High concentrations of NO_x are formed in the smaller combustor *F* almost to the point of dilution air admission, while in the larger size combustor *B* the gradual admission of intermediate and dilution air extends the NO_x formation through the intermediate zone at a lower rate. It is noticed, however, that combustor *F* produces more NO_x than combustor *B* due to the existence of larger regions near stoichiometric conditions in the flow file of the combustor. This emphasizes the importance of controlling the stoichiometry, especially early in the combustor, if the NO_x emissions are to be minimized. Figure 6 also shows that all the small concentration of NO_x formed at idle conditions occurs within the primary zone of the combustor. Figure 7 shows the total NO_x concentration at various axial locations for the three cases. The figure illustrates the cumulative concentrations in various zones of the combustor and shows that in both combustors no further formation of NO_x occurs beyond the locations of the dilution jets.

The calculated CO emissions for all combustor configurations are plotted against the measured data in Fig. 8. The good agreement shown in this figure indicates that the approach to calculate the CO emission through the evaluation of the CO formation in the primary zone and the subsequent conversion to CO_2 in downstream regions yields satisfactory results. More importantly, the calculation approach provides the details needed to point regions of excessive formation of CO and to enhance the conversion of CO later in the combustor. Figure 9 shows the initial formation of CO at two power conditions of combustor *E*. The primary zone of this can combustor operates at fuel-rich conditions due to the absence of dome swirler and the admittance of air through three rows of primary

Downloaded 02 Jun 2010 to 171.66.16.121. Redistribution subject to ASME license or copyright; see http://www.asme.org/terms/Terms_Use.cfm

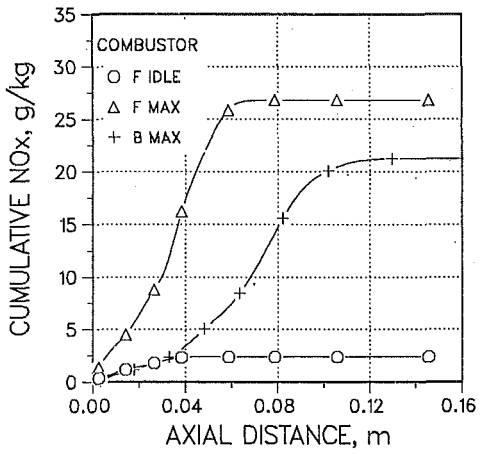

Fig. 7 Cumulative NO_x formation in combustor

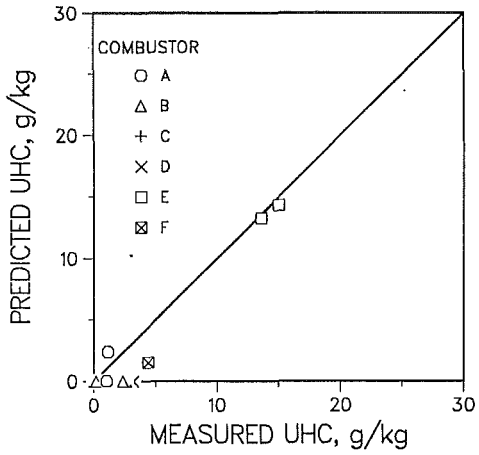

Fig. 10 Comparison between calculated and measured UHC

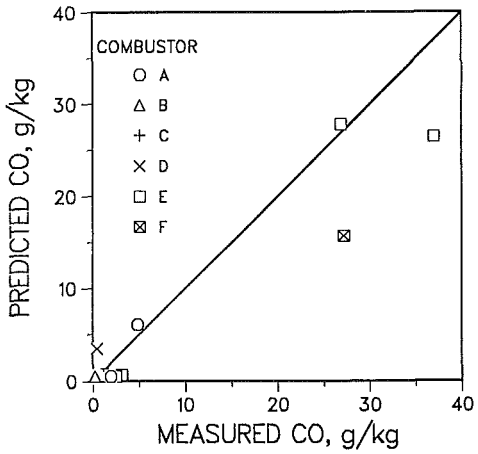

Fig. 8 Comparison between calculations and data of CO

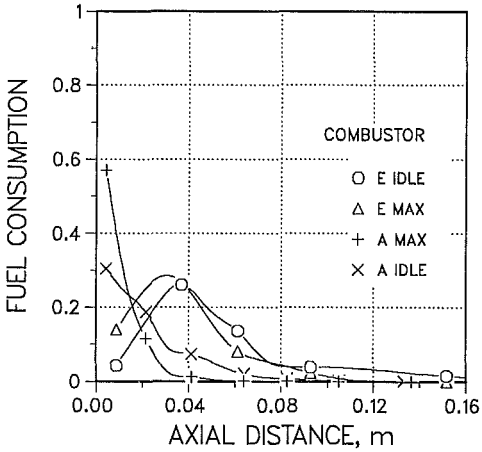

Fig. 11 Fraction of total fuel burned at different axial locations

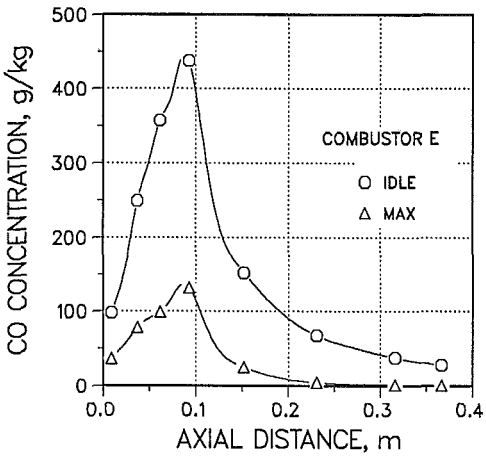

Fig. 9 Local concentration of CO in combustor

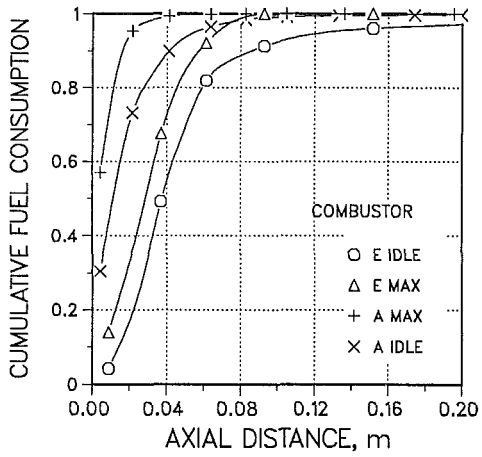

Fig. 12 Cumulative fuel consumption in combustor

jets. This explains the extended region of CO formation observed in Fig. 9. The trends of reduction in CO concentration at larger distances indicate that the conversion to CO_2 due to the availability of air far exceeds any further formation of CO in this region. Figure 9 also shows that the conversion process continues to happen throughout the combustor.

The unburned hydrocarbons calculated using the developed model are compared with the measurements obtained for various combustors under consideration in Fig. 10. Satisfactory agreement between the calculations and data is shown in this figure. The fractions of the total fuel burned at different axial locations in the annular combustor *A* and the can combustor *E* are given in Fig. 11. It is seen that the reaction rate is quite high early in combustor *A* even at idle conditions. In combustor *E*, the reaction of the fuel is initially at a much slower rate due to the insufficient air in the upstream region of the primary zone. Subsequent admission of air through the primary holes brings the fuel/air mixture closer to the stoichiometric value resulting in an increase in reaction rates. The results are better illustrated in cumulative forms in Fig. 12. For example, at an axial location of 0.04 m, almost all the fuel is burned in combustor *A* at maximum power conditions, while at the same location only 70 percent of fuel flow is reacted in combustor *E*. At idle, an appreciable amount of unburned fuel is present in the exhaust of combustor *E* as shown in the figure. This is attributed to the incomplete combustor near the liner walls.

Downloaded 02 Jun 2010 to 171.66.16.121. Redistribution subject to ASME license or copyright; see http://www.asme.org/terms/Terms_Use.cfm

The results discussed in this section indicate that the calculation of emissions using the capabilities of the three-dimensional combustor model combined with analitical expressions based on detailed kinetic schemes can provide insight into pollutant formation within the combustor. This information would certainly provide valuable assistance for the modification of current combustors or the development of new combustor concepts.

V Summary and Conclusions

A model to calculate the emissions of NO_x, CO, and unburned hydrocarbons from gas turbine combustors have been formulated. The model utilized a detailed chemical kinetic scheme to evaluate the key elements of poullutant formation and destruction in the combustor that was simulated by a number of stirred reactors representing various regions of the combustor. Based on the reaction rate calculations, a number of correlations were derived to estimate pollutant concentrations in terms of operating and geometric parameters such as temperature, residence time, and fuel/air ratio. The developed model utilizes the three-dimensional numerical computations to provide the flow and combustion characteristics of the combustor needed for use in the derived correlations. By this means, systematic modifications to the combustor can be made to minimize emissions while maintaining satisfactory combustion stability and performance.

The developed model was verified by analyzing a large number of combustor configurations that vary significantly in design and concept. The combustor configurations represented various classes of can-annular, through, and reverse flow annular combustors and operated on conventional fuels such as JP-4, JP-5, and DF-2 as well as high-density fuels. Satisfactory agreement between the calculations and the experimental data was obtained under various operating conditions. In addition to estimating the overall emissions of the combustor, the model provides insight into the local pollutant concentration in different zones of the combustor. For example, the calculations show that significant amounts of NO_x are formed in the hot region of the combustor in the primary and possibly the intermediate zones. The formation continues at a lower rate downstream depending on the configuration used for the subsequent admission of air into the combustor.

The calculations indicate that CO is formed in large quantities early in the primary zone. A significant proportion of CO is, however, converted to CO_2 in downstream zones of the combustor. The model also shows that in near-wall regions where the conditions dictate low-temperature reactions, partial combustion occurs. The CO formed in these regions has less chance to convert to CO_2 leading to higher CO emitted by the combustor. The arrangement of the radial air admission into the liner that controls the stoichiometry in various zones has been shown to play a major role on the CO emissions of different combustors.

The calculation of UHC using the developed approach has indicated that most of the unburned fuel exiting the combustor is due to incomplete combustion in low temperature regions of the combustor. These regions usually exist near the walls due to the chilling effects of the liner cooling air and the radial injection of air. For example, combustors operating on very rich mixtures in the primary zone due to the absence of dome swirlers demonstrate much slower reaction rates initially. Proper admission of radial jets is needed if complete combustion is to be achieved within the liner.

References

Ballal, D. R., and Lefebvre, A. H., 1981, "Flame Propagation in Heterogeneous Mixtures of Fuel Droplets, Fuel Vapor, and Air," *Eighteenth Symposium (Int.) on Combustion*, pp. 321-328.

Custer, J. R., and Rizk, N. K., 1988, "Influence of Design Concept and Liquid Properties on Fuel Injector Performance," *J. Propulsion and Power*, Vol. 4, No. 4, pp. 378-384.

Faeth, G. M., 1977, "Current Status of Droplet and Liquid Combustion," *Progress in Energy and Combustion Science*, Vol. 3, pp 191-224.

Fletcher, R. S., and Heywood, J. B., 1971, "A Model for Nitric Oxide Emissions From Aircraft Gas Turbine Engines," AIAA Paper No. 71-123.

Glassman, I., 1977, *Combustion*, Academic Press, New York.

Hammond, D. C., Jr., and Mellor, A. M., 1973, "Analytical Predictions of Emissions From and Within an Allison J-33 Combustor," *Comb. Sci. Tech.*, Vol. 6, pp. 279-286.

Hautman, D. J., Dryer, F. L., Schug, K. P., and Glassman, I., 1981, "A Multiple-Step Overall Kinetic Mechanism for the Oxidation of Hydrocarbons," *Comb. Sci. Tech.*, Vol. 25, pp. 219-235.

Launder, B. E., and Spalding, D. B., 1974, "The Numerical Computation of Turbulent Flow," *Comp. Methods Appl. Eng.*, Vol. 3, pp. 269-289.

Lefebvre, A. H., 1984, "Fuel Effects on Gas Turbine Combustion-Liner Temperature, Pattern Factor, and Pollutant Emissions," *AIAA Journal of Aircraft*, Vol. 21, No. 11, pp. 887-898.

Lefebvre, A. H., 1985, "Fuel Effects on Gas Turbine Combustion-Ignition, Stability, and Combustion Efficiency," ASME JOURNAL OF ENGINEERING FOR GAS TURBINES AND POWER, Vol. 107, pp. 24-37.

Mongia, H. C., and Reynolds, R. S., 1979, "Combustor Design Criteria Validation," Vol. III, USARTL-TR-78-SSC.

Mongia, H. C., Reynolds, R. S., and Srinivasan, R., 1986, "Multidimensional Gas Turbine Combustion Modeling: Applications and Limitations," *AIAA Journal*, Vol. 24, No. 6, pp 890-904.

Mosier, S. A., Roberts, R., and Henderson, R. E., 1973, "Development and Verification of an Analytical Model for Predicting Emissions From Gas Turbine Combustors During Low-Power Operation," *Atmospheric Pollution by Aircraft Engines*, AGARD CP No. 125.

Patankar, S. V., 1980, *Numerical Heat Transfer and Fluid Flows*, Hemisphere, Washington, DC.

Plee, S. L., and Mellor, A. M., 1979, "Characteristic Time Correlation for Lean Blowoff of Bluff-Body Stabilized Flames," *Combustion and Flame*, Vol. 35, pp. 61-80.

Rizk, N. K., and Lefebvre, A. H., 1985, "Drop-Size Distribution Characteristics of Spill Return Atomizers," *J. Propulsion and Power*, Vol. 1, No. 1, pp. 16-22.

Rizk, N. K., and Mongia, H. C., 1986, "Gas Turbine Combustor Design Methodology," AIAA Paper No. 86-1531.

Rizk, N. K., and Mongia, H. C., 1990a, "Ultra-low NO_x Rich-Lean Combustion," ASME Paper No. 90-GT-87.

Rizk, N. K., and Mongia, H. C., 1990b, "Lean Low NO_x Combustion Concept Evaluation," *Twenty-Third Symposium (Int.) on Combustion*, pp. 1063-1070.

Rizk, N. K., and Mongia, H. C., 1990c, "Three-Dimensional Combustor Performance Validation With High-Density Fuels," *J. Propulsion and Power*, Vol. 6, No. 5, pp. 660-667.

Rizk, N. K., and Mongia, H. C., 1991a, "Three-Dimensional Analysis of Gas Turbine Combustors," *J. Propulsion and Power*, Vol. 7, No. 3, pp. 445-451.

Rizk, N. K., and Mongia, H. C., 1991b, "Low NO_x Rich-Lean Combustion Concept Application," AIAA Paper No. 91-1962.

Rizk, N. K., and Mongia, H. C., 1993, "Semianalytical Correlations for No_x, CO, and UHC Emissions," ASME JOURNAL OF ENGINEERING FOR GAS TURBINES AND POWER, Vol. 115, this issue, pp. 612-619.

Sturgess, G. J., 1983, "Aerothermal Modeling: Phase I Final Report," NASA CR-168202.

Washam, R. M., and Mellor, A. M., 1979, "Correlation Technique for Ambient Effects on Oxides of Nitrogen," *AIAA Journal of Aircraft*, Vol. 16, No. 9, pp. 626-631.

Westbrook, C. K., and Pitz, W. J., 1984, "A Comprehensive Chemical Reaction Mechanism for Oxidation and Pyrolysis of Propane and Propene," *Comb. Sci. Tech.*, Vol. 37, pp. 117-152.

Downloaded 02 Jun 2010 to 171.66.16.121. Redistribution subject to ASME license or copyright; see http://www.asme.org/terms/Terms_Use.cfm

Semianalytical Correlations for NO_x, CO, and UHC Emissions

N. K. Rizk

H. C. Mongia

Allison Gas Turbine Division,
General Motors Corporation,
Indianapolis, IN 46206

To meet the future goals of reduced emissions produced by gas turbine combustors, a better understanding of the process of formation of various pollutants is required. Both empirical and analytical approaches are used to provide the exhaust concentrations of pollutants of interest such as NO_x, CO, and unburned hydrocarbon with varying degrees of success. In the present investigation, an emission model that simulates the combustor by a number of reactors representing various combustion zones is proposed. A detailed chemical kinetic scheme was used to provide a fundamental basis for the derivation of a number of expressions that simulate the reaction scheme. The model addresses the combined effects of spray evaporation and mixing in the reaction zone. The model validation included the utilization of a large data base obtained for an annular combustor of a modern turbopropulsion engine. In addition to the satisfactory agreement with the measurements, the model provided insight into the regions within the combustor that could be responsible for the excessive formation of emissions. Methods to reduce the emissions may be implemented in light of such information.

I Introduction

Gas turbine combustors will be required to operate under more severe conditions of pressure and temperature to meet the design requirements of next generation turbine engines. This fact, coupled with the expected trends of more stringent emission regulations, calls for the development of advanced combustion systems. To minimize the pollutant emissions produced by the combustor, while maintaining satisfactory combustion stability and performance, a better understanding of the various processes occurring simultaneously within the combustor is greatly needed.

The concentration levels of pollutants in the gas turbine exhaust are directly related to the operating temperature and pressure within the combustor, and to the residence time in various combustion zones. The achievement of efficient fuel atomization and rapid evaporation and mixing with the primary combustion air, and the subsequent admission of air into other combustor regions, can have a significant effect on emissions. In order to optimize the combustor design, both empirical and analytical tools are required to provide insight into the combustion and mixing processes within the combustor flow field. A typical empirical approach based on the extensive use of available experience and wide data base has been successfully adopted in various phases of the development process. Notable examples of empirical and semiempirical design tools are presented by Lefebvre (1984, 1985), Plee and Mellor (1978, 1979), and Mellor (1976). The success of such an approach relies on the accurate estimation of important parameters including length or volume occupied in combustion, recirculation zone characteristics, and fraction of total air utilized in primary zone combustion.

The obvious advantages offered by the empirical approach are the simplicity and the capability to give an estimate of combustor emissions and performance at various power modes. The applicability of the approach could be easily extended to other types of fuel provided that their relevant physical and chemical properties are known. The chemical reaction rate effects are represented in these empirical approaches by simple expressions that include the reaction temperature in an exponential term and the residence time. It has been shown by Rizk and Mongia (1991) that the simulation of the reaction mechanism could be significantly enhanced by the utilization of finite-rate chemistry calculations to provide the trends of emissions formation and consumption in various combustor zones.

The analytical and experimental studies reported in the literature have indicated that the reaction mechanism can proceed through a very large number of reactions. In fact, some of these models include all the possible reactions utilizing the capabilities of modern computers (Glassman, 1977; Westbrook and Pitz, 1984). In the present investigation, an approach to evaluate the emissions of the oxides of nitrogen (NO_x), carbon monoxide (CO), and the unburned hydrocarbon (UHC) has been formulated. The approach simulates the reaction in the combustor by a number of reactors that represent different zones of the combustor. A detailed chemical kinetic mechanism is used to provide a fundamental basis for the proposed model. The effects of spray evaporation and mixing in the reaction zone on emissions are addressed in the calculation procedure. The validation of the approach utilized a data base that covered a wide range of operating conditions. In the next section, the effort to correlate the experimental data with a number of conventional methods is described. The details of the kinetic

Contributed by the International Gas Turbine Institute and presented at the 37th International Gas Turbine and Aeroengine Congress and Exposition, Cologne, Germany, June 1-4, 1992. Manuscript received by the International Gas Turbine Institute February 6, 1992. Paper No. 92-GT-130. Associate Technical Editor: L. S. Langston.

Copyright © 1993 by ASME
Downloaded 02 Jun 2010 to 171.66.16.121. Redistribution subject to ASME license or copyright; see http://www.asme.org/terms/Terms_Use.cfm

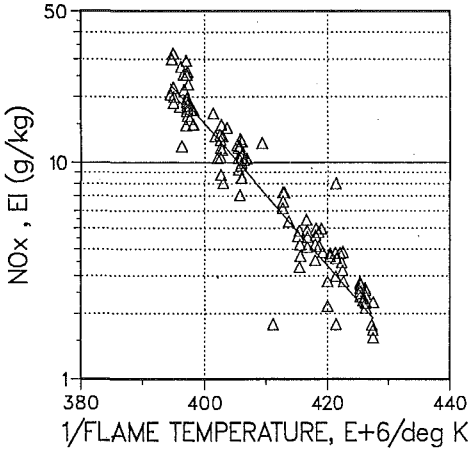

Fig. 1 The variation of NO_x with flame temperature

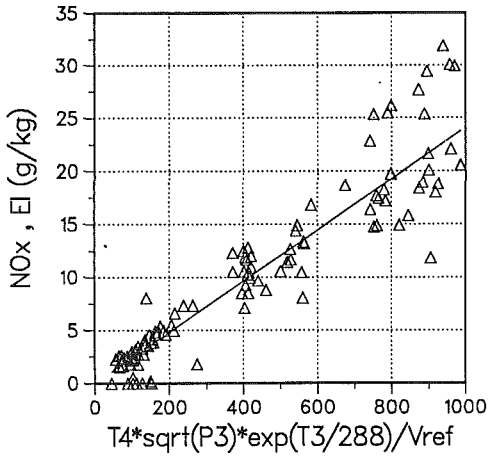

Fig. 2 Correlation of NO_x with reference velocity, temperature, and pressure

scheme and the proposed calculation approach are presented in later sections. Comparison between the calculations and measurements for NO_x, CO, and UHC pollutants and a summary of the main conclusions are given in the final sections of the paper.

II Emissions Correlations

The exhaust concentrations of the pollutants of importance are governed by the mean residence time in the combustion zone, the chemical reaction rates, and the mixing rates. Oxides of nitrogen NO_x are produced in the central hot region of the combustor by the oxidation of the atmospheric nitrogen, and most of the NO_x emitted in the exhaust is nitric oxide NO. If fuels contain organically bound nitrogen, then some of this nitrogen will eventually form fuel NO. Temperature has a less significant effect on the formation of fuel NO. The oxidation of atmospheric nitrogen involving hydrocarbon species in the flame zone has been observed to produce prompt NO, particularly with fuel-rich flames. In most cases the prompt NO is only a small fraction of the NO that forms in the post flame zone.

The strong correlation between temperature and NO_x emissions is illustrated in Fig. 1. In this figure, large numbers of NO_x measurements for an annular gas turbine combustor are plotted against the inverse of the flame temperature. The data were obtained over a wide range of engine operating conditions from sea level to altitude over P_3 from 0.1 to 1.5 MPa, T_3 from 430 to 720 K, and FAR from 0.007 to 0.024. The solid line represents the average of all data points. It is obvious that it is not sufficient to use the flame temperature by itself to estimate the NO_x emission since the scatter of the points around the average line is significant. For example, at the highest flame temperature the range of measured NO_x emissions index extends from about 10 up to a value of 30 g/kg.

When the effects of the combustor geometry, through the reference velocity V_{ref} and the system pressure P_3, are included in the NO_x correlation, significant improvement in the data correlation is observed at low power conditions, as shown in Fig. 2. The scatter in data around the average line, however, is still large at higher power modes. T_3 and T_4 are inlet and exit temperatures of the combustor.

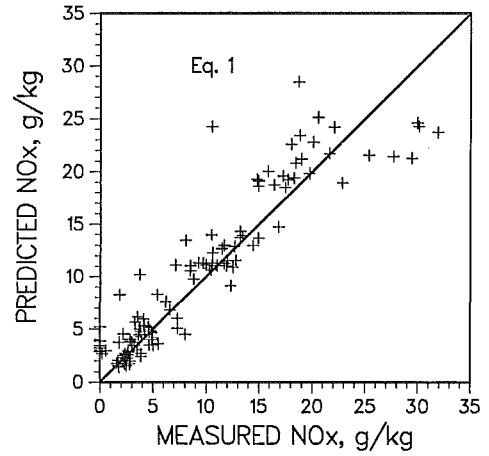

Fig. 3 NO_x calculation using approach of Lefebvre (1984)

Lefebvre (1984) utilized a large amount of data obtained for a number of production engines that operated on 13 different fuels to reach a quantitative relationship for NO_x. In this approach, the volume occupied in combustion V_c and the fraction of air utilized in the primary zone combustion F are selected to give the best fit to the data. Following this approach, the NO_x emission index of each operating condition was calculated and plotted against the measured value in Fig. 3. The following equation was used:

$$NO_x(g/kg) = 0.459\ E - 8P_3^{0.25}F\tau\ \exp(0.01T_{st}) \qquad (1)$$

where T_{st} is the stoichiometric temperature, K, P_3 is system pressure, kPa, and τ is the primary zone residence time, s, which is a function of V_c, F, and the primary zone temperature. The data correlation given in this figure shows less scatter in the results than the one illustrated in Fig. 2, which indicates that it contains most of the key parameters governing the operation of the combustor.

Nomenclature

B_M = mass transfer number
F = fraction of air to primary zone
FAR = fuel/air ratio
F_1, F_2, F_3 = emission model parameters
P_3 = inlet pressure, Pa
Pr = Prandtl number
Re = Reynolds number
SMD = Sauter mean diameter, m
T_c = reaction temperature, K
T_{pz} = primary zone temperature, K
T_{st} = stoichiometric temperature, K
V_c = combustion volume, m^3
V_{ref} = reference velocity, m/s
$\Delta P_3/P_3$ = nondimensional pressure drop
λ_{ev} = evaporation constant, m^2/s
τ = residence time, ms
ϕ = equivalence ratio

Downloaded 02 Jun 2010 to 171.66.16.121. Redistribution subject to ASME license or copyright; see http://www.asme.org/terms/Terms_Use.cfm

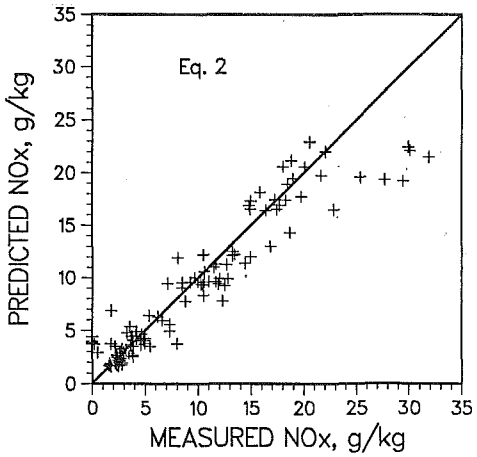

Fig. 4 Comparison between measurements and calculated NO_x given by Eq. (2)

The above equation was modified to include the effects of evaporation and mixing, which could be significant at low power modes, and to express the reaction term in a form compatible with the conventional reaction rate equations. The modified form is given by:

$$NO_x = 0.15\ E16(\tau - 0.5\tau_{ev})^{0.5} \cdot \exp(-71{,}100/T_{st})/(P_3^{0.05}(\Delta P_3/P_3)^{0.5}) \quad (2)$$

The mixing rate is simulated by the nondimensional liner pressure drop ($\Delta P_3/P_3$), and the evaporation time (τ_{ev}) is calculated using the values of the spray Sauter mean diameter (SMD) and the evaporation constant (λ_{ev}), which is given by:

$$\lambda_{ev} = \frac{8\ kg}{C_{pg}\rho_F} \log_e(1 + B_M)(1 + 0.3\ \mathrm{Re}^{0.5}\mathrm{Pr}^{0.33}) \quad (3)$$

where R_e and P_r are the Reynolds and Prandtl numbers based on gas properties at film temperature and instantaneous drop diameter; k_g, C_{pg}, and ρ_F are thermal conductivity and specific heat of gas, and fuel density; and B_M is mass transfer number (Faeth, 1977). Figure 4 illustrates that using Eq. (2) results in better correlation with the data in the low power range than the previous approach. At higher power range both equations give comparable results.

The presence of the CO pollutants in the combustor exhaust in large quantities is an indication of incomplete combustion of fuel due to inadequate burning rates in the primary zone, inadequate mixing, chilling effects of liner coolant, and/or insufficient residence time. CO is formed in the primary zone in amounts that exceed the equilibrium levels at fuel lean and stoichiometric mixtures. Under fuel-rich conditions higher levels of CO are formed, but in quantities less than the equilibrium values, due to the limited residence time in this zone. The subsequent admission of additional air downstream of the primary zone reduces the gas temperature and enhances the conversion of CO to CO_2.

The correlation for CO calculation presented by Lefebvre (1984) utilizes the same combustion volume (V_c) and the fraction of air to primary zone (F) estimated for the NO_x correlation. The expression for CO, following his concept, is given by:

$$CO(g/kg) = 0.333\ E\ 10\ \exp(-0.00275T_{pz})/(FP_3^{1.5}(\tau - 0.55\ \tau_{ev})(\Delta P_3/P_3)^{0.5} \quad (4)$$

In this correlation it is assumed that a significant proportion of the primary zone time τ is needed to evaporate the fuel. The calculated CO values are plotted against the measurements in Fig. 5. The correlation seems to give satisfactory agreement with data at the low end of the scale. However, less satisfactory correlation is observed at higher values of CO.

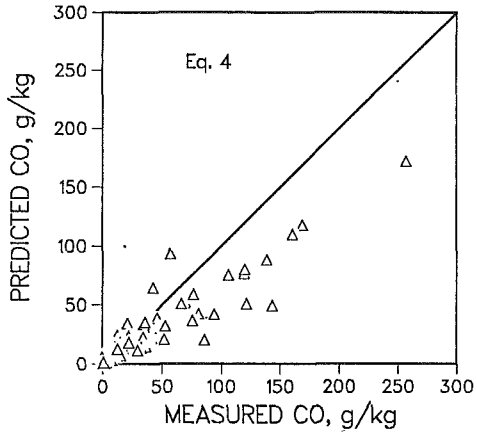

Fig. 5 CO calculation using approach of Lefebvre (1984)

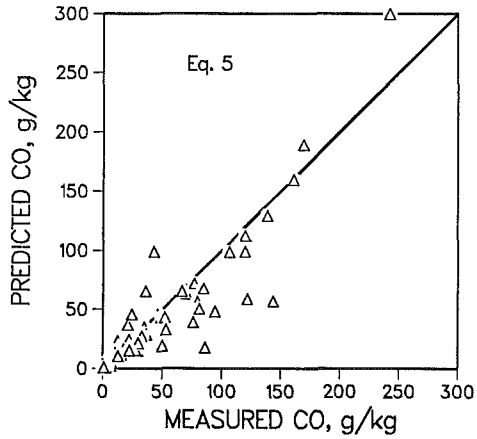

Fig. 6 Comparison between CO data and calculation using modified correlation (Eq. (5))

To express the term that represents the reaction in the usual reaction rate form, in the effort to enhance the correlation, the following equation was derived:

$$CO = 0.179\ E\ 9\ \exp(7800/T_{pz})/(P_3^2(\tau - 0.4\ \tau_{ev})(\Delta P_3/P_3)^{0.5}) \quad (5)$$

The comparison between the calculations and the measured data is presented in Fig. 6. The figures show better correlation at low power conditions where the CO emissions are generally high.

The emissions of the unburned hydrocarbon (UHC) are an indication of incomplete combustion in regions of the combustor where the burning rates of fuel are inadequate. Fuel droplets or vapor that escape the combustor hot core may not have the chance to burn fully due to the chilling effects of the cooling air and the subsequent admission of air downstream of the primary zone. Thus, enhanced atomization quality and mixing rate within the primary combustion zone are essential for the reduction of the UHC emissions.

Similar to the CO correlation derived by Lefebvre (1984), the UHC emission may be calculated in terms of reaction temperature (T_{pz}), system pressure, residence time in primary zone τ, and an evaporation time (τ_{ev}). The idea is to use the same combustion volume (V_c) and fraction of air to primary zone (F) that give the best correlation with the data in the calculation of the three pollutants. The expression used for the UHC emission is as follows:

$$UHC(g/kg) = 0.216\ E\ 10\ \exp(-0.00345\ T_{pz})/(FP_3^{1.5}(\tau - 0.55\ \tau_{ev})(\Delta P_3/P_3)) \quad (6)$$

Figure 7 shows that the calculation of UHC using Eq. (6) yields the right trend of increase of UHC emissions with the

Downloaded 02 Jun 2010 to 171.66.16.121. Redistribution subject to ASME license or copyright; see http://www.asme.org/terms/Terms_Use.cfm

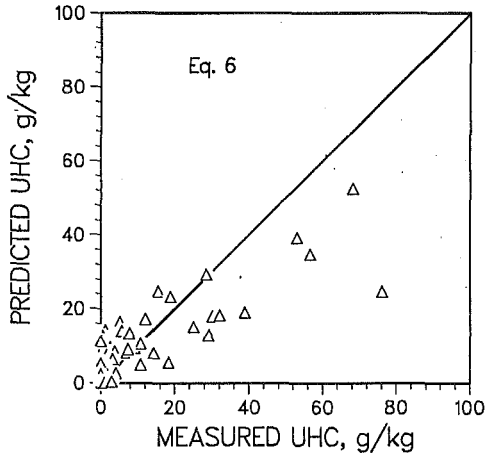

Fig. 7 UHC estimation following concept given by Lefebvre (1984)

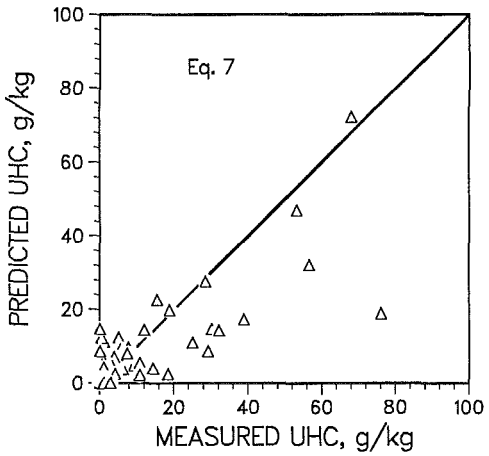

Fig. 8 Comparison between data and calculation of UHC using Eq. (7)

decrease in power setting. A large deviation from the perfect correlation line is observed at a higher level of UHC.

The reaction term in Eq. (6) was modified to the standard reaction form, and the correlation of the UHC data was performed to yield the following expression:

$$\text{UHC} = 0.755\ \text{E}\ 11 \exp(9756/T_{pz})/(P_3^{2.3}(\tau - 0.35\ \tau_{ev})^{0.1}(\Delta P_3/P_3)^{0.6}) \quad (7)$$

The comparison between the data and the calculations is illustrated in Fig. 8. The figure shows small improvement in the correlation at high levels of UHC over the previous equation.

The correlations presented in this section provide the overall emissions produced by the combustor using some parameters related to operating conditions and combustor configuration. In the next section, a model is proposed to calculate the emissions based on the local contributions of a number of reactors that simulate various combustor zones. Thus, the better understanding of the mechanisms of formation and destruction of various pollutants could be utilized in the effort to maintain the emissions below the specified goals.

III Emissions Model Development

1 Analytical Modeling Review. Several models have been proposed in the literature to correlate pollutant emissions formation within the combustor. These models consist of a number of chemical reactors in series and/or parallel that simulate various regions of the combustor. In the review given by Mellor (1976), a model based on the combination of a number of perfectly stirred reactors is described (Hammond and Mellor, 1973). A global finite rate mechanism was used in the model, and no droplet calculations were included in the approach. Volumes and flow splits were selected to yield best fits with the internal measurements of NO and CO. They concluded that the poor predictions of the variation of the emissions with combustor loading were due to neglecting the heterogeneous effects and to the concept used to simulate the primary zone.

Fletcher and Heywood (1971) modeled the combustor primary zone as a partially stirred reactor burning gaseous fuel over a distribution about the primary zone equivalence ratio, a lateral mixing reactor, and a plug flow reactor. Various operating parameters of the reactors were obtained from matching the model output with the measured exhaust NO emissions. Two model-fitting parameters were used in the model that gave satisfactory correlation except at low engine power. The discrepancy at low fuel/air ratios was attributed to ignoring the evaporation time of the fuel. No calculations of CO or UHC were offered in the model.

A review of the models that simulate the combustor by a number of streamtubes is given also by Mellor (1976). The streamtubes are allowed to exchange mass and heat by turbulent mixing, and droplet burning is allowed in the tubes surrounding a central recirculation zone by the combustion of fuel vapor (Mosier et al., 1973). An extended NO mechanism is used together with a global finite-rate expression for fuel oxidation, and partial equilibrium CO mechanism is assumed. Experience has allowed best selection of the arbitrary parameters of this model. A reasonable degree of agreement with the data was obtained using this model, particularly in regard to the trend of variation of the emissions with operating conditions.

The review of the emission models indicates clearly the importance of the accurate representation of the combustor regions and the inclusion of the effects of the droplet evaporation and burning. The flow allowed between these regions and the selection of the appropriate model parameters are the key aspects to the success of the model.

A flow model that simulates a combustor operating on the rich/lean combustion concept is presented by Rizk and Mongia (1991). It consists of a rich zone made up of two parallel stirred reactors feeding into a plug flow reactor. Mixer air is admitted consequentially into the system to form plug flow reactors that simulate quench and lean zones. A chemical kinetic mechanism that involves a large number of standard reactions has been used to evaluate the relative contribution of various combustion zones to the total NO_x formation. A number of expressions have been formulated to simulate the reaction mechanism in simpler terms, so that an accurate estimate of NO_x could be made without the need to use the detailed kinetic scheme. Satisfactory agreement with the measurements was obtained using this model.

2 Proposed Model Description. In the present investigation a similar approach has been followed to estimate the emissions of NO_x, CO, and UHC from conventional diffusion combustors. The combustor is simulated by a number of reactors, as shown in Fig. 9. The primary zone of the combustor consists of two central reactors in series: The first one contains the initial mixing and reaction of the fuel spray with the nozzle and swirler air, and defines a lean blowout zone (LBO), and the reaction continues through the second reactor (primary zone). Two other reactors occupy the near-wall region in the primary zone and are in parallel to the central reactors. The fuel, either in droplet or vapor form, that escapes the recirculation zone in the core of the combustor mixes with the rest of the dome air in the first near-wall reactor. The outcome of this reactor in addition to a fraction of the burning gas leaving the LBO reactor is fed into the second near-wall reactor, as shown in the figure.

The intermediate zone is simulated by two parallel reactors

Downloaded 02 Jun 2010 to 171.66.16.121. Redistribution subject to ASME license or copyright; see http://www.asme.org/terms/Terms_Use.cfm

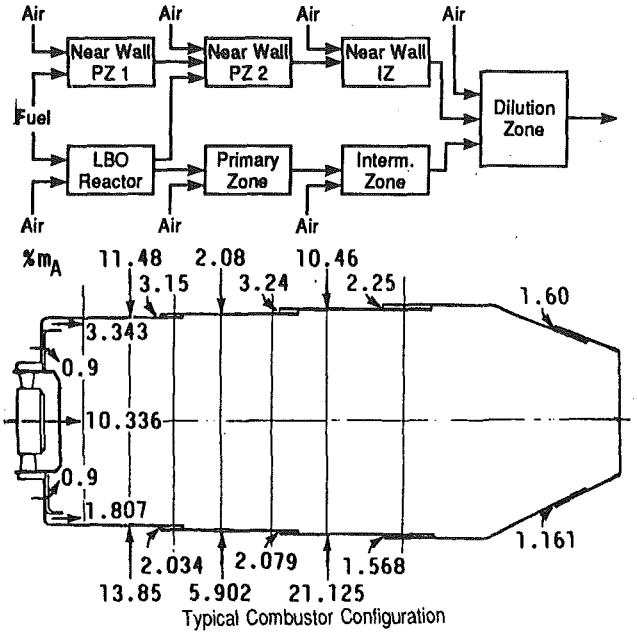

Fig. 9 Proposed combustor flow model

that occupy the core and the near-wall regions of this zone. These reactors involve a continuation of the reaction that is initiated upstream in the primary zone. The outcome of the two reactors mixes together to form a single plug flow reactor in the dilution zone. Jet and cooling air are admitted into the reactors of the three combustor zones according to the combustor configuration, and using an engineering estimate of the air split that is followed throughout the calculation procedure. For instance, all the primary zone cooling air goes into the second near wall reactor in this zone, while half the primary jet reaches the primary zone reactor, and the rest is split evenly between the intermediate zone reactor and the entrainment into the LBO reactor.

The cross-section area of each reactor is calculated based on the fraction of the total flow through the reactor at this location. The combustor length is divided into three parts: the primary zone extends from the dome to a location midway between primary and intermediate jets, the intermediate zone length extends to halfway between the intermediate and dilution jets, and the rest of the combustor belongs to the dilution zone. The primary zone length is split evenly between the LBO and the primary zone reactors, and similarly between the two near-wall reactors in this zone.

The concept followed to define the configuration and flow of various reactors should be similar for different combustors. However, two arbitrary parameters should be defined for each case: the fraction of total fuel reaching the near-wall mixing zone (F_1), and the fraction of the burning gases admitted into the second near wall reactor (F_3). A third parameter (F_2) is directly related to the swirler strength and geometry and defines the proportion of the swirler and dome air that goes into the LBO reactor.

The detailed reaction mechanism proposed by Westbrook and Pitz (1984) for the pyrolysis and oxidation of propane was used in the present investigation due to the similarity of the combustion properties of the propane to those of more complex practical fuels. The objective was to establish the trends of variation of the pollutant formation and destruction with operating conditions in various reactors of the flow model shown in Fig. 9. The mechanism involves a large number of elementary reactions that provide a more realistic picture of the combustion process. An extended Zeldovich mechanism described by Glassman (1977) was added to the kinetic model to calculate the NO_x formation within the combustor.

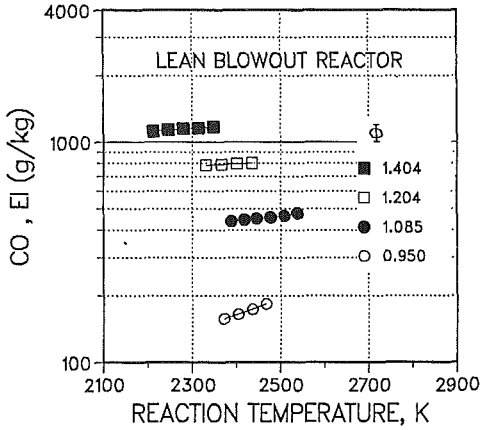

Fig. 10 Effect of reaction temperature on initial CO formation

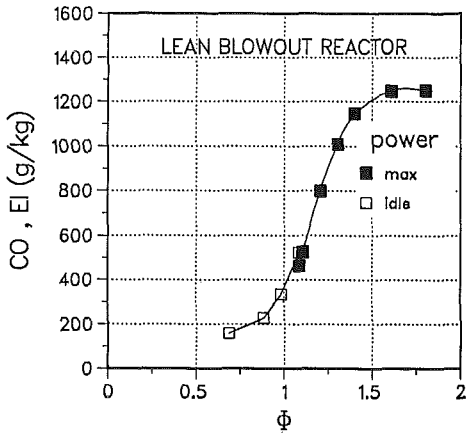

Fig. 11 Variation of CO concentration with equivalence ratio

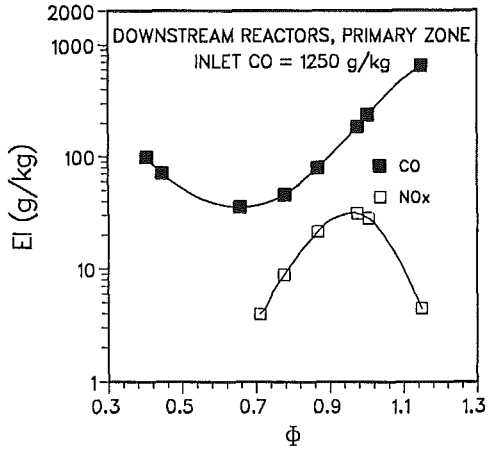

Fig. 12 CO and NO_x concentration variation with ϕ.

A wide range of operating parameters was covered in a parametric study using the chemical reaction program. The critical issues addressed in this effort were the effects of the equivalence ratio, residence time, the system pressure, and the interaction between various reactors on the local and overall concentrations of NO_x, CO, and UHC. Examples of the results of this study are illustrated in Figs. 10–14. Figure 10 shows that the formation of CO early in the primary zone reactors depends on the reactor temperature and the equivalence ratio in the reactor. High concentrations of CO are formed if a rich mixture exists in the reactor.

The CO formation at two power modes of a typical engine is illustrated in Fig. 11. The CO formed under lean conditions far exceeds the equilibrium levels. On the other hand, at rich fuel/air mixtures the equilibrium CO levels are much higher

Downloaded 02 Jun 2010 to 171.66.16.121. Redistribution subject to ASME license or copyright; see http://www.asme.org/terms/Terms_Use.cfm

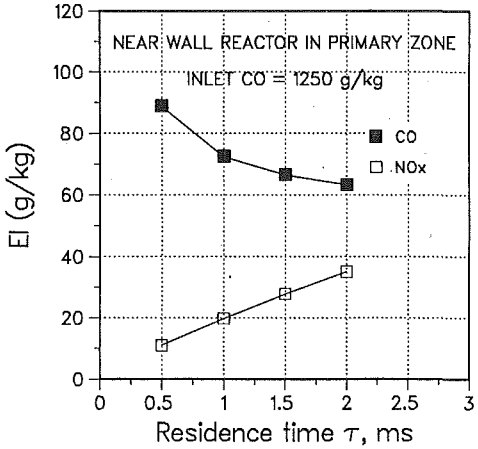

Fig. 13 Effect of residence time on CO and NO_x concentrations

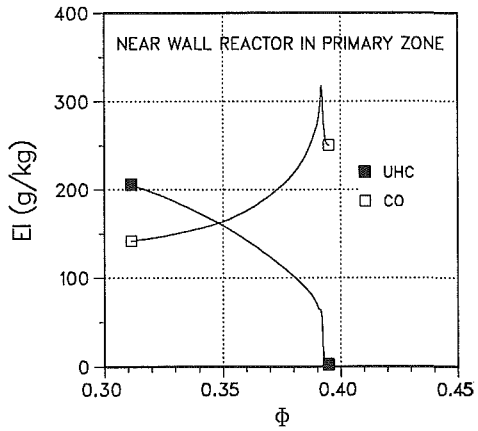

Fig. 14 UHC and CO concentrations in near-wall region

than the calculated CO concentrations. A longer residence time can bring the concentration closer to the equilibrium value.

The concentration of CO in downstream reactors in primary and intermediate zones is a balance between the formation of new CO and the oxidation of CO to CO_2 that is controlled by the reactor temperature and the equivalence ratio there. Figure 12 indicates that as the equivalence ratio, and consequently the reactor temperature, are reduced, the rate of conversion of CO to CO_2 exceeds the formation rate. Thus, the CO concentration entering these reactors is reduced in value. At much lower equivalence ratio and temperature, the trend of variation of CO concentration with the equivalence ratio is reversed and the conversion rate of CO slows down. The NO_x concentration reaches the highest levels near the stoichiometric mixture on the lean side, as shown in the same figure. Figure 13 illustrates the opposite effects of the reactor residence time on the CO and NO concentrations.

The investigation shows that the presence of most of the unburned hydrocarbons in the combustor exhaust is due to incomplete combustion in the near-wall reactors. The results indicate that there is a threshold temperature below which partial burning occurs, and the subsequent admission of air inhibits any further reaction in this region. Any changes in conditions that cause an increase of the reaction temperature, such as longer residence time, higher inlet temperature, or equivalence ratio, can produce a sudden drop in UHC concentration, as shown in Fig. 14. The formation of CO in the near-wall reactors is proportional to the extent of the fuel burning that takes place in these reactors. At high burning rates, the two processes of CO formation and conversion compete in the same manner mentioned earlier.

3 Emissions Formation Model.

Based on the results of these calculations, a number of expressions have been formulated to simulate the reaction mechanism in various reactors. The NO_x formation in the primary zone reactors is expressed by the following equation:

$$NO_x(g/kg) = 1\ E\ 13\ (P_3/1.4\ E\ 6)^{aa} \exp \times(-71{,}442/T_c)(7.56\ \phi^{-7.2} - 1.6)\tau^{0.64} \quad (8)$$

At equivalence ratios ϕ above 1.08, the following equation is used:

$$NO_x = 1\ E\ 13\ (P_3/1.4\ E\ 6)^{aa} \exp \times(-71{,}442/T_c)(5.21\ \phi^{-2.99} - 1.6)\tau^{0.64} \quad (9)$$

The exponent of the pressure term (aa) varies with the equivalence ratio as follows:

$$aa = 11.949 \exp(-\phi/5.76) - 10.0 \quad (10)$$

T_c is the reaction temperature based on the fuel/air ratio in the reactor and the inlet temperature and pressure to the system.

Additional NO_x is formed in downstream reactors if temperatures are high enough. Based on the results for the conditions prevailing in these reactors, the following equation is proposed:

$$NO_x = 1\ E\ 14\ (P_3/1.4\ E\ 6)^{aa} \exp \times(-71{,}442/T_c)(1.172\ \phi^{-4.56} - 0.6)\tau^{0.876} \quad (11)$$

The total NO_x formed in the combustor is the summation of the contribution from each reactor after correcting the NO_x concentration according to the fuel flow fraction through the reactor.

A similar approach was followed to simulate the CO formation given by the chemical kinetic model with a number of expressions. The initial formation of CO early in the primary zone (see Fig. 9) is calculated from:

$$CO(g/kg) = \exp(-CE/T_c)\,Cph\,(P_3/1.4\ E\ 6)^{a1}(\tau/0.5)^{a2} \quad (12)$$

The parameter CE is found to depend on ϕ according to the following relationship:

$$CE = 6.23\ E\ 4\ \phi^{3.8} \exp(-\phi/0.56)^{1.75} \quad (13)$$

and the function Cph is described by:

$$Cph = 4.54\ E\ 3\ \phi^4 \exp(-\phi/1.02)^{2.23} \quad (14)$$

The reaction temperature (T_c) is in K, and residence time (τ) is in ms. The exponents of the pressure and residence time terms are given by:

$$a1 = -0.447\ \phi^{-1.87} + 0.2 \quad (15)$$

$$a2 = -0.362^{-1.9} + 0.2 \quad (16)$$

A lower limit of $a1$ is set at -1.0 according to the kinetics results. A significant proportion of the CO formed early in the primary zone is converted to CO_2 in the downstream reactors in primary and intermediate zones. Additional formation of CO may also occur, especially if the reactor temperature is sufficiently high. The concentration of the CO at the exit of each reactor is given in terms of the inlet concentration to the reactor by:

$$CO = 2.52 \exp(-5000/T_c)(0.00017 \exp(\phi/1.26) + 0.05)CO_{IN}(P_3/1.4\ E\ 6)^{a3}\tau^{a4} \quad (17)$$

This equation describes the trend of variation of CO with reaction temperature in the temperature range higher than 2000 K. CO_{IN} is the inlet value of CO to the reactor, and the exponents $a3$ and $a4$ are given by:

$$a3 = 3.79 \exp(-1.56/\phi) - 0.8 \quad (18)$$

$$a4 = 0.875\ \phi^{0.94} - 1.0 \quad (19)$$

Downloaded 02 Jun 2010 to 171.66.16.121. Redistribution subject to ASME license or copyright; see http://www.asme.org/terms/Terms_Use.cfm

The trend of variation of CO at temperatures below 2000 K is described by:

$$CO = 0.122\ T_c^{-0.2}\ \phi^{-2.45} CO_{IN} (P_3/4.34\ E\ 5)^{a3} \tau^{a4} \quad (20)$$

In the near-wall reactors in the primary zone, when the conditions dictate fairly low reaction temperature, a partial combustion occurs. The following equation has been derived to represent the CO formation below a temperature of 1370 K (2006°F), which is found to be the lowest temperature for near complete combustion:

$$CO = (7.0\ E-15\ \exp\ (T_I/36.1) + 140)(P_3/4.34\ E\ 5)^{0.62} \quad (21)$$

The T_I is the reaction temperature corrected for the residence time as follows:

$$T_I = T_c \tau^{0.057} \quad (22)$$

The total CO concentration entering the dilution zone (CI_{ND}) is the summation of the outcomes of the two parallel reactors in the intermediate zone adjusted on the basis of the fuel flow fractions through the two reactors.

A further reduction in CO cencentration may occur in the dilution reactor according to:

$$CO = 0.122\ T_c^{-0.2}\ \phi^{-2.45} CI_{ND} (P_3/4.34\ E\ 5)^{-0.16} \tau^{a4} \quad (23)$$

The CO at the exit of the dilution zone reactor is not allowed in the calculation to exceed the inlet value to the reactor.

The main contributor to the presence of UHC in the combustor exhaust is the near-wall reactors, especially in the primary zone, due to incomplete combustion in this region. Below a temperature of 1370 K, the equation used to estimate the UHC is given by:

$$UHC\ (g/kg) = (1000 - 144.7\ \exp\ (TT^{5.1}/5.43\ E\ 15))F_1 \quad (24)$$

where the TT is the reaction temperature corrected for the residence time by:

$$TT = T_c \tau^{0.3} \quad (25)$$

At higher temperatures, the expression is as follows:

$$UHC = 1000 - 2215\ \exp(-1274/TT)F_1 \quad (26)$$

The F_1 parameter represents the fraction of the total fuel reaching the near-wall region. Appropriate fuel fraction is used for other reactors.

IV Emissions Model Validation

The data set used to evaluate the available emissions correlations in Section II of this paper was employed to validate the proposed emissions model. The model simulates the chemical reactor processes with a number of expressions that provide NO_x, CO, and UHC concentrations in each reactor. Certainly, the consideration of heterogeneous combustion and the limiting effects of the mixing process in the combustor could enhance the model capability to estimate the concentrations of these pollutants. The inclusion of the effects of droplet evaporation and mixing in the model is addressed in this section as applied to an annular combustor.

To evaluate the procedure used in Section III-2 to define the flow split and volume in each reactor, the kinetic reaction mechanism was used to calculate the LBO characteristics of the above combustor. The idle operating conditions were used in the calculation, and estimates of the three model parameters F_1, F_2, and F_3 that are related to the combustor configuration were made based on trends observed in normal operation of practical combustors. Ten percent of the fuel was assumed to reach the first near-wall reactor ($F_1 = 0.1$), the proportion of the swirler and dome air entering the so-called LBO reactor was 70 percent ($F_2 = 0.7$), and the fraction of the burning gases introduced into the second near-wall reactor of the primary zone was 30 percent ($F_3 = 0.3$). These three parameters were fixed throughout the calculations. The input value of the fuel flow rate used in the reaction model was reduced in small increments until a blowout eventually occurred in the lean blowout reactor. The fuel/air ratio of blowout was 0.0046 when the idle pressure and inlet temperature were 434 kPa (63 psi) and 456 K (361°F), respectively. The measured LBO fuel/air ratio for this combustor is in the range of 0.004–0.005, which agrees well with the calculations. This indicates that the estimates made for various model parameters, in particular those of the LBO reactor, were reasonable.

The emission model validation was then performed using the same data set mentioned earlier. The initial results showed that the calculated emissions followed the measured values closely, in particular at high power conditions. However, better matching to the data at lower power could be achieved by including the effects of the droplet evaporation in the model.

In the NO_x model, the fuel/air ratio (FAR) in the LBO zone is corrected to account for spray evaporation delay time by the following equation:

$$FAR = FAR_0(\tau - 0.5\ SMD^2/\lambda_{ev})/\tau \quad (27)$$

The FAR_0 is the overall fuel/air ratio in the reactor, and τ is residence time. The SMD is calculated using appropriate equations for both airblast and pressure atomization. Combined mode is also considered whenever a dual fuel circuit atomizer is employed provided that the fuel flow requires the operation of both circuits. The evaporation constant λ_{ev} is calculated using Eq. (3) for a spray of an average droplet diameter equal to the SMD. Similarly, the proposed correction for the fuel/air ratio used in the CO calculation is as follows:

$$FAR = FAR_0 \left(0.015 \left(\frac{\lambda_{ev}}{SMD^2}\right) \left(\frac{\Delta P_3}{P_3}\right)^{0.5}\right)^a \quad (28)$$

where $\Delta P_3/P_3$ is the nondimensional pressure drop, and the exponent a is estimated empirically and has a value of 0.1. The constant in the equation is a result of using the ratios of the parameters within the brackets to reference values. The effects of the mixing and system pressure on the degree of reaction near the wall are more pronounced. The equation used to modify the fuel/air ratio for UHC equation is as follows:

$$FAR = FAR_0 \left(0.059 \left(\frac{\lambda_{ev}}{SMD^2}\right)^{0.25} \left(\frac{\Delta P_3}{P_3}\right)^{0.5} P_3^{0.2}\right) \quad (29)$$

The values of NO_x, CO, and UHC calculated using the developed emission model are plotted in Figs. 15–17 against the measured data. Figure 15 shows that the present approach gives satisfactory agreement with the NO_x measurements, especially at the highest levels of NO_x. Similarly, the estimations of CO and UHC, shown in Figs. 16 and 17, are in good agreement with data, and in most cases indicate an improvement over the previous correlations described earlier.

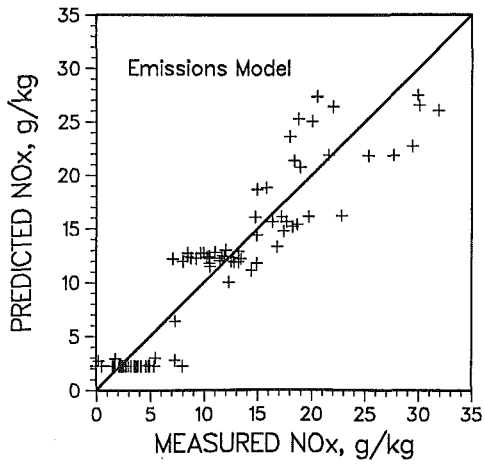

Fig. 15 Comparison between data and model calculation of NO_x

Downloaded 02 Jun 2010 to 171.66.16.121. Redistribution subject to ASME license or copyright; see http://www.asme.org/terms/Terms_Use.cfm

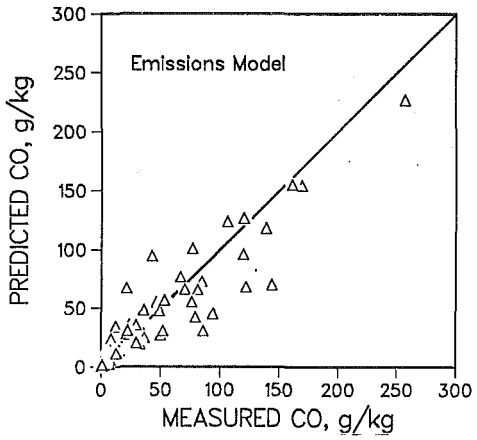

Fig. 16 CO calculation using developed model

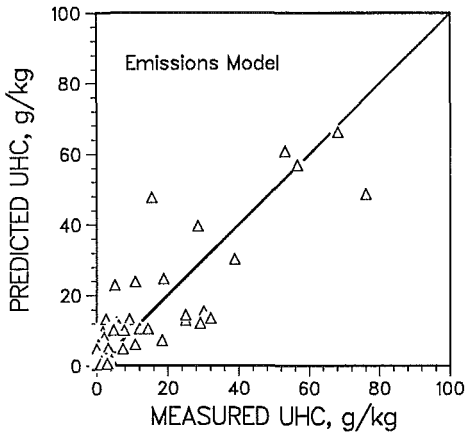

Fig. 17 Model calculation of UHC

The obvious advantage offered by the developed model is the capability to provide insight into the processes of pollutant formation within various regions of combustor. Thus, any effort to reduce the emissions from gas turbine engines could be more efficiently based on such information. The fact that the model utilizes a detailed kinetic scheme, through the derived expressions, makes the results more realistic with significantly less computation effort.

V Summary and Conclusions

To reduce further the pollutants produced by the gas turbine combustors, improved calculation techniques are needed to provide accurate estimates of the emissions. A large data set obtained for an annular combustor was used to investigate the capabilities of a number of expressions presented in the literature to calculate oxides of nitrogen, carbon monoxide, and unburned hydrocarbons. It has been found that the correlation with the data using these expressions is significantly improved by the proper inclusion of such terms as residence time, evaporation characteristics, and mixing rate. The modification of the reaction term in these equations to follow the standard form of reaction rate equation has enhanced the correlation in most cases.

A review of the analytical models applicable to the combustor has revealed the potential to use such models to point to the regions in the combustor that are responsible for excessive formation of pollutants. In these models, the combustor is divided into a number of reactors that simulate various regions of combustor. The success of this type of approach relies on the proper selection of the flow model and the reactor arrangement, in addition to the inclusion of means to account for spray evaporation and mixing in the combustion zone.

A model has been formulated in the present effort that contains a number of primary zone reactors simulating both core and near wall combustion. A reactor immediately downstream of the fuel nozzle is selected to define LBO characteristics of a combustor, and the outcomes of the primary zone reactors are admitted into intermediate and dilution zones reactors. A chemical kinetic scheme that includes large numbers of reactions and addresses NO_x formation was used to provide the trends of variation of the concentrations of various pollutants. Based on these results, expressions for NO_x, CO, UHC formation and/or destruction were derived for different regions of the combustor. The simulation of the chemical kinetics by the derived expressions is supplemented by the inclusion of the effects of the droplet combustion. Satisfactory agreement with the data was obtained using this model.

In addition to enhancing the capability to provide better estimates of the emissions over conventional methods, the model provides insight into the local formation of different species. For instance, the model illustrates the importance of the near wall region to the presence of UHC in the combustor exhaust. Changing the liner cooling schedule can have a significant effect on both CO and UHC emissions. The results also show that the rate of NO_x formation is highest in the core of the primary zone, and additional quantities of NO_x may form at a slower rate in downstream zones if the temperature is sufficiently high. Effects of system pressure, residence time, and combustor air distribution are better understood in light of the results offered by the derived model.

References

Faeth, G. M., 1977, "Current Status of Droplet and Liquid Combustion," *Progress in Energy and Combustion Science*, Vol. 3, pp. 191–224.

Fletcher, R. S., and Heywood, J. B., 1971, "A Model for Nitric Oxide Emissions From Aircraft Gas Turbine Engines," AIAA Paper No. 71-123.

Glassman, I., 1977, *Combustion*, Academic Press, New York.

Hammond, D. C., Jr., and Mellor, A. M., 1973, "Analytical Predictions of Emissions From and Within an Allison J-33 Combustor," *Combustion Sci. Tech.*, Vol. 6, pp. 279–286.

Lefebvre, A. H., 1984, "Fuel Effects on Gas Turbine Combustion-Liner Temperature, Pattern Factor, and Pollutant Emissions," *AIAA Journal of Aircraft*, Vol. 21, No. 11, pp. 887–898.

Lefebvre, A. H., 1985, "Fuel Effects on Gas Turbine Combustion—Ignition, Stability and Combustion Efficiency," ASME JOURNAL OF ENGINEERING FOR GAS TURBINES AND POWER, Vol. 107, pp. 24–37.

Mellor, A. M., 1976, "Gas Turbine Engine Pollution," *Prog. Energy Combust. Sci.*, Pergamon Press, Vol. 1, pp. 111–133.

Mosier, S. A., Roberts, R., and Henderson, R. E., 1973, "Development and Verification of an Analytical Model for Predicting Emissions From Gas Turbine Engine Combustors During Low-Power Operation," *Atmospheric Pollution by Aircraft Engines*, AGARD CP No. 125.

Plee, S. L., and Mellor, A. M., 1978, "Flame Stabilization in Simplified Prevaporizing Partially Vaporizing and Conventional Gas Turbine Combustors," *J. Energy*, Vol. 2, No. 6, pp. 346–353.

Plee, S. L., and Mellor, A. M., 1979, "Characteristic Time Correlation for Lean Blowoff of Bluff-Body-Stabilized Flames," *Combustion and Flame*, Vol. 35, pp. 61–80.

Rizk, N. K., and Mongia, H. C., 1991, "Low NO_x Rich-Lean Combustion Concept Application," AIAA Paper No. 91, 1962.

Westbrook, C. K., and Pitz, W. J., 1984, "A Comprehensive Chemical Kinetic Reaction Mechanism for Oxidation and Pyrolysis of Propane and Propene," *Combust. Sci. Tech.*, Vol. 37, pp. 117–152.

Downloaded 02 Jun 2010 to 171.66.16.121. Redistribution subject to ASME license or copyright; see http://www.asme.org/terms/Terms_Use.cfm

Comparison of Spectrometric Techniques for the Analysis of Liquid Gas Turbine Fuels

M. Lukas
Spectro Incorporated,
Littleton, MA 01460

High-temperature corrosion and fuel system fouling are major concerns that confront gas turbine users. Fuel treatment is a critical requirement for gas turbine operators burning alternative fuels, and even so-called "clean fuels." Spectrometric fuel analysis is used to determine the amount of treatment required as well as the efficiency of the treatment. In most cases, analytical techniques developed by chemists for use in laboratory environments have been adopted for field use. This paper describes the various spectrometric techniques available to the gas turbine user to analyze fuels for contaminants such as sodium, potassium, vanadium, lead, calcium, silicon, etc., and additives such as magnesium compounds. Atomic absorption spectroscopy (AAS) and various atomic emission spectroscopy (AES) techniques will be discussed and compared.

Introduction

Over the last 20 years, special gas turbines have been developed to be fueled by all types of liquid fuels including residual and crude oil. However, the fuel quality is not consistent or predictable, and the physical properties and contaminant levels of these fuels vary as a function of their source, refinery processing, handling, and storage [1].

A critical requirement for the use of heavy petroleum fuel oil in gas turbine is the pre-conditioning of the fuel before it reaches the gas turbine [2]. Fuel treatment has thus become an extremely important part of any gas turbine system burning alternate fuels. Spectrometric analysis is used to determine the amount of treatment required and the efficiency of that treatment.

In selecting an analytical instrument for gas turbine fuel analysis, several techniques are available, each capable of analyzing the primary six elements: sodium, potassium, calcium, lead, vanadium, and magnesium. However, the performance, capabilities, and limitations of these techniques vary based on the type of fuel and the physical location of the laboratory.

Since spectrometric analysis plays such an important role in the operation of a gas turbine, a basic understanding of its capabilities and limitations is important and must be taken into account. We often assume that we know and understand the differences among the various spectrometric techniques available to us. Unfortunately we often find out too late that what works in the laboratory does not necessarily work in the field, or that the salesman forgot to mention certain shortcomings or idiosyncrasies of his product in the analysis of actual fuel samples.

Contributed by the International Gas Turbine Institute and presented at the 37th International Gas Turbine and Aeroengine Congress and Exposition, Cologne, Germany, June 1–4, 1992. Manuscript received by the International Gas Turbine Institute February 20, 1992. Paper No. 92-GT-202. Associate Technical Editor: L. S. Langston.

This paper identifies the different spectrometric analytical techniques, describes how they work, compares the main features and characteristics, and evaluates them for application in either laboratory or field environments.

Chemical Analysis

Definition and Classification. Chemical analysis of a sample of matter is the determination of the chemical composition or chemical makeup of that sample. For the purposes of this paper, chemical analysis refers to determining and quantifying the concentration of the elements that cause high-temperature corrosion and the formation of deposits, or ash, in the hot section components of the gas turbine.

Chemical analysis procedures are classified in many ways. They typically fall into two categories: the analysis of the sample for *what* constituents are present, and the analysis of a sample for *how much* of each constituent is present. The former is called *qualitative* analysis, and the latter, *quantitative* analysis [3]. In gas turbine fuel analysis, both qualitative and quantitative analysis are important, and they must be considered together.

Analytical procedures can be further classified into two categories, instrumental procedures and wet procedures, Fig. 1 [3]. The instrumental procedures are considered to be modern techniques, which make use of state-of-the art instrumentation applying high technology and a great degree of computerization. The primary emphasis of this paper is to describe and compare the various techniques available. The wet techniques do not lend themselves to ON-SITE gas turbine fuel analysis. They employ chemical reactions and classical stoichiometry as their only basis for arriving at results.

Terms Used in Chemical Analysis. Every analytical measurement is subject to a certain number of uncertainties that

Copyright © 1993 by ASME
Downloaded 02 Jun 2010 to 171.66.16.121. Redistribution subject to ASME license or copyright; see http://www.asme.org/terms/Terms_Use.cfm

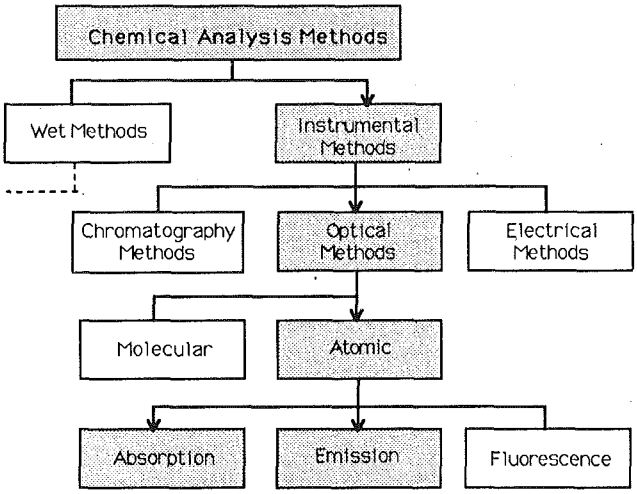

Fig. 1 Flow chart of analytical methods

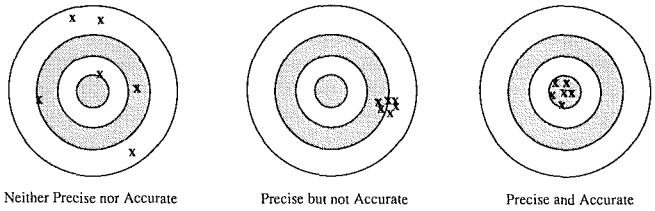

Fig. 2 Illustration of precision and accuracy

lead to scatter of data. The question, "Can I really trust these results?" is frequently raised. No single test can be applied for determining the accuracy and reliability of an analysis with absolute certainty. The question can only be answered with experience, the application of statistics, and an understanding of the analytical technique used.

The various analytical techniques available for fuel analysis have different attributes and capabilities that affect the quality of the data. In other words, "*the data are no better than the limitations of the analytical technique used.*" Although the emphasis of this paper is a comparison of these analytical techniques, we must have a general understanding of the statistics generally applied to evaluate a set (scatter) of analytical results. A definition and explanation of the primary statistical terms follows.

Mean and the Median. Mean and average ($\overline{X}$) are synonymous terms for the quantity that is obtained by dividing the sum of repeated measurements by the total number of results. In the formula below, X_i represents the individual analyses making up a set of N analyses:

$$\overline{X} = \frac{\sum_{j=1}^{N} X_i}{N}$$

The median, on the other hand, is that measurement about which all others are equally distributed. Ideally, the mean and median are equal and will more closely approximate each other as the number of analyses increases.

Precision. The term precision is used to describe how closely several measurements that have been carried out in exactly the same way relate to each other. Standard deviation is the most common measure of precision used in chemical analysis. Most fuel analyses consist of a small set of data, and the standard deviation is calculated by applying the formula shown below. Fortunately, most modern spectrometers have the built-in capability to calculate the standard deviation automatically

$$\sigma = \sqrt{\frac{\Sigma\,(\overline{X} - X_i)}{N-1}}$$

Standard deviation is frequently also quoted in relative terms by chemists and instrumentation manufacturers. The relative standard deviation (RSD) is obtained by dividing the standard deviation by the average of the set of analyses. It is expressed in percent as shown below:

$$\text{RSD} = (\sigma/\overline{X}) \times 100 \text{ percent}$$

Accuracy. The term accuracy refers to the correctness of the data or the closeness of the data to the accepted value. Accuracy is typically expressed in terms of "uncertainty of measurement," the difference between the true value and the measured value.

It is important to note the fundamental difference between accuracy and precision. Accuracy measures agreement between the analytical data and what is believed to be the true concentration of the element measured. Precision does not necessarily relate to accuracy but to how closely several measurements relate to each other. The difference between the two is made clear in Fig. 2. Good precision is no guarantee of good accuracy, but without good precision, accuracy does not exist.

The accuracy of data, or error, can occur in the analysis due to many sources, those that can be determined (determinate errors), and those that cannot be determined (indeterminate errors).

Determinate errors are avoidable mistakes that can be identified and are known to have occurred. They generally cause all results from a set of analyses from a specific fuel sample to be either high or low. Determinate errors fall into three categories: (1) *instrument errors*, which are attributable to imperfections in the spectrometer and instabilities in the power supply, (2) *method errors*, which arise from nonideal chemical or physical behavior such as sample preparation procedure, and (3) *personal errors*, which are caused by the carelessness, inattention, or physical or psychological limitations of the experimenter [4].

Indeterminate errors, also called random errors, are those that are impossible to avoid. They occur when a spectrometer is extended to its maximum capability. Such errors can be attributed to many factors; however, none can be positively identified. Indeterminate errors are therefore dealt with by applying statistics and the laws of probability. In a fuel sample, when low concentrations are important, the standard procedure is to analyze the same sample three to five times. The results are then compared, and if they agree to within a certain predetermined statistical set, they are averaged. Any results that fall outside of the predetermined limits are rejected before an average is calculated.

Atomic Absorption and Emission Spectroscopy

Principles of Spectroscopy. The term spectroscopy refers to the branch of science in which light radiation is resolved (separated) into its component wavelengths to produce a spectra. In accordance with this definition, a *spectrometer system* is a device that creates the condition for radiation to be absorbed or emitted, then separates the radiation into component wavelengths and identifies and quantifies the elemental components.

Atomic Emission Spectroscopy is a technique for detecting and quantifying the presence of elements in a material. It is based on the fact that each element has a unique atomic struc-

Downloaded 02 Jun 2010 to 171.66.16.121. Redistribution subject to ASME license or copyright; see http://www.asme.org/terms/Terms_Use.cfm

ture. When subjected to the addition of energy, each element emits light of specific wavelengths, or colors. A sodium solution gives off yellow color, potassium: violet color, copper: green color, and so on. Since no two elements have the same pattern of spectral lines, the elements can be differentiated. The intensity of the emitted light is proportional to the quantity of the element present in the sample, allowing the concentration of that element to be determined.

Figure 3 provides a simplified view of the events that take place in the optical spectroscopy process. Figure 3(*a*) shows a sketch of an atom in its ground state. Under normal conditions, prior to excitation, the electrons in the atomic structure of each element revolve in their lowest energy or "ground state." Eleven electrons are shown in Fig. 3, which would be the case for a sodium atom. During excitation, the energy of the source is imparted to the oil or fuel sample, causing it to vaporize. Atomic electrons absorb energy and are temporarily forced away from the nucleus of the atom into a higher, unstable orbit, as illustrated by Fig. 3(*b*). After reaching this unstable state, the electrons release this absorbed energy in the form of light at a specific wavelength as they return to the ground or stable state, Fig. 3(*c*). The energy released has a specific value corresponding to the particular electron transition that has occurred in the excited atom. The light has a specific frequency or wavelength (frequency is inversely proportional to wavelength) determined by the energy of the electronic transition. Since many transitions of different energy are possible for complicated atoms, which have many electrons, light of many different wavelengths is emitted. These spectral lines of light are unique to the atomic structure of only one element. The intensity of the spectral lines is proportional to the concentration of the element present in the sample. If more than one element is present in the sample, spectral lines of distinctively different wavelengths will appear for each element. These lines must be separated in order to identify and quantify the elements present in the sample. Usually only one spectral line among many possible choices is chosen to determine the concentration of a certain element. This line will be chosen for its intensity and freedom from spectral lines of other elements that may be too close to it and thus cause interference. To accomplish this, an optical system is required.

All spectrometer systems, based either on the atomic absorption or atomic emission technique, consist of the three main components shown in Fig. 4. These components are (1) an *excitation* source, (2) an *optical system* with *detector*(*s*), and (3) a *signal processing and readout system*.

1 The *excitation source* introduces energy to the sample causing electrons in the fuel sample to absorb that energy and reach an excited state. The form of energy can be either high-energy light as in AAS, or thermal energy as in AES.

2 The *optical system* separates and resolves the resulting radiation from that excitation into its component wavelengths. In AES systems, two types of optical system can be used: a monochromator, which detects the elements in the sample one at a time and in sequence, or a polychromator, which detects all the programmed elements at the same time. In AAS systems, radiation from a light source is absorbed and detected by a monochromator. The *detector* collects the light energy separated by the optical system and converts the radiant energy into an electrical current.

3 The *signal processing and readout system* measures the light that has been separated into its component wavelengths by the optical system and presents the information from the detectors to the operator in concentrations such as parts per million or percent. A computer is used in modern spectrometer systems to perform this function as well as the control of the entire system.

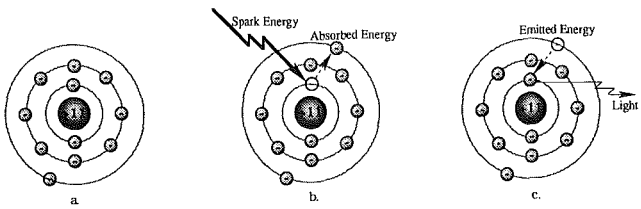

Fig. 3 Absorption and excitation process in an atom

Atomic Absorption Spectroscopy (AAS). In the flame atomic absorption spectroscopy (FLAAS) technique, Fig. 5, a small amount of the fuel sample, after appropriate dilution, is fed into and aspirated in a controlled flame, which is normally fueled by an acetylene–oxygen mixture. The flame vaporizes the sample, which causes the atoms to be in an elevated energy state so they can readily absorb light. A special hollow cathode lamp emits a high-intensity light beam corresponding to the exact energy required to cause the element of interest to be raised to an excited energy state. The monochromator is tuned to the desired wavelength and because of the chopper, receives a continuous reference signal from the hollow cathode lamp and an alternating absorbed signal from the flame. The absorbed light can be related to the concentration of the element present in the fuel [5], and a microprocessor or computer is then used to separate the signals and convert them into concentration.

Another AAS technique that has been found acceptable for fuel analysis is a nonflame type of atomizer known as graphite furnace atomic absorption spectroscopy (GFAAS). The equipment used for GFAAS is identical to flame atomic absorption method except for the addition of a small high-temperature furnace in place of the flame. There are various types of furnace currently in use, typically configured as either a small cylindrical carbon tube or cup to hold the sample. In GFAAS, a few microliters of the sample are first evaporated at a low temperature. The current through the furnace is then increased to a few hundred amperes, the temperature soars to approximately 2500°C, and the sample is atomized. The atomized metals in the sample then absorb light in the same manner as in standard FLAAS.

Atomic Emission Spectroscopy (AES). Most of the atomic emission spectrometers used in fuel analysis are either of the rotating disk electrode type (RDE) or of the inductively coupled plasma (ICP) type. The difference is only in the means used to excite the atoms of the elements in the fuel sample.

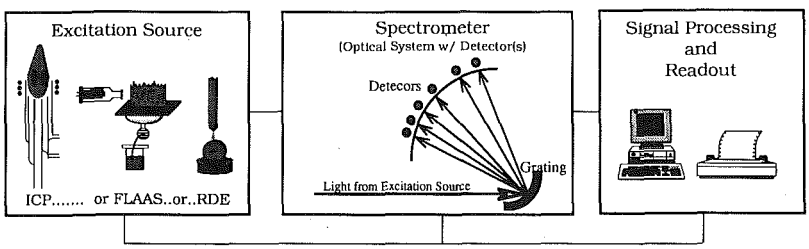

Fig. 4 Main components of spectrometer systems

Downloaded 02 Jun 2010 to 171.66.16.121. Redistribution subject to ASME license or copyright; see http://www.asme.org/terms/Terms_Use.cfm

In the RDE AES technique, a rotating counterelectrode brings a continuous sample into a gap formed between it and a stationary rod electrode. The sample is then struck with a high-voltage arc (Fig. 6), causing the individual metals in the sample to give off light or radiant energy. The ICP AES excitation technique is an electrode-free plasma created by a flow of inert gas (argon). The gas passes continuously through the plasma torch, which is located inside a two or three-turn R. F. coil connected to a radio frequency alternating current generator. The argon gas acts as a secondary coil of a transformer, thus heating the gas to extremely high temperatures. The fuel sample is aspirated through the center of the torch and into the plasma where the elements present are excited to give off radiant energy. In RDE AES and ICP AES systems, a lens or fiber optic is then used to gather and focus the radiant energy from the excitation source into the optical system. The energy that passes into the optical system strikes a concave diffraction grating, which disperses the light into the various spectral lines associated with the elements present. Photomultiplier tubes are used to detect and convert radiant energy into electrical energy. The output of the tube is an electrical current proportional to the amount of light it senses. This current is used to charge a low-leakage capacitor whose voltage is subsequently automatically measured with a precision digital voltmeter or computer. The result of the analysis is a measurement of the concentration of each metal present in the sample and is displayed on a video screen, or for permanent record, transcribed by an automatic typewriter.

Comparison of Analytical Techniques

The analytical techniques commonly used for gas turbine fuel analysis consist of:

FLAAS—Flame Atomic Absorption Spectroscopy
GFAAS—Graphite Furnace Atomic Absorption Spectroscopy
RDE AES—Rotating Disk Electrode, Atomic Emission Spectroscopy
ICP AES—Inductively Coupled Plasma, Atomic Emission Spectroscopy

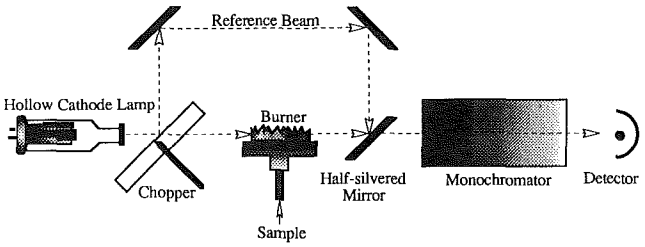

Fig. 5 Schematic diagram of an atomic absorption spectrometer

The FLAAS technique is the most established analytical method in use for elemental analysis. It has been used commercially for over 35 years, thousands of instruments are in use throughout the world, and a like number of applications-oriented publications are in existence. It is a single-element-at-a-time technique that is good for quantitative analysis but not for qualitative analysis. In the last ten years, it has reached a point in its life cycle where few improvements have been made except for developments in alternate means to atomize the sample [6]. The graphite furnace (GFAAS) applied to basic AAS offers more sensitivity, and is the most significant of these improvements.

The RDE AES technique has been in use for over 50 years for the analysis of a variety of samples. In some applications it was later replaced with the AAS technique, which offers greater sensitivity and capabilities to analyze more types of materials. For lubricating oil and fuel analysis, the RDE technique continues to be the preferred method, due to its simplicity of operation and reliability. Sample introduction is simple, and since it does not use nebulizers as in FLAAS and ICP AES, it also has the ability to analyze the larger particulates in the fuel or oil sample. It has actually made a comeback in the last 15 years because it is the only technique that readily lends itself to on-site analysis in all types of environment, while still providing reliable analytical performance.

The ICP AES technique was developed as an alternate method replacing AAS spectrometers. It offers greater sensitivity and analytical throughput due to its ability to make multi-element determinations and qualitative and quantitative analyses. It has enjoyed a successful commercial history in the last 15 years, and is continually improved and modified for a variety of applications.

All the above techniques are capable of analyzing gas turbine fuel samples ranging from light distillates to heavy residuals. Analytical performance, functional capabilities, and costs vary greatly, and are the subject of the paragraphs that follow, where a number of features important to fuel analysis are compared.

Analytical Performance. To compare the analytical performance of each technique, we must consider detection limit, short term precision, long term stability, dynamic range, and interferences.

Analytical Performance—Detection Limit. The detection

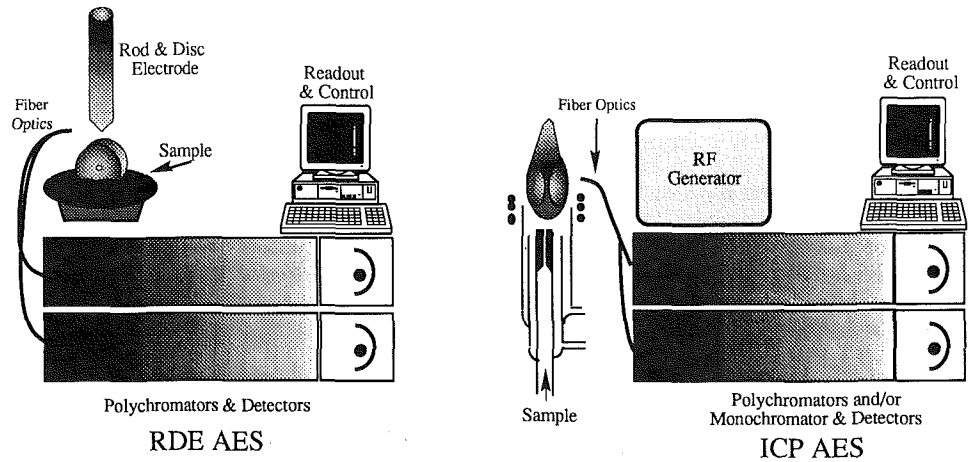

Fig. 6 Schematic diagram of RDE AES and ICP AES spectrometer systems

Downloaded 02 Jun 2010 to 171.66.16.121. Redistribution subject to ASME license or copyright; see http://www.asme.org/terms/Terms_Use.cfm

Table 1 Practical detection limits[1] (ppm) for oil and fuel samples

El.	AAS[2,3]	GFAAS	AE-RDE	AE-ICP [2]
Al	0.20	0.04	0.07	0.02
Ag	0.02	0.001	0.02	0.03
B	7.0	0.002	0.09	0.01
Ba	0.08	0.04	0.07	0.01
Ca	0.01	0.01	0.05	0.03
Cr	0.05	0.004	0.36	0.03
Cu	0.1	0.005	0.09	0.02
Fe	0.1	0.01	0.21	0.02
K	0.04	0.004	0.27	1.0
Mg	0.001	0.0002	0.01	0.20
Mo	0.25	0.03	0.45	0.08
Na	0.02	0.004	0.09	0.2
Ni	0.2	0.05	0.66	0.07
P	300	20	3	0.50
Pb	0.2	0.05	0.93	0.10
Ti	0.8	0.3	0.25	0.02
Si	2.0	0.6	0.38	0.10
Sn	0.02	0.03	0.88	0.30
V	0.8	0.2	0.45	0.05
Zn	0.03	0.001	0.57	0.02

(1) In parts per million (ppm) or μl/ml
(2) Based on typical dilution of 9:1 for lubricants and heavy fuel
(3) Based on air-acetylene or nitrous oxide-acetylene flame, from [8]

limit (DL) is an instrument measurement capability defined as the concentration that produces a net line intensity equivalent to three times the standard deviation of the background signal [7]. The "practical limit of detection" is, however, often greater than the calculated limit of detection by a factor of as much as 10.

The GFAAS totally consumes small quantities of the sample and for most elements, it provides superior detection limits. As a note of caution, however, the detection limit varies from element to element, operating conditions and between differing fuel types. Most published detection limits are measured in dilute aqueous solutions and represent the best that a system is capable of measuring [8]. They are thus calculated on ideal samples (water) and under ideal conditions (environmentally controlled laboratory and by a qualified chemist). A practical detection limit is one that is obtainable in actual situations, and is repeatable in almost any situation. Table 1 is a listing of practical detection limits calculated on actual oil and fuel samples.

As a rule the detection limits, with few exceptions, are best using GFAAS, followed by ICP AES, FLAAS, and RDE AES. A significant exception for the analysis of heavy fuels (those requiring dilution prior to analysis) is sodium. For these fuels, the RDE AES technique is preferred since the limit of detection is not increased due to the dilution requirement (see also "sample preparation" below).

Analytical Performance—Short and Long Term Precision. The short-term precision, as the name implies, is a confidence factor in the precision of the analysis. It is obtained by calculating the standard deviation for a small number of consecutive analyses without interruption. The smaller the standard deviation, the better the precision and the degree of confidence in the results [6]. Long-term precision, on the other hand, is calculated in a similar manner and over a longer period of time, typically 4 to 8 hours.

The short-term precision for the FLAAS and ICP AES techniques is similar, and typically in the 1 percent RSD range for fuel samples. The RDE AES technique short-term precision is in the 3 percent RSD range and the GFAAS 3–10 percent, depending on whether the sample is introduced automatically or manually. When low concentrations in the sample approach the detection limits of the respective technique, the precision is degraded, and the standard deviation is often used as the quantifiable figure of merit.

The long-term precision of FLAAS and ICP AES over an 8 hour period is also similar, and in the 2–3 percent RSD range. The RDE AES technique is the least susceptible to long-term drift, and the precision remains relatively constant over an 8 hour period. The GFAAS is the most prone to drifting due to graphite degradation, and RSD values ranging from 5 to 20 percent are typical.

Analytical Performance—Dynamic Range. The dynamic range refers to the concentration range for which the signal of the spectrometer system and sample concentration have a linear relationship. It is preferable to have a wide dynamic range in order to obtain accurate analytical results without the need to recalibrate, dilute, or preconcentrate the fuel sample. A wide dynamic range is beneficial in applications where fuels with wide concentration ranges such as distillates, crude oils, and/residual, may be analyzed.

The ICP AES technique has the widest dynamic range, and it spans over four to six decades. Even with 9:1 dilution necessitated by the heavier fuels, it still has the best dynamic range of all the techniques. Typically, one calibration curve is all that is required for most applications and one spectral line will cover the analytical range of interest.

The FLAAS and RDE AES techniques have a dynamic range of two to three decades, and more than one calibration may be required if a variety of fuels are analyzed. Sample preparation and changes in operating parameters are also typical requirements for FLAAS. Although sample preparation is not a prerequisite for the RDE AES technique, two spectral lines may be needed to cover the required spectral range. For example, two separate magnesium spectral lines must be used to cover the concentration range requirement for many fuels of 0 to 1500 parts per million; one for the low concentrations and another, less sensitive spectral line, for high concentrations over 500 parts per million.

The most restricted dynamic range is a characteristic of the GFAAS technique, which covers only about two decades. It is usually selected primarily for its low detection limit capabilities, while high concentrations in fuels are dealt with using one of the other techniques.

Analytical Performance—Interferences. Three types of interference are encountered: spectral, chemical, and physical. Each are effects that alter the measurement accuracy of the fuel sample. Spectral interferences are those caused by overlap or scatter of light from another element in the sample, or from continuous emissions from compounds in the sample. Chemical interferences are those resulting from chemical interactions between the elements in the sample and the sample matrix. Physical interferences are a result of sample transport and consumables.

The most frequently encountered spectral interference in fuel analysis is due to changes in background signal of the unknown sample as compared to the standard sample. A background correction system will compensate for most background signal changes, and is a requirement for accurate fuel analysis. It has also been shown that background correction systems that are capable of monitoring on either side of the spectral line and at user selected distances, improve accuracy [9].

The GFAAS technique has by far the fewest spectral interferences since almost all of the matrix is removed in the sample preparation process. The actual analysis consists almost entirely of the analyte. The other techniques all suffer to a greater extent from spectral interferences.

In today's modern spectrometers, most chemical interferences can be minimized with software corrections or selection of alternate spectral lines. Although many spectral interferences have been documented in the technical literature, little

Downloaded 02 Jun 2010 to 171.66.16.121. Redistribution subject to ASME license or copyright; see http://www.asme.org/terms/Terms_Use.cfm

has been published about gas turbine fuels. This is probably due to the wide variations in fuels throughout the world, and the limited market. The only sure way to detect, quantify, and subsequently eliminate spectral interferences is to analyze a sample of the fuel, and determine and measure the background signals near the wavelength of the interfered element. Spectrometers designed for fuel analysis have capabilities to perform such investigations and measurements.

ICP AES has the fewest chemical interferences, followed by FLAAS, then GFAAS with the most. The RDE AES technique suffers from chemical interferences when there are high concentrations of vanadium in the fuel, and with certain types of magnesium additive.

The main contributors to physical interference are sample transportand the cleanliness and purity of the consumables. ICP AES is the most susceptible to sample transport problems and GFAAS the least. Variations in sample quantity reaching the ICP torch for analysis due to contamination, viscosity differences, or the formation of droplets is the main contributor to this. The GFAAS has the fewest such problems since the entire sample is placed directly into the furnace for volatilization. Consumables such as graphite electrodes and the quality of the gases also contribute to physical interferences. Impurities in the electrodes of RDE AES, or the furnace of GFAAS, will appear in the analysis as an undesirable interference. Contamination in the gas or cylinders used to fuel FLAAS or ICP AES will have the same detrimental effect. Modern spectrometer systems use internal standards to reduce physical interferences. Changes in the signal of the internal standard are used to compensate and correct the concentrations of the elements analyzed.

Functional Capabilities. The functional capabilities of the standard analytical techniques vary greatly and are the most visible characteristics. They include fuel sample preparation requirements, sample throughput, and ease of operation.

RDE AES is the only technique capable of analyzing all types of fuel sample without any type of preparation. The only exceptions are residual fuels, which are solid at room temperatures, and must be heated so they can be poured into a sample vessel for analysis. Light distillates can be analyzed with FLAAS and ICP AES without dilution, but heavier fuels and most crude oil must be diluted prior to analysis. The GFAAS technique requires sample preparation as part of its procedure. Prior to analysis, the sample is first evaporated at a low temperature and later ashed at high temperatures.

It is appropriate to also point out that detection limits and accuracy can be improved by applying oxidation sample preparation procedures to a fuel sample prior to analysis with FLAAS or ICP AES. These procedures are grouped into wet or dry ashing techniques. Wet ashing is the method most often used. It makes use of gradual heating of the sample. Sulfuric, nitric, and perchloric acids are also introduced to decompose fuel samples [10]. Dry ashing is seldom used because it is not very reliable and cannot be applied for all elements. In its simplest form, it uses heat to burn off the matrix and to decompose the sample.

Sample throughput for fuel analysis is defined as the total time required to detect and quantify the basic six elements in the sample. Sample analysis with the RDE AES technique is less than one minute because sample preparation is not required, and all elements are analyzed at the same time. Without sample preparation, the ICP AES technique can also analyze one sample per minute but the time is at least double if sample dilution is necessary. The FLAAS technique requires at least two minutes per sample for an automatic system and four minutes or longer for a manual system. The GFAAS technique takes twenty minutes or more per sample because each element analyzed requires that the hollow cathode lamp be changed. The elements are analyzed individually, one after the other. The oxidation sample preparation procedures of wet and dry ashing can take as long as 4 to 8 hours per sample, depending on the fuel type and concentration of the elements in the sample.

Computers have made considerable contributions toward simplifying the operation of analytical techniques. RDE AES is by far the easiest and simplest technique to master. FLAAS and ICP AES are more complex and require a more skilled operator for routine analysis and periodic upkeep. GFAAS is much more susceptible to operator technique, and requires a trained laboratory technician in order to obtain accurate and repeatable data. The wet and dry ashing techniques must be performed by a chemist or highly trained technician. They employ hazardous acids, may cause an explosive reaction, and must be monitored throughout the entire procedure.

Costs. Like everything else, instrumentation acquisiton costs and costs per sample also vary among the techniques. Although analytical instrumentation is considered to be expensive, it is a small investment when compared to possible costly consequences due to poor or lack of fuel analysis, or when compared to the costs of the entire gas turbine installation.

The instrumentation cost of a FLAAS system starts at about $15,000 for the simplest single beam system, and can go up to as much as $60,000 for a completely automated system. The GFAAS is only slightly more expensive and starts at about $20,000. It can run as high as $90,000 for a system complete with all the options. The RDE AES system configured for gas turbine applications varies from $65,000 to $75,000, while the ICP AES systems start at $60,000 for a simple sequential system and can go up to as much as $100,000.

Many variables have to be considered in determining the per sample analysis cost for each technique. Some basic assumptions can be made for typical gas turbine fuel analysis applications, which simplifies matters. Typically, operation spans a 24 hour period and an average number of analyses in that period is 20 samples, including calibration. Based on these assumptions, the RDE technique has by far the lowest cost per sample. Total labor costs are less than 1 hour per day and variable costs per sample for consumables are approximately $0.50 per sample. In the typical gas turbine fuel analysis application, the other techniques are penalized equally, since they must be "on" and operating even when samples are not analyzed. Argon or nitrous-oxide acetylene are consumed continually for the ICP AES, FLAAS, and GFAAS techniques and its consumption becomes the basis of calculating costs per sample. These consumable costs vary from $0.75 to $5.00 per sample depending on whether liquid or gaseous argon and nitrous-oxide acetylene are used. Labor costs for ICP AES are typically 1 hour per day and 2 to 3 hours for FLAAS and GFAAS.

Selecting a Technique for Gas Turbine Fuel Analysis

The selection process of deciding which analytical technique to use for gas turbine fuel analysis is relatively easy if we identify and define the requirements for fuel analysis.

Timely fuel analysis is very important, since decisions for fuel treatment requirements and efficiency are made based on such analysis. Analytical results are therefore time sensitive and the capability to perform analyses must be close to the source of the fuel sample. On-site fuel analysis at the gas turbine site has become the norm in such applications.

The selection process, therefore, should be based on typical fuels encountered and performance requirements for instrumentation at the gas turbine site, situated either at or near the fuel treatment system. Petroleum based liquids, predominantly distillates, are the most widely used fuels in gas turbines; however, supplies of these are limited and crude oils as well as residual oils are frequently the fuel of choice. Fuel treatment

Downloaded 02 Jun 2010 to 171.66.16.121. Redistribution subject to ASME license or copyright; see http://www.asme.org/terms/Terms_Use.cfm

Table 2 Comparison summary of analytical techniques

Feature	FLAAS	GFAAS	RDE AES	ICP AES
Detection Limit	Very Good	Excellent	Good	Very Good
Short-term Precision	1%	3-10%	3%	1%
Long-term Precision	2-3%	5-20%	3%	2-3%
Dynamic Range	2-3 decades	1-2 decades	2-3 decades	4-6 decades
Sample Preparation	Yes	Yes	No	Yes
Sample Throughput	2-4 min.	20 min.	1 min.	1-2 min.
Ease of Operation	simple	complex	simpler	complex
Consumables (Daily & Capital)	acetylene, hollow cathode lamps	argon or nitrogen, graphite furnace, hollow cathode lamps	graphite electrodes	argon gas
Instrument Cost	$15-$60 K	$20-$90 K	$65-$75 K	$60-$100 K
Cost per Sample	$0.75-$5	$0.75-$5	$0.50-$1	$0.75-$5

based on chemical analysis is thus a requirement, and it is safe to assume that most applications are in less than ideal environment conditions and trained technicians to perform analyses are not always available.

The key considerations in selecting an analytical technique for on-site fuel analysis are identified below:

1 Environmental constraints
2 Ease of operation
3 Safety
4 Sample introduction/preparation requirements
5 Analytical performance
6 Availability of consumables
7 Cost per sample

When we compare the features of the analytical techniques in Table 2 with the items to consider for on-site fuel analysis, there is little doubt that the RDE technique is the best for the application. It is by far the easiest to use without requirements for special environmental controls. Sample preparation is not required for any type of fuel, and precision is sufficient to meet the requirements of ASTM D-2880 [11]. Total time to analyze a fuel sample is less than one minute per analysis. The only consumables required for the analysis are readily available graphite electrodes, which have an infinite shelf life and do not degrade with time.

We have ruled out FLAAS, GFAAS, and ICP AES since each requires a higher level of training for operation, and consumables are not readily obtainable at remote sites. A basic knowledge of chemical procedures and sample preparation is required for each of these techniques. Operation is dependent on the consumption of high-purity gases, which could create a logistics problem, and are difficult, if not impossible to obtain at remote locations. Wet and dry ashing techniques provide better precision, but do not lend themselves to on-site applications. They require a very high level of training, are slow, have poor repeatability, and present a possible safety hazard.

One exception would be if the gas turbine site has access to a nearby analytical laboratory staffed with trained laboratory technicians or chemists. In this instance, any of the techniques mentioned are applicable. A possible preference might be given to FLAAS or ICP AES using wet sample preparation techniques at the expense of timely analyses.

Summary

The analytical techniques available for gas turbine fuel analysis have been compared based on the requirements of typical applications. The techniques compared consist of flame atomic absorption spectroscopy (FLAAS), graphite furnace atomic absorption spectroscopy (GFAAS), atomic emission spectroscopy techniques using the rotating disk electrode (RDE AES), and the inductively coupled plasma (ICP AES).

The FLAAS technique is relatively simple to operate, offers good analytical performance, and is the least costly instrument to acquire. It is, however, a relatively slow technique, which requires sample preparation for most fuels and a different light source for each element analyzed. The availability of gases to fuel the burner is also a major consideration at remote locations.

The GFAAS technique works in conjunction with the FLAAS instrument and offers the best sensitivity of all the techniques. It is, however, very slow, requires sample preparation, and is very user dependent. As with FLAAS, the availability of gases to fuel the burner is also a major consideration at remote locations. At minimum allowable gas turbine fuel concentrations for sodium, the repeatability (difference between successive tests performed by different individuals at different laboratories) of the FLAAS and GFAAS techniques [12] make them marginal for fuel analysis.

The ICP AES technique has a wide dynamic range and features multi-element analysis capability. It also has excellent detection limits and precision. The only exception, critical for gas turbine fuel analysis, are the detection limits for alkali metals. Of all the available techniques, the detection limit for sodium is the worst with ICP AES if sample dilution is required. ICP AES systems are relatively difficult to operate, require sample preparation for most gas turbine alternate fuels, and the nonavailability of argon to support the plasma can be a major limitation at remote locations.

Downloaded 02 Jun 2010 to 171.66.16.121. Redistribution subject to ASME license or copyright; see http://www.asme.org/terms/Terms_Use.cfm

Of the techniques available for fuel analysis, RDE AES is the only one capable of fulfilling the requirements for on-site fuel analysis at remote locations. It is the only technique capable of fulfilling the operational and analytical fuel analysis requirements at nonlaboratory installations. It is simple to operate in all types of environments, has multi-element capabilities, and consumables are readily available. It does not have the best detection limits of all the techniques, but they are sufficient to meet the fuel specification requirements of ASTM D 2880.

The various techniques available for fuel analysis vary in cost, complexity of operation, and analytical performance. All are designed for other applications and need to be optimized and calibrated for gas fuel analysis. They are modern instruments with the necessary software capabilities to compensate for common fuel analysis problems such as matrix effects and interferences. Regardless of the technique selected, applications support and experience with fuel analysis by the instrument supplier is imperative to optimize performance and accuracy.

Acknowledgments

The author wishes to thank Mr. Ken Koch of Petrolite Research, Mr. Aneesh Bakshi of Alfa-Laval Separator Co., Mr. Shlomo Dreymann, and Sue Franz for their encouragement to prepare this paper and the many valuable suggestions they provided.

References

1 Lukas, M., "Spectrometric Analysis of Residual Fuel," ASME Paper No. 78-GT-93, 1978.

2 McConvey, M. G., "Alternative Fuels and Fuel Treatment for Industrial CHP Schemes," presented at the First International Combined Heat and Power Symposium, London, Apr. 1989.

3 Kentel, J., *Analytical Chemistry for Technicians*, Lewis Publishers Inc., MI, 1989, p. 2.

4 Skoog, D. A., West, D. M., and Holler, J. F., *Analytical Chemistry*, Saunders College Printing, New York, 1988, pp. 15, 568.

5 Sawyer, J. W., *Sawyer's Turbomachinery Maintenance Handbook*, Turbomachinery International Publications, CT, 1980, p. 8–5.

6 Routh, M. W., "Comparison of Atomic Spectroscopic Techniques," Applied Research Laboratories.

7 Thompson, M., and Walsh, J. N., *A Handbook of Inductively Coupled Plasma Spectrometry*, Blackie, Glasgow, 1986, p. 33.

8 Bruno, T. J., and Svoronos, P. D. N., *CRC Handbook of Basic Tables for Chemical Analysis*, CRC Press, Boca Raton, FL, 1989, pp. 367–390.

9 Spectro Inc., "Final Test Report on Fuel Samples for Petrolite Research and Development," 1990.

10 Petrolite Research, "Wet Ash Procedure for Analysis of Trace Metals Contained in Organic Matrix," Method M6-86.

11 Annual Book of ASTM Standards, "Standard Specification for Gas Turbine Fuel Oil," Vol. 05.02, D-2880-88.

12 Annual Book of ASTM Standards, "Standard Test Method for Trace Metals in Gas Turbine Fuels by Atomic Absorption and Flame Emission Spectroscopy," Vol. 05.03, D-3605-87.

Downloaded 02 Jun 2010 to 171.66.16.121. Redistribution subject to ASME license or copyright; see http://www.asme.org/terms/Terms_Use.cfm

Coal Gas Cleaning and Purification With Inorganic Membranes

D. E. Fain

G. E. Roettger

Oak Ridge K-25 Site,[1]
Martin Marietta Energy Systems, Inc.,
Oak Ridge, TN 37831-7271

The economic viability of coal gasification could depend on the ability to clean and purify the coal gases at elevated temperatures. Inorganic membranes have the potential for being used for that purpose. Efforts have been undertaken at the Oak Ridge K-25 Site to develop membranes that would be useful for separating hydrogen from the coal gas at the high operating temperatures. This paper will give a brief review of some fundamentals of gas separation with membranes. Also, a brief discussion of the theory derived to guide the development process will be given. The theory can be used to indicate the pore size needed to achieve good separation. In addition, some experimental results that have been obtained with some of the membranes that have been fabricated will be discussed.

Introduction

The economic viability of coal gasification could well depend on the ability to clean and purify the coal gases at elevated temperatures. Inorganic membranes have the potential for being stable and useful at very high temperatures. Therefore, they have the potential for being used to clean and purify the gasified coal.

Under the sponsorship of the U.S. Department of Energy (DOE) Office of Fossil Energy's Advanced Research and Technology Development (AR&TD) Materials Program, a project has been undertaken at the K-25 Site to develop membranes that would be useful in the coal gasification process (Fain et al., 1991a, 1991b; Egan et al., 1992). This project has been directed toward developing a membrane that can separate hydrogen from coal gas at operating temperatures. Since hydrogen has economic value as a pure process gas, separation of some of the hydrogen from the coal gas for resale will significantly improve the economics of the process. A second phase of the development project will be to develop membranes to remove acid gases from the coal gas.

Fundamentals of Gas Separation by Membranes

Separation of a gas mixture using a membrane is accomplished by passing the mixture (feed stream) across one side of the membrane. A fraction of the gas (enriched stream) passes through the membrane and the remaining fraction of the gas (depleted stream) is collected and not allowed to pass through the membrane. The ratio of the enriched stream flow rate to the feed flow rate will be referred to as the cut. A driving force is needed to produce transport through the membrane. That driving force is a difference in the partial gas density of any given component on the two sides of the membrane. The transport will be in the direction of decreasing partial density. The difference in partial density can be achieved by a difference in pressure, temperature, or mole fraction. Controlling the boundary conditions of any of these three variables on the two sides of the membranes will provide a driving force and produce a transport of different gases through the membrane. The membranes themselves affect these variables by influencing, differently, the rates at which different gas molecules are transported through the membrane. The influence of the membrane depends on the physical and chemical interaction of the gases with the membrane.

With organic membranes, the transport appears to be influenced mostly by a solution diffusion model. It appears that both the solution and diffusion are affected by the chemical interaction of the gases with the membrane, the free volume in the membrane, and the flexibility of the organic matrix. In organic membranes, the free volume is usual fairly small, 15 percent or much less, but it can vary depending on the flexibility of the material. There is little or no interest in pores or pore size distributions.

Inorganic membranes are usually porous with much more variable free volumes, perhaps 20 to 70 percent, and relatively little or no flexibility. The pore size and pore size distribution of the free volume are of fundamental importance. There are potentially many different transport mechanisms in such a membrane. The transport by the different mechanisms is greatly influenced (in different ways) by one or more of the mean dimensions of the distribution of path lengths in the free volume. The chemical interaction between the gas molecules and the membrane surfaces also influences the transport. The best known and understood mechanism is free molecule diffusion or Knudsen flow. This type of flow occurs when the molecular density is such that the mean free path between collisions with a membrane wall is small in comparison to the mean free path for collisions between molecules and when the pore size is large in comparison to the size of the molecules. Under these conditions, the diffusion coefficient for transport through the membrane is proportional to the mean molecular velocity and

[1]The Oak Ridge K-25 Site is managed by Martin Marietta Energy Systems, Inc. for the U.S. Department of Energy under contract No. DE-AC05-84OR21400.

Contributed by the International Gas Turbine Institute and presented at the 37th International Gas Turbine and Aeroengine Congress and Exposition, Cologne, Germany, June 1-4, 1992. Manuscript received by the International Gas Turbine Institute March 5, 1992. Paper No. 92-GT-359. Associate Technical Editor: L. S. Langston.

Copyright © 1993 by ASME
Downloaded 02 Jun 2010 to 171.66.16.121. Redistribution subject to ASME license or copyright; see http://www.asme.org/terms/Terms_Use.cfm

Table 1 Typical coal gas mixture

Gas	Mole Fraction	Molecule Diameter
Hydrogen (H_2)	0.391	2.97
Water (H_2O)	0.005	2.82
Carbon Monoxide (CO)	0.189	3.59
Hydrogen Sulfide (H_2S)	0.005	3.73
Methane (CH_4)	0.113	3.88
Carbon Dioxide (CO_2)	0.297	4.00

the mean path length between collisions with the membrane walls. The separation factor is equal to the square root of the ratio of the molecular weights. For most commercial applications, a square root of molecular weight separation factor is too small to be economical. The challenge is to design membranes that will increase the transport of the desired gas and decrease the transport of the other gases and provide effective separation factors much larger than the square root of the molecular weight ratio.

The most common way that membranes are used to separate a gas mixture is to fix the pressure on the two sides of the membrane. The ratio of the pressures on the two sides of the membrane is a most important parameter. The largest change in mole fraction, ΔC^*, will occur when the ratio of the low-side pressure to the high-pressure, W, approaches zero and is zero when the ratio approaches unity. The change in mole fraction across an ideal membrane is

$$\Delta C = \Delta C^*(1 - W)$$

where

$$\Delta C = C_1 - C_0,$$

$$\Delta C^* = \frac{C_1(1 - C_1)(\alpha - 1)}{\alpha(1 - C_1) + C_1}.$$

Even when the separation factor is infinite (the membrane passes only the desired gas), the partial pressure on the high side of the membrane cannot be reduced below the pressure that is fixed for the low side.

The amount of recovery of the desired gas depends on the separation factor, the pressure ratio, and the cut. The economics of a separation system depend on the separation factor, the operating conditions for the process, and considerable ingenuity in optimizing the design of the separation unit to achieve maximum economy. The design of a unit for a binary mixture will be simpler than the design of a unit for a mixture with many gases. The separation factor tends to lose its meaning for a mixture of many gases. For a multicomponent mixture, it is more meaningful to consider the relative gas velocity instead of a separation factor. The relative gas velocity can be defined as the ratio of a gas velocity to that of the velocity of the slowest gas molecule in the mixture that passes through the membrane. If a gas is not transported through the membrane, its relative velocity will be zero.

Table 2 Mole fractions for an ideal Knudsen membrane with a 25 percent total volume cut

Gas	Relative Velocity	Mole Fraction		Individual Gas Cut
		Enriched	Depleted	
H_2	4.69	0.673	0.297	0.430
H_2O	1.57	0.003	0.006	0.172
CO	1.26	0.106	0.217	0.140
H_2S	1.37	0.003	0.006	0.128
CH_4	1.66	0.081	0.124	0.182
CO_2	1.00	0.134	0.351	0.113

Table 3 Mole fractions for a perfect membrane that passes only hydrogen with 50 percent recovery of hydrogen

Gas	Relative Velocity	Mole Fraction		Individual Gas Cut
		Enriched	Depleted	
H_2	1	1	0.243	0.5
H_2O	0	0	0.006	0.0
CO	0	0	0.235	0.0
H_2S	0	0	0.006	0.0
CH_4	0	0	0.140	0.0
CO_2	0	0	0.369	0.0

The gas components in a representative coal gas mixture are shown in Table 1. The mole fractions of the enriched and depleted streams for the maximum mole fraction change that can be obtained with an ideal Knudsen membrane are shown in Table 2, and corresponding values for a perfect membrane that passes only hydrogen are shown in Table 3. The individual gas cut is the ratio of the amount of that gas in the enriched stream to the amount of that gas in the feed stream.

Figures 1 and 2 provide graphic comparisons of model calculation for several different types of membranes. The enriched stream mole fractions for various amounts of hydrogen recovery are shown in Fig. 1. The cut, the fraction of the feed gas that passes through the membrane, needed to achieve a fractional hydrogen recovery is shown in Fig. 2. Two curves are shown for each membrane; in Fig. 1, the upper curve is for zero pressure ratio and the lower curve is for a pressure ratio of 0.233 (high-side pressure of 430 psia and low-side pressure of 100 psia); in Fig. 2, the curves are oppositely oriented, the upper curve is for a pressure ratio of 0.233 and the lower curve is for a pressure ratio of zero. These figures show the importance of a large separation factor in achieving a highly enriched recovery of hydrogen. A Knudsen membrane can produce only a moderately enriched product stream of hydro-

Nomenclature

A, and C = temperature-dependent constants
α = separation factor
C_0 = feed mole fraction
C_1 = enriched mole fraction
ΔC = $C_1 - C_0$
ΔC^* = maximum ideal value for $C_1 - C_0$
M_i = molecular weight of the ith gas molecule
F_i = flow rate in standard cc per second
v_i = molecular velocity of the ith gas molecule
ΔP_i = partial pressure drop of the ith gas molecule
P_o = standard pressure
T = temperature
T_o = standard temperature
W = pressure ratio
f_i = momentum accommodation coefficient of the ith gas molecule
l = capillary length
r = capillary radius
δ_i = radius of the ith gas molecule
t_i = the adsorbed film thickness for the ith gas molecule

Downloaded 02 Jun 2010 to 171.66.16.121. Redistribution subject to ASME license or copyright; see http://www.asme.org/terms/Terms_Use.cfm

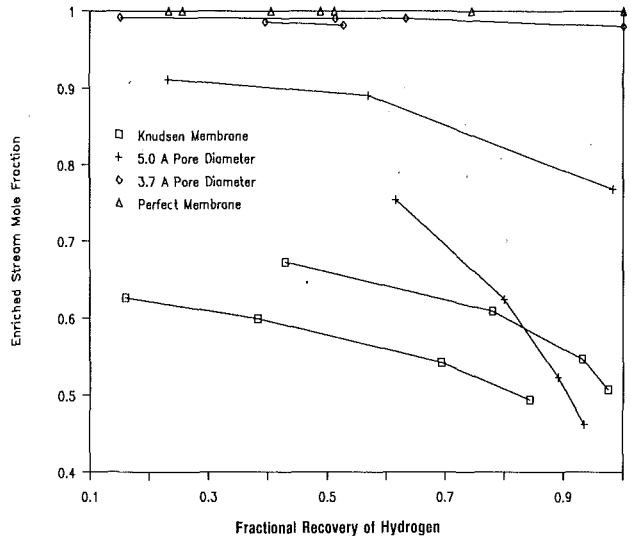

Fig. 1 Mole fraction of the enriched stream for various amounts of hydrogen recovery

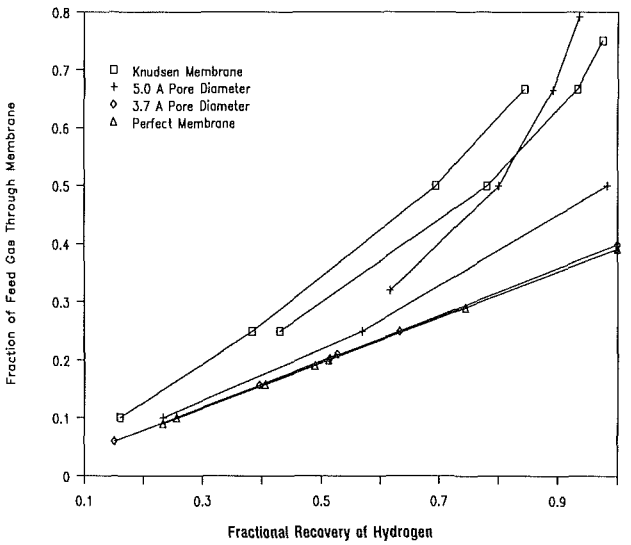

Fig. 2 Fraction of feed gas passing through the membrane to achieve a fractional hydrogen recovery

gen. The separation factor for hydrogen and carbon dioxide with a 5.0 Å pore diameter membrane is about 40; it is infinite for a 4.0 Å pore diameter. The small deviations between the 3.7 Å pore diameter and the perfect membrane shown in Fig. 2 are caused by the transport of small amounts of carbon monoxide and water.

If membranes that pass only one specific gas could be produced, then a separation unit using these specific membranes in series could be used to remove the individual gases one at a time. It is, therefore, very important to have some guidelines or a theoretical model to provide a basis for designing and developing membranes appropriate for separating individual gases.

A Simple Model for Gas Separation by Inorganic Membranes

The usefulness of any model will depend greatly on the accuracy of the assumed mechanisms for the transport process. The difficulty of the task is emphasized by the fact that there may be a multiplicity of transport mechanisms and the degree of multiplicity may vary among the different gases.

The modeling should start with and use as much as possible that which is already known. The problem of viscous laminar flow and free molecule diffusion or Knudsen flow through porous materials with pore radii down to about 100 Å is approximately solved by assuming the additivity of Poiseuille and Knudsen flow (sometimes referred to as Maxwell slip flow in this approximation) (Pollard and Present, 1948). There are other more sophisticated solutions, but this is generally adequate for porous materials.

The membranes of interest will generally have pore sizes much less than 100 Å pore radii. Thus, in the development of a model, viscous flow will be ignored. Viscous flow can be simply added later if it is needed. The equation for free molecule diffusion of a gas in a circular capillary in standard cc/sec is

$$F = 2/3\bar{v}\pi r^3 \frac{T_o \Delta P}{T P_o l}, \tag{1}$$

and the separation factor for a binary mixture is given by the ratio of the flow per unit pressure difference for each gas

$$\alpha = \frac{\bar{v}_i}{\bar{v}_i} = \sqrt{\frac{M_j}{M_i}}. \tag{2}$$

Knudsen or free molecule flow is generally considered to represent the mechanism for binary gas separation factors that approach the square root of the gas molecular weight ratio. Present and deBethune have developed an excellent theory for this type of separation (Present and deBethune, 1949). Experimental validity of the essentials of this theory has been demonstrated (Fain and Brown, 1974). This type of separation has been demonstrated repeatedly in membranes that have effective pore sizes that are very large compared to the size of the gas molecules. However, when the pore size of the membrane approaches the size of the gas molecules other considerations become important. The diffusion process associated with Knudsen flow considers the gas molecule as a point with no physical dimensions. In fact, molecules do have a finite size. As a first approximation we may consider a membrane as made up of capillaries with smooth walls and the gas molecules as hard spheres with a fixed diameter. Diffusion is a random walk process in which molecules move a given (variable) distance, then change direction in a random way, independent of the direction from which it came. The transport through the membrane by Knudsen diffusion is the product of the diffusion coefficient, the area, and the density gradient. The diffusion coefficient is proportional to the product of a mean distance between collisions with the capillary walls and the mean molecular velocity. The mean distance between wall collisions is calculated by averaging the distance from a point on the wall of a capillary to all visible points on other walls weighted by the cosine law distribution of paths from the wall's surface. At least in the first approximation, the closest approach to the capillary wall by the hard sphere molecule is the radius of the hard sphere molecule. Therefore, the actual mean distance between wall collisions for a molecule is proportional to the difference between the mean distance to a wall and the diameter of the hard sphere molecule. In the case of a capillary, it would be the difference between the capillary diameter and the molecule diameter. In addition, the area open to flow is the area calculated by using a diameter equal to the difference between the diameter of a capillary and the diameter of the hard sphere molecule. In this approximation, the diffusion coefficient and the area depend on the diameter of the gas molecule. The equation for Knudsen flow is then given by

Downloaded 02 Jun 2010 to 171.66.16.121. Redistribution subject to ASME license or copyright; see http://www.asme.org/terms/Terms_Use.cfm

$$F_i = 2/3\bar{v}\pi(r-\delta_i)^3 \frac{T_o \Delta P}{T P_o l}. \quad (3)$$

For a binary mixture, the separation factor is the ratio of the specific flows of the two components. For point molecules, the separation factor is simply the square root of the ratio of the molecular weights. For hard sphere molecules, the separation factor is

$$\alpha = \frac{(r-\delta_i)^3}{(r-\delta_j)^3}\left(\frac{M_j}{M_i}\right)^{1/2}. \quad (4)$$

The separation factor calculated for hard sphere molecules, using Eq. (4) for several binary mixtures, is shown in Fig. 3. The separation factor can become very large as the pore size approaches the size of the larger molecule. However, this figure assumes only the free molecule diffusion component of transport. The effect of the other components of transport must also be taken into account.

As the pore radii decrease below 100 Å, other transport components become significant. One of these components is usually referred to as surface flow. Surface flow is associated with the adsorption of gases on the membrane surfaces and the transport is thought of as diffusion of molecules on the surface. In addition to the enhanced flow due to the diffusion on the surface, the molecules adsorbed on the surface change the effective radius of the pores and, therefore, the amount of transport from other flow mechanism. As the pore radii become still smaller, as indicated above, the size of the molecule itself becomes significant. The effective pore radius is the pore radius minus the effective thickness of the adsorbed layer and minus the radius of the molecule. This makes the effective pore radius different for different size molecules.

We can use satistical arguments to infer the effect on the transport diameter by adsorbed molecules. In the hard sphere approximation, the effect of one monolayer of adsorbed molecules will be simply to decrease the radius of the capillary by the diameter of the adsorbed molecules. If less than a monolayer is adsorbed, sometimes the jump distance will not be affected; at other times the jump distance will be decreased by one adsorbed molecule diameter and other times the jump distance will be reduced by two adsorbed molecule diameters. On the average the jump distance will be decreased by an amount equivalent to twice the average thickness of the adsorbed layer. The average thickness will be equal to the product of the fraction of a monolayer and the thickness of a single monolayer. It follows that the effective thickness is the product of the fractional number of monolayers and the thickness of a single monolayer.

The adsorbed molecules can move around on the surface in a two-dimensional sense. This surface diffusion will contribute to the transport and for a first approximation may be considered simply additive to the gas phase diffusion. Surface diffusion is considered a two-dimensional transport with the diffusion coefficient proportional to the product of the mean velocity and the mean molecular jump distance on the surface. The flow rate is proportional to the perimeter of the flow passage and the driving force is the surface density gradient. For the current data, the adsorption of gases is much less than a monolayer. Therefore, only Henry's Law adsorption is considered. That can be modified when the adsorption is much higher.

It has been well recognized in the literature (Kennard, 1938) that there is often a variation in the momentum accommodation coefficient when molecules collide with different surfaces. This phenomenon is observed with both Maxwell slip flow and with Knudsen flow. It has generally been concluded that the effect is the same for both types of flow. However, there are theoretical and experimental data that suggest the

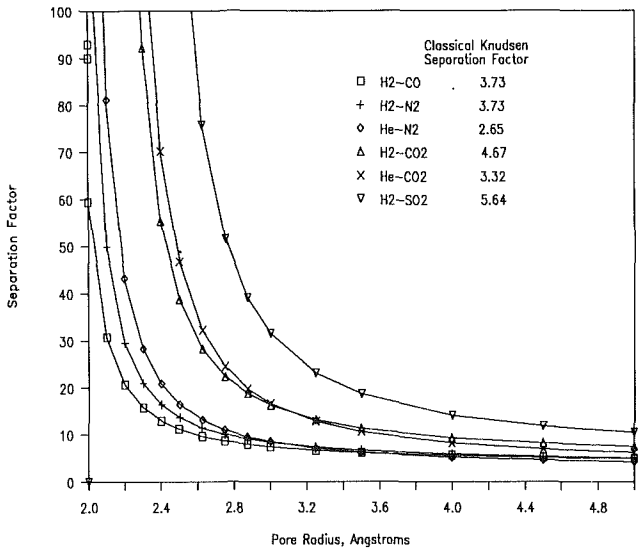

Fig. 3 Separation factors for ideal Knudsen flow of hard sphere molecules

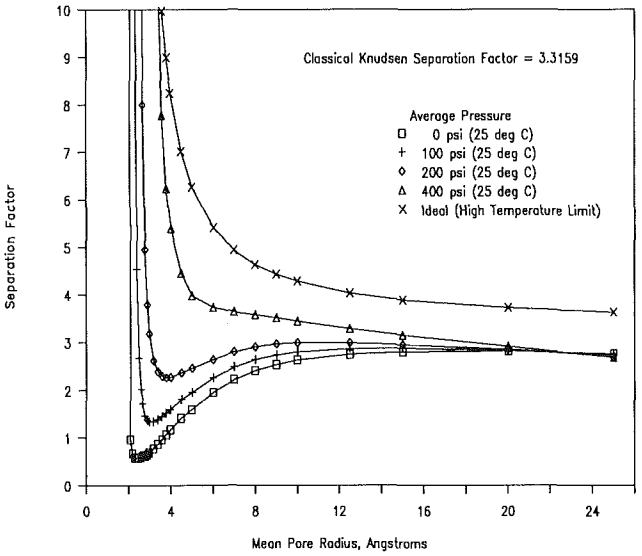

Fig. 4 He-CO_2 separation factors calculated from the transport model for individual pure gas flows

effect of accommodation coefficients less than unity is different for the two types of flow (Fain, 1981). In the transport equations the accommodation coefficients should be taken into account. The accommodation coefficient is simply a multiplicative factor on the Knudsen diffusion coefficient. The functional form of the equation that takes all of these transport mechanism into account is

$$F_i = \frac{C\bar{v}_i \Delta P_i}{Tl}(r-\delta_l-t_i-t_g)^3\left[\frac{1}{f_i}+A\left(1-\frac{\delta_i}{r}\right)^{-2}\right]. \quad (5)$$

There are several constants in Eq. (5) that have been combined into the single constant C. These constants can be estimated from various types of data, such as adsorption isotherms and single component transport measurements. These constants have been evaluated from such measurements with helium and carbon dioxide. The separation factors calculated using Eq. (5) are shown in Fig. 4 plotted against pore diameter. The initial decrease in separation factor as the pore size decreases is due to an increase in the surface flow of carbon dioxide. However, as the temperature is increased, the surface flow and

Downloaded 02 Jun 2010 to 171.66.16.121. Redistribution subject to ASME license or copyright; see http://www.asme.org/terms/Terms_Use.cfm

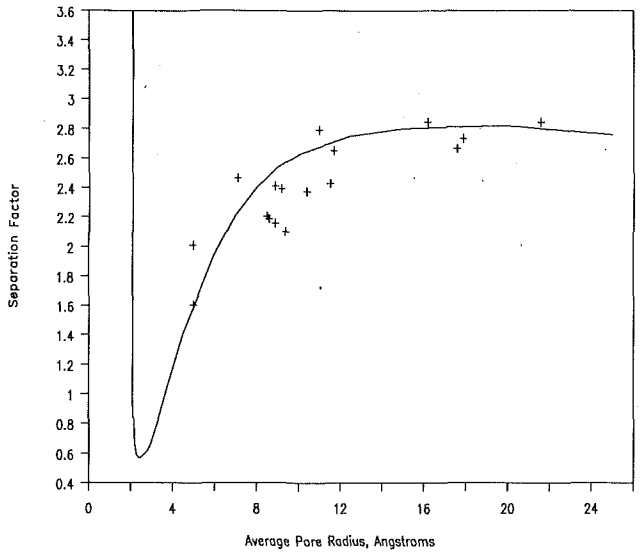

Fig. 5 Comparison of separation factors calculated from He and CO_2 pure gas flow measurements with calculations from the transport model

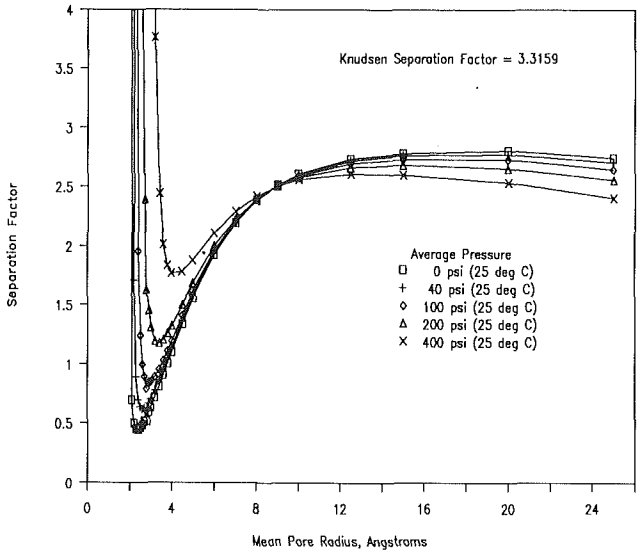

Fig. 7 He-CO_2 separation factors from the gas transport model for gas mixture flows (without momentum transfer)

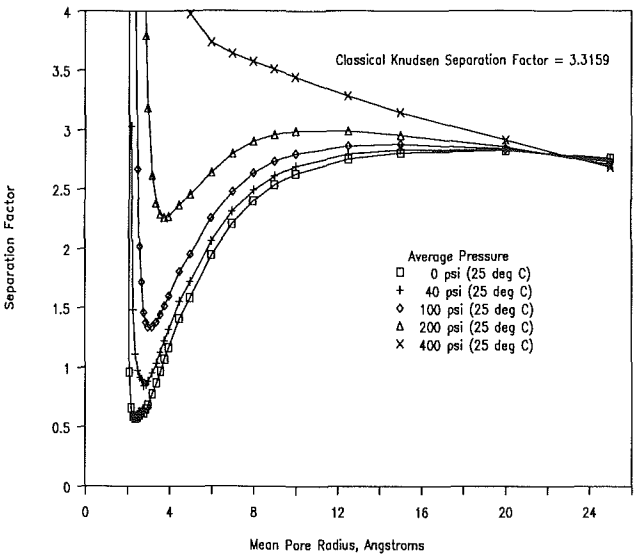

Fig. 6 He-CO_2 separation factors from the gas transport model using individual pure gas flows

adsorption of carbon dioxide should decrease and the separation factor should approach the high temperature limit estimated by Eq. (4) and shown in Fig. 3.

Experimental Results

To date in this project, a large number of alumina membranes have been fabricated and characterized. As part of the characterization, pure gas flow rates have been measured on some of these alumina membranes having mean pore diameters between 10 and 50 Å. The flow measurements were made at room temperature using helium, nitrogen, and carbon dioxide as test gases. Adsorption isotherms were also measured at room temperature. The constants needed in Eq. (5) have been approximated from these data. The separation factors calculated with these data are shown in Fig. 5 for direct comparison with the experimental data. As can be seen, the agreement between the calculated and measured separation factors is quite good.

The separation factors calculated from the model for the individual gas flows and for several pressures are again shown in Fig. 6 on a different scale. It is common practice to use the method of measuring pure gas flow rates to estimate the separation factor for a binary mixture. However, the adsorption of one gas on the walls of a membrane will also affect the transport of the other molecular component. This will be the case when an actual binary separation is measured. The separation factors for the same conditions shown in Fig. 6, but with the flow of a binary mixture, are shown in Fig. 7. The calculations in Fig. 7 take into account the effect of the adsorption on both gases, i.e., the effect of the adsorption of the carbon dioxide on the transport of the helium, which would not occur for the individual gas transport. However, no interaction or momentum exchange between the two species was considered. It is likely that momentum exchange and momentum accommodation coefficients less that unity for either or both gas molecules will occur in practice. Therefore, the separation factor in Fig. 7 show only the effects of surface flow and adsorption. A comparison of the results shown in Figs. 6 and 7 indicates the importance of making actual separation measurements at an early date to verify the assumption. Momentum exchange and variations in accommodation coefficients could make the differences even larger than shown in Figs. 6 and 7.

Conclusions

Much progress has been made in reducing the pore size of inorganic membranes and learning about the physical characteristics of these membranes. However, the experimental data alone might have suggested that the development effort would not be successful since the separation factors have been decreasing with smaller pore radii. But the mathematical model has indicated that the development work is proceeding as should be expected. With the mathematical model the data are encouraging and we have incentive and direction to vigorously continue the development effort. To achieve high separation factors for hydrogen separation from coal gas, the model clearly indicates the need for smaller pores than have been achieved to date. We believe there are techniques for reducing pore size further. A particular problem is appropriately measuring the membrane pore size to continue to track the fabrication methods and control the development process. High-temperature flow and separation measurements are expected to confirm the higher separation factors before the end of this year.

Downloaded 02 Jun 2010 to 171.66.16.121. Redistribution subject to ASME license or copyright; see http://www.asme.org/terms/Terms_Use.cfm

References

Egan, B. Z., Fain, D. E., Roettger, G. E., and White, D. E., 1992, "Separating Hydrogen From Coal Gasification Gases With Alumina Membranes," ASME JOURNAL OF ENGINEERING FOR GAS TURBINES AND POWER, Vol. 114, pp. 367–370.

Fain, D. E., and Brown, W. K., 1974, "Neon Isotope Separation by Gaseous Diffusion Transport in the Transition Flow Regime With Regular Geometries," K-1863, Union Carbide Corporation, Nuclear Division, Oak Ridge Gaseous Diffusion Plant.

Fain, D. E., 1981, "A Comparison of the Effect of Nonrandom Surface Scattering on Free-Molecule and Slip Flow Through Capillaries," *Rarefied Gas Dynamics*, Vol. 74 (Pt. 1), pp. 218–236.

Fain, D. E., Roettger, G. E., and White, D. E., 1991a, "Development of Ceramic Membranes for High-Temperature Hydrogen Separation," *Proceedings of the Fifth Annual Conference on Fossil Energy Materials*, Martin Marietta Energy Systems, Inc., Oak Ridge National Laboratory, Oak Ridge, TN, ORNL/FMP-91/1, pp. 55–64.

Fain, D. E., Roettger, G. E., and White, D. E., 1991b, "Development of Ceramic Membranes for Gas Separation—FY 1990 Development Activities," K/QT-413, Martin Marietta Energy Systems, Inc., Oak Ridge K-25 Site, Oak Ridge, TN.

Kennard, E. H., 1938, *Kinetic Theory of Gases*, McGraw-Hill, New York–London.

Pollard, W. G., and Present, R. D., 1948, *Phys. Rev.*, Vol. 73, p. 762.

Present, R. D., and deBethune, A. J., 1949, *Phys. Rev.*, Vol. 75, p. 1050.

Downloaded 02 Jun 2010 to 171.66.16.121. Redistribution subject to ASME license or copyright; see http://www.asme.org/terms/Terms_Use.cfm

Coal Mineral Matter Transformation During Combustion and Its Effects on Gas Turbine Blade Deposition and Erosion

S. Rajan

J. K. Raghavan[1]

Department of Mechanical Engineering and Energy Processes,
Southern Illinios University at Carbondale,
Carbondale, IL 62901

The reaction pathways along which mineral matter is transformed during pulverized coal combustion and the corresponding characteristics of the ash formed are especially important from the standpoint of coal-fired gas turbine operation. Using a novel FT-IR technique and EDX analysis, these mineral matter transformations are investigated when coal is burned in a pulverized coal-dust burner. The mineral transformations of quartz, gypsum, calcite, dolomite, pyrite, and those of the aluminosilicate minerals, kaolinite and montmorillonite, have been evaluated. Discussion of the results focuses on the effect of these mineral transformations on the deposition and erosive characteristics of the resulting combustion-generated ash.

Introduction

Despite technological challenges, plentiful supplies of coal, both in the U.S. and abroad, make it a viable fuel for stationary power generation via Brayton cycle turbines. This attractiveness of coal is further enhanced by the feasibility of combined cycle operation with Rankine bottoming cycles. A variety of furnaces are also currently under development for the coal-fired gas turbine, including the slagging furnace and the fluidized bed boiler among others.

Two primary objectives in the direct use of coal as a heat source for gas turbines are the mitigation of turbine blade erosion and the reduction of ash deposition in the stator and rotor blade passages. Both these factors affect the plant performance, while blade erosion also directly influences plant life. They are directly influenced by the coal ash transformation characteristics during combustion. Nor is the problem completely eliminated by coal beneficiation and deep cleaning, although the quantity and size distribution of the ash are thereby reduced.

The source for this combustion-generated ash, namely the mineral matter in coal, may be distributed throughout the coal or can occur as discrete inclusions. In low rank lignites and sub-bituminous coals, they can be bonded by ion exchangeable cations to carboxyl groups or occur as organometallic compounds. The discrete mineral phases occurring in coal often consist of quartz, calcite, gypsum, kaolinite, pyrite, etc. Higher concentrations of silicates and clays are also frequently observed as the rank of the coal increases. The types of minerals present in U.S.A. coals and their mode of occurrence are outlined by Gluskoter [1].

During combustion, the temperature and pressure history to which the mineral matter is subjected strongly influences its transformation. Depending on the type of minerals present, the ash morphology and size distribution vary. Tazaki et al. [2] suggest that this morphology results from the noncombustible mineral matter being first melted at the high coal particle temperatures, followed by cooling temperature gradients as the combustion gases flow in the vicinity of the heat exchanger tubes or turbine blade passages. Irregular hollow grains composed predominantly of aluminum and silicon were found to be most prevalent in the samples observed by these investigators. Vaporization and condensation phenomena, in conjunction with oxidation and nucleation processes, also influence the particle size distribution of fly ash from coal combustion [3]. In the drop tube studies conducted with Montana lignite by these investigators [3], the amount of metal oxides produced was significantly higher at particle temperatures of 2800 K than at particle temperatures of 2500 K. Further, the possibility exists of the more volatile mineral components condensing on the high melting point compounds, thus influencing both the size and morphology of the ash particles.

Deposits on furnace tubes and turbine blades often consists of an initial layer of dust comprised of silica and alumina particles of the order of 10 μm in size [4] or calcium and sodium sulfates 2 μm of less is diameter [5]. The stickiness of this initial layer of particles is enhanced by the presence of quartz, illite, pyrite, or hematite. For pyrites, this sticking temperature (that is, the temperature of the metal surface that signals the initiation of the particle-to-wall adhesion process) can be as low as 533 K [6]. Aluminosilicates originating from the clay minerals such as montmorillonite and kaolnite add to these

[1]Current address: Battelle Laboratories, Columbus, OH.

Contributed by the Environmental Control Division and presented in initial form at the 35th International Gas Turbine and Aeroengine Congress and Exhibition, Brussels, Belgium, June 11–14, 1990. Manuscript received by the Environmental Control Division July 19, 1991. Associate Technical Editor: H. E. Hesketh.

Copyright © 1993 by ASME
Downloaded 02 Jun 2010 to 171.66.16.121. Redistribution subject to ASME license or copyright; see http://www.asme.org/terms/Terms_Use.cfm

initial deposits and, if the temperatues are suitable, may result in glassy deposits in the outer layers.

Investigation of the mechanism of ash deposition and erosion of turbine blade passages requires a basic understanding of the coal mineral transformations occuring during the combustion process. Information on the reaction pathways of the mineral components is especially useful in forming mitigation strategies. Data on the morphology, size distribution, stickiness, and state of the ash particles, whether molten or solid, will assist in analyzing the actual turbine blade deposits to determine how deposits and erosion may be reduced. Therefore, the objective of the present work was to investigate the transformation of selected minerals considered important from the standpoint of ash formation, adhesion, and deposition during pulverized coal combustion. Emphasis is placed on analyzing the reaction pathways of the mineral transformations and their subsequent impact on deposition and erosion.

The minerals investigated are the aluminosilicate clay minerals illite, kaolinite, and montmorillonite, the silicate mineral quartz, the carbonate minerals calcite and dolomite, and the sulfate mineral gypsum. While a variety of analytical techniques have been used in the past including x-ray diffraction analysis [7, 8], x-ray absorption fine structure spectroscopy [9], Mossbauer spectroscopy, scanning auger microprobe and secondary ion mass spectroscopy [2], etc., very little effort has been made to utilize the recent advances in Fourier Transform Infrared (FTIR) spectroscopy in mineral matter analysis. The analysis technique used in the present investigation is based on the work by Painter et al. [10] for the above minerals. Energy dispersive x-ray analysis was also employed to detect the elements Al, Si, S, Cl, K, Ca, and Fe. Analysis of mineral transformations and subsequent deposition characteristics are examples of problems where the FTIR and EDX techniques can be of assistance to designers of combustion turbine blades, blade clearance passages, etc.

The selected coal was burned in a unique one-dimensional coal-dust–air flame supported on a burner of the type used previously by Milne et al. [11]. The coal was burned under a rich stoichiometry since this is an essential condition required for good flame stability. In addition, during staged combustion in modern furnaces, coal is burned first under fuel-rich conditions in the burner first stage followed by fuel-lean combustion to reduce the production of nitrogen oxides instrumental in smog production and acid rain deposition. The raw coal and the ash samples collected at different burner heights have been analyzed to determine the mineral matter transformations during combustion. The data are interpreted with particular reference to adhesion, deposition, and erosion of metal surfaces. Details of the experimental apparatus, techniques used, and the results obtained are given in the following sections.

Apparatus and Experimental Techniques

(a) Apparatus. The combustion tests were performed under controlled laboratory conditions in order to minimize the specific influences of a particular furnace design such as flow patterns, turbulence characteristics, etc. Hence, a one-dimensional coal-dust–air burner shown schematically in Fig. 1 and employed in previous investigations by Milne and et al. [11] and Altenkirch et al. [12] was selected for the experiments. The coal used in the experiments was an Illinois No. 6 coal with the proximate and ultimate analyses as shown in Table 1. A suspension of fine coal ground 90 percent $<$ 325 mesh was fed from a fluidized bed-coal-dust feeder as shown in Fig. 1. The off-take tube from this coal-dust feeder conveyed a fine suspension of coal-dust in air to the base of the burner where additional combustion air was supplied. A uniform coal feed rate to the burner was ensured by controlling the back pressure of the fluidized bed feeder, which is mounted on a load cell to monitor weight loss changes. During the experiments, it was found necessary to vibrate both the fluidized bed coal feed column, and the burner body on which the flame was stabilized. All air flows were metered with rotameters as shown.

Using a 0.46 cm i.d. stainless steel water cooled probe to which a Pt/Pt 13 percent Rh thermocouple was attached for temperature measurement, gas and particulate samples were extracted from different heights of the coal-dust air flame. The solid ash and unburned coal particles were collected on teflon membranes for the analysis of the mineral matter transformations using FT-IR spectroscopy and energy dispersive x-ray analysis techniques.

(b) Low-Temperature Ashing. To ensure that any residual unburned organic constituents did not interfere with the mineral matter determinations, the raw coal, as well as the

Table 1 Bands used for subtraction

Mineral	Characteristic bands
Quartz	1080, 798, 778
Kaolinite	1030, 1015
Calcite	872, 712
Illite	1025, 1122
Montmorillonite	1034
Dolomite	883, 723
Gypsum	667, 603

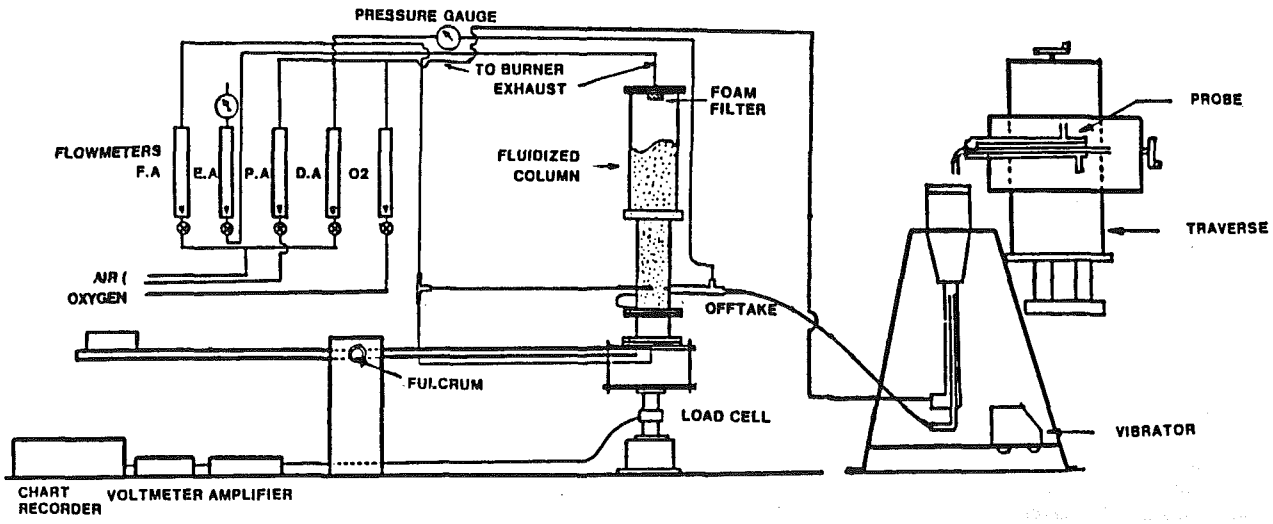

Fig. 1 Layout of experimental coal-dust burner

Downloaded 02 Jun 2010 to 171.66.16.121. Redistribution subject to ASME license or copyright; see http://www.asme.org/terms/Terms_Use.cfm

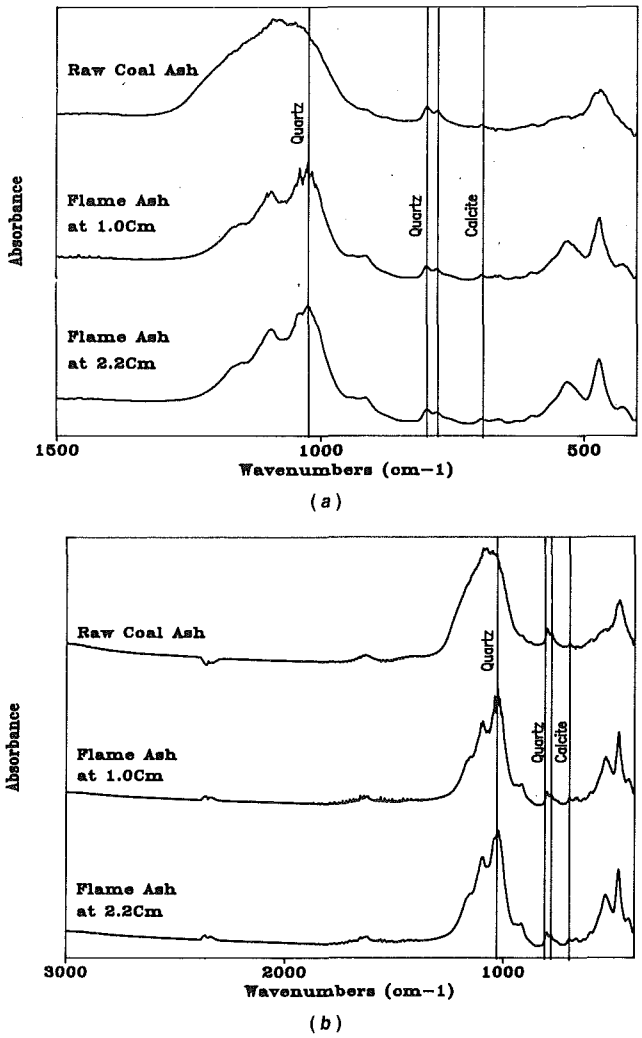

Fig. 2 FT-IR spectra of mineral matter in unburned coal and flame-generated ash samples

combustion-generated ash samples, were subjected to a low-temperature ashing process. Approximately 50 to 75 mg of the sample particulates were ashed in a single chamber oxygen-plasma furnace using the procedures of Frazer and Belcher [13]. The oxygen pressure, flow rate, and radio-frequency power level were of the same range as that used by Frazer and Belcher, and the ashing procedure was usually carried out for a period of 36 hours at 100°C. The residues left behind after the low-temperature ashing procedure were verified to be free of organic components.

(c) FT-IR Analysis. The solid ash from the low-temperature ashing process was analyzed to determine the koalinite, illite, montmorillonite, gypsum, quartz, and calcite concentration using FT-IR spectroscopy. Since the primary objective was to be able to quantify these minerals present in the ash sample, it was very important that accurate weighings and consistent sample preparation procedures were adopted. Typically about 0.2–0.4 mg of the low temperature ash was mixed with 250 mg of KBr and ground for 25 minutes in a Wig-L-Bug grinder. The grinding was done in cycles of 10–10–5 minutes to prevent overheating. The mixture was pressed into a pellet form using a press and die at 12,000 psi. The pellet was inspected for defects and stored carefully in a desiccator before recording the spectra.

A Nicolet 20Dx FT-IR spectrometer was used to obtain two hundred scans of interferograms of the pellet sample in the mid-IR region. These interferograms were then averaged and Fourier transformed to obtain the spectra. The spectra were baseline corrected and normalized and then transferred to an IBM computer system for spectral processing. For the purpose of quantification of the various minerals present in the coal ash sample, the spectral subtraction procedure of Painter et al. [10] has been used. In this procedure the spectrum of a known standard mineral, like quartz, gypsum, etc., is subtracted successively from the spectrum of the low temperature ash of the sample. The spectra of the pure mineral, referred to as standard spectra, were obtained by the same method as that of the low-temperature ashed coal samples. Due to the impurities present in the clay samples of kaolinite, illite, and montmorillonite, the spectra of these minerals were repeated several times before a fairly consistent spectrum was selected to be used as a standard for spectral subtraction. Other minerals like quartz and gypsum were obtained with less labor.

(d) Spectral Analysis of Mineral Matter. The baseline corrected and normalized spectra of the low-temperature ash obtained from the unburned raw coal, and combustion-generated samples at heights of 1.0 and 2.2 cm within the flame, are shown in Fig. 2. Figure 2(*a*) shows the full spectrum as measured in the mid-IR region, while in Fig. 2(*b*) the portion of the spectrum between 1500 and 400 cm^{-1} has been shown expanded for clarity. The spectra incorporate the characteristic mineral peaks required for the quantitative evaluation of the various minerals.

Quantitative determination of the mineral matter concentrations from the spectra such as those shown in Fig. 2 was accomplished by processing the band intensity data using specialized computer software. This is illustrated in Figs. 3 and 4 with respect to the quantitative measurement of the quartz and kaolinite concentrations, respectively. The unburned coal mineral matter spectrum is shown in the middle curve in Fig. 3, above which is the standard spectrum of quartz. The characteristic bands attributable to quartz occur at 1080, 798, and 778 cm^{-1} as indicated by the arrows in the quartz standard spectrum. The intensities of these bands are directly in proportion to the quartz concentration in the standard. By successive trial and error procedures or by software-controlled sequential operation, a constant is determined with which the standard quartz spectrum is multiplied and the product thus obtained is subtracted from the raw coal spectrum, such that the intensities of the quartz peaks at 1080, 798, and 778 cm^{-1} are eliminated from the raw coal spectrum. If this constant K is too high, the quartz bands in the raw coal spectrum will become negative, while too small a constant will result in residual intensities in the quartz bands. The bottom curve in Fig. 3 shows the raw coal spectrum with the wide arrows indicating the locations where the quartz bands have been subtracted out and the slope of the curve at 1080, 798, and 778 cm^{-1} is zero. The quartz concentration is then determined as discussed below from Eq. (1).

The presence of kaolinite ($Al_4Si_4O_{10}(OH)_8$) is indicated by a variety of bands at 3695, 3620, 1100, 1030, 1015, 913, 797, 753, 537, and 473 cm^{-1} [14]. However, many of these bands overlap with those from other species resulting in interference in the subtraction procedure outlined above. Hence following Painter et al. [10], the bands at 1030 and 1015 cm^{-1} have been employed exclusively for quantitative determination of kaolinite. Figure 4 shows the mineral matter spectrum of the flame-generated ash sampled at 2.2 cm height within the flame in the curve at the center of the figure. The bottom spectrum illustrates the result of subtracting out the kaolinite standard bands shown at the top of the figure. Table 1 enumerates the characteristic bands employed in this work to identify the minerals under investigation.

(e) Data Analysis and Quantification. The mineral standards were individually subtracted from the spectra obtained with the raw coal and the ash samples collected from within

Downloaded 02 Jun 2010 to 171.66.16.121. Redistribution subject to ASME license or copyright; see http://www.asme.org/terms/Terms_Use.cfm

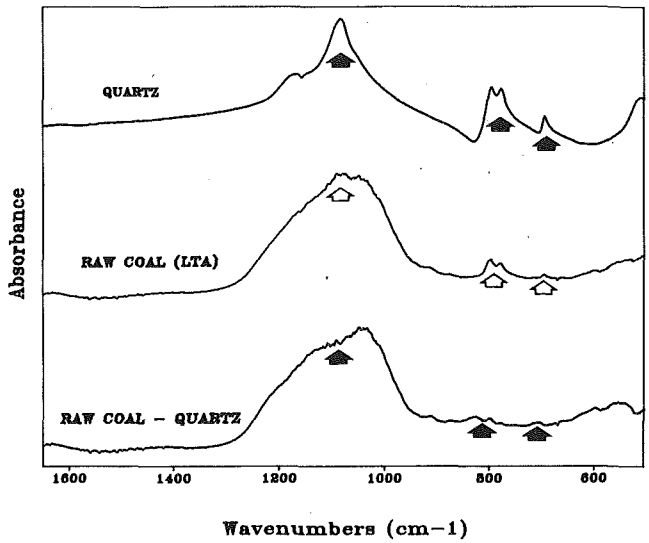

Fig. 3 Method of Quantitative determination of quartz in raw coal

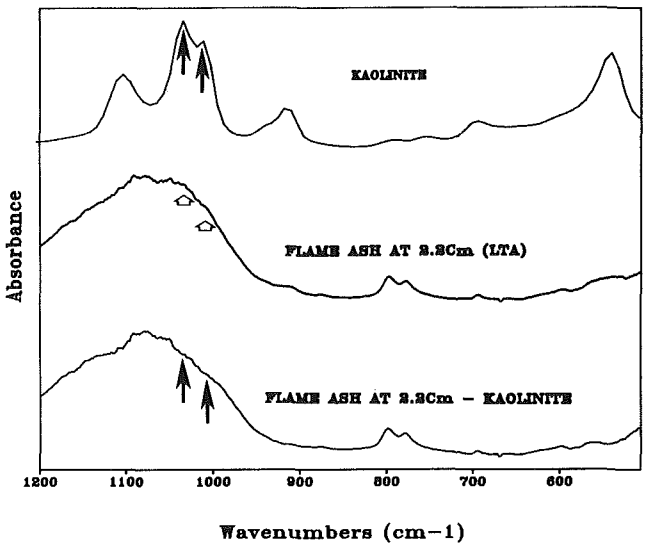

Fig. 4 Quantitative determination of kaolinite in flame-generated sample

the flame. Since the concentration of the individual standards was known, the weight fraction of the minerals in the low-temperature ash mixture is than given by:

$$y_m = K * W_s / W_m \quad (1)$$

where K = subtraction factor, obtained by eliminating the contribution of the standard in the mixture.

W_s = weight of the standard (mg)

W_m = weight of the mixture (mg)

Another technique of quantitatively evaluating the concentrations of the minerals present is to fit the spectra of a number of mineral standards to the spectrum of the test ash sample by a least-squares analysis procedure [15]. Although it has been reported that the least-squares technique of estimation gives a better accuracy in quantification, it is also known that the least-squares technique requires an extensive library of standard spectra and spurious analysis of low-concentration components must be carefully avoided. However, the accuracy of estimation using the spectral subtraction procedure as described above is essentially the same as that of the least-squares technique and is considered better than other analytical procedures such as x-ray diffraction [5, 6, 8]. It was therefore adopted in the present analysis.

Table 2 Proximate and ultimate analysis of the raw coal

Proximate Analysis:	
Moisture	3.82 percent
Fixed carbon	58.60 percent
Vol. matter	34.29 percent
Ash	3.75 percent
Ultimate Analysis:	
Carbon	75.04 percent
Hydrogen	4.94 percent
Nitrogen	1.82 percent
Oxygen.	18.20 percent

Table 3 Analysis of sulfur forms in raw coal

Total sulfur	0.8400 percent
Organic sulfur	0.5473 percent
Sulfate sulfur	0.0333 percent
Pyritic sulfur	0.2594 percent

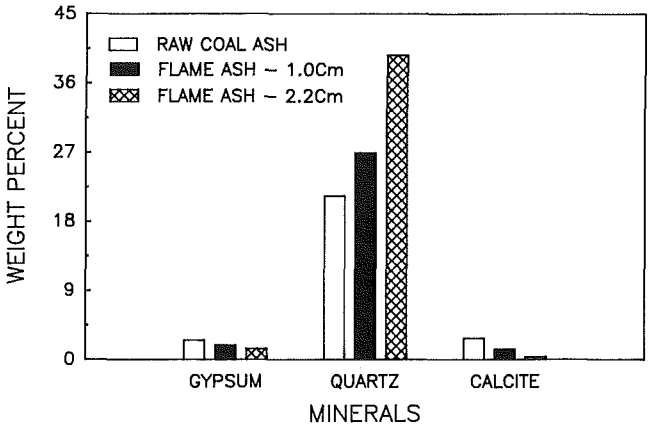

Fig. 5 FT-IR data on quartz, gypsum, and calcite concentration variations during combustion

Results and Discussion

The proximate and ultimate analyses of the raw coal used in the present experiments are shown in Table 2. The ash content of the coal is 3.75 percent. Of this 3.75 percent, and SEM-EDX analysis of the raw coal indicates a high percentage of silicon (32 percent) and aluminum (16.5 percent). The raw coal also contained 6.4 percent iron, 3.3 percent potassium and 2.1 percent calcium compounds. Its sulfur content was 11.04 percent. All these percentages are with reference to the 3.75 percent total ash content. Its rather high sulfur content in comparison to the iron present indicates that most of the sulfur is organically bound. This is borne out by the sulfur forms analysis shown in Table 3, where more than half the total sulfur present is found to exist inorganic form. Other possible modes of occurrence of sulfur species common in Illinios coals include pyrite and gypsum.

Effect of Combustion on Mineral Matter

Quartz Transformations. The combustion-derived transformations of quartz, gypsum, and calcite, as determined from the FT-IR analysis, are illustrated in Fig. 5. Quartz is one of the major components of the test coal, and its concentration is observed to increases in the combustion ash samples. In bituminous coals, which contain a relatively high proportion of the vitrinite macerals, the quartz mineral inclusions are generally distributed throughout the coal matrix. During combustion of these high vitrinite content coals, the probability of cenosphere formation is high and fine molten quartz particles adhere to the inner walls of the receding cenospheres as the organic constituents are burned away. With the final collapse of the cenosphere walls, the molten quartz layers coalesce to form ash droplets, Fig. 6.

Downloaded 02 Jun 2010 to 171.66.16.121. Redistribution subject to ASME license or copyright; see http://www.asme.org/terms/Terms_Use.cfm

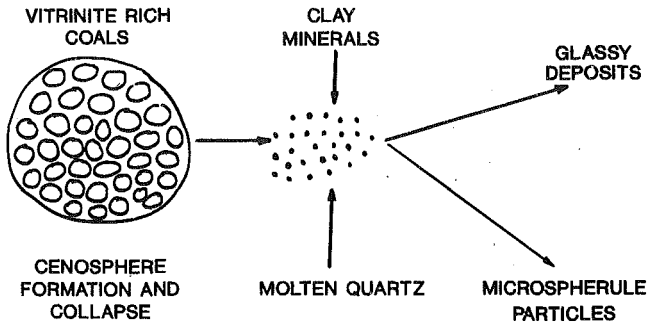

Fig. 6 Quartz transformations during combustion

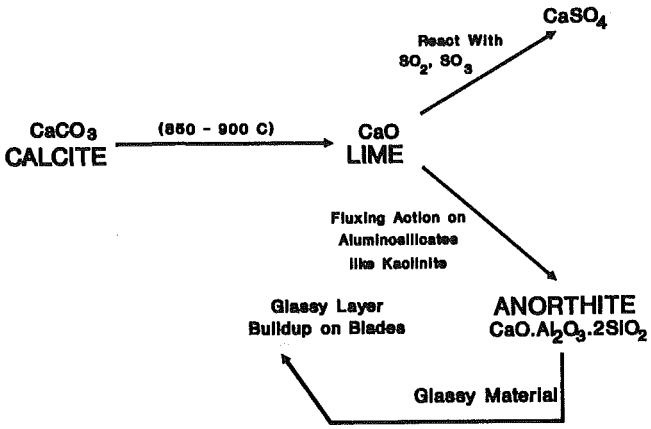

Fig. 7 Combustion-influenced calcite transformations

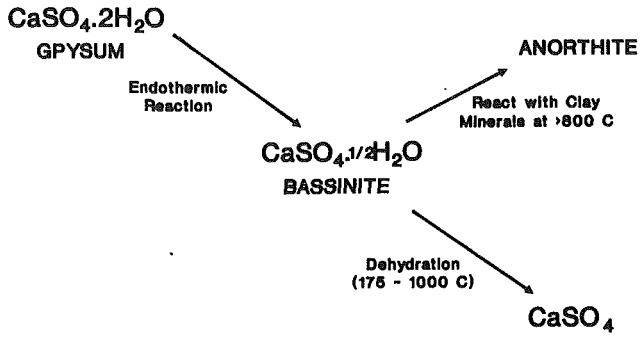

Fig. 8 Reaction pathway for gypsum transformations

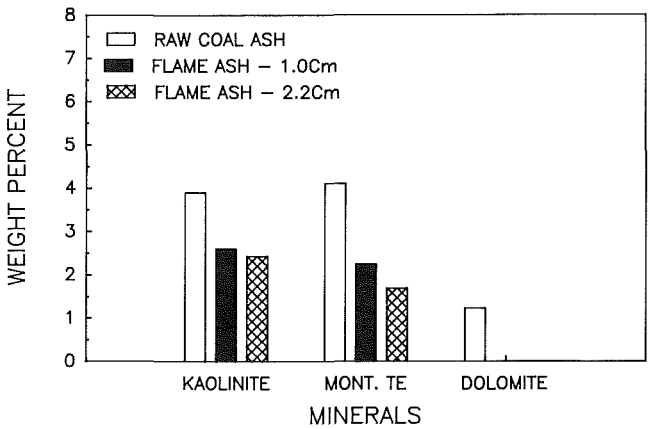

Fig. 9 FT-IR data on kaolinite, montmorillonite, and dolomite concentration variations during combustion

In experiments where the low-temperature ash from coals has been heated progressively from 400°C to 1400°C at 100°C intervals [16], it was found that quartz persisted in original form up to 1100°C, while at temperatures of 1200°C and beyond it transforms to a glass. However, during actual furnace operation, the combustible organic components of coal subject the quartz to different temperature histories in the presence of other minerals and clays. Due to the rich stoichiometry of the present tests, gas temperatures as high as 1000°C were measured, and it is estimated that particle temperatures were in the neighborhood of 1100–1200°C. At these and higher temperatures, other minerals can be incorporated into the amorphous quartz matrix to form slag or microspherule particles [2], Fig. 6. Should the temperature be high and the particles arrive in the molten state at the turbine blades, a combination of impaction and viscosity effects will determine the buildup of the ash layer on the blades. At lower temperatures, these microspherule particles would have solidified upon arrival at the turbine blade passages and the concern here would be its erosive characteristics.

Gypsum and Calcite Transformations. The transformation of the calcium-bearing mineral gypsum ($CaSO_4 \cdot 2H_2O$) and calcite ($CaCO_3$) can also be deduced from Figs. 5, 7, and 8. With the simultaneous formation of sulfur compounds from the oxidation of the coal sulfur during the combustion process some of the calcite is converted to calcium sulfate. The concentration of calcite in the original coal is quite small, and depending on its dispersion in the coal matrix and its association with other minerals, the calcite is transformed along a variety of pathways. One valid change is simply to convert to lime CaO, which occurs around 850–900°C, Fig. 7. Some of this CaO reacts with sulfur in the char and oxygen to form calcium sulfate. A competing reaction is the incorporation of the lime in molten clays to form anorthite ($CaO \cdot Al_2O_3 \cdot 2SiO_2$), which is a lower melting silicate brought about by the fluxing action of calcite on the clay minerals such as kaolinite. This aluminosilicate glass can arrive as fly ash at the turbine blades and will adhere to the initial sticky deposit layers contribution to deposit buildup.

The known thermal behavior of gypsum [7, 16] suggests that the weight loss characteristics observed in Fig. 5 are partially the result of endothermic dehydration reactions, which occur in two steps, Fig. 8. Bassinite ($CaSO_4 \cdot 1/2\ H_2O$) is first formed, followed by complete dehydration to anhydrite ($CaSO_4$) in the low-temperature regions of the flame at temperatures of about 175–1000°C, depending on residence time–temperature history. The bassinite formed during dehdyration can react with clay minerals to form anorthite at particle temperatures above 800°C.

Dolomite and Aluminosilicate Mineral Transformations. The FT-IR data of Fig. 9 show that dolomite, the other possible calcium-bearing mineral, is initially present in very small quantities in the coal tested, but is not detected in the flame ash samples. The Ca, Mg carbonates are transformed to the oxides and travel along reaction pathways similar to the oxides from calcite and gypsum. Also shown in Fig. 9 are the compositional changes due to the aluminosilicate clays kaolinite and montmorillonite. No illite was detected in the original coal sample. Initial weight loss changes of the montmorillonite result from dehydration between 100–150°C followed by dehydroxylation. Dehydroxylation of the kaolinite produces metakaolinite. Further decomposition of both the montmorillonite and kaolinite yields in some instances free quartz, which could also be contributing to the increase in the quartz concentration of the flame ash samples observed in Fig. 5. The breakdown of the kaolinite and montmorillonite structures at the higher temperature regions within the flame, especially in the presence of iron and calcium compounds that act as fluxing agents, results in the formation of glassy deposits. These transformations are illustrated in Fig. 10.

Downloaded 02 Jun 2010 to 171.66.16.121. Redistribution subject to ASME license or copyright; see http://www.asme.org/terms/Terms_Use.cfm

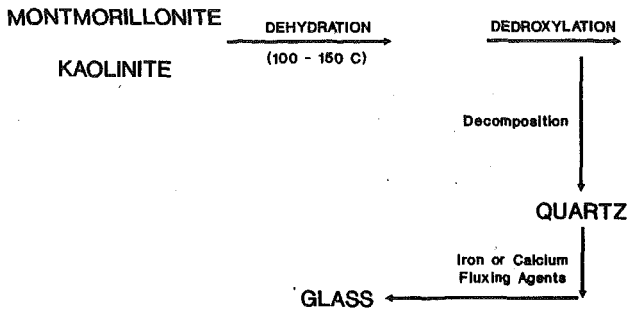

Fig. 10 Reaction pathways for clay mineral transformations

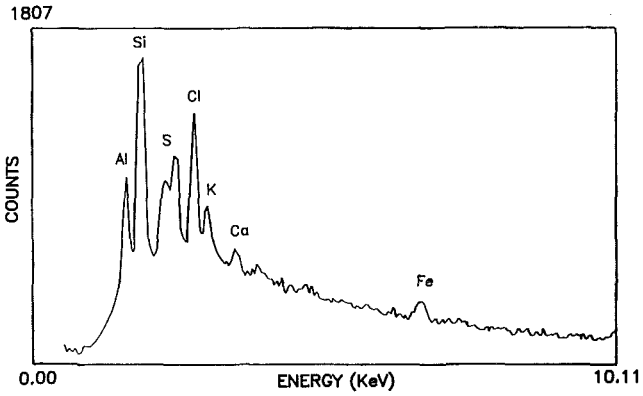

Fig. 11 EDX elemental data on unburned coal

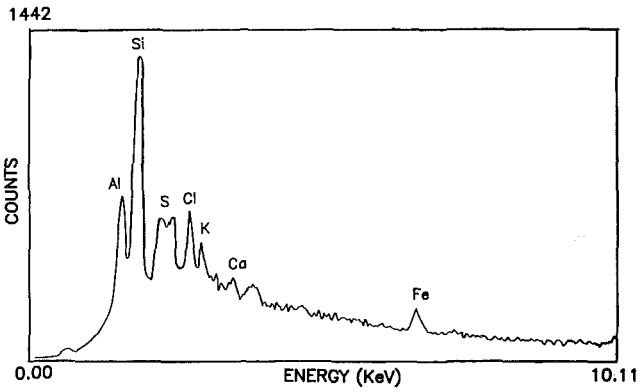

Fig. 12 EDX elemental data on combustion-generated ash at 2.2 cm height in burner

EDX Elemental Results. Figures 11 and 12 show the distribution of the predominant species in the raw coal and the combustion sample, respectively, at a height of 2.2 cm in the flame as determined by the energy dispersive x-ray analysis. Silicon is the most abundant component, followed closely by aluminum residing mostly in the quartz, and the aluminosilicate mineral kaolinite and montmorillonite. Trace amounts of sodium were detected in the coal, on the order of 1 percent of the total mineral content, while 3.25 percent of the mineral matter in the raw coal was potassium. Since illite is considered as the most likely source of potassium in bituminous coals, and no illite was detected in the FT-IR analysis, it is suspected that the potassium is probably connected via carboxyl-bound sites through a cation exchange process as in lower rank coals.

The fate of the alkali species during combustion is illustrated in Fig. 13. During combustion, the alkaki species tend to vaporize, forming the hydroxide, which in the presence of sulfur species converts to the sulfate. These molten alkali sulfates are transported in the hot combustion gases and can cause rapid

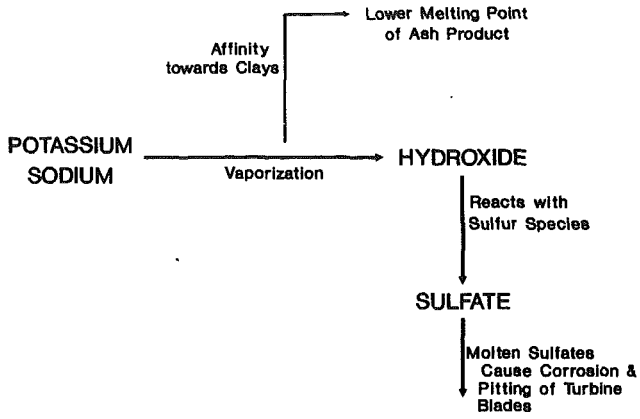

Fig. 13 Fate of the alkali metals

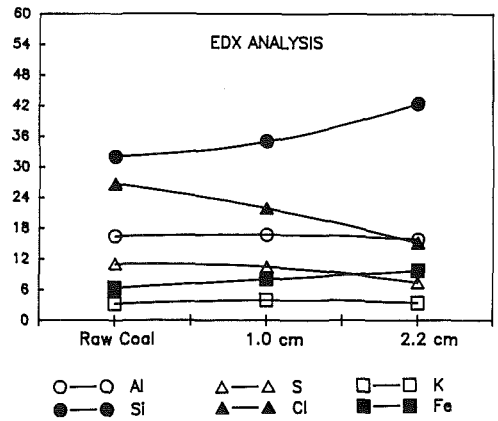

Fig. 14 Variation of significant elemental species along burner height

deterioration and corrosive pitting of turbine blades if present in sufficient quantity. The volatile alkaki also have a strong affinity toward the clay minerals kaolinite, montmorillonite, etc. by which they are absorbed, thereby lowering the melting point of the final ash product [4, 16]. The EDX data indicate that the potassium concentration in the burned samples has in fact increased slightly implying not that its mass has increased, but that there is very little loss of potassium through vaporization.

Figure 14 compares the concentrations of various elements as they are transformed at different heights in the flame. The increase in quartz concentration in Fig. 14 is again the result of the quartz melting but being retained in the coal ash, while other minerals have indeed been reduced in concentration. Reduction of the chlorine and sulfur in the ash samples is expected, HCl being considered the primary vehicle for the release of chlorine compounds, although a thorough investigation that we conducted also indicates the formation of metallic chlorides [17]. Sulfur compounds produced are generally the oxide SO_2 and SO_3.

Iron Transformations. A noticeable increase in the iron concentration in Fig. 14 signals some interesting transformations. In bituminous coals, pyrite is a common mode of occurrence, and the sulfur forms analysis in Table 3 does indicate 0.26 percent pyritic sulfur in the raw coal. Pyrite transformations during coal combustion are characterized by both exothermic and endothermic reactions, Fig. 15. Initial dissociation to pyrrhotite ($Fe_{(1-x)}S$) is endothermic, and it has been suggested that it occurs in two stages [18]. This is followed by melting and exothermic oxidation to the magetite, which occurs at the fairly low gas temperatures measured in the coal-dust flame. Furnace and turbine blade deposits are often found to

Downloaded 02 Jun 2010 to 171.66.16.121. Redistribution subject to ASME license or copyright; see http://www.asme.org/terms/Terms_Use.cfm

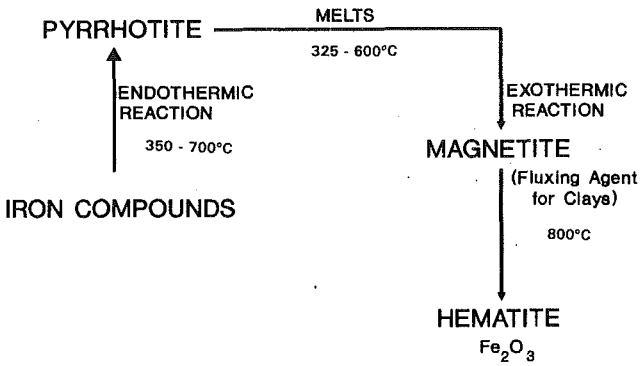

Fig. 15 Reaction pathway for iron transformations

contain an initial iron-rich layer due to the adhesion of the molten iron oxide (Fe_3O_4) to the cooler walls. In addition, the magnetite and other iron oxides act as fluxing agents for quartz and clays promoting glassy deposit formation. Magnetite reverts slowly to hematite (Fe_2O_3) at lower temperatures. Hence from the standpoint of deposit formation and blade performance, iron compounds play a very important part and should be extracted from the combustion gases before expansion in the turbine blades. This could be accomplished up front via coal beneficiation or during combustion as with the slagging combustor.

Conclusions

The FT-IR technique employed for the quantitative determination of clays and other mineral matter in coal offers a reliable method for the quantitative determination of these minerals. Supplemented by the EDX analysis used in this investigation, a comprehensive picture of mineral matter transformations during coal combustion can be obtained. With particular reference to turbine blade erosion and deposition, the data show that (*a*) the clay minerals are important from the standpoint of being the precursors for microspherule particulate formation as well as glassy deposit buildup, (*b*) both iron compounds and alkali metals can act as fluxing agents reducing the melting point of the glassy deposits, and (*c*) pyrite transformations are especially significant, as they are responsible for the initial deposit layer because of the melting point compounds formed and their fairly low sticking temperatures.

References

1 Gluskoter, H. J., "An Introduction to the Occurrence of Mineral Matter in Coal," in: *Ash Deposits and Corrosion Due to Impurities in Combustion Gases*, R. W. Bryers, ed., Hemisphere Publishing Corporation, 1978, pp. 3–19.

2 Tazaki, K., Fyte, W. S., Sahu, K. S., and Powell, M., "Observations on the Nature of Fly Ash Particles," *Fuel*, Vol. 68, 1989, pp. 727–734.

3 Neville, M., Quann, R. J., Haynes, B. S., and Sarofim, A. F., "Vaporization and Condensation of Mineral Matter During Pulverized Coal Combustion," *Proceedings, Eighteenth Symposium (International) on Combustion*, The Combustion Institute, 1981, pp. 1267–1274.

4 Bryers, R. W., "The Fate of Mineral Matter in Coal After Combustion," *Proceedings, International Symposium on Coal Combustion*, Beijing, China, 1987, pp. 101–108.

5 Zygarlicke, C. J. Steadman, E. N., Benson, S. A., and Puffe, W. H., "Studies of Transformations of Inorganic Constituents in a Texas Lignite During Combustion," *ACS Division of Fuel Chemistry Preprints*, Vol. 34, No. 2, 1989, pp. 355–361.

6 Austin, L. G. Abbott, F., and Kinneman, W. P., "Upper Wall Slag Deposits From American Coals in Utility Boilers: A Progress Report on Recent Work," *Journal of the Institute of Energy*, Dec. 1986.

7 Mitchell, R. S., and Gluskoter, H. J., "Minerology of Ash of Some American Coals: Variations With Temperature and Source," *Fuel*, Vol. 55, 1976, pp. 90–96.

8 Paulson, L. E., Beckering, W., and Fowkes, W. W., "Separation and Identification of Minerals From Northern Great Plains Province Lignite," *Fuel*, Vol. 51, 1972, pp. 224–227.

9 Huffman, G. P., Huggins, F. E., Levasseur, A. A., Durant, J. F., Lytle, F. W., and Mehta, A., "Investigation of Atomic Structures of Calcium in Ash and Deposits Produced During the Combustion of Lignite and Bituminous Coal," *Fuel*, Vol. 68, 1989, pp. 238–242.

10 Painter, P. C., Coleman, M. M., Jenkins, R. G., Whang, P. W., and Walker, P. L., "Fourier Transform Infrared Study of Mineral Matter in Coal. A Novel Method of Quantitative Mineralogical Analysis," *Fuel*, Vol. 57, 1978, pp. 337–344.

11 Milne, T. A., Beachey, J. E., and Greene, F. T., "Direct Mass Spectrometric Sampling of Corrosion-Related Species From Laboratory Pulverized Coal-Air Flames," *Proceedings of the International Conference on Ash Deposits and Corrosion From Impurities in Combustion Gases*, R. W. Bryers, ed., Hemisphere Corporation, 1978, pp. 217–231.

12 Altenkirch, R. A., Peck, R. E., and Chen, S. L., "The Appearance of Nitric Oxide and Cyanide in One-Dimensional Coal Dust/Oxidizer Flames," *Combustion Science and Technology*, Vol. 20, 1978, pp. 49–58.

13 Frazer, F. W., and Belcher, C. B., *Fuel*, Vol. 52, 1973, p. 41.

14 Van der Marel, H. W., and Beutelspacher, H., in: *Atlas of Infrared Spectroscopy of Clay Minerals and Their Admixtures*, Elsevier, 1976.

15 Painter, P. C., Rimmer, S. M., Snyder, R. W., and Davis, A., "A Fourier Transform Infrared Study of Mineral Matter in Coal: The Application of a Least Squares Curve-Fitting Technique," *Applied Spectroscopy*, Vol. 35, No. 1, 1981, pp. 102–106.

16 O'Gorman, J. V., and Walker, P. L., "Thermal Behavior of Mineral Fractions Separated From Selected American Coals," *Fuel*, Vol. 52, 1973, pp. 71–79.

17 Rajan, S., and Koropchak, J., "Chlorine Species Transformation Under Fuel-Rich Reaction Conditions," Final Report, submitted jointly to CRSC and EPRI, 1988.

18 Srinivasachar, S., Helble, J. J., and Boni, A. A., "A Physical and Chemical Basis for Understanding Inorganic Mineral Transformations in Coals Based on Model-Mineral Experiments," *197th ACS National Meeting*, 1989, pp. 347–351.

Downloaded 02 Jun 2010 to 171.66.16.121. Redistribution subject to ASME license or copyright; see http://www.asme.org/terms/Terms_Use.cfm

J. Kim

M. G. Dunn

A. J. Baran

Calspan Corporation,
Advanced Technology Center,
Buffalo, NY 14225

D. P. Wade

E. L. Tremba

Defense Nuclear Agency,
Alexandria, VA 22310-3398

Deposition of Volcanic Materials in the Hot Sections of Two Gas Turbine Engines

This paper reports the results of a series of tests designed to determine the melting and subsequent deposition behavior of volcanic ash cloud materials in modern gas turbine engine combustors and high-pressure turbine vanes. The specific materials tested were Mt. St. Helens ash and a soil blend containing volcanic ash (black scoria) from Twin Mountain, NM. Hot section test systems were built using actual engine combustors, fuel nozzles, ignitors, and high-pressure turbine vanes from an Allison T56 engine can-type combustor and a more modern Pratt and Whitney F-100 engine annular-type combustor. A rather large turbine inlet temperature range can be achieved using these two combustors. The deposition behavior of volcanic materials as well as some of the parameters that govern whether or not these volcanic ash materials melt and are subsequently deposited are discussed.

Introduction

During the past ten years, there have been several instances in which commercial aircraft have traversed volcanic dust clouds with potentially disastrous results. Some notable instances are the 1980 Trans America Lockheed L-382 aircraft (Allison T56 turboprop engines) encounter with the Mt. St. Helens volcanic cloud near Seattle, WA, the June, 1982, encounter of a British Airways Boeing 747 aircraft (Rolls Royce RB-211 engines) and a Singapore Airlines Boeing 747 aircraft (Pratt and Whitney JT9-D engines) with volcanic clouds from the Mt. Galunggung volcano near Bandung, Indonesia, and the December, 1989, encounter of a KLM Boeing 747 aircraft (General Electric CF6 engines) with the Mt. Redoubt volcanic cloud near Anchorage, AK. In all instances, substantial deposition on the engine hot section components was experiences, which caused significant difficulty in operating the engines (Campbell, 1990).

Previous measurement programs (Dunn et al., 1987a, b; Batcho et al., 1987) have indicated that some of the effects leading to engine damage and possibly engine failure when traversing dust clouds are: (1) compressor erosion resulting in the loss of surge margin, (2) deposition of glassified material on engine hot section components reducing flow area at the high-pressure turbine inlet, (3) partial or complete blockage of combustor fuel nozzles adversely influencing atomization, and (4) partial or complete blockage of vane and blade cooling air holes influencing metal temperature. Situations arise for which it is important to determine quickly and inexpensively the behavior of specific soil and volcanic materials while traversing an engine. Rather than investing the time and money required to obtain an appropriate engine, it was decided that a HSTS made from the hot sections of representative engines would provide a realistic environment in which to perform the necessary measurements. From this perspective, the T56 HSTS represents the older can-type combustors and the F-100 HSTS represents the more modern annular-type combustors. Damage modes 2, 3, and 4 described above can be tested in such systems relatively quickly and inexpensively. Furthermore, effects that would be very difficult to study in a full engine (such as increasing or decreasing the vane metal temperature by varying the cooling air supply) can be studied in such an HSTS. In the final analysis, full-scale engine testing cannot be avoided, and it also is an ongoing part of this research. However, this paper will be confined to a summary of the results of four studies (Padova et al., 1987; Moller and Dunn, 1989; Dunn and Kim, 1991; Kim et al., 1991) performed using the two HSTS.

Matching of Engine and HSTS Operating Parameters

To simulate the flow through the engine combustor accurately, four conditions need to be satisfied: (1) The airflow distribution within the engine combustor must be duplicated. This can be performed by keeping the HSTS flow function, given by

$$FF = \frac{\dot{m}\sqrt{T}}{P}$$

close to the value of FF in the engine. It is seen that the ratio of airflow through the HSTS to that in the engine can be below unity as long as the pressure is reduced a corresponding amount. (2) The residence time of the particles within the combustor must be duplicated. If the flow function and temperature levels within the HSTS are matched, this condition will be satisfied

Contributed by the International Gas Turbine Institute and presented at the 37th International Gas Turbine and Aeroengine Congress and Exposition, Cologne, Germany, June 1-4, 1992. Manuscript received by the International Gas Turbine Institute February 21, 1992. Paper No. 92-GT-219. Associate Technical Editor: L. S. Langston.

Copyright © 1993 by ASME
Downloaded 02 Jun 2010 to 171.66.16.121. Redistribution subject to ASME license or copyright; see http://www.asme.org/terms/Terms_Use.cfm

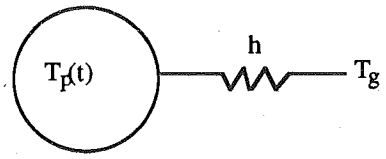

Fig. 1 Model of dust particle moving in a gas

since both the pressure and mass flow change by the same amount. (3) The temperatures within the HSTS must be the same as those in the engine. The fuel/air ratio can be adjusted to achieve this. (4) The thermal behavior of the particle in the HSTS should be similar to that in the engine. A rough measure of the particle thermal behavior is given by the thermal time constant of the particle (τ_t), i.e., the time it takes for the initial particle-to-gas temperature difference to decay by a factor $1/e$. For the lumped mass system shown in Fig. 1, the thermal time constant can be calculated to be

$$\tau_t = \frac{m_p c_p}{hA} = f\left(\frac{d_p}{h}\right)$$

where the subscript p refers to the particle. It is necessary to keep τ_t for the HSTS equal to τ_t for the engine combustor. It can be shown (Kim et al., 1991) that this leads to the condition

$$\left(\frac{d_{p,1}}{d_{p,2}}\right) = \left(\frac{\rho_{g,1}}{\rho_{g,2}}\right)^{0.429} = \left(\frac{P_{g,1}}{P_{g,2}}\bigg|_{T=\text{const}}\right)^{0.429}$$

The ratio of particle diameter in the engine to that in the HSTS was calculated to be less than 1.5 for both HSTS. Since the particle sizes entering the combustor in the engine are not known to this level of accuracy, the differences in the heat transfer behavior of the particles entering the HSTS and the engine combustor may be neglected.

Determination of Dust Feed Rate

Because the air ingested by the engine at the inlet is compressed in making its way to the combustor, the dust concentration at the combustor inlet is significantly higher than it is at the engine inlet. The rate at which dust is fed into the HSTS must reflect this compression ratio. The HSTS air is compressed by external compressors after which the duct blend is added to this already compressed air stream. Mass balances on the dust and air at the compressor inlet (subscript 1) and exit (subscript 2) are given by

$$\dot{m}_{\text{dust}} = c_1\dot{V}_1 = c_2\dot{V}_2 \Rightarrow \frac{c_2}{c_1} = \frac{\dot{V}_1}{\dot{V}_2}$$

$$\dot{m}_{\text{air}} = \rho_2\dot{V}_2 = \frac{P_2}{RT_2}\dot{V}_2 \Rightarrow \dot{V}_2 = \frac{\dot{m}_{\text{air}}RT_2}{P_2}.$$

Combining the above two equations yields the dust concentration magnification factor (M) as

$$M = \frac{c_2}{c_1} = \frac{\dot{V}_1 P_2}{\dot{m}_{\text{air}}RT_2} = \frac{\rho_2}{\rho_1}$$

The magnification factor is thus the compressor exit (combustor inlet) to compressor inlet air density ratio. Like the engine, the HSTS also has a magnification factor.

It is necessary to compute M for both the engine and the HSTS in order to compute dust feed rates. For a given dust concentration (c) at the engine inlet, the concentration at the compressor exit is simply the concentration at the engine inlet multiplied by the engine magnification factor (M_{engine})

$$c_{2,\text{engine}} = M_{\text{engine}}c_{1,\text{engine}}.$$

The dust concentration provided to the HSTS Must be the same as the engine combustor would experience. For a given HSTS magnification factor (M_{HSTS}), the dust concentration at the HSTS inlet is given by

$$c_{1,\text{HSTS}} = \frac{c_{2,\text{HSTS}}}{M_{\text{HSTS}}} = \frac{c_{2,\text{engine}}}{M_{\text{HSTS}}} = \frac{M_{\text{engine}}}{M_{\text{HSTS}}}c_{1,\text{engine}}.$$

The dust feed rate (F) is then given by

$$F = \dot{V}_{1,\text{HSTS}}c_{1,\text{HSTS}}.$$

where $\dot{V}_{1,\text{HSTS}}$ is the volume flow rate of air at the HSTS compressor inlet (which is at atmospheric pressure).

Experimental Apparatus and Dust Blend Description

It was decided early on to use actual engine hardware for the test series in order best to simulate conditions encountered during engine operation in volcanic clouds. In both HSTS, actual engine hardware including the combustion chamber, fuel nozzles, ignitors, and high pressure turbine vanes were used. A brief description of two HSTS built from the T56 and F-100 engine hardware follows.

T56 Hot Section Test System. A schematic of the T56 HSTS is shown on Fig. 2. Compressed air is supplied by a series of 42.5 m^3/min (1500 scfm) positive displacement compressors. This compressed air enters a 17.1-cm-ID by 5.5-m-long pipe into which dust is injected. The long pipe length ensures the dust and air are in equilibrium before entering the combustor. The hot section consists of (1) the can-type combustor from the Allison T56 engine, (2) a single entry, dual orifice fuel nozzle, (3) three air-cooled TIT thermocouple probes, and (4) four pairs of high-pressure turbine vane units (eight vane passages). The hot gases discharge into an exhaust chamber, then exit the facility through a pair of choke flaps. These flaps are movable, enabling the pressure in the combustion chamber to be changed. Postrun inspection of the combustor and vanes was performed by borescoping through the ignitor port, or by disassembling the HSTS.

A schematic of the dust injection system (DIS) is shown in

Nomenclature

A = area
a = acceleration
BPRR = burner pressure rise ratio
c = concentration, mass/unit volume
c_p = specific heat
C_d = drag coefficient
d = diameter
F = dust feed rate, mass/unit time
FF = flow function
h = heat transfer coefficient
ICV = independently cooled vane
HSTS = hot section test system
M = magnification factor
m = mass
MSH = Mt. St. Helens ash
P = pressure, absolute
R = gas constant
T = temperature, absolute
t = time
TIT = turbine inlet temperature
t = time
V = volume
v = velocity
μ = viscosity
ν = μ/ρ
ρ = density
τ_t = thermal time constant

Superscripts

$\cdot$ = per unit time

Subscripts

g = gas
p = particle

Downloaded 02 Jun 2010 to 171.66.16.121. Redistribution subject to ASME license or copyright; see http://www.asme.org/terms/Terms_Use.cfm

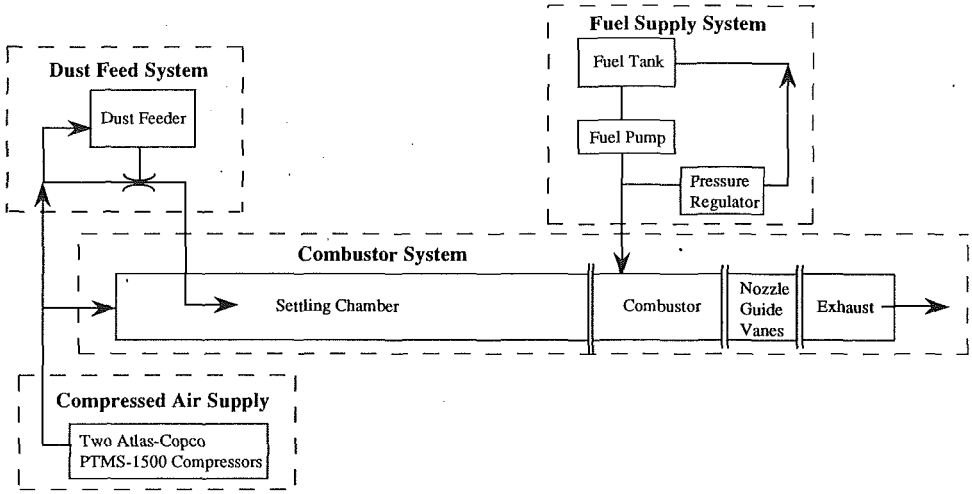

Fig. 2 Schematic of T56 HSTS

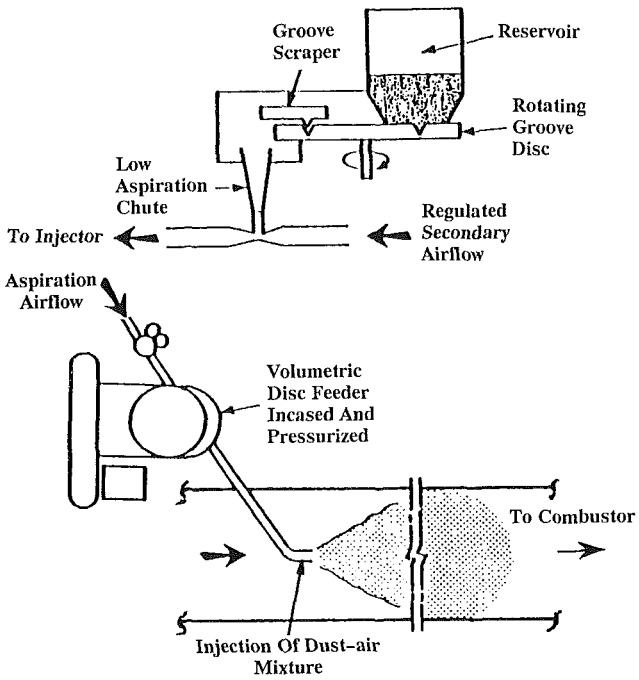

Fig. 3 Schematic of dust injection system

Fig. 3. A volumetric disk feeder was selected for the DIS because of its ability to provide continuous, accurate feeding of small quantities of dry materials. Since the feeder was not designed to operate with a pressure drop across it, the feeder is housed in a vessel that can be pressurized to the pressure of the discharge environment. The feeder therefore sees no pressure differential during operation.

The HSTS parameters measured were combustor inlet temperature and pressure, fuel flow, combustor pressure, and turbine inlet temperature. An IBM PC along with a Keithley 600 were used for data acquisition and processing. The reader is referred to Padova et al. (1987) for a complete description of the T56 HSTS.

F-100 Hot Section Test System

Testing of annular-type combustors is significantly more difficult than testing can-type combustors. To test all of the annuli would have required a prohibitive number of external compressor units. Therefore, only one quarter of the combustor (four out of sixteen fuel nozzles) was used as the test section. The remainder was filled with a high-temperature castable ceramic (Al_2O_3, ZrO_2). The mass flow rate through the test section was also reduced by two thirds to decrease the number of compressors needed. The combustor entry flow function (*FF*) was matched to that in the engine by lowering the combustor entry pressure to one third of the engine operating pressure.

Figure 4 shows a schematic of the F-100 HSTS. The air enters a high-pressure (1.06 MPa) chamber where it is metered. A dust/air mixture generated using the same DIS system that was used for the T56 HSTS is injected into the inlet of the 3.96-m-long low-pressure section and allowed to come into equilibrium with the main air before entering the combustor. The pressure within the combustor is set by adjusting the choke flap area at the exit of the exhaust duct. Due to the high temperature of the exhaust gases, water jets downstream of the vanes were used to lower the exhaust gas temperature to an acceptable level. A photograph of the test section showing the combustor with the vanes in place along with the water injection nozzles is given in Fig. 5. A general view of the HSTS is shown in Fig. 6. Provision was made to cool two of the vanes independently of the remainder of the vane row. This allowed us to determine the effect of vane metal temperature (achieved by increasing or decreasing cooling air to the vane) on material deposition. These vanes are hereafter referred to as ICVs (independently cooled vanes). One of these ICVs had a 1.0-mm-dia Pt-Rh thermocouple placed in the wall at 20 percent chord on the pressure side so that the temperature of this ICV could be monitored continuously. The reader is referred to Kim et al. (1991) for a complete description of the F-100 HSTS.

The data acquisition and processing system for the F-100 HSTS measurements was the same as that used in the T56 HSTS measurements. Similarly, postrun inspection of the combustor and vanes was performed by borescoping through the ignitor port, or by disassembling the HSTS.

Description of Material Tested

The two HSTS described above were used to investigate the deposition behavior of two volcanic materials. The first was Mt. St. Helens ash (MSH). The second was a mixture of two types of soil (sand and clay), black scoria (the volcanic ash material), and a small amount of a claylike additive. The sand was decomposed granite obtained from the Santa Monica mountains. The clay was material obtained from near Corona, CA. The black scoria was obtained from the Twin Mountain

Downloaded 02 Jun 2010 to 171.66.16.121. Redistribution subject to ASME license or copyright; see http://www.asme.org/terms/Terms_Use.cfm

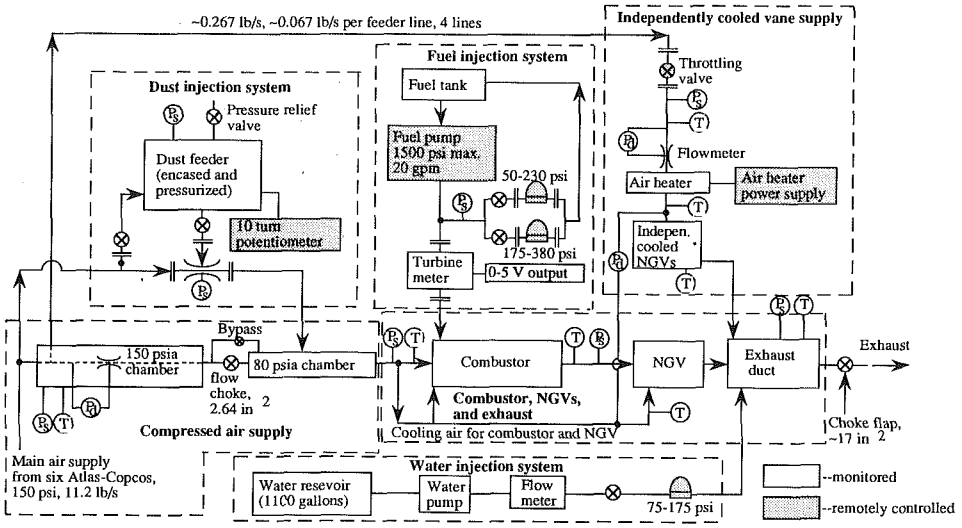

Fig. 4 Schematic of F-100 HSTS

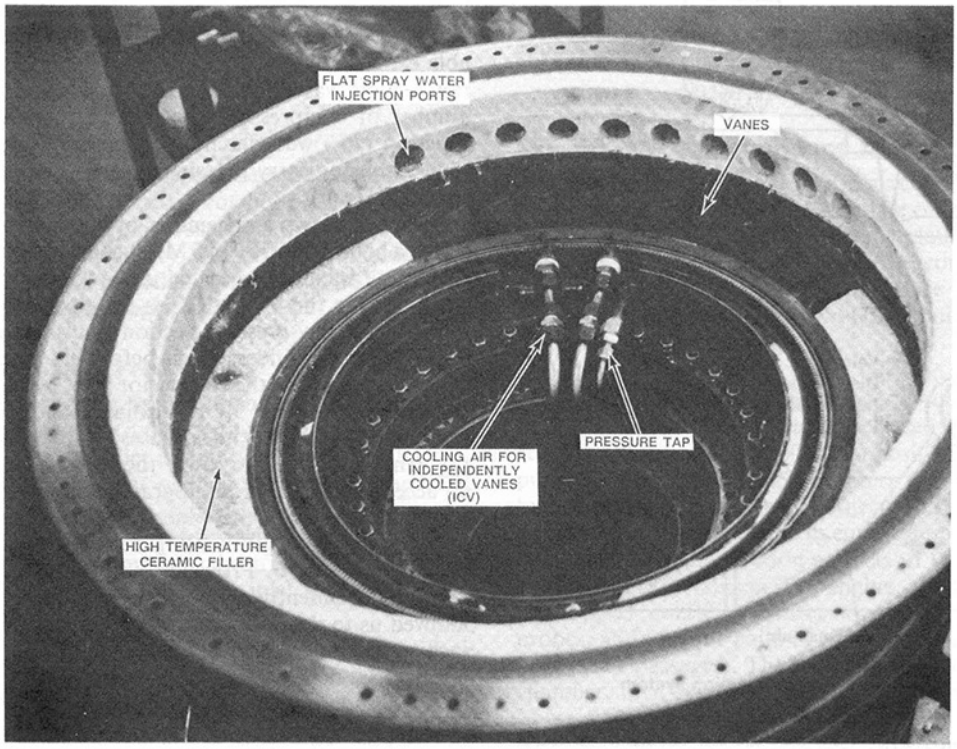

Fig. 5 Internal view of F-100 HSTS

quarry near Des Moines, NM. The claylike additive was bentonite. The above materials were mixed according to the recipe

blend 2 = 26 percent Hollywood sand + 26 percent Corona clay + 42 percent black scoria + 6 percent bentonite

This mixture will hereafter be referred to as blend 2.

The important physical properties of the dust particles that affect their behavior in air are size, shape, and weight. These characteristics were measured at Calspan and independently at other laboratories. A summary of the general properties of MSH and each of the comopnents of blend 2 is shown in Table 1. SEM micrographs of these materials are shown in Fig. 7. Differences in particle shape, particle surface texture amount of natural fines, and tendency to agglomerate are readily apparent. All of the particles are very nonspherical in shape.

Table 1 Raw material characteristics

Material	Color	Moisture content	Bulk density (g/cm^3)	Appearance
Mt. St. Helens	Gray granular composition of white to black grains	0.23%	1.273	Coarse to fine sand grains.
Black scoria	Black	19.6%	1.053	Pumiceous rocks with very little medium or fine grains. Unbreakable under finger pressure.
Corona clay	Reddish, mostly uniform	10.46%	1.157	Rock-granular plus fine soil-like material. Rocks are unbreakable under finger pressure.
Hollywood sand	Dark tan-gray with some small white grains	4.56%	1.28	Fine soil-like plus coarse grains of rock. Rock layers break easily under finger pressure.
Bentonite	Silver gray	7.92%	0.823	Fine, soft (talcum-like) powder.

Downloaded 02 Jun 2010 to 171.66.16.121. Redistribution subject to ASME license or copyright; see http://www.asme.org/terms/Terms_Use.cfm

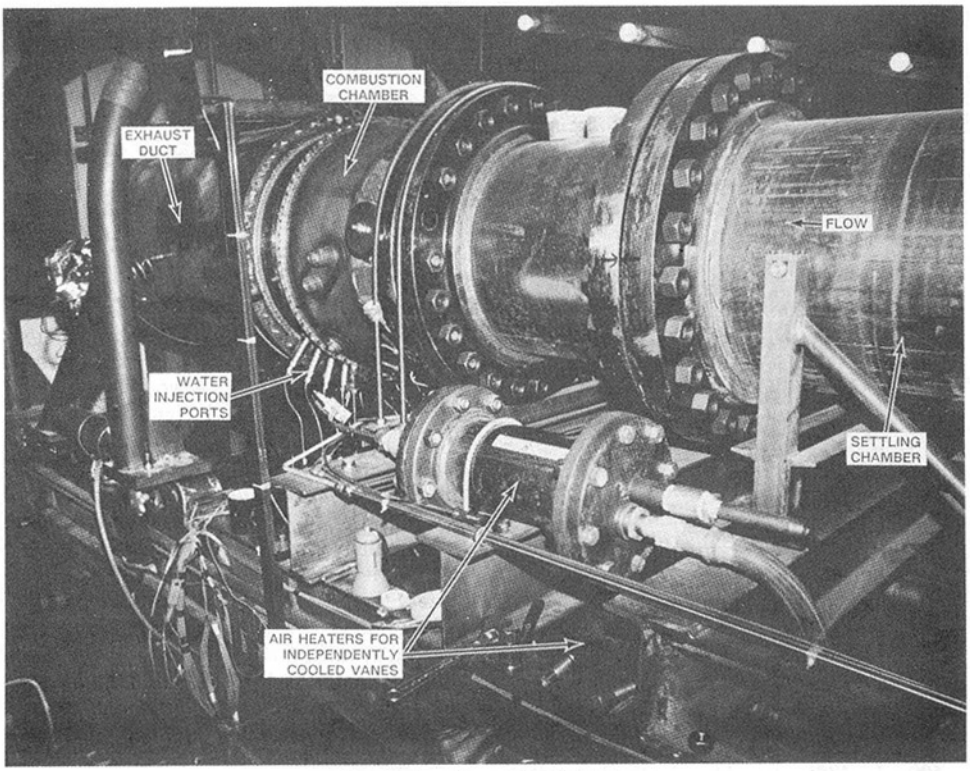

Fig. 6 Overview of F-100 HSTS

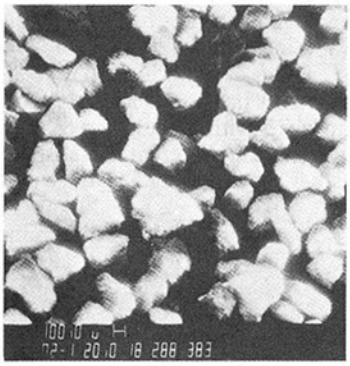

a) Micrograph of MSH magnified 20 times

b) Micrograph of Black Scoria magnified 100 times

c) Micrograph of Bentonite magnified 50 times

d) Micrograph of Corona Clay magnified 20 times

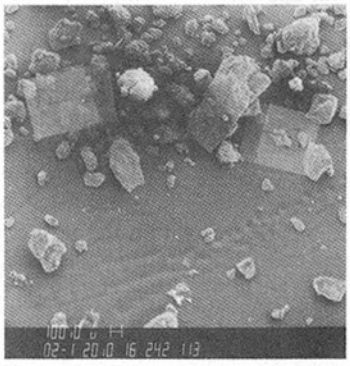

e) Micrograph of Hollywood Sand magnified 20 times

Fig. 7 Micrographs of Mt. St. Helens ash (MSH) and each component of blend 2

The mean size of the particles entering the combustion chamber of engines exposed to volcanic materials is, in general, not well known. However, some experimental results have been published for a Pratt and Whitney JT3D engine indicating that the fan and compressor pulverize the material. In the particular case mentioned, the average particle size of the incoming material was about 38 μm and the average particle size at the compressor discharge was determined to be on the order of 7 μm (Dunn et al., 1987a). The average particle diameter of the materials used in this test series is summarized in Table 2. The

Downloaded 02 Jun 2010 to 171.66.16.121. Redistribution subject to ASME license or copyright; see http://www.asme.org/terms/Terms_Use.cfm

Table 2 Median particle sizes of the materials used

Material	Average particle diameter (μm)
Mt. St. Helens	23
Black Scoria	73
Quartz	5
Clay	7
Feldspar	12

Table 3 Results of runs for blend 2 and black scoria, T56 HSTS

Run	Material	Conc. (mg/m^3)	TIT (K) (°F)	Exposure time (min.)	Mass of deposits (g)	Capture ratio
23	Blend 2	500	1339 (1950)	7	0.	0.0
24	Blend 2	500	1283 (1850)	7	0.	0.0
27	Blend 2	500	1228 (1750)	7	0.	0.0
30	Blend 2	100	1389 (2040)	7	2.09	0.023
32	Blend 2	250	1383 (2030)	7	6.01	0.027
33	Black scoria	250	1222 (1740)	7	9.38	0.0417
34	Black scoria	250	1283 (1850)	7	10.65	0.0474
41	Blend 2	500	1394 (2050)	7	12.50	0.028
42	Blend 2	500	1386 (2035)	14	33.61	0.037
44	Blend 2	500	1506 (2250)	7	16.91	0.038

quartz, clay, and feldspar had particle sizes similar to those expected in the engine. The particle size of MSH was not too far off what one would expect. The black scoria particles, however, were considerably larger than expected. Larger particles have higher thermal mass, and do not melt as easily as smaller particles. If black scoria is observed to be deposited in the HSTS, one would expect deposition to be more severe in the engine hot sections. Larger particles also do not follow the flow as well as finer particles. This may cause deposition patterns in the HSTS that are different than in the engine.

Furnace tests were performed to determine the melting temperature of MSH, black scoria, and blend 2. Samples of each material were placed in ceramic crucibles and then in a furnace, which was initially at 922 K (1200°F). The temperature was increased in 55.6 K (100°F) increments up to a maximum of 1478 K (2200°F). The samples were allowed to soak for ten minutes after the furnace reached its target temperature before the samples were removed and allowed to cool for inspection. All three materials began to agglomerate at 1311 K-1366 K (1900°F-2000°F), and all melted between 1366 K-1422 K (2000°F-2100°F). Since the temperatures within the primary combustion zone of combustors are typically much higher than this (~2200 K), the particles traversing this zone should melt if their residence time is sufficiently long.

The component in the volcanic materials most likely to deposit is what the geologists refer to as glass. An analysis of the scoria and MSH performed by the University of Nebraska and the National Soil Survey Laboratory found glass fractions by weight of 85 and 25 percent for the scoria and MSH ash, respectively. For blend 2, the glass fraction was 36 percent. A modal analysis of the ejected material (ash) from the Mt. Galunggung eruption of 1982–1983 (Katili and Sudradjat, 1984) found glass fractions of between 1 and 46 percent over a nine month period. The cloud composition even for a particular volcano varies on a daily basis as illustrated by the Mt. Galunggung data just noted. The amount of glass in the cloud is an important parameter in determining how the engine will respond. Unfortunately, this value is very difficult to predict even for a specific volcano. The percent glass in the materials used in the engine tests is well within the range of the measured glass content of ejected volcanic materials.

Results and Discussion

T56 HSTS Results

Deposition Behavior of Blend 2. No deposition was observed during runs made with pure Corona clay and a blend of Corona clay and Hollywood sand at TITs up to 1394 K (2050°F). Black scoria and blend 2 (which contains black scoria) were observed to be deposited under some conditions. A summary of the runs made with blend 2 and black scoria is shown on Table 3. The dust concentration cited in Table 3 is the equivalent dust concentration that the engine would see at the inlet prior to compression. In no instances were deposits observed on the combustor liner. Deposition for blend 2 is first observed on the vanes at a threshold TIT of between 1339 K (1950°F) and 1394 K (2050°F). An important parameter to be derived from the measurements is the capture ratio, i.e., the mass of material deposited on the vanes divided by the total mass of material ingested. It is seen from runs 30, 32,and 41 (the concentration was varied while the TIT and exposure time was held constant in these runs) that the capture ratio is quite independent of dust concentration, suggesting that the mass of deposition is proportional to concentration over the range of concentrations tested. The conclusion one can draw from a comparison of runs 41 and 42 (runs of various test duration) is that the capture ratio increases with time, implying that the vanes become better captors of material as the deposits on the vanes increase. Insufficient data were available to determine how the capture ratio varies with time, however. Finally, comparing runs 41 and 44 (runs at different TITs) shows that the capture ratio increases with increasing TIT once the threshold TIT for deposition (~1367 K) is exceeded. This behavior is thought to be mainly due to the increase in the amount of mass available for deposition since more of the particles melt during their traverse through the hot section of the combustor at the higher temperature. Again, insufficient data were available to determine how the capture ratio varies with TIT. Another important parameter that influences deposition behavior is the vane surface temperature. It was not until the F-100 HSTS tests were performed that this parameter could be controlled, however.

The results for pure black scoria show that for the given temperature range, the capture ratio is relatively constant and is consistently higher than that of blend 2 (containing 42 percent black scoria) at higher temperatures. This is felt to be due to more molten material being available for deposition on the vanes than was available for the blend 2 runs.

A photograph of the vanes after a typical elevated temperature run for which blend 2 was used is shown in Fig. 8. The deposits ranged from a grainy agglomerate at TITs just above deposition threshold to a glazelike deposit in which the grain-like texture was lost at higher TITs. Similar types of deposits were observed for black scoria. In all cases where blend 2 and black scoria were deposited, all the deposits were easily removed from the surfaces. In many cases, the metal surface, upon removal of the deposits, appeared cleaner and shiner than before it had been exposed, indicating that the oxide layer originally on the vane surface had been removed.

The type of surface onto which the molten material was deposited appears to have had an effect on the characteristics of the deposited material. In some of the thicker deposits of blend 2, the outer layers of the deposit were molten while those

Downloaded 02 Jun 2010 to 171.66.16.121. Redistribution subject to ASME license or copyright; see http://www.asme.org/terms/Terms_Use.cfm

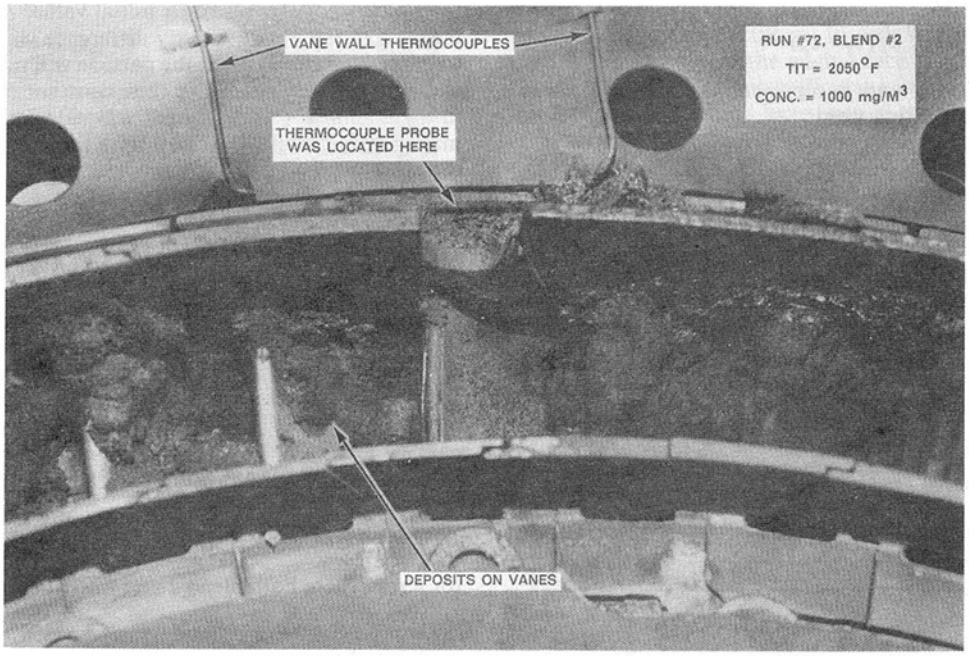

Fig. 8 Results for T-56, blend 2 containing black scoria

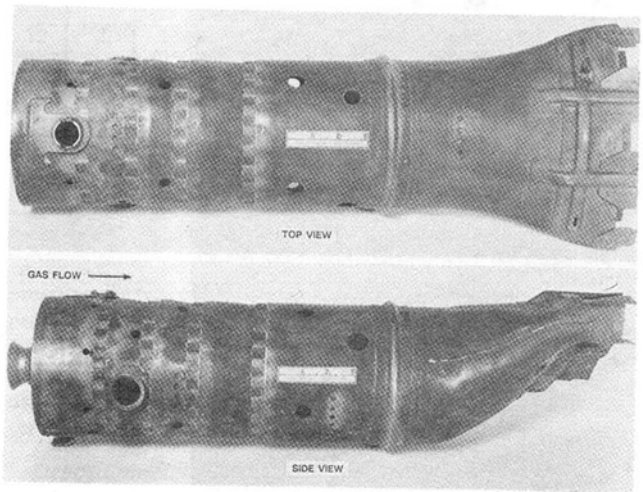

Fig. 9 Top and side views of T-56 combustor liner

nearest the surface were almost always an agglomeration. Because the flame temperature was kept constant during each run, the apparent layering of phases cannot be the result of hotter particles impinging on solid surfaces later in the run. It is suggested that the thermal conductivity at the surface of a deposit covered vane is lower than that of a clean vane because the deposits are good insulators; they are porous and made up primarily of oxides. This means that the layers being deposited on a clean metal surface will have their heat conducted effectively to the metal but will form a thermal barrier coating to the subsequently deposited material.

Deposit location and distribution. The locations at which deposits occur appear to be dependent on surface and flame temperature and on the acceleration field within the vanes near the deposit location. The regions of rapid flow deceleration near the surface were the first places for deposits to form. Any deposits on the suction side appeared to be the result of droplets of molten material moved there by drag forces from the free stream and from locations near the leading edge or the outer shroud.

Surface and gas temperature and the acceleration field in the immediate proximity of the vanes are not the only strong influence on deposition pattern. As seen in Fig. 8, little of the material is deposited on the vanes at small span values while a considerable amount is deposited toward the outer shroud. This observation suggests that the combustor liner is centrifuging particles in a way that increases their number density at large vane span values. An examination of the combustion chamber shown in Fig. 9 suggest that this centrifuging arises aft of the cylindrical portion of the liner in the transition to the guide vanes. The combustor has a bellylike shape, which flares outward to meet the vanes. To move through this transition, the flow must follow an S shape (as viewed from the side) and distribute itself radially outward (as viewed from the top). Particles that are unable to follow this flow path will tend to be centrifuged and deposited on the vane surfaces closer to the outer shroud. This behavior is strongly influenced by the particle size, shape, and density. Finer, lighter particles will tend to follow the flow more readily, while coarser, heavier particles will tend to be centrifuged. Similarly, particles of irregular shape will tend to follow the flow better than smooth particles due to their higher drag coefficient. It has been noted earlier that the black scoria particles used in this test were considerably larger than what one would expect in an engine environment. A deposition pattern more uniform across the leading edge of the vanes than observed in Fig. 8 would probably have been observed had the particles been closer in size to those expected in an engine environment.

The above hypothesis is supported by the following analysis. Consider a spherical particle placed in a uniform flow. The force on the particle is the drag on the particle due to the difference in speed between the particle and the carrier air, i.e.,

$$\text{Force} = ma = m\frac{dv}{dt} = \rho_p \frac{\pi d_p^3}{6}\frac{dv}{dt} = \text{Drag}$$

From the definition of drag coefficient, an expression for the drag on a spherical particle can be obtained as

$$\text{Drag} = C_d \frac{1}{2}\rho_g \frac{\pi d_p^2}{4}(v_g - v_p)^2$$

where

Downloaded 02 Jun 2010 to 171.66.16.121. Redistribution subject to ASME license or copyright; see http://www.asme.org/terms/Terms_Use.cfm

$$C_d = \frac{24}{\mathrm{Re}_p} = \frac{24\nu}{d_p(v_g - v_p)} \quad \text{for } 0 < \mathrm{Re}_p < 100$$

and the subscripts g and p represent the gas and particle, respectively. Substituting yields

$$\frac{d_p^2}{18\nu}\frac{\rho_p}{\rho_g}\frac{dv_p}{(v_g - v_p)} = K\frac{dv_p}{(v_g - v_p)} = dt$$

The above equation is easily integrated to obtain

$$\frac{v_g - v_p}{v_g} = \exp(-t/K)$$

where $K = d_p^2/18\nu\ \rho_p/\rho_g$ is the time constant, and represents the time it takes for the initial particle to fluid velocity difference to decay to $1/e$ of its initial value. A large value of K means that the initial velocity difference will take a long time to decay, and implies that the particle will not follow a rapidly changing velocity field. The time constant of a scoria particle in the combustor environment was calculated to be approximately 10 ms, while the time it took for the particle to traverse the S-shaped region in the combustor was approximately 4 ms. It is therefore not surprising that the scoria particles were centrifuged in the flow.

Table 4 Burner pressure rise ratio (BPRR) for various runs

Run	Material	Conc. (mg/m^3)	TIT (K) (°F)	BPRR
72	Blend 2	1000	2050 (1394)	0.0479
75	MSH	1000	2050 (1394)	0.0295

Impact of dust on rig behavior. Burner pressure measurements during a run have been found to be an excellent indicator as to whether or not deposition is occurring on the vanes. Since the compressors used are of the positive displacement type, the flow rate remains constant for all discharge pressures. Experience has shown that an increase in burner pressure is indicative of vane deposition because of a decrease to the vane passage area due to deposits. Table 4 summarizes measured values of the burner pressure rise ratio (BPRR), defined as

$$\mathrm{BPRR} = \frac{\text{Burner pressure rise}}{\text{Initial burner pressure}}$$

for a run where both blend 2 and MSH deposited. The burner

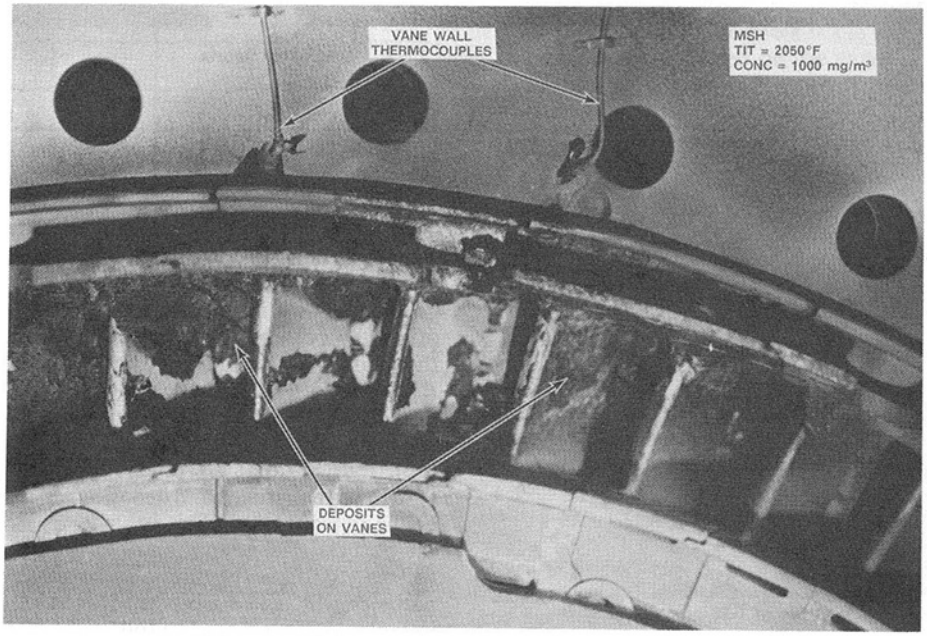

Fig. 10(*a*) Results from exposure to Mt. St.Helens ash, front view

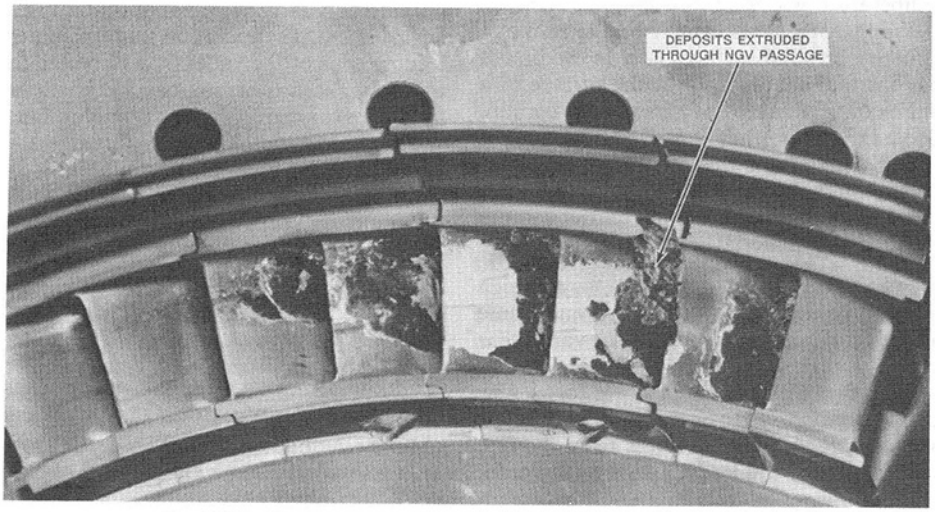

Fig. 10(*b*) Results from exposure to Mt. St. Helens ash, rear view

Downloaded 02 Jun 2010 to 171.66.16.121. Redistribution subject to ASME license or copyright; see http://www.asme.org/terms/Terms_Use.cfm

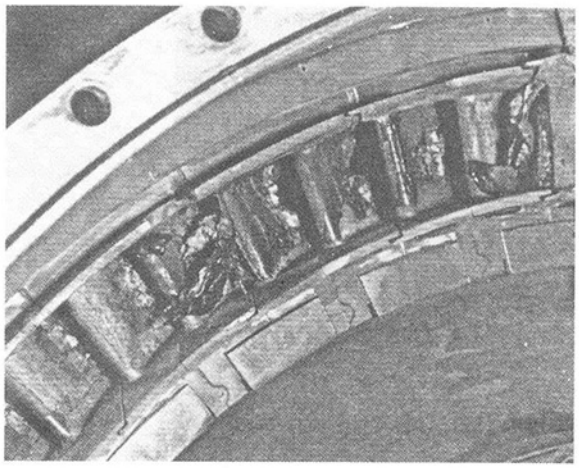

Fig. 11 Deposition of Mt. St. Helens ash in the T-56 engine (flight results)

Table 5 Summary of test runs; test duration was 7 min for all runs

Run	Blend	TIT (K) (°F)	Engine face dust conc. (mg/m^3)	Comments
11	2	1450 (2150)	200	Glass-like deposits on TITs, no deposits on vanes.
12	2	1644 (2500)	500	Glass-like deposits on TITs, little deposits on vanes.
13	2	1644 (2500)	1000	Glass-like deposits on TITs, little deposits on vanes.
14	2	1644 (2500)	500	With decreased airflow to ICV. Glass-like deposits on TITs, significant deposits found on ICV pair.

pressure rise was computed as the difference between the burner pressure 30 s before dust shut off and 30 s after dust on. The BPRR values quoted in Table 4 translate into burner pressure increases on the order of 17.2 kPa (2.5 psi). Burner pressure did not increase during the runs where deposits were not observed.

Deposition Behavior of Mt. St. Helens Ash. Deposition of MSH was first observed for a TIT = 1394 K (2050°F) and an equivalent engine inlet concentration of 1250 mg/m^3. The average rate of accumulation for these runs was 1.9 g/min. At the same inlet concentration and a TIT = 1494 K (2230°F), the accumulation rate decreased to 1.5 g/min. The deposits were observed to have a greenish-black coloration and the physical appearance of a relatively thin glaze applied to the metal surface. The deposits had very characteristic ripples. The decrease in the accumulation rate at the higher temperature, the physical appearance of the deposits, and the amount of glassified material deposited downstream of the vanes suggested that molten material was continuously being blown away when operating at a high temperature. A video camera monitoring the exhaust confirms this mechanism. Photographs of the deposits are shown in Figs. 10(*a*) and 10(*b*). Figure 10(*b*) shows how the molten material has extruded through a vane pair. A comparison of the above photos and the deposits on the vanes from the T56 engine that flew through the Mt. St. Helens volcanic cloud (Fig. 11) shows the similarity between the HSTS and in-flight results.The deposits were very hard and glassy, and were difficult to remove from the surface. Capture ratios for MSH could not be reliably computed.

F-100 HSTS Results. Blend 2 was also used as the dust material introduced into the F-100 HSTS. For the initial test, the hot sections were exposed to a dust concentration equivalent to 200 mg/m^3 at the engine face for 7 min at a TIT of 1644 K (2500°F). For this particular run, the vane temperature was lower than it would have been in the engine (by ~390 K) because air to the combustor was supplied by the external compressors (air exit temperature of ~340 K) instead of the engine compressor (air exit temperature of ~730 K). However, it was anticipated on the basis of the T56 HSTS results that deposits would be found on the vanes in the HSTS. A postrun borescope of the HSTS revealed TIT probes that were covered with glass. The vanes had a reddish dust coat on them, but no signs of glassy deposits as experienced in the T56 HSTS were observed.

It was hypothesized that three main points of difference between the T56 andF-100 HSTS were significant. The first hypothesis was that since the T56 HSTS was operated at a lower TIT, it was possible that the TIT needed to be lowered in the F-100 HSTS to get blend 2 to be deposited. A run at a TIT of 1450 K (2150°F) was selected to test this hypothesis since deposition of blend 2 was observed at this TIT in the T56 HSTS. The second hypothesis was that the dust concentration needed to be increased for deposition to occur, since the equivalent engine inlet concentration of blend 2 used in the T56 HSTS was 1000 mg/m^3, in contrast to a concentration of 200 mg/m^3 used in the F-100 HSTS. Runs were therefore made with increased dust concentration. The third hypothesis was that the vane metal temperature was significant, since the vanes in the T56 HSTS ran much hotter (as hot as 1422 K) than in the F-100 HSTS (~670 K). A run was therefore made with reduced cooling air to the ICV pair to determine the effect of vane surface temperature on deposition.

The results of four runs using the F-100 HSTS to test the above three hypothesis are summarized on Table 5. Results from run 11 (test of first hypothesis) found TIT probes covered with a glasslike deposit, but no deposits on the vanes, confirming that lowering the TIT does not increase the likelihood of glass deposition on the vanes. Some deposits were found on the leading edges of the vanes after runs 12 and 13 (test of second hypothesis), but not nearly as much as was observed in the T56 HSTS. The rig was taken apart and the deposits were collected.It was interesting to note that deposits usually occurred at locations where the vane had been damaged (the local vane temperature at these points was sufficiently high to cause melting of the vane surface). A photograph taken of the vanes before and after the deposits were removed (Fig. 12*a*, *b*) illustrates this point. This observation suggests that the surface temperature onto which the particles impact must be above a certain threshold temperature if deposition is to occur. Inspection of the above photographs reveals another damage mechanism (one separate from deposition) that can occur in engines. Close inspection of the leading edges of the vanes shows that the showerhead cooling air holes have been plugged with dust, resulting in a decrease in film cooling effectiveness. Such plugging can allow the surface temperature of the vanes to increase above their melting temperature, resulting in damage to the vanes. Figure 13 is a close-up view of the leading edges of a vane that shows clogging of the cooling holes and the resultant damage to the vane. The third hypothesis was tested by decreasing the cooling air to one of the ICVs to increase the vane temperature with an equivalent dust concentration of 500 mg/m^3. The ICV temperature reached a maximum of ~1089 K (1500°F) during the run. A postrun borescope examination revealed significant amounts of deposits on the ICV vane. Smaller amounts of deposits were found on the other vanes as indicated in Table 6. The TIT probes were covered with glass. Increasing the vane metal temperature increased the amount of deposits significantly. This parameter appears to be one of the major factors determining whether or not a particular dust blend is deposited.

Downloaded 02 Jun 2010 to 171.66.16.121. Redistribution subject to ASME license or copyright; see http://www.asme.org/terms/Terms_Use.cfm

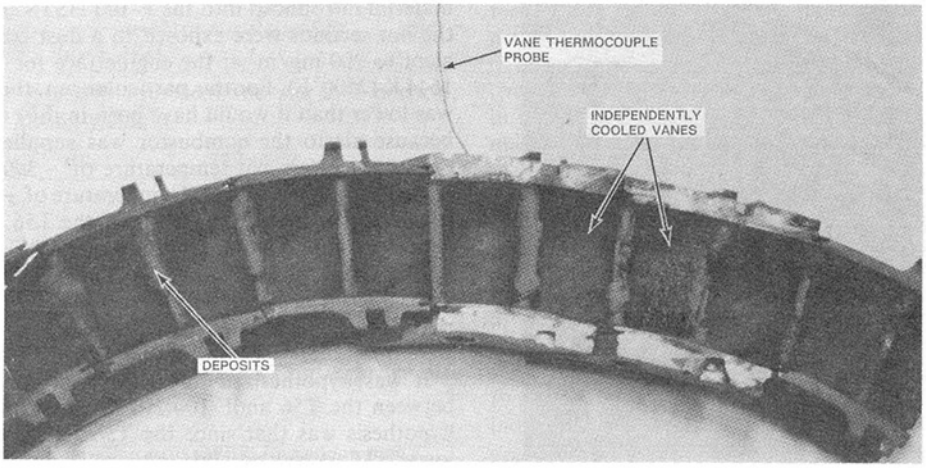

Fig. 12(*a*) NGV row before removal of deposits (after run 13)

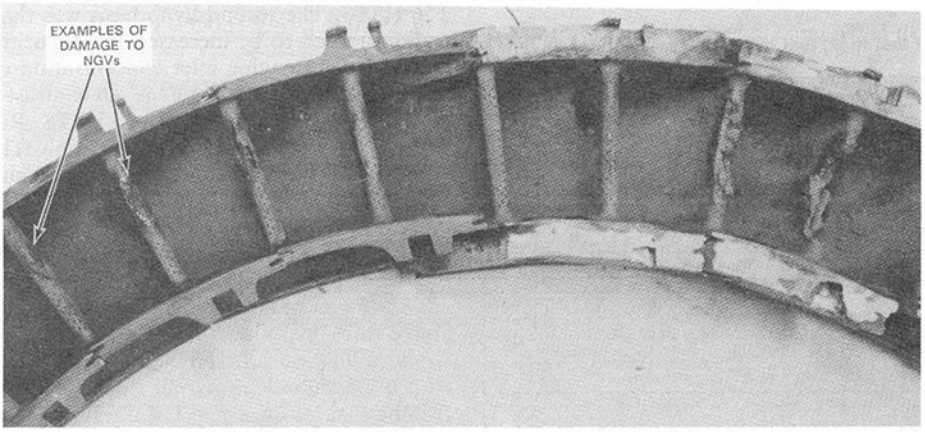

Fig. 12(*b*) NGV row after removal of deposits (after run 13)

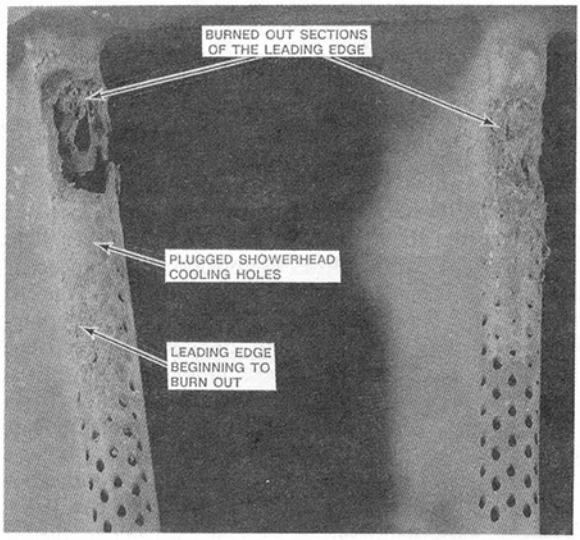

Fig. 13 Closeup view of vane leading edges showing burnout and clogging of cooling holes

Location and Distribution of Deposits. An examination of Fig. 12(*a*) shows that the vane leading edges toward the outer shroud have significant deposits, while lesser deposition occurs on the leading edges at small span values, similar to what was observed for the T56 vanes. The centrifuging mechanism discussed earlier in connection with deposit distribution in the T56 HSTS is applicable to deposition behavior in the F-100 HSTS as well. The construction of the F-100 combustion chamber is such that the flow along the inner diameter must follow an S-shaped path to reach the vanes. Particles not able to follow the flow would be centrifuged outward and would deposit on the vanes near the outer shroud.

Table 6 Deposit distribution on vanes after run 14

Location	Mass of dust collected (g)
From ICV	15.96
From vane next to ICV	5.50
From remainder of vanes	6.98

Conclusions

Two hot-section test systems were designed and built using the combustors, igniters, fuel nozzles, and first stage high-pressure turbine vanes from Allison T56 and Pratt and Whitney F-100 engines to study the behavior of two volcanic materials when they are ingested into gas turbine engines. The T56 hardware represents the older can-type combustors while the F-100 hardware represents the more modern annular-type combustors. The HSTS were operated at the same flow function and temperature levels as would occur in the engines. Mt. St. Helens ash, and a blend of Hollywood sand, Corona clay, bentonite, and Twin Mountain black scoria (a second volcanic ash material) were the materials tested. The main conclusions from this series of tests are:

Downloaded 02 Jun 2010 to 171.66.16.121. Redistribution subject to ASME license or copyright; see http://www.asme.org/terms/Terms_Use.cfm

1 Two significant engine parameters that influence whether or not a particular material deposits are turbine inlet temperature, and vane surface temperature.
2 Deposition was observed to occur in some cases on the turbine inlet temperature probes and the nozzle guide vanes. No deposition was observed in the combustor liner.
3 Once deposition begins, the mass of material deposited is proportional to dust concentration for a given TIT and dust exposure time.
4 The rate at which deposition occurs increases with time for a given TIT and dust concentration, i.e., the vanes become better captors of material as the deposits on the vanes increases.
5 Damage to the vanes can occur even when the deposition is not initially present if dust blocks the showerhead cooling holes. Such blockage can cause vanes to burn out under normal turbine inlet temperature operating conditions.
6 The distribution of deposits is strongly influenced by whether or not the particles are able to follow the flow.

Acknowledgments

This work was supported by the Defense Nuclear Agency under contract No. DNA 001-89-C-0060.

References

Batcho, P. F., Moller, J. C., Padova, C., and Dunn, M. G., 1987, "Interpretation of Gas Turbine Response Due to Dust Ingestion," ASME JOURNAL OF ENGINEERING FOR GAS TURBINES AND POWER, Vol. 109, pp. 344–352.

Campbell, E. E., 1990, "Volcanic Ash," *Proceedings of the 747 Flight Operations Symposium*, Seattle, WA, Oct. 9–11, Boeing Commercial Aircraft Company, pp. 2.3.1–2.3.34.

Dunn, M. G., Padova, C., and Adams, R. E., 1987a, "Operation of Gas Turbine Engines in Dust-Laden Environments," AGARD-Advanced Technology Aero Engine Components, Paris, France.

Dunn, M. G., Padova, C., Moller, J. E., and Adams, R. E., 1987b, "Performance Deterioration of a Turbofan and a Turboject Engine Upon Exposure to a Dust Environment," ASME JOURNAL OF ENGINEERING FOR GAS TURBINES AND POWER, Vol. 109, pp. 336–343.

Dunn, M. G., and Kim, J., 1991, "The 'Most Probable' Dust Blend and Its Response in the T56 Hot Section Test System (HSTS)," to be submitted to DNA.

Katili, J. A., and Sudradjat, A., 1984, *Galunggung, the 1982–1983 Eruption*, Volcanological Survey of Indonesia, Directorate General of Geology and Mineral Resources, Department of Mines and Energy, Republic of Indonesia.

Kim, J., Baran, A. J., and Dunn, M. G., 1991, "Description of a F-100 Engine Hot Section Test System (HSTS) for Dust Phenomonology Testing," DNA-TR-91-159.

Kim, J., Dunn, M. G., and Baran, A. J., 1991, "The 'Most Probable' Dust Blend and Its Response in the F-100 Hot Section Test System (HSTS)," DNA-TR-91-160.

Moller, J. C., and Dunn, M. G., 1989, "Dust and Smoke Phenomenology Testing in a Gas Turbine Hot Section Simulator," DNA-TR-90-72-V2.

Padova, C., Dunn, M. G., and Moller, J. C., 1987, "Dust Phenomenology Testing in the Hot-Section Simulator of an Allison T56 Gas Turbine," Calspan Report No.7389-A-1.

Downloaded 02 Jun 2010 to 171.66.16.121. Redistribution subject to ASME license or copyright; see http://www.asme.org/terms/Terms_Use.cfm

J. F. Zievers

P. Eggerstedt

Industrial Filter & Pump Mfg. Co.,
Cicero, IL 60650

E. C. Zievers
Universal Porosics, Inc.,
LaGrange, IL 60525

D. Nicolai
SETEC GmbH,
Bietigheim, Federal Republic of Germany

What Affects the Cost of Hot Gas Filter Stations?

This technical paper examines the various aspects of hot gas filter station design that ultimately affect both initial and operational costs. Process conditions such as temperature and pressure, and design constraints such as face velocity, are discussed with respect to their bearing on filter station costs. More subtle parameters, such as pulse gas cleaning requirements and filter element geometry, also directly impact filter design and hence, cost. As all of the information presented is based upon actual filter applications, it will provide useful insight for those involved in filter designing and recommendations.

Introduction

The "filter stations" referred to in the title are of the closed pressure vessel(s) type, utilizing ceramic filter elements, which are supported by a tube sheet or similarly functioning plenum and are cleaned by a reverse jet pulse of high-pressure gas.

Although filter element types that capture solids on the outside (S.O.) and those that capture solids on the inside (S.I.) are both discussed, the emphasis of the paper and the cost data are based on S.O. type elements.

In this paper, the authors attempt to use their accumulated experience from sizing and pricing many hot gas filter stations [1–23] to set forth some obvious interrelationships and indicate the cost effect.

Finally, these interrelationships will be utilized to create some cost estimating curves that may be of help to other engineers.

Process Parameters

It is obvious from the gas laws that the temperature and pressure of the gas stream to be filtered will affect the volume flow of gas and therefore, the size of the filter station. To a certain extent, the volume of gas is also affected by the type of fuel feed. For example, a 50/50 coal/water slurry feed will produce a larger flow of gas at the filter station as compared to a "dry" coal feed. A 75/25 coal/water "paste" will have a lesser effect, but the influence is still present. In the same vein, if "sorbents" are fed as a liquid slurry, the liquid portion increases the gas volume and consequently the cost of the filter station.

The gas temperature and required vessel skin temperature both affect the thickness of refractory lining as well as the ultimate vessel diameter and cost.

Filter Vessel Size

Since refractory thickness can vary widely, the authors have found it useful to begin pressure vessel design by defining the Useful Interior Diameter (UID). UID is the diameter into which the required quantity of filter elements can be fitted in an appropriate pattern. The UID must have an added provision for any gas inlet baffle and refractory lining in order to arrive at vessel diameter. In preparing cost estimates that are referred to later in this paper, UID's were calculated and a uniform refractory thickness of 12.5 cm was added to arrive at vessel diameters that were then cost estimated.

Design Pressure and Temperature

The design pressure of the filter system obviously affects the vessel wall thickness. Gas temperature and allowable pressure differential affect the tube sheet material of construction, thickness, and method of suspension, and the choice of ceramics to be used for filter elements, and bring about a decision as to whether the tube sheet will be cooled or uncooled. All of the aforementioned have a direct bearing on filter station cost. The method of cooling the tube sheet can increase overall heat loss and result in higher process costs. Line pressure directly affects the pressure of the jet pulse gas and, of course, the cost of compressing that jet pulse gas to operating level.

Materials

It should be pointed out that the choice of ceramic materials for filter elements is also affected by the feed gas chemistry and the ultimate corrosive nature of the feed gas. The ceramic material selected will also affect the cost, as shown in Fig. 1.

Contributed by the International Gas Turbine Institute and presented at the 37th International Gas Turbine and Aeroengine Congress and Exposition, Cologne, Germany, June 1–4, 1992. Manuscript received by the International Gas Turbine Institute February 21, 1992. Paper No. 92-GT-221. Associate Technical Editor: L. S. Langston.

Copyright © 1993 by ASME
Downloaded 02 Jun 2010 to 171.66.16.121. Redistribution subject to ASME license or copyright; see http://www.asme.org/terms/Terms_Use.cfm

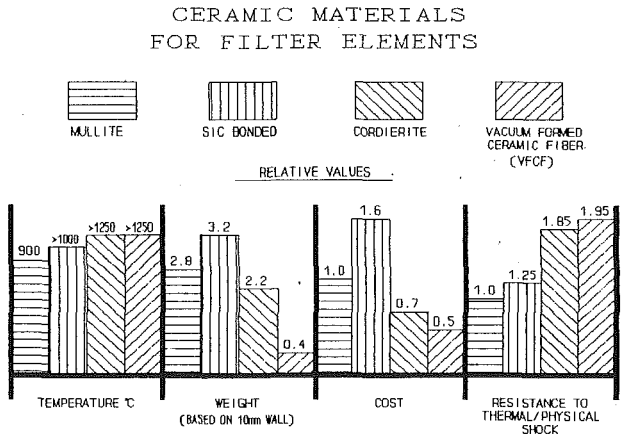

Fig. 1

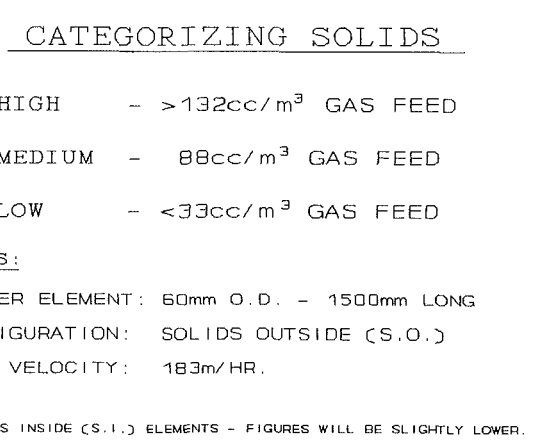

Fig. 2

Figure 1 also illustrates the relative characteristics of some commonly used ceramic materials.

If a ceramic is chosen that has poor resistance to thermal shock, it may be necessary to heat the jet pulse gas. The heating of jet pulse gas can be expensive itself and can also affect the choice and cost of jet pulse delivery valves and measuring instrument probes. On at least one occasion, in order to prevent the intrusion of corrosive gas into the jet pulse nozzles, a small amount of jet pulse gas had to be constantly metered through the nozzles, resulting in additional cost.

The choice of ceramic material and supplier can affect quality control costs. On the matter of quality control, a decision must be made as to what minimum tests will satisfactorily determine the suitability of product for process use and what percentage of the product must be tested. How and where will such quality control records be kept, and by whom? The authors feel that each ceramic element should have a serial number and a locator code, but this also is a cost.

The number of ceramic elements needed to do a given job is determined by the volume of gas and the design face velocity, but these are not the only considerations. The volume of particulate, the particle size, and particle size distribution must also be considered.[1] Note the word volume was used. Often, particulate loading is measured in terms of weight. In sizing a filter, the volume of solids used in conjunction with the attainable cake thickness at a given allowable pressure drop may have a greater effect on the size of the filter station than the volume of gas to be filtered. Although true particle density is often cited, filter sizing, element spacing, and other filter design considerations are based upon the dry bulk density of the dust. In such cases, the alternate cost of additional cyclones must be considered.

[1]Particle size distribution of dust can be manipulated using selected dust or selected "sorbents." See U.S. Patent No. 4,865,629.

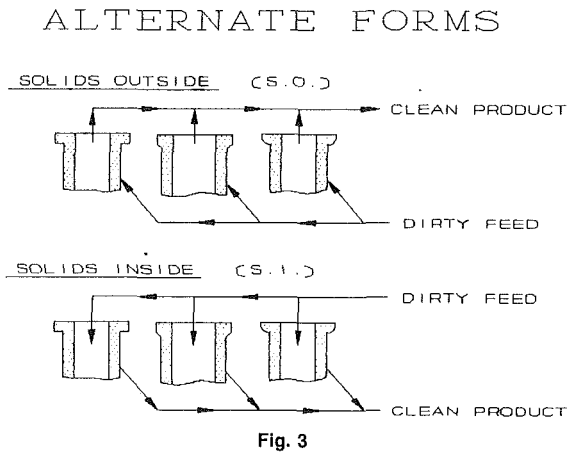

Fig. 3

In categorizing solids loads reaching the filter elements, the authors use the following criteria calculated from candles 60 mm × 1500 mm long and operating at a FV of 183 m/h, as illustrated in Fig. 2

- High solids loads produce a cake 6 mm or more thick in 15 min (132 cc/m^3 gas feed).
- Medium solids loads produce a cake approximately 4 mm thick in 15 min (88 cc/m^3 gas feed).
- Low solids loads produce a cake 1.5 mm or less thick in 15 min (33 cc/m^3 gas feed).

Element Geometry

Beside the ceramic material used for the filter elements [24], the physical size of the elements will ultimately affect the filter station cost. Further examination may prove fruitful. First, and generally speaking, two ceramic filter element configurations are currently commerically available (see Fig. 3):

(A) 60 mm o.d. × 1500 mm long, monolithic, solids outside (S.O.),

(B) 172 mm i.d. × 3000 mm long, sectioned, solids inside (S. I.).

S.O. elements may be obtained in a fluted design as well. A fluted element of any given outside diameter will yield more filtration surface. To date, denser ceramic structures (those of silicon carbide, mullite, and alumina) are made with a non-fluted i.d., resulting in the following considerations:

1 Should the design engineer utilize the entire fluted surface area? As dust accumulates radially outward, it will tend to change the actual filtration surface, the effects of which can be determined in testing.

2 At a selected design face velocity, what effect does an increase in surface area per element have on the velocity of clean gas through the orifice of the filter element? This velocity can reach a point of criticality, the effects of which are covered below and in Fig. 4.

Fluted elements made of a less dense, vacuum-formed material (Alumino-silicate, mullite, etc.) usually have a uniform wall thickness, since both the o.d., and i.d. are fluted. To maintain orifice velocity, the o.d. may be adjusted to 80 mm with a 50 mm i.d.

Critical Orifice Velocity

The 60 mm o.d. elements are available in two i.d.'s; 40 mm and 30 mm. While the available filtration surface areas are identical, one must consider the interior area of the element at the flange as a restrictive orifice. When the velocity of the filtered gas at the element flange exceeds about 30 m/s, the flange orifice begins to contribute a considerable additional

Downloaded 02 Jun 2010 to 171.66.16.121. Redistribution subject to ASME license or copyright; see http://www.asme.org/terms/Terms_Use.cfm

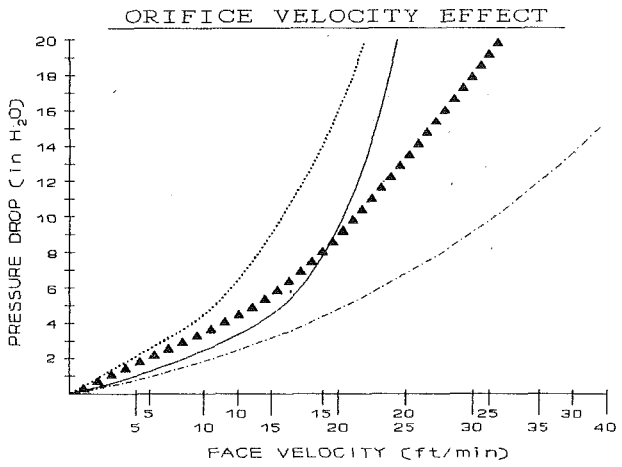

SYMBOL	I.D.(mm)	LGTH.(mm)	m^2
———	30	1500	.26
	30	2000	.35
.....	30	1500 FLUTED	.35
(THEORETICAL)	30	1500 FLUTED	.44*
-.-.-.-.-.	40	1500	.26
▲▲▲▲	40	2000	.35

* READ UPPER F.V. SCALE

Fig. 4

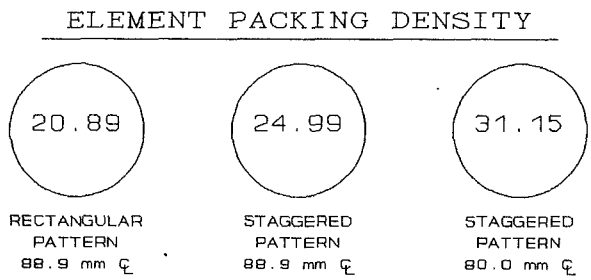

Fig. 5

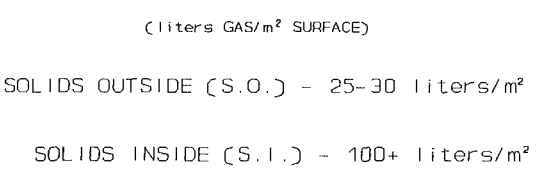

Fig. 6

pressure drop. This added pressure drop can effectively limit the selection of design face velocity and therefore, affect the cost. For want of a better term, the authors will call this the Critical Orifice Velocity (COV) [25]. The relationship between COV and 60 mm o.d. candle dimensions is shown in Fig. 4. Notice that a 2.0 m-long candle has been included because such elements are now in limited presence in the market. The very existence of a 2.0 m-long element deserves another comment on cost. It is this: When planning a filter station it seems prudent to include the cost of extra filter vessel height to allow for possible future use of 2.0 m-long elements.

Jet Pulse Volume

Jet Pulse Volume (JPV) may be defined as that volume (in liters) of jet pulse gas that must be delivered to the filter in order to clean 1 m^2 of filter surface. Typically, because of the geometry involved in filter designs currently on the market, JPV for S.O. filter elements will be in the 25–30 l/m^2 range. For S.I. elements the JPV can reach considerably above 100 l/m^2. Obviously, JPV affects the installation and operating costs of a hot gas filter station.

Perhaps a little mathematics would be in order here. Assume a filter with 50 m^2 surface, a JPV of 25 l/m^2, operating at a face velocity of 400 m/h, and a pulse frequency of 4 times per hour. This filter will clean 20,000 m^3 of gas and will utilize 5,000 liters of jet pulse gas per hour at 6–8 bar over line pressure. If, on the other hand, the JPV is 100 l/m^2, the jet pulse gas requirement would rise to 20,000 liters per hour.

Element Packing Density

Element Packing Density (EPD) is still another factor. If one considers the diameter of the filter element itself, plus anticipated cake accumulation, plus some dimensional safety (clearance) as comprising a small circle, the EPD is derived from the number of those small circles that can be arranged in a large circle, which is the filter vessel UID. Strictly defined, EPD is the number of square meters of filtering surface per cubic meter of filter vessel that is occupied by the filter elements. In calculating EPD, the total volume, including the volume occupied by the filter elements themselves, is used. The space beneath the filter elements (i.e., cake hopper, etc.), however, is not used. Figure 5 illustrates some examples using 60 mm o.d. × 1500 mm-long candles on varying centerline spacings.

Staggered patterns for element centerlines result in greater EPD values. Fluted S.O. elements with a reasonable COV will usually yield 12–17 percent greater EPD than their S. I. counterparts, which would seemingly have an advantage, but normally these are made with a greater o.d. (to accommodate cake in the i.d.), thereby reducing the EPD value.

Element Fixing

EPD is also affected by the method of fixing and sealing the elements in the tube sheet [4]. Often element fixing and sealing can have more effect on the size of the "small circle" mentioned earlier than the cake thickness and clearance factor. Besides affecting EPD, the method of fixing and sealing filter elements in the tube sheet directly relates to original equipment cost, installation cost, and maintenance costs. Operating pressure does not greatly affect fixing cost; it does not affect EPD at all. If the tube sheet is cooled, allowance for the cooling serpentine will most certainly affect EPD, filter vessel size, and cost. A good general statement is "the more complicated, the more costly."

Jet Pulse System

The "more complicated, more costly" statement above can also be made about the jet pulse system. The cost of the jet pulse system is ultimately determined by:

1 Required volume of jet pulse gas used per unit of time (say, per hour), volume of solids, size of solids, nature of solids, (stickiness), and allowable pressure drop, all of which must be considered. Volume of jet pulse gas is also affected by the internal volume of the filter elements, in the case of solids outside elements (S.O.), or by the internal volume of the filter housing section, in the case of solids inside elements (S.I.). Typical values for jet pulse volume are given in Fig. 6. The data used in compiling Fig. 6 were obtained from commercial literature, laboratory tests, and the referenced papers.

2 Required pressure of jet pulse gas is determined by feed gas line pressure, inherent pressure drop across the porous ceramic elements, and the nature of the particulate.

Downloaded 02 Jun 2010 to 171.66.16.121. Redistribution subject to ASME license or copyright; see http://www.asme.org/terms/Terms_Use.cfm

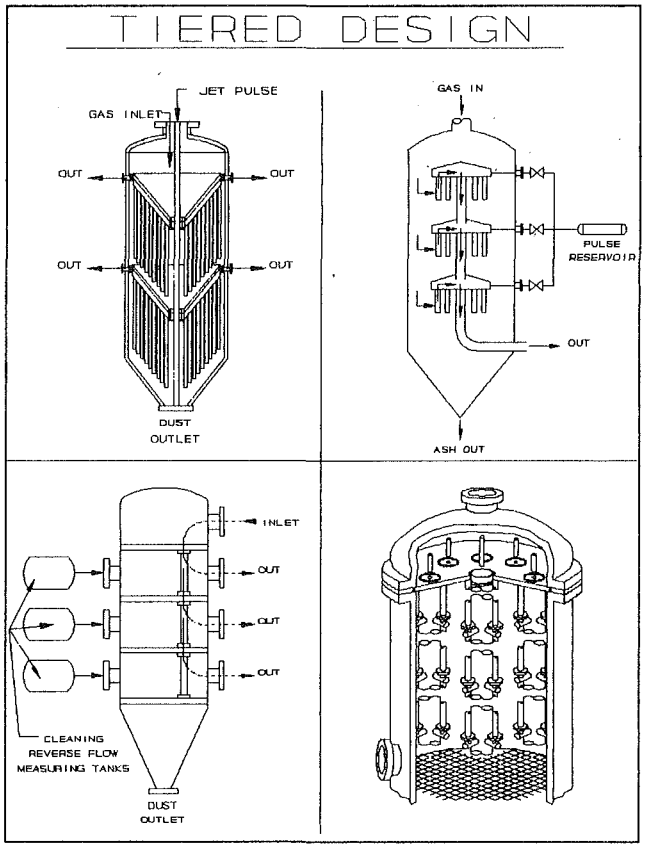

Fig. 7

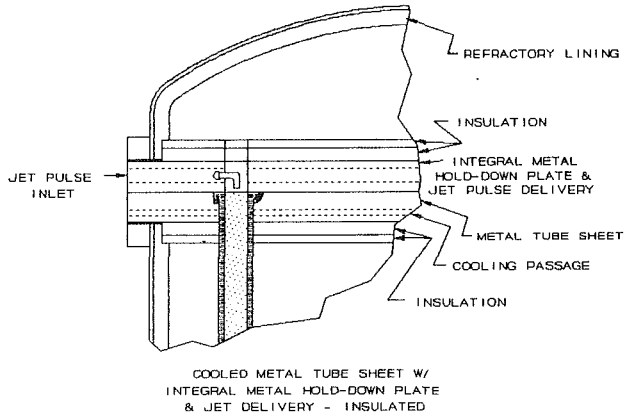

COOLED METAL TUBE SHEET W/
INTEGRAL METAL HOLD-DOWN PLATE
& JET DELIVERY - INSULATED

Fig. 8(A)

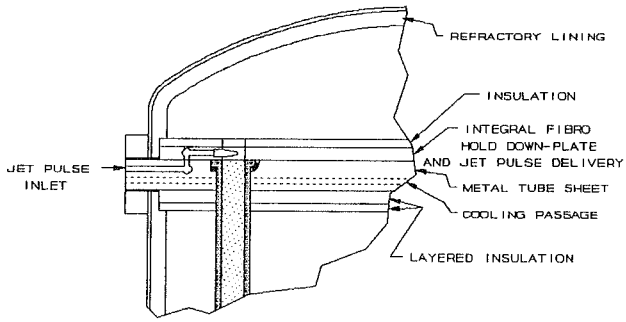

COOLED METAL TUBE SHEET & INTEGRAL
FIBRO HOLD DOWN PLATE AND JET DELIVERY

Fig. 8(B)

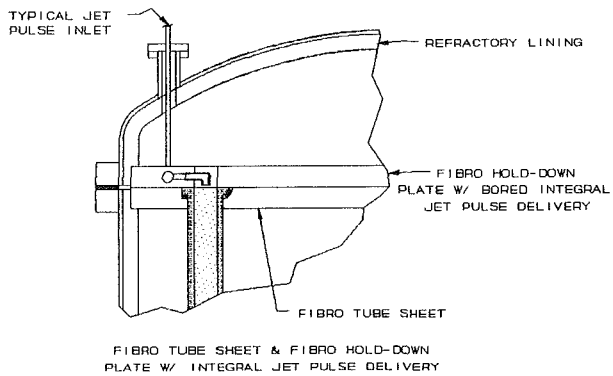

FIBRO TUBE SHEET & FIBRO HOLD-DOWN
PLATE W/ INTEGRAL JET PULSE DELIVERY

Fig. 8(C)

3 Required temperature of jet pulse gas is mainly governed by the capability of the ceramic elements to withstand thermal shock.

4 The materials used for construction of the jet pulse delivery system will be determined by the operating temperature and the gas chemistry.

Lastly, the physical design(s) of the jet pulse delivery system will also affect the manufacturing cost, the installation cost, and maintenance costs. Items 1, 2, and 3 will define the size and cost of the jet pulse gas compressor system. In all cases, the simpler and more compact, the better.

Tiered Designs

The overall cost of a hot gas filter station can theoretically be lowered, and possibly overall plant geometry improved as well, by installing 2 or 3 tiers (levels) of filter elements in a common pressure housing. Tiered designs have been proposed for both S.O. and S.I. type elements. At this point in time, tiered S.I. type filters are more widely used. To date, no really large tiered filters have been reported. Figure 7 illustrates four types of tiered design.

Integral Tubesheet System

In a series of earlier papers [26–28], the authors compared:

- "Hard" (SiC, mullite, cordierite) versus "soft" (Al_2O_3/SiO_2) ceramic fiber ("Fibro") filter elements
- Metal versus ceramic tubesheets
- Metal versus ceramic filter element positioning systems
- Metal versus ceramic "integral" jet pulse delivery systems

The general conclusions drawn were:

1 Soft ceramic fiber ("Fibro") filter, elements are lighter in weight (by a factor of 8–10), have superior tolerance for thermal shock, have equal removal efficiency, and are less expensive than their hard ceramic counterparts.

2 Ceramic fiber ("Fibro") tubesheets have very low coefficients of thermal expansion, can operate at temperatures of +1500°C, are lighter in weight (by a factor of 8–10), are relatively insensitive to temperature variations, and are less expensive than alloy tubesheets.

3 Whether metal or ceramic, the simplest and least expensive filter element fixing/positioning system is the "hold down plate."

The hold down plate lends itself to the integral system, wherein the jet pulse delivery system is incorporated within the hold down plate and the tube sheet. Integral systems can be designed as:

(A) Metal/Metal—A cooled metal tube sheet and metal hold down plate with integral jet pulse delivery system.

(B) Metal/Fibro—Cooled metal tube sheet with ceramic ("Fibro") hold down plate and integral ceramic jet pulse delivery system.

(C) Fibro/Fibro—Ceramic ("Fibro") tube sheet and ceramic

Downloaded 02 Jun 2010 to 171.66.16.121. Redistribution subject to ASME license or copyright; see http://www.asme.org/terms/Terms_Use.cfm

RELATIVE COST EFFECT

COST FACTOR	$	$$	$$$
ELEMENT PACKING DENSITY (m^2/m^3)	28-35	22-27	< 20
FACE VELOCITY (m/Hr.)	400	200	100
SOLIDS (cc/m^3)	.32	88	132
JET PULSE VOLUME (l/m^2)	< 20	24-30	> 40
MATERIAL (INTERNALS)	ALL CERAMIC	ALLOY & SOFT CERAMIC	ALLOY & HARD CERAMIC

Fig. 9

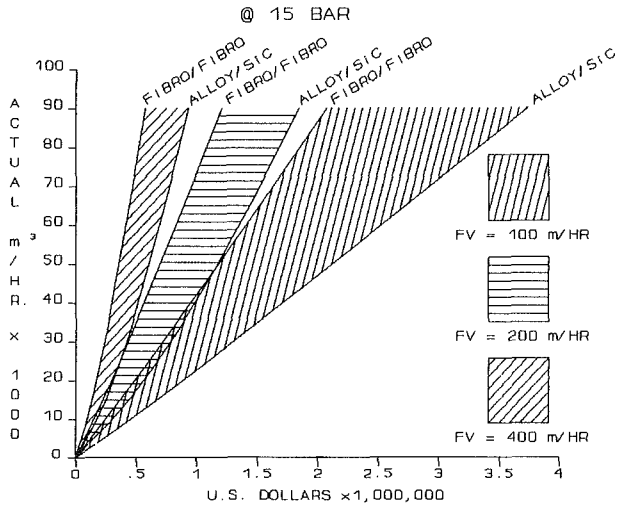

Fig. 10

("Fibro") hold down plate with integral jet pulse delivery system.

Combinations A, B, and C are illustrated in Fig. 8.

After cooling, at either programmed or unprogrammed down times, the integral system can be lifted out in one piece and quickly replaced with a complete one-piece spare. In the case of a Fibro/Fibro system, overall down time is shortened considerably due to a shorter "cool down" time.

Failure Detection System

Use of the expression "unprogrammed down times" above implies a failure in the filter system. Should one or more filter elements fail for any reason it is important to know of the failure as early as possible. Passing particulate can be detected by placing a small filter element on the clean gas side of the filter and operating it at approximately 10 or more times the filter station design face velocity. Variation in pressure drop across this "sentinel" will signal an element failure.

Conclusion

The authors have attempted to incorporate all of the statements made to this point into Figs. 9, 10, and 11, which illustrate that the cost of a hot gas filter station can vary by as much as 30–50 percent once the incoming volume of gas has been defined.

In preparing the rather extensive cost data, the authors categorized the cost-affecting factors discussed in this paper as low, medium, or high in terms of their potential affect on costs and used the specific ranges shown in Fig. 9. Note: Tiered

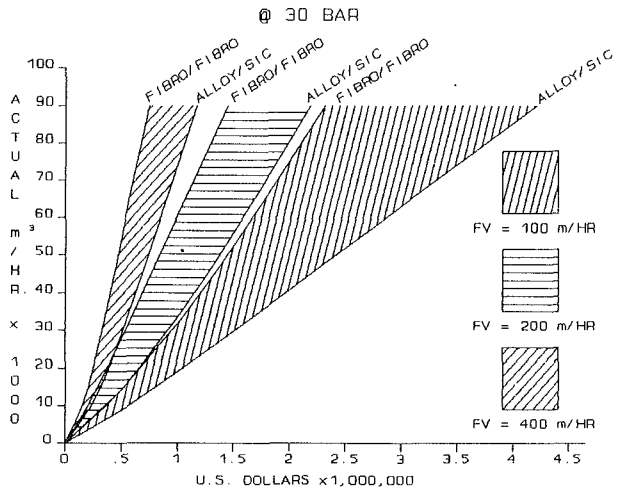

Fig. 11

designs have not been included in preparation for Figs. 8, 9, 10, or 11.

Gas flows, temperature, pressure, efficiency, fuel, etc., all were taken from a presentation made at the EPRI filtration workshop in San Francisco, November 1989 [29]. In that presentation, gasifier and PFBC 100 MWE power plants were compared.

Because the inputs for Figs. 10 and 11 are identical, with the exception of operating pressure, they can be discussed together. Included in the costs were the pressure vessel, refractory lining (in the field), tube sheet, raw materials, machining and/or milling as required, filter candles, gaskets, fixing system for candles, jet pulse delivery system, jet pulse measuring tank, jet pulse solenoids, and jet pulse system auto control. Also included was the pressure drop measuring equipment, a high solids detection and monitoring device on the "clean side" with an alarm triggered by a small "sniffer" candle, temperature sensors and engineering for all of the above. All of the above were based on "Ex works" prices.

Not included in the cost buildups were freight to site, erection/installation, start up assistance, spare components, main line valves, lock hoppers, or license fees, etc.

Some comparisons may be of interest. Since the specifications of the pressure vessel did not change, variables were assigned to the projected cost of some of the components of a complete filter at 15 bar. Here are some interesting multiples, taking the vessel as a 1.0 multiplier:

- Cooled metal tube sheet 0.6
- Cooled metal tube sheet—metal hold down plate with integral jet pulse 1.0
- Cooled metal tube sheet—Fibro hold down plate with integral jet pulse 0.65
- SiC candles 1.25
- Fibro candles 0.65

In summary, many factors contribute to the final cost of a hot gas filter station. Some are dictated by process conditions and cannot be changed, while others are a function of the filter design itself and can be tailored to any given application.

As hot gas filtration technology continues to evolve, design breakthroughs will produce more cost effective filter systems. Advances in materials of construction, particularly in the area of ceramic structural components, will allow for greater component selection, durability, and corrosion resistance.

Finally, as with any expanding market, competition between suppliers will effectively help keep costs "in check."

References

1 Hemplemann, W., "Incineration of Low Level Radioactive Waste," Karlsruhe, Aug. 1978.

Downloaded 02 Jun 2010 to 171.66.16.121. Redistribution subject to ASME license or copyright; see http://www.asme.org/terms/Terms_Use.cfm

2 Patel, J. G., and Jones, F. L., "Performance of Utah Bituminous Coal in the U-Gas Gasifier," presented at the Fifth EPRI Contractors Conference on Coal Gasification, June 1985.

3 Laux, S., Schiffer, H., and Renz, U., "Performance of Ceramic Filter Elements for Combined Cycle Power Plant High Temperature Gas Clean-Up," presented at the ASME Fluidized Bed Combustion Meeting, 1991.

4 Tassicker, O. J., Leitch, A. J., Burnard, G. K., Reed, G. P., "Performance of a Large Filter Module Utilizing Porous Ceramics on a Pressurized Fluidized Bed Combustor," presented at the Tenth International Conference on Fluidized Bed Combustion, Apr. 30–May 3, 1989.

5 Leitch, A. J., "A Summary of the EPRI Hot Gas Filter Experience at the Grimethorpe PFBC Establishment," EPRI Workshop, Nov. 29–30, 1989.

6 Lee, S. H. D., Sscmalzer, D. K., Steindler, M. J., and Swift, W. M., "Measurement of Alkali Vapors in PFBC Exhaust," *Proceedings of the Seventh Annual Coal-Fueled Heat Engines and Gas Stream Cleanup Systems Contractors Review Meeting*, U.S. DOE, Morgantown, WV, Mar. 1990.

7 Cowell, L. H., Hasen, A. M., Lecren, R. T., and Stephenson, M. D., "Coal-Fueled Two-Stage Slagging Combustion Island and Cleanup System for Gas Turbine Application," presented at the 35th International Gas Turbine & Aeroengine Congress & Expo, Brussels, Belgium, June, 1990.

8 Baird, M. J., Jarr, L. A., Longanbach, J. R., Williams, M. C., *Proceedings of the Separations Technology Workshop for Coal Gasification*, Dec. 8, 1988.

9 Jensen, R., Mahagaokar, U., and Krewinghaus, A., "SCGP—Progress in a Proven, Versatile, and Robust Technology," presented at the Ninth EPRI Conference on Coal Gasification Power Plants, Sept. 1990.

10 Wilkes, C., Santanam, C. B., DeJulio, G. M. C., and Eggerstedt, P., "Gas Stream Cleanup Program for Coal-Fueled Gas Turbines," presented at the U.S. DOE, METC Heat Engines Conference, Morgantown, WV, Mar. 25–28, 1990.

11 Hudson, D. M., Twigg, A. N., Clark, R. K., Holbrow, P., and Leitch, A. J., "Durability of Ceramic Filtration Systems for Particulate Removal at High Temperature," presented at the ASME Fluidized Bed Combustion Meeting, 1991.

12 Durst, M., Reinhardt, A., Vollmer, H., and Koch, W., "The Performance of High Efficiency High Temperature Ceramic Gas Filter Elements," presented at the Vth World Filtration Congress, June 5–8, 1990.

13 Sawyer, J., Vass, R. J., Brown, N. R., and Brown, J. J., "Corrosion and Degradation of Ceramic Particulate Filters in Direct Coal-Fired Turbine Applications," presented at the 35th International Gas Turbine & Aeroengine Congress & Expo, Brussels, Belgium, June, 1990.

14 Stringer, J., Bakker, W., Oakey, J., Semler, C., and Durst, M., "Materials Considerations for Removing Dust at High Temperature From Reducing Gases," presented at E.P.R.I. Workshop, San Francisco, CA, Nov. 1989.

15 Alvin, M. A., Lippert, T. E., and Lane, J. E., "Assessment of Porous Ceramic Materials for Hot Gas Filtration Applications," presented at the AIChE Annual Meeting, Nov. 11–16, 1990.

16 Seville, J. P. K., Clift, R., Withers, C. J., and Keidel, W., "Rigid Ceramic Media for Filtering Hot Gases," *Filtration & Separation*, July/Aug. 1989.

17 Withers, C. J., West, A. A., Twigg, A. N., Courtney, R. S., Seville, J. P. K., and Clift, R., "Improvements in the Performance of Ceramic Media for Filtration of Hot Gases," presented at Filtration Society Filtech '89, Karlsruhe, Germany.

18 Bower, C. J., Arnold, M. St. J., Oakey, J. E., and Cross, P. J. I., "Hot Particulate Removal for Coal Gasification Systems," British Coal Corporation, Coal Research Establishment, Stoke Orchard, Glos. United Kingdom.

19 Jahkola, A. Jalovaara, J., and Hulkkomen, S., "Testing of Ceramic Candle Filters at Otaniemi PFBC Test Rig," presented at the ASME Fluidized Bed Combustion Meeting, 1991.

20 Stringer, J., Leitch, A. J., and Clark, R. K., "The EPRI Hot Gas Filter Pilot Plant at Grimethorpe: What Worked, What Broke and Where Do We Go Now?" presented at the ASME Meeting, Fluidized Bed Combustion, 1991.

21 Zievers, J. F., Eggerstedt, P., Aguilar, P., and Zievers, E. C., "Some Operating Experience With Porous Ceramic Filter," presented at the Seminar on Fluidized Bed Combustion Technology for Utility Applications, Palo Alto, CA, May 3–5, 1988.

22 Zievers, E. C., Zievers, J. F., and Eggerstedt, P., "Porous Ceramics Can Be Tailored to the Hot Gas Filtration Job," presented at the Eighth International Conference on Thermal Destruction of Hazardous, Radioactive, Infectious & Mixed Wastes, May 2–5, 1989.

23 Zievers, J. F., "Comparison of Cylindrical Porous Ceramic Elements Used for Hot Gas Filtration," presented at the Vth World Filtration Congress, June 5–8, 1990.

24 Cheung, W., Seville, J. P. K., Clift, R., Withers, C. J., and Keidel, W., "Rigid Ceramic Media for Filtering Hot Gases," Department of Chemical & Process Engineering, University of Surrey, Guildford, Surrey, United Kingdom.

25 Eggerstedt, P., "Effect of High Candle I.D. Velocities on Differential Pressure," 1987, reissued 1991, Lab Report 61587, issued by the R&D Dept. of Industrial Filter & Pump Mfg. Co., Cicero, IL.

26 Zievers, J. Z., Eggerstedt, P., and Zievers, E. C., "Cylindrical Porous Ceramic Elements for Hot Gas Filtration in the Chemical Industry," presented at the American Institute of Chemical Engineers Meeting, Chicago, IL, Nov. 1990.

27 Zievers, E. C., Zievers, J. F., Eggerstedt, P., and Aguilar, P., "Porous Ceramics in Medical Waste Incineration," presented at the 1991 Incineration Conference, Knoxville, TN, May 13–17, 1991.

28 Zievers, J. F., Eggerstedt, P., Zievers, E. C., and Nicolai, D., "Lightweight Ceramic Materials Make High Temperature Gas Filtration Simpler," Deutsche Keramische Gesellschaft e.V. (DKG), Erlangen/Nurnberg, Oct. 17, 1991.

29 Tassicker, O., lecture presented at the EPRI Gas Filtration Workshop, San Francisco, CA, Nov. 1989.

Downloaded 02 Jun 2010 to 171.66.16.121. Redistribution subject to ASME license or copyright; see http://www.asme.org/terms/Terms_Use.cfm

T. E. Lippert

R. A. Newby

M. A. Alvin

D. M. Bachovchin

G. J. Bruck

E. E. Smeltzer

Westinghouse Electric Corporation,
Science & Technology Center,
Pittsburgh, PA 15235

Development of Hot Gas Cleaning Systems for Advanced, Coal-Based Gas Turbine Cycles

Westinghouse is developing hot gas cleaning systems for advanced, coal-based gas turbine cycles. This paper summarizes the Westinghouse hot gas filter concept and reports on recent in-house and field test programs supporting its design and development. Basic materials issues related to ceramic material stability and hot metals structures are reviewed. Results of recent filter system testing are presented, comparing candle and crossflow designs operating in both "simulated" and actual coal-derived gas streams. Laboratory tests and analysis are reported relating to integrating sulfur and alkali control with the particle filter function.

Introduction

Hot gas cleaning using ceramic barrier filter systems can enhance the future use of clean coal technologies such as Pressurized Fluidized Bed Combustion (PFBC), Integrated Coal Gasification Combined Cycle (IGCC), and Direct Coal-Fueled Turbines (DCFT). In these applications the hot gas filter removes sufficient ash and waste materials to protect downstream equipment from particle fouling and erosion effects and allows the cleaned gas to meet environmental emission requirements upon discharge without further flue gas treatment. The hot gas particle filter may also be integrated with the sulfur, alkali, or other gas phase contaminant removal processes. This is accomplished by injecting upstream of the filter appropriate sorbent particles that react with the gas phase contaminant and collecting the reacted sorbent particles as part of the filter cake. The filter cake is removed by pulse jet cleaning methods. In this integrated approach, the particle filter may serve as either the primary device or as a polishing device in the gas phase contaminant removal process.

The Westinghouse hot gas filter is shown schematically in Fig. 1. The system consists of a refractory lined, coded pressure vessel that contains arrays of the ceramic filter element assemblies. The arrays are formed by attaching individual candle elements (Item 1) to a common plenum (Item 2) and discharge pipe. The arrays are cleaned from a single pulse nozzle source. For efficient packaging, several of the individual plenum assemblies are arranged vertically from a common support structure, forming a filter cluster (Item 3). The filter cluster represents the basic module needed for constructing a large filter system. The individual clusters are supported from a common, high alloy tubesheet and expansion assembly (Item 4) that spans the pressure vessel and divides it into "clean" and "dirty" gas sides. The cluster concept provides a modular approach to scaleup and permits maintenance and replacement of individual filter elements. In the Westinghouse system, the cluster concept has been adapted to ceramic candles, crossflow, and bag filter elements. Currently, activity is focused on the development and demonstration of the key technologies needed for the successful commercialization of this design concept, namely:

- Selection and qualification of the ceramic filter elements
- Design and qualification of the hot metal structure
- Specification and design of a reliable, high-pressure pulse cleaning system
- Integrated process design and operation.

Ceramic barrier filter devices currently under development include candles, crossflow, tubes, bags, and granular beds. Under the auspices of the U. S. Department of Energy (DOE), Westinghouse has pioneered crossflow filter development, and with the Electric Power Research Institute (EPRI) the application of ceramic candle filters for PFBC. In recent years, the Westinghouse hot gas cleaning activity has focused on integrated filter system development. Specialized test facilities have been built and operated, and field test programs conducted in support of this activity. This paper provides an overview of the current status and test results from these program areas.

Development of Hot Gas Filter Systems

The criteria for successful use and operation of porous filters as a viable advanced particulate removal concept requires not only thermal, chemical, and mechanical stability of the ceramic materials, but also long-term structural durability of each individual filter elements, and high reliability of the integrated process design features. These system and material development issues are being addressed in dedicated test facilities built

Contributed by the International Gas Turbine Institute and presented at the 37th International Gas Turbine and Aeroengine Congress and Exposition, Cologne, Germany, June 1–4, 1992. Manuscript received by the International Gas Turbine Institute March 17, 1992. Paper No. 92-GT-431. Associate Technical Editor: L. S. Langston.

Copyright © 1993 by ASME
Downloaded 02 Jun 2010 to 171.66.16.121. Redistribution subject to ASME license or copyright; see http://www.asme.org/terms/Terms_Use.cfm

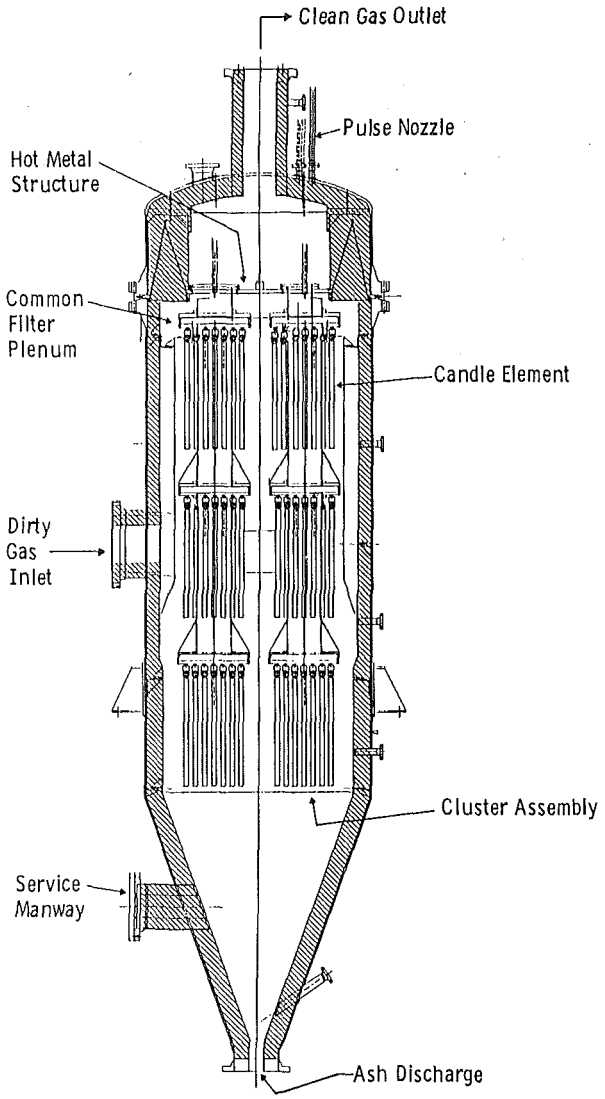

Fig. 1 Westinghouse candle filter system concept

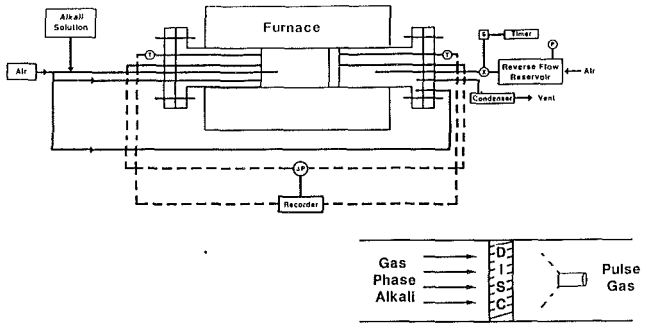

Fig. 2 Schematic of the high-temperature flow-through alkali/ceramic test facility

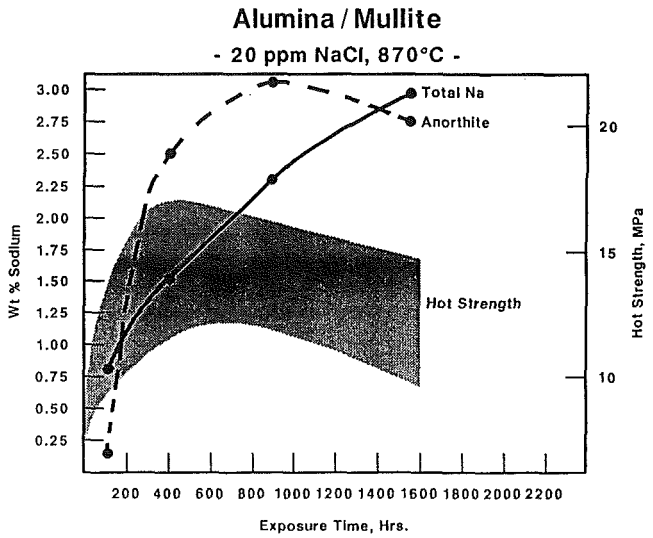

Fig. 3 Effects of alkali exposure on alumina/mullite filter material

and operated by Westinghouse at the Science and Technology Center (STC) and through pilot scale field programs.

Materials Development

Ceramic Filter Materials. Ceramic filter materials that are used in the manufacturing of porous hot gas filters include oxides such as alumina/mullite ($Al_2O_3/3Al_2O_3 \cdot 2SiO_2$), cordierite ($2MgO \cdot 2Al_2O_3 \rightleftharpoons 5SiO_2$), and aluminosilicate foam ($xAl_2O_3 \rightleftharpoons ySiO_2$); nonoxides such as clay bonded silicon carbide (SiC), and reaction bonded or sintered silicon nitride (Si_3N_4); and oxide-nonoxides such as cordierite-silicon nitride ($2MgO \rightleftharpoons 2Al_2O_3 \cdot 5SiO_2$–$Si_3N_4$). The stability of each of these materials has been under investigation for both advanced coal combustion and gasification systems [1, 2].

Westinghouse has designed, constructed, and operated two high-temperature flow-through test facilities (Fig. 2) for the purposes of evaluating porous ceramic filter material stability in controlled process gas environments (i.e., alkali, steam and air) that include thermal cycling conditions, which simulate pulse gas filter cleaning [3].

Under actual process gas applications, steam and/or coal-released gas phase alkali are expected to react with silica-containing phases present in each ceramic filter material, forming either volatile silica species or eutectic alkali silicate species, respectively [4–6]. Additional reactions have been proposed between iron, which is present in ash or char particulates, and the silica-containing phases, which are present in each ceramic filter material [7]. These reactions are expected to lead to the formation of localized iron silicate melts ($FeSiO_4$ or Fe_2SiO_4). When eutectic or molten phases are formed, closure of 1–10 μm pores may result, thus reducing gas permeability through the porous filter structure. Similarly when fines adhere or bond to the eutectic or molten phases, the effectiveness of pulse cleaning for particulate removal may be reduced. The formation of the eutectic or molten phases is known to soften or weaken the ceramic microstructure at high temperature, ultimately limiting the strength of the filter at process operating conditions.

Of particular interest to hot gas filtration have been the alumina/mullite and clay bonded silicon carbide materials (8, 9). Although the concentration of alkali and steam varies with process application, Westinghouse has demonstrated the relative inertness of alumina/mullite in both high-temperature simulated and subpilot-scale process gas environments [3]. At high temperature (~700–870°C) alumina/mullite undergoes conversion of its amorphous or glass containing phase(s) to a crystalline anorthite ($CaO \cdot Al_2O_3 \cdot 2SiO_2$) structure, which imparts high-temperature strength to the filter matrix. Conversion or crystallization is enhanced by the presence of steam and gas phase sodium species. As shown in Fig. 3, the extent of sodium sorption into the alumina/mullite matrix initially enhances conversion of the amorphous phase to the crystalline anorthite structure, which directly parallels an increase in the hot strength of the matrix. With time, sodium sorption continues, leading to the conversion of the anorthite and/or re-

Downloaded 02 Jun 2010 to 171.66.16.121. Redistribution subject to ASME license or copyright; see http://www.asme.org/terms/Terms_Use.cfm

sidual amorphous phase to tridymite (SiO_2), which may lead to a decrease or leveling-off in the hot strength of the alumina/mullite matrix. The shaded area reflects strength differences seen between alkali exposed surfaces and surfaces exposed to both alkali and cold gas pulsing.

Unlike the alumina/mullite matrix, Westinghouse has shown that the clay bonded silicon carbide matrix has a higher affinity for reaction with gas phase alkali, forming glassy sodium silicates particularly within the binder phase of this material. As a result of sodium silicate formation, the clay bonded silicon carbide structure tends to undergo a reduction in strength at process temperatures due to softening and plasticity of the binder phase.

Evaluation of filter elements from field tests has demonstrated that both the oxide and nonoxide porous ceramic filters experience overall loss of material cold strength. This is attributed to the thermal cycling effects of pulse gas cleaning. Although exact temperature gradients through the porous walls of the filters are not known during the pulse cleaning event, microcracking is considered to occur along the clean gas surface of either the crossflow or the candle filter, which reduces the cold strenght of the matrix. Efforts are being undertaken to demonstrate whether microcracking similarly influences the hot strength of the ceramic materials.

For process applications where the temperature is less than 700–800°C, both oxide and nonoxide porous ceramic filter materials are expected to remain relatively inert in the combustion or gasification process gas environment, and thus are expected to survive long-term operation (> 1000–10,000 hours). At temperatures greater than 700–800°C, particularly for the nonoxide ceramic materials, long-term filter operation is expected to be influenced by both temperature and gas phase reactions. Efforts to assure proper filter manufacturing through quality control and nondestructive evaluation measures, optimization of filter design and geometry considerations, and strengthening of the binder phases and/or overall filter matrix are being undertaken, all of which are expected to have a significant impact on the longevity of hot gas filters for use in advanced coal-powered systems.

Hot Metal Structures. The hot metal tubesheet and expansion assembly in the Westinghouse design represents the primary support structure for the filter system and must maintain satisfactory mechanical properties and resist oxidation and corrosive attack for prolonged cyclic service at elevated temperatures. While several scale-resistant iron, nickel, and cobalt-based alloys can be fabricated in sizes suitable for tubesheet and support structures, qualification of these alloys must also consider such factors as creep-induced distortion, growth of defects to critical flaw size, and weldability of the materials—both during original manufacture and during repair operation after prolonged service. Four superalloy materials that have been investigated for hot gas cleaning tubesheet application include nickel-based Rolled Alloys RA333, Inconel I617, cobalt-based Haynes H188, and iron-based Haynes H556. All four alloys show good resistance to oxidation and corrosion under conditions similar to or more severe than those encountered in PFBC systems.

A test program was undertaken to compare weldability and fatigue life of the alloys. Evaluation tests included visual, radiographic, Charpy V-Notch toughness, Varestraint weldability, and low cycle fatigue. All four alloys showed weldability in the range of other widely welded alloys such as Type 316 stainless steel and Incoloy 800. Normal precautions are advised to minimize hot cracking when welding all of these alloys. Fatigue life tests predicted the best performance for H188 followed by H556 and RA333.

Filter System Testing. Two dedicated high-temperature, high-pressure (HTHP) filter test facilities have been constructed and operated since 1988. These test facilities are intended to provide simulated HTHP dirty gas environments for evaluating ceramic filter element operating characteristics, cleaning, performance, and material durability. Ash or char materials from operating PFBC and coal gasification facilities are used. The PFBC simulator facility is designed for a gas flow up to 680 kg/h, combusting methane to provide the thermal input. A gravimetric dust feeder and a pneumatic transport line are used to re-entrain the ash into the hot gas entering the filter unit. The second HTHP test system is a closed loop that is electrically heated and designed to provide either a reducing or an inert gas environment, permitting the feeding of char/ash material. In this facility, up to 680 kg/h of gas flow is recirculated using a specially designed HTHP eductor. Approximately 10 percent of the gas is used as the motive flow for the eductor. Utilizing these facilities over 10,000 test hours of experience have been achieved on ceramic candle and crossflow filters. Recent test experience has included:

- Over 2000 operating hours on crossflow filters operating under simulated PFBC conditions with face velocity ranging from 1.5 to 5 cm/s.
- Approximately 2000 hours of testing was also completed utilizing gasifier fines re-entrained in an inert gas environment at temperatures ranging from 177°C to 650°C at system pressures from about 0.6–1.0 MPa and face velocities ranging from 1 to 2.5 cm/s.
- Approximately 400 hours of testing on 11 and 5 element candle filter arrays under simulated PFBC conditions with face velocities ranging from about 1.7 to 3.5 cm/s.
- Tests on both candles and crossflow filters to simulate PFBC plant thermal transients (startup, turbine trip) including accelerated pulse cleaning cycles.

In general, in all these tests the high performance potentials of both crossflow and candle filters have been demonstrated. Outlet dust loadings, based on isokinetic sampling, have ranged far below NSPS, averaging about 1 ppm or less.

In addition to filtration efficiency, the performance of these filters is determined by their long-term pressure drop characteristics, expressed as filter permeance. Figures 4 and 5 show measured filter permeance ratios for both the PFBC and gasifier ash testing. These simulator developed data that have been reported. Both crossflow and candle filter data are shown.

Although the PFBC simulator facilities are methane fired, major constituents of the gas composition are reasonably similar to actual plant conditions. Operating at the same system temperature and pressure in the simulator with re-entrained ash essentially reproduces the relevant filtration properties (gas particles density ratio viscosity) of the actual PFBC. Equation (1) shows that at the same face velocity (V) and solids loading, the filter pressure drop characteristics for the two cases should be similar assuming equivalent filter and cake permeance, (K_f, K_c).

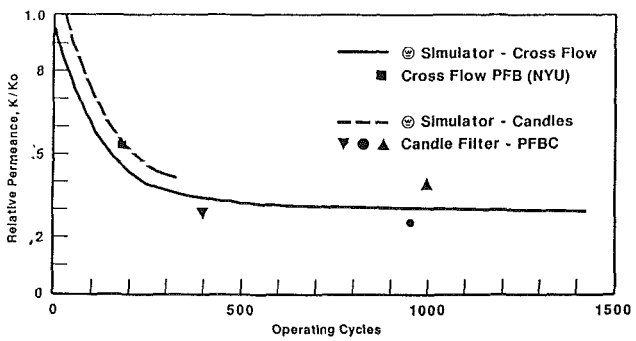

Fig. 4 Comparison of Westinghouse simulator PFBC and plant experience

Downloaded 02 Jun 2010 to 171.66.16.121. Redistribution subject to ASME license or copyright; see http://www.asme.org/terms/Terms_Use.cfm

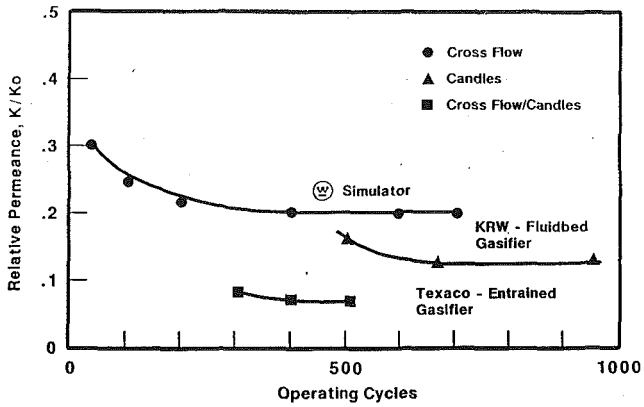

Fig. 5 Comparison of Westinghouse gasifier simulator and plant experience

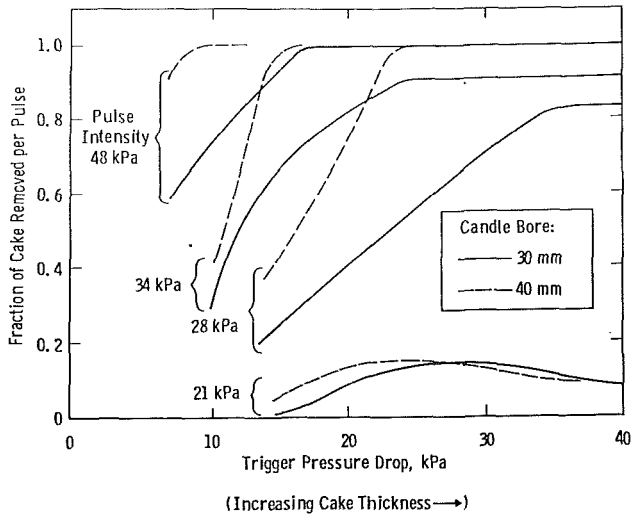

Fig. 6 Model calculations showing effect of cleaning pulse intensity and cake thickness on filter cleaning

$$\Delta p = \frac{\mu V}{K_f} + \frac{\mu C V^2 \theta}{\rho_c K_c} \tag{1}$$

where

μ = gas viscosity
V = filter face velocity
C = dust (ash) concentration
θ = time
ρ_c = bulk density of the dust cake
K_f = filter permeance
K_c = cake permeance

The cake permeance (K_c) in the simulator should be reasonably reproduced if the actual PFBC ash is used, even if the fines fraction of the re-entrained ash remains as agglomerated particles (assuming that these agglomerates are formed in the actual PFBC cake). Redepositing this entrained ash should provide a similar cake structure.

The filter permeance (K_f) establishes the baseline pressure after cleaning. Fine particulate entrained in the gas may reach the filter surface and become trapped in the pore structure, resulting in a decrease in K_f with time. By comparing the relative permeance ratio (K_f/K_{f0}) of the filters over time (or operating cycles) the effect of initial filter permeability is normalized. Data shown in Fig. 4 suggest filters operated in actual PFBC or in simulator facilities exhibit very similar permeance trends and that the tested candles and crossflows have "conditioned" similarly.

Westinghouse pilot plant test experience using both candles and crossflow filters in the entrained gasifier environments show considerable deviation from the inert gas simulator testing, Fig. 5. The low filter permeance shown in the entrained gasifier field testing reflects the relatively high operating pressure drop (accompanied by short cleaning cycles) that was experienced. It is interesting to note, however, that both crossflow and candles experienced similar low permeance values in the pilot plant testing, suggesting that the observed effect is not filter geometry related. As operated, the simulator facility could not reproduce the complex gas chemistry and potential gas/solid interaction and filter cake adhesion that may be occurring in the actual gasifier environment. Also, analysis of captured ash material from the pilot plant tests show low bulk density with a large fines fraction (8 percent $< 1.5\ \mu$, 14 percent $< 2.3\ \mu$m). These factors combine to provide bulk cake properties that exhibit high flow resistance and perhaps of more importance, high re-entrainment after a pulse.

Pulse Jet Filter Cleaning. The characteristics and properties of the ash cake, in addition to establishing the filter operating characteristics, affect the cleanability of the filter and therefore the design of the pulse gas cleaning system. Barrier filter systems are cleaned online by simple pulse jet methods. This approach utilizes a short burst of high-pressure gas, controlled by the action of a fast response valve and enhanced by the use of an educator, to cause a reverse flow back through the filter to dislodge the deposited dust cake. Test experience shows that different degrees of filter cleaning may result depending on ash and pulse jet conditions. If the pressure rise at the filter cake interface generated by the cleaning pulse exceeds the force of adhesion between the filter wall and dust cake, the cake will be removed. The pressure rise depends on reservoir pressure, piping resistance, valve characteristics, eductor design, design of the filter plenum, filter area and flow resistance, ash cake thickness and resistance, and filter operating conditions (P, T).

Partial cleaning of a filter element may occur because of nonuniformities in the dust cake properties (adhesion porosity) and thickness (distribution over the filter), pulse gas kinetic energy effects and nonuniformities in the filter wall (porosity, thickness). Once partial cleaning is initiated, the pulse cleaning gas redistributes according to the resulting variation in resistance and exacerbates the problem. Testing of filters has shown that by alternating pulse cleaning conditions or adjusting the amount of cake deposited prior to cleaning, efficient cleaning and stable base pressure drop can be recovered.

Utilizing a detailed computer model that accounts for the above effects to simulate the dynamics of cake buildup and partial cake removal, a rational basis can be developed for the design of the pulse cleaning system and operation of the filter. This is demonstrated by model calculations shown in Figs. 6 and 7. In these curves, the pulse intensity refers to the pulse gas static pressure generated in the plenum section of the filter element mount (i.e., prior to entering the filter cavity). The trigger pressure drop is the operating point at which filter cleaning is initiated. Baseline pressure drop refers to the operating point the filter retains after the cleaning event. The calculations are for PFBC conditions using candle filters of two different inside bore diameters, 30 and 40 mm. These results show:

1 Increasing the trigger pressure drop is generally beneficial because a thicker ash cake provides a higher pressure force between the filter and cake interface and also reduces pulse flow distribution effects over the filter surface.

2 Cleaning can be very "patchy" at low pulse intensities. In such cases, raising the trigger pressure drop may be detrimental because of the greater redirection of the pulse gas flow through areas already cleaned.

Downloaded 02 Jun 2010 to 171.66.16.121. Redistribution subject to ASME license or copyright; see http://www.asme.org/terms/Terms_Use.cfm

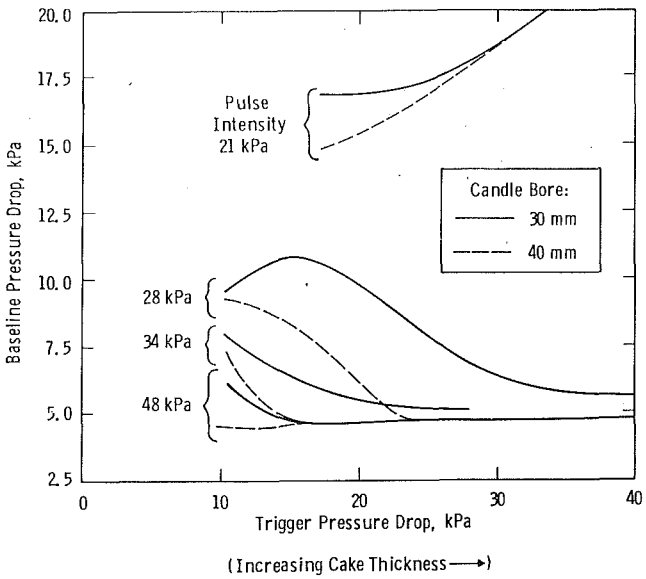

Fig. 7 Model calculations showing effect of cleaning pulse intensity and cake thickness on filter baseline pressure drop

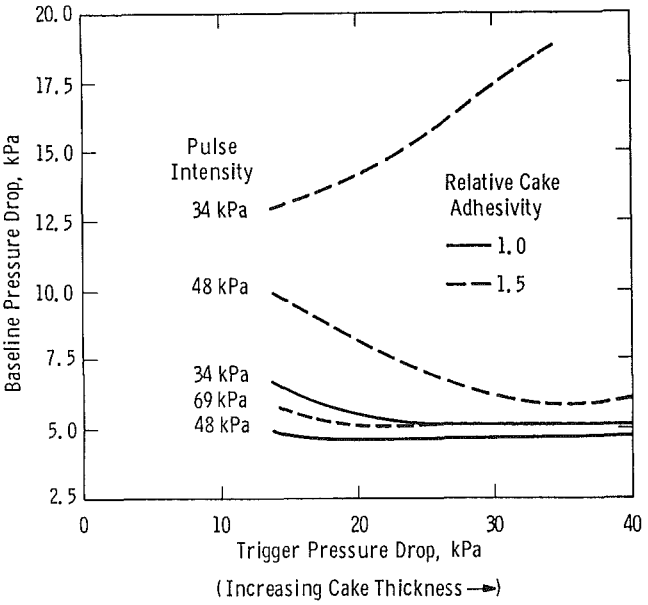

Fig. 8 Model calculations showing effect of ash cake adhesivity on filter cleaning

3 High pulse intensity is important in achieving good cleaning.

4 Increasing the candle bore from 30 to 40 mm can be beneficial because flow distribution (both in filtration and pulse cleaning) over the filter is improved. This will be more pronounced at higher face velocity.

Filter pulse cleaning systems should be designed with sufficient margin to meet a wide range of process conditions. Figure 8 illustrates the case of insufficient design margin allowed for the pulse cleaning system. In this example, a fixed design is assumed for the pulse valve system based on "low adhesion" cake characteristics—solid lines. Changes may occur in process conditions or feed stock that result in "high ash adhesion" characteristics and as illustrated, dashed lines, adversely impact filter operation unless sufficient margin is available to generate considerably higher pulse intensity.

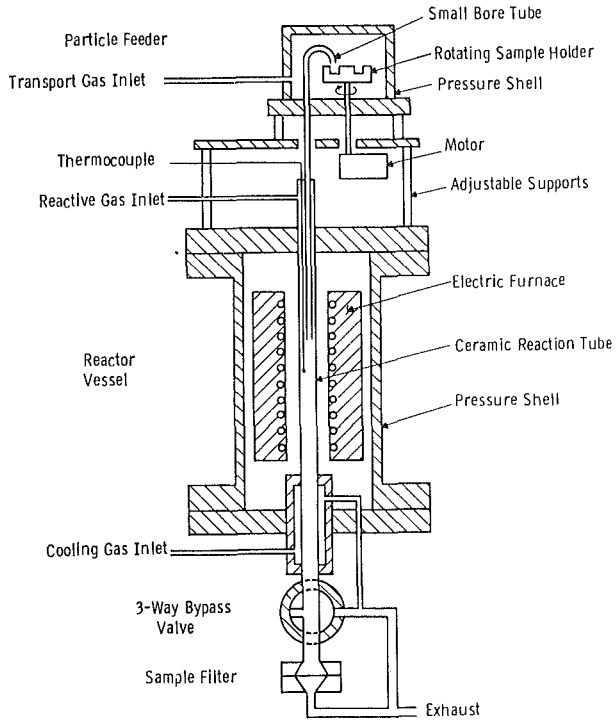

Fig. 9 Entrained reactor configuration

Integrated Hot Gas Cleaning Systems

In addition to the filter component and systems development activity described above, work is being conducted to develop process designs for integrating gas phase contaminant controls with the particle filter, i.e.,

- Ceramic barrier filter particulate control
- Sulfur sorbent injection into high-temperature gas streams
- Alkali sorbent injection into high-temperature gas streams

This approach is particularly suited to direct coal-fueled gas turbine power generation. Summarized below are results of bench-scale testing conducted into high-temperature gas flows (either oxidizing or reducing) and collected on a downstream ceramic barrier filter.

Entrained Sulfur Removal. The SO_2 removal portential under entrained, calcium-based sorbent condition has been evaluated by:

- Modeling calcium-based particle sulfation kinetics and SO_2 removal under cocurrent, entrained reactor conditions.
- Analyzing kinetic data collected in an atmospheric-pressure entrained test reactor [10], a 0.61 MPa entrained DCFT dilution zone [11], and the Westinghouse STC pressurized entrained reactor.
- Estimating commercial SO_2 performance and limitations based on the kinetic data and models generated.

Dolomitic limestone, calcitic limestone, hydrated lime, and hydrated dolomitic lime were tested utilizing the pressurized reactor shown in Fig. 9 and their performance determined by analyzing the product sorbent for their extent of sulfation. Forty-three, high-pressure 1.0 MPa tests at low Ca/S ratios were completed, looking primarily at the influence of temperature (1000°C–1260°C) and residence time (80–270 ms) in a combustion gas environment.

Using a kinetic form [12] developed from the data, the resulting design equation is

$$(E^* - E)^{0.5} = [E^*]^{0.5} - (\mathrm{Ca/S})C_o^{0.5}\, kt_r^{0.5} \qquad (2)$$

where E is the sulfur removal efficiency, E^* is the sulfur removal efficiency at equilibrium at the prevailing temperature and inlet gas composition, Ca/S is the molar calcium-to-sulfur

Downloaded 02 Jun 2010 to 171.66.16.121. Redistribution subject to ASME license or copyright; see http://www.asme.org/terms/Terms_Use.cfm

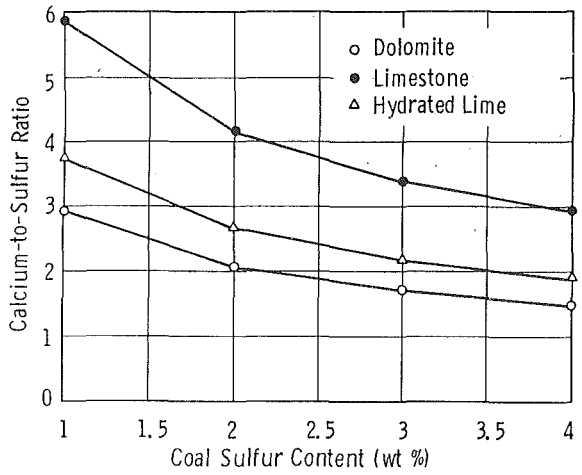

Fig. 10 Projected entrained sulfur removal performance for 1850°F temperature

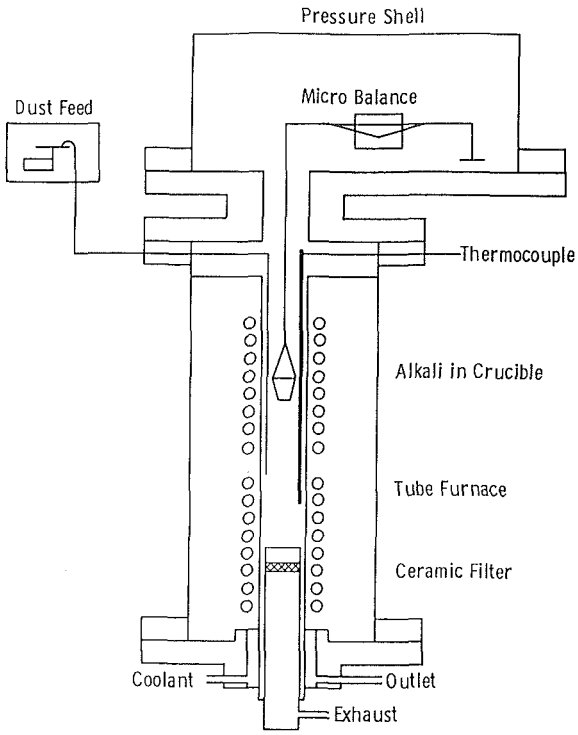

Fig. 11 Schematic of the alkali removal reactor with ceramic filter

feed ratio, C_o is the SO_2 concentration at the point of sorbent injection, and t_r is the sorbent-gas contact time in the system. Values of the constant k were determined from the data, as a function of the gas temperature for dolomitic limestone, calcitic limestone, hydrated lime, and dolomitic hydrate.

Figure 10 shows the required Ca/S ratio as a function of the coal sulfur content to meet 90 percent sulfur removal at temperatures of 1010°C. Little overall difference is found at a higher temperature of 1150°C because the higher reactivity at 1150°C is countered by the greater thermodynamic limitation at the higher temperature. At 1150°C the Ca/S ratio will rise dramatically if the coal sulfur content is reduced below 1.1 wt percent due to equilibrium limitations. If the temperature is increased beyond 1150°C the sulfur removal performance will also become poor.

Entrained Alkali Removal. The objective of alkali sorbent laboratory-scale testing has been to determine the reactivity of

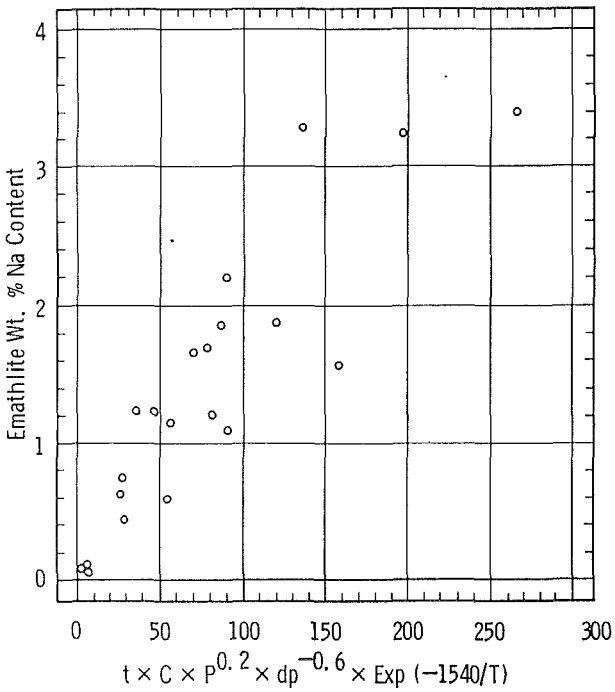

Fig. 12 NaC1-emathlite conversion data correlation

as alkali sorbents, such as emathlite [(CaO MgO) $\times Al_2O_3 \cdot ySiO_2$], at temperatures from 1010°C to 1150°C, and to project the alkali removal performance of fine alkali sorbent particles injected into the combustion products of coal-based turbine cycles.

Utilizing the entrained alkali test reactor illustrated in Fig. 11, nine alkali tests were completed and have been analyzed [12]. All the tests were at a nominal reaction temperature of 1010°C and a pressure of 1.0 MPa. Six of the tests were conducted by first loading emathlite on the internal filter disk by feeding emathlite powder (−400 mesh) for 15 minutes under hot conditions, but without alkali vapor in the gas. The gas was nitrogen containing a small amount of water vapor. A total of about 0.2 g of emathlite powder was accumulated on the filter. Then the alkali crucible was lowered into the heated zone to vaporize sodium chloride (NaCl), the vapor being carried into the reaction zone and through the emathlite layer on the filter disk. This was continued for 15 minutes of alkali exposure. The reacted emathlite sample was removed and analyzed for total sodium content. Three other tests were conducted by feeding emathlite powder for 15 minutes simultaneously with the release of alkali vapor to compare the entrained performance with the filter cake performance. The particles resided in the entrained reaction zone for about 2 seconds, and accumulated on the filter disk for an average residence time of 7.5 minutes on the filter during the test period.

The tests were conducted at different levels of alkali vapor in the gas, controlled by the temperature position of the alkali crucible within the reactor. The gas temperature profiles were measured through the reactor zone and were fairly uniform, but the filter disk temperature was about 65°C lower than the average entrained zone temperature.

The gas phase NaCl contect is estimated both from the thermobalance crucible weight record during the test period, and by the externally measured crucible weight loss over the test period. The alkali vapor content of the gas was varied over a range of 1.3 to 28.5 ppmv. These levels of alkali are representative of expectations for many coal-based gas turbine cycles. The sample sodium content shows a clear trend to increase as the gas alkali vapor content increased, and was

Downloaded 02 Jun 2010 to 171.66.16.121. Redistribution subject to ASME license or copyright; see http://www.asme.org/terms/Terms_Use.cfm

higher in the entrained tests than in the filter cake tests for comparable conditions. The unreacted emathlite powder contains 0.13 wt percent sodium, and totally saturated emathlite is expected to contain about 20 wt percent sodium.

The data collected have been correlated and compared with priori alkali removal data collected in this program (in oven tests) and in other Westinghouse STC programs that utilized emathlite pellets [13]. These test results, shown in correlated form in Fig. 12, are consistent with prior testing. The tests performed here are representative of alkali removal under reducing conditions, where the primary alkali form would be NaCl. Prior testing has shown that the alkali form (NaCl, Na_2SO_4, KCl, etc.) is not important when using emthalite or hectorite for removal, and the difference between reducing and oxidizing conditions will not be significant.

It has been concluded that:

- Emathlite is an effective alkali sorbent at temperatures up to at least 1150°C.
- The affinity of emathlite for reaction with NaCl, KCl, and Na_2SO_4 is comparable over this temperature range.
- It is expected that the gas alkali content of the combustion gas may range between 1 and 10 ppmv in many advanced technologies for a typical bituminous coal over the range of temperatures of interest. The acceptable level of alkali in the gas is uncertain, but is expected to range from 20 to 50 ppbv. Roughly, 99 percent alkali removal is required.
- The estimated maximum emathlite feed rate is about 10 times the stoichiometric feed rate, and the corresponding emathlite mass feed rate is less than about 0.5 percent of the coal feed rate.
- Westinghouse has also developed an emathlite packed bed process for alkali removal, which reduces emathlite consumption rates to near stoichiometric levels.

Conclusions

Successful development of hot gas filtration for advanced coal-based power generation requires understanding of materials behavior, component integration, and process constraints. These factors are being investigated for system demonstration through structured pilot test programs and systems modeling. Ceramic barrier filter devices such as candle and crossflow have shown highest potential for achieving performance goals consistent with gas turbine tolerance and environmental emission requirements. Westinghouse test results show the oxide-based filters will have high tolerance to both alkali and steam. The feasibility of integrating gas phase control, such as alkali and sulfur removal, with the filter function has also been demonstrated in bench-scale testing.

Several of the U. S. DOE Clean Coal programs, representing a broad range of applications, are currently considering the implementation of hot gas filtration. These programs will serve as a key vehicle for the commercial demonstration of hot gas filtration.

References

1 Alvin, M. A., Lane, J. E., and Lippert, T. E., "Thermal/Chemical Degradation of Ceramic Cross Flow Filter Materials," Topical Report, DOE contract No. DE-AC21-88MC25034, Westinghouse Science & Technology Center, 1989.

2 Sawyer, J., Brown, J. J., Brown, N., and Vass, R. J., "Chemical/Thermal Degradation of Ceramic Candle Filter Materials: Topical Report," DOE Contract No. DE-AC21-88MC25203, Acurex Corp., 1989.

3 Alvin, M. A., Bachovchin, D. M., Lane, J. E., and Lippert, T. E., "Thermal/Chemical Stability of Ceramic Cross Filter Materials," *Proceedings of the Eleventh Annual Gasification and Gas Stream Cleanup Systems Contractors Review Meeting*, Morgantown, WV, Aug. 1991.

4 Jacobsen, N. S., Smialke, J. L., and Fox, D. S., "Molten Salt Corrosion of SiC and Si_3N_4," NASA TM-101346, Nov. 1988.

5 Stern, K. H., "Oxidation of Silicon, Silicon Carbide and Silicon Nitride," NRL Memorandum Report 5447, June 4, 1986.

6 Tressler, R. E., "Corrosion of Advanced Structural Ceramics," Center for Advanced Materials Research Newsletter, Vol. 2, No. 1, 1988, pp. 1-6.

7 Perkins, R. A., and Lavendel, H. W., "Reaction of Silicon Carbide With Fused Coal Ash," Technical Planning Study 76-623, Final Report, Lockheed Palo Alto Research Laboratory for EPRI, Nov. 1976.

8 Stringer, J.,and Leitch, A. J., "Ceramic Candle Filter Performance at the Grimethorpe (UK) Pressurized Fluidized Bed Combustor," ASME JOURNAL OF ENGINEERING FOR GAS TURBINES AND POWER, Vol. 114, pp. 371-379.

9 Lippert, T. E., Alvin, M. A., Bachovchin, D. M., Haldipur, G. B., Newby, R. A., and Smeltzer, E. E., "Cross Flow Filter Development for Advanced Fossil Power Generation," presented at the ASME 1990 International Joint Power Generation Conference, Boston, MA, Oct. 24, 1990.

10 Milne, C. R., "High Temperature Short-Time Sulfation of Calcium-Based Sorbents," Ph.D. Thesis, Univ. of Utah.

11 Solar Turbines, Inc., "Advanced Coal-Fueled Industrial Cogeneration Gas Turbine System," Semi Annual Report to DOE/METC, Dec. 2, 1988-June 1, 1989.

12 Newby, R. A., et al., "Integrated Low-Emissions Cleanup Systems for DCFT," *Proceedings of the 7th Annual Coal-Fueled Heat Engines and Gas Stream Cleanup Systems Contractors Review Meeting*, Morgantown, WV, Mar. 1990.

13 Mulik, P. R., et al., "Simultaneous High Temperature Removal of Alkali and Particulates in a Pressurized Gasification Systems," Final Report, DOE/MC/16372-1548, Sept. 1983.

Downloaded 02 Jun 2010 to 171.66.16.121. Redistribution subject to ASME license or copyright; see http://www.asme.org/terms/Terms_Use.cfm

L. R. White
New Products Department.

T. L. Tompkins

K. C. Hsieh

D. D. Johnson

Ceramic Materials Department.

3M Center,
St. Paul, MN 55144-1000

Ceramic Filters for Hot Gas Cleanup

This paper reviews the properties of high-temperature ceramic fibers and relates why strength, thermal shock resistance, chemical inertness, and high-temperature capability are important properties for high-temperature filter media. The use of candle filters, fabric filters, and composite filters will be discussed for removal of particulates from hot gas streams in electrical power generation systems, metal refining, chemical processing, and Diesel engine exhaust applications.

Introduction

Environmental concern and passage of the U.S. Clean Air Act have focused attention on the removal of pollutants from hot gas streams. Application of high-performance, high-temperature particulate control ceramic filters is expected to be beneficial not only to the advanced fossil-fuel processing technologies, but also to high-temperature industrial processes, waste incineration processes, and to Diesel soot filtration.

Development and utilization of hot gas filtration depends on the creative design and use of new high-temperature materials. A potential building block for these ceramic filters is the Nextel™[1] family of continuous ceramic fibers, which are capable of withstanding temperatures above 1100°C. This paper reviews the properties of ABS fibers and details three areas of hot gas filter development: (1) ceramic fabric filters, (2) diesel particulate traps, and (3) ceramic composite filters, currently in progress at 3M.

ABS Fiber Family

ABS fibers are continuous, polycrystalline metal oxide fibers, typically 10–12 μm in diameter, transparent and nonporous.

The continuous nature of the ceramic fibers allows processing them into engineered yarns for conversion into many textile shapes and forms using conventional textile weaving and braiding processes and equipment. The resultant textile shapes and forms are useful for a variety of applications at temperatures greater than 1100°C.

Table 1 lists the chemistry and physical properties for four fibers. Fibers designated 312 and 440 have been commercially available for some time. Two newly developed fibers, 550 and 610, are also shown since they may have future applications in the filtration area.

Ceramic Filters for Hot Gas Filtration

Ceramic filters utilized for hot gas filtration of fossil-fueled industrial processes will be exposed to a variety of conditions in addition to heat. The gas may contain acid vapors, have reducing or oxidizing potential, and may also be pressurized. Table 2 illustrates the temperature ranges and the corresponding process operating conditions that may be encountered in several hot gas filtration applications for ceramic filters (Alvin et al., 1991).

Diesel Soot Filters

The mechanical properties, ease in handling, durability, and temperature resistance of ABS fibers make them an attractive medium for producing filters for the collection of soot from Diesel engine exhausts. Wound cartridge filters will not crack when exposed to severe thermal or mechanical stress due to the nonrigid nature of these fibers. Individual fibers will move relative to one another to relieve the stress.

Cartridge filters have been made by winding ABS continuous yarns around a perforated metal tube. There is normally a nonperforated area on each end of the tube to seal against exhaust leakage. Figure 1 is a schematic of such a filter cartridge. In use, one end of the tube is blocked. This forces the exhaust gas through the ceramic fiber of the filter cartridge where the soot particles are captured. A diesel trap system usually contains a number of these individual filter cartridges.

Figure 2 shows the pressure drop vesus flow rate for clean and soot-loaded filters. Once the filter has been loaded and the pressure drop reaches a predetermined value, the filter will then be regenerated. Regeneration is simply burning the soot to clean the filter. Filter cartridges are compatible with all regeneration systems used today such as electric heaters, burners, engine throttling, fuel additives, and catalysts.

[1] Nextel™ fibers are composed of alumina, boria, and silica and are denoted as ABS fibers in the rest of this paper.

Contributed by the International Gas Turbine Institute and Presented at the 37th International Gas Turbine and Aeroengine Congress and Exposition, Cologne, Germany, June 1–4, 1992. Manuscript received by the International Gas Turbine Institute February 27, 1992. Paper No. 92-GT-313. Associate Technical Editor: L. S. Langston.

Copyright © 1993 by ASME
Downloaded 02 Jun 2010 to 171.66.16.121. Redistribution subject to ASME license or copyright; see http://www.asme.org/terms/Terms_Use.cfm

Table 1 Properties of ABS fibers

Property	Units	312	440	550	610
Filameter diameter	μm	10–12	10–12	10–12	10–12
Crystal size	nm	< 500	< 500	< 500	< 500
Crystal type		$9Al_2O_3:2B_2O_3$ + amorph. SiO_2	gamma Al_2O_3 + mullite + amorph. SiO_2	gamma/delta Al_2O_3 + amorph. SiO_2	alpha Al_2O_3
Density	g/cc	2.7–2.9	3.05	3.03–3.04	3.7–3.8
Filament tensile strength (51 mm gage)	MPa	1700	2000	2000	1900
Filament tensile modulus	GPa	150	190	193	373
Surface area	m^2/g	< 0.2	< 0.2	< 0.2	< 0.2
Composition	wt %	62 Al_2O_3 24 SiO_2 14 B_2O_3	70 Al_2O_3 28 SiO_2 2 Bi_2O_3	73 Al_2O_3 27 SiO_2	> 99 Al_2O_3 0.2–0.3 SiO_2 0.4–0.7 Fe_2O_3
Thermal expansion (100–1100°C)	ppm/°C	3	4–5.3	—	—
Dielectric constant (@ 9.375 Ghz)		5.2	5.7	~5.8	~9

Table 2 Conditions for ceramic filter applications

Filter applications	Temperature (°C)	Pressure (atm)	Composition	Particulate loading (ppm)	Life requirements (h)
Fossil fuel combustion					
Fluidized bed combustion	500–1000	3–20	Oxidizing	1000–10,000	> 10,000
Coal gasification	700–800	10–20	Reducing	1000–10,000	> 10,000
Direct coal fired turbine	1000–1350	10–20	Oxidizing	1000	> 10,000
Waste incineration	600–800	1	Oxidizing	1000–10,000	> 10,000
Industrial processes					
Plasma	500–800	1	Oxidizing	100,000	> 10,000
Metals	400–1000	1	Oxidizing and Reduction	30,000	> 10,000
Diesel filtration	600–1100	1	Oxidizing	< 1000	> 10,000

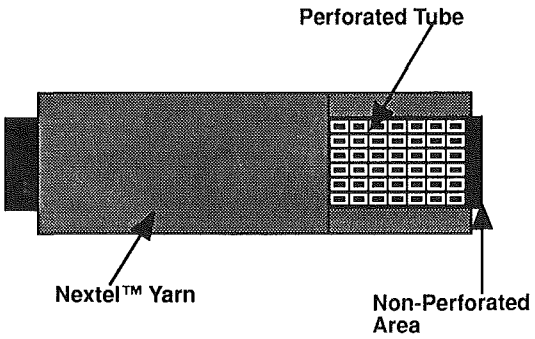

Fig. 1 3M Diesel filter cartridge

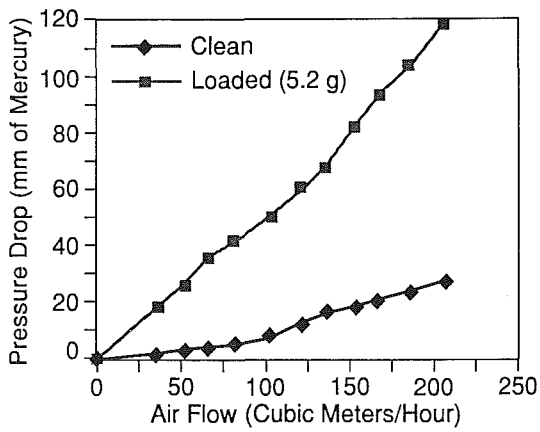

Fig. 2 Pressure drop versus flow rate; flow is from inside to outside and cartridge dimensions are: 38.1 mm i.d., 63.5 mm o.d., and 508 mm long

Filtration efficiency and soot holding capacity are dependent variables that can be adjusted within limits to satisfy requirements. Cartridge filters have been evaluated on various bus, truck, and small vehicle engines. The procedure for measuring filter cartridge efficiency was to pump a known volume of gas through a membrane filter that had been conditioned in a controlled temperature and humidity environment for at least 8 hours. Exhaust gas both upstream and downstream of the filter cartridge was sampled simultaneously for a set period of time. The particulate-laden membrane filters were then weighed after they had again been conditioned for 8 hours. Percent efficiency was then calculated as:

$$\%E = (\text{Upstream concentration} - \text{Downstream concentration}) \times \frac{100}{\text{Upstream}}$$

where both downstream and upstream mass concentrations were determined by:

$$\text{Mass concentration} = \frac{(\text{Soiled filter weight} - \text{Clean filter weight})}{(\text{Measured exhaust volume sampled})}$$

Efficiency varies from around 65 to 90 percent depending on face velocity. Efficiency data points versus face velocity are shown in Fig. 3. Each data point in the figure is an average of at least three tests. Tests have demonstrated that filters can be made to meet the new standards for diesel particulate emissions.

Filter cartridges of the type described here are being used successfully in diesel soot filters for both on and off-road vehicles. Filter cartridges with built-in electrical heaters for regeneration have been demonstrated in daily use on several city buses in various parts of the country.

Ceramic Fabric Filters

The continuous and flexible nature of ABS fibers allows the weaving of many speciality fabrics for use at high temperature. One particular design, a seamless filter bag, was developed

Downloaded 02 Jun 2010 to 171.66.16.121. Redistribution subject to ASME license or copyright; see http://www.asme.org/terms/Terms_Use.cfm

and patented as a filtration fabric (White et al., 1986). This fabric forms the basis for an advanced technology in electrical power generating plants that use coal. Using a high-temperature filtration system means substantial saving for these generating plants, because waste gases need no longer be cooled prior to filtration and it is possible that with many industrial gas streams above 480°C, a considerable amount of heat can be recovered.

University of North Dakota Study. The Electric Power Research Institute (EPRI) and the Energy & Environmental Research Center of the University of North Dakota tested seamless woven filter bags in a high temperature baghouse with reverse pulse jet cleaning. A slipstream of flue gas containing fly ash from a stoker-fired boiler at the University of North Dakota steam plant was used for the test. Results reported by Weber and Schelkoph (1990) are in Table 3. Phase I was a 1000-hour test, phase II was a 16,000+ hour test using an improved fabric. The filtration efficiencies ranged from 99.19 to 99.99 percent by Environmental Protection Agency (EPA) Method 5 sampling at operating temperatures of 427°C to 538°C.

Tensile strength of the filter bags was measured several times during the test program. Periodically, a filter bag would be removed for strength testing and replaced with a new bag. Figure 4 shows that after 16,728 hours of operation the filter bags retained 85 percent of their initial strength. The original filter bags were in excellent condition with no flaws at the conclusion of this test program.

U.S. Department of Energy—Clean Coal II Program. The SO_x, NO_x, ROX, BOX™ (SNRB) process, or the Babcock & Wilcox patented hot catalytic scrubbing baghouse, is an advanced air pollution control system for the combined removal of sulfur oxides, nitrogen oxides, and particulates emitted from fossil-fired boilers or processes. The key to the SNRB process is a high-temperature baghouse in which simultaneous SO_x, NO_x, and particulate removal occurs.

SO_x, removal is accomplished by injecting a dry sorbent such as hydrated lime or sodium bicarbonate into the flue gas at 480–590°C. NO_x removal is accomplished in part by ammonia injection with a selective NO_x reduction catalyst located inside each filter bag assembly. Finally, the particulates and spent SO_x sorbent are collected in a high-temperature baghouse at 370–455°C using ABS filter bags. The SNRB process offers the advantages of high removal efficiencies of SO_x, NO_x, and particulate with only a single major component—a high-temperature baghouse. Additional benefits include simplicity in handling of dry materials, increased catalyst life, and the potential for improving the boiler/turbine cycle efficiency.

Laboratory-Scale Pilot Testing. A laboratory scale 0.5 megawatt electric (MWe) pilot furnace, insulated duct work, a solids injection system, an ammonia injection system, a water-cooled heat exchanger to simulate the economizer section of an utility boiler, and a high-temperature baghouse, were used to evaluate the SNRB process (Chu et al., 1991). The high-temperature baghouse contained 12 commercial size bag/catalyst arrangements. Each bag was 15.56 cm in diameter and 6.1 m in length, yielding a total collection area of about 2.98 m^2. The baghouse employed an on-line pulse jet cleaning system with a differential pressure switch to trigger baghouse cleaning. The baghouse utilized high-temperature, woven ABS bags for particulate removal and a vanadium-free, zeolite catalyst from the Norton Company to promote NO_x reduction by NH_3.

A medium-sulfur Ohio #8 coal (2–2.5 percent sulfur) was burned in the pilot test furnace to produce flue gas containing approximately 1500–2000 ppm SO_2, 600–800 ppm NO_x, and 3–4 percent O_2. The SO_2, NO_x, and O_2 compositions were continuously monitored at the furnace outlet at the baghouse inlet, and at the baghouse outlet.

The baghouse was operated at temperatures up to 455°C. One of the project objectives was to achieve particulate emis-

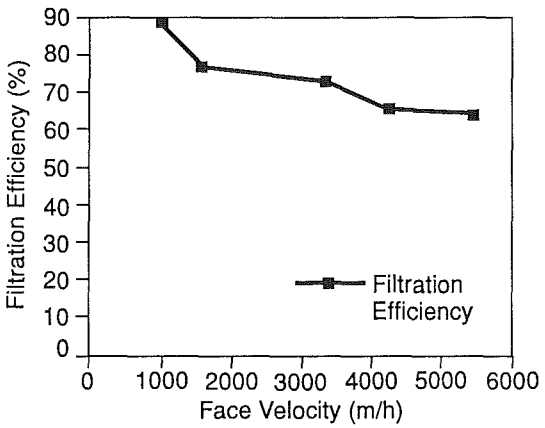

Fig. 3 Filtration efficiency versus face velocity

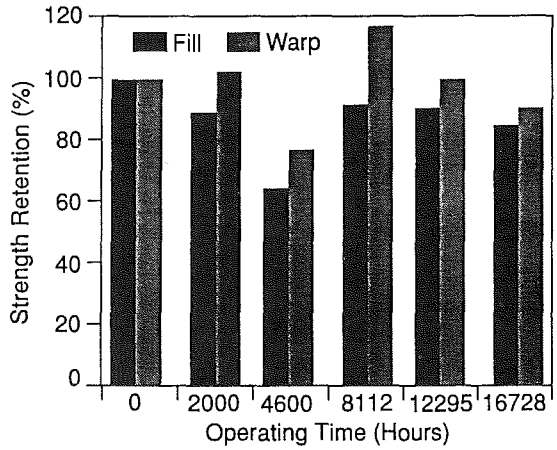

Fig. 4 Strength retention versus time

Table 3 Test results from University of North Dakota

	Phase I	Phase II
Efficiency	99.19–99.96 percent	99.66–99.99 percent
Test method	EPA method 5	EPA method 5 and 8
Total test time	1022 hours	16877 hours (3441 cleaning cycles)
Particulate	Fly ash	Fly ash
Operating temperature	427° to 510°C (800° to 950°F)	427° to 538°C (800° to 1000°F)
Face velocity	0.9 m/min (3.0 ft/min)	1.8 m/min (6.0 ft/min)
Mass median diameter	2.3 μm	2.6–14.8 μm
Mass concentration	>3.4 g/m^3 (>1.5 grain/ft^3)	>3.4 g/m^3 (>1.5 grain/ft^3)

Downloaded 02 Jun 2010 to 171.66.16.121. Redistribution subject to ASME license or copyright; see http://www.asme.org/terms/Terms_Use.cfm

sions less than the New Source Performance Standards (NSPS) requirement of 12.9 g/10^9 J (0.03 lb/10^6 Btu). Particulate emissions downstream of the baghouse were determined using EPA Methods 5 and 17 and emissions less than 12.9 g/10^9 J were observed (Fig. 5). This corresponds to particulate collection efficiencies greater than 99.9 percent. The baghouse operating temperature did not appear to affect particulate collection efficiency over the range of temperatures evaluated.

Figure 6 shows that increasing temperature led to higher SO_x and NO_x removal rates, thus demonstrating the advantage of a hot baghouse.

B&W is currently being funded by the U.S. Department of Energy (DOE) and the Ohio Coal Development Office (OCDO) under the DOE Innovative Clean Coal Technology Demonstration program to demonstrate the feasibility of the SNRB technology in a 5-MWe field demonstration at a coal-fired utility boiler. The project involves a team approach with B&W, Norton Company (catalyst supplier), Minnesota Mining and Manufacturing (bag manufacturer). Ohio Edison (host utility), and EPRI. This demonstration will be operational in early 1992.

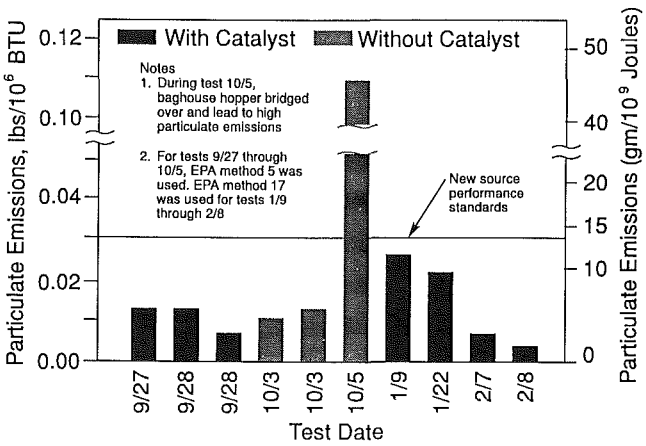

Fig. 5 Pilot facility particulate emissions

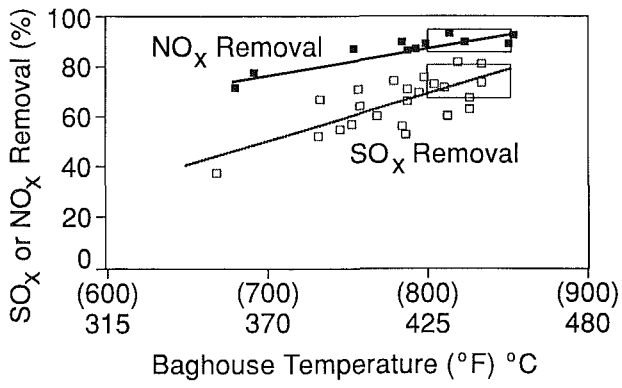

Fig. 6 SO_x/NO_x operating compatibility

Other Filter Bag Applications. ABS filter bags have also been used to filter particulate in several industrial operations. They have been operating several years removing catalyst fines from a spent catalyst bin vent in a catalytic cracking unit. New applications include removing fine powdered metals from hot gas streams and high-temperature metal separations where one element is gaseous.

Composite Filters. Since the oil crisis of 1973, more efficient coal to energy processes have been sought. Pressurized fluidized bed combustion and coal gasification combined cycle are attractive technologies; however, both require hot gas cleanup for turbine protection. High-efficiency cyclones have been used but do not remove particles smaller than about 5 μm so that additional cleanup is needed in order to satisfy environmental constraints. Hot gas filtration using rigid ceramic filters has demonstrated dust removal at high efficiency and an acceptable pressure loss. Major concerns have been thermal shock caused by pulse-cleaning, chemical attack by alkali vapor, and cleanability of the rigid filter.

The ceramic filters which have been tested at PFBC conditions more than any others are called candles, are tubular in shape, and are made from ceramic particles and fibers which are bonded with a glassy phase. The gas path through them is 15 mm in length, and they are heavy, each one weighing about six kilograms.

A new filter is being developed as an alternative to candles (White, 1991). It is being constructed from a ceramic fiber reinforced ceramic matrix composite material, the reinforcement is ABS fiber and the matrix is silicon carbide.

The filter is fabricated by first making a preform of ceramic fibers and then depositing the matrix by chemical vapor deposition. Filters made so far weigh 1.2 to 1.3 kilograms and have a gas path of 2.5 to 3.5 mm. This represents an 80 percent reduction in weight and wall thickness, so they are light and thin in comparison to candles.

Table 4 shows the effect of thermal shock created by immersing a specimen heated to 1000°C into water. Two different ceramic composite filters are shown labeled A and B. These differ in the way the filtering surface is made. Structurally they are similar but B has a layer of ceramic felt which is the filtering surface. Monolithic refers to a commercially available candle. Strength loss occurred for all filters but was most severe for Monolithic. B suffered delamination of the outer layer of felt. Studies of polished sections showed that the felt was not well-bonded to the underlying surface during fabrication.

Water cycle tests are severe and may be unrealistic and a pulse tester was used to assess damage caused by cleaning pulses. This pulse tester consisted of a heated enclosure in which a filter was suspended and air was passed through it from outside to inside. Periodically, a cleaning pulse was sent down the axis of the filter.

A filter of type B was tested for about 1000 hours with a total of 100,000 pulses. Temperature was 850–900°C, air flow was 27–31 m^2/h, pressure drop across the filter was 51–61 cm of water (50–60 mbar), pulse reservoir pressure was 5.5–6.2 bar, and pulse duration was 0.1 second. Pulse frequency was twice per minute and was set at that value because measure-

Table 4 Thermal shock resistance

Cycles = 1000°C/Water Immersion					
Filter A		Filter B		Monolithic	
Cycles	Burst pressure (bar)	Cycles	Burst pressure (bar)	Cycles	Burst pressure (bar)
0	37.0	0	32.0	0	60.0
1	25.0	1	16.0	1	10.0
2	14.0	2	5.9	2	N/A
4	8.4	4	6.1	4	Too weak
8	9.9	8	N/A	8	Too weak
		Delaminated on second cycle			

Downloaded 02 Jun 2010 to 171.66.16.121. Redistribution subject to ASME license or copyright; see http://www.asme.org/terms/Terms_Use.cfm

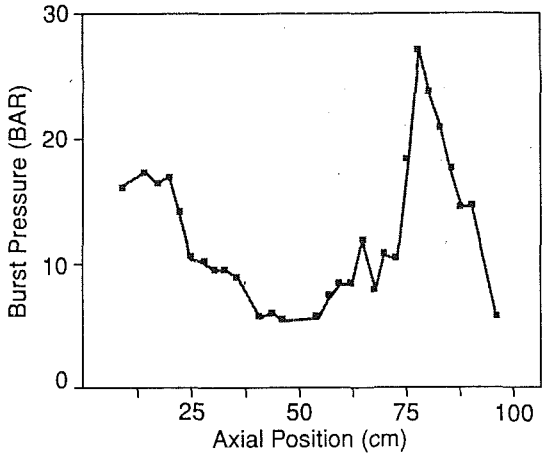

Fig. 7 Type B filter; burst strength after pulse testing

ments of temperature indicated that equilibration between pulses required about thirty seconds. The total number of pulses corresponds to one year of service if filters are cleaned once every five minutes.

Figure 7 shows burst strength of the pulse-tested filter. Air pulsing, exposure to temperature, or both have weakened it, but it was strong enough to withstand pulsing, i.e., it did not break during testing. The spike in burst strength at an axial position of 75 cm is not understood and may be due to the dynamics of pulse cleaning.

Development of composite filters is not complete but results indicate that light, strong filters can be made. Improvements in bonding the filtering surface to the underlying substrate are needed and work is in progress to solve that problem.

Summary

ABS fibers have sufficient strength and chemical resistance to be used in ceramic filters for temperatures up to 1000°C. Flexibility and strength permit development of textile shapes and forms for many diverse applications. The fibers are resistant to oxidizing and reducing atmospheres at the temperatures of interest for most fossil fuel combustion processes.

Diesel soot filters have been developed and successfully demonstrated on several test vehicles using several cartridge systems.

Ceramic fabric filters have been installed on a coal-fired boiler and operated at >99 percent efficiency for a period equal to two years of continuous use. This fabric has also been successfully tested in the SNRB process with >99.9 percent collection efficiency. This work is currently being scaled up to a 5 MWe demonstration at a coal-fired utility boiler.

ABS fibers have also been used as the reinforcement in a ceramic fiber, ceramic matrix composite material. Strong, lightweight, thermal shock resistant structures can be made and tailored for both strength and filtration properties.

Ceramic fibers are building blocks that can be creatively engineered into unique structures. They can be engineered to protect the space shuttle during re-entry or they can be used to remove several forms of pollution from hot gas streams, protect our environment, and at the same time conserve energy.

References

Alvin, M. A., Lippert, T. E., and Lane, J. E., 1991, "Assessment of Porous Ceramic Materials for Hot Gas Filtration Applications," *American Ceramic Society Bulletin*, Vol. 70, No. 9.

Chu, P., Kudlac, G. A., Wilkinson, J. M., and Korbett, G. A., 1991, "Simultaneous SO_x/NO_x/Particulate Removal in a High Temperature Baghouse," presented at the American Flame Research Institute Spring Meeting, Hartford, CT, Mar. 18–19.

Weber, G. F., and Schelkoph, G. L., 1990, "Pilot Scale Performance/Durability Evaluation of 3M Company's High Temperature Nextel™ Filter Bags," Final Project Report submitted to EPRI under EPRI Contract 1336-16, Feb.

White, L. R., Forester, R. J., O'Brien, D. L., and Schmidt, G. A., 1986, "Ceramic Fabrics for Filtration at High Temperatures," 290–870°C," *I. Chem. E. Symposium Series*, No. 99, p. 263–281.

White, L. R., 1991, "Ceramic Filters for Use at High Temperature," presented at the 9th Particulate Control Symposium, EPRI, Williamsburg, VA, Oct. 15–18.

Downloaded 02 Jun 2010 to 171.66.16.121. Redistribution subject to ASME license or copyright; see http://www.asme.org/terms/Terms_Use.cfm

Utility Perspective of Selecting Air Filter for Simple-Cycle, Heavy-Duty Combustion Turbines

J. W. Lyons
Combustion Turbine Technologies.

A. Morrison

Southern Company Services, Inc.,
Power and System Engineering—
Mechanical,
Birmingham, AL 35202-2625

The combustion turbines evaluated for this study range in size (nominal) from 80 MW to 100 MW and operate at a compression ratio between 10 and 14. Under these conditions the compressor ingests about 500,000 to 725,000 cubic feet of air per minute for its rated output. With this volume of air, even low concentrations of contaminants can result in a significant total amount of contaminants entering the unit, which may cause compressor erosion, fouling, and foreign object damage in the compressor section and cooling air passage blockage, locking of turbine blade roots, and hot corrosion or sulfidation in the turbine section. Adequate protection against the above-mentioned degradation or damage due to poor air quality may be obtained by using properly designed air filters. An inadequate filter system or total lack of one results in a reduction in power and efficiency over the life of the unit and may significantly decrease the intervals between maintenance and thereby increase the cost of maintenance. Consideration should be given to adding an air inlet filter when or after the combustion turbine without air filter is overhauled to reduce future maintenance costs. This study investigates the need for an inlet air filtration system for simple-cycle, heavy-duty combustion turbines from a cost/benefit and operation standpoint. Options for inlet air filters include a self-cleaning pulse type filter, a surface loading cartridge filter without pulse feature, and a three-stage depth loading type media type filter. Benefits are determined by estimates of improvements in performance and effects on the combustion turbine's longevity and maintenance.

Air Quality Analysis

Airborne contamination may be defined in terms of the following:

- Dust or particulate concentration.
- Particle size distribution.
- Identification of specific contaminants.

Particulate concentration is the weight of contamination per unit volume of air. The unit for particulate concentration can be designated as mg/m^3 of air, μg/m^3, g/1000 ft^3, grains/1000 ft^3, or parts per million (ppm). This analysis considers the unit parts per million, i.e., the mass of contaminants per million units mass of air. Contaminants may be categorized as low (<0.1 ppm by weight), moderate (>0.1 ppm and <0.3 ppm), and high (>0.3 ppm).

The size distributions of airborne dusts are variable with respect to time and place. In general, high values of dust concentration tend to be associated with coarse dust and low values with fine dust. Approximately 80 percent of the particles in the atmosphere are 0.1 μm or less and contribute only 1 percent of the total weight of the contaminants. Most of the weights of the contaminants are associated with contaminants larger than 1 μm [1].

Specific contaminants such as sodium, potassium, vanadium, and lead may exist in the air in the smaller particle size range. When these contaminants are known to be in the environment, high-efficiency filter devices are required to protect against hot corrosion.

Reasons for Air Filtration

Following are the reasons for an inlet air filtration system for a simple-cycle, heavy-duty combustion turbine [2].

The compressors of typical heavy-duty combustion turbines range in size from 80 MW to 100 MW and ingest about 500,000 to 725,000 cubic feet of air per minute for their rated output. Figure 1 gives the total mass of particulates ingested by the combustion turbine within a year for 300 hours of peaking operation at 95°F based on moderate particulate concentration of 0.15 ppm by weight.

Figure 1 shows that the quantity of dust that is ingested can be appreciable when totaled over 20 to 30 years of operation.

FLOW (scfm)	NO. OF HOURS	TOTAL PARTICULATE (DUST) WEIGHT (lb.)
500,000	300	97
725,000	300	141

Fig. 1

Contributed by the International Gas Turbine Institute and presented at the 37th International Gas Turbine and Aeroengine Congress and Exposition, Cologne, Germany, June 1–4, 1992. Manuscript received by the International Gas Turbine Institute February 21, 1992. Paper No. 92-GT-321. Associate Technical Editor: L. S. Langston.

Copyright © 1993 by ASME
Downloaded 02 Jun 2010 to 171.66.16.121. Redistribution subject to ASME license or copyright; see http://www.asme.org/terms/Terms_Use.cfm

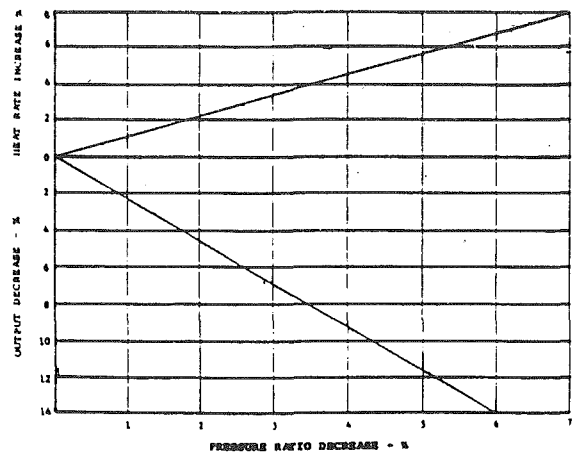

Fig. 2

Compressor Foreign Object Damage. Foreign object damage is caused by objects of sufficient size. Wire trash screens as a first component of the air filter system can stop large foreign objects like birds or stones.

Effect of Particulate (Dust) on Compressor Blade Erosion. Erosion of compressor blading is caused by airborne particulate above 5 to 10 μm (0.0004 in.). Erosion causes blunting of the leading edge, which changes the air angle of attack, and causes thinning of the blade trailing edge, which impairs the fatigue strength. Degradation of overall performance results.

Effect of Particulate (Dust) on Compressor Fouling. Ingestion of "adhesive" materials, such as oil vapor, smoke, sea salt, or industrial vapor, causes fouling of compressor blades. These contaminants are generally in the 0.1–0.5 μm range. Fouling reduces compressor efficiency, lowers compressor discharge pressure, and results in reduced output for a given turbine inlet/exhaust temperature with a corresponding reduction in efficiency, i.e., high heat rate. Figure 2 indicates the effect of the decrease in pressure ratio on output and heat rate.

Effect of Particulate (Dust) on Turbine Air Cooling Passage. Poor air quality can also affect the turbine section since the cooling flow is extraced from the compressor. Particles smaller than 5 μm may block internal cooling passages to blades, vanes, and rotor. The process is slow, and the damage may be detected during major overhauls. Blocking of air passages causes less air flow for cooling, thereby increasing thermal stress of the turbine section.

Locking of Turbine Blade Roots. Locking of turbine blade roots can be caused by accumulation of dust and corrosion residues in the clearance areas.

Effect of Particulate on Hot Section Corrosion. Inadequate air filtration is associated with the ingestion of certain metals, such as sodium, potassium, vanadium, and lead, which, after combining with sulfur and/or oxygen during the combustion process, deposit on the surface of parts along the hot gas path. These parts include combustion liners, transition pieces, nozzle partitions, and turbine buckets. The rate of hot corrosion is directly related to gas stream temperature, the level of trace elements (metals), and the temperature and surface pressure of the blade metal. The hot corrosion has posed a continuing problem to combustion turbine users since the advent of higher firing temperatures.

Selection of Type of Inlet Air Filtration System for Peaking Operation

This study assumes that the number of annual hours the combustion turbine will operate is limited (300 to 500 h/yr). The selection of the air filter system is based on the following factors [3]:

- Environment
- Media type
- Efficiency
- Initial cost
- Operating cost

ENVIRONMENT	FILTER TYPE
Moderately contaminated area; particulate concentration of 0.15 ppm by weight.	Three-stage with weatherhood and trash screen as first stage, prefilter as second stage, and high efficiency depth loading media type filter as third stage. (See Figure 4.)

Fig. 3

Media Type. Two types of media are available in the industry:

- Surface loading media
- Depth loading media

Surface Loading Media. The surface loading media depend upon large surface area and the dust cake built on that surface. The initial efficiency of this kind of filter is low until the dust cake is formed. For peaking units with short operation hours (300 to 500 h/yr), surface loading media will take several years to achieve good particle size efficiency (over 95 percent). Since the natural life of most filters is 4 to 6 years, this will make the filter ineffective for peaking operation. Self-cleaning filters use surface loading media and are ineffective since the filter needs to be changed due to its natural life before pulsation occurs. Filters of this type can be purchased precoated to improve initial efficiency; however, precoating will increase initial pressure drop and corresponding loss of output and increased heat rate.

Depth Loading Media. The depth loading media depend upon the particles occupying the spaces within the structure of the media. The initial efficiency of this type of filter is high (over 95 percent) and, therefore, is extremely suitable for peaking operation. However, depth loading media start leaching dirt to the clean side of the filter around 2 1/2 to 3 in. of pressure drop and, therefore, need to be replaced around that pressure drop. In the presence of water or high humidity conditions, leaching may occur at lower pressure drop if the media are not water resistant or not provided with an added nonpermeable layer. For peaking units with limited numbers of operating hours, the changeout time usually occurs after several years.

Environment. Environment may be classified as clean, dusty, or contaminated. Since the peaking units will operate a limited number of hours (300 to 500 h/yr), Figs. 3 and 4 show the recommended filtration system for a moderately contaminated area with a particulate concentration of 0.15 ppm by weight. The same filter system may be used in a highly contaminated area (>0.3 ppm), but the filters need to be replaced more frequently than in a moderately concentrated area. For a clean area (<0.1 ppm), a two-stage filter appears reasonable.

If the combustion turbine is to be operated in cold climates, a bypass door with heat tracing may be installed to bypass air during transient inlet icing conditions. However, if the icing condition occurs repeatedly, an anti-icing system may be installed to mitigate the problem. Usually a weather hood, which

Downloaded 02 Jun 2010 to 171.66.16.121. Redistribution subject to ASME license or copyright; see http://www.asme.org/terms/Terms_Use.cfm

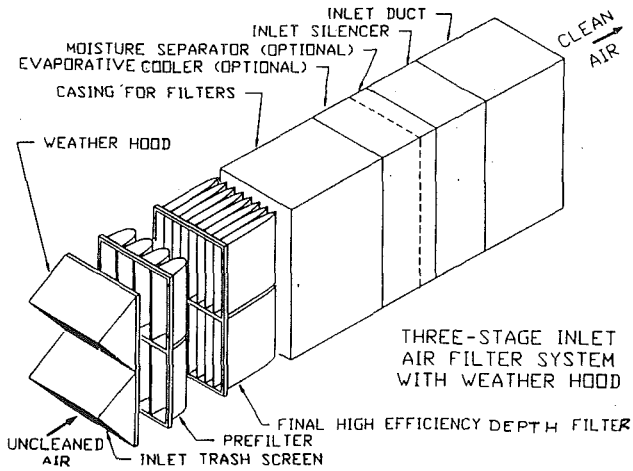

Fig. 4

DAMAGE	PARTICLE SIZE RANGE
Erosion	> 5 - 10 microns
Fouling	0.1 - 5 microns
Hot Corrosion	0.1 - 5 microns
Blocking of Cooling Holes	0.1 micron and over

Fig. 5

MICRON SIZE	PREFILTER EFFICIENCY	FINAL FILTER EFFICIENCY	COMBINED EFFICIENCY
.5 - 1.0	25%	95%	96%
1.0 - 2.0	40%	99%	99.5%
2.0 - 3.0	65%	99.9%	99.5%
3.0 - 4.0	80%	99.9%	99.9%
4.0 AND ABOVE	90 - 99%	99.9%	99.9%

Fig. 6

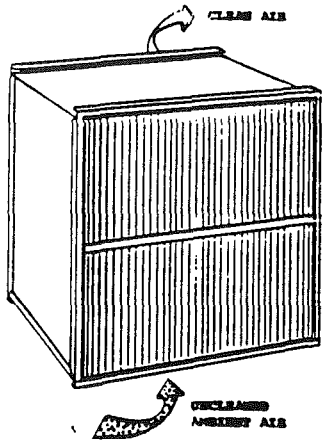

Fig. 7

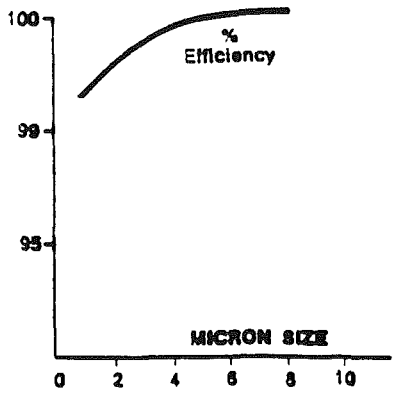

Fig. 8

reduces ingestion or precipitation with a heat traced bypass door, is effective in cold climates for peaking operation. Use of an evaporative cooler is site specific and is not discussed in this study.

Efficiency. Figure 5 shows the effect of particle size on the damage of the combustion turbine.

It is, therefore, necessary to install filters with high particle efficiency. In the industry, efficiency is defined as follows:

- ASHRAE atmospheric dust spot efficiency.
- ASHRAE arrestance or AC fine test dust mass efficiency.
- Particle size efficiencies.

ASHRAE atmospheric dust spot efficiency is defined as the ability of the device to remove dust from the test air. The method of determining this quantity is on a light transmission basis. It does not provide efficiency based on particle size [4].

ASHRAE arrestance or AC fine test duct mass efficiency (arrestance) does not provide efficiency based on particle size. The arrestance is calculated based on the weight of dust entering and the weight of dust leaving [4].

For safe operation of the combustion turbine, filter efficiency shall be based on particle size. Manufacturers of air filters have available technology to provide particle efficiency. Typical particle efficiency required for safe combustion turbine operation for peaking operation is shown in Fig. 6.

Periodic compressor water wash is required to clean off small particles deposited on the compressor. Figure 7 shows a typical high efficiency filter, and Fig. 8 shows typical filter efficiency versus particle size curve.

Cost Evaluation. The cost (capital and O&M) of an inlet air filtration system depends on the following:

- Total flow through the inlet.
- Type of filter system.
- Clean pressure drop.
- Dirty or final pressure drop.
- Dust-holding capacity of the filter.
- Filter efficiency.
- Installed cost.

A detailed present worth analysis was performed based on the following:

- Flow through the combustion turbine was considered to be 500,000 CFM.
- Total clean pressure drop through the three-stage filter was considered to be 1.25 in.
- Prefilter was changed at 1.5 in. of pressure drop.
- Final filter was changed at 2.5 in. of pressure drop.
- Annual operation was considered to be 300 hours.
- Installation cost was based on experience on actual installation.
- Average arrestance was considered.
- Life of the combustion turbine was considered to be 30 years.
- Output loss due to inlet air filter is considered to be 1.42 percent for 4 in. of water gage (w.g.) inlet pressure drop [5].
- Heat rate increase is considered to be 0.45 percent for 4 in. w.g. inlet pressure drop [5].

Downloaded 02 Jun 2010 to 171.66.16.121. Redistribution subject to ASME license or copyright; see http://www.asme.org/terms/Terms_Use.cfm

TYPE OF AIR FILTER SYSTEM	PRESENT WORTH OF CAPITAL COST INCLUDING INSTALLATION COST ($)	PRESENT WORTH OF PENALTY INCURRED DUE TO OUTPUT LOSS ($)	PRESENT WORTH OF HEATRATE PENALTY	PRESENT WORTH OF MAINTENANCE COST ($)	TOTAL PRESENT WORTH ($)	DIFFERENTIAL COST ($)
NO AIR FILTER	0.0	1,215,000	280,000	3,000,000	4,495,000	3,897,000
THREE-STAGE HIGH EFFICIENCY DEPTH LOADING TYPE FILTER	495,000	BASE	BASE	103,000	598,000	BASE
CARTRIDGE FILTER WITH SELF-CLEANING FEATURE	497,000	607,500	140,000	1,700,000	2,944,500	2,346,500
CARTRIDGE FILTER (SURFACE LOADING) WITHOUT SELF-CLEANING FEATURE	460,000	607,500	140,000	1,700,000	2,907,500	2,309,500

Fig. 9 Present worth of inlet air filter system in 1992 dollars based on 30 equal payments

- The positive impact of not having inlet filtration on power output and heat rate was considered.
- The natural life of the filter media was considered to be 5 years.
- Net output loss in a combustion turbine without air filter, due to compressor fouling and other degradation, was considered to be 0.5 percent the first year, with a subsequent increase of 0.5 percent every year for 10 years, at which point the compressor is rebladed [2].
- The net heat rate increase is considered to be 0.25 percent every year with a subsequent increase of 0.25 percent every year for 10 years, at which point the compressor is rebladed.
- The negating effect of compressor waterwash on compressor fouling was considered.
- Output loss and heat rate increase due to the use of low initial efficiency surface loading media (cartridge) is considered to be half that of the combustion turbine with no filter.
- The fuel considered is natural gas.
- Turbine and hot gas path maintenance is considered every 15 years for a combustion turbine without an air filter and every 20 years for a combustion turbine with a surface load type air filter.
- The present worth analysis is based on 30 equal payments.
- The interest rate is considered to be 10 percent and fixed charge rate is considered to be 13.67 percent.
- Figure 9 shows the total present worth of the inlet air filter system in 1992 dollars.

Conclusion

The following can be concluded based on the above discussions:

- An inlet air filter is required and is cost/benefit justified as shown in this paper for heavy-duty simple-cycle combustion turbine to protect it from damage caused by airborne particulates. It reduces the operating cost of the combustion turbine and protects the combustion turbine from loss of output and decrease of efficiency.
- Consideration should also be given to adding an inlet air filter system to existing heavy-duty combustion turbines operating without an air filter after overhaul to extend the next maintenance.
- For peaking operation typically between 300 to 500 h/yr in a moderately contaminated area with a contaminant concentration of 0.15 ppm by weight, a three-stage high-efficiency depth loading media type filter is favored, since the initial efficiency of this kind of filter is high and the life cycle cost of this filter system is cheaper than the other options.
- A surface loading type filter is not favored since the initial efficiency of this kind of filter is low and the life cycle cost of this filter is more than that of a three-stage high efficiency depth loading media type filter. It will take several years for surface loading type filters to become efficient for peaking units typically operating between 300 to 500 hours per year.
- The efficiency of filters should be based on particle efficiency and not mass efficiency or arrestance.

References

1 "Turbo Power and Marine Systems—Air Filtration for FT4C-3F Gas Turbines," Report No. TPM-769.

2 "Basic Gas Turbine Engine Technology," Home Study Course Published by the ASME International Gas Turbine Institute.

3 Mund, M. G., and Murphy, T. E., "The Gas Turbine-Air Cleaner Dilemma," ASME Paper No. 63-AHGT-63, 1963.

4 "Method of Testing Air-Cleaning Devices Used in General Ventilation for Removing Particulate Matter," ASHRAE Standard 52-76.

5 General Electric Model PG711EA Gas Turbine Estimated Performance, Fig. No. 499HA733.

Downloaded 02 Jun 2010 to 171.66.16.121. Redistribution subject to ASME license or copyright; see http://www.asme.org/terms/Terms_Use.cfm

Performance of Gas Turbine Compressor Cleaners

H. J. Kolkman
Materials Department,
National Aerospace Laboratory NLR,
1006 BM Amsterdam,
The Netherlands

Deposits are regularly removed from compressor blades and vanes of installed jet engines and gas turbines by compressor washing. A compressor cleaner is sprayed into the compressor while operating at reduced or normal rpm. Recently developed compressor cleaners are claimed to be ecologically sound. In addition, many new compressor cleaners contain a corrosion inhibitor. The cleaning efficiency of eight (old and new) compressor cleaners was determined by means of simulated compressor washing of compressor blades that had become fouled in service. For the situation simulated, the cleaning efficiency of new, ecologically sound cleaners turned out to be poor as compared with old compressor cleaners. The corrosion inhibition offered by those cleaners that contain a corrosion inhibitor was found to be satisfactory.

Introduction

Compressor Cleaning. During the operation of jet engines and gas turbines, dust, sand, organic matter, sea salt, etc. are deposited on compressor blades and vanes. The nature of such a deposit is exemplified in Fig. 1. Generally speaking the chemical composition of a compressor deposit will depend on the engine type, the operating conditions, and the environment (i.e., the intake air). However, basically the following constituents can be distinguished: (*a*) Water-insoluble compounds: These are mainly soil (represented by the silicon peak in Fig. 1) and especially organic compounds (represented by the carbon and oxygen peaks). (*b*) Water-soluble compounds: A detailed analysis is presented elsewhere [1]. A number of these compounds cause corrosion, since they are hygroscopic and/or contain chlorides (Fig. 1) that promote pitting corrosion.

One of the measures used to combat compressor corrosion [2] is to remove the water-soluble compounds by rinsing with distilled or tap water. This measure is, however, hindered by the fact that the water-soluble compounds are embedded in the water-insoluble compounds (which are not corrosive).

Moreover, all constituents of the deposits (including the water-insoluble compounds) adversely affect engine performance [3]. Therefore compressor *washing* is applied in addition to *rinsing*.

Compressor washing is carried out by spraying a compressor cleaner solution into an installed jet engine or gas turbine operating at reduced rpm (cranked or cold washing) or at normal rpm (hot or fired washing).

Recent Developments. Recently many new compressor cleaners have been developed because of the following reasons:

1 Safety and Environmental Issues. Cleaning with water/kerosene mixtures can result in compressor fires and surges if the kerosene separates from the water. Aromatic hydrocarbons containing compressor cleaners are now thought to be harmful to the health of people upon skin contact or inhalation. Soil pollution of airfields by compressor cleaners containing mineral oils and/or hydrocarbons is not permitted by the Water Authorities.

2 Corrosion Inhibition. A number of new compressor cleaners contain "corrosion inhibitors." These corrosion inhibitors are claimed to inhibit corrosion during a certain period. This is important for, e.g., jet engines that are frequently not reoperated immediately after compressor washing, so that a dryout run has to be applied in order to prevent corrosion of the wet compressor. This time-consuming dryout running after washing can be omitted as long as the engine is reoperated within the inhibition period.

The aim of the present work was to investigate the cleaning efficiencies and corrosion inhibition offered by a number of compressor cleaners, listed in Table 1.

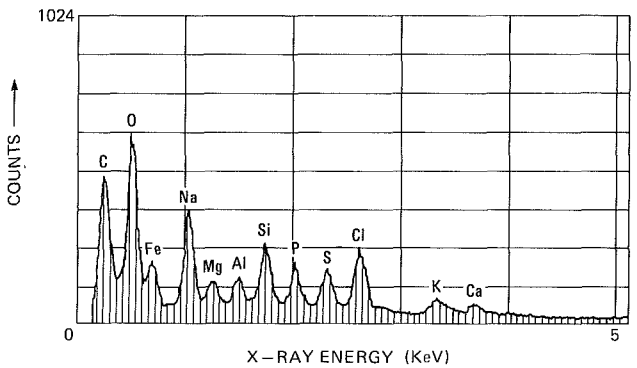

Fig. 1 EDX spectrum of deposits scraped off compressor blades of a fighter jet engine

Contributed by the International Gas Turbine Institute and presented at the 37th International Gas Turbine and Aeroengine Congress and Exposition, Cologne, Germany, June 1-4, 1992. Manuscript received by the International Gas Turbine Institute February 24, 1992. Paper No. 92-GT-360. Associate Technical Editor: L. S. Langston.

Copyright © 1993 by ASME
Downloaded 02 Jun 2010 to 171.66.16.121. Redistribution subject to ASME license or copyright; see http://www.asme.org/terms/Terms_Use.cfm

Table 1 Compressor cleaners tested

Cleaner *	Dilution Parts cleaner: Parts water	After-rinse required	Dry-out run required
B and B 3100	1:4	yes	yes
ARDROX 6322	1:4	yes	yes
BRULIN 512 M (≡ 715 N)	1:5	yes	yes
TURCO JET WASH K	1:4	no	no
JALEX ZOK 27	1:4	no	no
Kent L 9020 (≡ Turboclean)	1:4	no	yes
R-MC	ready foruse	no	yes
ARDROX 634	1:4	?	?
Demineralized water	not applicable	n.a.	n.a.

* The first three compressor cleaners are regarded as well-known "old" cleaners.
The last five cleaners are claimed to be new, ecologically sound compressor cleaners.

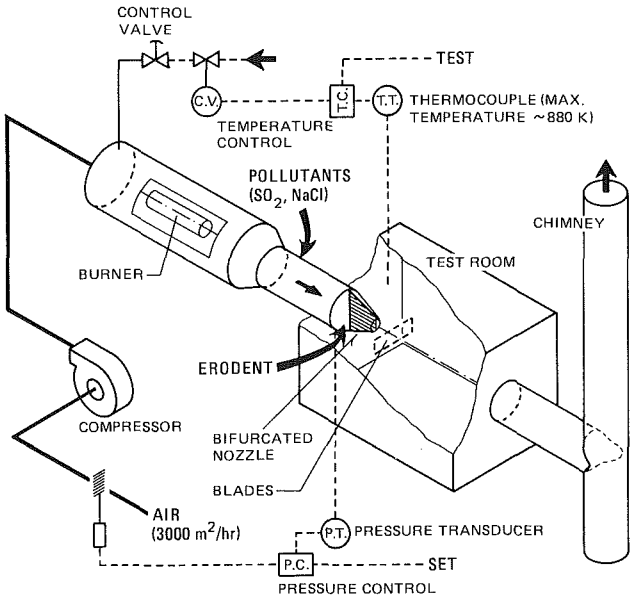

Fig. 2 The NLR compressor rig (schematic)

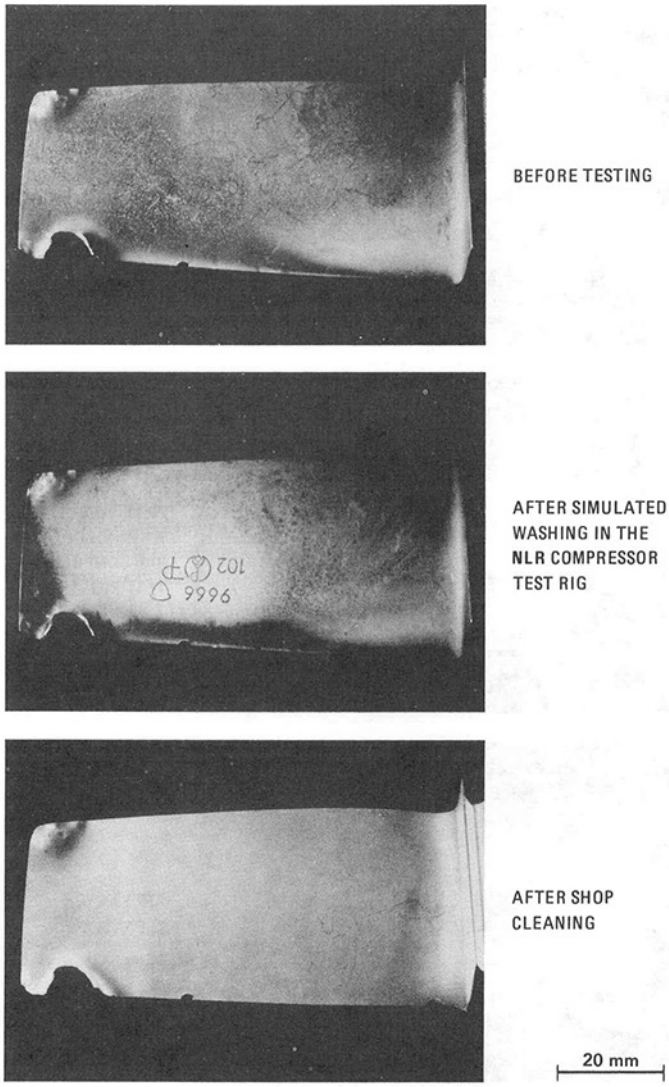

Fig. 3 The effect of washing with B and B 3100

Cleaning Efficiency

Test Method. These are standardized tests to determine the cleaning efficiency of a compressor cleaner [4, 5]. In these tests aluminum test coupons are artificially fouled with a carbon deposit. The cleaner solution is sprayed onto a rotating test coupon. The result is given as the weight percentage of the deposit removed by the cleaner. Disadvantages are that real components (e.g., with the correct surface roughness) and real deposits are not used.

Therefore it was decided to simulate reality as closely as possible by using the NLR compressor test rig to simulate the engine conditions during compressor washing and to use compressor blades that had been fouled in practice.

The NLR compressor test rig (Fig. 2) is especially used to test compressor components under simulated corrosive and/or erosive service conditions [1, 2, 6]. Air is compressed in a centrifugal compressor and is heated with natural gas. Nozzles are provided to inject pollutants and erodent. For the present application no pollutants or erodent were injected. Instead the cleaner solution was sprayed through the nozzle that is normally used to inject salt water as pollutant.

The test specimens were fourth-stage compressor blades of a fighter jet engine that had been rejected because of FOD, etc. These blades are made of a titanium alloy and are uncoated. There is a washing procedure for cranked washing. Since the compressor under consideration is very corrosion resistant this procedure is not applied normally. Hence the blades were severely fouled. Six blades were used per cleaner. The air velocity, air temperature, washing time, etc., were adjusted to correspond to realistic conditions.

The blades were weighed and photographed before testing. After washing in the NLR compressor test rig the blades were soaked in distilled water to remove remnants of the cleaner, dried, weighed, and photographed. In order to determine the quantity of the remaining deposits, the blades were subjected to shop cleaning, weighed, and photographed.

Results. By comparison of the macrographs made before and after simulated washing (e.g., the upper and center macrographs in Figs. 3 and 4) it was found that all cleaners removed the deposits partly but not completely. The remnant deposits could not be removed by doubling the air velocity or the washing time. The "old" cleaners removed more deposits than the new, ecologically sound cleaners. This can be seen by comparing the data inscribed in the airfoils, which are clearly

Downloaded 02 Jun 2010 to 171.66.16.121. Redistribution subject to ASME license or copyright; see http://www.asme.org/terms/Terms_Use.cfm

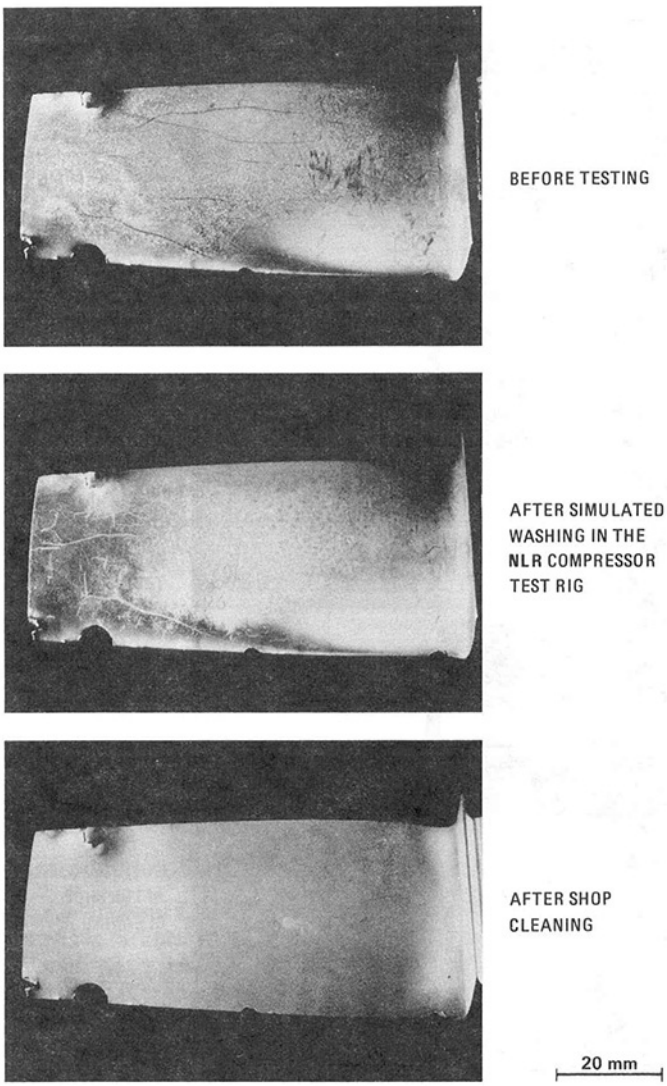

Fig. 4 The effect of washing with Jalex Zok 27

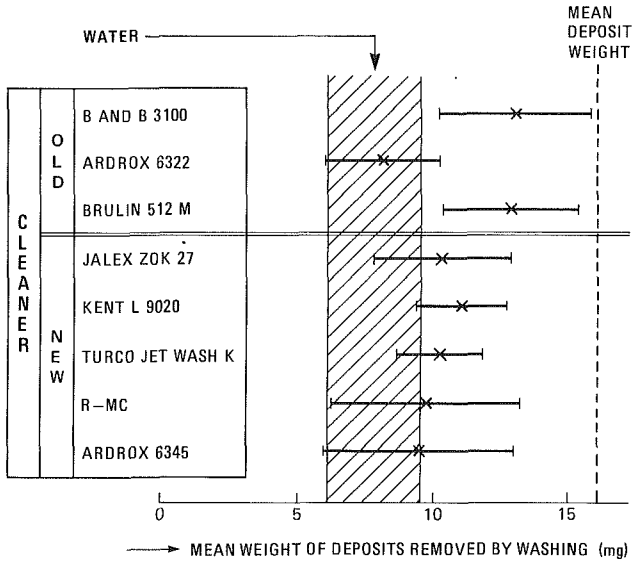

Fig. 5 Mean weight of deposits removed by simulated washing in the NLR compressor test rig

visible after washing with an old cleaner (center macrograph in Fig. 3) and barely visible after washing with a new cleaner (center macrograph in Fig. 4).

Shop cleaning removed all remaining deposits and did even more than that. As seen in the lower macrographs in Figs. 3 and 4, the aforementioned inscribed data were removed by shop cleaning. Therefore the question arose whether shop cleaning attacked the base metal. This turned out to be the case. A second shop cleaning (of the already clean blades) resulted in a weight loss of 12.1 ± 1.5 mg (which is very small as compared with the mean blade weight of 44.2 g).

A graphic presentation of the deposit weight losses by simulated washing in the NLR compressor test rig is given in Fig. 5. For each cleaner the mean and standard deviation of six measurements are plotted. The scatter band for "washing" with demineralized water is indicated by the dashed area. Washing with water removed the deposits partly, apparently because of physical action or because the water-soluble part of the deposits was concerned. All cleaners were diluted with water (see Table 1). Thus if a cleaner itself has any effect, its diluted solution in water should perform better than water. Thus the more the data for a particular cleaner are located to the right-hand side of the water scatter band, the better its performance.

The results of the weight measurements (presented in Fig. 5) agree with the results of the macroscopic observations (exemplified in Figs. 3 and 4):

- None of the cleaners was able to remove all deposits from the severely fouled blades.
- The best-performing cleaners were "old" cleaners
- Most of the ecologically sound new cleaners performed only slightly better than water. Hence ecologically sound compressor washing may require more frequent washing.

Corrosion Inhibition

Test Specimens. The titanium alloy compressor blades used to investigate the cleaning efficiency are very resistant to atmospheric corrosion and hence were not suitable for investigating the corrosion inhibition offered by some cleaners. Instead 60 × 30 × 2 mm^3 410 and 17-4 PH steel test coupons were used. The 17-4 PH coupons were used to investigate the corrosion inhibition offered by Jalex Zok 27, Kent L 9020, and Turco Jet Wash K (= Turboclean). The 410 steel test coupons were used only to test Jalex Zok 27.

Test Method. To simulate atmospheric corrosion in a polluted and humid environment during shut-down periods, the test coupons were stored in a climate room for 28 days under the following conditions: RH (relative humidity) = 94–95 percent; temperature = 20.0 ± 0.5°C; SO_2 concentration = 3.0 ± 0.5 ppm.

To simulate washing, the test coupons were periodically soaked. Different soaking media and soaking frequencies were used, as will be explained in the next subsection.

Test Results. The (originally clean and dry) test coupons that were stored in the climate room without any soaking simulated the atmospheric exposure of compressor components after washing with a cleaner without inhibitor, and the rinsing and drying. These coupons are indicated by a cross on the vertical scale in Fig. 6; it is seen from Fig. 6(*b*) that 410 steel is prone to atmospheric corrosion, whereas Fig. 6(*a*) shows that 17-4 PH steel is not.

This situation changes if one simulates omission of rinsing and dryout running. Upon washing, the salt deposits on the blades and vanes dissolve in the wash water. If no rinsing and dryout running are applied, a dilute salt solution will be left behind on the blades and vanes. From practice it is known that the wash water left behind can contain about 200 ppm

Downloaded 02 Jun 2010 to 171.66.16.121. Redistribution subject to ASME license or copyright; see http://www.asme.org/terms/Terms_Use.cfm

	SOAKING IN:	SIMULATES:
×	NOT SOAKED	WASHING WITH RINSING AND DRYING
●—●	200 PPM NaCl	WASHING WITHOUT RINSING AND DRYING
○ ○	200 PPM NaCl +CLEANER	WASHING WITH CLEANER WITHOUT RINSING AND DRYING
□ □	CLEANER	IDEM, LESS SEVERE CIRCUMSTANCES

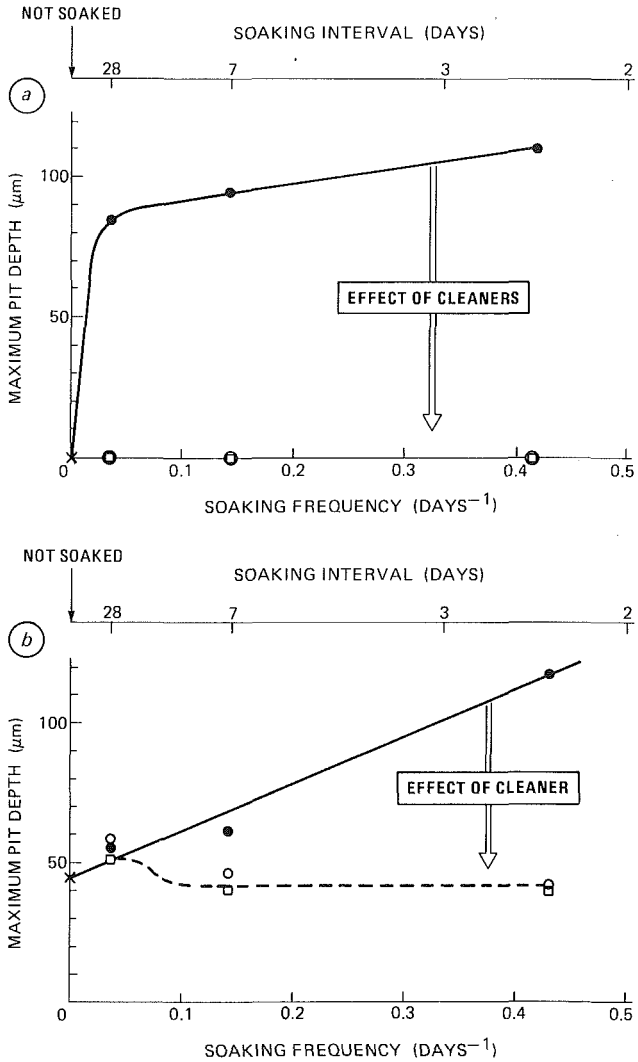

Fig. 6 Effect of soaking frequency and soaking medium on maximum pit depth for (*a*) 17-4 PH coupons; (*b*) 410 coupons

sodium chloride [1]. Thus, to simulate the omission of rinsing and dryout running, coupons were periodically soaked in a 200 ppm sodium chloride solution. Although this solution is very diluted, it had a strong influence on the atmospheric corrosion, as indicated by full circles in Fig. 6: The 17-4 PH coupons—which were completely resistant to atmospheric corrosion in the absence of salt—exhibited pitting corrosion in the presence of salt (Fig. 6*a*). For 410 steel the pit depth increased with increasing soaking (washing) frequency if a salt solution was left behind after washing (Fig. 6*b*). This shows the benefit of rinsing and dryout running—which removes the salt solution—after washing.

The question arises whether the same benefit can be gained with a cleaner with an inhibitor. In other words: Can the rinsing and dryout running be omitted if the water left behind on the blades and vanes after washing contains a corrosion inhibitor (originating from the cleaner) in addition to salt? In order to investigate this, coupons were soaked in a cleaner solution with 200 ppm salt. The results are indicated by the open circles in Fig. 6. Indeed it is seen that the inhibitor in the cleaners neutralized the influence of the salt. For 17-4 PH coupons the pitting corrosion was completely eliminated by the (inhibitor in the) cleaners (Fig. 6*a*). This holds for all three cleaners investigated, i.e., Jalex Zok 27, Kent L 9020, and Turco Jet Wash K. For the 410 coupons only the first cleaner was investigated. In this case it was found (Fig. 6*b*) that pitting was not completely eliminated by the presence of the inhibitor, but was reduced to the level that is representative for washing with rinsing and dryout running.

Thus for all cases (material and cleaner combinations) investigated it had to be concluded that the presence of an inhibitor in the cleaner enabled omission of the time-consuming rinsing and dryout run after compressor washing.

Conclusions

1 For the situation simulated, the cleaning efficiency of new, ecologically sound cleaners turned out to be poor as compared with old compressor cleaners. However, one might legitimately argue that the intention in practice is to keep an initially clean engine from becoming fouled in service. In such cases the new cleaners may perform better if frequently applied.

2 The corrosion inhibition offered by those cleaners that contain a corrosion inhibitor was found to be satisfactory.

Acknowledgments

This work was supported by the Royal Netherlands Air Force and the Royal Netherlands Navy.

References

1 Kolkman, H. J., "Coatings for Gas Turbine Compressors," in: *Materials Development in Turbo-Machinery Design*, D. M. R. Taplin, J. F. Knott, and M. H. Lewis, eds., The Institute of Metals, London, Book 456, 1989, pp. 224–230.

2 Kolkman, H. J., and Mom, A. J. A., "Corrosion and Corrosion Control in Gas Turbines, Part I: The Compressor Section," ASME Paper No. 84-GT-255, 1984.

3 Becker, B., and Bohn, D., "Operating Experience With Compressors of Large Heavy-Duty Gas Turbines," ASME Paper No. 84-GT-133, 1984.

4 "Cleaning Fluid for Compressors of Gas Turbine Engines," sixth draft, specification TS 10268A, The Director of Quality Assurance/Materials Centre E135/1, Royal Arsenal East, London, July 3, 1984.

5 "Cleaning Efficiency of Turbine Gas Path Cleaners," SAE ARP 1862, Society of Automotive Engineers, 1986.

6 Kolkman, H. J., "New Erosion Resistant Compressor Coatings," ASME Paper No. 88-GT-186, 1988.

Downloaded 02 Jun 2010 to 171.66.16.121. Redistribution subject to ASME license or copyright; see http://www.asme.org/terms/Terms_Use.cfm